Assessing the optical properties of chalcogenide glasses and fibres: towards the development of new light sources.



Yuanrong Fang, MSc

Supervisors:

Prof. Trevor Benson and Prof. Angela B Seddon

Thesis submitted to the University of Nottingham for the degree of Doctor of Philosophy

March 2019

Abstract

Owing to their properties of mid-infrared (MIR) transparency, high refractive index, low phonon energy, high optical non-linearity, and an ability to dope them with rare-earth element ions, chalcogenide glasses are a promising candidate for planar photonic integrated circuits, and narrow- and broad-band fibre-based laser sources and amplifiers for the MIR. Although much research effort has been paid to the development and characterisation of chalcogenide glasses for photonics, relatively little refractive index dispersion data are presently available at MIR wavelengths. Therefore, the aim of this Project is to assess the optical properties, especially refractive index, material dispersion and thermo-optic coefficient, of the chalcogenide glasses and fibres ($As_{40}Se_{60}$, $Ge_{16}As_{24}Se_{15.5}Te_{44.5}$, $Ge_{20}Sb_{10}Se_{70}$ and $Ge_{20}Sb_{10}Se_{67}S_3$ at. % (atomic %)) fabricated for developing MIR light source and fibre-sensing.

As a well-know technique to determine the refractive index with a high accuracy, the minimum deviation method is applied to determine the refractive index of the chalcogenide glasses investigated in this Project. The errors in each part of the minimum deviation measurement using our experimental setup are analysed using a commercial LAF850322 right-angled prism. The refractive indices of different chalcogenide glass prisms are then successfully measured at wavelengths of ~1500 nm, 3100 nm, 3800 nm and 6450 nm with a standard deviation of less than 0.001 refractive index unit (RIU)) using different light sources. The results obtained are taken as the benchmark values for the techniques developed later.

After analysing in the literature the refractive index change with changing composition of Ge-As-Se-Te, an interpolation modelling scheme for estimating the refractive index of $Ge_xAs_{z-x}Se_{100-z-y}Te_y$ within the range of $10 \leq x \leq 25$, $40 \leq y \leq 50$ and $30 \leq z \leq 40$ is set up with an error of less than 0.22 %.

To investigate a suitable refractive index model to describe the refractive index dispersion of chalcogenide glasses in the MIR region, several refractive index models (the Cauchy and Sellmeier models) are applied to fit the refractive index data points of the $Ge_{16}As_{24}Se_{15.5}Te_{44.5}$ at. %, $As_{40}Se_{60}$ at. %, $Ge_{10}As_{23.4}Se_{66.6}$ at. %, $Ge_{16.5}As_{16}Ga_{3}Se_{64.5}$ at. % and Pr^{3+} doped $Ge_{16}As_{21}Ga_{1}Se_{62}$ at. % glasses made in-house, obtained using spectroscopic ellipsometry at MIR wavelengths. A two-term Sellmeier model, with one resonant optical bandgap electronic absorption and one resonant MIR fundamental vibrational absorption, is verified to be unique and sufficient to describe the refractive index dispersion of the chalcogenide glasses within their transparent windows. The numerical aperture of a step-index fibre based on an $As_{40}Se_{60}$ at. % core and $Ge_{10}As_{23.4}Se_{66.6}$ at. % cladding and a step-index fibre based on the $Ge_{16}As_{24}Se_{15.5}Te_{44.5}$ at. % and $Ge_{10}As_{23.4}Se_{66.6}$ at. % glass pair is respectively calculated to be larger than 0.97 and 1.86 over the wavelength range from 0.5 to 30 μm. The two-term Sellmeier fits to the measured refractive index data are also used to calculate material dispersion characteristics for these compositions.

The well-known method presented by Swanepoel can be used to determine the refractive index dispersion of thin films over the wavelength range from 0.7 to 2 μm from wavelength values at maxima and minima, only, of the transmission interference fringes. In order to extend this method into the MIR spectral region (measurements described are over the wavelength range from 2 to 25 μm), the method is improved by using a two-term Sellmeier model instead of the Cauchy model as the dispersive equation. The refractive index dispersion of hot-pressed chalcogenide thin films is determined by the improved method with a standard deviation of less than 0.002. The accuracy of the method is shown to be within 0.4% with of a benchmark refractive index value obtained from prism measurements at a wavelength of 3.1 μm. The refractive indices of other compositions investigated in this Project were also determined using this method.

A simple technique is proposed to determine the small refractive index contrast of a low numerical aperture (NA) glass pair. A core fibre ($Ge_{20}Sb_{10}Se_{70}$ at. %) is hot-pressed together with a cladding fibre ($Ge_{20}Sb_{10}Se_{67}S_3$ at. %) to form a two-composition thin film with the advantages of the two glasses having the same thermal history and post-fibre processing. The refractive index contrast can be simply determined with an error of less than ±0.002 only using their FTIR (Fourier transform infrared) transmission spectra. Moreover, a 3 at. % substitution of S for Se in the Ge-Sb-Se glass system is shown to blue-shift the visible (VIS) optical bandgap, the MIR fundamental vibrational absorption bands, the zero dispersion wavelength and lower the refractive index.

In this Project, the effect of temperature on the optical properties of chalcogenide glasses, including their transparent windows, impurity and multiphonon absorptions, refractive index, zero dispersion wavelengths and thermo-optic coefficients of the chalcogenide glasses is investigated. In order to obtain the continuous thermo-optic coefficient of a chalcogenide glass at MIR wavelengths, the FTIR continuous *dn/dT* method is proposed based on the FTIR transmission spectra at upper and lower temperatures. It is shown that this method can successfully determine the thermo-optic coefficients of the chalcogenide glass thin films ($Ge_{16}As_{24}Se_{15.5}Te_{44.5}$ at. % and $As_{40}Se_{60}$ at. %) over the wavelength range from 2 to 20 μm with an error of less than ±7.5 ppm (parts per million) /℃. The proposed method is shown to provide a much lower error than the minimum deviation method and the improved Swanepoel method.

In summary, some techniques are successfully developed to obtain the refractive index, material dispersion data and thermo-optic coefficients for bulk chalcogenide glasses and chalcogenide glass thin films in the MIR region in this Project. These data are useful for the design of step-index fibres for new MIR light sources and fibre-sensing.

Publications

Fang, Y., Jayasuriya, D., Furniss, D., Tang, Z.Q., Markos, C., Sujecki, S., Seddon, A.B. and Benson, T.M., 2016, July. Characterising refractive index dispersion in chalcogenide glasses. In *Transparent Optical Networks (ICTON), 2016 18th International Conference on* (pp. 1-5). IEEE.

Sojka, L., Tang, Z., Furniss, D., Sakr, H., Fang, Y., Beres-Pawlik, E., Benson, T.M., Seddon, A.B. and Sujecki, S., 2017. Mid-infrared emission in Tb^{3+}-doped selenide glass fiber. *Journal of the Optical Society of America B Optical Physics*, *34*(27), p.A70.

Fang, Y., Jayasuriya, D., Furniss, D., Tang, Z.Q., Markos, C., Sujecki, S., Seddon, A.B. and Benson, T.M., 2017. Determining the refractive index dispersion and thickness of hot-pressed chalcogenide thin films from an improved Swanepoel method. *Optical and Quantum Electronics*, *49*(7), p.237.

Fang, Y., Jayasuriya, D., Furniss, D., Tang, Z.Q., Seddon, A.B. and Benson, T.M., 2019. Determining small refractive index contrast in chalcogenide glass pairs at mid-infrared wavelengths. *Manuscript accepted by Optical Material Express for publication.*

Publications *in press* and *in preparation*

Fang, Y., Jayasuriya, D., Furniss, D., Tang, Seddon, A.B. and Benson, T.M., 2019. Determining the continuous thermo-optic coefficients of chalcogenide glass thin films in the MIR region using FTIR transmission spectra. *Submitted for publication.*

Fang, Y., D., Furniss, Jayasuriya, D., Parnell, H., Seddon, A.B. and Benson, T.M., 2019. Methods for determing the refractive index of chalcogenide glasses at MIR wavelengths. *To be submitted.*

Acknowledgements

I would like to express my sincere gratitude to my supervisors, Prof. Trevor Benson and Prof. Angela Seddon for their continuous support of my PhD study. It is my honour to be a PhD student under their supervision. Their patience, inspiration, guidance and knowledge helped me in all the time of research and writing of this thesis. I really appreciate what they have taught me in these three years.

I would also like to thank Dr. David Furniss, who gave me lots of useful suggestions and help during the experiments. He is one of the most knowledgeable, creative and humble scientists I have met. Another person I would like to thank is Dr. Zhuoqi Tang, who always let me know how to be a better scientist.

I would like to thank Dr. Dinuka Jaysuriya and Dr. Harriet Parnell for providing me the high-quality chalcogenide glasses used in this work and useful knowledge of glass science. I am also very grateful to Mr. Wojciech Rozwadowski for helping with the design of a temperature-controlled sample holder.

The last but no means least, thanks go to mum, dad and my wife for their love, understanding and unbelievable support in these three years. They are the most important people in my life. Thank you!

Glossary of symbols and abbreviations

Elements			
As	Arsenic	**In**	Indium
Ce	Cerium	**O**	Oxygen
Ga	Gallium	**Pr**	Praseodymium
Ge	Germanium	**S**	Sulfur
H	Hydrogen	**Sb**	Antimony
HF	Hydrofluoric acid	**Se**	Selenium

Techniques, properties and miscellaneous	
at. %	Atomic %
AOS	All-optical switching
BB	Broadband
CONM	Chemically ordered network model
CVD	Chemical vapor deposition
dn/dT	Thermo-optic coefficient
DTGS	Deuterated triglycine sulfate
EXAFS	Extended X-ray absorption fine structure
E_g	Optical bandgap
Et al.	Et alia (and others)
FIR	Far-infrared
FTIR	Fourier transform infrared
Glo	Globar
ICL	Interband cascade laser
IR	Infrared
KBr	Potassium bromine
MCN	Mean coordination number
MCT	Mercury cadmium telluride
MDM	Minimum deviation method
MIR	Mid-infrared
NA	Numerical aperture
NIR	Near-infrared
NRL	Naval Research Laboratory
p	Vapour pressure
PBS	Phosphate buffer solution

Abbreviations/ miscellaneous (cont.)	
PDS	Photothermal deflection spectroscopy
PLD	Pulsed laser deposition
ppm	Parts per million
QCL	Quantum cascade laser
RAM	Regional approach method
RBS	Rutherford backscattering spectroscopy
Ref.	Reference
RF	Radio frequency
RIU	Refractive index unit
SC	Spin-coating
SCG	Supercontinuum generation
s.d.	Standard deviatoin
SE	Spectroscopy ellipsometry
SIF	Step index fibre
SM	Single mode
$\mathbf{T_c}$	Crystallisation temperature
$\mathbf{T_f}$	Fictive temperature
$\mathbf{T_g}$	Glass transition temperature
$\mathbf{T_m}$	Melting temperature
TE	Thermal evaporation
TEC	Thermal expansion coefficient
TMA	Thermal mechanical analysis
TPC	Thermal polarisability coefficient
UV	Ultra-violet
VIS	Visible
WAT	Weak absorption tail
wt. %	Weight %
XPS	X-ray photoelectron spectroscopy
ZDW	Zero dispersion wavelength
5N/6N	99.999 %/ 99.9999 % purity
ΔT	Temperature variation
α	Apex angle
λ	Wavelength
nm	Nanometer
μm	Micrometre

Abbreviations/ miscellaneous (cont.)	
mm	Milimeter
θ	Angle
$\underline{\boldsymbol{n}}$	Complex refractive index
$\boldsymbol{n}$	Refractive index
$\boldsymbol{n_2}$	Nonlinear refractive index coefficient
$\boldsymbol{\kappa}$	Extinction coefficient
$\underline{\boldsymbol{\varepsilon_r}}$	Complex relative permittivity
$\boldsymbol{\varepsilon_r}$	Real part of complex relative permittivity
$\widetilde{\boldsymbol{\varepsilon_r}}$	Imaginary part of complex relative permittivity

Table of contents

Chapter 1: Introduction 1

1.1 Aims and objectives of the Project 3

1.2 Structure of thesis 3

References 5

Chapter 2: Background and literature review 8

2.1 Glass science fundamentals 8

2.2 Optical fibres 11

2.3 Chalcogenide glasses 12

2.3.1 Chalcogenide glass 12

2.3.2 Structure of chalcogenide glasses 14

2.3.3 Optical properties of chalcogenide bulk glasses and comparison with thin films 22

2.4 Applications of chalcogenide glasses 40

2.4.1 Active applications 41

2.4.2 Passive applications 42

2.5 Methods for determination of the optical properties of chalcogenide glasses… 45

2.5.1 Minimum deviation method 45

2.5.2 Prism coupler 47

2.5.3 Spectroscopic ellipsometry 49

2.5.4 Envelope method 54

2.4.5 Determine the optical constants of a thin film only from the values of wavelength at each extreme of the transmission spectrum. 58

2.5.6 Digital refractometry 59

2.6 Section summary 61
References 61
Chapter 3: Experimental techniques 80
3.1 List of chemical used 80
3.2 Hot pressing codes 82
3.3 Glass melting 86
3.3.1 Silica ampoule preparation 86
3.3.2 Glass melting of different compositions 87
3.4 Prism preparation 90
3.5 Hot pressing 95
3.5.1 Hot pressing technique 95
3.5.2 Chalcogenide glass thin film preparation 97
3.5.3 Ellipsometry sample preparation 100
3.6 Fourier transform infrared (FTIR) spectroscopy 101
3.6.1 Basic theory 101
3.6.2 Bulk-glass sample preparation for FTIR measurements 102
3.6.3 Method for bulk glass characterisation 103
3.6.4 Measuring the transmission spectra of an interband cascade laser (ICL) and SuperK supercontinuum source using FTIR spectroscopy 103
3.6.5 Thin-film FTIR measurements using FTIR spectroscopy 107
3.7 Thermal mechanical analysis (TMA) 117
3.7.1 Viscosity-temperature characterisation of bulk glasses 118
3.7.2 Thermal expansion coefficient (TEC) 119

3.8 Thermal performance of a new thermal prism/thin-film holder to be used for thermo-optic coefficient measurements 121

3.8.1 Thermal performance of heating chalcogenide prisms 121

3.8.2 Thermal performance of the temperature-controlled holder for heating and cooling chalcogenide thin films 127

3.9 Chapter summary 130

References 131

Chapter 4: Measuring the refractive index of chalcogenide glasses using the minimum deviation method 133

4.1 Basic theory of the minimum deviation method. 133

4.2 Experimental setup and operations. 135

4.3 Analysis the errors of the minimum deviation measurements in our laboratory using a commercial LAF 850322 right-angled prism 137

4.3.1. The LAF 850322-silica-glass prism 137

4.3.2. The results of the refractive index of LAF 850322 prism 139

4.3.3. Errors in the minimum deviation measurement using the LAF 850322 prism…. 143

4.3.4 Section summary 152

4.4 Measuring the refractive indices of chalcogenide glasses using the minimum deviation method 153

4.4.1 The refractive indices of $Ge_{7.5}As_{25.5}S_{67}$, $As_{40}Se_{60}$, $Ge_{16}As_{24}Se_{15.5}Te_{46}$ at. % and $Ge_{20}Sb_{10}Se_{70}$ at. % at different wavelengths. 153

4.4.2 The refractive indices of other chalcogenide glasses at wavelengths of 3.1 μm, 3.8 μm and 6.45 μm. 161

4.4.3 Repeatability of the minimum deviation measurements using the 3100 nm ICL source 163

4.4.4 Section summary.....165

4.5 Extrapolating the refractive index data of the $Ge_xAs_{z-x}Se_{100-z-y}Te_y$ at. % glass system.....166

4.6 Chapter summary 169

References 171

Chapter 5: Refractive index models for chalcogenide glasses..... 172

5.1 Refractive index models.....173

5.1.1 Complex refractive index and permittivity 173

5.1.2 Cauchy model.....174

5.1.3 Sellmeier model 175

5.2 Refractive index dispersion measurements on chalcogenide glasses by means of spectroscopic ellipsometry.....176

5.3 Optically transparent window.....179

5.4 Fits to the ellipsometry data 179

5.4.1 Fits to the ellipsometry data (real part of the refractive index) over the wavelength range from the lower wavelength edge of the transparent window to 2.5 μm… 180

5.4.2 Fits to the ellipsometry data (real part of the refractive index) over the whole transparent window 187

5.5 Physical interpretation of parameters of the two-term Sellmeier model...196

5.6 Step-index fibre and numerical aperture 199

5.7 Material dispersion 200

5.8 Chapter summary 202

References 204

Chapter 6: Swanepoel's method to determine the refractive index of chalcogenide glasses…… 207

6.1 Reproducing the original Swanepoel method 208

6.1.1 The basic theory of the original Swanepoel method.....209

6.1.2 Reproducing the results given in Swanepoel's paper using Matlab. .215

6.2 Determining the refractive index of $Ge_{16}As_{24}Se_{15.5}Te_{44.5}$ at. % and $As_{40}Se_{60}$ at. % thin films using the original Swanepoel method.....221

6.2.1 Determining the order numbers at each extreme for the $Ge_{16}As_{24}Se_{15.5}Te_{44.5}$ at. % and $As_{40}Se_{60}$ at. % thin films. 224

6.2.2 Determining n from the order number m for the $Ge_{16}As_{24}Se_{15.5}Te_{44.5}$ at. % and $As_{40}Se_{60}$ at. % thin films. 226

6.2.3 Determining *n* from the dispersion equation for the $Ge_{16}As_{24}Se_{15.5}Te_{44.5}$ at. % and $As_{40}Se_{60}$ at. % thin films. 230

6.2.4 Determining *n* from the transmittance of the interference spectrum for the $Ge_{16}As_{24}Se_{15.5}Te_{44.5}$ at. % and $As_{40}Se_{60}$ at. % thin films. 232

6.2.5 Determining the final thickness and refractive index of the $Ge_{16}As_{24}Se_{15.5}Te_{44.5}$ at. % and $As_{40}Se_{60}$ at. % thin films.....235

6.3 Modifying the Swanepoel method by using three-term Cauchy, one-term Sellmeier and two-term Sellmeier models. 238

6.3.1 The basic theory of the modified Swanepoel method by using the three-term Cauchy, one-term Sellmeier and two-term Sellmeier models 239

6.3.2 Determining the refractive index of $As_{40}Se_{60}$ at. % thin film over the wavelength range from 0.7 to 2 μm using the modified Swanepoel methods..245

6.3.3 Determining the refractive index of $Ge_{16}As_{24}Se_{15.5}Te_{44.5}$ at. % and $As_{40}Se_{60}$ at. % thin film in mid-infrared (MIR) region using the improved Swanepoel method. 263

6.4 Refractive indices and material dispersions of Ge-As-Se-Te glasses. 282

6.4.1 Refractive indices of the Ge-As-Se-Te thin films.....283

6.4.2 The numerical apertures of the ultra-high NA and low-NA fibres. ...285

6.4.3 Material dispersions of Ge-As-Se-Te glasses 286

6.5 The refractive index of other chalcogenide glasses.....288

6.6 Effect of fast quenching. 290

6.7 Determining small refractive index contrast in chalcogenide glass pairs at mid-infrared wavelengths.....292

6.7.1 Ge-Sb-Se/S glasses: molecular structure 292

6.7.2 Analysis of observed MIR vibrational absorption bands.....293

6.7.3 Simple approach for determining which material has the larger refractive index in the two-composition (Ge-Sb-Se and Ge-Sb-Se-S) thin film 295

6.7.4 Determining the refractive indices of Ge-Sb-Se and Ge-Sb-Se-S glasses in the two-composition thin film. 298

6.7.5 Numerical aperture and dispersion. 304

6.7.6 Section summary.....306

6.7 Chapter summary. 307

References 310

Chapter 7: The effect of temperature on the optical properties of chalcogenide glasses…… 313

7.1 Thermal-FTIR analysis for chalcogenide glasses.....314

7.1.1 Thermal-FTIR analysis for $Ge_{16}As_{24}Se_{15.5}Te_{44.5}$ at. % bulk glass 315

7.1.2 Thermal-FTIR analysis for $Ge_{20}Sb_{10}Se_{70}$ at. % and $Ge_{20}Sb_{10}Se_{67}S_3$ at. % bulk glasses 318

7.1.3 Analysis of multiphonon combination bands in $As_{40}S_{60}$ at. % 322

7.2 Thermo-optic coefficients of chalcogenide glasses using the minimum deviation method. 324

7.2.1 Thermo-optic coefficient (dn/dT) and thermal polarisability coefficient of a chalcogenide glass 325

7.2.2 Thermo-optic and thermal polarizability coefficients of $As_{40}Se_{60}$ at. % and $Ge_{16}As_{24}Se_{15.5}Te_{44.5}$ at. % obtained from prism measurements. 328

7.2.3 Thermo-optic and thermal polarisability coefficients obtained from the $Ge_{20}Sb_{10}Se_{70}$ at. % and $Ge_{20}Sb_{10}Se_{67}S_3$ at. % prism measurements. 338

7.3 A FTIR continuous dn/dT method to determine the thermo-optic coefficient of chalcogenide glasses. 344

7.3.1 Basic theory.....344

7.3.2 Determining thermo-optic coefficients of chalcogenide glasses ($As_{40}Se_{60}$ at. % and $Ge_{16}As_{24}Se_{15.5}Te_{44.5}$ at. %) using the FTIR continuous dn/dT method… 346

7.3.3 Assessing the thermal properties of Ge-As-Se-Te thin films with different compositions using the novel method.....363

7.4 Chapter summary 370

References 373

Chapter 8: Conclusions and suggestions for future work 376

8.1 Conclusions 376

8.1.1 Measuring the refractive index of chalcogenide glasses using the minimum deviation method (chapter 4) 376

8.1.2 Refractive index models for chalcogenide glasses in near-infrared (NIR) and mid-infrared (MIR) regions (chapter 5) 380

8.1.3 Swanepoel's method to determine the refractive index of chalcogenide glasses (chapter 6).....384

8.1.4 The effects of temperature on the optical properties of chalcogenide glasses (chapter 7).....388

8.2 Future work 393

8.2.1 Prism minimum deviation measurements.....394

8.2.2 Spectroscopic ellipsometry.....395

8.2.3 Improved Swanepoel method 395

References 396

Appendix A - 1 -

Appendix B - 7 -

Chapter 1: Introduction

The mid infrared (MIR) spectral region, referred to as the spectral region from 3 to 50 μm [1.1], is a domain of interest to many areas of science and technology since it covers the important atmospheric windows (3-5 μm and 8-12 μm) [1.2], and the molecular fingerprints of numerous gases, liquids and solids [1.1,1.3]. Since molecular species exhibit fundamental vibrational absorption bands with large extinction coefficients within this spectral region [1.4], MIR spectroscopy potentially provides extremely sensitive chemical analysis, which, therefore, attracts lots of interest in developing discrete and broadband MIR light sources. In order to develop new MIR light sources, chalcogenide glasses (ChGs) are considered as good candidates as some compositions have been shown to be able to transmit light out to 25 μm [1.5].

A chalcogenide glass is a glass consisting of one or more Group 16 elements of the Periodic Table, sulfur (S), selenium (Se), or tellurium (Te), usually formulated with additions of germanium, arsenic or antimony to increase glass stability and robustness [1.6]. Since chalcogenide glasses provide a wide range of glass compositions, different physical properties can be achieved, including variation in refractive index. The properties of MIR transparency, high refractive index, low phonon energy, high optical non-linearity [1.7], and an ability to doped them with rare-earth element ions [1.8-1.12], make chalcogenide glasses attractive for use in planar photonic integrated circuits [1.13,1.14], and narrow- and broad-band fibre-based laser sources [1.15,1.16] and amplifiers [1.17-1.19] for the MIR. Although much research effort has been paid to the development and characterisation of chalcogenide glasses for photonics, relatively little refractive index dispersion data are presently available at MIR wavelengths, see for example: [1.20-1.25].

Refractive index, and very often its wavelength dispersion, is one of the key parameters that influences the design of optical components. Techniques commonly used for refractive index measurement include the modelling of transmission or reflection spectroscopic data [1.26,1.27], spectroscopic ellipsometry [1.20,1.24], prism coupling [1.28], grating coupling [1.29], and the measurement of the minimum deviation angle of light passing through a prism [1.30]. Several of these techniques require intensive sample preparation, are time consuming, and are costly to conduct. More importantly, it has until recently been difficult to apply some of these techniques to the MIR spectral region because of the paucity of suitable beam sources [1.28]. Carlie *et al.* modified a commercial system prism coupling system (Metricon model 2010) using additional laser sources, detectors, and a GaP prism in order to enable the measurement of refractive index dispersion at spot wavelengths over the 1.5–10.6 μm range and used it to determine the refractive index of As_2Se_3 bulk glass and thin films across this wavelength region to an accuracy of ± 0.001 [1.28]. Due to the high accuracy of the method the authors were able to compare the refractive indices of as-deposited and annealed As_2Se_3 films with those of the parent bulk glasses. In [1.22], the continuous linear refractive index dispersion was reported at ambient temperature of two bulk chalcogenide glasses, $As_{40}Se_{60}$ at. % and $Ge_{10}As_{23.4}Se_{66.6}$ at. %, over the 0.4 μm-33μm wavelength range obtained by means of spectroscopic ellipsometry. A two-term Sellmeier equation, with one resonant optical bandgap electronic absorption and one resonant MIR fundamental vibrational absorption, was determined as sufficient and appropriate for fitting the refractive index dispersion over the wavelength range for which the extinction coefficient was less than 0.0005. The fitting accuracy was better than 0.1%. Nevertheless, the accuracy in measuring the refractive index by means of spectroscopic ellipsometry is inherently limited by surface effects [1.31] as a thin contamination layer, oxide layer, or small defects on the surface can all potentially yield different optical constants for the glass.

1.1 Aims and objectives of the Project

The overall aim of this Project is to develop a technique based on the Swanepoel method to determine optical properties, especially refractive index and material dispersion, of chalcogenide glasses in the MIR region. These data will be significantly useful to core-cladding fibre design for MIR supercontinuum generation (SCG), fibre-lasing or fibre-sensing. It is highly possible that the temperature of the chalcogenide fibres will be increased when generating a supercontinuum broadband beam or pumping by narrow-band laser for fibre-lasing. The effect of temperature on the optical properties of chalcogenide glasses will thus be also investigated in this Project. To achieve the overall aim, this Project has several objectives:

1. To investigate the refractive index of different chalcogenide glasses using the minimum deviation method.

2. To find out the best refractive index model for chalcogenide glasses in the MIR region.

3. To modify the Swanepoel method in order to extend it into the MIR region.

4. To assess the optical properties (transparent window, refractive index, material dispersion and numerical aperture) of chalcogenide glasses used for MIR SCG and fibre sensing.

5. To investigate the effect of temperature on the optical properties of chalcogenide glasses.

1.2 Structure of thesis

A brief layout of the chapters presented in this Thesis is provided in this section.

Chapter 2 provides a review of background material and literature relevant to the field of study.

Chapter 3 describes the experimental techniques employed in the preparation and characterisation of all glass systems reported in this thesis. Moreover, the manufacturing procedures for chalcogenide glass prisms and thin films are given in this chapter. Chapter 3 also describes the thermal performance of a temperature controlled holder for heating or cooling a chalcogenide prism or thin film, newly built as part of the present Project.

Chapter 4 presents the basic theory of the minimum deviation method and the experimental setup in our laboratory. The refractive indices at different wavelengths of the chalcogenide glasses used for MIR SCG or fibre-sensing will be measured using the minimum deviation method. These values will be considered as benchmark values for measurements reported in chapter 6.

Chapter 5 presents the refractive index results obtained from spectroscopic ellipsometry. Two commonly used refractive index models (the Cauchy and Sellmeier models) will be introduced and applied to fit the data points. The appropriate refractive index models, which will be used to improve the Swanepoel method [1.26] in chapter 6, can be via the best fitting qualities to the experimental data.

In Chapter 6, the results presented in Swanepoel's paper [1.26] will be reproduced using Matlab code developed by the author. The best refractive index model determined in chapter 5 will be applied to modify the Swanepoel method in order to extend this method into the MIR region. The optical properties of some chalcogenide glasses fabricated for MIR SCG and fibre-sensing will be assessed in this chapter. A two-composition hot-pressed thin film was fabricated to determine a very small refractive index contrast between core and cladding glass compositions.

Chapter 7 presents the effect of temperature on the optical properties of chalcogenide glasses. The FTIR continuous *dn/dT* method is developed in this chapter to determine the thermo-optic coefficients of chalcogenide hot-pressed thin films.

Chapter 8 draws conclusions from the work presented in this thesis. The major findings will be outlined in this chapter. Finally, some suggestions for future work will also be made.

References

[1.1] Seddon, A.B., Tang, Z., Furniss, D., Sujecki, S. and Benson, T.M., 2010. Progress in rare-earth-doped mid-infrared fiber lasers. *Optics Express*, *18*(25), pp.26704-26719.

[1.2] Tao, G., Shabahang, S., Ren, H., Yang, Z., Wang, X. and Abouraddy, A.F., 2014, March. Multimaterial rod-in-tube coextrusion for robust mid-infrared chalcogenide fibers. In *Optical Components and Materials XI* (Vol. 8982, p. 898223). International Society for Optics and Photonics.

[1.3] Eggleton, B., Luther-Davies, B. and Richardson, K., 2011. Chalcogenide photonics'. *Nature Photonics*, *5*(3), pp.141-148.

[1.4] Rothman, L.S., Barbe, A., Benner, D.C., Brown, L.R., Camy-Peyret, C., Carleer, M.R., Chance, K., Clerbaux, C., Dana, V., Devi, V.M. and Fayt, A., 2003. The HITRAN molecular spectroscopic database: edition of 2000 including updates through 2001. *Journal of Quantitative Spectroscopy and Radiative Transfer*, *82*(1-4), pp.5-44.

[1.5] Kubat, I., Petersen, C.R., Møller, U.V., Seddon, A., Benson, T., Brilland, L., Méchin, D., Moselund, P.M. and Bang, O., 2014. Thulium pumped mid-infrared 0.9–9μm supercontinuum generation in concatenated fluoride and chalcogenide glass fibers. *Optics Express*, *22*(4), pp.3959-3967.

[1.6] Seddon, A.B., 1995. Chalcogenide glasses: A review of their preparation, properties and applications. *Journal of Non-Crystalline Solids*, *184*, pp.44-50.

[1.7] Zakery, A. and Elliott, S.R., 2003. Optical properties and applications of chalcogenide glasses: a review. *Journal of Non-Crystalline Solids*, *330*(1-3), pp.1-12.

[1.8] Sanghera, J.S. and Aggarwal, I.D., 1999. Active and passive chalcogenide glass optical fibers for IR applications: a review. *Journal of Non-Crystalline Solids*, *256*, pp.6-16.

[1.9] Cole, B., Shaw, L.B., Pureza, P.C., Mossadegh, R., Sanghera, J.S. and Aggarwal, I.D., 1999. Rare-earth doped selenide glasses and fibers for active applications in the near and mid-IR. *Journal of Non-Crystalline Solids*, *256*, pp.253-259.

[1.10] Sanghera, J.S., Shaw, L.B. and Aggarwal, I.D., 2009. Chalcogenide glass-fiber-based mid-IR sources and applications. *IEEE Journal of Selected Topics in Quantum Electronics*, *1*(15), pp.114-119.

[1.11] Tang, Z., Furniss, D., Fay, M., Sakr, H., Sójka, L., Neate, N., Weston, N., Sujecki, S., Benson, T.M. and Seddon, A.B., 2015. Mid-infrared photoluminescence in small-core fiber of praseodymium-ion doped selenide-based chalcogenide glass. *Optical Materials Express*, *5*(4), pp.870-886.

[1.12] Falconi, M.C., Palma, G., Starecki, F., Nazabal, V., Troles, J., Adam, J.L., Taccheo, S., Ferrari, M. and Prudenzano, F., 2017. Dysprosium-doped chalcogenide master oscillator power amplifier (MOPA) for mid-IR emission. *Journal of Lightwave Technology*, *35*(2), pp.265-273.

[1.13] Seddon, A.B., Pan, W.J., Furniss, D., Miller, C.A., Rowe, H., Zhang, D., McBrearty, E., Zhang, Y., Loni, A., Sewell, P. and Benson, T.M., 2006. Fine embossing of chalcogenide glasses–a new fabrication route for photonic integrated circuits. *Journal of Non-Crystalline Solids*, *352*(23-25), pp.2515-2520.

[1.14] Abdel-Moneim, N.S., Mellor, C.J., Benson, T.M., Furniss, D. and Seddon, A.B., 2015. Fabrication of stable, low optical loss rib-waveguides via embossing of sputtered chalcogenide glass-film on glass-chip. *Optical and Quantum Electronics*, *47*(2), pp.351-361.

[1.15] Gattass, R.R., Shaw, L.B., Nguyen, V.Q., Pureza, P.C., Aggarwal, I.D. and Sanghera, J.S., 2012. All-fiber chalcogenide-based mid-infrared supercontinuum source. *Optical Fiber Technology*, *18*(5), pp.345-348.

[1.16] Petersen, C.R., Møller, U., Kubat, I., Zhou, B., Dupont, S., Ramsay, J., Benson, T., Sujecki, S., Abdel-Moneim, N., Tang, Z., Furniss, D., Seddon, A.B. and Bang, O., 2014. Mid-infrared supercontinuum covering the 1.4-13.3 mum molecular fingerprint region using ultra-high NA chalcogenide step-index fibre. *Nature Photonics*, *8*, pp.830-834.

[1.17] Hu, J., Menyuk, C.R., Wei, C., Shaw, L.B., Sanghera, J.S. and Aggarwal, I.D., 2015. Highly efficient cascaded amplification using Pr 3+-doped mid-infrared chalcogenide fiber amplifiers. *Optics Letters*, *40*(16), pp.3687-3690.

[1.18] Anashkina, E.A., 2018. Design and Numerical Modeling of Broadband Mid-IR Rare-Earth Doped Chalcogenide Fiber Amplifiers. *IEEE Photonics Technology Letters*, *30*(13), pp. 1190-1193.

[1.19] Shen, M., Furniss, D., Tang, Z., Barny, E., Sojka, L., Sujecki, S., Benson, T.M. and Seddon, A.B., 2018. Modeling of resonantly pumped mid-infrared Pr 3+-doped chalcogenide fiber amplifier with different pumping schemes. *Optics Express*, *26*(18), pp.23641-23660.

[1.20] Orava, J., Kohoutek, T., Wagner, T., Cerna, Z., Vlcek, M., Benes, L., Frumarova, B. and Frumar, M., 2009. Optical and structural properties of Ge–Se bulk glasses and Ag–Ge–Se thin films. *Journal of Non-Crystalline Solids*, *355*(37-42), pp.1951-1954.

[1.21] Qiao, H.A., Anheier, N.C., Musgrave, J.D., Richardson, K. and Hewak, D.W., 2011. Measurement of chalcogenide glass optical dispersion using a mid-infrared prism coupler. In *Window and Dome Technologies and Materials XII* (Vol. 8016, p. 80160F). International Society for Optics and Photonics.

[1.22] Dantanarayana, H.G., Abdel-Moneim, N., Tang, Z., Sojka, L., Sujecki, S., Furniss, D., Seddon, A.B., Kubat, I., Bang, O. and Benson, T.M., 2014. Refractive index dispersion of chalcogenide glasses for ultra-high numerical-aperture fiber for mid-infrared supercontinuum generation. *Optical Materials Express*, *4*(7), pp.1444-1455.

[1.23] Gleason, B., Richardson, K., Sisken, L. and Smith, C., 2016. Refractive index and thermo-optic coefficients of Ge-As-Se chalcogenide glasses. *International Journal of Applied Glass Science*, *7*(3), pp.374-383.

[1.24] Wang, Y., Qi, S., Yang, Z., Wang, R., Yang, A. and Lucas, P., 2017. Composition dependences of refractive index and thermo-optic coefficient in Ge-As-Se chalcogenide glasses. *Journal of Non-Crystalline Solids*, *459*, pp.88-93.

[1.25] Fang, Y., Jayasuriya, D., Furniss, D., Tang, Z.Q., Markos, C., Sujecki, S., Seddon, A.B. and Benson, T.M., 2017. Determining the refractive index dispersion and thickness of hot-pressed chalcogenide thin films from an improved Swanepoel method. *Optical and Quantum Electronics*, *49*(7), p.237.

[1.26] Swanepoel, R., 1985. Determining refractive index and thickness of thin films from wavelength measurements only. *Journal of the Optical Society of America A*, *2*, pp.1339-1343.

[1.27] Marquez, E., González-Leal, J.M., Prieto-Alcón, R., Vlcek, M., Stronski, A., Wagner, T. and Minkov, D., 1998. Optical characterization of thermally evaporated thin films of $As_{40}S_{40}Se_{20}$ chalcogenide glass by reflectance measurements. *Applied Physics A*, *67*(3), pp.371-378.

[1.28] Carlie, N., Petit, L., Musgraves, J.D., Richardson, K., Anheier Jr, N.C., Qiao, H.A., Bernacki, B. and Phillips, M.C., 2011. Measurement of the refractive index dispersion of As_2Se_3 bulk glass and thin films prior to and after laser irradiation and annealing using prism coupling in the near-and mid-infrared spectral range. *Review of Scientific Instruments*, *82*(5), pp.053103-053103.

[1.29] Laniel, J.M., Ménard, J.M., Turcotte, K., Villeneuve, A., Vallée, R., Lopez, C. and Richardson, K.A., 2003. Refractive index measurements of planar chalcogenide thin film. *Journal of Non-Crystalline Solids*, *1*(328), pp.183-191.

[1.30] Fang, Y., Sojka, L., Jayasuriya, D., Furniss, D., Tang, Z.Q., Markos, C., Sujecki, S., Seddon, A.B. and Benson, T.M., 2016. Characterising refractive index dispersion in chalcogenide glasses. In *18th International Conference on Transparent Optical Networks*. IEEE.

[1.31] Poelman, D. and Smet, P.F., 2003. Methods for the determination of the optical constants of thin films from single transmission measurements: a critical review. *Journal of Physics D Applied Physics*, *36*, pp.1850-1857.

Chapter 2: Background and literature review

The goal of this Project is to assess the optical properties of chalcogenide bulk glasses and thin films. Based on this goal, this chapter provides an introduction to the theory, structure, optical properties and recent progress in chalcogenide bulk glasses and thin films. Section 2.1 will provide a brief overview of glass science, covering their fundamental characteristics and properties. Section 2.2 will introduce the basic theory and structure of optical fibres. Section 2.3 will provide an introduction to chalcogenide glasses, which includes the definition, structure, optical properties of chalcogenide bulk glasses and thin films, specifically the compositions ($As_{40}Se_{60}$ at. %, $Ge_{20}Sb_{10}Se_{70}$ at. %, $Ge_{16}As_{24}Se_{15.5}Te_{44.5}$ at. %) investigated in this Project. The applications of chalcogenide glasses will be shown in section 2.4. As this Project mainly aims to determine the refractive index of the chalcogenide glasses, different methods for determining the refractive index of the chalcogenide glasses will be discussed in section 2.5. Finally, the summary of this chapter will be given in section 2.6.

2.1 Glass science fundamentals

In 1945, the American Society for Testing Material proposed one of the most frequently quoted definitions of glass, which describes as “Glass is an inorganic product of fusion which has cooled to a rigid condition without crystallizing.” [2.1]. However, this restrictive definition does not consider the fact that glass can be formed by organic material, e.g. glycerol, and fabricated by other routes, such as vapour deposition or a sol gel route. To meet this difficulty, a committee of the U.S. National Research Council proposed a more general definition in 1976, which describes as “an X-ray amorphous material which exhibits the glass transition, this being defined as that phenomenon in which a solid amorphous phase exhibits with

changing temperature a more or less sudden change in derivative thermo-dynamic properties, such as heat capacity and expansion co-efficient, from crystal like to liquid like values" [2.2].

As a useful way to discuss glass formation, and the relationship between glassy, liquid and solid states, the volume-temperature diagram is shown in Figure 2.1-1 [2.3]. When a liquid (point a in Figure 2.1-1) is cooled down to its liquidus (point b in Figure 2.1-1), this is accompanied by a gradual decrease in enthalpy as it begins to contract. The decrease in volume on cooling is attributed partly to the decreasing amplitude of atomic vibrations and partly to changes in structure which results in it becoming more compact as temperature falls [2.3]. At temperatures near the melting points, T_m, these structure changes can occur very rapidly depending on different rate of cooling. If the rate of cooling is sufficiently lower than the crystallisation rate, the melt starts to crystallise on the cooling; this is accompanied by a marked increase in density (the volume decreases from point b to point c in Figure 2.1-1) at the melting points, T_m. On further cooling the stable crystal will continue to contract (point f in Figure 2.1-1). If the crystallisation rate is sufficiently lower than the rate of cooling, no crystallisation happens on cooling. The volume of the supercooled liquid decreases gradually from point b to point d as shown in Figure 2.1-1. A decrease in slope, which is a result of the reduced amplitude of atomic vibration [2.3], is then found when the supercooled liquid enters a glass transition temperature, T_g, range. Generally, T_g can be defined as the temperature at which the shear viscosity equals 10^{12} pa [2.4] or where the liquid and vitreous portions of Figure 2.1-1 intersect, which is usually at $2T_m/3$ [2.4]. Only below T_g is it correct to describe the material as a glass.

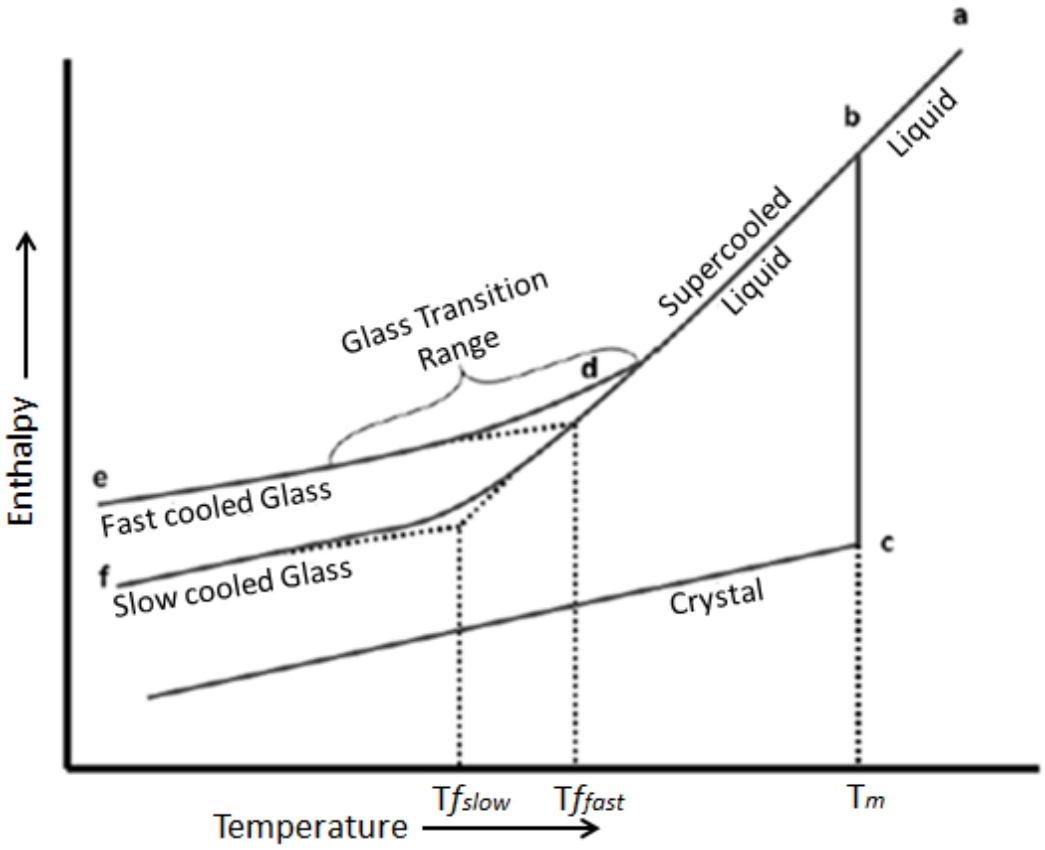


Figure 2.1- 1. Volume per mass (or enthalpy) vs. temperature graph demonstrating the relationship between the glassy, liquid and solid state. Adapted from [2.3].

Once the supercooled liquid has entered the glass transition region, different glasses with different density can be obtained for different cooling rates. On faster cooling (to point e in Figure 2.1-1), a glass with larger volume (lower in density) will be formed. If the cooling rate is slower (to point f in Figure 2.1-1), a glass with smaller volume (larger in density) will be formed since a slower cooling rate allows more time for changes in configuration to occur [2.3].

The fictive temperature of a glass, T*f*, defines the structure of a glass and can be found upon reheating [2.5]. The concept of a "fictive temperature" is valuable in discussing the changes in configuration and physical properties which occur when a glass is heat treated in the vicinity of T_g. By extrapolating along the glass line to the intersection with the equilibrium liquid line, the fictive temperature can be determined (Tf_{fast} and Tf_{slow} in Figure 2.1-1) [2.5]. Therefore, both T_g and T*f* depend

on the cooling rate of the glass and it is often assumed that the two are equal [2.6,2.7].

2.2 Optical fibres

The basic structure of an optical fibre is that a core material, which has a higher refractive index (n_{core}), is surrounded by a cladding material, which has a lower refractive index ($n_{cladding}$), as shown in Figure 2.2-1(a). When light incident at the core/cladding interface with an incident angle of θ, the total internal reflection occurs when θ is larger than the critical angle θ_c ($\sin\theta_c = \frac{n_{cladding}}{n_{core}}$), as shown in Figure 2.2-1(b). The basic principle of light guiding within the core material is by total internal reflection. The maximum half conical angle incident from air to the core of the optical fibre, which is achieving total internal reflection, is referred to the angle of acceptance α (see Figure 2.2-1(b)). The relationship between α and the refractive indices of the three mediums incorporated into the fibre, those of air, cladding and core, are unified by the numerical aperture (NA) [2.8].

$$\mathrm{NA} = \sin\alpha = \sqrt{{n_{core}}^2 - {n_{cladding}}^2} \quad \text{(no units)} \qquad (2.1)$$

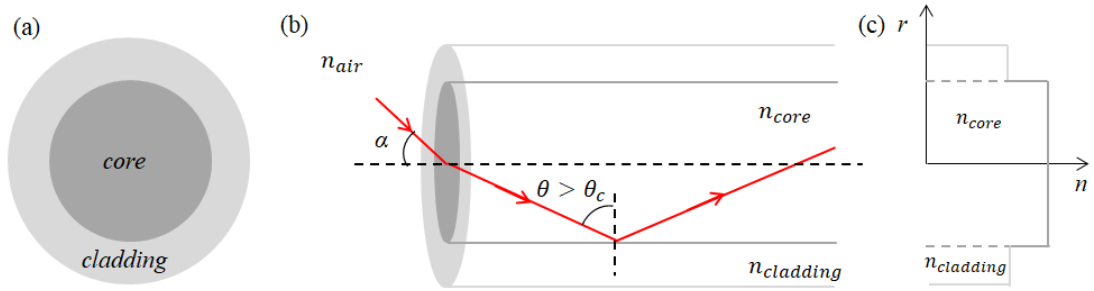


Figure 2.2- 1. (a) Schematic diagram showing (a) cross section of a step-index fibre, (b) light guiding by total internal reflection by the core, where α is the angle of acceptance, θ is the incident angle at the core/cladding interface and θ_c is the critical angle, and (c) refractive index profile of the step-index fibre.

Optical fibres can have a variety of structures to help guide light and the simplest of these is the step-index fibre (SIF) (see Figure 2.2-1). The refractive index profile of the SIF is shown in Figure 2.2-1(c). Note that the compositions investigated in this Project were all designed for fabricating SIFs. Therefore, other refractive index profile fibres (depressed index, dispersion shifted, dispersion flattened) will not be further discussed here.

2.3 Chalcogenide glasses

Since the goal of this Project is to characterise the optical properties of the chalcogenide glasses, specifically $As_{40}Se_{60}$ at. %, $Ge_{20}Sb_{10}Se_{70}$ at. %, $Ge_{20}Sb_{10}Se_{67}S_3$ at. % and $Ge_{16}As_{24}Se_{15.5}Te_{44.5}$ at. %, it is essential to realize the theory, structure, optical properties of the chalcogenide glasses investigated in this Project. The $As_{40}Se_{60}$ at. % and $Ge_{16}As_{24}Se_{15.5}Te_{44.5}$ at. % glasses were fabricated for MIR supercontinuum generation [2.9], and the $Ge_{20}Sb_{10}Se_{70}$ at. % and $Ge_{20}Sb_{10}Se_{67}S_3$ at. % glasses were fabricated for MIR fibre-sensing [2.10].

2.3.1 Chalcogenide glass

A chalcogenide glass is a glass consisting one or more Group 16 elements of the Periodic Table, sulfur (S), selenium (Se), or tellurium (Te), usually formulated with additions of gallium (Ga), germanium (Ge), arsenic (As) or antimony (Sb) to increase glass stability and robustness [2.11]. Since chalcogenide glasses provide a wide range of glass compositions, different physical properties can be achieved, including refractive index [2.12]. Chalcogenide glasses can be doped by rare-earth ions, such as Er^{3+}, Dy^{3+}, Pr^{3+}, Ce^{3+}, etc. and hence many applications of active optical devices have been proposed [2.13-2.16]. The main properties of chalcogenide glasses include:

1. Chalcogenide glasses transmit to longer wavelengths into the infrared (IR) than silica and fluoride glasses (see Figure 2.3-1) which makes chalcogenide glasses

suitable for passive MIR applications such as radiometric thermometry and CO_2 laser power delivery [2.17-2.19], and active applications such as broadband MIR supercontinuum generation (SCG) fibre sources [2.20].

2. Chalcogenide glasses have a higher nonlinear refractive index coefficient (n_2) compared to silica glass (see Figure 2.3-2) (at 1550 nm wavelength silica glass exhibits n_2 = 0.03 x 10^{-14} cm^2/W while for chalcogenide glass: n_2 = $As_{40}Se_{60}$ at. % 10 x 10^{-14} cm^2/W, $Ge_{10}As_{10}Se_{60}Te_{20}$ at. % 20 x 10^{-14} cm^2/W and 3 x 10^{-14} cm^2/W for $As_{40}S_{60}$ at. % [2.21-2.23], and therefore can be used for all-optical switching (AOS).
3. Chalcogenide glasses exhibit a longer wavelength multi-phonon edge and a wider band gap compared to silicon [2.24, 2.25].
4. The low phonon energy of the chalcogenide glasses relates to longer wavelength transparency. The phonon energy of sulfides ranges from ~ 400 - 450 cm^{-1}, and that for selenides and tellurides from ~ 230 - 350 cm^{-1} [2.26-2.29].
5. The chalcogenide glasses can exhibit a high optical damage threshold and environmental stability [2.30-2.32].

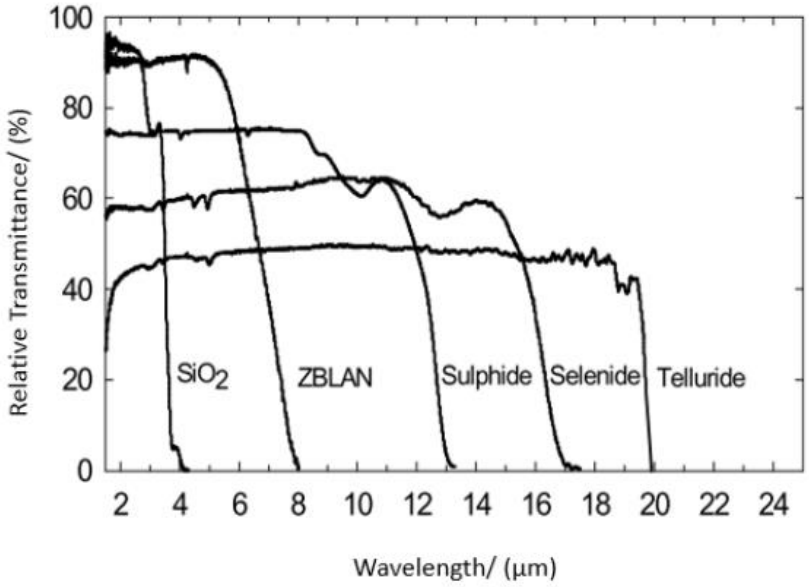


Figure 2.3- 1. Bulk transmission spectra for SiO_2, ZBLAN, sulfide, selenide and telluride glasses [2.17]. Note that the relative transmittance values shown do not allow for Fresnel reflection.

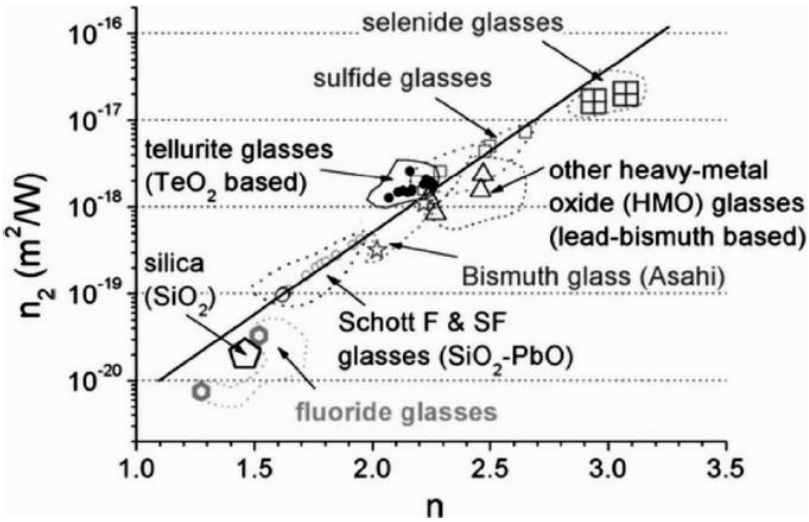


Figure 2.3- 2. Linear refractive index (*n*) related to the nonlinear refractive index coefficient (n_2) for various glass systems [2.33].

2.3.2 Structure of chalcogenide glasses

Different compositions of chalcogenide glasses usually exhibit different structures, leading to different optical properties. In this subsection, the structures of the chalcogenide glasses investigated in this Project will be discussed. Moreover, Dantanarayana *et al.* [2.34] claimed that a more physically comprehensive refractive index model can be achieved by identifying the position of the MIR fundamental vibrational absorption band of a chalcogenide glass. Therefore, some studies of the MIR fundamental vibrational absorption bands in the glass systems studied in this Project will also be provided here.

The structure of chalcogenide glasses cannot be described by means of a continuous random network which is isotropic in three dimensions; As_2S_3, As_2Se_3, GeS_2, and $GeSe_2$ at. % can be locally layer-like and pure S and Se are chain like. For all these materials, the weak van der Waal's bonding between the layers and chains leads to a considerable flexibility of the structure [2.35] and, therefore, changes in the structure can be relatively easily accommodated.

Structural and dynamic information of a chalcogenide glasses can be obtained by Raman (or inelastic) scattering of light in the material. The nondestructive nature of the probe, and flexibility in sampling arrangements, has opened up many potentially new areas where Raman measurements have proved valuable [2.36,2.37]. The structure of a chalcogenide glass can be analysed by NIR Raman spectroscopy. Using the VIS (visible) part of the spectrum as the excitation wavelength one can obtain the Raman spectrum of photosensitive compounds without interference from photoreactions caused by the probe beam.

Raman spectra of $As_{40}Se_{60}$, $As_{40}S_{30}Se_{30}$, $As_{40}S_{45}Se_{15}$, $As_{40}S_{60}$, $As_{32}S_{34}Se_{34}$ and $As_{24}S_{38}Se_{38}$ at. % were obtained with NIR excitation at a wavelength of 840 nm, as shown in Figure 2.3-3 [2.38]. The dominant feature in binary sulfide and selenide compounds are bands at 345 cm^{-1} for $As_{40}S_{60}$ at. % and 230 cm^{-1} for $As_{40}Se_{60}$ at. %, respectively [2.38]. For $As_{40}S_{60}$ at. %, the strong band observed at ~345 cm^{-1} in Figure 2.3-3 is attributed to the antisymmetric As-S-As stretching vibration in an AsS_3 pyramid unit. For $As_{40}Se_{60}$ at. %, the strong band observed at ~230 cm^{-1} in Figure 2.3-3 is attributed to the antisymmetric As-Se-As stretching vibration in an $AsSe_3$ pyramid unit. Figure 2.3-3 also shows that, in ternary compounds with a S/Se=1 molecular ratio, a progressive decrease in the intensity of these broad bands is observed with decreasing As content; this indicates a decrease in the number of As-containing pyramidal sites. Moreover, new bands at 255 and 440 cm^{-1} to 480 cm^{-1} start to appear with decreasing As content, and are attributed to Se-Se homopolar bonds. These units serve as chalcogen chains connecting the remaining pyramid units. In Figures 2.3-3 e and f, a weak small band at 495 cm^{-1} is attributed to the small numbers of S-S bonds; this suggests that, for equal concentrations of S and Se, S stays with the remaining pyramids and that it is the Se which dominates the connecting chain units.

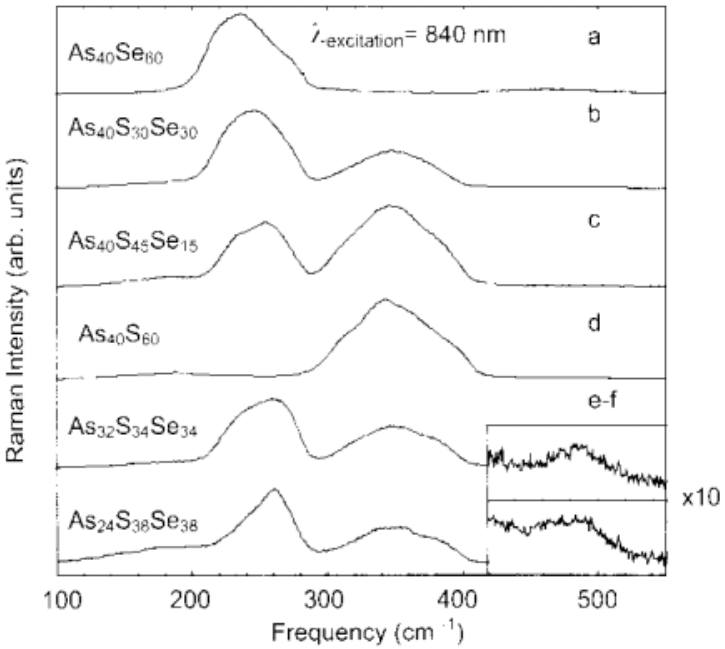


Figure 2.3- 3. Raman spectra of $As_{40}Se_{60}$, $As_{40}S_{30}Se_{30}$, $As_{40}S_{45}Se_{15}$, $As_{40}S_{60}$, $As_{32}S_{34}Se_{34}$ and $As_{24}S_{38}Se_{38}$ at. %, which were obtained with NIR excitation at a wavelength of 840 nm. Spectral resolution is 1.5 cm^{-1} [2.38].

Due to the fact they are less toxic than their arsenic-containing counterparts [2.39], the Ge-Sb-Se glass system has attracted more and more interest for applications in a variety of forms *i.e.* bulk, fibre or thin films [2.40-2.53]. It is reported that, within the composition range of 5-35 atomic % (at. %) Ge, 5-40 at. % Sb and the remainder Se [2.54], the Ge-Sb-Se glass system exhibits robustness, relatively good thermal, mechanical and chemical properties and high transparency across the 2-16 μm wavelength range [2.54-2.57]. Like other chalcogenide systems, the physical properties of Ge-Sb-Se glasses are dependent on their composition, which can be described by a number of structural models. One is the chemically ordered network model (CONM) [2.58]. This model assumes that the formation of heteropolar bonds are preferred over homopolar bonds and gives rise to a Ge-Sb-Se system made up of tetrahedral-like [$GeSe_4$] and pyramidal-like [$SbSe_3$] chemically stable units [2.59]. In topological models, which invoke the 'Constraint Theory' [2.60] and structural dimensionality considerations [2.61], the glass properties are proposed to be dependent on the mean coordination number (MCN). This model described two

topological thresholds where the network changes from a floppy state to a rigid network, with a subsequent change from a two- to three-dimensional structure, at MCN = 2.4, and MCN = 2.67, respectively [2.60,2.61]. However, since, for the Ge-Sb-Se glasses, the Sb has a larger atomic radius than its neighbouring Ge or Se (133 pm, 125 pm and 103 pm, respectively [2.62]), topological models are not as accurate in predicting their physical properties [2.41,2.63].

Apart from Ge-Sb-Se glasses, the properties of the Ge-Sb-Se-S glass will also be assessed in this Project. Unlike Se-based glasses, which usually undergo catastrophic damage once a laser damage threshold is exceeded, S-based glasses are unlikely to have this damage. As the Se element in Ge-Sb-Se glasses is progressively replaced by S element, the damage threshold rises and the tendency for the surface to "burn" disappears [2.64]. The structure of $Ge_{15}Sb_{20}Se_{65-x}S_x$ at. % glasses was studied by Wang *et al.* recently [2.65]. Raman spectra of $Ge_{15}Sb_{20}Se_{65-x}S_x$ at. % (x=0; 16.25; 32.5; 48.75 and 65) glasses are shown in Figure 2.3-4(a). For Se-based structural units, the band at around 203 cm^{-1} and 218 cm^{-1} might be attributed to the vibrational modes in the corner-sharing and edge-sharing $GeSe_{4/2}$ tetrahedral units, respectively [2.66,2.67]. The Raman peaks at 190 cm^{-1} and 177 cm^{-1} might be attributed to the pyramidal $SbSe_{3/2}$ structure units. For S-based structure units, bands at 344 cm^{-1} and 395cm^{-1} in Figure 2.3-4 are attributed to $GeS_{4/2}$ tetrahedral vibration modes [2.68-2.70]. The pyramidal $SbS_{3/2}$ structural units have the peaks at 280 cm^{-1} and 308 cm^{-1}, [2.70,2.71] and the S chains or rings have a vibration around 475 cm^{-1} [2.70,2.72,2.73]. The evolution of the structural units in this glass system was also quantified by decomposing the Raman spectra into multiple Gaussians as shown in Figure 2.3-4(a). The relative intensity of Raman bands derived from spectral decomposition is shown in Figure 2.3-4(b). It was found that all the spectra were dominated by the heteropolar bonds Ge–Se/S and Sb–Se/S vibrations; the number of the Se-related chemical bonds (Ge–Se, Sb–Se and Se–Se) increased and that of S-related chemical bonds (Ge–S, Sb–S and S–S) decreased gradually with increasing

Se content.

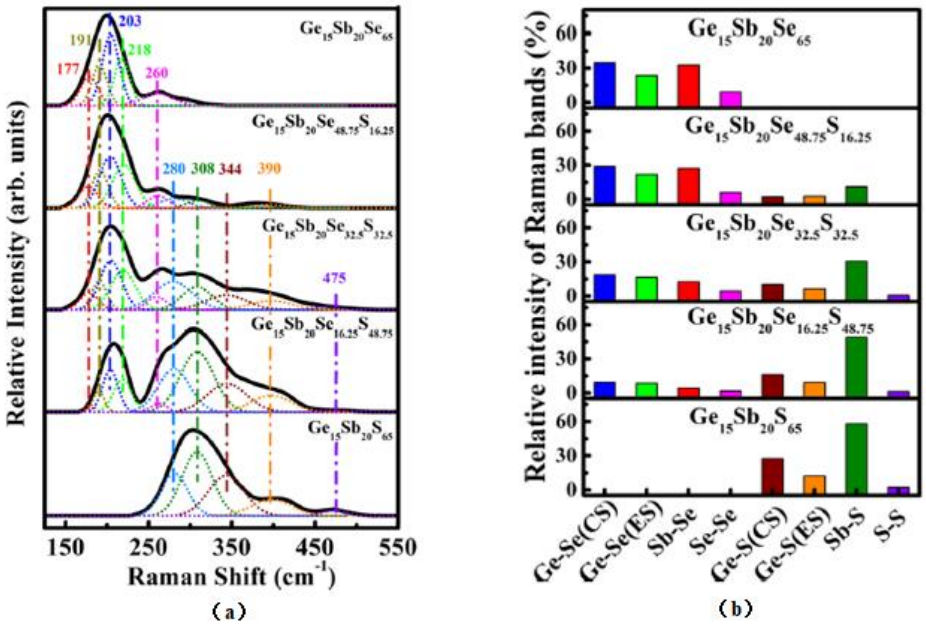


Figure 2.3- 4. (a) Raman spectra of the $Ge_{15}Sb_{20}Se_{65-x}S_x$ at. % glasses with different chemical compositions and their decompositions into multiple Gaussians; (b) Relative intensity of the different Raman bands as derived from spectral decomposition [2.65].

Another glass system investigated in this Project is Ge-As-Se-Te. Substitution of the Te atom into the Ge-As-Se glass system allows robustness and sufficient thermal stability, which is defined as the stability towards devitrification during melt-cooling and stability towards devitrification on glass reheating above T_g or stability towards crystallisation during shaping [2.74]. Nguyen *et al.* investigated the structure of Ge-As-Se-Te by Raman scattering measurement [2.75]. The Raman spectra of $Ge_{30}As_{10}Se_{60-x}Te_x$ at. % (x=25; 28; 30 and 35) are shown in Figure 2.3-5(a). In Figure 2.3-5(a), the band between 140 and 190 cm^{-1} is associated with Ge-chalcogen tetrahedral units; this association is made because the spectra of germanium selenide glasses have a band centred at around 190 cm^{-1} which is due to the fundamental symmetric stretching vibration of $GeSe_{4/2}$ units as clearly shown in Figure 2.3-5(a) for $Ge_{33}As_{12}Se_{55}$ at. % glass [2.76]. With the presence of Te, this band shifts to lower frequencies because of the increased reduced mass due to Te. (The atomic mass of

Te is 127.6 compared with 78.96 for Se.) Therefore, this band can be assigned to [$GeSe_{4-x}Te_x$] tetrahedral units. In Figure 2.3-5(a), the band between 190 and 230 cm^{-1} locates close to the vibrational band (240 cm^{-1}) found in As_2Se_3 glass which is attributed to $AsSe_{3/2}$ pyramidal units [2.77]. Due to the presence of Te, modified structural units were proposed by Nguyen *et al.* as [$AsSe_{3-x}Te_x$] structural units [2.75]. The band position shifts to smaller wave number as the Te content increases from 25 to 35 at.%, as shown in Figure 2.3-5(a); this shift is also attributed to the larger atomic mass of Te compared with that of Se. The shoulder between 190 and 230 cm^{-1} observed in Figure 2.3-5 might be attributed to the vibration of [$AsSe_{3-x}Te_x$] mixed pyramidal units. Moreover, a small band was observed between 230 and 280 cm^{-1}. Since the fundamental stretching vibration asscociated with $GeSe_{4/2}$ structural units is located at ~262 cm^{-1} [2.76], this small band between 230 and 280 cm^{-1} is associated with [$GeSe_{4-x}Te_x$] tetrahedral units. When Te is substituted for Se in the $Ge_{30}As_{10}Se_{60-x}Te_x$ at. % glass system, the structure can be schematically represented as shown in Figure 2.3-5(b). The Se and Te atoms are bonded to As and Ge atoms so that the main structural units present are the [$AsSe_{3-x}Te_x$] mixed pyramids, [$GeSe_{4-x}Te_x$] mixed tetrahedral, and Ge-Te-Ge chains with Ge-Ge, As-As, Ge-As, and Se-Te bonds connected together to form an amorphous structure [2.75].

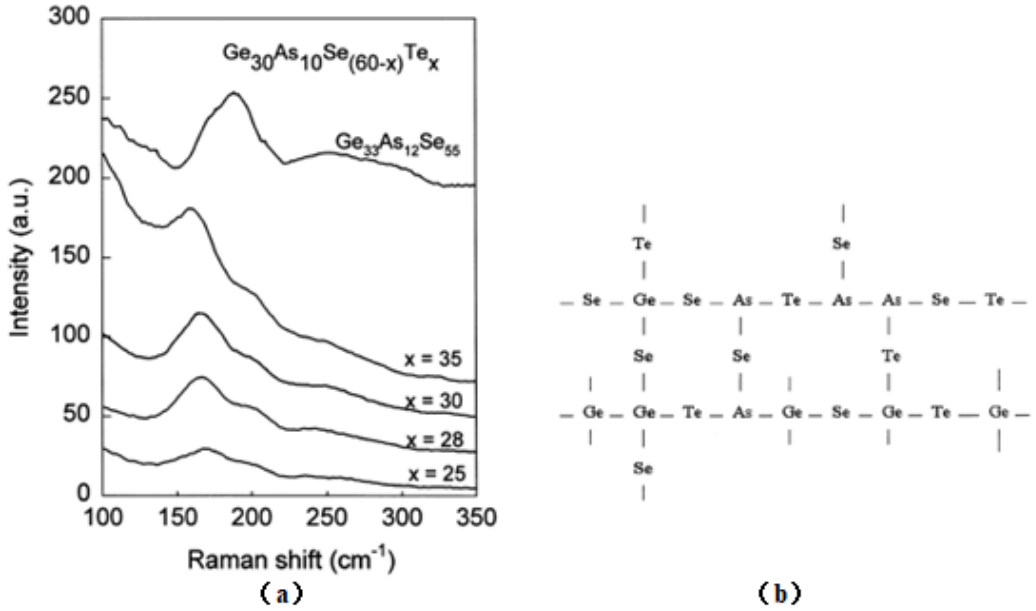


Figure 2.3- 5. (a) Room temperature Raman spectra of chalcogenide $Ge_{30}As_{10}Se_{60-x}Te_x$ at. % glasses as a function of Te content; (b) Schematic representation of glasses in the $Ge_{30}As_{10}Se_{60-x}Te_x$ at. % system [2.75].

Another approach to investigate the atomic configuration of glasses in the vitreous state is by comparing the IR (infrared) spectra of the glasses with their crystalline counterparts. The comparison implies that the basic structural units in the glasses are essentially the same as those found in the corresponding crystal. The IR transmission spectra for the glass system $Ge_{28-x}Sb_xSe_{72}$ at. % (x=0; 8; 16 and 24) in the spectral range of 500-200 cm^{-1} are shown in Figure 2.3-6 [2.78]. The absorption bands at 220 and 285 cm^{-1} are mainly attributed to $GeSe_4$ (fundamental vibrational mode) and $GeSe_2$ (Raman mode). The band at 220 cm^{-1} is close to that obtained by Lisista *et al.* [2.79] and Nemanich *et al.* [2.80] for crystalline $GeSe_2$ in the Raman spectra. Since Se rings and chains formed by an excess of Se atoms are interlinked by both Ge and Sb atoms, the absorption peaks at ~227 and 247 cm^{-1} have been assigned to the Se polymeric chain and Se_8 polymeric rings, respectively. In Figure 2.3-6, as the percentage of Sb increases from 8 to 24 %, the probability of forming Se_8 rings increases. In order to allow an assignment of the bonds to $SbSe_3$ structural units, a comparison between the published results and the experimental spectrum was made

[2.78]. The band situated at 247 cm^{-1} in Figure 2.3-6 is close to the value of 250 cm^{-1} calculated by Quiroga [2.81], which has also been assigned to $GeSe_4$ units. The abundance of these units in this band has a small $SbSe_3$ contribution relative to the pyramid units. The frequency 285 cm^{-1} is in agreement with the frequency assigned by Goyal and Maan [2.82] for the $GeSe_4$ structural units in a GeSbSe alloy. Therefore, the intense feature at 247 cm^{-1} observed in the experimental spectrum can be assigned to $GeSe_4$ units. The absorption due to Ge–Se–Ge is also expected to contribute about 304 cm^{-1}.

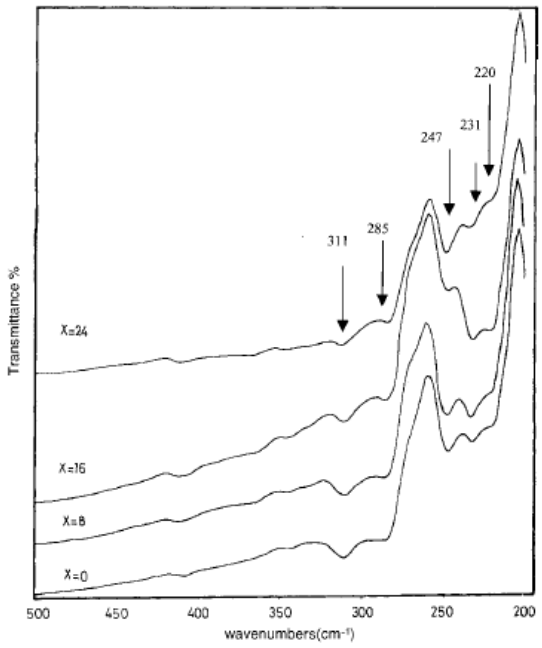


Figure 2.3- 6. FIR transmission spectra of amorphous $Ge_{28-x}Sb_xSe_{72}$ (x=0; 8; 16 and 24) glasses at room temperature [2.78].

Other techniques, including EXAFS (extended X-ray absorption fine structure) [2.83], RBS (Rutherford backscattering spectroscopy) [2.84] and XPS (X-ray photoelectron spectroscopy) [2.85] can also be extensively employed for investigating the structure of chalcogenide glasses, but will not be further discussed here. The knowledge of the fundamental vibrational band will be useful for physically interpretating the parameters of the two-term Sellmeier refractive index model, which will be further discussed in section 5.5.

2.3.3 Optical properties of chalcogenide bulk glasses and comparison with thin films

This Project aims to charaterise the optical properties of chalcogenide bulk glasses and thin films, including optical transmission, refractive index, material dispersion and thermo-optic performance. Therefore, in this subsection, these optical properties in some chalcogenide glasses studied in this Project will be reviewed.

2.3.3.1 Optical transmission theory

The optical transmission window of chalcogenide glasses is affected by electronic absorption at short wavelengths, multiphonon absorption at long wavelengths, and Rayleigh scattering in between [2.86]. Besides, extrinsic losses are often observed within this window and arise from impurities in the glass. In practice, the attenuation of a chalcogenide glass can be understood as the sum of the absorption loss and the scattering loss. The absorption loss can be expressed as [2.86]:

$$\text{Absorption loss} = A_0 \exp\left(\frac{A}{\lambda}\right) + B_0 \exp\left(\frac{-B}{\lambda}\right) + \sum c_i C_i + D_0 \exp\left(\frac{D}{\lambda}\right) \qquad (2.2)$$

where $A_0 \exp\left(\frac{A}{\lambda}\right)$ represents the intrinsic electronic absorption, $B_0 \exp\left(\frac{-B}{\lambda}\right)$ represents the multiphonon absorption, $\sum c_i C_i$ describes extrinsic absorption due to impurities and $D_0 \exp\left(\frac{D}{\lambda}\right)$ represents the weak absorption tail. The scattering loss can be expressed as [2.86]:

$$\text{Scattering loss} = \frac{E}{\lambda^4} + \frac{F}{\lambda^4} + \frac{G}{\lambda^2} + H \qquad (2.3)$$

where $\frac{E}{\lambda^4}$ represents the intrinsic Rayleigh scattering, $\frac{F}{\lambda^4}$ represents the extrinsic Rayleigh scattering, $\frac{G}{\lambda^2}$ describes the Rayleigh-Gans scattering and H represents the wavelength-independent scattering. The optical transmission windows of some chalcogenide glasses are listed in Table 2.3-1.

Table 2.3- 1. Approximate transmission windows of some chalcogenide bulk glasses.

Glass-forming system	Transmission window (μm)	Reference
Ga-La-S	0.57-9.5	[2.87]
As-S	0.6-10	[2.30]
Ge-Sb-S	0.64-11	[2.88]
As-S-Se	0.75-12.5	[2.88]
Ge-As-Se	0.84-16	[2.87]
As-Se	0.85-17.5	[2.88]
Ge-As-Se-Te	1.0-17	[2.30]
As-Se-Te	1.23-18.52	[2.88]
Ge-Se-Te	1.7-17	[2.87]
Te-As-Se	2.0-16	[2.89]

The short wavelength limit of the optical transmission window is governed by the electronic absorption edge [2.90,2.91]. It is useful to consider chalcogenide glasses as amorphous semiconductors with a characteristic energy gap, E_g. The optical absorption near electronic absorption edge of an amorphous semiconductor can be characterised into three regions as shown in Figure 2.3-7(a) [2.92]. The region A in Figure 2.3-7(a) is referred to the bandgap edge; the absorption within this region is usually too large to measure. Region B is the broadening of that edge, similar to Urbach tails observed in crystals, and is generally observed as the UV (ultra-violet) absorption edge. Region C is the weak absorption tail (WAT); this absorption tail is associated with the medium range order in the glass structure and localised energy states. The weak absorption tail is sensitive to glass purity and thermal history [2.93]. The optical absorptions near the electronic edge of some chalcogenide glasses ($Ge_{28}Sb_{12}Se_{60}$, $Ge_{33}As_{12}Se_{55}$, and $As_{40}S_{60}$ at. %) were obtained by Wood and Tauc, as shown in Figure 2.3-7(b) [2.92]. In all these three chalcogenide glasses, the

Urbach tail and WAT can be easily observed. The WAT generally extends from the UV edge across the transmission window to the multiphonon edge, and for high-quality chalcogenide glasses, dominates the optical loss spectrum over Rayleigh scattering [2.87].

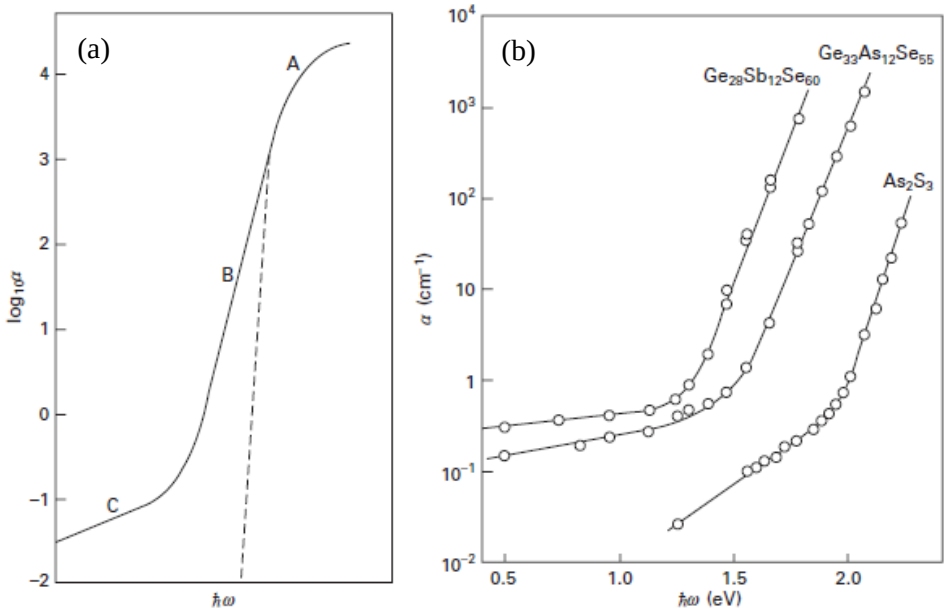


Figure 2.3- 7. (a) Three principal regions of optical absorption near the short wavelength cut-off: band gap edge (A), Urbach tail (B) and weak absorption tail (C) [2.93].(b) Optical absorption for three amorphous chalcogenide glasses near the short wavelength cut-off demonstrating the transition from Urbach tail to WAT [2.92].

Another division of the optical absorption near the electronic absorption edge of a chalcogenide glass is given based on the value of its absorption coefficient [2.94]. When the absorption coefficient $\alpha \geq 10^4 cm^{-1}$, a square root dependence is found with frequency. For the spectrum where $10^4 cm^{-1} \geq \alpha \geq 10^0 cm^{-1}$ (see Figure 2.3-7(b)), the dependence is exponential ('Urbach' edge). For $\alpha \leq 10^0 cm^{-1}$ (see Figure 2.3-7(b)), an exponential dependence is also found with frequency (WAT).

In order to obtain the absorption coefficients of chalcogenide glasses, several techniques can be used for as-deposited, annealed, photodarkened films and in fabricated waveguides. At shorter wavelengths (high absorption coefficient), a conventional spectrometer could be used with correction for reflection losses using

the method described in [2.95]. At wavelengths beyond band edge (low absorption coefficient), photothermal deflection spectroscopy (PDS) is suitable for measuring the relative absorption coefficient in the long-wavelength region [2.96]. For determining the optical band gap energy of a chalcogenide glass, the most widely used method is to plot $(\alpha h\nu)^{1/2}$ versus $h\nu$ (h is Planck's constant (eV s); ν is the frequency) above the Urbach edge yielding a striaight line; it is generally accepted that the optical band-gap of the amorphous chalcogenide glass can be determined using the intersection of this straight line with the energy axis. Table 2.3-2 shows the optical band gap for some bulk chalcogenide glasses, and Table 2.3-3 shows the results of optical-gap measurements for chalcogenide thin films.

Table 2.3- 2. Optical band gaps for some bulk chalcogenide glasses.

Glass composition / at. %	E_g / (eV)	Reference	Glass	E_g / (eV)	Reference
$As_{40}S_{60}$	2.4	[2.98]	$Ge_{30}Sb_{10}Se_{60}$	1.57	[2.100]
$As_{40}Se_{60}$	1.77	[2.99]	$Ge_{27.5}Sb_{10}Se_{62.5}$	1.69	[2.100]
$Ge_{25}Se_{75}$	2.07	[2.99]	$Ge_{25}Sb_{10}Se_{65}$	1.77	[2.100]
$Ge_{28}Sb_{12}Se_{60}$	1.8	[2.99]	$Ge_{20}Sb_{10}Se_{70}$	1.71	[2.100]
$Ge_{25}Se_{65}Te_{10}$	1.73	[2.99]	$Ge_{15}Sb_{10}Se_{75}$	1.64	[2.100]
$As_{40}S_{60}$	2.25	[2.97]	$Ge_{10}Sb_{10}Se_{80}$	1.59	[2.100]
$As_{40}S_{55}Se_{5}$	2.13	[2.97]	$Ge_{17}Sb_{15}Se_{68}$	1.61	[2.100]
$Ge_{25}As_{12}Se_{40}Te_{23}$	1.18	[2.97]	$Ge_{15}Sb_{20}Se_{65}$	1.58	[2.100]
$Ge_{30}As_{10}Se_{30}Te_{30}$	1.17	[2.97]	$Ge_{17}Sb_{23}Se_{60}$	1.38	[2.100]
$Ge_{32.5}Sb_{10}Se_{57.5}$	1.47	[2.100]	$Ge_{15}Sb_{25}Se_{60}$	1.35	[2.100]

Table 2.3- 3. Optical band gaps for some chalcogenide thin films.

Thin film composition / at. %	Manufacturing technique	E_g (eV)	Reference
$As_{40}S_{60}$	PLD deposited	2.26	[2.96]
As_3Se_{97}	Thermal evaporation	1.77	[2.101]
$As_{22}Se_{78}$	Thermal evaporation	2.07	[2.101]
$As_{41}Se_{59}$	Thermal evaporation	1.79	[2.101]
$As_{39}Se_{61}$	Thermal evaporation	1.79	[2.101]
$Ge_9As_{25}Se_{66}$	Thermal evaporation	1.922	[2.101]
$Ge_5As_{35}Se_{60}$	Thermal evaporation	1.828	[2.101]
$Ge_2As_{40}Se_{58}$	Thermal evaporation	1.783	[2.101]
$Ge_{28}Sb_{12}Se_{60}$	As-deposited thermal evaporation	1.63	[2.102]
$Ge_{28}Sb_{12}Se_{60}$	As-annealed thermal evaporation	1.66	[2.102]
$Ge_{28}Sb_{12}Se_{60}$	As-deposited radio-frequency magnetron sputtering	1.59	[2.102]
$Ge_{28}Sb_{12}Se_{60}$	As-annealed radio-frequency magnetron sputtering	1.61	[2.102]

The infrared (long-wavelength) cutoff is determined by the multiphonon absorption edge, which is governed by vibrational resonances of the atomic network and which in turn depends on atomic mass and bond strength [2.101]. For some chalcogenide glasses with larger atoms and weaker bonds, the infrared cutoff shifts to longer wavelengths. For example, Katsuyama and Matsumura showed that increasing the concentration of Te in the ternary Ge–Se–Te glass shifts the multiphonon edge to longer wavelengths (see Figure 2.3-8) [2.103]. However, generally, shifting the multiphonon edge to longer wavelengths also shift the short wavelength edge to longer wavelengths. For example, in the $xAs_2S_3 + (1\text{-}x)As_2Se_3$ glass system, the substitution of S for Se shifts both the electronic edge (Figure 2.3-9(a)) and the multiphonon edge to shorter wavelengths (Figure 2.3-9(b)) [2.88].

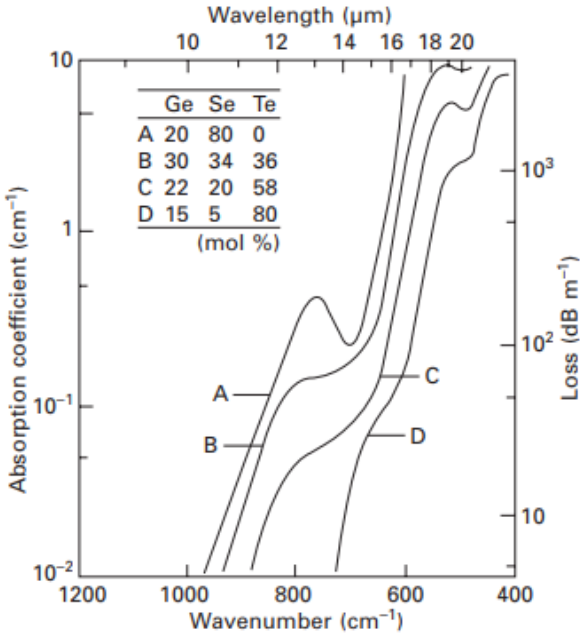


Figure 2.3- 8. Effect of increasing Te concentration on multiphonon absorption edge in Ge–Se–Te glass [2.103].

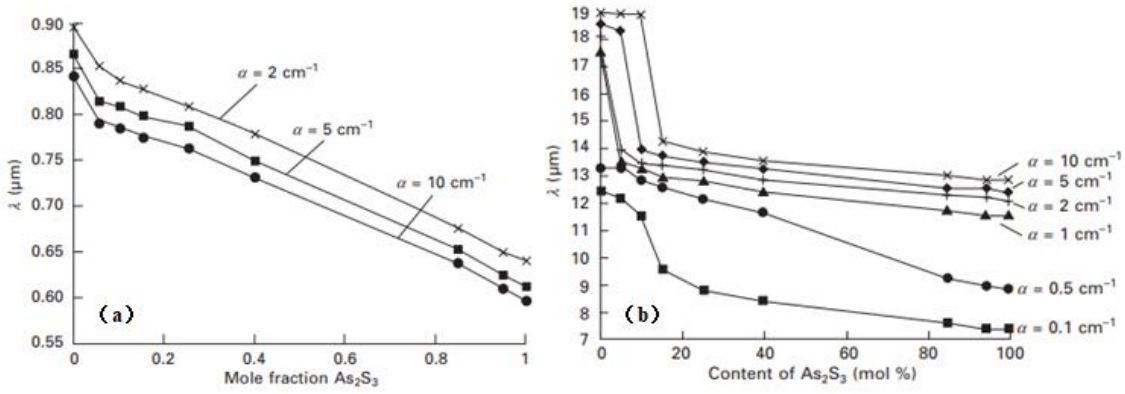


Figure 2.3- 9. (a) Spectral position of the electronic edge as a function of As_2S_3 content in the xAs_2S_3 + (1-x)As_2Se_3 glass system. The absorption coefficient corresponding to the electronic edge position is represented by the three curves, from the top down, 2, 5, and 10 cm^{-1} [2.88]; (b) Spectral position of the multiphonon edge as a function of As_2S_3 content in the xAs_2S_3 – (1-x)As_2Se_3 glass system. The absorption coefficient corresponding to the multiphonon edge position is represented by the six curves, from the top down, 10, 5, 2, 1, 0.5, and 0.1 cm^{-1} [2.88].

2.3.3.2 Impurity absorptions

The abundance of characteristic absorption peaks in the MIR region has led to the prominence of infrared spectroscopy for chemical sensing and identification. These

same absorptions are problematic for optical transmission when impurities are present in chalcogenide glasses. The wavelengths of the impurity and atmosphere absorption bands in the MIR spectral region has been summarised by Dr. Helen Rowe and Dr. Dinuka Jayasuriya in their University of Nottingham PhD theses [2.9,2.104]. Here some important impurity absorption bands across the MIR spectral band in the chalcogenide glasses relevant to the present work are listed in Table 2.3-4. Theoretically, the impurity absorptions can be eliminated so long as nucleation is fully suppressed. However, in practice, it is extremely difficult to remove: hydrogen, oxygen, and water, which form R–O and R–H bonds (where R is the chalcogen and group 4B or 5B elements) in the glass matrix [2.105]. For chalcogenide optical fibres, lots of effort has been applied to minimize the effect of the impurity absorption. For example, Sanghera *et al.* [2.106] have shown that purification of precursor chemicals can significantly reduce the presence of extrinsic losses. Their fibre attenuation spectra are shown in Figure 2.3-10 for As–S–Se fibres.

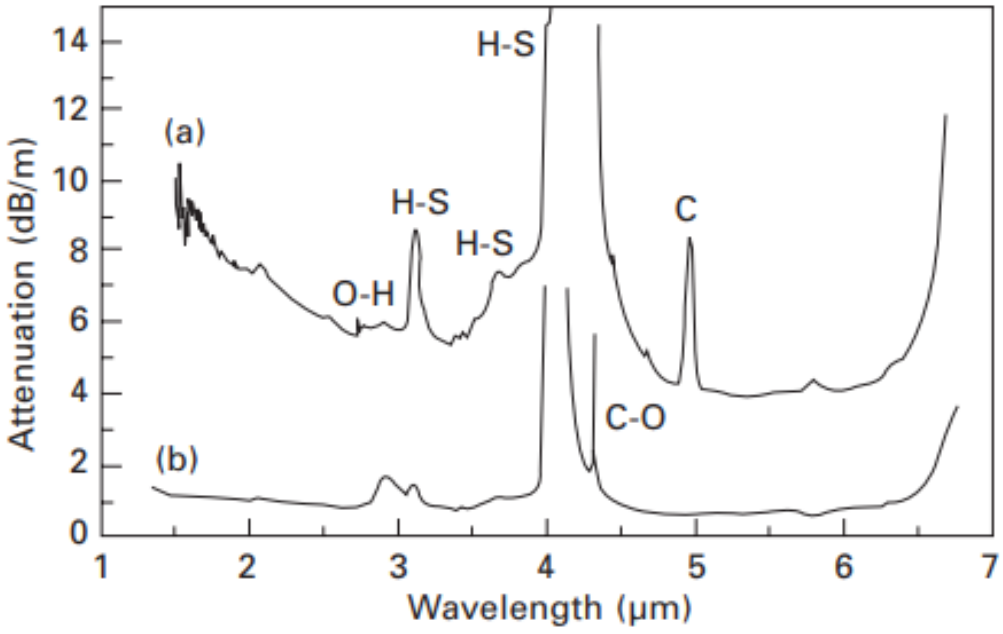


Figure 2.3- 10. Optical attenuation spectra of As–S–Se fibres fabricated with commercially available chemical precursors, curve (a), and purified chemical precursors, curve (b), which demonstrates a reduction in extrinsic impurity absorption and minimum attenuation [2.106].

Table 2.3- 4. Impurity absorptions in some chalcogenide glasses.

Band /μm	Impurity bond	Glass composition	Reference
2.05	S-H	As-S	[2.107]
	S-H $_{(w)}$	-	[2.108]
	S-H$_{(overtone)}$	As-S	[2.109]
2.24	O-H $_{(m)}$	-	[2.108]
2.29	SO-H$_{(combination)}$	As-S	[2.109]
2.32	Se-H	As-Se	[2.107]
	Se-H $_{(w)}$	-	[2.108]
2.54	S-H$_{(combination)}$	As-S	[2.110]
2.54	S-H $_{(w)}$	-	[2.108]
2.77	$H_2O_{(molecular)}$	As-S	[2.109]
2.78	O-H $_{(m)}$	-	[2.108]
	OH	As-Se	[2.110]
2.79	H_2O	As-S/As-Se	[2.107]
2.84	OH	As-Se	[2.110]
2.86	H_2O	As-S/As-Se	[2.107]
2.91	SO-H$_{(fundamental)}$	As-S	[2.109]
2.92	OH^-	As-Se	[2.107]
	SeO-H	As-Se	[2.110]
	O-H	Ge-As-Se	[2.109]
2.93	O-H $_{(vs)}$	-	[2.108]
3.11	S-H	As-S	[2.107]
	S-H $_{(m)}$	-	[2.108]
	S-H$_{(combination)}$	As-S	[2.109]
3.41	C-H $_{(m)}$	-	[2.108]
3.5	C-H $_{(m)}$	-	[2.108]
3.53	Se-H	As-Se	[2.107]
	Se-H $_{(w)}$	-	[2.108]
	Se-H	As-Se	[2.110]
3.65	S-H	As-S	[2.107]
3.7	S-H $_{(m)}$	-	[2.108]
3.69	S-H$_{(combination)}$	As-S	[2.109]
4.0	S-H	$As_{40}S_{60}$	[2.111]
4.01	S-H	As-Se	[2.107]
	S-H $_{(s)}$	-	[2.108]
4.03	S-H$_{(fundamental)}$	As-S	[2.109]
4.12	Se-H	As-Se	[2.107]
	Se-H $_{(m)}$	-	[2.108]
	Se-H	As-Se	[2.110]

Band /μm	Impurity bond	Glass composition	Reference
4.33	CO_2	As-S/As-Se	[2.107]
	CO_2	As_2S_3	[2.111]
4.5	Se-H	As_2S_3	[2.111]
4.57	Se-H	As-Se	[2.107]
	Se-H $_{(s)}$	-	[2.108]
	Se-H	As-Se	[2.110]
	Se-H	Ge-As-Se	[2.109]
4.65	CS_2	As-S	[2.107]
4.94	Carbon	As-S	[2.109]
4.95	Ge-H	As-S/As-Se	[2.107]
	COS	$As_{40}S_{60}$	[2.111]
5.48	AsO-H	As-S	[2.109]
6.3	O-H $_{(s)}$	-	[2.108]
	$H_2O_{(molecular)}$	As-Se	[2.110]
6.31	H_2O	As-S/As-Se	[2.107]
6.32	$H_2O_{(molecular)}$	As-S	[2.109]
6.68	CS_2	As-S	[2.107]
7.8	CSe_2	As-Se	[2.107]
	Se-H	As-Se	[2.107]
7.9	Ge-O	As-S/As-Se	[2.107]
	Oxide	Ge-As-Se	[2.109]
8.63	S-O	$As_{40}S_{60}$	[2.111]
9.27	Si-O $_{(vs)}$	-	[2.108]
9.1-9.6	Si-O	As-S/As-Se	[2.107]
10.4	Ge-O $_{(m)}$	-	[2.108]
10.6	Se-O	As_2S_3	[2.111]
10.67	Se-O	As-Se	[2.107]
	Se-O $_{(w)}$	-	[2.108]
10.77	Ge-O $_{(s)}$	-	[2.108]
10.8	AsO-H	As-S	[2.109]
11.06	Se-O	As-S/As-Se	[2.107]
	Se-O $_{(vs)}$	-	[2.108]
11.40	Ge-O $_{(vs)}$	-	[2.108]
12.40	Ge-O $_{(vs)}$	-	[2.108]
12.5	Si-O $_{(m)}$	-	[2.108]
12.8	Ge-O	As-S/As-Se	[2.107]
13.55	Sb-O $_{(m)}$	-	[2.108]
13.96	Se-O $_{(s)}$	-	[2.108]
14.53	Sb-O $_{(s)}$	-	[2.108]
17.60	Sb-O $_{(s)}$	-	[2.108]
18.18	Ge-O $_{(m)}$	-	[2.108]

2.3.3.3 Optical constants of chalcogenide bulk glasses.

The refractive index of a chalcogenide glass is essential for designing chalcogenide-glass-based optical devices. One big goal in this Project is to determine the refractive index of the chalcogenide glasses fabricated for developing MIR light sources and fibre sensors. Here, the refractive indices of some chalcogenide glass systems relevant to the present work are reviewed and discussed.

Due to the considerable degree of polarisability of the chalcogen elements, chalcogenide glasses have larger refractive indices than other glasses. Since chalcogenide glasses provide a wide range of glass compositions, the refractive index for chalcogenide glasses can vary from 2.0 for germanium sulfides [2.112] to 3.4 for glasses with large tellurium concentrations [2.113]. Different techniques, such as the minimum deviation method [2.114-2.116], prism coupling [2.117,2.118] and ellipsometry [2.34,2.119-2.122] can characterise the refractive index of bulk chalcogenide glasses. Table 2.3-5 lists some refractive index results from different bulk glass systems. From the data shown in Table 2.3-5, some general refractive index trends are indicated. From Table 2.3-5, replacing selenium in As_2Se_3 with larger, more polarisable tellurium increases refractive index, while the lighter, less polarisable sulfur decreases refractive index. Moreover, according to [2.11], the addition of germanium or silicon lowers the refractive index, while lead, tin and antimony increase it. Therefore, with the polarisability of the chalcogen elements increased, the refractive index also increases. By increasing the temperature of a chalcogenide glass, the polarisability of the glass will be either increased or decreased depending on its composition [2.123]. The increased polarisability with temperature (thermal polarisability) leads to an increased refractive index with temperature, and the reduced polarisability with temperature results in a reduced refractive index with temperature. Therefore, the polarisability of a chalcogenide glass varies with temperature, which thus leads to a change in refractive index.

Further details on the variation of refractive index with temperature will be discussed in section 2.3.3.6 and chapter 7.

Table 2.3- 5. Refractive index (*n*) of some chalcogenide glasses.

Glass composition / at. %	*n* at 1.55 μm	Reference	Glass composition / at. %	*n* at 2 μm	Reference
$As_{40}S_{60}$	2.45	[2.124]	$Ge_{14}As_4Se_{82}$	2.4747	[2.122]
$As_{40}S_{50}Se_{10}$	2.49	[2.124]	$Ge_{14}As_{20}Se_{66}$	2.5845	[2.122]
$As_{40}S_{40}Se_{20}$	2.55	[2.124]	$Ge_{14}As_{32}Se_{58}$	2.6127	[2.122]
$As_{40}S_{30}Se_{30}$	2.62	[2.124]	$Ge_{17}As_{12}Se_{71}$	2.5200	[2.122]
$As_{40}S_{20}Se_{40}$	2.70	[2.124]	$Ge_{33}As_{12}Se_{55}$	2.5398	[2.122]
$As_{40}S_{10}Se_{50}$	2.76	[2.124]	$Ge_{15}As_{15}Se_{17}Te_{53}$	3.250	[2.113]
$As_{40}Se_{60}$	2.81	[2.124]	$Ge_{15}As_{15}Se_{11}Te_{59}$	3.370	[2.113]
$As_{39}Se_{61}$	2.81	[2.124]	$Ge_{15}As_{15}Se_5Te_{65}$	3.447	[2.113]
$As_{40}Se_{55}Cu_5$	2.93	[2.124]	$Ge_{20}As_{20}Se_{14}Te_{46}$	3.200	[2.113]
$A_{s25}S_{55}Te_{20}$	2.52	[2.124]	$Ge_{15}As_{25}Se_{14}Te_{46}$	3.267	[2.113]

2.3.3.4 Chalcogenide thin films and comparison with the bulk

In the present work, the thin films, with a thickness from 20 μm to 30 μm, were fabricated by a hot-pressing technique and their optical properties were assessed. Currently, chalcogenide thin films are mostly prepared by deposition techniques, and used for integrated optical devices [2.125]. The optical properties of the thin films vary with deposition techniques, compositions and thermal history [2.126]. Therefore, a chalcogenide glass thin film usually exhibits different optical properties to its bulk form. In this subsection, the optical properties of thin films prepared by different current techniques will be discussed.

In general, chalcogenide glass thin films can be prepared by thermal evaporation (TE) [2.127], sputtering [2.128], pulsed laser deposition (PLD) [2.129], spin-coating

(SC) [2.130], or chemical vapour deposition (CVD) [2.131]. The refractive index of a chalcogenide thin film is mostly obtained using transmission-curve or prism-coupling techniques [2.132] or a grating-coupling technique [2.133].

Thermal evaporation is the simplest technique used for preparing chalcogenide thin films. The starting material is heated to evaporation by resistive heating or electron bombardment, and is collected on a substrate. Since this technique is low-cost, relatively simple, and reproducible, and capable of deposition over a large substrate area, it is attractive for good glass-forming binary chalcogenides like As-S (Se), Ge-S (Se) [2.134]. Sputtering is the most versatile technique for depositing chalcogenide thin films; this technique can be used for depositing any binary (e.g., a-As-S, a-Ge-S, a-Ge-Te) [2.135], ternary (e.g., a-Ge-Ga-S, a-Ge-Sb-Te) [2.136], multi-component (e.g., a-Ag-In-Sb-Te, a-Ge-As-Se-Te) [2.137], or rare-earth doped glasses (e.g., a-Er-Ga-La-S) [2.138]. Energetic ions from a low pressure plasma bombard and erode the target, which is subjected to a radio frequency (RF) field. The film is deposited on a substrate at a low rate. Compared to thermally evaporated films, sputtered films tend to have the same stoichiometry as the target because sputtering rates of atoms and clusters do not vary with atomic type as much as evaporation rates. Chen *et al.* prepared $Ge_{28}Sb_{12}Se_{60}$ at. % chalcogenide films using either thermal evaporation or radio-frequency (RF) magnetron sputtering techniques [2.139]. The composition difference to the bulk glass was less than 3 atomic %. The refractive indices of the films were obtained from the transmission spectra based on an envelope method developed by Swanepoel [2.140], and the optical band gaps were derived from optical absorption spectra using the Tauc plot [2.22]. Figure 2.3-11 shows the refractive index of the bulk glass, TE and RF sputtered films. A further increase in refractive index after annealing the as-deposited films (see Figure 2.3-11 and Table 2.3-6) is mainly attributed to the rearrangement of the chemical bonds that has been demonstrated in [2.141].

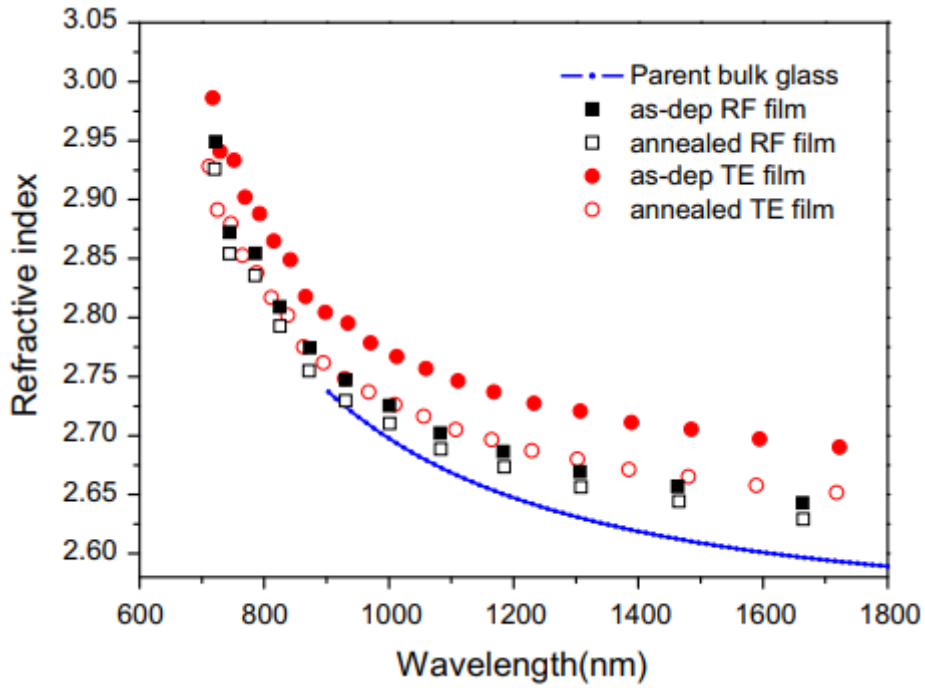


Figure 2.3- 11. Spectral dependences of refractive index of the bulk $Ge_{28}Sb_{12}Se_{60}$ at. % glass, thermally evaporated (TE) and radio-frequency (RF) sputtered films [2.139].

Table 2.3- 6. Refractive index (*n*) of evaporated chalcogenide films [2.38].

Composition/ at. %	*n* at 1.53 μm	*n* at 1.53 μm	Film status
$As_{40}S_{60}$	2.4035	2.4050	annealed
$As_{40}S_{60}$	2.3439	2.3439	not annealed
$As_{40}Se_{60}$	2.8318	2.8318	annealed
$As_{40}Se_{60}$	2.7842	2.7707	not annealed
$As_{32}S_{34}Se_{34}$	2.5400	2.5414	annealed
$As_{32}S_{34}Se_{34}$	2.5050	2.5041	not annealed
$As_{24}S_{38}Se_{38}$	2.4666	2.4650	annealed
$As_{24}S_{38}Se_{38}$	2.4445	2.4445	not annealed
$As_{18}S_{41}Se_{41}$	2.3764	2.3745	annealed
$As_{18}S_{41}Se_{41}$	2.3691	2.3673	not annealed

Pulsed-laser deposition (PLD) [2.142], as a relatively new physical deposition technique for the deposition of a vast range of materials including chalcogenide thin films, is able to produce high-quality films that do apparently not require annealing. The stoichiometry of the target is then well preserved in the deposited film even for multi-component or rare-earth doped compositions. Chalcogenide films deposited by PLD can often be obtained containing structural units similar to those in the

corresponding bulk glass (target material) (see Figure 2.3-12) [2.143]. PLD is a complex deposition technique with many technological aspects reviewed in detail elsewhere [2.142,2.143-2.145]. However, since it uses high energy (~ 1 J), low repetition rate (10-100 Hz) nanosecond laser pulses, PLD can lead to high scattering losses in the thin films. To overcome this problem, an ultrafast PLD process, which employs short (less than 50 ps), low-energy (~μJ), high repetition rate (10^5-10^8 Hz) pulse trains, was developed [2.146,2.147] and it is possible to produce high optical quality $As_{40}S_{60}$ at. % chalcogenide thin films [2.148]. In general, annealing removes stress and strain in the PLD thin films and hence produces a more relaxed glass structure. The effect of annealing at different temperatures on the refractive index of a PLD thin film is shown in Figure 2.3-13 [2.149]. PLD has been used in the deposition of a variety of chalcogenide thin films, for example sulfides (As-S [2.148], Ge-S [2.150], Ge-Ga-S [2.151], Ga-La-S [2.152], Ge-Ga-S-Cs-I [2.153]), selenides (As-Se [2.154], Ge-Se [2.155], Ge-Ga-Se [2.156]) and telluride (Ge-Sb-Te [2.157]) films. PLD also permits the deposition of rare-earth doped chalcogenide amorphous films, which exhibit near-infrared PL, such as Ge-Ga-Sb-S:Dy_2S_3 [2.158], Ge-Ga-Se:Er_2S_3 [2.159] and Ge-Ga-S-Cs-I:Pr_2S_3 [2.151].

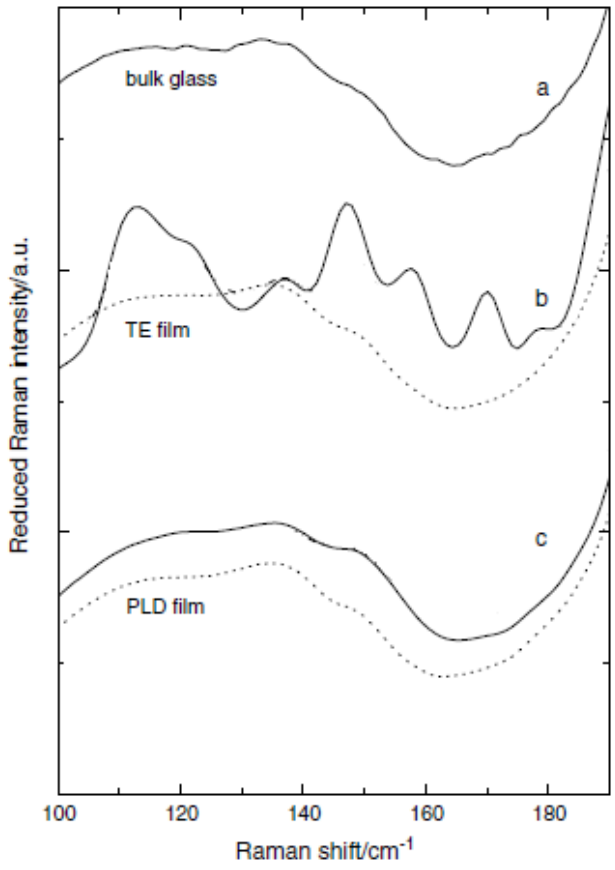


Figure 2.3- 12. Raman spectra (region 100–180 cm^{-1}) of (a) bulk $As_{40}Se_{60}$ at. % glass, (b) as-deposited, and annealed thermally evaporated (TE) As-Se thin film and (c) as-deposited, and annealed pulse-laser deposited (PLD) As–Se thin film (full line: as-deposited films; dotted line: annealed films) [2.143].

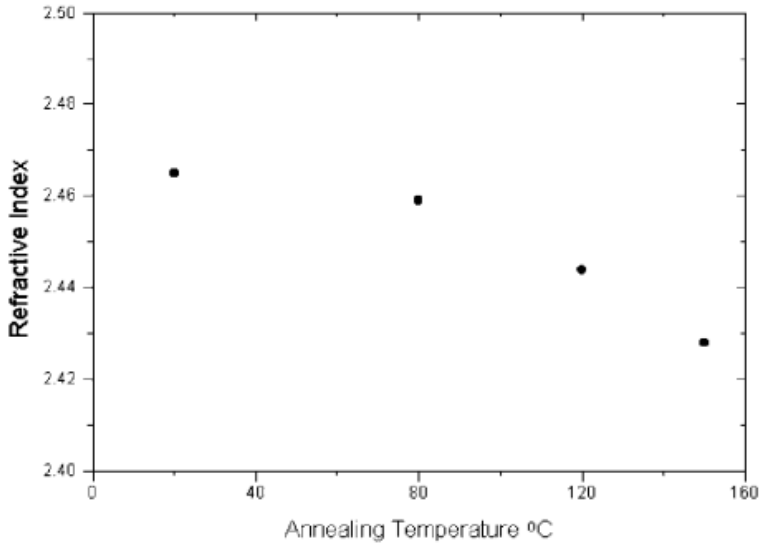


Figure 2.3- 13. Effect of annealing on the refractive index at a wavelength of 810 nm of an $As_{40}S_{60}$ at. % film prepared by PLD [2.149].

Additionally, chalcogenide thin films can also be prepared by spin-coating and chemical vapour deposition, which will not be discussed in detail in this literature review. Spin-coating (SC) is a solution-based process developed for low-cost deposition of thin films of materials ranging from polymers (as organic photoresists) to functional inorganic films including amorphous [2.160] and crystalline chalcogenides [2.161]. Chemical vapour deposition (CVD) is an important technique, particularly promising for conformal deposition of chalcogenide thin films into embedded 1D, 2D and 3D structures [2.162]. CVD is a method where gaseous precursors react either in the gas phase or at the substrate–gas interface, producing a thin film on the substrate.

In the present work, a hot-pressing technique was developed for fabricating a thicker chalcogenide glass thin film (compared to the as-deposited thin films) and its optical properties were charaterised as discussed in chapter 6.

2.3.3.5 Photoinduced changes in chalcogenide glasses

Chalcogenide glasses exhibit photoinduced phenomena, including photocrystallisation, photopolymerisation, photodecomposition, photocontraction, photovaparozation, photodissolution and light-induced change in local atomic configuration [2.163,2.164]. These changes are accompanied by changes in optical constants, such as changes in the band gap, refractive index and optical absorption coefficient. Depending on whether the bandgap moves to longer or shorter wavelength, the photoinduced changes are respectively defined as photodarkening or photobleaching.

Figure 2.3-14(a) shows that the refractive index of Ge-Sb-S thin films prepared by TE and spin-coating deposition increases after exposure to UV lamp light (main peak wavelength 365 nm, 156 mW cm^2) for 60 mins [2.165]. The refractive index of these two thin films was measured by spectroscopic ellipsometry. A light induced change in the optical band gap was also observed, as shown in Figure 2.3-14(b). These

light-induced changes in chalcogenide glasses are attributed to the structural flexibility of the glass and also attributed to their high-lying lone-pair p states in the valence band. Annealing chalcogenide glasses can also affect the photoinduced changes (see Figures 2.3-14(a) and 2.3-14(b)).

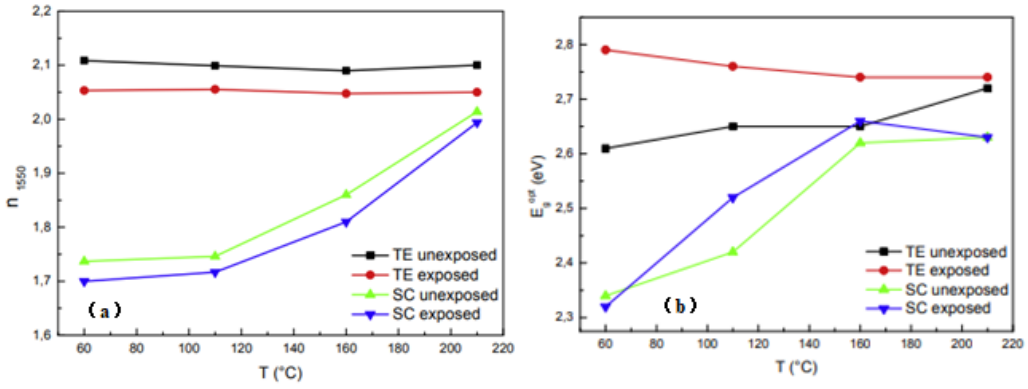


Figure 2.3- 14. (a) The refractive index of studied spin-coated (SC) a thermally evaporated (TE) $Ge_{20}Sb_5S_{75}$ at. % thin films obtained from spectroscopic ellipsometry in dependence on annealing temperature; (b) The optical bandgaps (E_g) of spin-coated (SC) a thermally evaporated (TE) $Ge_{20}Sb_5S_{75}$ at. % thin films obtained from spectroscopic ellipsometry and their dependence on annealing temperature [2.165].

2.3.3.6 Thermo-optic coefficient (dn/dT)

The variation in the refractive index of a chalcogenide glass with a change in temperature is described as thermo-optic behaviour (thermo-optic coefficient (dn/dT)), and is crucial for IR optical design [2.166]. The refractive index change with temperature is attributed to the thermal excitation of phonons (and electrons in some cases), and can be either positive or negative in sign depending on the composition of the glass. Prod'homme *et al.* proposed a thermal Lorentz-Lorenz model to describe the thermo-optic coefficient [2.167]. In this model, the thermo-optic coefficient is related to the thermal polarisability coefficient and thermal expansion coefficient. This model will be further discussed in detail in chapter 7. Here, some published and commercial thermo-optic coefficient data for the chalcogenide glasses investigated in the present work are reviewed.

Table 2.3-7 summarises the dn/dT data of some chalcogenide glasses. Composition variation in chalcogenide glasses leads to different dn/dT values as shown in Table 2.3-7. Recently, the composition dependence of thermo-optic coefficient in Ge-As-Se chalcogenide glasses was investigated by Wang *et al.* using an IR variable angle spectroscopic ellipsometer (IR-VASE, J.A. Woollam Co. Inc., Lincoln, NE) equipped with a temperature controllable sample chamber [2.12]. Thermo-optic coefficients in the Ge-As-Se glass system increased with increasing the mean coordination number, as shown in Figure 2.3-15(a). Moreover, thermo-optic coefficient varies at different wavelengths (see Figure 2.3-15(b)). More details on the dn/dT behaviour of chalcogenide glasses will be provided in chapter 7, where the temperature effect on the optical properties of some chalcogenide glasses ($As_{40}Se_{60}$ at. %, $Ge_{20}Sb_{10}Se_{70}$ at. %, $Ge_{20}Sb_{10}Se_{67}S_3$ at. % and $Ge_{16}As_{24}Se_{15.5}Te_{44.5}$ at. %), especially their thermo-optic coefficients, was investigated by using the minimum deviation method and a novel method developed in the present work.

Table 2.3- 7. Thermo-optic coefficients (dn/dT) of some chalcogenide glasses.

Composition / at. %	dn/dT (at a wavelength of 4.515 μm)	Ref.	Composition / at. %	dn/dT (at a wavelength of 4.515 μm)	Ref.
$As_{40}Se_{60}$	31.7	[2.123]	$Ge_{25}As_{26.25}Se_{48.75}$	63.2	[2.123]
$Ge_5As_{38}Se_{57}$	30.2	[2.123]	$As_{30}Se_{70}$	-43.8	[2.123]
$Ge_{10}As_{36}Se_{54}$	24.7	[2.123]	$Ge_5As_{28.5}Se_{66.5}$	-6.8	[2.123]
$Ge_{15}As_{34}Se_{51}$	59.2	[2.123]	$Ge_{10}As_{27}Se_{63}$	25.2	[2.123]
$Ge_{20}As_{32}Se_{48}$	58.7	[2.123]	$Ge_{15}As_{25.5}Se_{59.5}$	32.7	[2.123]
$As_{35}Se_{65}$	-6.3	[2.123]	$Ge_{20}As_{24}Se_{56}$	38.2	[2.123]
$Ge_5As_{33.25}Se_{61.75}$	29.9	[2.123]	$Ge_{25}As_{22.5}Se_{52.5}$	53.7	[2.123]
$Ge_{10}As_{31.5}Se_{58.5}$	18.2	[2.123]	$Ge_{10}As_{40}Se_{50}$	22.7	[2.168]
$Ge_{15}As_{29.75}Se_{55..25}$	21.0	[2.123]	$Ge_{28}Sb_{12}Se_{60}$	64.7	[2.169]
$Ge_{20}As_{28}Se_{52}$	36.5	[2.123]	$As_{40}Se_{60}$	35.2	[2.170]

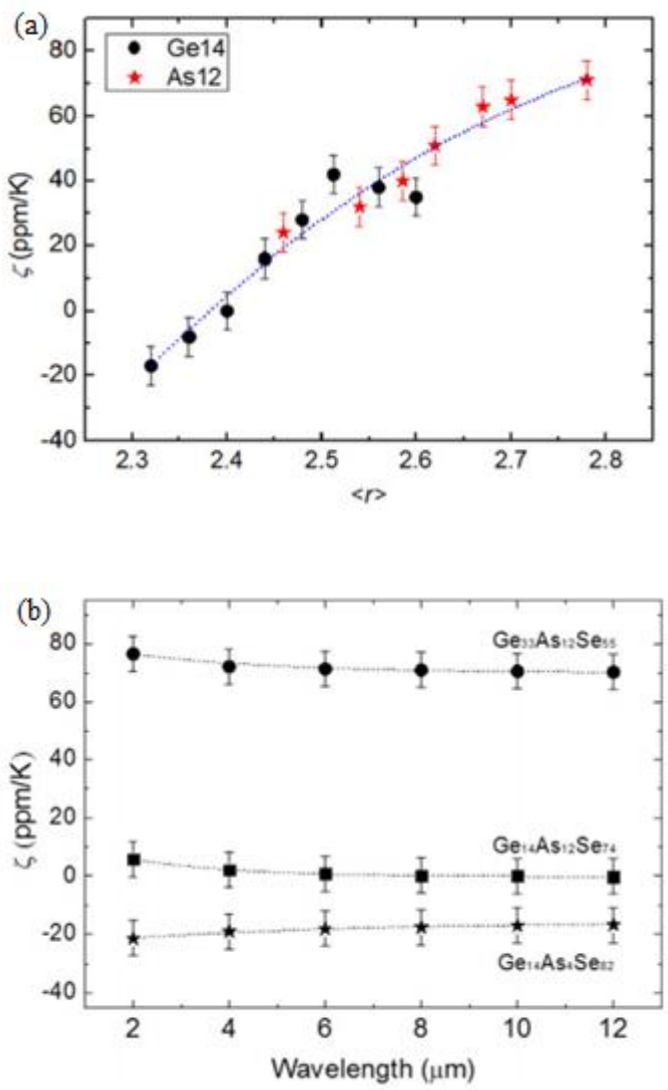


Figure 2.3- 15. (a) The thermo-optic coefficient as a function of the mean coordination number <r> in $Ge_{14}As_xSe_{86-x}$ at. % and $Ge_xAs_{12}Se_{88-x}$ at. % glasses; (b) Plot of thermo-optic coefficient against wavelength for $Ge_{33}As_{12}Se_{55}$, $Ge_{14}As_{12}Se_{74}$, and $Ge_{14}As_4Se_{82}$ at. % glasses. [2.12]

2.4 Applications of chalcogenide glasses

The applications of chalcogenide glasses can conveniently be divided into two groups, which are passive applications and active applications. Active applications modify the light propagating through a fibre, other than that due to scattering, absorption and reflection associated with the fibre [2.17]. Passive applications utilize chalcogenide fibres as a light conduit from one location to another one without

changing the optical properties, other than that due to scattering, absorption and reflection associated with the fibre [2.17].

2.4.1 Active applications

Since the MIR wavelength range corresponds to the characteristic molecular absorption or vibrational energy bands of most gases, liquids, and solid phases, lots of studies have been aiming at developing active MIR light sources based on chalcogenide glass fibres. One approach is to utilise the infrared nonlinear properties of chalcogenide fibres to achieve supercontiuum generation (SCG) [2.20,2.171-2.174] and chalcogenide glass Raman fibre lasers [2.175-2.178]. The first SCG in chalcogenide fibres has focused on $As_{40}S_{60}$ at. % fibre, where a spectrum from 2 to 4.6 μm has been reported in an $As_{40}S_{60}$ at. % step-index fibre by pumping in the normal dispersion regime [2.179]. After this study, lots of effort has been paid to develop the broadest MIR supercontiuum [2.170-2.174]. A broad SCG based on chalcogenide fibres was demonstrated by Petersen *et al.* [2.174]. By launching intense short pulses (with a central wavelength of 6.3 μm) into an ultra-high numerical-aperture chalcogenide fibre (core: As-Se, cladding Ge-As-Se), a mid-infrared supercontiuum spanning 1.4 μm to 13.3 μm was generated. (see Figure 2.4-1) [2.174].

Another approach towards MIR light sources has been to use chalcogenide glasses as hosts for rare-earth ions [2.180-2.185], or nanoscale doped crystals. Despite lots of research on rare-earth-doped chalcogenide glass fibres since the 1990s, there has been only limited success to date [2.186,2.187]. In order to achieve MIR fibre lasing based on chalcogenide fibres, a better understanding on the local rare earth ion environment to obviate unwanted non-radiative decay, lower optical loss in rare-earth-doped chalcogenide fibres and a better understanding of the impact of host chalcogenide glass native defects on the doped rare-earth-ion fluorescence are required [2.186].

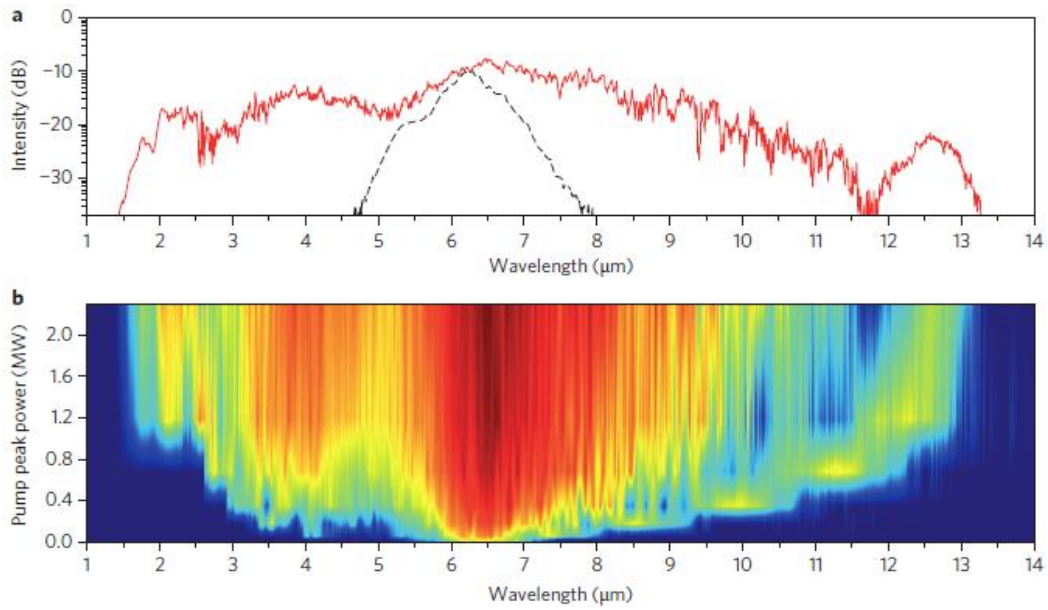


Figure 2.4- 1. Experimental SCG results with the pump centred at 6.3 μm. a, Input pump spectrum (dashed line) and spectral profile at maximum pump power (solid line), showing a broad, flat supercontinuum (1.64–11.38 μm at –20 dB) followed by a strong spectral peak extending the spectrum all the way to 13.3 μm. b, Spectral evolution with increasing pump peak power, showing the gradual redshift of a distinct spectral peak at the long-wavelength edge and the corresponding formation and blueshift of dispersive waves [2.20].

2.4.2 Passive applications

Chalcogenide glass fibres can transmit to longer wavelengths in the infrared than silica and fluoride glasses, which makes them suitable for MIR passive applications, such as laser power delivery [2.188-2.190], chemical sensing [2.191-2.196], temperature monitoring [2.197], thermal imaging [2.198-2.201], near field microscopy [2.202,2.203] and fibre-based multimode beam combiners [2.204].

For **laser power delivery**, sulfide fibres have been proven to be tolerant to a high power CO laser operating at 5.4 μm with a power density of ~ 125 kW/cm^2 without damage [2.188]. Later, Busse *et al.* demonstrated that tellurite fibres could tolerate a high power CO laser operating at 10.6 μm with a power density of ~ 54 kW/cm^2 without damage [2.189]. Recently, Sincore *et al.* demonstrated mechanically robust and low loss single-mode arsenic sulfide fibres with anti-reflection coatings for delivering high power mid-infrared sources [2.190]. These fibres were able to

transmit a laser power of 10.3 W at a wavelength of 2053 nm. This study indicates that improving the anti-reflection coatings and using a high beam quality mid-infrared source, chalcogenide fibres can reliably deliver ≥ 10 W in a single mode, potentially out to 6.5 μm.

Chalcogenide fibres are extremely suitable for **chemical sensing** because most molecular species vibrate in the MIR region. Different sensing techniques, including evanescent/ATR (attenuated total reflectance) [2.191-2.193], diffuse reflectance and absorption spectroscopy [2.194-2.196], have been applied to detect many species such as aqueous, non-aqueous, toxic liquids and solids [2.191-2.196].

In 1992, the application of **temperature monitoring** using As-S fibres with a Telflon cladding was reported by Ueda *et al.* [2.197]. The first application of chalcogenide fibres for **thermal imaging** was demonstrated by Kapany and Simms [2.198]. After this demonstration, lots of studies on thermal imaging using chalcogenide fibres were reported. For example, the use of a 1000 chalcogenide fibre bundle for collecting the image of an electric iron at 773 K was demonstrated by Saito *et al.* [2.199]. Moreover, Nishii *et al.* reported that the thermal imaging of an operating integrated circuit in the 3 to 5.4 μm region was collected by a flexible fibre bundle containing 8400 Telfon coated fibres, and then was recorded using an InSb detector [2.200]. Gibson *et al.* [2.201] reported a convenient method for fabricating novel infrared layered chalcogenide glass lenses (see Figure 2.4-2(a)) for thermal imaging. The thermal imaging of a man obtained using these multi-layered lenses, with an uncooled LWIR imaging core, is shown in Figure 2.4-2(b).

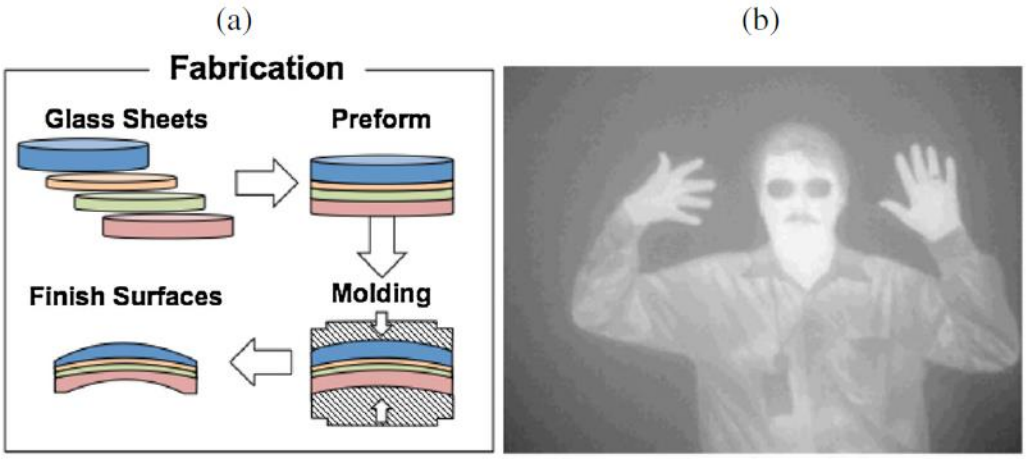


Figure 2.4- 2. (a) Layered optical design and fabrication process overview of a chalcogenide glass based lens. (b) Thermal image obtained using the multi-layered lens with an uncooled mid-infrared imaging core. [2.201]

For the application of chalcogenide fibres in **near field spectroscopy**, the Naval Research Laboratory (NRL) reported that high quality singlemode and multimode chalcogenide fibres could be used to demonstrate about 20 nm topographic resolution and about 200 nm spectral resolution for polycrystalline diamond [2.202], pancreatic cells [2.203], biofilms and semiconductor samples.

Multimode fibre combiners allow for the incoherent power and spectral combination of multiple light sources. A 7 × 1 infrared fibre optic multimode combiner based on an arsenic sulfide infrared fibre was fabricated by Gattass *et al.* [2.204] with transmission over a wide range of infrared wavelengths (see Figure 2.4-3(a)). Multiple sources with different wavelengths have also been successfully combined with a multimode fibre combiner by coupling two distinct quantum cascade laser sources and a laser diode (see Figure 2.4-3(b)).

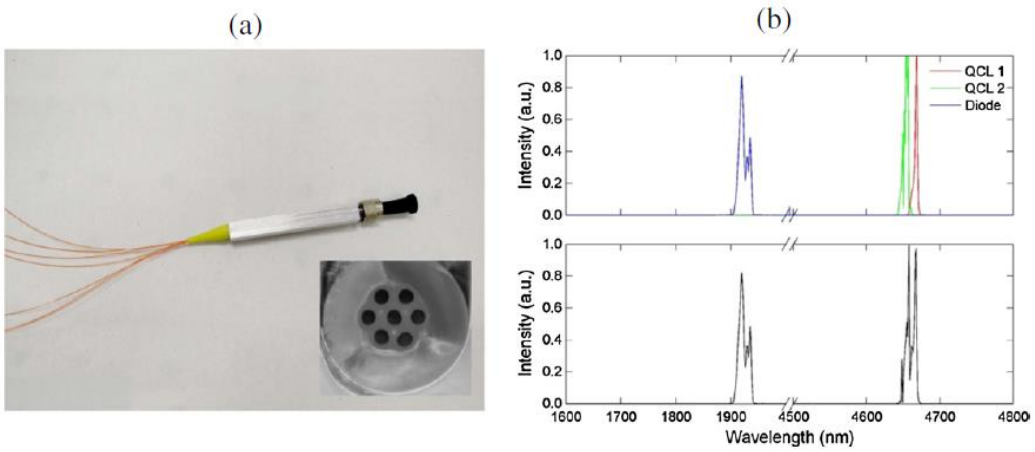


Figure 2.4- 3. (a) 7 × 1 infrared fibre optic multimode combiner based on an arsenic sulfide infrared fibre and (b) the spectral output of the sources separately (top) and combined (bottom) [2.204].

2.5 Methods for determination of the optical properties of chalcogenide glasses

In this section, some techniques previously developed for determining the refractive index of some bulk chalcogenide glasses or chalcogenide thin films will be discussed. The advantages and disadvantages of these refractive index techniques will also be covered. Since the principal goal of this Project is to develop a technique to determine the refractive index of a chalcogenide glass in the MIR region, this background study will provide a solid foundation for this Project.

2.5.1 Minimum deviation method

If a light beam travels from the air through an isotropic solid material in the form of a prism or crystal, the refractive index n is given by:

$$n = \frac{\sin[(\alpha+\theta)/2]}{\sin(\alpha/2)} \qquad (2.4)$$

where α is the apex angle of prism, and θ is the minimum deviation angle. The definitions of the apex angle and the minimum deviation angle will be given in section 4.1.

The minimum deviation method has been proven to determine the refractive index of materials in the range from 1.3 to 2.0 with an accuracy of 1×10^{-6} [2.205-2.207], and with the accuracy of measurement of both α and θ less than 1". This technique proved to be suitable for measuring the refractive index of PbTe [2.208], PbSe [2.208], Ge-As-Se [2.209, 2.210], Ge-As-S [2.211], Ga-Ge-Sb-Se [2.212], As-Se [2.213], and Ge-As-Se-Te [2.213] at certain wavelengths. For example, Zhang *et al.* used the minimum deviation method to determine the refractive indices of $Ge_{22}As_{20}Se_{58}$ at. % and $Ge_{20}Sb_{15}Se_{65}$ at. %, which were measured at ambient temperature to be 2.4944 and 2.5842 at a wavelength of 10 μm, respectively, with an error of ±0.00015 [2.209].

Based on the minimum deviation method, a commercial M^3 minimum deviation refractometer (M^3 Measurement System, Inc.) was developed to measure the refractive index of a chalcogenide glass at the mid-infrared wavelengths [2.214-2.216]. For instance, Novak *et al.* ultilised the M^3 minimum deviation refractometer to obtain the refractive index of As-Se at wavelengths of 2, 4, 6, 8, 10 and 12 μm before and after a thermal moulding (See Figure 2.5-1) [2.216]. This technique can yield refractive index results accurate to the 4^{th} decimal place at room temperature if a prism has a sufficiently flat surface.

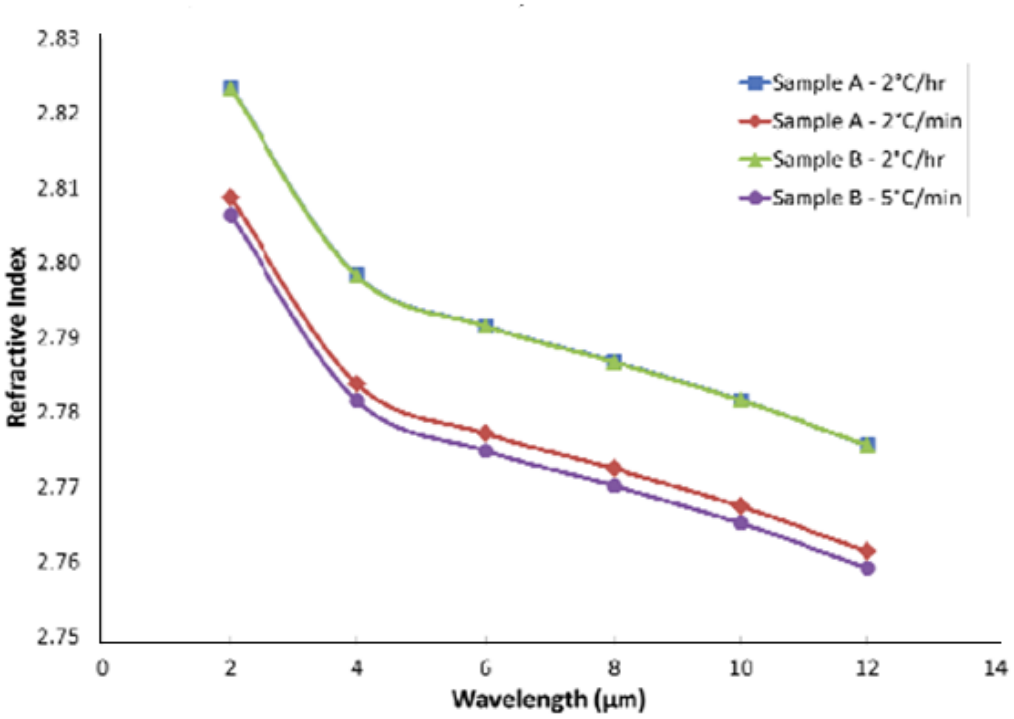


Figure 2.5- 1. The refractive index of $As_{40}Se_{60}$ at. % at wavelengths of 2, 4, 6, 8, 10 and 12 µm before and after a thermal moulding [2.216].

2.5.2 Prism coupler

The prism coupling technique has been utilized to measure the refractive index in the near- and mid-IR spectral region of chalcogenide glasses in bulk and thin film form. The prism coupling technique essentially measures a laser beam reflected off of a prism base which is in close contact with the sample to be measured. For the bulk material characterisation, the refractive index is determined by measuring the critical angle at which total internal reflection occurs at the interface between the prism and sample. For the thin film characterisation, the laser beam tunnels across the narrow air gap between the prism and the film at certain discrete values of the incident angles to become a guided optical propagation mode within the thin film; this is accompanied by a drop in the intensity of light at each coupling angle. The refractive index of a thin film can be obtained by analysing the locations of the intensity dips and the width between the dips [2.117].

A commercial system (Metricon model 2010) has been modified with additional laser sources, detectors, and a GaP prism to allow the measurement of refractive index dispersion over the 1.5–10.6 μm range (see Figure 2.5-2). The instrumental error was found to be ±0.001 refractive index units across the entire wavelength region examined. Carlie *et al.* [2.117] provided the refractive index measurement of $As_{40}Se_{60}$ at. % bulk glasses and the comparison of the refractive indices of as-deposited and annealed $As_{40}Se_{60}$ at. % films with those of the parent bulk glasses in their paper. Qiao *et al.* [2.118] used this method to measure the refractive indices of several chalcogenide glass families (see Table 2.5-1) over the 1.5–10.6 μm range with an accuracy of $\pm 1 \times 10^{-3}$. In 2016, Gleason *et al.* [2.123] ultilised a modified Metricon Inc. prism coupler (2010M) to measure the refractive index and the thermo-optic coefficient of chalcogenide glasses. In this work, this technique yielded the refractive index of a chalcogenide glass within an error of ± 0.0005.

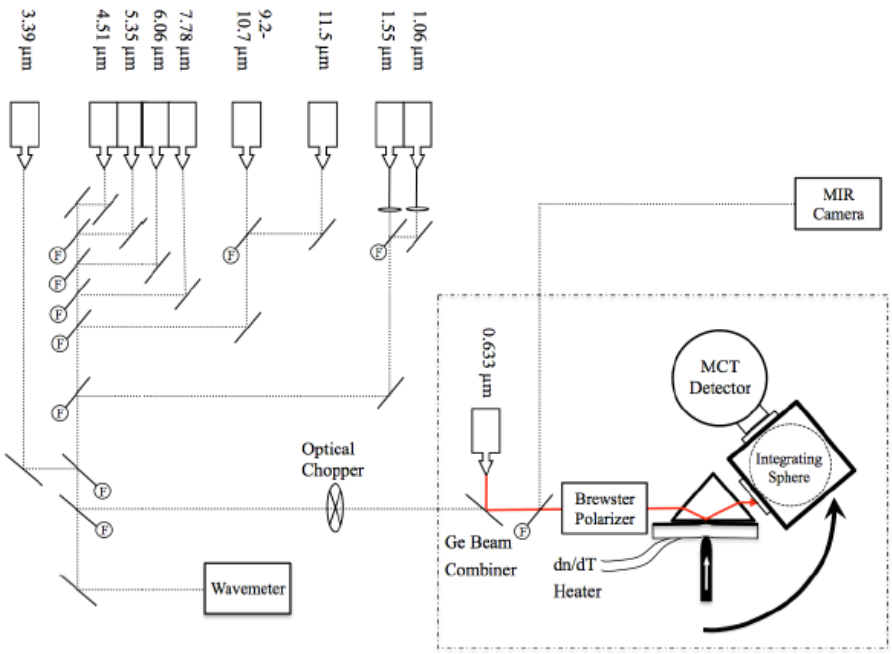


Figure 2.5- 2. The modified Metricon model 2010 prism coupling system with a wavelength range spanning the visible, near-infrared and mid-infrared wavelengths [2.118].

Table 2.5- 1. The refractive indices of several chalcogenide glass families measured by Qiao *et al.* using a prism coupler [2.118].

Glass family	Compositoin / at. %	Wavelength/ μm					
		0.633	1.547	3.391	5.351	9.294	10.591
Schott IG glass [2.217, 2.218]	$As_{12}Ge_{33}Se_{55}$	n/a	2.659	2.625	2.618	2.609	2.605
	$As_{40}Ge_{19}Se_{50}$	2.793	2.544	2.516	2.509	2.499	2.495
As-S/Ge-S [2.118]	$As_{42}Se_{58}$	2.584	2.416	2.398	2.372	2.472	2.365
	$As_{36}Ge_6S_{58}$	2.471	2.319	2.315	2.306	2.291	2.282
	$As_{36}Sb_6S_{58}$	2.665	2.465	2.454	2.445	2.427	2.417
	$Ge_{23}Sb_7S_7$	2.245	2.152	2.140	2.131	2.111	2.100
Southampton GLS glass	$Ga_{26}La_{14}S_{58}O_2$	2.457	2.360	2.340	2.325	2.276	2.252
	$Ga_{38}La_{11}S_{44}O_7$	2.319	2.241	2.224	2.204	2.131	2.091
	$Ga_{33}La_{15}S_{34}O_{18}$	2.292	2.216	2.200	2.179	2.110	2.065
	$Ga_{33}La_{10}S_{54}O_{23}$	2.442	2.343	2.326	2.311	2.263	2.239

The prism coupling method offers many advantages, including fast, high-resolution index sample characterisation, and simple data analysis. Additionally, this technique can be used to measure bulk materials as well as films, and no specific sample preparation is generally necessary making the prism coupling technique very attractive. However, oxide layer on films and bulk samples will affect the accuracy of measuring refractive index.

2.5.3 Spectroscopic ellipsometry

Spectroscopic ellipsometry (SE) is a widely used technique for characterising surfaces, interfaces and multilayer structures non-destructively and non-invasively. It provides precise measurement of optical constants of the materials over a wide wavelength range from the ultraviolet (UV) to the infrared (IR). Moreover, it can also be used to characterise composition, roughness, thickness, crystalline nature, doping concentration, electrical conductivity and other material properties. The basic principle of ellipsometry is to measure the change of polarisation upon reflection or transmission, and compare it to a model. Figure 2.5-3 shows a schematic figure of ellisopmetry measurements. Electromagnetic radiation from a light source passes

through a polariser and optical compensator and falls on the sample. After reflection by the sample, the reflected radiation will pass through a compensator and analyser placed before reaching a detector. Ellipsometry uses the information from polarised light to characterise materials; this makes ellipsometry measurements insensitive to the fluctuation of light intensity, electronic drift, or scattered light loss.

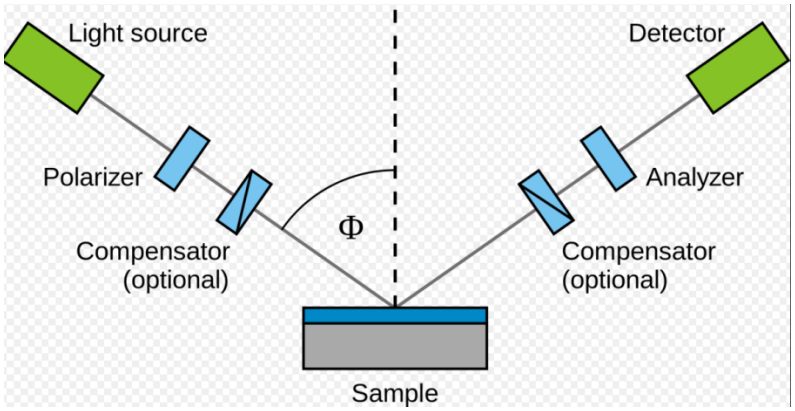


Figure 2.5- 3. Schematic setup of an ellipsometry measurement [2.219].

The first ellipsometer was demonstrated by Drude in 1887 although it was not named as an ellipsometer at that time [2.220,2.221]. The early ellipsometer was based on the extinction light method with simple instrumental configuration, and is involved in a large amount of data processing and complicated calculations, which takes a long time to collect all the data [2.222]. The first ellipsometer with an autorotation pick-up device was built by Cahan and Spanier in 1969 [2.223]. In the middle of the 1970s, Aspnes studied an ellipsometer in which the optical properties could be measured over a wider wavelength range by using a grating monochromator [2.224]. In 1990, a widely used online spectral ellipsometer was developed by the team from Pennsylvania State University [2.225]. Due to the commercialisation of spectral ellipsometers, the research based on ellipsometry dramatically increased. In the 1990s, SE was mainly used to characterise the thickness and optical properties of semiconductor materials. Until now, some companies, such as J. A. Woollam Co. Inc., Angstrom Sun Technologies Inc. and HORIBA, Ltd., supply commercial spectroscopic ellipsometers for charaterising the optical properties of materials. For

characterising the refractive index of a chalcogenide glass in the MIR region, the traditional prism measurement and prism coupling technique are limited by the fact that light sources of all wavelengths are not readily available. The spectroscopic ellipsometer is considered as an effective tool by many researchers to obtain the refractive index data of a chalcogenide bulk glass [2.12,2.34,2.119,2.226,2.228] or thin film [2.229-2.238] in the MIR region.

SE relies on fitting refractive index data to an appropriate model. The most commonly used refractive index models for chalcogenide glasses are Cauchy, Sellmeier, Drude, Tauc-Lorentz and Cody-Lorentz models, which have been discussed by Dantanarayana [2.239]. These models will be discussed in detail in chapter 5.

Bulk glass characterisation. Němec *et al.* [2.226] reported the linear refractive index of chalcogenide glasses ($As_{40}Se_{60}$ at. % and $Ge_{28}Sb_{12}Se_{60}$ at. %) by using spectroscopic ellipsometry (J A Woollam Co. Inc.) (see Figure 2.5-4). A Cauchy-like dispersion model was adopted to derive refractive indices in the NIR-MIR spectral range. In Figure 2.5-4, the curves are referred to the results obtained from the spectroscopic ellipsometer while the cross dots in Figure 2.5-4 represent the experimental data obtained from the prism coupling method. The comparison shown in Figure 2.5-4 validates the reliability of infrared spectroscopic ellipsometry. In [2.34], spectroscopic ellipsometry was used to determine the refractive index dispersion of As-Se and Ge-As-Se in MIR region using a Sellmeier model as the refractive index model, which yielded an accuracy of better that 0.1%. Dantanarayana *et al.* claimed that unlike the Cauchy model, which does not encompass the entire transparent window of a chalcogenide glass, a two-term Sellmeier model, with one resonant VIS absorption and one resonant FIR absorption, could effectively describe the refractive index dispersion of a chalcogenide glass across the whole MIR region of transparency [2.34]. Recently, Wang *et al.* [2.12]

measured the refractive indices and thermo-optic coefficients of $Ge_{14}As_xSe_{86-x}$ at. % (x = 4, 8, 12, 16, 20, 23.2, 28, 32) and $Ge_xAs_{12}Se_{88-x}$ (x = 17, 21, 23.3, 25, 27.5, 29, 33) glasses in the 2 μm–12 μm MIR range, but detailed information regarding the fitting model was not mentioned in the paper. In the study of Wang *et al.*, spectroscopic ellipsometry could yield the refractive index accurate to the 4th decimal place. Table 2.5-2 summarises some of the recent applications of spectroscopic ellipsometry to the measurement of chalcogenide glasses.

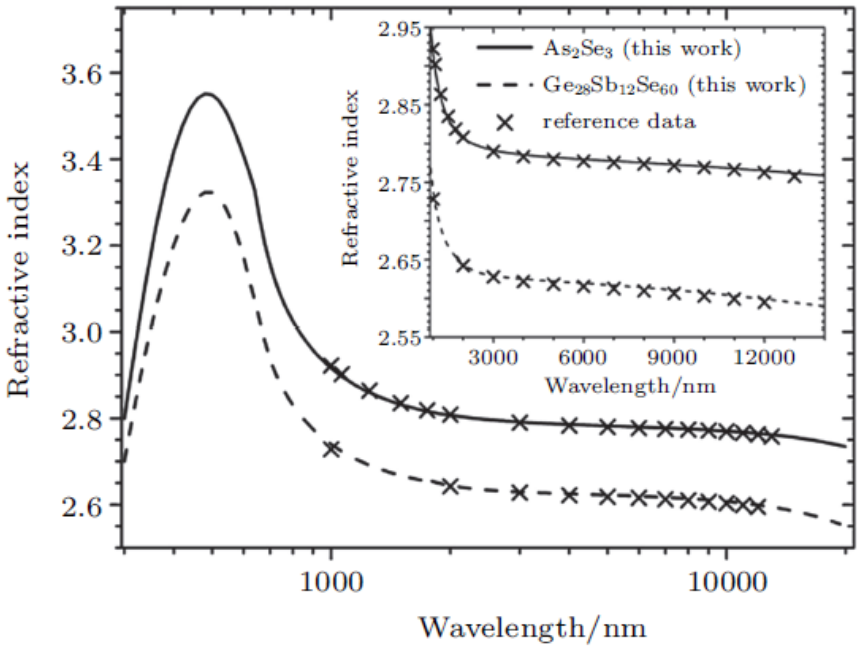


Figure 2.5- 4. Curves of refractive index dispersion of bulk $As_{40}Se_{60}$ at. % (full curves) and $Ge_{28}Sb_{12}Se_{60}$ at. % (dashed curves) glasses determined by the spectroscopic ellipsometer [2.226]. Cross dots represent the data published by the commercial producers. The inset shows the 900 nm–14000 nm spectral range in detail.

Table 2.5- 2. Recent applications of the spectroscopic ellipsometry to the refractive index measurement of chalcogenide glasses. Adapted from [2.227]

Composition/ at. %	Model	Wavelength range	Refractive index model	Ref.
Ge-As-Se	IR-VASE, J A Woollam, Lincoln, NE	1 μm–13 μm		[2.12]
Ge-As-Te	VASE, J A Woollam, Co., Inc., Lincoln, NE	0.3 μm–20 μm	Cody-Lorentz, Sellmeier	[2.228]
$As_{40}Se_{60}/Ge_{10}As_{23.4}Se_{66.6}$	VASE, J. A. Woollam, Lincoln, NE	0.4 μm–33 μm	Sellmeier	[2.34]
$As_2Se_3/Ge_{28}Sb_{12}Se_{60}$	VASE/IR-VASE	0.3 μm–2.3 μm/1.7 μm–20 μm	Cody-Lorentz	[2.226]
$As_{33}\ S_{67-x}Se_x$	VASE J A Woollam Co., Inc	0.3 μm–2.3 μm	Tauc-Lorentz	[2.119]

Thin film characterisation. In 2008, the reversible photostructural effects and metastable photorefraction in As_4Se_3 films were investigated using spectroscopic ellipsometry [2.229]. It is found that the as-deposited film has a maximum refractive index compared with the annealed and irradiated films, and significant metastable reversible photorefraction is accompanied by photodarkening. Later, Todorov *et al.* [2.230] investigated the optical properties of thin As–S–Se films. In [2.230], binary $As_xS(Se)_{100-x}$ at. % systems exhibited the maximum refractive index of 3.301 when the composition was $As_{40}Se_{60}$ at. %, and exhibited a minimum refractive index of 2.458 when when the composition was $As_{40}S_{60}$ at. %. Moreover, the photodarkening effect was observed when the films were exposed to light irradiation. In the past few years, spectroscopic ellipsometry was also applied to characterise the refractive index [2.229-2.238], optical band gap [2.234, 2.235] and annealing effect [2.238] of a chalcogenide thin film. Table 2.5-3 summarises the recent applications of the spectroscopic ellipsometry to the measurement of chalcogenide glass thin films.

Table 2.5- 3. Recent applications of the spectroscopic ellipsometry to the measurement of chalcogenide glass thin films. Adapted from [2.227].

Composition / at. %	Model	Wavelength range	Refractive index model	Ref.
As_4Se_3	VASE, J A Woollam Co., Inc.	0.5 μm–2.3 μm	-	[2.229]
$GeTe/Sb_2Te_3$	VASE, J A Woollam Co., Inc.	-	-	[2.230]
$Ge_{90}Te_{10}$	VASE, J A Woollam Co., Inc.	3 μm–12 μm	Gaussian	[2.232]
MoS_2	-	-	Tauc-Lorentz	[2.233]
$Inx(As_2Se_3)1−x$ (x = 0, 0.01, 0.05)	VASE, J A Woollam Co., Inc.	1.9 eV–4.5 eV	-	[2.234]
$ZnSe_xTe_{1−x}$	J A Woollam, M-2000	0.4 μm–1.1 μm	-	[2.235]
W doped $Ge_2Sb_2Te_5$(GSTW)	VASE, J A Woollam Co., Inc.	0.3 μm–6.2 μm	Tauc-Lorentz and Dude	[2.236]
GeTe/GaSb	V-Vase	0.275 μm–1.77 μm	Tauc-Lorentz	[2.237]
$Ge_5Te_{20}Se_{75}$	J A Woollam, M-2000	0.245 μm–1.7 μm	Cody-Lorentz, Gaussian and Tauc-Lorentz	[2.238]

The advantage of ellipsometry is the surface sensitivity which is also its weakness. A very thin contamination on a thin film will yield different results for the optical constants [2.227].

2.5.4 Envelope method

In 1976, Manifacier *et al.* [2.240] provided a method to determine the refractive index and thickness of a thin film using optical transmission spectra. This method was further developed by Swanepoel [2.241] and also found its way into commercial thin film software [2.242,2.243]. Appreciable interference fringes in the thin film transmission spectrum are required in this method (the extremes of the interference fringes T_M and T_m (shown in Figure 2.5-5) are measured to an accuracy of better than 1 %). From the transmission spectrum (see Figure 2.5-5), envelopes around the transmission maxima and minima are constructed, and T_M and T_m were considered

as to be continuous functions of wavelength λ, as shown by the envelopes in Figure 2.5-5. The envelopes around the maxima and minima are considered as $T_M(\lambda)$ and $T_m(\lambda)$ at each wavelength. Refractive index can then be calculated using $T_M(\lambda)$ and $T_m(\lambda)$.

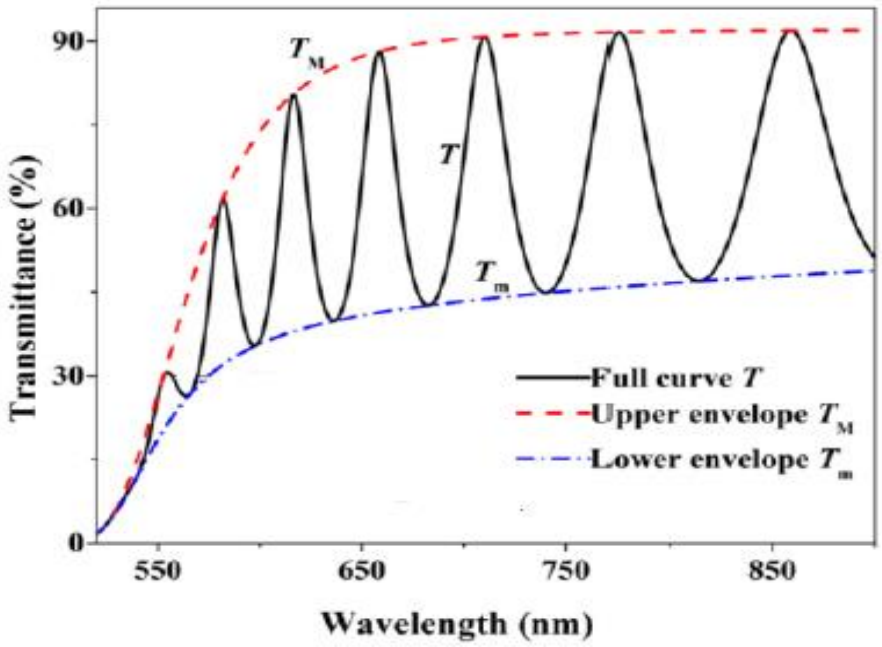


Figure 2.5- 5. Transmission curve of a 1 µm film of Si-H on a finite glass substrate. Adapted from [2.246].

In 1983, Swanepoel successfully calculated the refractive index, absorption coefficient and thickness for $\alpha - \mathrm{Si{:}H}$ film to an accuracy of the order of 1 % using the envelope method [2.241]. A year later, an improved method [2.244] was provided by him to determine the surface roughness and optical constants of $\alpha - \mathrm{Si{:}H}$ thin film from transmission envelopes. This improved method could not only determine the refractive index and thickness to an accuracy of 0.1 % but also calculate the variation of the surface of the thin film.

In 2011, Shaaban *et al.* checked the validity of the method provided by Swanepoel by determining the optical constants of different thicknesses of amorphous $Ge_{25}Cd_5Se_{70}$ at. % films [2.245]. The study showed that the refractive indices and

thicknesses of $Ge_{25}Cd_5Se_{70}$ at. % thin films were determined with an accuracy of better than 1 %. Moreover, the study showed that the refractive index could be extrapolated by a Cauchy dispersion model over the whole spectral range, which extended from 400 to 2500 nm, and that the refractive index *n* increased with the film thickness.

Recently, Jin *et al.* [2.246] proposed a tangency point method (TPM) based on the envelope method developed by Swanepoel [2.241] to derive the thickness and optical constants of chalcogenide thin films from their transmission spectra. The TPM was able to solve the problem of the abnormal value of thickness in the strong absorption region obtained by the envelope method [2.241]. The accuracy of determining the thickness and refractive index was proved to be better than the envelope method presented in [2.241]. A regional approach method (RAM) was further recently demonstrated by this group to extend the envelope method to an arbitrary wavenumber [2.247]. The thickness and refractive index of a Ge-Sb-Se thin film were determined over the wavelength range from 555-5000 nm to an accuracy of better than 0.5 % using this method.

However, a few pitfalls of the envelope method were provided by Poelman and Smet [2.248]:

1. There is no right way to construct the envelopes of interference fringes. They are usually constructed using parabolic interpolation, but this is in fact an arbitrary choice.
2. The envelopes should be constructed from the tangent points touching the transmission spectrum. Some efforts have been paid to increase the accuracy of constructing these envelopes [2.249,2.250].
3. It is difficult to construct the envelopes when absorption features, such as CO_2 absorption band, water absorption band, impurity absorption and multiphonon absorption features, fall in between interference extremes.

4. The accuracy of the method decreases with decreasing the thickness of the thin film, because the interference extremes are spaced further apart and interpolation between them becomes more difficult when decreasing the thickness of thin films.
5. The method fails (i) if the absorption in the film is so high that interference fringes are not visible and (ii) if the upper envelope $T_M(\lambda)$ and lower envelope $T_m(\lambda)$ curves coincide at longer wavelengths.

Some efforts have been undertaken to increase the accuracy of the envelope method [2.251] and to refine the method to avoid multiple solutions [2.252,2.253]. A way to minimize the error in the envelope method for determination of optical constants of a thin film was presented by Kar in 2010 [2.254]. The algorithm for the determination of optical constants of a weakly absorbing thin film from the envelope method was modified to minimise the error in the estimated values of extinction coefficient (k) as a function of wavelength. The method led to a significant improvement in the evaluated values of extinction coefficient k or absorption coefficient α over a wide spectral region, especially in the weak absorption region. The upper wavelength limit was shown to depend on the sensitivity of the measured values of T_M and T_m (the extremes of the interference fringes) to low value of k.

However, this envelope method was mostly used to determine the refractive index of a thin film in the NIR region. The fact that this method is based on a Cauchy model and cannot provide an accurate result when absorption features (CO_2 absorption band, water absorption band, impurity absorption and multiphonon absorption features) fall in between interference extremes limits the use of the envelope method to determine refractive index of chalcogenide glasses in the MIR spectral region.

2.4.5 Determine the optical constants of a thin film only from the values of wavelength at each extreme of the transmission spectrum.

In 1985, a method was provided by Swanepoel [2.255] that allowed the dispersive refractive index and thickness in the transparent region to be determined by two transmission spectra, one at normal incidence and another at oblique incidence (see Figure 2.5-6). The envelope method required that $T_M(\lambda)$ and $T_m(\lambda)$ be measured to an accuracy better than 0.5 % to yield an accuracy of 1 % in refractive index. Even small inhomogeneities have a large influence on the experimental values of T_M and T_m (the extremes of the interference fringes around maxima and minima) and can result in errors up to 100 % in determining the thickness of thin film [2.255]. Therefore, a method based only on the wavelength at which maxima and minima occur could reduce the errors caused by T_M and T_m; this yielded values of refractive index and thickness of a-Si:H thin film.

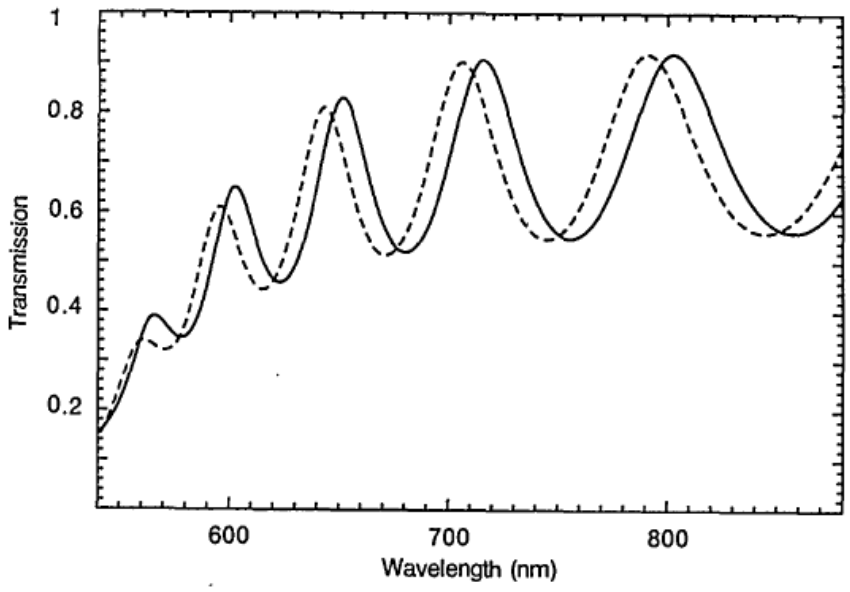


Figure 2.5- 6. Transmission spectra of a 1-μm film of a-Si:H on a glass substrate for normal incidence (solid line) and an angle of incidence of 30 °(broken line) [2.255].

Corrales *et al.* used the method in [2.255] to determine the refractive index and thickness of As_2Se_3 and Se thin films which were prepared by thermal evaporation

[2.249]. The paper showed that the method yielded values for refractive index and average thickness to an accuracy of better than 3 % [2.256].

This method is expected to be suitable for determining the refractive index of a chalcogenide glass thin film in the mid-infrared spectral region, which is a big goal in this Project, since it is not so sensitive to the absorption features compared to the envelope method. However, since the original dispersive model in this method (a Cauchy model) cannot encompass the entire chalcogenide-glass transparent window (0.4 – 33 μm) [2.34], a suitable model is required in order to extend this method into mid-infrared region. In chapter 6, the best refractive model for fitting the refractive index of a chalcogenide glass in the mid-infrared region was determined as a two-term Sellmeier model, and this method was successfully applied to the refractive index dispersion determinations for chalcogenide glass thin films.

2.5.6 Digital refractometry

In 1987, Collet [2.257] proposed a technique which was based on a simplification in Fresnel's reflection equations [2.258] at an incident angle of 45 º. Since it measured the refractive index of materials using only optical and electronic components, this technique was named as Digital Refractometry. The configuration of Digital Refractometry demonstrated by Collet is shown in Figure 2.5-7.

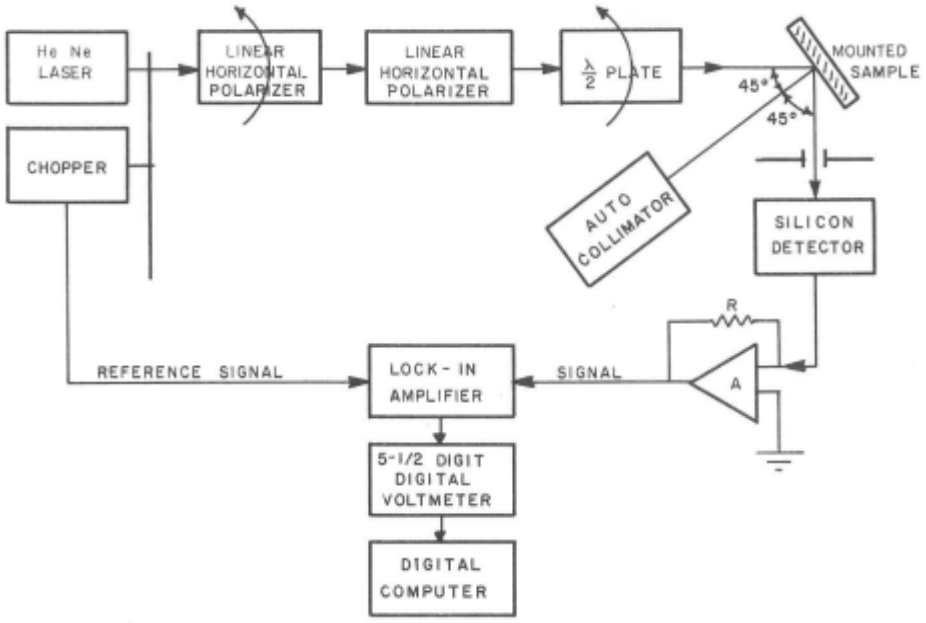


Figure 2.5- 7. Single-beam configuration for Digital Refractometry [2.257].

When a s-polarised beam (i.e the plane of polarisation is perpendicular to the plane of incidence) is incident on an optical surface of a sample with an incident angle of 45 º, the intensity of the reflected beam becomes [2.257]:

$$I_{max} = I_0(1 - sin2r)/(1 + sin2r) \qquad (2.5)$$

where I_0 is the intensity of the incident beam and r is the angle of reflection. When a p-polarised beam (i.e the plane of polarisation is now parallel to the plane of incidence) with a same intensity, I_0, is incidents on an optical surface of the same sample with the same incident angle, the intensity of the reflected beam becomes [2.257]:

$$I_{min} = I_0(1 - sin2r)^2/(1 + sin2r)^2. \qquad (2.6)$$

After obtaining I_{max} and I_{min}, the refractive index of a sample can be determined using [2.257]:

$$n^2 = (R + 1)\left[(R + 1) + \sqrt{4R}\right]/(R - 1)^2 \qquad (2.7)$$

where R is the ratio of the maximum and minimum intensities, I_{max}/I_{min}. Based on the configuration shown in Figure 2.5-7, the refractive index of a sample of BK7 glass was determined to be n = 1.5150 ± 0.0001 at a wavelength of 632 nm; this value is in very good agreement with the published value [2.259]. Since only a single surface is required and the sample can be very small, this method was expected to be an attractive alternative to the minimum deviation prism method [2.257]. However, similar to the minimum deviation method, Digital Refractometry required multiple beam sources in order to obtain refractive index data at different wavelengths.

Until now, it is still challenging to directly obtain the refractive index of chalcogenide glass fibres. However, by grinding and polishing a chalcogenide fibre with a larger diameter (≥ 300 μm) to obtain a sufficient flat surface area [2.260], it may be possible to determine the refractive index of a chalcogenide fibre using Digital Refractometry. This will be proposed as future work for this Project in chapter 8.

2.6 Section summary

In this section, the theory, structure, optical properties and recent progress in chalcogenide bulk glasses and thin films were reviewed. Moreover, some current refractive index techniques for bulk chalcogenide glasses and chalcogenide glass thin films were also discussed. Since the principal goal of this Project is to develop a technique to determine the refractive index of a chalcogenide glass in the MIR region, this background study provides a solid foundation for this Project.

References

[2.1] *ASTM Standards on Glass and Glass Products*. April 1955, prepared by ASTM Committee C14, American Society for Testing Materials.

[2.2] Wong, J. and Angell, C.A., 1976. *Glass: structure by spectroscopy* (p. 36). New York: M. Dekker.

[2.3] Rawson, H., 1980. *Properties and applications of glass*. North-Holland.

[2.4] Debenedetti, P.G. and Stillinger, F.H., 2001. Supercooled liquids and the glass transition. *Nature*, *410*, pp.259-267.

[2.5] Badrinarayanan, P., Zheng, W., Li, Q. and Simon, S.L., 2007. The glass transition temperature versus the fictive temperature. *Journal of Non-Crystalline Solids*, *353*(26), pp.2603-2612.

[2.6] Moynihan, C.T., 1994. Phenomenology of the structural relaxation process and the glass transition. In *Assignment of the glass transition*. ASTM International.

[2.7] Moynihan, C.T., Easteal, A.J., De Bolt, M.A. and Tucker, J., 1976. Dependence of the fictive temperature of glass on cooling rate. *Journal of the American Ceramic Society*, *59*(1-2), pp.12-16.

[2.8] Kolimbiris, H., 2004. *Fiber optics communications*. Saddle River: Pearson/Prentice Hall.

[2.9] Jayasuriya, D., 2018. *Towards mid-infrared fibre-optic device and systems for sensing, mapping and imaging* (Doctoral dissertation, University of Nottingham).

[2.10] Parnell, H., 2018. *Towards a Ge-Sb-Se/S hyperspectral imaging probe for early cancer diagnosis (Do*ctoral dissertation, University of Nottingham).

[2.11] Seddon, A.B., 1995. Chalcogenide glasses: a review of their preparation, properties and applications. *Journal of Non-Crystalline Solids*, *184*, pp.44-50.

[2.12] Wang, Y., Qi, S., Yang, Z., Wang, R., Yang, A. and Lucas, P., 2017. Composition dependences of refractive index and thermo-optic coefficient in Ge-As-Se chalcogenide glasses. *Journal of Non-Crystalline Solids*, *459*, pp.88-93.

[2.13] Mori, A., Ohishi, Y., Kanamori, T. and Sudo, S., 1997. Optical amplification with neodymium-doped chalcogenide glass fiber. *Applied Physics Letters*, *70*(10), pp.1230-1232.

[2.14] Tawarayama, H., Ishikawa, E., Yamanaka, K., Itoh, K., Okada, K., Aoki, H., Yanagita, H., Matsuoka, Y. and Toratani, H., 2000. Optical Amplification at 1.3 μm in a Praseodymium-Doped Sulfide-Glass Fiber. *Journal of the American Ceramic Society*, *83*(4), pp.792-796.

[2.15] Bornstein, A. and Reisfeld, R., 1982. Laser emission cross-section and threshold power for laser operation at 1077 nm and 1370 nm; chalcogenide mini-lasers doped by Nd^{3+}. *Journal of Non-Crystalline Solids*, *50*(1), pp.23-27.

[2.16] Reisfeld, R. and Bornstein, A., 1978. Fluorescence of Er^{3+} doped La_2S_3. $3Ga_2S_3$ glasses. *Journal of Non-Crystalline Solids*, *27*(1), pp.143-145.

[2.17] Aggarwal, I.D. and Sanghera, J.S., 2002. Development and applications of chalcogenide glass optical fibers at NRL. *J. Optoelectron. Adv. Mater*, *4*(3), pp.665-678.

[2.18] Sanghera, J.S., Shaw, L.B. and Aggarwal, I.D., 2002. Applications of chalcogenide glass optical fibers. *Comptes Rendus Chimie*, *5*(12), pp.873-883.

[2.19] Nishii, J., Morimoto, S., Inagawa, I., Iizuka, R., Yamashita, T. and Yamagishi, T., 1992. Recent advances and trends in chalcogenide glass fiber technology: a review. *Journal of Non-Crystalline Solids*, *140*, pp.199-208.

[2.20] Petersen, C.R., Møller, U., Kubat, I., Zhou, B., Dupont, S., Ramsay, J., Benson, T., Sujecki, S., Abdel-Moneim, N., Tang, Z., Furniss, D., Seddon, A.B. and Bang, O., 2014. Mid-infrared supercontinuum covering the 1.4–13.3 μm molecular fingerprint region using ultra-high NA chalcogenide step-index fibre. *Nature Photonics*, *8*(11), p.830.

[2.21] Boyd, R.W., 2003. *Nonlinear optics*. Elsevier.

[2.22] Zakery, A. and Elliott, S.R., 2003. Optical properties and applications of chalcogenide glasses: a review. *Journal of Non-Crystalline Solids*, *330*(1-3), pp.1-12.

[2.23] Agrawal, G.P., 2000. Nonlinear fiber optics. In *Nonlinear Science at the Dawn of the 21st Century* (pp. 195-211). Springer, Berlin, Heidelberg.

[2.24] Hurlbut, W.C., Lee, Y.S., Vodopyanov, K.L., Kuo, P.S. and Fejer, M.M., 2007. Multiphoton absorption and nonlinear refraction of GaAs in the mid-infrared. *Optics Letters*, *32*(6), pp.668-670.

[2.25] Bindra, K.S., Bookey, H.T., Kar, A.K., Wherrett, B.S., Liu, X. and Jha, A., 2001. Nonlinear optical properties of chalcogenide glasses: Observation of multiphoton absorption. *Applied Physics Letters*, *79*(13), pp.1939-1941.

[2.26] Fallahkhair, A.B., Li, K.S. and Murphy, T.E., 2008. Vector finite difference modesolver for anisotropic dielectric waveguides. *Journal of Lightwave Technology*, *26*(11), pp.1423-1431.

[2.27] Prasad, A., Zha, C.J., Wang, R.P., Smith, A., Madden, S. and Luther-Davies, B., 2008. Properties of $Ge_xAs_ySe_{1-xy}$ glasses for all-optical signal processing. *Optics Express*, *16*(4), pp.2804-2815.

[2.28] Black, R. and Pask, C., 1984. Equivalent optical waveguides. *Journal of Lightwave Technology*, *2*(3), pp.268-276.

[2.29] Cole, B., Shaw, L.B., Pureza, P.C., Mossadegh, R., Sanghera, J.S. and Aggarwal, I.D., 1999. Rare-earth doped selenide glasses and fibers for active applications in the near and mid-IR. *Journal of Non-Crystalline Solids*, *256*, pp.253-259.

[2.30] Sanghera, J.S. and Aggarwal, I.D., 1999. Active and passive chalcogenide glass optical fibers for IR applications: a review. *Journal of Non-Crystalline Solids*, *256*, pp.6-16.

[2.31] Schweizer, T., Hewak, D.W., Payne, D.N., Jensen, T. and Huber, G., 1996. Rare-earth doped chalcogenide glass laser. *Electronics Letters*, *32*(7), pp.666-667.

[2.32] Koester, C.J. and Snitzer, E., 1964. Amplification in a fiber laser. *Applied Optics*, *3*(10), pp.1182-1186.

[2.33] Price, J.H., Monro, T.M., Ebendorff-Heidepriem, H., Poletti, F., Horak, P., Finazzi, V., Leong, J.Y., Petropoulos, P., Flanagan, J.C., Brambilla, G. and Feng, X., 2007. Mid-IR supercontinuum generation from nonsilica microstructured optical fibers. *IEEE Journal of Selected Topics in Quantum Electronics*, *13*(3), pp.738-749.

[2.34] Dantanarayana, H.G., Abdel-Moneim, N., Tang, Z., Sojka, L., Sujecki, S., Furniss, D., Seddon, A.B., Kubat, I., Bang, O. and Benson, T.M., 2014. Refractive index dispersion of chalcogenide

glasses for ultra-high numerical-aperture fiber for mid-infrared supercontinuum generation. *Optical Materials Express*, *4*(7), pp.1444-1455.

[2.35] Elliott, S.R., 1986. A unified model for reversible photostructural effects in chalcogenide glasses. *Journal of Non-Crystalline Solids*, *81*(1-2), pp.71-98.

[2.36] Colomban, P. and Corset, J., 1999. Foreword to the special issue on Raman (micro) spectrometry and materials science. *Journal of Raman Spectroscopy*, *30*(10), pp.863-866.

[2.37] Weber, W.H. and Merlin, R. eds., 2013. *Raman scattering in materials science* (Vol. 42). Springer Science & Business Media.

[2.38] Richardson, K., Cardinal, T., Richardson, M., Schulte, A., Seal, S. and Kolobov, A.V., 2003. Engineering glassy chalcogenide materials for integrated optics applications. *Photo-Induced Metastability in Amorphous Semiconductors*, pp.383-402.

[2.39] Wei, W.H., Fang, L., Shen, X. and Wang, R.P., 2014. Transition threshold in $Ge_xSb_{10}Se_{90-x}$ glasses. *Journal of Applied Physics*, *115*(11), pp.113510-113510.

[2.40] Wang, T., Wei, W.H., Shen, X., Wang, R.P., Davies, B.L. and Jackson, I., 2013. Elastic transition thresholds in Ge–As (Sb)–Se glasses. *Journal of Physics D: Applied Physics*, *46*(16), p.165302.

[2.41] Wei, W.H., Wang, R.P., Shen, X., Fang, L. and Luther-Davies, B., 2013. Correlation between structural and physical properties in Ge–Sb–Se glasses. *The Journal of Physical Chemistry C*, *117*(32), pp.16571-16576.

[2.42] Zhang, W., Dai, S., Shen, X., Chen, Y., Zhao, S., Lin, C., Zhang, L. and Bai, J., 2013. Rib and strip chalcogenide waveguides based on Ge–Sb–Se radio-frequency sputtered films. *Materials Letters*, *98*, pp.42-46.

[2.43] Němec, P., Olivier, M., Baudet, E., Kalendova, A., Benda, P. and Nazabal, V., 2014. Optical properties of $(GeSe_2)_{100-x}(Sb_2Se_3)_x$ glasses in near-and middle-infrared spectral regions. *Materials Research Bulletin*, *51*, pp.176-179.

[2.44] Tanwar, N. and Saraswat, V.K., 2014. A study of kinetics of phase transformation of $Ge_{10}Se_{75}Sb_{15}$ chalcogenide glass. *Journal of Non-Crystalline Solids*, *394*, pp.1-5.

[2.45] Chen, L., Chen, F., Dai, S., Tao, G., Yan, L., Shen, X., Ma, H., Zhang, X. and Xu, Y., 2015. Third-order nonlinearity in Ge–Sb–Se glasses at mid-infrared wavelengths. *Materials Research Bulletin*, *70*, pp.204-208.

[2.46] Zhang, B., Yu, Y., Zhai, C., Qi, S., Wang, Y., Yang, A., Gai, X., Wang, R., Yang, Z. and Luther-Davies, B., 2016. High brightness 2.2–12 μm mid-infrared supercontinuum generation in a nontoxic chalcogenide step-index fiber. *Journal of the American Ceramic Society*, *99*(8), pp.2565-2568.

[2.47] Baudet, E., Cardinaud, C., Girard, A., Rinnert, E., Michel, K., Bureau, B. and Nazabal, V., 2016. Structural analysis of RF sputtered Ge-Sb-Se thin films by Raman and X-ray photoelectron spectroscopies. *Journal of Non-Crystalline Solids*, *444*, pp.64-72.

[2.48] Lee, J.H., Lee, W.H., Park, J.K., Yi, J.H., Shin, S.Y., Park, B.J., So, B., Heo, J., Choi, J.H., Kim, H.J. and Choi, Y.G., 2016. Thermal properties of ternary Ge–Sb–Se chalcogenide glass for use in molded lens applications. *Journal of Non-Crystalline Solids*, *431*, pp.41-46.

[2.49] Lee, J.H., Yi, J.H., Lee, W.H. and Choi, Y.G., 2017. Broken chemical order in Ge-Sb-Se glasses for use as infrared-transmitting lenses. *Journal of Non-Crystalline Solids*, *456*, pp.27-32.

[2.50] Ghayebloo, M., Tavoosi, M. and Rezvani, M., 2017. Compositional modification of Se-Ge-Sb chalcogenide glasses by addition of arsenic element. *Infrared Physics & Technology*, *83*, pp.62-67.

[2.51] Luo, B., Wang, Y., Sun, Y.N., Dai, S., Yang, P., Zhang, P., Wang, X., Chen, F. and Wang, R., 2017. Fabrication and characterization of bare Ge-Sb-Se chalcogenide glass fiber taper. *Infrared Physics & Technology*, *80*, pp.105-111.

[2.52] Han, X., You, C., Dai, S., Zhang, P., Wang, Y., Guo, F., Xu, D., Luo, B., Xu, P. and Wang, X., 2017. Mid-infrared supercontinuum generation in a three-hole $Ge_{20}Sb_{15}Se_{65}$ chalcogenide suspended-core fiber. *Optical Fiber Technology*, *34*, pp.74-79.

[2.53] Lin, L., Wang, G., Shen, X., Dai, S., Xu, T. and Nie, Q., 2017. Photo-induced structural changes in Ge-Sb-Se films. *Infrared Physics & Technology*, *81*, pp.59-63.

[2.54] Savage, J.A., Webber, P.J. and Pitt, A.M., 1978. An assessment of Ge-Sb-Se glasses as 8 to 12 μm infra-red optical materials. *Journal of Materials Science*, *13*(4), pp.859-864.

[2.55] Hilton, A.R. and Hayes, D.J., 1975. The interdependence of physical parameters for infrared transmitting glasses. *Journal of Non-Crystalline Solids*, *17*(3), pp.339-348.

[2.56] Frumar, M., Tichá, H., Klikorka, J. and Tomíška, P., 1973. Optical absorption in vitreous $GeSb_2Se_4$. *Journal of Non-Crystalline Solids*, *13*(1), pp.173-178.

[2.57] Rechtin, M.D., Hilton, A.R. and Hayes, D.J., 1975. Infrared transmission in Ge-Sb-Se glasses. *Journal of Electronic Materials*, *4*(2), pp.347-362.

[2.58] Bicerano, J. and Ovshinsky, S.R., 1985. Chemical bond approach to the structures of chalcogenide glasses with reversible switching properties. *Journal of Non-Crystalline Solids*, *74*(1), pp.75-84.

[2.59] Mahadevan, S., Giridhar, A. and Singh, A.K., 1983. Elastic properties of Ge-Sb-Se glasses. *Journal of non-crystalline solids*, *57*(3), pp.423-430.

[2.60] Phillips, J.C. and Thorpe, M.F., 1985. Constraint theory, vector percolation and glass formation. *Solid State Communications*, *53*(8), pp.699-702.

[2.61] Tanaka, K., 1989. Structural phase transitions in chalcogenide glasses. *Physical Review B*, *39*(2), p.1270.

[2.62] Vinod, E.M., Ramesh, K. and Sangunni, K.S., 2015. Structural transition and enhanced phase transition properties of Se doped $Ge_2Sb_2Te_5$ alloys. *Scientific Reports*, *5*, pp.8050-8050.

[2.63] Opletal, G., Drumm, D.W., Petersen, T.C., Wang, R.P. and Russo, S.P., 2015. Ab Initio Comparison of Bonding Environments and Threshold Behavior in $Ge_xAs_{10}Se_{90-x}$ and $Ge_xSb_{10}Se_{90-x}$ Glass Models. *The Journal of Physical Chemistry A*, *119*(24), pp.6421-6427.

[2.64] Wang, R., Yan, K., Yang, Z. and Luther-Davies, B., 2015. Structural and physical properties of $Ge_{11.5}As_{24}S_{64.5-x}Se_{64.5\cdot(1-x)}$ glasses. *Journal of Non-Crystalline Solids*, *427*, pp.16-19.

[2.65] Wang, R., Xu, Q., Liu, H., Sheng, Y. and Yang, X., 2018. Structure and physical properties of $Ge_{15}Sb_{20}Se_{65-x}S_x$ glasses. *Journal of the American Ceramic Society*, *101*(1), pp.201-207.

[2.66] Wang, R.P., Smith, A., Prasad, A., Choi, D.Y. and Luther-Davies, B., 2009. Raman spectra of $Ge_xAs_ySe_{1-x-y}$ glasses. *Journal of Applied Physics*, *106*(4), p.043520.

[2.67] Su, X., Wang, R., Luther-Davies, B. and Wang, L., 2013. The dependence of photosensitivity on composition for thin films of $Ge_xAs_ySe_{1-x-y}$ chalcogenide glasses. *Applied Physics A*, *113*(3), pp.575-581.

[2.68] Mei, Q., Saienga, J., Schrooten, J., Meyer, B. and Martin, S.W., 2003. Preparation and characterization of glasses in the $Ag_2S+B_2S_3+GeS_2$ system. *Journal of Non-Crystalline Solids*, *324*(3), pp.264-276.

[2.69] Julien, C., Barnier, S., Massot, M., Chbani, N., Cai, X., Loireau-Lozac'h, A.M. and Guittard, M., 1994. Raman and infrared spectroscopic studies of Ge-Ga-Ag sulphide glasses. *Materials Science and Engineering: B*, *22*(2-3), pp.191-200.

[2.70] Frumarova, B., Němec, P., Frumar, M., Oswald, J. and Vlček, M., 1999. Synthesis and optical properties of the Ge–Sb–S: $PrCl_3$ glass system. *Journal of Non-Crystalline Solids*, *256*, pp.266-270.

[2.71] Kotsalas, I.P., Papadimitriou, D., Raptis, C., Vlcek, M. and Frumar, M., 1998. Raman study of photostructural changes in amorphous $Ge_xSb_{0.4-x}S_{0.6}$. *Journal of Non-Crystalline Solids*, *226*(1-2), pp.85-91.

[2.72] Becucci, M., Bini, R., Castellucci, E., Eckert, B. and Jodl, H.J., 1997. Mode assignment of sulfur α-S_8 by polarized Raman and FTIR studies at low temperatures. *The Journal of Physical Chemistry B*, *101*(12), pp.2132-2137.

[2.73] Musgraves, J.D., Wachtel, P., Gleason, B. and Richardson, K., 2014. Raman spectroscopic analysis of the Ge–As–S chalcogenide glass-forming system. *Journal of Non-Crystalline Solids*, *386*, pp.61-66.

[2.74] Sharda, S., Sharma, N., Sharma, P. and Sharma, V., 2014. Glass transition and crystallization kinetics analysis of Sb–Se–Ge chalcogenide glasses. *Journal of Thermal Analysis and Calorimetry*, *115*(1), pp.361-366.

[2.75] Nguyen, V.Q., Sanghera, J.S., Freitas, J.A., Aggarwal, I.D. and Lloyd, I.K., 1999. Structural investigation of chalcogenide and chalcohalide glasses using Raman spectroscopy. *Journal of Non-Crystalline Solids*, *248*(2-3), pp.103-114.

[2.76] Ball, G.J. and Chamberlain, J.M., 1978. Infrared structural studies of Ge_ySe_{1-y} glasses. *Journal of Non-Crystalline Solids*, *29*(2), pp.239-248.

[2.77] Saitoh, K., Uemura, O., Usuki, T. and Kameda, Y., 1995. The structure of amorphous As-X-I (X: S, Se). *Journal of Non-Crystalline Solids*, *192*, pp.286-291.

[2.78] El-Sayed, S.M., 2003. Far-infrared studies of the amorphous $Sb_xGe_{28-x}Se_{72}$ glassy semiconductor. *Semiconductor Science and Technology*, *18*(4), p.337.

[2.79] Lisitsa, M.P., Artamonov, V.V., Berezhinskii, L.I., Bletskan, D.I. and Valakh, M., 1976. Raman Spectra of Ge and Sn Chalcogenides. *Ukrainskii Fizichnii Zhurnal*, *21*(2), pp.218-220.

[2.80] Nemanich, R.J., 1983. Low frequency Raman scattering in chalcogenide glasses. *Journal of Non-Crystalline Solids*, *59*, pp.851-854.

[2.81] Quiroga, I., Corrector, C., Bellido, F., Valázquez, J., Villares, P. and Garay, R.J., 1996. Infrared studies of a $Ge_{0.20}Sb_{0.05}Se_{0.75}$ glassy semiconductor. *Journal of Non-Crystalline Solids*, *196*, pp.183-186.

[2.82] Goyal, D.R. and Maan, A.S., 1995. Far-infrared absorption in amorphous $Sb_{15}Ge_xSe_{85-x}$ glasses. *Journal of Non-Crystalline Solids*, *183*(1-2), pp.182-185.

[2.83] Asal, R., Rivers, P.E. and Rutt, H.N., 1997. A structural study of gallium lanthanum sulphide glass bulk and thin films by X-ray absorption fine structure spectroscopy. *Journal of Physics: Condensed Matter*, *9*(29), p.6217.

[2.84] Rivero, C., Sharek, P., Li, W., Richardson, K., Schulte, A., Braunstein, G., Irwin, R., Hamel, V., Turcotte, K. and Knystautas, E., 2003. Structural analysis of chalcogenide waveguides using Rutherford backscattering spectroscopy. *Thin Solid Films*, *425*(1-2), pp.59-67.

[2.85] Seal, S., Richardson, K.A., Lopez, C., Graham, A., Verma, D.K., Saliminia, A., Galstian, T. and Villeneuve, A., 2002. Structure and chemical studies of As_2S_3 glasses used for waveguide applications. *Physics and Chemistry of Glasses*, *43*(1), pp.59-65.

[2.86] Sanghera, J. and Gibson, D., 2014. Optical properties of chalcogenide glasses and fibers. In *Chalcogenide Glasses*(pp. 113-138).

[2.87] Brady, D.J., 1998. Transmission of chalcogenide glass. In *Properties, Processing and Applications of Glass and Rare Earth-Doper Glasses for Optical Fibres*. INSPEC, The Institution of Electrical Engineers London.

[2.88] Snopatin, G.E., Shiryaev, V.S., Plotnichenko, V.G., Dianov, E.M. and Churbanov, M.F., 2009. High-purity chalcogenide glasses for fiber optics. *Inorganic Materials*, *45*(13), p.1439.

[2.89] Bureau, B., Maurugeon, S., Charpentier, F., Adam, J.L., Boussard-Pl édel, C. and Zhang, X.H., 2009. Chalcogenide glass fibers for infrared sensing and space optics. *Fiber and Integrated optics*, *28*(1), pp.65-80.

[2.90] Weaire, D. and Thorpe, M.F., 1971. Electronic properties of an amorphous solid. I. A simple tight-binding theory. *Physical Review B*, *4*(8), pp.2508-2520.

[2.91] Thorpe, M.F. and Weaire, D., 1971. Electronic properties of an amorphous solid. II. Further aspects of the theory. *Physical Review B*, *4*(10), pp.3518-3527.

[2.92] Wood, D.L. and Tauc, J., 1972. Weak absorption tails in amorphous semiconductors. *Physical Review B*, *5*, pp.3144-3151.

[2.93] Kanamori, T., Terunuma, Y., Takahashi, S. and Miyashita, T., 1984. Chalcogenide glass fibers for mid-infrared transmission. *Journal of Lightwave Technology*, *2*(5), pp.607-613.

[2.94] Zarzycki, J., 1996. *Materials Science and Technology, Glasses and Amorphous Materials* (Vol. 9). Wiley-VCH.

[2.95] Goldschmidt, D., 1984. Determination of the absorption edge of a thin film from transmission measurements. *Journal of the Optical Society of America A*, *1*, pp.275-277.

[2.96] Zakery, A., Ruan, Y. and Rode, A., 2003. Low-loss Waveguides in Ultrafast Laser-deposited As 2 S 3 Chalcogenide Films'. *Journal of the Optical Society of America B*, *20*(9), pp.1844-1852.

[2.97] Nguyen, V.Q., Sanghera, J.S., Kung, F.H., Aggarwal, I.D. and Lloyd, I.K., 1999. Effect of temperature on the absorption loss of chalcogenide glass fibers. *Applied Optics*, *38*(15), pp.3206-3213.

[2.98] Vogel, E.M., Weber, M.J. and Krol, D., 1991. Nonlinear optical phenomena in glass. *Physics and Chemistry of Glasses*, *32*(6), pp.231-254.

[2.99] Lenz, G., Zimmermann, J., Katsufuji, T., Lines, M.E., Hwang, H.Y., Spälter, S., Slusher, R.E., Cheong, S.W., Sanghera, J.S. and Aggarwal, I., 2000. Large Kerr effect in bulk Se-based chalcogenide glasses. *Optics Letters*, *25*(4), pp.254-256.

[2.100] Dai, S., Chen, F., Xu, Y., Xu, Z., Shen, X., Xu, T., Wang, R. and Ji, W., 2015. Mid-infrared optical nonlinearities of chalcogenide glasses in Ge-Sb-Se ternary system. *Optics Express*, *23*(2), pp.1300-1307.

[2.101] Tichý, L., Ticha, H., Nagels, P., Callaerts, R., Mertens, R. and Vlček, M., 1999. Optical properties of amorphous As–Se and Ge–As–Se thin films. *Materials Letters*, *39*(2), pp.122-128.

[2.102] Chen, Y., Shen, X., Wang, R., Wang, G., Dai, S., Xu, T. and Nie, Q., 2013. Optical and structural properties of Ge–Sb–Se thin films fabricated by sputtering and thermal evaporation. *Journal of Alloys and Compounds*, *548*, pp.155-160.

[2.103] Katsuyama, T. and Matsumura, H., 1989. Infrared optical fibers. *Adam Hilger Series on Optics and Optoelectronics, Bristol: Adam Hilger, 1989*.

[2.104] Rowe, H., 2008. *Infra-red transmitting optical fibres with potential use in medical diagnosis and treatment* (Doctoral dissertation, University of Nottingham).

[2.105] Nishii, J. and Yamashita, T., 1998. Chalcogenide glass-based fibers. *Infrared Fiber Optics*, pp.143-184.

[2.106] Sanghera, J.S., Nguyen, V.Q., Pureza, P.C., Miklos, R.E., Kung, F.H. and Aggarwal, I.D., 1996. Fabrication of long lengths of low-loss IR transmitting $As_{40}S_{(60-x)}Se_x$ glass fibers. *Journal of Lightwave Technology*, *14*(5), pp.743-748.

[2.107] Borisevich, V.G., Voitsekhovsky, V.V. and Scripachev, I.V., 1991. Investigation of the influence of extrinsic hydrogen on the optical properties of chalcogenide glasses in the system As-Se. *Vysokochist Vesch*, *1*, p.65.

[2.108] Lezal, D., 2003. Chalcogenide glasses-survey and progress. *Journal of Optoelectronics and Advanced Materials*, *5*(1), pp.23-34.

[2.109] Kanamori, T., Terunuma, Y., Takahashi, S. and Miyashita, T., 1985. Transmission loss characteristics of $As_{40}S_{60}$ and $As_{38}Ge_5Se_{57}$ glass unclad fibers. *Journal of Non-Crystalline Solids*, *69*(2-3), pp.231-242.

[2.110] Moynihan, C.T., Macedo, P.B., Maklad, M.S., Mohr, R.K. and Howard, R.E., 1975. Intrinsic and impurity infrared absorption in As_2Se_3 glass. *Journal of Non-Crystalline Solids*, *17*(3), pp.369-385.

[2.111] Churbanov, M.F., Snopatin, G.E., Shiryaev, V.S., Plotnichenko, V.G. and Dianov, E.M., 2011. Recent advances in preparation of high-purity glasses based on arsenic chalcogenides for fiber optics. *Journal of Non-Crystalline Solids*, *357*(11-13), pp.2352-2357.

[2.112] Wang, W.H., Dong, C. and Shek, C.H., 2004. Bulk metallic glasses. *Materials Science and Engineering: R: Reports*, *44*(2-3), pp.45-89.

[2.113] Tikhomirov, V.K., Furniss, D., Seddon, A.B., Savage, J.A., Mason, P.D., Orchard, D.A. and Lewis, K.L., 2004. Glass formation in the Te-enriched part of the quaternary Ge–As–Se–Te system and its implication for mid-infrared optical fibres. *Infrared Physics & Technology*, *45*(2), pp.115-123..

[2.114] Seddon, A.B. and Laine, M.J., 1997. Chalcogenide glasses for acousto-optic devices. II. As–Ge–Se systems. *Journal of Non-Crystalline Solids*, *213*, pp.168-173.

[2.115] Boudebs, G., Cherukulappurath, S., Guignard, M., Troles, J., Smektala, F. and Sanchez, F., 2004. Linear optical characterization of chalcogenide glasses. *Optics Communications*, *230*(4-6), pp.331-336.

[2.116] Zhang, X.H., Guimond, Y. and Bellec, Y., 2003. Production of complex chalcogenide glass optics by molding for thermal imaging. *Journal of Non-Crystalline Solids*, *326*, pp.519-523.

[2.117] Carlie, N., Anheier Jr, N.C., Qiao, H.A., Bernacki, B., Phillips, M.C., Petit, L., Musgraves, J.D. and Richardson, K., 2011. Measurement of the refractive index dispersion of As_2Se_3 bulk glass and thin films prior to and after laser irradiation and annealing using prism coupling in the near-and mid-infrared spectral range. *Review of Scientific Instruments*, *82*(5), p.053103.

[2.118] Qiao, H.A., Anheier, N.C., Musgrave, J.D., Richardson, K. and Hewak, D.W., 2011, May. Measurement of chalcogenide glass optical dispersion using a mid-infrared prism coupler. In *Window and Dome Technologies and Materials XII* (Vol. 8016, p. 80160F). International Society for Optics and Photonics.

[2.119] Orava, J., Šik, J., Wagner, T. and Frumar, M., 2008. Optical properties of $As_{33}S_{67-x}Se_x$ bulk glasses studied by spectroscopic ellipsometry. *Journal of Applied Physics*, *103*(8), p.083512.

[2.120] Orava, J., Kohoutek, T., Wagner, T., Cerna, Z., Vlcek, M., Benes, L., Frumarova, B. and Frumar, M., 2009. Optical and structural properties of Ge–Se bulk glasses and Ag–Ge–Se thin films. *Journal of Non-Crystalline Solids*, *355*(37-42), pp.1951-1954.

[2.121] Pamukchieva, V., Szekeres, A., Todorova, K., Svab, E. and Fabian, M., 2009. Compositional dependence of the optical properties of new quaternary chalcogenide glasses of Ge–Sb–(S, Te) system. *Optical Materials*, *32*(1), pp.45-48.

[2.122] Wang, Y., Qi, S., Yang, Z., Wang, R., Yang, A. and Lucas, P., 2017. Composition dependences of refractive index and thermo-optic coefficient in Ge-As-Se chalcogenide glasses. *Journal of Non-Crystalline Solids*, *459*, pp.88-93.

[2.123] Gleason, B., Richardson, K., Sisken, L. and Smith, C., 2016. Refractive Index and Thermo-Optic Coefficients of Ge-As-Se Chalcogenide Glasses. *International Journal of Applied Glass Science*, *7*(3), pp.374-383.

[2.124] Harbold, J.M., Ilday, F.Ö., Wise, F.W., Sanghera, J.S., Nguyen, V.Q., Shaw, L.B. and Aggarwal, I.D., 2002. Highly nonlinear As–S–Se glasses for all-optical switching. *Optics Letters*, *27*(2), pp.119-121.

[2.125] Eggleton, B., Luther-Davies, B. and Richardson, K., 2011. Chalcogenide photonics'. *Nature Photonics*, *5*(3), pp.141-148.

[2.126] Sharma, P., Sharma, N., Sharda, S., Katyal, S.C. and Sharma, V., 2016. Recent developments on the optical properties of thin films of chalcogenide glasses. *Progress in Solid State Chemistry*, *44*(4), pp.131-141.

[2.127] Bulla, D.A.P., Wang, R.P., Prasad, A., Rode, A.V., Madden, S.J. and Luther-Davies, B., 2009. On the properties and stability of thermally evaporated Ge–As–Se thin films. *Applied Physics A*, *96*(3), pp.615-625.

[2.128] Tan, W.C., Solmaz, M.E., Gardner, J., Atkins, R. and Madsen, C., 2010. Optical characterization of a-As_2S_3 thin films prepared by magnetron sputtering. *Journal of Applied Physics*, *107*(3), p.033524.

[2.129] Pan, R.K., Tao, H.Z., Zang, H.C., Lin, C.G., Zhang, T.J. and Zhao, X.J., 2011. Structure and optical properties of amorphous GeS_x films prepared by PLD. *Journal of Non-Crystalline Solids*, *357*(11-13), pp.2358-2361.

[2.130] Krbal, M., Wagner, T., Kohoutek, T., Nemec, P., Orava, J. and Frumar, M., 2007. The comparison of Ag–$As_{33}S_{67}$ films prepared by thermal evaporation (TE), spin-coating (SC) and a pulsed laser deposition (PLD). *Journal of Physics and Chemistry of Solids*, *68*(5-6), pp.953-957.

[2.131] Huang, C.C., Hewak, D.W. and Badding, J.V., 2004. Deposition and characterization of germanium sulphide glass planar waveguides. *Optics Express*, *12*(11), pp.2501-2506.

[2.132] Gill, D.S., Eason, R.W., Zaldo, C., Rutt, H.N. and Vainos, N.A., 1995. Characterisation of Ga-La-S chalcogenide glass thin-film optical waveguides, fabricated by pulsed laser deposition. *Journal of Non-Crystalline Solids*, *191*(3), pp.321-326.

[2.133] Laniel, J.M., Menard, J.M., Villeneuve, A., Vallee, R., Lopez, C. and Richardson, K.A., 2003, February. Refractive index measurements of planar chalcogenide waveguide. In *Applications of Photonic Technology 5* (Vol. 4833, pp. 670-677). International Society for Optics and Photonics.

[2.134] Tichý, L., Ticha, H., Nagels, P., Callaerts, R., Mertens, R. and Vlček, M., 1999. Optical properties of amorphous As–Se and Ge–As–Se thin films. *Materials Letters*, *39*(2), pp.122-128.

[2.135] Tan, W.C., Solmaz, M.E., Gardner, J., Atkins, R. and Madsen, C., 2010. Optical characterization of a-As_2S_3 thin films prepared by magnetron sputtering. *Journal of Applied Physics*, *107*(3), p.033524.

[2.136] Simpson, R.E., Krbal, M., Fons, P., Kolobov, A.V., Tominaga, J., Uruga, T. and Tanida, H., 2009. Toward the ultimate limit of phase change in $Ge_2Sb_2Te_5$. *Nano Letters*, *10*(2), pp.414-419.

[2.137] Seddon, A.B., Pan, W.J., Furniss, D., Miller, C.A., Rowe, H., Zhang, D., McBrearty, E., Zhang, Y., Loni, A., Sewell, P. and Benson, T.M., 2006. Fine embossing of chalcogenide glasses–a new fabrication route for photonic integrated circuits. *Journal of Non-Crystalline Solids*, *352*(23-25), pp.2515-2520.

[2.138] Frantz, J.A., Sanghera, J.S., Shaw, L.B., Villalobos, G., Aggarwal, I.D. and Hewak, D.W., 2006. Sputtered films of Er^{3+}-doped gallium lanthanum sulfide glass. *Materials Letters*, *60*(11), pp.1350-1353.

[2.139] Chen, Y., Shen, X., Wang, R., Wang, G., Dai, S., Xu, T. and Nie, Q., 2013. Optical and structural properties of Ge–Sb–Se thin films fabricated by sputtering and thermal evaporation. *Journal of Alloys and Compounds*, *548*, pp.155-160.

[2.140] Swanepoel, R., 1983. Determination of the thickness and optical constants of amorphous silicon. *Journal of Physics E Scientific Instruments*, *16*, pp.1214-1222.

[2.141] Kincl, M. and Tichý, L., 2008. Thermally and optically induced irreversible changes in some Ge–As–S amorphous thin films. *Materials Chemistry and Physics*, *110*(2-3), pp.322-327.

[2.142] Eason, R., 2007. *Pulsed laser deposition of thin films: applications-led growth of functional materials*. John Wiley & Sons.

[2.143] Frumar, M., Frumarova, B., Nemec, P., Wagner, T., Jedelsky, J. and Hrdlicka, M., 2006. Thin chalcogenide films prepared by pulsed laser deposition–new amorphous materials applicable in optoelectronics and chemical sensors. *Journal of Non-Crystalline Solids*, *352*(6-7), pp.544-561.

[2.144] Gamaly, E.G., Rode, A.V., Luther-Davies, B. and Tikhonchuk, V.T., 2002. Ablation of solids by femtosecond lasers: Ablation mechanism and ablation thresholds for metals and dielectrics. *Physics of Plasmas*, *9*(3), pp.949-957.

[2.145] Gamaly, E.G., Rode, A.V. and Luther-Davies, B., 2006. Ultrafast Laser Ablation and Film Deposition. *Pulsed Laser Deposition of Thin Films: Applications-Led Growth of Functional Materials*, pp.99-129.

[2.146] Gamaly, E.G., Rode, A.V. and Luther-Davies, B., 1999. Ultrafast ablation with high-pulse-rate lasers. Part I: Theoretical considerations. *Journal of Applied Physics*, *85*(8), pp.4213-4221.

[2.147] Rode, A.V., Luther-Davies, B. and Gamaly, E.G., 1999. Ultrafast ablation with high-pulse-rate lasers. Part II: Experiments on laser deposition of amorphous carbon films. *Journal of Applied Physics*, *85*(8), pp.4222-4230.

[2.148] Rode, A.V., Zakery, A., Samoc, M., Charters, R.B., Gamaly, E.G. and Luther-Davies, B., 2002. Laser-deposited As_2S_3 chalcogenide films for waveguide applications. *Applied Surface Science*, *197*, pp.481-485.

[2.149] Zakery, A., 2002. Low loss waveguides in pulsed laser deposited arsenic sulfide chalcogenide films. *Journal of Physics D: Applied Physics*, *35*(22), p.2909.

[2.150] Ogura, H., Matsuishi, K. and Onari, S., 2000. Raman scattering and photodarkening of amorphous $Ge_{1-X}S_X$ ($0 \leqslant X \leqslant 0.62$) films. *Journal of Non-Crystalline Solids*, *270*(1-3), pp.147-153.

[2.151] Martino, M., Caricato, A.P., Fernandez, M., Leggieri, G., Jha, A., Ferrari, M. and Mattarelli, M., 2003. Pulsed laser deposition of active waveguides. *Thin Solid Films*, *433*(1-2), pp.39-44.

[2.152] Youden, K.E., Grevatt, T., Eason, R.W., Rutt, H.N., Deol, R.S. and Wylangowski, G., 1993. Pulsed laser deposition of Ga-La-S chalcogenide glass thin film optical waveguides. *Applied Physics Letters*, *63*(12), pp.1601-1603.

[2.153] Caricato, A.P., De Sario, M., Fernandez, M., Ferrari, M., Leggieri, G., Luches, A., Martino, M., Montagna, M., Prudenzano, F. and Jha, A., 2003. Chalcogenide glass thin film waveguides deposited by excimer laser ablation. *Applied Surface Science*, *208*, pp.632-637.

[2.154] Kalyva, M., Siokou, A., Yannopoulos, S.N., Wagner, T., Krbal, Orava, J. and Frumar, M., 2008. Soft x-ray induced Ag diffusion in amorphous pulse laser deposited $As_{50}Se_{50}$ thin films: An x-ray photoelectron and secondary ion mass spectroscopy study. *Journal of Applied Physics*, *104*(4), p.043704.

[2.155] Gmachl, C., Hwang, H.Y., Paiella, R., Sivco, D.L., Baillargeon, J.N., Capasso, F. and Cho, A.Y., 2001. Quantum cascade lasers with low-loss chalcogenide lateral waveguides. *IEEE Photonics Technology Letters*, *13*(3), pp.182-184.

[2.156] Němec, P., Frumar, M., Frumarova, B., Jelınek, M., Lančok, J. and Jedelský, J., 2000. Pulsed laser deposition of pure and praseodymium-doped Ge–Ga–Se amorphous chalcogenide films. *Optical Materials*, *15*(3), pp.191-197.

[2.157] Wágner, T., Havel, J., Houška, J., Peña-Méndez, E.M., Přikryl, J., Pavlišta, M. and Frumar, M., 2007, September. Thin films of $Ge_2Sb_2Te_5$ prepared by pulsed laser deposition, properties and plume particles analysis. In *European Symposium on Phase Change and Ovonic Science* (pp. 1-4).

[2.158] Nazabal, V., Němec, P., Jedelský, J., Duverger, C., Le Person, J., Adam, J.L. and Frumar, M., 2006. Dysprosium doped amorphous chalcogenide films prepared by pulsed laser deposition. *Optical Materials*, *29*(2-3), pp.273-278.

[2.159] Dwivedi, P.K., Sun, Y.W., Tsui, Y.Y., Tonchev, D., Munzar, M., Koughia, K., Haugen, C.J., DeCorby, R.G., McMullin, J.N. and Kasap, S.O., 2005. Rare-earth doped chalcogenide thin films fabricated by pulsed laser deposition. *Applied Surface Science*, *248*(1-4), pp.376-380.

[2.160] Chern, G.C. and Lauks, I., 1982. Spin-coated amorphous chalcogenide films. *Journal of Applied Physics*, *53*(10), pp.6979-6982.

[2.161] Schwartz, R.W., Narayanan, M. and Mitzi, D.B., 2009. Solution Processing of Inorganic Materials.

[2.162] Orava, J., Kohoutek, T. and Wagner, T., 2014. Deposition techniques for chalcogenide thin films. In *Chalcogenide Glasses* (pp. 265-309).

[2.163] Owen, A.E., Firth, A.P. and Ewen, P.J.S., 1985. Photo-induced structural and physico-chemical changes in amorphous chalcogenide semiconductors. *Philosophical Magazine B*, *52*(3), pp.347-362.

[2.164] Ewen, P.J.S. and Owen, A.E., 1992. High-performance glasses. *Blackie, London*, p.287.

[2.165] Slang, S., Janicek, P., Palka, K., Loghina, L. and Vlcek, M., 2018. Optical properties and surface structuring of $Ge_{20}Sb_5S_{75}$ amorphous chalcogenide thin films deposited by spin-coating and vacuum thermal evaporation. *Materials Chemistry and Physics*, *203*, pp.310-318.

[2.166] Musgraves, J.D., Danto, S. and Richardson, K., 2014. Thermal properties of chalcogenide glasses. In *Chalcogenide Glasses* (pp. 82-112).

[2.167] Prod'homme, L., 1960. A new approach to the thermal change in the refractive index of glasses. *Physics and Chemistry of Glasses*, *1*(4), pp.119-122.

[2.168] Schott Glass Inc., 2013. Schott Infrared Chalcogenide Glasses – IRG 22.

[2.169] Schott Glass Inc., 2013. Schott Infrared Chalcogenide Glasses – IRG 23.

[2.170] Schott Glass Inc., 2013. Schott Infrared Chalcogenide Glasses – IRG 25.

[2.171] Hudson, D.D., Dekker, S.A., Mägi, E.C., Judge, A.C., Jackson, S.D., Li, E., Sanghera, J.S., Shaw, L.B., Aggarwal, I.D. and Eggleton, B.J., 2011. Octave spanning supercontinuum in an As_2S_3 taper using ultralow pump pulse energy. *Optics Letters*, *36*(7), pp.1122-1124.

[2.172] Domachuk, P., Wolchover, N.A., Cronin-Golomb, M., Wang, A., George, A.K., Cordeiro, C.M.B., Knight, J.C. and Omenetto, F.G., 2008. Over 4000 nm bandwidth of mid-IR supercontinuum generation in sub-centimeter segments of highly nonlinear tellurite PCFs. *Optics Express*, *16*(10), pp.7161-7168.

[2.173] Yang, P., Zhang, P., Dai, S., Wu, Y., Wang, X., Tao, G. and Nie, Q., 2015. Tapered chalcogenide–tellurite hybrid microstructured fiber for mid-infrared supercontinuum generation. *Journal of Modern Optics*, *62*(9), pp.729-737.

[2.174] Gao, W., Duan, Z., Asano, K., Cheng, T., Deng, D., Matsumoto, M., Misumi, T., Suzuki, T. and Ohishi, Y., 2014. Mid-infrared supercontinuum generation in a four-hole As_2S_5 chalcogenide microstructured optical fiber. *Applied Physics B*, *116*(4), pp.847-853.

[2.175] Bernier, M., Fortin, V., Caron, N., El-Amraoui, M., Messaddeq, Y. and Vallée, R., 2013. Mid-infrared chalcogenide glass Raman fiber laser. *Optics letters*, *38*(2), pp.127-129.

[2.176] Slusher, R.E., Lenz, G., Hodelin, J., Sanghera, J., Shaw, L.B. and Aggarwal, I.D., 2004. Large Raman gain and nonlinear phase shifts in high-purity As_2Se_3 chalcogenide fibers. *Journal of the Optical Society of America B Optical Physics*, *21*, pp.1146-1155.

[2.177] Bernier, M., Fortin, V., El-Amraoui, M., Messaddeq, Y. and Vallée, R., 2014. 3.77 μm fiber laser based on cascaded Raman gain in a chalcogenide glass fiber. *Optics Letters*, *39*(7), pp.2052-2055.

[2.178] Thielen, P.A., Shaw, L.B., Sanghera, J.S. and Aggarwal, I.D., 2003. Modeling of a mid-IR chalcogenide fiber Raman laser. *Optics Express*, *11*(24), pp.3248-3253.

[2.179] Gattass, R.R., Shaw, L.B., Nguyen, V.Q., Pureza, P.C., Aggarwal, I.D. and Sanghera, J.S., 2012. All-fiber chalcogenide-based mid-infrared supercontinuum source. *Optical Fiber Technology*, *18*(5), pp.345-348.

[2.180] Heo, J., 2003. Rare-earth doped chalcogenide glasses for fiber-optic amplifiers. *Journal of Non-Crystalline Solids*, *326*, pp.410-415.

[2.181] Sojka, L., Tang, Z., Furniss, D., Sakr, H., Oladeji, A., Bereś-Pawlik, E., Dantanarayana, H., Faber, E., Seddon, A.B., Benson, T.M. and Sujecki, S., 2014. Broadband, mid-infrared emission from Pr^{3+} doped GeAsGaSe chalcogenide fiber, optically clad. *Optical Materials*, *36*(6), pp.1076-1082.

[2.182] Tang, Z., Zhu, H., Bereś-Pawlik, E., Furniss, D., Seddon, A.B., Benson, T.M. and Sujecki, S., 2012. Study of mid-infrared laser action in chalcogenide rare earth doped glass with Dy^{3+}, Pr^{3+} and Tb^{3+}. *Optical Materials Express*, *2*(11), pp.1632-1640.

[2.183] Tanabe, S., 2002. Rare-earth-doped glasses for fiber amplifiers in broadband telecommunication. *Comptes Rendus Chimie*, *5*(12), pp.815-824.

[2.184] Ohishi, Y., Mori, A., Kanamori, T., Fujiura, K. and Sudo, S., 1994. Fabrication of praseodymium-doped arsenic sulfide chalcogenide fiber for 1.3-μm fiber amplifiers. *Applied physics letters*, *65*(1), pp.13-15.

[2.185] Shen, M., Furniss, D., Tang, Z., Barny, E., Sojka, L., Sujecki, S., Benson, T.M. and Seddon, A.B., 2018. Modeling of resonantly pumped mid-infrared Pr^{3+}-doped chalcogenide fiber amplifier with different pumping schemes. *Optics express*, *26*(18), pp.23641-23660.

[2.186] Seddon, A.B., Tang, Z., Furniss, D., Sujecki, S. and Benson, T.M., 2010. Progress in rare-earth-doped mid-infrared fiber lasers. *Optics Express*, *18*(25), pp.26704-26719.

[2.187] Jackson, S.D., 2012. Towards high-power mid-infrared emission from a fibre laser. *Nature Photonics*, *6*, pp.423-431.

[2.188] Nishii, J., Morimoto, S., Inagawa, I., Iizuka, R., Yamashita, T. and Yamagishi, T., 1992. Recent advances and trends in chalcogenide glass fiber technology: a review. *Journal of Non-Crystalline Solids*, *140*, pp.199-208.

[2.189] Busse, L.E., Moon, J.A., Sanghera, J.S. and Aggarwal, I.D., 1996. Chalcogenide fibers deliver high IR power. *Laser Focus World*, *32*(9), pp.143-150.

[2.190] Sincore, A., Cook, J., Tan, F., El Halawany, A., Riggins, A., McDaniel, S., Cook, G., Martyshkin, D.V., Fedorov, V.V., Mirov, S.B. and Shah, L., 2018. High power single-mode delivery of mid-infrared sources through chalcogenide fiber. *Optics express*, *26*(6), pp.7313-7323.

[2.191] Heo, J., Rodrigues, M., Saggese, S.J. and Sigel, G.H., 1991. Remote fiber-optic chemical sensing using evanescent-wave interactions in chalcogenide glass fibers. *Applied optics*, *30*(27), pp.3944-3951.

[2.192] Sanghera, J.S., Kung, F.H., Busse, L.E., Pureza, P.C. and Aggarwal, I.D., 1995. Infrared evanescent absorption spectroscopy of toxic chemicals using chalcogenide glass fibers. *Journal of the American Ceramic Society*, *78*(8), pp.2198-2202.

[2.193] Zhang, X.H., Duhamel, M.V., Ma, H.L., Blanchetiere, C. and Lucas, J., 1993. Application of the TeX glass fibers as chemical sensors. *Journal of Non-Crystalline Solids*, *161*, pp.327-330.

[2.194] Sanghera, J. and Aggarwal, I.D., 1998. *Infrared fiber optics*. CRC Press.

[2.195] Melling, P., Commercial Literature. *Remspec Inc*.

[2.196] Saito, M. and Kikuchi, K., 1997. Infrared optical fiber sensors. *Optical Review*, *4*(5), pp.527-538.

[2.197] Ueda, T., Yamada, K. and Sugita, T., 1992. Measurement of grinding temperature of ceramics using infrared radiation pyrometer with optical fiber. *Journal of Engineering for Industry*, *114*(3), pp.317-322.

[2.198] Kapany, N.S. and Simms, R.J., 1965. Recent developments in infrared fiber optics∗. *Infrared Physics*, *5*(2), pp.69-80.

[2.199] Saito, M., Takizawa, M., Sakuragi, S. and Tanei, F., 1985. Infrared image guide with bundled As–S glass fibers. *Applied optics*, *24*(15), pp.2304-2308.

[2.200] Nishii, J., Yamashita, T., Yamagishi, T., Tanaka, C. and Sone, H., 1991. Coherent infrared fiber image bundle. *Applied Physics Letters*, *59*(21), pp.2639-2641.

[2.201] Gibson, D., Bayya, S., Sanghera, J., Nguyen, V., Scribner, D., Maksimovic, V., Gill, J., Yi, A., Deegan, J. and Unger, B., 2014, July. Layered chalcogenide glass structures for IR lenses. In *Infrared Technology and Applications XL* (Vol. 9070, p. 90702I). International Society for Optics and Photonics.

[2.202] Schaafsma, D.T., Mossadegh, R., Sanghera, J.S., Aggarwal, I.D., Luce, M., Generosi, R., Perfetti, P., Cricenti, A., Gilligan, J.M. and Tolk, N.H., 1999. Fabrication of single-mode chalcogenide fiber probes for scanning near-field infrared optical microscopy. *Optical Engineering*, *38*(8), pp.1381-1386.

[2.203] Sanghera, J.S., Shaw, L.B., Busse, L.E., Talley, D.B. and Aggarwal, I.D., 1999, April. Infrared-transmitting fiber optics for biomedical applications. In *Specialty Fiber Optics for Medical Applications* (Vol. 3596, pp. 178-188). International Society for Optics and Photonics.

[2.204] Gattass, R.R., Shaw, L.B., Kung, F.H., Gibson, D.J., Nguyen, V.Q., Chin, G.D., Busse, L.E., Aggarwal, I.D. and Sanghera, J.S., 2013. Infrared Fiber N×1 Multimode Combiner. *IEEE Photonics Journal*, *5*(5), pp.7100905-7100905.

[2.205] Tilton, L.W., 1931. Prism size and orientation in minimum-deviation refractometry. *Nat. Bur. Stand. J. Research*, *6*, p.59-76.

[2.206] Malitson, L.H., 1965. Interspecimen Comparison of the Refractive Index of Fused Silica. *Journal of the Optical Society of America*, *55*(1205), pp.1917-1983.

[2.207] Tentori, D. and Lerma, J.R., 1990. Refractometry by minimum deviation: accuracy analysis. *Optical Engineering*, *29*(2), pp.160-168.

[2.208] Walton, A.K. and Moss, T.S., 1963. Determination of refractive index and correction to effective electron mass in PbTe and PbSe. *Proceedings of the Physical Society*, *81*(3), p.509.

[2.209] Zhang, X.H., Guimond, Y. and Bellec, Y., 2003. Production of complex chalcogenide glass optics by molding for thermal imaging. *Journal of Non-Crystalline Solids*, *326*, pp.519-523.

[2.210] Seddon, A.B. and Laine, M.J., 1997. Chalcogenide glasses for acousto-optic devices. II. As–Ge–Se systems. *Journal of Non-Crystalline Solids*, *213*, pp.168-173.

[2.211] Guillevic, E., Zhang, X., Pain, T., Calvez, L., Adam, J.L., Lucas, J., Guilloux-Viry, M., Ollivier, S. and Gadret, G., 2009. Optimization of chalcogenide glass in the As–Se–S system for automotive applications. *Optical Materials*, *31*(11), pp.1688-1692.

[2.212] Ma, H.L., Guimond, Y., Zhang, X.H. and Lucas, J., 1999. Ga–Ge–Sb–Se based glasses and influence of alkaline halide addition. *Journal of Non-Crystalline Solids*, *256*, pp.165-169.

[2.213] Fang, Y., Jayasuriya, D., Furniss, D., Tang, Z.Q., Markos, C., Sujecki, S., Seddon, A.B. and Benson, T.M., 2017. Determining the refractive index dispersion and thickness of hot-pressed chalcogenide thin films from an improved Swanepoel method. *Optical and Quantum Electronics*, *49*(7), p.237.

[2.214] Novak, J., Pini, R., Moreshead, W.V., Stover, E. and Symmons, A., 2013, October. Investigation of index of refraction changes in chalcogenide glasses during molding processes. In *Electro-Optical and Infrared Systems: Technology and Applications X* (Vol. 8896, p. 889602). International Society for Optics and Photonics.

[2.215] Novak, J., Novak, S., Huddleston, J., Moreshead, W., Symmons, A. and Stover, E., 2017, August. Compositional dependence of properties and lens performance of As-Se chalcogenide glass. In *Advanced Optics for Defense Applications: UV through LWIR II* (Vol. 10181, p. 101810Q). International Society for Optics and Photonics.

[2.216] Novak, J., Symmons, A., Novak, S. and Stover, E., 2016, May. Applicability of an annealing coefficient for precision glass molding of $As_{40}Se_{60}$. In *Advanced Optics for Defense Applications: UV through LWIR* (Vol. 9822, p. 98220A). International Society for Optics and Photonics.

[2.217] Schott Glass Inc., 2013. Schott Infrared Chalcogenide Glasses – IRG 2.

[2.218] Schott Glass Inc., 2013. Schott Infrared Chalcogenide Glasses – IRG 3.

[2.219] Wikipedia. 2010. Ellipsometry. [ONLINE] Available at:https://en.wikipedia.org/wiki/Ellipsometry. [Accessed 29 November 2018].

[2.220] Vedam, K., 1998. Spectroscopic ellipsometry: a historical overview. *Thin SolidFfilms*, *313*, pp.1-9.

[2.221] Collins, R.W., Koh, J., Fujiwara, H., Rovira, P.I., Ferlauto, A.S., Zapien, J.A., Wronski, C.R. and Messier, R., 2000. Recent progress in thin film growth analysis by multichannel spectroscopic ellipsometry. *Applied Surface Science*, *154*, pp.217-228.

[2.222] Budde, W., 1962. Photoelectric analysis of polarized light. *Applied Optics*, *1*(3), pp.201-205.

[2.223] Cahan, B.D. and Spanier, R.F., 1969. A high speed precision automatic ellipsometer. *Surface Science*, *16*, pp.166-176.

[2.224] Aspnes, D.E. and Studna, A.A., 1975. High precision scanning ellipsometer. *Applied Optics*, *14*(1), pp.220-228.

[2.225] Muller, R.H. and Farmer, J.C., 1984. Fast, self-compensating spectral-scanning ellipsometer. *Review of Scientific Instruments*, *55*(3), pp.371-374.

[2.226] Němec, P., Olivier, M., Baudet, E., Kalendova, A., Benda, P. and Nazabal, V., 2014. Optical properties of $(GeSe_2)_{100-x}(Sb_2Se_3)_x$ glasses in near-and middle-infrared spectral regions. *Materials Research Bulletin*, *51*, pp.176-179.

[2.227] Wei, N.N., Yang, Z., Pan, H.B., Zhang, F., Liu, Y.X., Wang, R.P., Shen, X., Dai, S.X. and Nie, Q.H., 2018. Variable angle spectroscopic ellipsometry and its applications in determining optical constants of chalcogenide glasses in infrared. *Chinese Physics B*, *27*(6), p.067802.

[2.228] Hawlová, P., Verger, F., Nazabal, V., Boidin, R. and Němec, P., 2014. Accurate determination of optical functions of Ge–As–Te glasses via spectroscopic ellipsometry. *Journal of the American Ceramic Society*, *97*(10), pp.3044-3047.

[2.229] Němec, P. and Frumar, M., 2008. Photoinduced phenomena in As_4Se_3 amorphous thin films prepared by pulsed laser deposition. *Thin Solid Films*, *516*(23), pp.8377-8380.

[2.230] Todorov, R., Paneva, A. and Petkov, K., 2010. Optical characterization of thin chalcogenide films by multiple-angle-of-incidence ellipsometry. *Thin Solid Films*, *518*(12), pp.3280-3288.

[2.231] Park, J.W., Baek, S.H., Kang, T.D., Lee, H., Kang, Y.S., Lee, T.Y., Suh, D.S., Kim, K.J., Kim, C.K., Khang, Y.H. and Da Silva, J.L., 2008. Optical properties of (GeTe, Sb 2 Te 3) pseudobinary thin films studied with spectroscopic ellipsometry. *Applied Physics Letters*, *93*(2), p.021914.

[2.232] Lee, C.C. and Ku, S.L., 2011. Study on the optical property and crystallinity of $Ge_{90}Te_{10}$ films deposited by electron beam evaporation. *Thin Solid Films*, *519*(6), pp.1794-1797.

[2.233] Yim, C., O'Brien, M., McEvoy, N., Winters, S., Mirza, I., Lunney, J.G. and Duesberg, G.S., 2014. Investigation of the optical properties of MoS_2 thin films using spectroscopic ellipsometry. *Applied Physics Letters*, *104*(10), p.103114.

[2.234] Amin, G.A.M., 2015. Studies on In $_x(As_2Se_3)_{1-x}$ thin films using variable angle spectroscopic ellipsometry (VASE). *Materials Science-Poland*, *33*(3), pp.501-507.

[2.235] Shaaban, E.R., El-Hagary, M., Emam-Ismail, M., Elnaeim, A.A., Moustafa, S.H. and Adel, A., 2015. Optical characterization of polycrystalline $ZnSe_{1-x}Te_x$ thin films using variable angle spectroscopic ellipsometry and spectrophotmetery techniques. *Materials Science in Semiconductor Processing*, *39*, pp.735-741.

[2.236] Guo, S., Ding, X.J., Zhang, J.Z., Hu, Z.G., Ji, X.L., Wu, L.C., Song, Z.T. and Chu, J.H., 2015. Intrinsic evolutions of dielectric function and electronic transition in tungsten doping $Ge_2Sb_2Te_5$ phase change films discovered by ellipsometry at elevated temperatures. *Applied Physics Letters*, *106*(5), p.052105.

[2.237] Velea, A., Socol, G., Popescu, M. and Galca, A.C., 2015. In-situ characterization of the optical and electronic properties in GeTe and GaSb thin films. *Journal of Applied Physics*, *118*(13), p.135712.

[2.238] Abdel-Wahab, F., Merazga, A., Rasheedy, M.S. and Montaser, A.A., 2016. Optical characterization of the annealing effect on $Ge_5Te_{20}Se_{75}$ thin films by variable angle of-incidence spectroscopic ellipsometry. *Optik-International Journal for Light and Electron Optics*, *127*(8), pp.3871-3877.

[2.239] Dantanarayana, H.G., 2012. *Application of TLM for optical microresonators* (Doctoral dissertation, University of Nottingham).

[2.240] Manifacier, J.C., Gasiot, J. and Fillard, J.P., 1976. A simple method for the determination of the optical constants n, k and the thickness of a weakly absorbing thin film. *Journal of Physics E: Scientific Instruments*, *9*(11), p.1002.

[2.241] Swanepoel, R., 1983. Determination of the thickness and optical constants of amorphous silicon. *Journal of Physics E: Scientific Instruments*, *16*(12), p.1214.

[2.242] Essential MacLeod, Thin Film Center Inc., Tucson, AZ, USA, https://www.thinfilmcenter.com.

[2.243] FilmStar, FTG Software Asociates, Princeton, NJ, USA, https://www.ftgsoftware.com/design.htm.

[2.244] Swanepoel, R., 1984. Determination of surface roughness and optical constants of inhomogeneous amorphous silicon films. *Journal of Physics E: Scientific Instruments*, *17*(10), p.896.

[2.245] Shaaban, E.R., Yahia, I.S. and El-Metwally, E.G., 2012. Validity of Swanepoel's method for calculating the optical constants of thick films. *Acta Physica Polonica-Series A General Physics*, *121*(3), p.628.

[2.246] Jin, Y., Song, B., Jia, Z., Zhang, Y., Lin, C., Wang, X. and Dai, S., 2017. Improvement of Swanepoel method for deriving the thickness and the optical properties of chalcogenide thin films. *Optics Express*, *25*(1), pp.440-451.

[2.247] Jin, Y., Song, B., Lin, C., Zhang, P., Dai, S., Xu, T. and Nie, Q., 2017. Extension of the Swanepoel method for obtaining the refractive index of chalcogenide thin films accurately at an arbitrary wavenumber. *Optics Express*, *25*(25), pp.31273-31280.

[2.248] Poelman, D. and Frederic Smet, P., 2003. Methods for the determination of the optical constants of thin films from single transmission measurements: a critical review. *Journal of Physics D Applied Physics*, *36*, pp.1850-1857.

[2.249] McClain, M., Feldman, A., Kahaner, D. and Ying, X., 1991. An algorithm and computer program for the calculation of envelope curves. *Computers in Physics*, *5*(1), pp.45-48.

[2.250] Minkov, D., 1992. Singularity of the solution when using spectrum envelopes for the computation of the optical constants of a thin dielectric layer. *Optik*, *90*(2), pp.80-84.

[2.251] Sisonyuk, A.G., 1996. A posteriori error of the transmission interference method of thin film refractive index calculation. *Journal of Physics D: Applied Physics*, *29*(4), p.1068.

[2.252] Minkov, D. and Swanepoel, R., 1993. Computerization of the optical characterization of a thin dielectric film. *Optical Engineering*, *32*(12), pp.3333-3338.

[2.253] González-Leal, J.M., Prieto-Alcón, R., Angel, J.A., Minkov, D.A. and Márquez, E., 2002. Influence of substrate absorption on the optical and geometrical characterization of thin dielectric films. *Applied Optics*, *41*(34), pp.7300-7308.

[2.254] Kar, M., 2010. Error minimization in the envelope method for the determination of optical constants of a thin film. *Surface and Interface Analysis*, *3*(42), pp.145-150.

[2.255] Swanepoel, R., 1985. Determining refractive index and thickness of thin films from wavelength measurements only. *Journal of the Optical Society of America A*, *2*, pp.1339-1343.

[2.256] Corrales, C., Ramírez-Malo, J.B., Fernández-Peña, J., Villares, P., Swanepoel, R. and Márquez, E., 1995. Determining the refractive index and average thickness of AsSe semiconducting glass films from wavelength measurements only. *Applied Optics*, *34*(34), pp.7907-7913.

[2.257] Collet, E., 1987. Digital refractometry. *Optics Communications*, *63*(4), pp.217-224.

[2.258] Born, M. and Wolf, E., 2013. *Principles of optics: electromagnetic theory of propagation, interference and diffraction of light*. Elsevier.

[2.259] Schott Catalog-Optical Glass, Schott Optical Glass, Inc. Yor Ave., Duryea, PA 18642, USA.

[2.260] Athanasiou, G.S., 2013. *The fabrication of chalcogenide glass fibre photonic components* (Doctoral dissertation, University of Nottingham).

Chapter 3: Experimental techniques

This chapter provides a detailed overview of all the experimental procedures used to fabricate, process and characterise the chalcogenide glasses investigated during the work described in this thesis. Section 3.1 will list all the chemicals used during this Project. In section 3.2, the personal codes will be listed as well as the corresponding as-batched compositions, target thickness and other information for all thin films that will be referred to later in this thesis. In section 3.3, the experimental techiniques for making chalcogenide bulk glasses will be described, and section 3.4 presents the technique for preparing chalcogenide glass prisms. Section 3.5 describes the hot-pressing technique developed for making chalcogenide glass thin films and bulk samples for ellipsometry measurements. Section 3.6 then introduces the Fourier transform infrared (FTIR) spectroscopy used for bulk glass characterisation, thin film measurements and measuring the emission spectra of external beam sources. Section 3.7 describes thermal mechanical analysis (TMA) for measuring the viscosity-temperature properties and thermal expansion coefficient (TEC) of chalcogenide glasses. Section 3.8 presents the thermal performance of a new thermal prism/thin-film holder developed as part of the present work. Finally, a summary of this chapter will be made in section 3.9. Note that the T_gs (glass transition temperatures) of the glass compositions investigated in the hot-pressing were kindly provided by Drs. Jaysuriya and Parnell (formerly PhD students of the MIR photonics Group, University of Nottingham, UK).

3.1 List of chemical used

Table 3.1-1 lists all the chemicals used for glass synthesis whilst Table 3.1-2 lists the chemicals used elsewhere in this research.

Table 3.1- 1. The chemicals used for glass synthesis in this project with their suppliers and purities.

Melting chemical	Supplier	Purity /%
Germanium	Materion	99.999
Arsenic	Furakawa	99.999995
Antimony	Cerac	99.9999
Selenium	Materion	99.999
Sulfur	Materion	99.999
Tellurium	Materion	99.999
Ga	Alfar Aesar	99.99999
In	Alfar Aesar	99.99995
Pr-foil	Alfar Aesar	99.9
Ce-foil	Alfar Aesar	99.9

Table 3.1- 2. Supplier, purity and purpose of chemicals used in this project.

Chemical	Supplier	Purity	Purpose
Acetone	Fisher chemicals	99.8+ %	All glass samples and relevant equipment were washed x3 with acetone and then x3 with isopropanol
Isopropanol	Fisher chemicals	HPLC (99.9+ %)	
Propylamine	Sigma-Aldrich	99 mol. %	Etch fibres to remove the oxide layers
Polishing oil	Buelher	-	Polishing and cutting glass preforms
1000 ppm SiC grinding powder	Buelher	-	Grinding glass samples
0.25 – 6 µm diamond paste	Buelher	-	Polishing glass samples
Nitrogen	BOC	99.998 %	Purge gas
Oxygen	BOC	Standard	Oxy-propane torch
Propane	Calor gas	Standard	Oxy-propane torch
Liquid nitrogen	BOC		Cold traps

Key: - means not known; ppm means parts of million.

3.2 Hot pressing codes

Table 3.2-1 lists the sample codes as well as the corresponding as-batched glass compositions, target thickness and other information for all the hot-pressed thin films that will later be referred to in this report.

Table 3.2- 1. The information of the thin films hot-pressed in this project.

Hot pressing code	Composition / at. %	Melting code	Annealing and quenching	No. of thin films obtained (No. of fibres pressed)	Propylamine etching	Target thickness /μm	Note
YRFFP001	$As_{40}Se_{60}$	M130MINSCGDJ	Well-annealed	4 (4)	No	No shim	First attempt
YRFFP002	$As_{40}Se_{60}$	M130MINSCGDJ	Well-annealed	2 (4)	No	25	Well hot-pressed
YRFFP003	$As_{40}Se_{60}$	M130MINSCGDJ	Well-annealed	3 (4)	No	25	Well hot-pressed
YRFFP004	$As_{40}Se_{60}$	M130MINSCGDJ	Well-annealed	0 (4)	No	20	Fail
YRFFP005	$Ge_{16}As_{24}Se_{15.5}Te_{44.5}$	M140MINSCGDJ	Well-annealed	0 (4)	No	20	First attempt to obtain Ge-As-Se-Te thin films.
YRFFP006	$Ge_{16}As_{24}Se_{15.5}Te_{44.5}$	M140MINSCGDJ	Well-annealed	1 (4)	No	30	
YRFFP007	$Ge_{16}As_{24}Se_{15.5}Te_{44.5}$	M140MINSCGDJ	Well-annealed	2 (4)	No	20	Well hot-pressed
YRFFP008	$Ge_{20}Sb_{10}Se_{70}$	M135HAP	Well-annealed	0 (4)	No	20	Fail
YRFFP009	$Ge_{20}Sb_{10}Se_{70}$	M135HAP	Well-annealed	1 (4)	No	30	Well hot-pressed
YRFFP010	$Ge_{20}Sb_{10}Se_{70}$	M135HAP	Well-annealed	1 (4)	No	20	
YRFFP011	$Ge_{20}Sb_{10}Se_{70}$	M135HAP	Well-annealed	1 (4)	No	20	

Table 3.2- 1. The information of the thin films hot-pressed in this project. (continued)

YRFFP012	$Ge_{16}As_{24}Se_{15.5}Te_{44.5}$	M140MINSCGDJ	Well-annealed	3 (4)	Yes	30	Test the reproducibility
YRFFP013	Tb doped Ge-As-Ga-Se	ZQT081	Well-annealed	4 (4)	Yes	25	Large thickness variation
YRFFP014	Tb doped Ge-As-Ga-Se	ZQT081	Well-annealed	2 (4)	Yes	25	Well hot-pressed
YRFFP015	$Ge_{20}Sb_{10}Se_{67}S_3$	M157HAP	Well-annealed	3 (7)	Yes	20	
YRFFP016	$Ge_{14.3}As_{27}Se_{15.5}Te_{43.2}$	M178DJ	Well-annealed	2 (7)	Yes	30	
YRFFP017	$Ge_{20}As_{20}Se_{14}Te_{46}$	M112DJ	Well-annealed	4 (7)	Yes	20	
YRFFP018	$Ge_{15}As_{25}Se_{19}Te_{41}$	M193DJ	Well-annealed	3 (7)	Yes	25	
YRFFP019	$Ge_{16}As_{24}Se_{15.5}Te_{44.5}$	M188SCGDJ	Well-annealed	3 (4)	Yes	25	Distilled preform
YRFFP020	$Ge_{16}As_{24}Se_{15.5}Te_{44.5}$	M188SCGDJ	Fast-quenched	0 (4)	Yes	25	Samples were broken
YRFFP021	$Ge_{16}As_{24}Se_{15.5}Te_{44.5}$	M188SCGDJ	Fast-quenched	0 (4)	Yes	25	Samples were broken
YRFFP022	$Ge_{16}As_{24}Se_{15.5}Te_{44.5}$	M188SCGDJ	Fast-quenched	0 (4)	Yes	25	Samples were broken
YRFFP023	$Ge_{16}As_{24}Se_{15.5}Te_{44.5}$	M188SCGDJ	Fast-quenched	2 (4)	Yes	25	Distilled preform
YRFFP024	$Ge_{14.3}As_{27}Se_{15.5}Te_{43.2}$	M178DJ	Fast-quenched	0 (4)	Yes	25	Samples were broken

Table 3.2- 1. The information of the thin films hot-pressed in this project. (continued)

YRFFP025	$Ge_{14.3}As_{27}Se_{15.5}Te_{43.2}$	M178DJ	Fast-quenched	2 (4)	Yes	25	Well hot-pressed
YRFFP026	$Ge_{16}As_{24}Se_{15.5}Te_{44.5}$ and $As_{40}Se_{60}$	M188SCGDJ and M130MINSCGDJ	Slow-quenched		Yes	25	Three-compositions thin film
YRFFP027	$Ge_{20}Sb_{10}Se_{70}$ and $Ge_{20}Sb_{10}Se_{67}S_3$	M135HAP and M157HAP	Slow-quenched	1 (3)	Yes	25	Two-compositions thin film
YRFFP028	$Ge_{20}Sb_{10}Se_{70}$ and $Ge_{20}Sb_{10}Se_{67}S_3$	M135HAP and M157HAP	Slow-quenched	1 (3)	Yes	25	Two-compositions thin film

Key: YRF= authors' initials; FP= fibre-pressed; M= melt; SCG=supercontinuum generation; DJ, ZQT and HAP=the person leading the melt, i.e. Dinuka Jayasuriya, Zhuoqi Tang and Harriet Parnell, respectively;

3.3 Glass melting

The steps for making chalcogenide glasses are listed in the flow chart of Figure 3.3-1, and described in the following sub-sections.

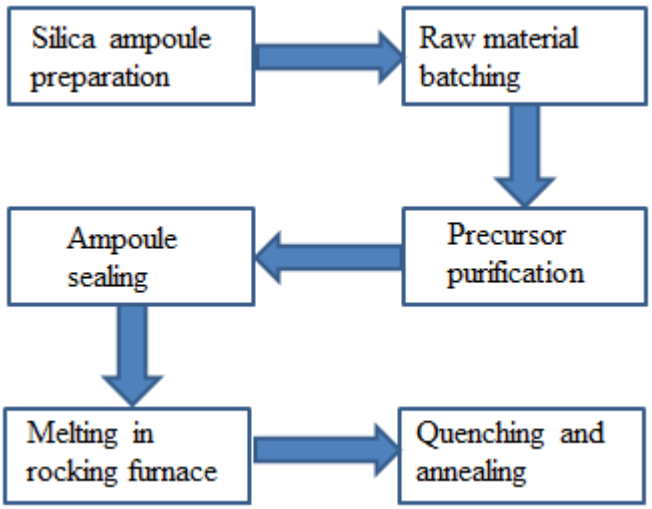


Figure 3.3- 1. Flowchart of chalcogenide-glass making steps.

3.3.1 Silica ampoule preparation

Silica ampoules (< 1 ppm OH) used as containment when making the chalcogenide glasses were supplied by both Baumbach UK, and Multilab UK. In order to minimise the oxide/hydride impurities, the prepared ampoule was etched by hydrofluoric acid (HF) for ~ 5 mins, and was then rinsed three times with distilled water in a fume cupboard.

The ampoule was subsequently air and vacuum baked to drive off physisorbed and chemisorbed water from the inside surface of the ampoule. The schedules of both procedures are shown in Table 3.3-1. For the air baking, the ampoule was placed vertically, with the open end upwards, in a tube furnace (TF105/4.5/1ZF, Instron). The ampoule was heated gradually to 1000 ℃ to remove carbon deposits. After the air baking, the ampoule was connected to a vacuum turbo pump (Purifier Ltd) using a vacuum valve (under vacuum ~10^{-3} Pa at gauge, Purifier). The same heat-treat

schedule as that used for the air baking was applied to remove any physisorbed and chemisorbed water from the internal surface of the ampoule, with the turbo pump applying a vacuum of 10^{-3} $^{\pm 1}$Pa. After the vaccum baking, the ampoule was kept under vacuum using the vacuum valve and transferred to a nitrogen atmosphere glovebox (MBraun 150B-G, ≤ 0.1 ppm O_2, ≤ 0.1 ppm H_2O).

Table 3.3- 1. The heat-treat schedule for the air baking and vacuum baking of the ampoule.

Step	Schedule
1	Ramp to 1000 ℃ @ 200 ℃/h
2	Dwell for 6 h at 1000 ℃
3	Ramp to 70 ℃ @ 200 ℃/h
4	Dwell for 100 h at 70 ℃ (until taken out of furnace)

3.3.2 Glass melting of different compositions

In this Project, the main glass compositions investigated are $As_{40}Se_{60}$, $Ge_{16}As_{24}Se_{15.5}Te_{44.5}$, $Ge_{20}Sb_{10}Se_{70}$/ $Ge_{20}Sb_{10}Se_{67}S_3$ at. %. The procedures of glass melting, annealing and quenching will be described in this sub-section.

(a) $As_{40}Se_{60}$ at. %

In preparing the glass $As_{40}Se_{60}$ at. % composition studied in this project, the As (7N purity, Furakawa Denshi) and Se (5N purity, Materion) elemental precursors were heat-treated under vacuum (10^{-3} Pa) at 310 ℃ and 260 ℃, respectively, in order to purify them by driving off volatile oxides. The elements were subsequently batched under a nitrogen atmosphere in an MBraun glove-box (≤ 0.1 ppm H_2O and ≤ 0.1 ppm O_2) into a vitreous silica ampoule (Multi-Lab Ltd, UK). After batching, the silica ampoule was sealed (under ~10^{-3} Pa vacuum) using an oxy-propane (CALOR Gas) torch (Jensons, Junior Jet 7), and placed in a rocking furnace to melt and homogenise the glass at ~ 800 ℃ / 12 h for the $As_{40}Se_{60}$ at. % composition. The

melts were quenched and annealed for 1h at the on-set T_g of 180 ℃ before slowly cooling them down to room temperature. The details of the melting, quenching and annealing schedules are shown in Table 3.3-2. This produced glass rod which were ~ 10 mm in diameter and ~ 70 mm in length. The $As_{40}Se_{60}$ at. % samples used in this project were prepared by Dr. Dinuka Jayasuriya at the time the work was undertaken a PhD candidate in the MIR Photonics Group, University of Nottingham UK.

Table 3.3- 2. Typical, melting, quenching and annealing schedule of the chalcogenide glasses investigated in this Project.

Steps	$As_{40}Se_{60}$ at. %	$Ge_{16}As_{24}Se_{15.5}Te_{44.5}$ at. %	$Ge_{20}Sb_{10}Se_{70}$/ $Ge_{20}Sb_{10}Se_{67}S_3$ at. %
Melting Schedule			
Initial temperature ramp	25 ℃ to 300 ℃ @ 40 ℃/h.	25 ℃ to 450 ℃ @ 40 ℃/h.	25 ℃ to 450 ℃ @ 40 ℃/h.
Slow temperature ramp (rocking on)	300 ℃ to 800 ℃ @ 40 ℃/h.	450 ℃ to 850 ℃ @ 40 ℃/h.	450 ℃ to 900 ℃ @ 40 ℃/h.
Dwell (rocking on)	12 h	12 h	12 h
Temperature ramp	800 ℃ to 650 ℃ @ 40 ℃/h. (rocking on)	850 ℃ to 560 ℃ @ 60 ℃/h. (Vertical hold)	900 ℃ to 700 ℃ @ 50 ℃/h. (Vertical hold)
Dwell time before quenching	2 h @ 650 ℃.	1 h @ 560 ℃.	1 h @ 700 ℃.
Quenching			
Air-quenching	(a) Quench in air to ambient (0.5 - 2.0 mins). (b) Quench in small tube furnace set at T_g (0.5 - 2.0 mins). (c) Progressively quench chalcogenide glass, from top to bottom of the boule, with nitrogen gas.		
Annealing			
1	Dwell for 1 h @ T_g	Dwell for 1 h @ T_g	Dwell for 0.5 h, 10 ℃ below T_g
2	Turn furnace off and allow to cool to RT (~24 h).	Turn furnace off and allow to cool to RT (~24 h).	Turn furnace off and allow to cool to RT (~24 h).

Key: T_g= glass transition temperature; RT= room temperature.

(b) $Ge_{16}As_{24}Se_{15.5}Te_{44.5}$ at. %

For preparing the $Ge_{16}As_{24}Se_{15.5}Te_{44.5}$ at. % glass studied in this project, the As (7N purity, Furakawa Denshi) and Se (5N purity, Materion) elemental precursors were heat-treated under vacuum (10^{-3} Pa) at 310 ℃ and 260 ℃, respectively, in order to purify them by driving off volatile oxides. Ge (5N purity, Materion) and Te (5N purity, Materion) were untreated. The elements were subsequently batched under a nitrogen atmosphere in an MBraun glove-box ($\leq$ 0.1 ppm H_2O and $\leq$ 0.1 ppm O_2) into a prepared silica ampoule (Multi-Lab Ltd, UK). After batching, the silica ampoule was sealed (under ~10-3 Pa vacuum) and placed in a rocking furnace to melt and homogenise the glass, at ~ 850 ℃ / 12 h for the $Ge_{16}As_{24}Se_{15.5}Te_{44.5}$ at. % composition. The melts were quenched and annealed for 1h at the on-set T_g of 175 ℃ before slowly cooling them down to room temperature. The details of the melting, quenching and annealing schedules are shown in Table 3.3-2. This produced glass rod which were ~ 10 mm in diameter and ~ 70 mm in length. The Ge-As-Se-Te samples investigated in this Project were also prepared by Dr. Dinuka Jayasuriya.

(c) $Ge_{20}Sb_{10}Se_{70}$ at. % / $Ge_{20}Sb_{10}Se_{67}S_3$ at. %

The $Ge_{20}Sb_{10}Se_{70}$ at. % and $Ge_{20}Sb_{10}Se_{67}S_3$ at. % glass compositions studied here were prepared by the traditional melt-quench technique. The Se (99.999 %; Materion, ABSCO Materials, Suffolk, UK) and Sb (99.9999 %, Cerac, ABSCO Materials) elemental precursors were purified via a bake-out procedure to remove oxide impurities. Ge (5 N purity, Materion) was untreated as elemental Ge and Ge-oxides have low, and similar vapour pressures, even at high temperatures. As-supplied Ge (99.999%, Materion) was batched into the prepared silica ampoule (Baumbach, Suffolk, UK/ Multilab, Newcastle, UK), along with purified Sb and Se / S, under a nitrogen atmosphere (99.998 % BOC, white-spot) in a MBraun glove-box ($\leq$ 0.1 ppm H_2O and $\leq$ 0.1 ppm O_2). After batching, the silica ampoule with raw materials was sealed under vacuum (10^{-3} Pa) using an oxy-propane (BOC gas) torch (Jencons,

Junior Jet 7, East Grinstead, UK) and placed in a rocking furnace to melt and homogenise the glass, at ~ 900 ℃ / 24 h. After cooling to 700 ℃, the ampoule was removed from the furnace and was quenched and the chalcogenide glass was annealed *in situ* at the onset-T_g for 0.5 h, before cooling down to room temperature. The details of the melting, quenching and annealing schedules are shown in Table 3.3-2. This produced glass rods which were ~ 10 mm in diameter and ~ 70 mm in length. The $Ge_{20}Sb_{10}Se_{70}$ at. % and $Ge_{20}Sb_{10}Se_{67}S_3$ at. % samples investigated in this project were prepared by Dr. Harriet Parnell at the time the work was undertaken a PhD candidate in the MIR Photonics Group, University of Nottingham UK.

3.4 Prism preparation

The procedure used for making chalcogenide glass prisms was as follows:

1. An as-synthesised, as-annealed chalcogenide glass rod of ~ 10 mm diameter, prepared as described in section 3.3, was placed on a home-made metal holder and a diamond embedded blade (Isomet saw, Buehler Ltd, LECO Instruments Ltd) was used to cut through the glass rod in order to make a glass rod section 10-15 mm long.
2. The glass rod was placed in a plastic holder with some silicon spray (Supplier: Force) on its internal surface. Monomer epoxy liquid (Supplier: Easycomposites^{TM}) was poured on to the rod to completely immerse it. The holder with the sample was left for 24 hours for polymerisation to occur.
3. The polymer-encapsulated glass rod sample was taken out of the holder and hot mounted on a home-made metal holder at ~ 80 ℃ using wax (Buehler, Coventry, UK), as shown in Figure 3.4-1 (a). The holder with the sample was placed on the Buehler saw and was cut through at the dotted line shown on Figure 3.4-1(a). After cutting, the sample looks like the schematic shown in Figure 3.4-1(b). The chalcogenide glass sample was ground using 400 ppm and 1000 ppm SiC grinding powder (Supplier: Buehler), and then polished to a 1μm

finish using 6 µm, 3 µm and 1 µm diamond paste (Supplier: Buehler) progressively.

4. The one-face-polished sample was removed from the holder and mounted on a second holder whose top had been machined to the desired prism angle (Figure 3.4-1(c)). A futher cut was made, as indicated by the dotted line in Figure 3.4-1(c), using the saw, and grinding and polishing then performed to a 1 µm finish. The final prism with the desired apex angle is shown schematically in Figure 3.4-1(d). As will be described in section 4.3, an increase in the apex angle reduces the standard deviation of the resulting refractive index measurement. However, if the apex angle is too large, the beam is unable to pass through the prism. A 20 ° prism apex angle is a good choice for chalcogenide glasses (for refractive indices 2.2 to 3.5). The grinding and polishing schedule for manufacturing chalcogenide prisms is shown in Table 3.4-1

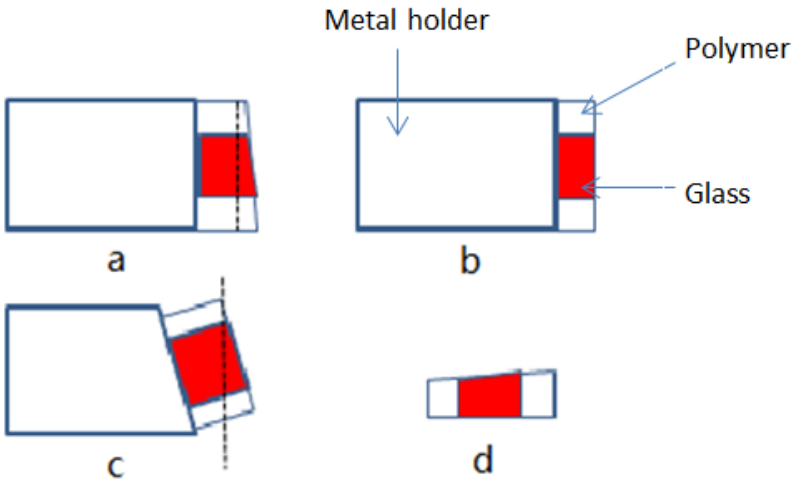


Figure 3.4- 1. Schematic diagrams showing the prism preparation procedure

Table 3.4- 1. The grinding and polishing schedule of manufacturing chalcogenide prisms.

Powders	Time (Surface1)	Time (Surface2)
Silicon carbide powders (diameter: 63.5 μm, supplier: Struers)	40 minutes	40 minutes
Silicon carbide powders (diameter: 25.4 μm)	10 minutes	10 minutes
Diamond polishing compound (diameter: 6 μm, supplier: Metadi)	20 minutes	20 minutes
Diamond polishing compound (diameter: 3 μm, supplier: Metadi)	13 minutes	13 minutes
Diamond polishing compound (diameter: 1 μm, supplier: Metadi)	10 minutes	10 minutes

The chalcogenide prisms manufactured by the procedure presented here are shown in Table 3.4-2.

Table 3.4- 2. The personal prism code, composition and melting code, and target apex angle of the prisms fabricated in this Project.

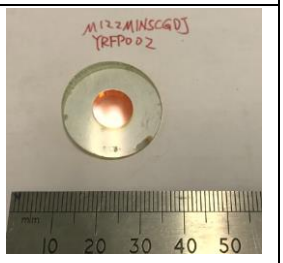
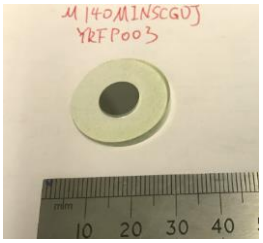
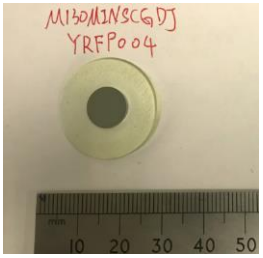
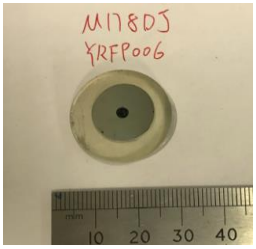
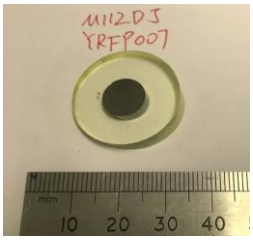
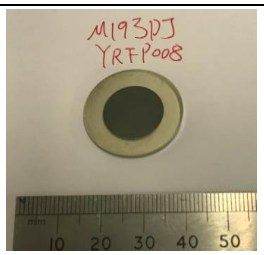
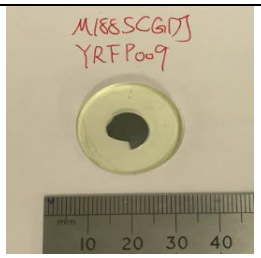
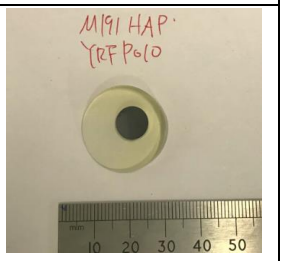
Prism code	Composition / at. %	Melting code	Target apex angle / °	Picture
YRFP001	$Ge_{7.5}As_{25.5}S_{67}$	M122MINSCGDJ	20	
YRFP002	$Ge_{7.5}As_{25.5}S_{67}$	M122MINSCGDJ	10	
YRFP003	$Ge_{16}As_{24}Se_{15.5}Te_{44.5}$	M140MINSCGDJ	10	
YRFP004	$As_{40}Se_{60}$	M130MINSCGDJ	10	
YRFP005	$Ge_{20}Sb_{10}Se_{70}$	M135HAP	20	

Table 3.4- 2. The personal prism code, composition and melting code, and target apex angle of the prisms fabricated in this project. (continued)

Prism code	Composition / at. %	Melting code	Target apex angle / °	Picture
YRFFP006	$Ge_{14.3}As_{27}Se_{15.5}Te_{43.2}$	M178DJ	20	
YRFFP007	$Ge_{20}As_{20}Se_{14}Te_{46}$	M112DJ	10	
YRFFP008	$Ge_{15}As_{25}Se_{19}Te_{41}$	M193DJ	10	
YRFP009	$Ge_{16}As_{24}Se_{15.5}Te_{44.5}$	M188SCGDJ	10	
YRFP010	$Ge_{20}Sb_{10}Se_{67}S_3$	M191HAP	20	

3.5 Hot pressing

A hot-pressing technique developed during the project will be presented in this section. With the advantage of achieving good surface finish, this technique was found suitable for fabricating both thin films and ellipsometry samples [3.1].

3.5.1 Hot pressing technique

Figures 3.5-1 and 3.5-2 show photographs of the hot pressing equiment used in preparing thin film samples and ellipsometry samples. There were two flat aluminium plates (diameter: ~150mm) inside the vacuum chamber as shown in Figure 3.5-1. The base plate could be moved up to reach the top plate for pressing. Inside each plate there was a thermocouple to measure the temperature of the plate, which was controlled by the temperature controller (see Figure 3.5-2). A bell jar was used as the chamber which was evacuated by a rotary pump. In the control panel (see Figure 3.5-2), movement controllers could control the movement of the base plate up and down. The load controller could increase the pressure between the two plates during hot pressing, and the pressure could be read out on the applied load readout. Moreover, a height readout measuring the changing height of the base plate up to 0.01 mm accuracy was placed in the panel, as shown in Figure 3.5-2.

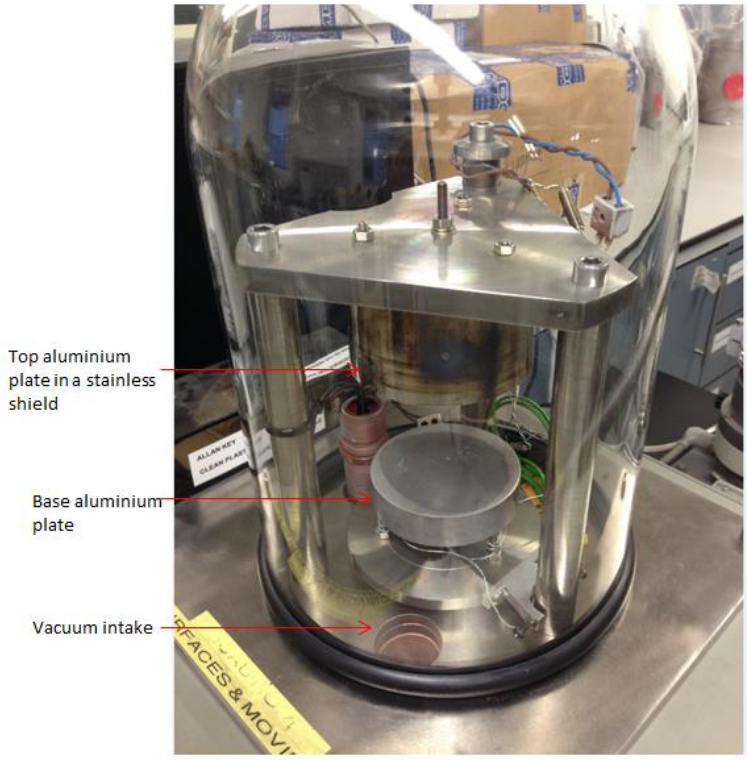


Figure 3.5- 1. Photograph of the vacuum chamber of the hot pressing equiment showing the top and base alluminium plates used for hot pressing.

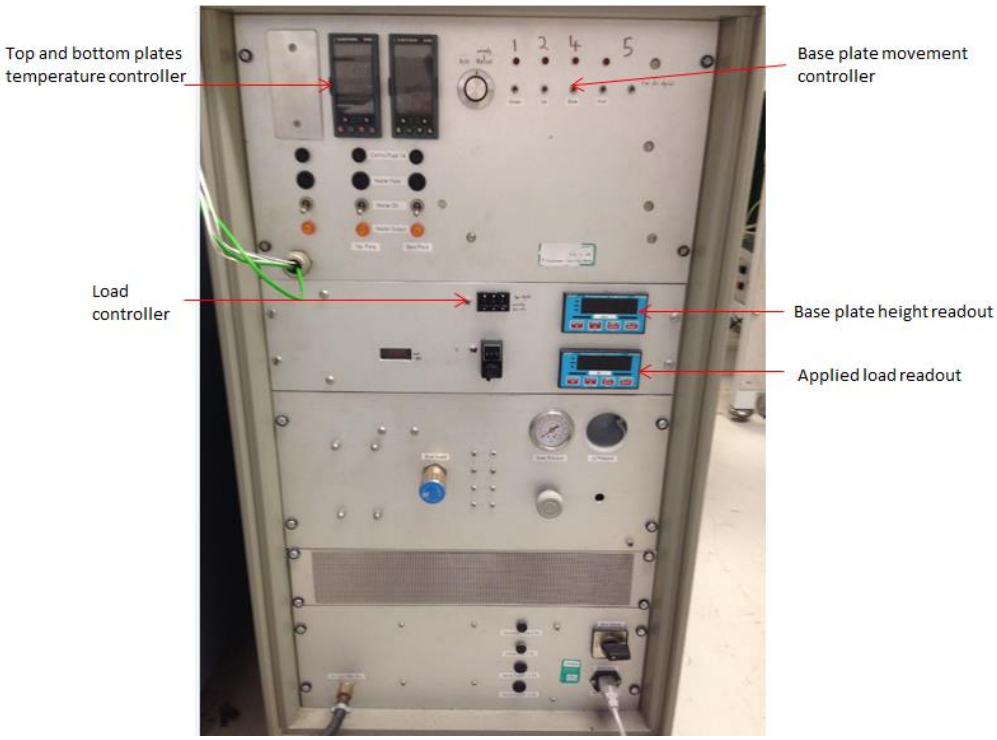


Figure 3.5- 2. Photograph of the control panel of hot pressing equiment.

3.5.2 Chalcogenide glass thin film preparation

A hot-pressing technique was developed to prepare thin films of chalcogenide glass (see section 3.5.1); this involved the hot-pressing of *circa* 20 mm lengths of fibre, with a nominal diameter of 250 μm, using the hot-press previously described in [3.2-3.4] and in section 3.5.1. The as-annealed preforms (~ 10 mm diameter and ~ 70 mm length) of chalcogenide glasses (e.g. $Ge_{16}As_{24}Se_{15.5}Te_{44.5}$ at. % and $As_{40}Se_{60}$ at. %), prepared as in section 3.3, were drawn into optical fibres using a customised Heathway draw-tower in a 10,000- Class clean-room. The fibres were drawn under a N_2 flow (BOC white-spot) at a viscosity of around $10^{4.5}$ Pa.s. The final fibre diameter was 250 ±10 μm. The outer surface of the fibres was shiny and no defects could be seen by the naked eye. Four chalcogenide fibres, each of about 250 μm diameter and 20 mm length, were cleaved from the chalcogenide fibre. The four 20 mm lengths of chalcogenide fibre were each immersed in propylamine (Sigma-Aldrich 99 mol.%) for 30 mins at room temperature under atmospheric pressure to remove the oxide layer on the outer surface. Subsequently the etched fibres were taken out of the propylamine and were immersed in acetone (99.8%, Sigma Aldrich) for 10 minutes and subsequently each fibre was individually cleaned carefully using isopropanol (IPA, HPLC grade, Fisher Chemical) with optical lens tissues. A silica glass ampoule (Multi-Lab Ltd, UK) was used as the container for the propylamine-etching; this was rinsed with distilled water and dried under vacuum (~10^{-3} Pa). The four propylamine-etched 20 mm long fibres were then placed on a tungsten carbide plate (800 mm diameter, of flatness 0.08 μm and of surface finish 0.009 μm) surrounded by a thick stainless steel shim (Supplier: Hollinbrow Ltd, UK) with the choice of thickness of 20, 25 and 30 μm, as shown in Figure 3.5-3(a), and then covered by a second tungsten carbide plate, as shown in Figure 3.5-3(b). The fibre samples were hot-pressed under vacuum (10^{-4} Pa) at T_g +40 ℃ (viscosity ~10^{8} Pa s) with a maximum pressure of 700 N between the two plates. A schematic figure of the hot-pressing of chalcognenide fibres is shown in Figure 3.5-3(b). For the preparation

of standard single-material thin films, the samples were then annealed at the onset-T_g and allowed to cool with the tungsten carbide plates. For manufacturing "fast-quenched" thin films, nitrogen was filled into the hot-pressing chamber after releasing the pressure, causing the samples to be cooled down at a rate of ~ 75 ℃/h. The hot pressing temperature-pressure versus time schedule used for manufacturing the $As_{40}Se_{60}$ at. % (M130MINSCGDJ) thin films (YRFFP002) is shown in Figure 3.5-3(b) as an example. In order not to damage the samples while opening the press, solvents (acetone and if necessary IPA) were squirted into the gap between the two tungsten carbide plates. The single-material thin films prepared using the techniques described in this section were listed in Table 3.2-1. The as-annealed chalcogenide glass single-material thin films prepared using this technique will be investigated in section 6.3 to yield their refractive indices and material dispersions. The fast-quenched single-material thin film will be used to investigate the effect of annealing on the hot-pressed thin film in section 6.6.

In order to determine a very small refractive index contrast of the core and cladding compositions of an intended low numerical aperture step-index fibre [3.5], an unstructured fibre of the core composition ($Ge_{20}Sb_{10}Se_{70}$ at. % (M135HAP)) was hot-pressed together with an unstructured fibre of the cladding composition ($Ge_{20}Sb_{10}Se_{67}S_3$ at. % (M157HAP)) to form a two-composition thin film, with the advantages of the two glasses having the same post-fibre processing thermal history. For fabricating the two-composition chalcogenide glass thin films, the pre-treated $Ge_{20}Sb_{10}Se_{70}$ at. % and $Ge_{20}Sb_{10}Se_{67}S_3$ at. % fibres (each fibre was cleaved to be ~ 20 mm long and etched by propylamine for 30 mins) were placed on a tungsten carbide plate surrounded by a 25 μm thick stainless steel shim and then covered by a second tungsten carbide plate. The distance between the two fibres: $Ge_{20}Sb_{10}Se_{70}$ at. % and $Ge_{20}Sb_{10}Se_{67}S_3$ at. % was, from experience, set at 1 mm to allow the two materials to spread until touching during pressing but not move into each other. The fibre samples were hot-pressed under vacuum (10^{-4} Pa) at 260 ℃ (temperature at

which the viscosities of both glasses were ~ 10^8 Pa s) for 15 h with a maximum pressure of 700 N between the two plates. The pressure was removed at the temperature of 260 ℃. The samples were then cooled down at a slow rate (10 ℃/h) across the T_g region (from 230 to 200 ℃) and then allowed to cool down naturally with the equipment under the vacuum to room temperature. The optical properties of this two-composition ($Ge_{20}Sb_{10}Se_{70}$ at. % and $Ge_{20}Sb_{10}Se_{67}S_3$ at. %) thin film will be investigated in section 6.7.

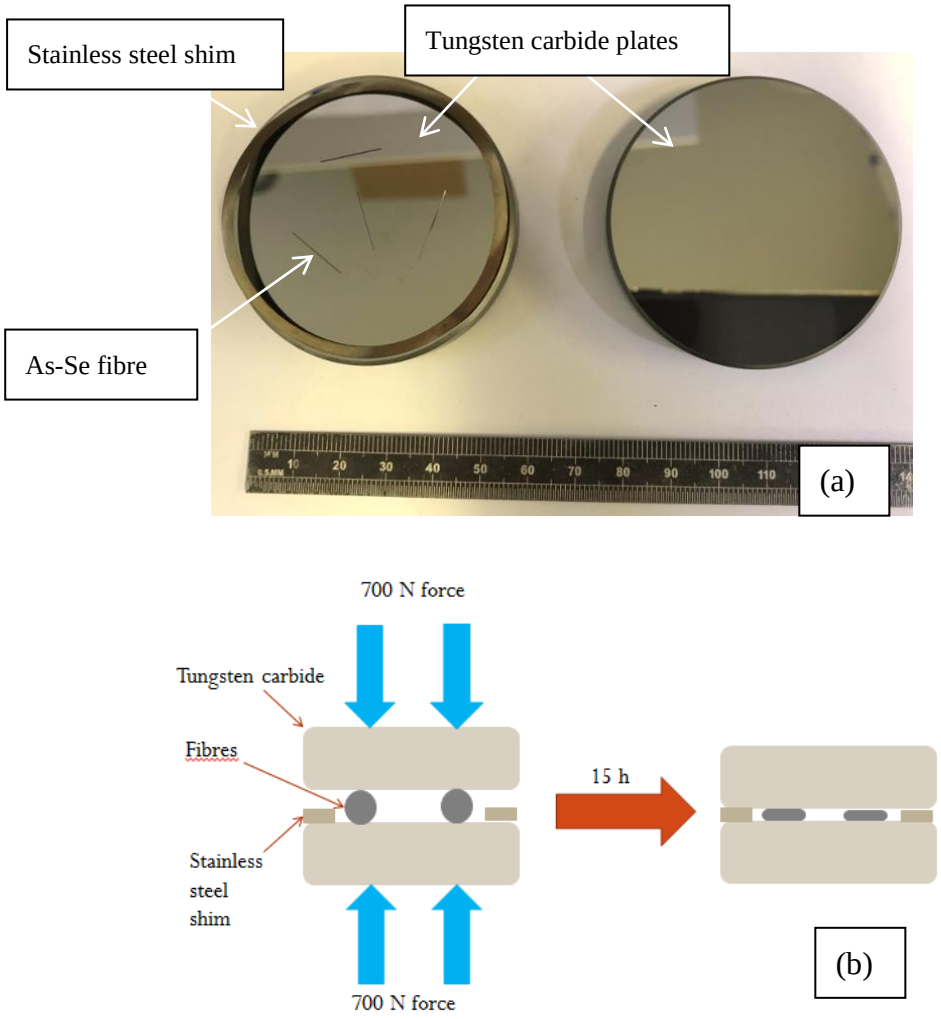


Figure 3.5- 3. (a) The picture of four $As_{40}Se_{60}$ at. % (M130MINSCGDJ) fibres and a stainless steel shim placed on a tungsten carbide plate and a second tungsten carbide plate; (b) Schematic figure of hot-pressing chalcogenide fibres.

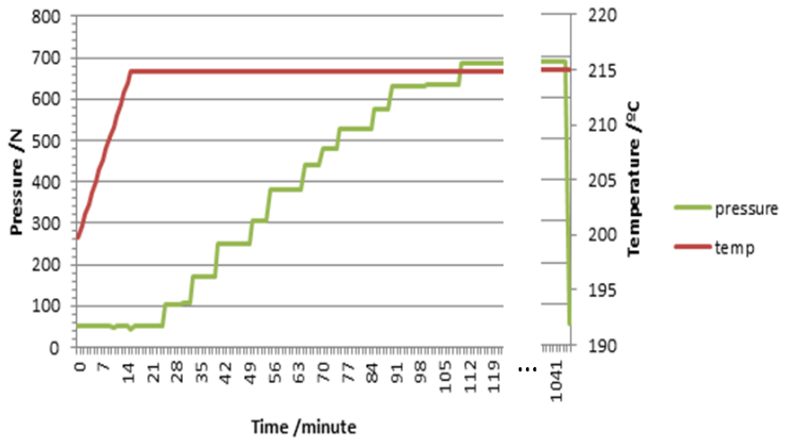


Figure 3.5- 4.The hot-pressing schedule used for making $As_{40}Se_{60}$ at. % (M130MINSCGDJ) thin films (YRFFP002).

3.5.3 Ellipsometry sample preparation

For the preparation of pressed samples for ellipsometry studies, the as-annealed chalcogenide glass rod (see section 3.3), with a diameter of 10 mm, was saw cut using a diamond embedded blade (Isomet saw, Buehler Ltd, LECO Instruments Ltd) to a ~ 3 mm thick disc sample. Disc faces were ground for 1 minute using 1000 grit silicon carbide (SiC) powder (see Table 3-2) with polishing oil (manufacturer, see Table 3.1-2), and successively polished from 6 µm, 3 µm, to a 1 µm finish using 6 µm, 3 µm and 1 µm diamond paste (Supplier: Buehler), respectively. To ensure that the opposite faces of the discs were both flat, orthogonal to the rod axis and parallel, the well-polished disc samples were lightly hot-pressed (pressure: 450 N) for 45 mins under vacuum at T_g + 25 ℃, between two tungsten carbide plates (diameter: 100 mm; flatness: 0.08 µm; surface finish: 0.0009 µm). The pressure was then released. The sample was annealed at the on-set T_g and allowed to cool down naturally to room temperature under vacuum. After the hot-pressing, the back face of the sample was re-roughened using using 1000 grit silicon carbide (SiC) powder (see Table 3.1-2) with polishing oil while the other surface was protected with Parafilm M©. The sample thickness was measured using a micrometre. These well-prepared ellipsometry samples were sent to J. A. Woollam Co. Inc. (Lincoln, NE68508, U.S.)

for spectroscopic ellipsometry analysis. The results obtained from the spectroscopic ellipsometry analysis will be discussed in detail in chapter 5.

3.6 Fourier transform infrared (FTIR) spectroscopy

In this Project, Fourier-transform infrared (FTIR) spectroscopy (Bruker IFS 66 v/s) was used to obtain the transmission spectra of a bulk-glass sample or a thin film sample. For characterizing a bulk-glass sample, information about the absorptions of impurities (see section 7.1), the transparent window (see sections 5.3) and multi-phonon absorptions (see section 7.1) can be obtained. For the thin-film samples prepared as described in section 3.5, the transmission spectra measured using FTIR spectroscopy can be used to determine the refractive index and thickness of the thin film (see chapter 6).

3.6.1 Basic theory

A Fourier transform spectroscope is a Michelson interferometer with a movable mirror and a stationary mirror (see Figure 3.6-1). The beam splitter, the source and the detector must match in operating wavelengths for the region to be studied. A source beam, whose size can be controlled by an aperture, is split into two beams by a beam splitter. One beam is reflected off a stationary mirror; the other is reflected by a movable mirror, the measurement of which can cause a time delay in the reflected signal. By scanning the movable mirror over some distance, an interference pattern is produced that encodes the spectrum of the source and which turns out to be its Fourier transform [3.6]. The combined beam passes through the sample and the resulting interferogram is collected using the detector. The data obtained from the detector is analysed using the in-built Bruker software (OPUS).

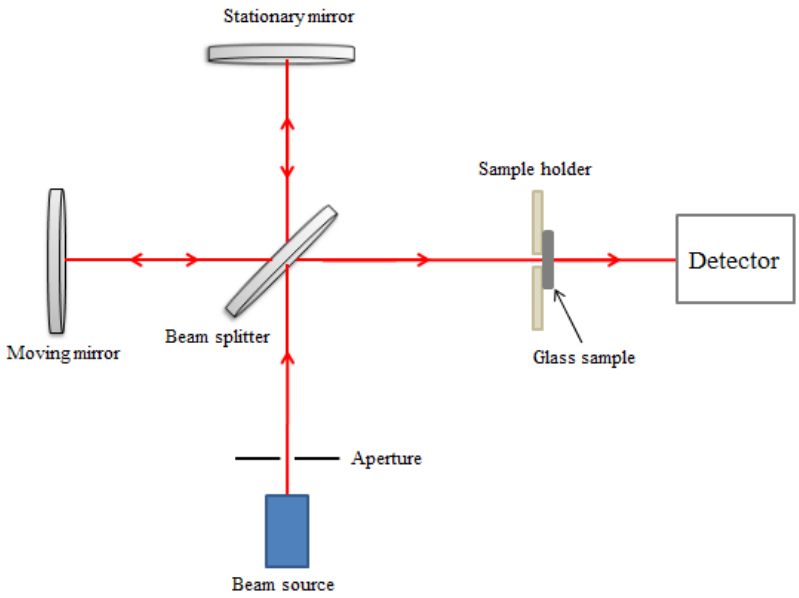


Figure 3.6- 1. The schematic diagram of the FTIR spectrometer configuration.

3.6.2 Bulk-glass sample preparation for FTIR measurements

An as-annealed chalcogenide glass rod, with a diameter of ~10 mm, was saw cut using a diamond embedded blade (Isomet saw, Buehler Ltd, LECO Instruments Ltd) to a ~ 4 mm (bulk-glass FTIR sample) or ~ 2mm (thin FTIR sample for infrared FTIR measurements) thick disc sample. The disc sample was then mounted on to an in-house built polishing jig and ground for ~ 2 mins using 1000 grit silicon carbide (SiC) powder (manufacturer, see Table 3.1-2) with polishing oil (manufacturer, see Table 3.1-2) to attain a parallel surface. After that, the sample was polished progressively from 6 µm, 3 µm, to a 1 µm finish using 6 µm, 3 µm and 1 µm diamond paste, respectively. For each grit, the polishing time was ~ 6 mins. The one-face-polished sample was re-mounted on to the polishing jig for grinding and polishing the other surface. The well-polished surface was protected by a layer of wax (Buehler). The second surface was ground and polished to a 1 µm finish following the same procedure as that used for the first surface. Note that careful cleaning using acetone and isopropanol was required after each grinding and polishing step. After obtaining two well-polished surfaces, acetone was used to clean

the sample and remove the wax. The thickness of the FTIR sample was measured using a micrometer.

3.6.3 Method for bulk glass characterisation

For near-infrared (NIR) spectroscopy, a tungsten-lamp source, a CaF_2 beam-splitter and an InGaAs detector were set up in the FTIR spectrometer. MIR spectroscopy, the setup for the FTIR spectrometer was a GlobarTM source, a KBr beam splitter and a DLaTGSD301 detector. In this Project, the main focus was on MIR spectroscopy. Before measurements, the FTIR spectrometer was purged with dry air (Parker Filtration, FTIR purge gas generator, 75-52-12VDC) for 15 mins to minimise the effect of air absorptions (O-H band at ~ 2.9 µm [3.7, 3.8], CO_2 absorption at 4.2 µm [3.8] and molecular H_2O bending absorption at 6.2 µm [3.8, 3.9]). Then a background spectrum was recorded using the chosen aperture size of 12 mm. This background spectrum was automatically removed by Bruker software during the sample run. After the background collection, the bulk-glass FTIR sample was mounted on the aperture (diameter: 5 mm) of an in-house built sample holder using blue plasticine. Then the sample holder was replaced in its slot in the FTIR spectrometer and the spectrum was collected after 15 mins of dry-air purging.

3.6.4 Measuring the transmission spectra of an interband cascade laser (ICL) and SuperK supercontinuum source using FTIR spectroscopy

An interband cascade laser (ICL) fabricated at the Naval Research Laboratory (NRL), USA, (which emitted > 200 mW cw at 25 °C) and SuperK mid-infrared supercontinuum source (1.1-4.2 µm, 450 mW) from NKT Photonics, used in conjunction with a band pass filter (centre wavelength: 3.8 µm; FWHM: 180 nm) will be amongst the light sources used in the prism minimum deviation measurements reported in chapter 4 of this thesis. Therefore, it was important to measure the operating wavelengths of the ICL and SuperK sources.

3.6.4.1 Experimental setup

The experimental setup for obtaining the emission spectra of the ICL and SuperK sources is shown in Figure 3.6-2. When obtaining the emission spectrum of the ICL, the KBr beam splitter and DLaTGSD301 detector were set up in the FTIR spectrometer (Bruker IFS 66v/s) and the ICL output was carefully launched into the FTIR spectrometer as shown in Figure 3.6-2. The resolution used was set to be 2 cm^{-1} and the scan time was set to be 30 mins. When obtaining the emission spectrum of the SuperK source, a CaF_2 beam-splitter and DLaTGSD301 detector were set up in the FTIR spectrometer (Bruker IFS 66v/s). The SuperK source was carefully aligned into the FTIR spectrometer, as shown in Figure 3.6-2, and the scan time was set to be 30 mins with a resolution of 2 cm^{-1}.

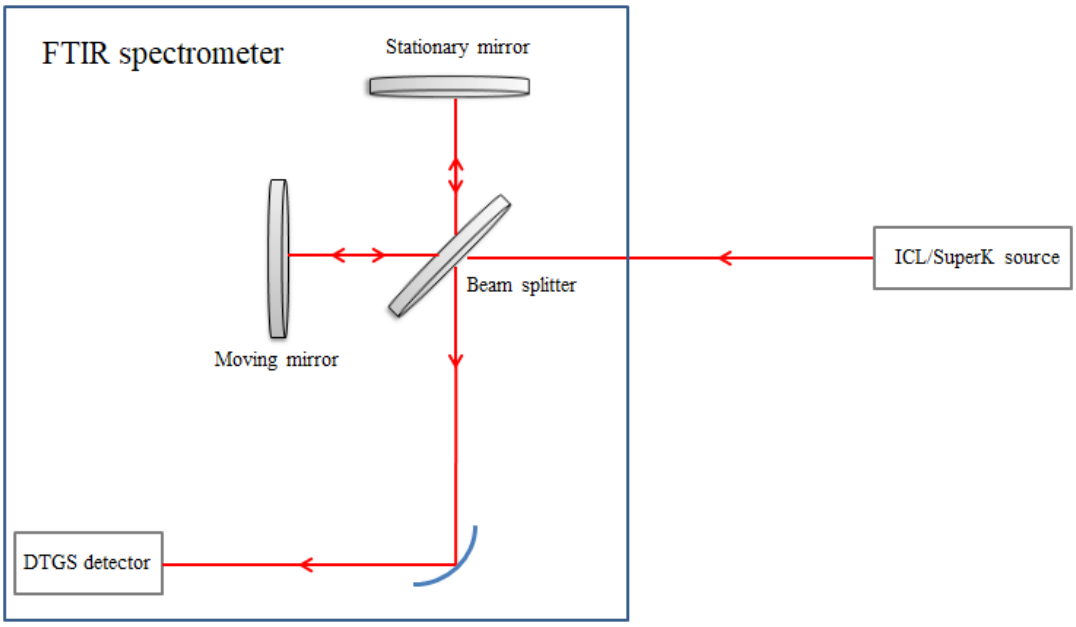


Figure 3.6- 2. Schematic of the FTIR spectrometer scheme used for measuring the operating wavelengths of ICL or SuperK sources.

3.6.4.2 Emission spectrum of the ICL using FTIR spectroscopy

The output intensity of the ICL was controlled by a laser diode driver (Thorlabs, LDC205C). The operation temperature of the ICL was controlled by a temperature controller (Thorlabs, TED200C). The drive current of the ICL was set to be 258.7 mA with an operating temperature of 23 ℃. The output emission spectrum of the ICL measured using the FTIR spectrometer is shown in Figure 3.6-3. It is found that the centre wavelength of the ICL located at ~ 3.107 μm, with a full width at half maximum (FWHM) of less than 0.011 μm, as shown in the inset of Figure 3.7-3. Second overtone and third overtone bands are observed at the wavelengths of ~ 1.504 μm and ~ 1.036 μm, respectively.

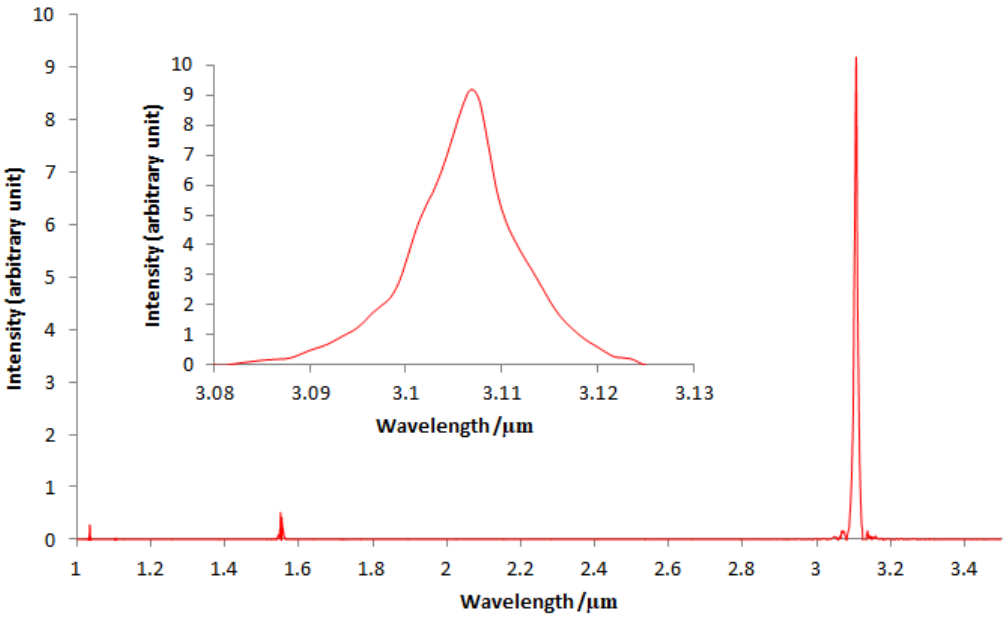


Figure 3.6- 3. The FTIR emission spectrum of the ICL when operated at 23 ℃ with a drive current of 258.7 mA. Inset: Detail of the emission around the centre wavelength of the ICL.

To further investigate the effect of temperature on the output of the ICL, the operating temperature was set to be 23 ℃, 24 ℃ and 25 ℃, respectively, using the Thorlabs temperature controller. The emission spectra of the ICL, obtained via FTIR spectrometry at these different temperatures, are shown in Figure 3.6-4. The drive current was kept constant at 258.7 mA. Figure 3.6-4 shows that, with temperature

increased, the central wavelength of the ICL shifts to longer wavelengths. At an operating temperature of 23 ℃, the central wavelength locates at ~ 3.107 μm. With the operating temperature increased to 24 ℃ and 25 ℃, the central wavelength shifted to ~ 3.108 μm and ~ 3.109 μm, respectively, as shown in Figure 3.6-4. The amplitude of the emission spectrum reduced as the operating temperature increased, as shown in Figure 3.6-4. To obtain the exact values of the output power, a Power Max 500A laser power meter (Molectron Detector Inc.) was placed in front of the ICL, at a distance of 40 mm. The measured output power was 4.29 mW, 2.44 mW and 0.32 mW for operating temperatures of 23 ℃, 24 ℃ and 25 ℃, respectively.

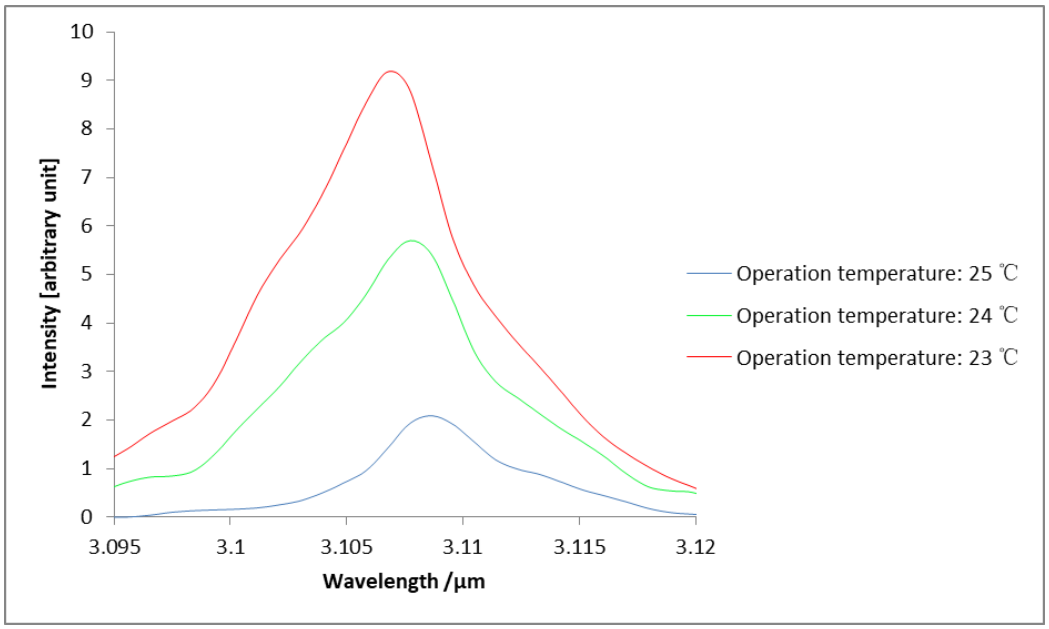


Figure 3.6- 4. The emission spectra of the ICL, obtained using FTIR spectroscopy at the temperatures of 23 ℃, 24 ℃ and 25 ℃. The drive current was kept constant at 258.7 mA.

3.6.4.3 Emission spectra of SuperK source with a band pass filter

The experimental setup for obtaining the emission spectrum of the SuperK source using FTIR spectroscopy was shown in Figure 3.6-2. The emission spectrum of the SuperK source obtained using FTIR spectroscopy is shown as the blue curve in Figure 3.6-5. A band pass filter (centre wavelength: 3.8 μm; FWHM: 180 nm) was placed in front of the SuperK source; the resulting emission spectrum is shown as the

green curve in Figure 3.6-5. The centre wavelength of the SuperK source locates at the wavelength of ~ 3.80 μm with a FWHM of less than 0.16 μm. The SuperK source used in conjunction with this bandpass filter will be used to measure the refractive index of chalcogenide prisms using the minimum deviation method, as will be described in chapter 4.

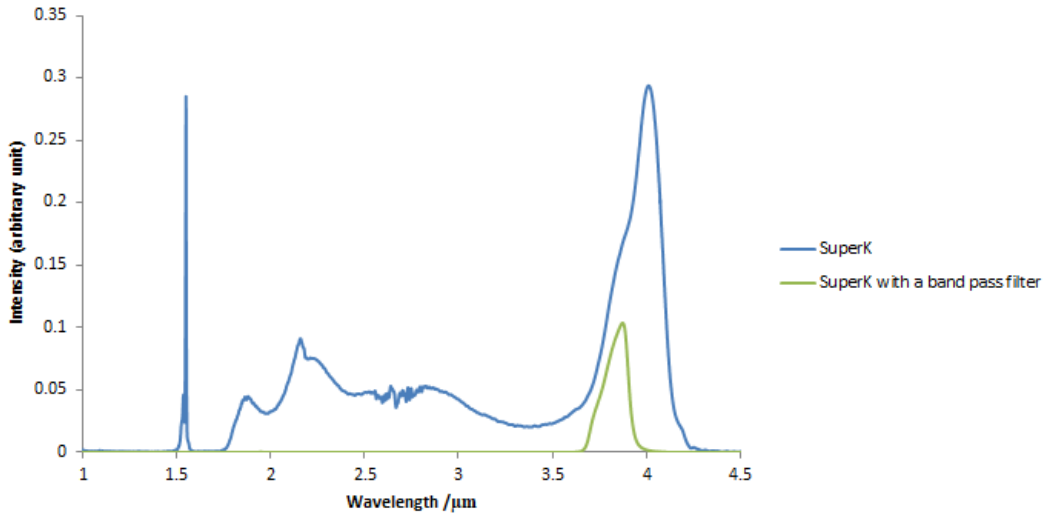


Figure 3.6- 5. The emission spectra of the SuperK source and the SuperK source used in conjunction with a 3.8 μm band pass filter obtained using FTIR spectroscopy.

3.6.5 Thin-film FTIR measurements using FTIR spectroscopy

One big goal in this Project is to determine the refractive index of a chalcogenide thin film using the Swanepoel method [3.9]. The chalcogenide thin films for this work were successfully manufactured by the hot-pressing technique, as described in section 3.5. In order to determine the refractive index of the resulting chlacogenide glass thin film, FTIR spectroscopy was used to obtain the transmission spectra of the thin films.

3.6.5.1 Experimental operation and results

A Globar^{TM} source, KBr beam splitter and DLaTGSD301 detector were set up in the FTIR spectrometer (Bruker IFS 66v/s) to measure the transmission spectra of the

thin films in the wavelength range from 1 to 25 μm; 25 μm was the maximum wavelength possible with this set-up in the Bruker FTIR. Because of the low efficiency of the KBr beam splitter and the DLaTGSD301 detector at wavelengths below 2 μm, clear extrema in the transmission spectra were only obtained over the wavelength range from 2 to 25 μm.

Before measurements, the FTIR spectrometer was purged with dry air and a background spectrum was then recorded using the chosen aperture size of 1 mm. As discussed above, the background spectrum was automatically removed by Bruker software during the sample run. The hot-pressed thin film, prepared using the hot-pressing technique described in section 3.5.1, was mounted on a home-made rotation stage, which was accurate up to 0.1 º, installed in the sample compartment of the Bruker 66 v/s FTIR spectrometer. In the FTIR spectrometer a He-Ne beam, which was used for alignment, indicated the position of the Globar^{TM}. Careful alignment was undertaken to ensure that the axis of rotation went through the surface of the thin film at the focal point of the He-Ne beam and that no lateral displacement of the light took place during rotation. The location of normal incidence was determined by ensuring that equivalent transmission spectra were obtained after rotation through equal angles in a clockwise and anticlockwise sense. Before recording the spectrum of the thin film, a 15-min dry-air purging was allowed to minimise the effect of air absorptions. After obtaining the transmission spectrum at normal incidence, the rotation stage was rotated by an angle of 30 ºto obtain the transmission spectrum with an incident angle of 30 º. Then the rotation stage was rotated back to the normal incident position, and was rotated by an angle of 30 ºin the other direction. The transmission spectrum with an incident angle of -30 ºwas obtained using the FTIR spectroscopy.

3.6.5.2 Error analysis

The factors influencing the wavelengths at which extrema in the transmission spectra of the chalcogenide glass thin films occur are analysed in this sub-section. These influence the errors which occur when using these extrema to measure the refractive index and thickness of the thin films using an improved Swanepoel method (defined in chapter 6), as will be described in detail in chapter 6.

(a) Thickness variation of the thin film

The chalcogenide thin films used in this project were prepared by the hot-pressing technique described in section 3.5. Although a stainless steel shim, with a thickness of 20, 25 or 30 μm, was used during the hot pressing to maintain the surface flatness, a thickness variation still existed in the thin films produced. Since the surface finish of the tungsten carbide plate is ± 0.009 μm, the thickness variation of the hot-pressed thin films was mainly attributed to the fact that the thin film was not completely hot-pressed down to the target thickness. This leads to a wedge-shape thin film. In order to investigate the thickness variation across the thin film, the transmission spectra of different regions (see Figure 3.6-6) of a Pr^{3+}-ion doped Ge-As-Se-Ga thin film (YRFFP013) were measured using FTIR spectroscopy. Results are shown in Figure 3.6-7. For normal incidence on a film with the thickness *d*, the wavelengths of the transmission extrema are given by [3.10]:

$$2n_0 d = m\lambda_0 \qquad (3.1)$$

where λ_0 is the wavelength at the maxima or minima of the normal incidence transmission spectrum, n_0 is the refractive index of the material at λ_0, and *m* is the order number which has integer values for the maxima and half-integer values for the minima in the case where the thin film has no substrate or the refractive index of thin film is larger than that of the substrate [3.10].

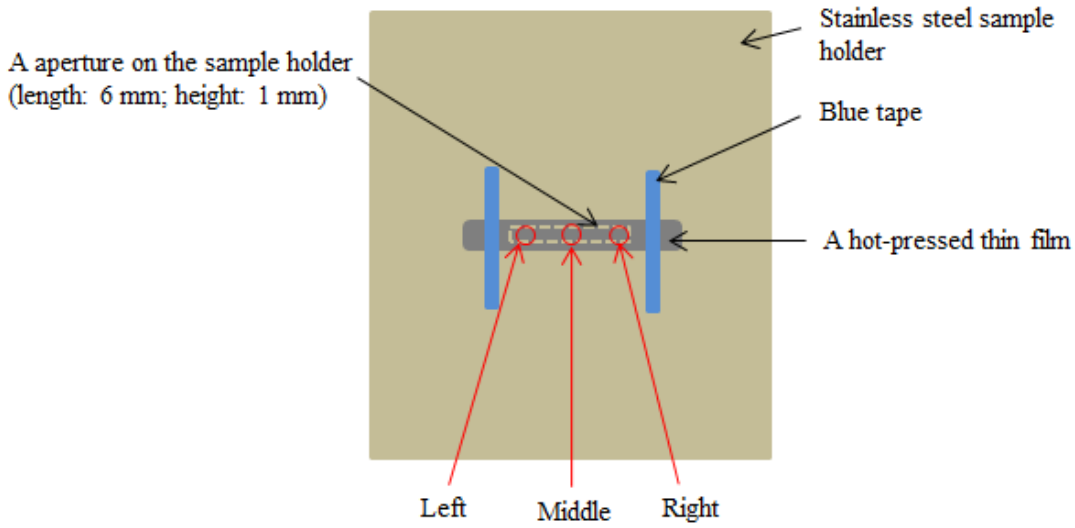


Figure 3.6- 6. Schematic figure of a thin glass film sample mounted on the sample holder with a aperture (length: 6 mm; height: 1 mm) using blue tape. Red circles outline the different parts of a Pr^{3+}-ion doped Ge-As-Se-Ga thin film (YRFFP013) measured.

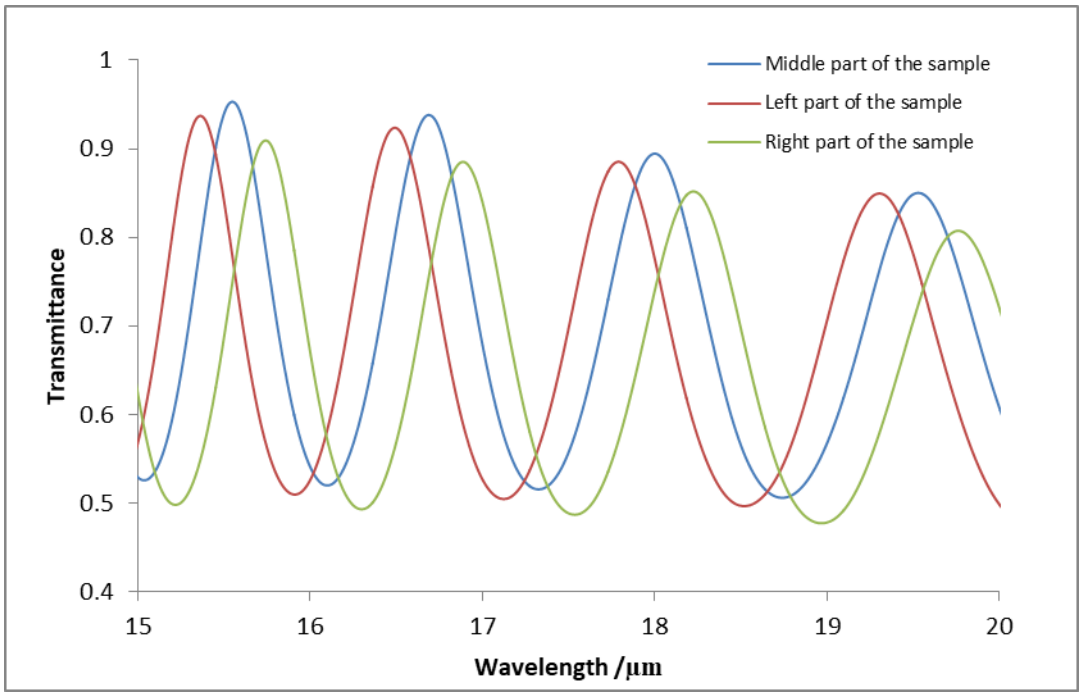


Figure 3.6- 7. The transmission spectra at normal incidence at different parts (see Figure 3.6-6) of a Pr^{3+}-ion doped Ge-As-Se-Ga thin film (YRFFP013). The shifts at the extrema are due to the thickness variation across the thin film sample.

Figure 3.6-7 shows that the wavelengths of the extrema are slightly different for the different parts of the thin films. The transmission spectrum obtained at the left

part of the thin film shows that extrema occur at shorter wavelengths. As the measured region shifted to the left part of the thin film via the middle part, the extrema in the transmission spectra progressively shifted to longer wavelengths. According to Eq. (3.1), since refractive index at different parts of the thin film can be assumed the same (the thin film is assumed homogeneous), the difference in the positions of the extrema can be attributed to a thickness variation across the thin film. Therefore, in this case, the thin film was wedge-shape with a smaller thickness at the left part and a larger thickness at the right part.

The interference transmission spectra at normal incidence of a chalcogenide wedge-shaped thin film with a smaller thickness variation (Pr^{3+} doped Ge-As-Se-Ga, YRFFP014) and that with a larger thickness variation (Pr^{3+} doped Ge-As-Se-Ga, YRFFP013) are compared in Figure 3.6-8. The blue-curve spectrum is obtained from a chalcogenide thin film (Pr^{3+} doped Ge-As-Se-Ga, YRFFP014) with smaller thickness variation while the red-curve spectrum represents that of the same film (Pr^{3+}-ion doped Ge-As-Se-Ga, YRFFP013) but with a larger thickness variation. It can be seen that the interference pattern shrinks dramatically, especially, at lower wavelengths if the thickness is not uniform.

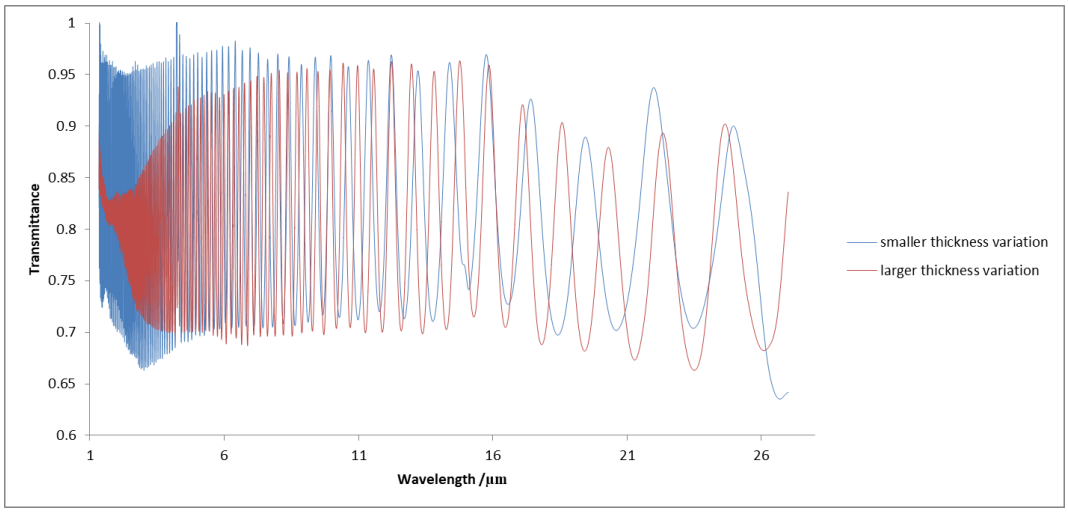


Figure 3.6- 8. The interference transmission spectra at normal incidence of a chalcogenide glass thin film with a smaller thickness variation (Pr^{3+}-ion doped Ge-As-Se-Ga, YRFFP014) and that with a larger thickness variation (Pr^{3+}-ion doped Ge-As-Se-Ga, YRFFP013).

According to [3.11], for a thin film with a thickness variation Δd over the probe beam diameter, the interference pattern will be destroyed at the point of $\lambda = 4n\Delta d$. In Figure 3.6-8, the extrema are distinguishable over the wavelength range from 1 μm to 27 μm in the blue-curve spectrum, which indicates that the thickness variation is less than 0.1 μm over the beam size of 1 mm assuming the refractive index n is ~ 2.6. For the red-curve spectrum in Figure 3.6-8, the extrema are no longer distinguishable at a wavelength of ~ 2 μm; this indicates that the thickness variation is ~ 0.2 μm over the 1 mm bean size. When $\lambda < 4n\Delta d$, a second interference pattern starts to appear but, since it is not of practical importance, it will not be considered further.

In this Project, the values of the wavelength at extrema will be used to determine the refractive index of the thin film using an improved Swanepoel method, as will be described in chapter 6. For the blue-curve spectrum with a smaller thickness variation in Figure 3.6-8, the values of the wavelength at extrema can be accurately obtained over the wavelength from 2 to 25 μm. For the red-curve spectrum with a larger thickness variation in Figure 3.6-8, the values of the wavelength at extrema

can be accurately obtained over the wavelength from 3 to 25 μm. Therefore, the thickness variation on the thin film will affect the wavelength range over which the refractive index measurement technique developed later is accurate (see section 6.3).

(b) Size of aperture

A small thickness variation (usually wedge-shape) typically exists across the hot-pressed thin film as previously discussed. An effective way to reduce the error caused by this thickness variation is to reduce the beam size by selecting a smaller aperture in the FTIR spectrometer. The interference transmission spectrum of an illustrative chalcogenide glass thin film (Pr^{3+}-ion doped Ge-As-Se-Ga, YRFFP013) at normal incidence using an aperture of 6 mm in the FTIR spectrometer is shown as the blue curve in Figure 3.6-9. The blue curve in Figure 3.6-9 shows that the transmission spectrum variation shrinks at a wavelength of ~ 8 μm; this indicates the thickness variation across the illuminated area of the thin film (diameter: 6 mm) was ~ 0.77 μm (assuming n = 2.6) according to $\lambda = 4n\Delta d$. When $\lambda < 4n\Delta d$, a second interference pattern started to appear as shown in Figure 3.6-9. In this case, the possible wavelength range of the refractive index measurement was thus from 9 μm to 25 μm. When the aperture was reduced from 6 mm to 1 mm, the extrema could not be resolved for wavelengths below 2 μm (see the red curve in Figure 3.6-9), which indicates the thickness variation across the illuminated region of the thin film (diameter: 1 mm) is ~ 0.19 μm. Therefore, the values of the wavelength at extrema could now be accurately obtained over the wavelength range from 3 to 25 μm. Figure 3.6-9 shows that reducing the incident beam size can effectively increase the lower wavelength at which extrema can be distinguished and hence the wavelength range of the refractive index measurements.

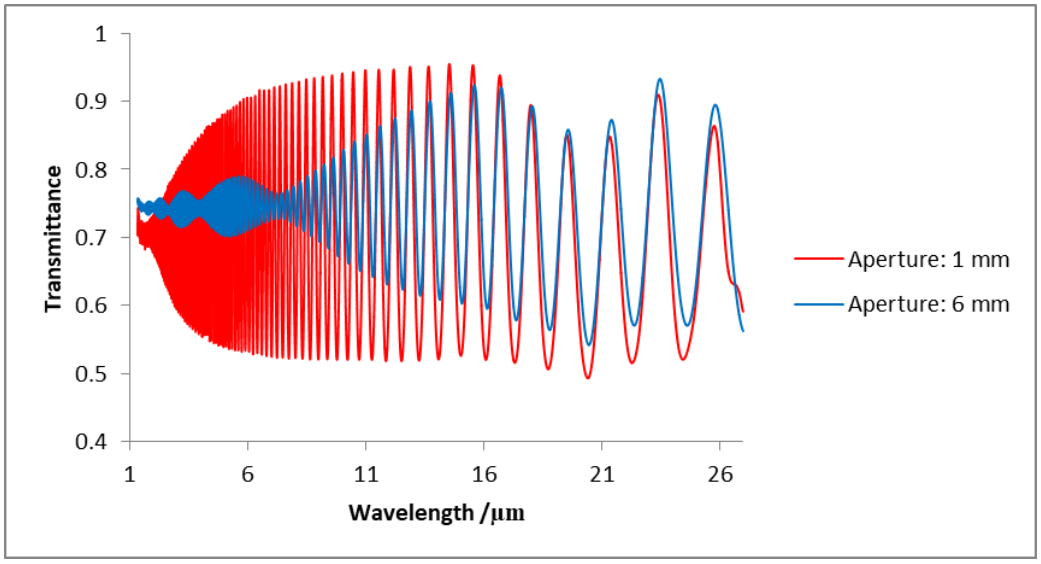


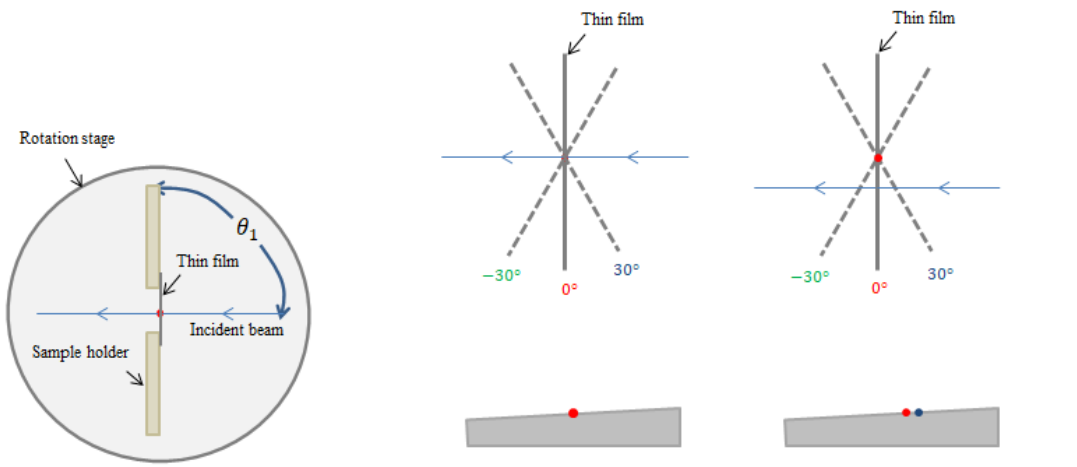
Figure 3.6- 9. The interference transmission spectra of a chalcogenide glass thin film (Pr^{3+}-ion doped Ge-As-Se-Ga, YRFFP013) at normal incidence using a beam with a diameter of 6 mm (blue curve) and 1 mm (red curve) in the FTIR spectrometer. Note that a smaller aperture enables the extrema of the transmission curve to be correctly resolved at lower wavelengths.

(c) Alignment

In the thin film measurement using FTIR spectroscopy, a misalignment of the wedge-shaped thin film with the rotation stage and the beam can cause an error in determining the refractive index of the thin film. The error caused by this misalignment will be analysed in this sub-section.

Figure 3.6-10(a) shows the schematic figure of the best alignment condition. The thin film was aligned at the rotation centre of the rotation axis, and the incident beam is aligned to travel through the rotation centre. As described in section 3.6.5.1, the transmission spectra of a thin film at incident angles of 0 º, 30 º and - 30 º was required for determining thin film refractive index dispersion and thin film thickness. The positions of the thin film with a thickness variation at incident angles of 0 º, 30 º and - 30 º are shown schematically in Figure 3.6-10(b). Figure 3.6-10(b) shows that, when the incident beam was well-aligned with the rotation centre and the beam path, the measured point on the thin film with an assumed systematic thickness variation would be located at the same spot. Since a thickness variation usually exists in a

hot-pressed thin film, using the same measurement spot on the sample for the incident angles of 0 °, 30 ° and – 30 ° can minimize the errors caused by any misalignments. When the incident beam was not well aligned, the measurement spots with incident angles of 30 °and – 30 °would locate at different positions on the sample to that for normal incidence, as shown schematically in Figure 3.6-10(c). Since a systematic thickness variation may have existed in the thin film, the thickness of the thin film at the measurement spot for normal incidence (red spot in Figure 3.6-10(c)) was potentially different from that for oblique incident angles. According to Eq. (3.1), a different thickness will have led to a shift of the wavelengths at extrema in the transmission spectra; this will have resulted in errors in determining the refractive index of a chalcogenide thin film.



(a) Thin film was aligned at the rotation center of the rotation stage.

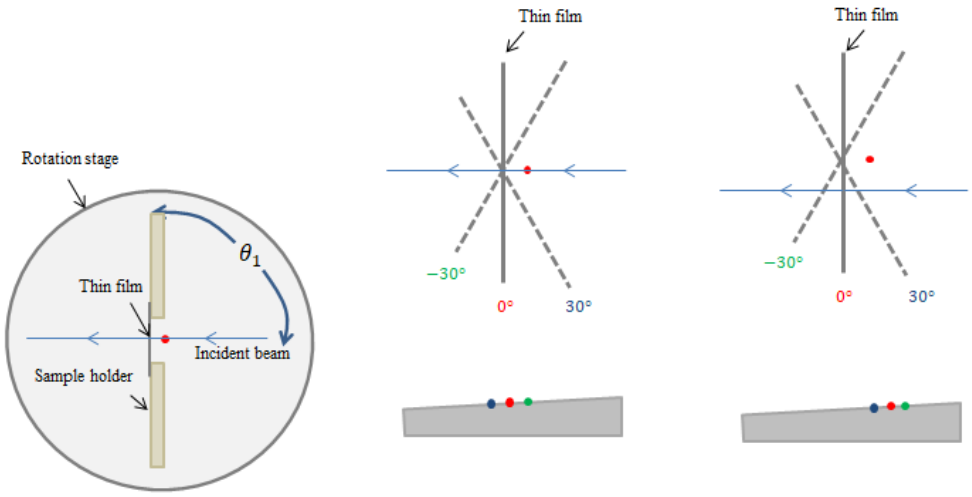
(b) Upper figure: Schematic figure of the positions of the thin film during the measurements.
Lower figure: measured points on the thin film (all the measured points at three positions are on the red spots).

(c) Upper figure: Schematic figure of the positions of the thin film during the measurements.
Lower figure: measured points on the thin film (normal incident at the red spot; incident with angles of 30° and − 30° at the blue spot).

Figure 3.6- 10. (a) Schematic diagram of a thin film sample aligned at the rotation centre of the rotation stage; (b) schematic diagram showing three different thin film positions during the measurements with a well-aligned incident beam, and the measurement spots on the thin film; (c) schematic diagram showing three different thin film positions during the measurements with a poorly-aligned incident beam, and the corresponding measurement spots on the thin film.

Figure 3.6-11(a) shows schematically the situation where a thin film is not placed at the rotation centre of the stage. The positions of a thin film with a systematic

thickness variation at incident angles of 0 º, 30 ºand – 30 º, with a well-aligned incident beam, are shown in Figure 3.6-11 (b). From Figure 3.6-11 (b), it is shown that the measurement points on the wedge-shape thin film will be located at different spots, which would result in errors in determining the refractive index. When the incident beam was not well aligned, the measured spots with incident angles of 0 º, 30 ºand -30 ºwill locate at different positions as shown in Figure 3.6-11 (c), which will also lead to errors in determining the refractive index.



（a） Thin film was not aligned at the rotation center of the rotation stage.

（b）Upper figure: Schematic figure of the positions of the thin film during the measurements.
Lower figure: measured points on the thin film (0°: red spot; 30°: blue spot; − 30°: green spot).

（c）Upper figure: Schematic figure of the positions of the thin film during the measurements.
Lower figure: measured points on the thin film (0°: red spot; 30°: blue spot; − 30°: green spot).

Figure 3.6- 11. (a) Schematic diagram of a thin film sample that was not aligned at the rotation centre of the rotation stage; (b) schematic diagram showing three different thin film positions during the measurements with a well-aligned incident beam, and the corresponding measurement spots on the thin film; (c) schematic diagram showing three different thin film positions during the measurements with a poorly-aligned incident beam, and the corresponding measurement spots on the thin film.

In summary, since a thickness variation of the chalcogenide thin film may have existed, a carefully alignment was required to make sure the same incident points at different incident angles (0 º, 30 ºand – 30 º).

(d) Air absorptions

In the FTIR thin film transmission measurements, any air absorption in the optical path in the measurement range (1 µm to 27 µm) will have distorted the observed interference fringes. Figure 3.6-12 shows the transmission spectra of a $Ge_{16}As_{24}Se_{15.5}Te_{44.5}$ at. % (M140MINSCGDJ) thin film (YRFFP007) over the wavelength range from 2 µm to 8 µm taken without carefully collecting the background spectrum. The noticeable absorption bands observed were: CO_2 absorption at around 4.2 and H-O-H absorption at around 2.7 and 6.2 µm [3.6-3.8]. A background spectrum was collected immediately before each thin film transmission measurement, without the sample present, with care to ensure that the measurement conditions remained the same; this considerably reduced the effect of air absorption.

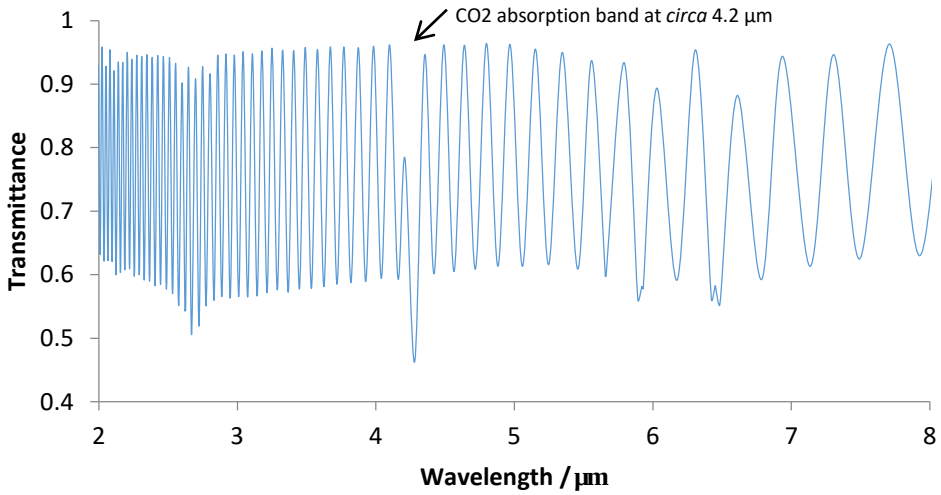


Figure 3.6- 12. The transmission spectrum of a $Ge_{16}As_{24}Se_{15.5}Te_{44.5}$ at. % (M140MINSCGDJ) thin film (YRFFP007) of a nominal thickness 20 µm without careful background collection. The effect of CO_2 absorption can be observed at a wavelength of 4.2 µm and the effect of water absorption can be seen at wavelengths of 2.7 µm and 6.2 µm.

3.7 Thermal mechanical analysis (TMA)

Thermal mechanical analysis (TMA) is a technique used to study the physical properties of a material with changing temperature. Carried out in a Perkin Elmer

TMA-7, both the viscosity-temperature and thermal expansion coefficient (TEC) of chalcogenide glass samples were investigated in this Project.

The TMA samples were cut from extruded rods [3.12] with a diameter of 4.7±0.2 mm. For viscosity investigation, the samples were cut with a height of either 2.0 mm or 4.5 mm so that a viscosity range between ~$10^{4.5}$ – 10^{8} Pa.s could be recorded [3.5]. For TEC investigation, the height of the sample was 10 mm [3.5]. Note that, for TEC and viscosity-temperature measurements, extra care was taken to ensure the surfaces of each sample were cut to be flat and parallel. To see whether the cut surfaces of the sample were indeed parallel, a micrometer was used to take several thickness measurements between the top and bottom surfaces at different locations.

3.7.1 Viscosity-temperature characterisation of bulk glasses

3.7.1.1 Sample preparation

Samples cut for viscosity-temperature investigations had a height of either 1.6 mm or 4.1 mm so that a viscosity range between ~$10^{4.5}$ – 10^{8} Pa.s could be recorded. The data was used to determine suitable temperatures for use when hot-pressing (viscosity: ~$10^{8.0}$ Pa.s) or fibre-drawing (viscosity: ~$10^{7.5}$ Pa.s) a composition.

Before testing, samples were carefully washed three times in acetone and isopropanol (see Table 3.1-2), so to remove any residual wax, and then both their heights and diameters were measured.

3.7.1.2 Method

Viscosity-temperature measurements using the parallel-plate method [3.13] were carried out on a Perkin Elmer TMA 7 thermomechanical equipment with flowing He (BOC) at 20 ml/min. The materials of the parallel plate were stainless steel. The equipment was calibrated by using a National Institute of Standards (NIS) standard glass 717a with known viscosity-temperature behaviour. For a sample with a height

of 1.6 mm, a load of 50 mN was applied to achieve a viscosity measurement range of 10^{5-3} Pas [3.5]. For a sample with a height of 4.1 mm, a load of 400 mN was applied to achieve a viscosity measurement range of 10^{8-5} Pas [3.5]. Samples were heated at 40 ℃/min to a temperature approximately 150 ℃ above T_g or until the programme was stopped by the user; this was to ensure the samples had not expanded so far that they touched the sides of the machine. Depending on the probe position, the stopping position (selected minimum height of the sample) was determined. The data recorded was height of the sample as a function of temperature. The viscosity was calculated according to [3.14]:

$$\eta = \frac{2\pi F h^5(t)}{sV[dh(t)/dt](2\pi h^3(t)+V)} \qquad (3.2)$$

where η is viscosity, h is instantaneous sample height, F is total applied force, V is sample volume, t is time and dh/dt is sample height deformation rate.

3.7.2 Thermal expansion coefficient (TEC)

Thermal expansion coefficient can be defined as the fractional rate of change of volume of a material with temperature. It is thus related to the change of density (mass per unit volume) with temperature. The thermal expansion coefficient in a volume of a glass sample (TEC_v) can be determined from:

$$TEC_v = \frac{1}{V}\left(\frac{\Delta V}{\Delta T}\right) \qquad (3.3)$$

where V is the volume of the glass sample at the initial temperature and $\frac{\Delta V}{\Delta T}$ is the variation in volume with temperature. According to Figure 3.7-1, the Morse-Condon curves [3.15,3.16] shows that thermal expansion is an effect related to the mean intermolecular bond length increasing as temperature increases. The energy stored in chemical bonds increases with temperature, with the heat uptake shifting the mean equilibrium position of the bond, which leads to a mean expansion when heating and

contraction while cooling. This response can be represented as a coefficient of thermal expansion. Since amorphous glasses have isotropic properties (same properties in all directions) as long as the glasses are not stressed, chalcogenide glasses exhibit linear thermal expansion with temperature.

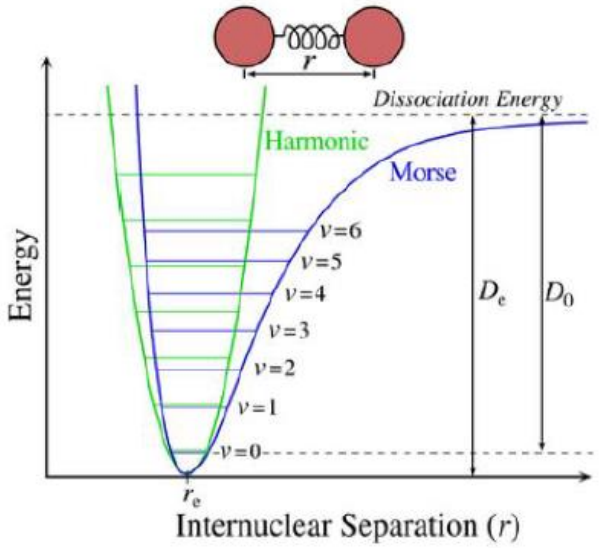


Figure 3.8- 1. Morse-Condon potential energy curves. Weakly bonded materials exhibit a shallower and more asymmetric potential well. Therefore, they exhibit a higher expansion coefficient, which is a greater shift in the mean position of the interatomic separation [3.14]. D_e is the dislocation energy and D_0 is the actual energy required for dislocation.

3.7.2.1 Sample preparation

TEC samples were cut from a ~4.7 mm diameter extruded rod with a height of ~10 mm, taking into consideration the width of the diamond cutting blade. Just like the viscosity-temperature samples, TEC samples were carefully washed three times in acetone and isopropanol in order to remove any residual wax, and both their heights and diameters were measured using a micrometer.

3.7.2.2 Method

The experimental setup (TMA-7 thermomechanical equipment) was similar to that used for measuring viscosity-temperature properties (see section 3.7.1.2). Samples

were placed in the TMA holder. A constant load of 100 mN was applied to the sample under a 30 ml/min He (BOC) flow. Samples were heated at a rate of 5 ℃/min to a temperature ~40 ℃ above T_g before being cooled at a rate of 10 ℃/min. In practice, the linear expansion coefficient is measured from the readings of the TMA and is calculated as

$$\mathrm{TEC}_L = \frac{1}{L_0}\left(\frac{\Delta L}{\Delta T}\right) \qquad (3.4)$$

where $\frac{\Delta L}{\Delta T}$ is the change in sample height with temperature, and L_0 is the initial height of sample. The measured TECs will be used to determine the thermo-optic coefficients of chalcogenide glass thin films, as discussed in section 7.3.

3.8 Thermal performance of a new thermal prism/thin-film holder to be used for thermo-optic coefficient measurements

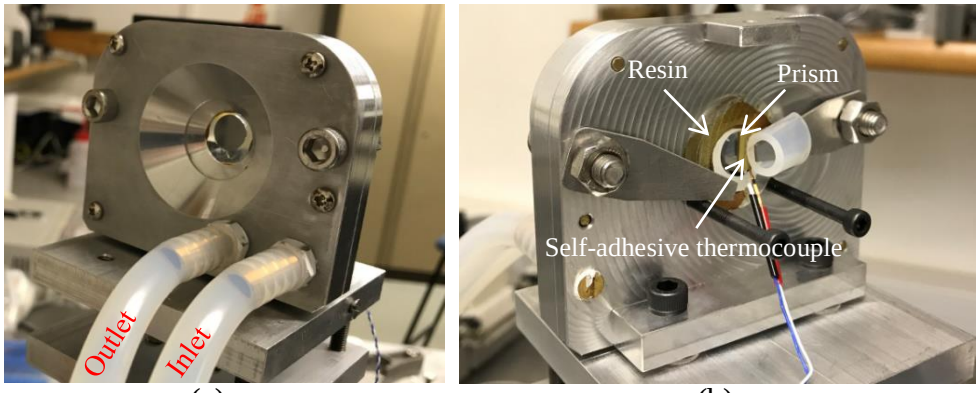
One goal of the Project is to investigate the thermal properties of bulk chalcogenide glasses and chalcogenide glass thin films. The details of a new aluminium sample holder designed to control the temperature of the samples are presented in Appendix A. The thermal performance of the sample holder when heating and cooling chalcogenide glass prisms will be discussed in section 3.8.1. The thermal performance of the holder when heating or cooling chalcogenide glass thin films will then be presented in section 3.8.2.

3.8.1 Thermal performance of heating chalcogenide prisms

3.8.1.1 Experimental setup

A chalcogenide glass prism held within its epoxy polishing block (as described in section 3.4) was mounted on the home-made aluminium temperature-controlled prism holder as shown in Figure 3.8-1. Thermal grease (supplier: APIEZON) was

applied between the resin and the prism holder to improve the thermal contact. The prism holder was connected to a water bath system (NESLAB RTE 740, Thermo Electron co.) by two pipes (outer diameter: 10 mm; inner diameter: 6 mm) as shown in Figure 3.8-1(a). The water was heated or cooled to a set temperature and flowed into the prism holder from one pipe. Then the heated or cooled water flowed around the prism holder and returned back to the water bath from the other pipe (see Figure 3.8-1(a)). The temperature of the holder was controlled by the heated or cooled water from the water bath. The epoxy resin around the prism was directly attached to the aluminium holder, as shown in Figure 3.8-1(b). Hence, the heat was transferred from the heated prism holder to the chalcogenide prism itself via the resin. This will cause a small temperature variation from the edge to the middle of the prism. After the water reaching a set temperature, the prism was left for 20 minutes in order to obtain a stable temperature. A self-adhesive thermocouple (K-type) was used to measure the temperature of the prism (see Figure 3.8-1), and investigate the temperature difference between the resin and prism. A nylon enclosure (see Figure 3.8-6(b)) was designed to cover the temperature-controlled holder in order to reduce the air flow.



(a) (b)

Figure 3.8- 1. (a) The front view of the temperature controlled prism holder with a prism mounted on it; (b) the back view of the temperature controlled prism holder with a prism mounted on it with a self-adhesive thermocouple attached to the surface of the prism.

3.8.1.2 Thermal performance of heating chalcogenide prisms

The thermal performance of heating and cooling the chalcogenide glass prisms ($Ge_{16}As_{24}Se_{15.5}Te_{44.5}$ at. % (M140MINSCGDJ), $As_{40}Se_{60}$ at. % (M130MINSCGDJ), $Ge_{20}Sb_{10}Se_{70}$ at. % (M135HAP) and $Ge_{20}Sb_{10}Se_{67}S_3$ at. % (M191HAP)) using the temperature-controlled holder will be shown in this sub-section. This data will be used for dn/dT calculation in section 7.2.

In the first measurement, a $Ge_{16}As_{24}Se_{15.5}Te_{44.5}$ at. % prism (YRFP003, see section 3.4) was used. The temperature of the water bath (NESLAB RTE 740, Thermo Electron co.) was increased from 15 ℃ to 80 ℃ in intervals of 5 ℃. A self-adhesive thermocouple was attached to the middle of the prism and then attached to the resin in order to measure their actual temperatures. Figure 3.8-2 shows that, as temperature increased, the temperature difference between the resin and the prism increases. When the temperature of the water bath was set to be 80 ℃, the temperature variation between the resin and the prism was up to 3.7 ℃.

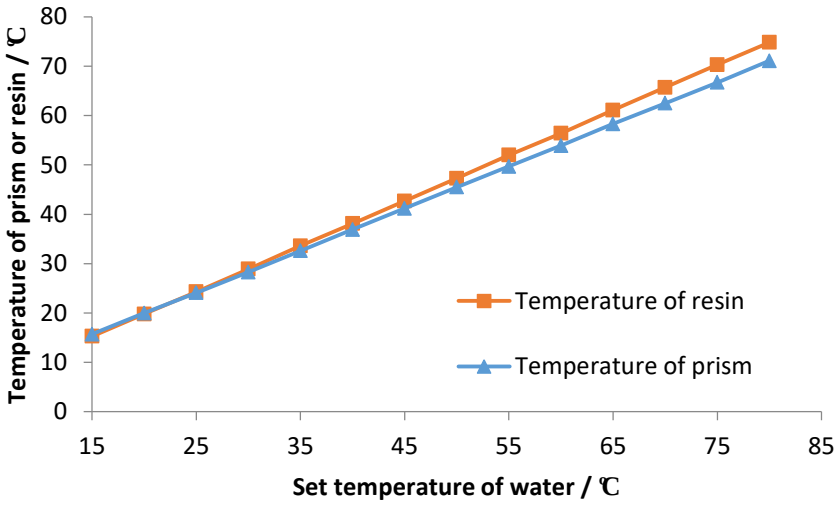


Figure 3.8- 2. Temperature of $Ge_{16}As_{24}Se_{15.5}Te_{44.5}$ at. % (M140MINSCGDJ) prism (YRFP003) and the resin measured using a thermocouple with the water temperature set from 15 ℃ to 80 ℃ in intervals of 5 ℃

In a similar measurement using the $As_{40}Se_{60}$ at. % prism (YRFP004, see section 3.4), the temperature of the water bath was set to be 15 ℃ and then from 20 ℃ to

80 ℃ in intervals of 10 ℃. The measured temperatures of the prism and the resin around the prism are displayed in Figure 3.8-3 as a function of the set temperature. The temperature variation between the resin around the prism and the prism itself is again seen to increase with an increase in the set water temperature. When the temperature of the water bath was set to be 80 ℃, the temperature variation between the resin around the prism and the prism itself was up to 5.1 ℃.

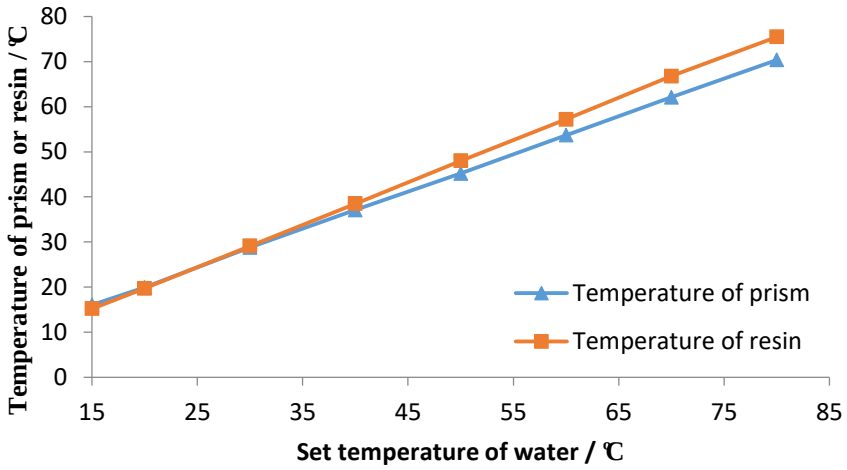


Figure 3.8- 3. Temperature of $As_{40}Se_{60}$ at. % (M130MINSCGDJ) prism (YRFP004) and the resin measured using a thermocouple with the water temperature set be 15 ℃ and then increasing from 20 ℃ to 80 ℃ in intervals of 10 ℃.

For heating or cooling the $Ge_{20}Sb_{10}Se_{70}$ at. % (YRFP005, see section 3.4) and $Ge_{20}Sb_{10}Se_{67}S_3$ at. % (YRFP010, see section 3.4) prisms using the temperature-controlled holder, the temperature of the water bath was in turn set to be 15 ℃, 40 ℃, 60 ℃ and 80 ℃. The measured temperatures of the resin around the prisms and the $Ge_{20}Sb_{10}Se_{70}$ at. % and $Ge_{20}Sb_{10}Se_{67}S_3$ at. % prisms themselves are shown in Figures 3.8-4 and 3.8-5. The maximum temperature variations between the resin and the prism was 2.5 ℃ for $Ge_{20}Sb_{10}Se_{70}$ at. % when the water temperature was set to be 80 ℃, as shown in Figure 3.8-4. For $Ge_{20}Sb_{10}Se_{67}S_3$ at. %, the temperature variation becomes 1.4 ℃ as shown in Figure 3.8-5.

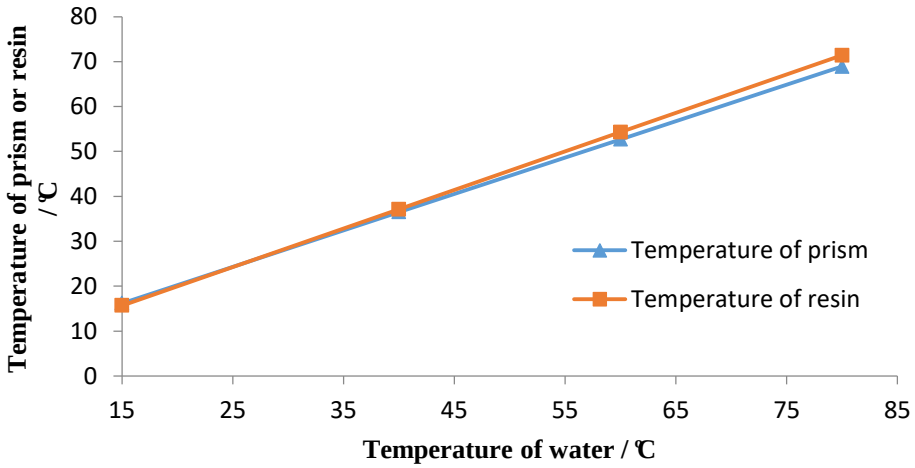


Figure 3.8- 4. Temperature of the $Ge_{20}Sb_{10}Se_{70}$ at. % (M135HAP) prism (YRFP005) and the resin measured using a thermocouple with the water temperature set be 15, 40, 60 and 80 ℃.

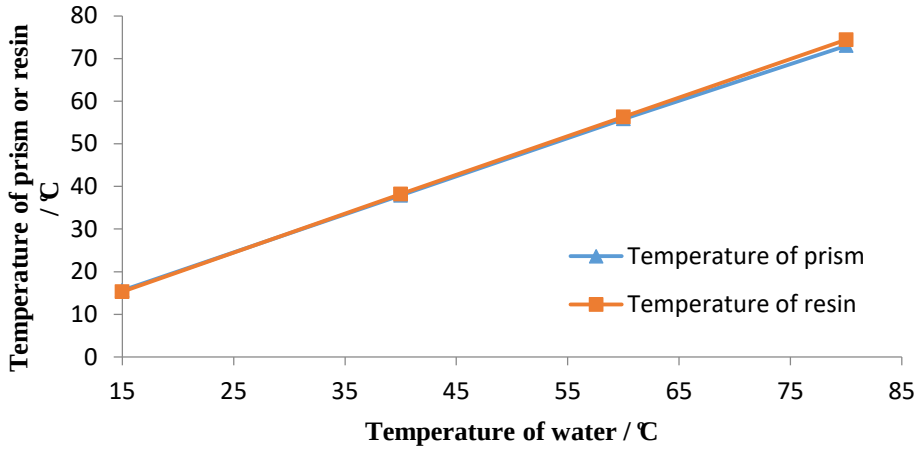


Figure 3.8- 5. Temperature of the $Ge_{20}Sb_{10}Se_{67}S_3$ at. % (M191HAP) prism (YRFP010) and the resin measured using a thermocouple with the water temperature set be 15, 40, 60 and 80 ℃.

3.8.1.3 Repeatability of measuring the temperature of a prism

As a way to determine the repeatability of the temperature measurements on the prism using the new thermal prism holder, the temperature of the $Ge_{16}As_{24}Se_{15.5}Te_{44.5}$ at. % (M140MINSCGDJ) prism (YRFP003) was measured as a function of set water bath temperature at different times.

The temperatures of the $Ge_{16}As_{24}Se_{15.5}Te_{44.5}$ at. % prism measured from 15 ℃ to 80 ℃ in intervals of 5 ℃ on different days are shown in Table 3.8-1. During these six days, the minimum room temperature was measured to be 24.7±0.1 ℃ and the maximum room temperature was measured to be 25.7 ±0.1 ℃. The temperatures of the $Ge_{16}As_{24}Se_{15.5}Te_{44.5}$ at. % prism measured at different set temperatures (temperature of the water bath) across 6 days of measurements was within a variation of ΔT_{prism} less than 0.3 ℃. Table 3.8-1 also shows that, when the set temperature is close to room temperature, the relative error is small. As the temperature of the water bath was increased away from room temperature, the variation of ΔT_{prism} increased.

Table 3.8- 1. The temperatures of the $Ge_{16}As_{24}Se_{15.5}Te_{44.5}$ at. % (M140MINSCGDJ) prism (YRFP003) measured from set water temperature of 15 ℃ to 80 ℃ in intervals of 5 ℃ across six days.

T_{water} / ℃	T_{prism} / ℃ (day 1)	T_{prism} / ℃ (day 2)	T_{prism} / ℃ (day 3)	T_{prism} / ℃ (day 4)	T_{prism} / ℃ (day 5)	T_{prism} / ℃ (day 6)	ΔT_{prism} / ℃
15	15.7	15.6	15.7	15.8	15.7	15.7	0.2
20	20	20.1	20	20.1	20.1	20	0.1
25	24.1	24.1	24.1	24.1	24.1	24.1	0
30	28.3	28.2	28.2	28.4	28.3	28.4	0.2
35	32.6	32.5	32.6	32.6	32.7	32.6	0.2
40	36.9	36.8	36.9	37.0	37.0	36.9	0.2
45	41.2	41.2	41.1	41.2	41.4	41.1	0.3
50	45.5	45.5	45.4	45.6	45.5	45.5	0.2
55	49.7	49.5	49.8	49.7	49.8	49.7	0.3
60	53.9	54	53.9	54	53.8	53.9	0.2
65	58.3	58.2	58.4	58.1	58.3	58.4	0.3
70	62.5	62.4	62.6	62.5	62.7	62.6	0.3
75	66.7	66.5	66.7	66.8	66.7	66.6	0.3
80	71.1	71	71	71.1	71.2	70.9	0.3

3.8.2 Thermal performance of the temperature-controlled holder for heating and cooling chalcogenide thin films

3.8.2.1 Experimental setup

A thin-film holder with a slit (width: 8mm, height: 1 mm) was designed to enable the hot-pressed thin film samples to be mounted on the temperature-controlled holder. The design detail of this thin film holder is presented as Figure A4 in Appendix A.

A chalcogenide glass thin film was mounted on the thin-film holder, which was then mounted on the thermal holder, as shown in Figure 3.8-6(a). Thermal grease (supplier: APIEZON) was applied between the resin and the prism holder to improve the thermal contact. A 3-axis stage was designed and manufactured to connect the rotation stage and the thermal thin-film holder, as shown in Figure 3.8-6(b). The design detail of this 3-axis stage is presented as Figures A5 and A6 in Appendix A. The whole setup was then mounted on the FTIR base plate as shown in Figure 3.8-6(b). When heating or cooling a chalcogenide glass thin film, the thin film was left for 20 minutes to obtain a stable temperature after the water reaching a set temperature.

For measuring the temperature of the thin film, the self-adhesive thermocouple was attached directly on to the thin film as shown in Figure 3.8-7. The thermal performance of heating or cooling the thin film using the temperature controlled thin-film holder will be discussed in section 3.8.2.2.

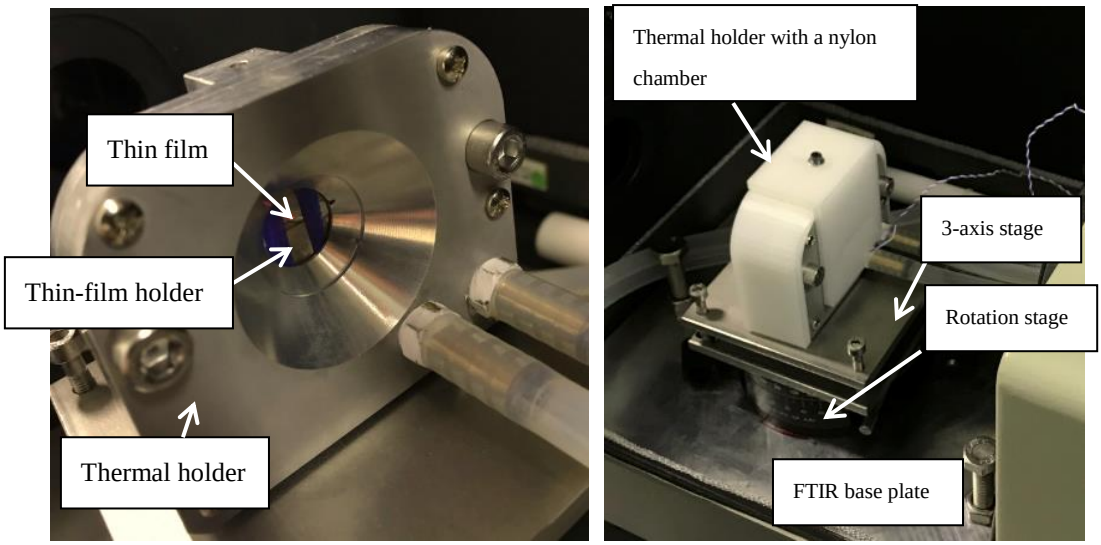


Figure 3.8- 6. (a) The front view of the thin-film holder with a thin film mounted and with the whole assembly mounted on the temperature-controlled holder; (b) the thin-film and temperature-controlled holder covered by a nylon chamber mounted in the cavity of the FTIR spectrometer.

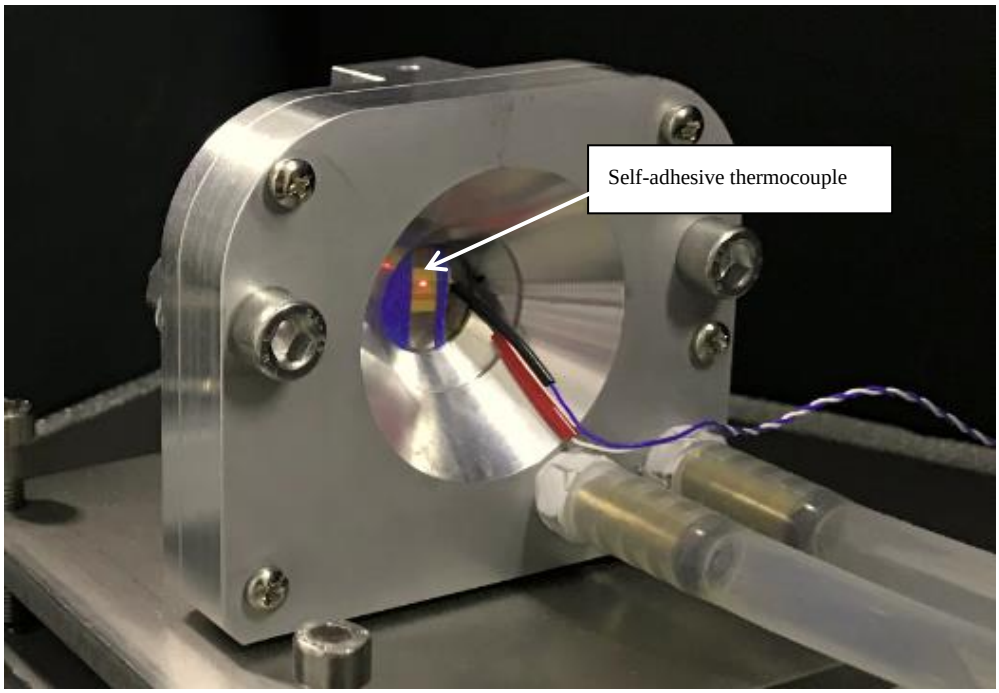


Figure 3.8- 7.Photograph showing a self-adhesive thermocouple attached to a thin-film sample.

3.8.2.2 Thermal performance of heating and cooling the thin film

In the measurements of glass thermo-optic coefficient using this temperature-controlled thin-film holder, some thin films were measured without

covering the temperature-controlled holder by a nylon chamber (see Figure 3.8-6(a)) while some were measured using the nylon chamber (see Figure 3.8-6(b)). Therefore, in this sub-section, the thermal performance of heating and cooling the hot-pressed thin film in these two cases will be discussed.

The measured temperatures of the thin film on different days without using the nylon chamber are shown in Table 3.8-2. The temperature of the water bath was set to be 20 and 80 ℃. There is little variance in the measured thin film temperature from day to day, as shown in Table 3.8-2. The average temperature of the thin film across 6 days of measurements is 21.6 ℃ when the set temperature is 20 ℃, and varies by less than 0.2 ℃. When the temperature of water bath is set to be 80 ℃, the average temperature of the thin film is 74.6 ℃ with a variation of $\Delta T_{thin\text{-}film}$ less than 0.5 ℃. The average ΔT (higher temperature (80 ℃) - lower temperature (20 ℃)) is 53.0 ℃ with a variation of $\Delta T_{thin\text{-}film}$ of less than 0.6 ℃.

Table 3.8- 2. The temperatures of the thin film measured at the temperature of the water bath set to be 20 and 80 ℃ across six days without being covered by a nylon chamber.

T_{water} / ℃	$T_{thin\ film}$ / ℃ (day 1)	$T_{thin\ film}$ / ℃ (day 2)	$T_{thin\ film}$ / ℃ (day 3)	$T_{thin\ film}$ / ℃ (day 4)	$T_{thin\ film}$ / ℃ (day 5)	$T_{thin\ film}$ / ℃ (day 6)	$\Delta T_{thin\text{-}film}$ / ℃
20	21.6	21.6	21.5	21.6	21.7	21.6	0.2
80	74.6	74.3	74.8	74.6	74.5	74.8	0.5
ΔT	53.0	52.7	53.3	53.0	52.8	53.2	0.6

When the nylon chamber was used to cover the holder (see Figure 3.8-6(b)), the measured temperatures of the thin film at the set temperatures of 20 and 80 ℃ on different days are as shown in Table 3.8-3. The average temperature of the thin film measured using the self-adhesive thermocouple across the 6 days of measurements is 20.9 ℃ when the set temperature was 20 ℃, and varies by less than 0.2 ℃. When the temperature of water bath was set to be 80 ℃, the average measured temperature of the thin film is 76.2 ℃ with a variation of $\Delta T_{thin\text{-}film}$ of less than 0.6 ℃. From Tables 3.8-2 and 3.8-3, it is found that using a nylon chamber can increase the

average ΔT (higher temperature (80 ℃) - lower temperature (20 ℃)) from 53.0 ℃ to 55.3 ℃.

Table 3.8- 3. The temperatures of the thin film measured at the temperature of the water bath set to be 20 and 80 ℃ across six days with being covered by a nylon chamber.

T_{water} / ℃	$T_{thin\ film}$ / ℃ (day 1)	$T_{thin\ film}$ / ℃ (day 2)	$T_{thin\ film}$ / ℃ (day 3)	$T_{thin\ film}$ / ℃ (day 4)	$T_{thin\ film}$ / ℃ (day 5)	$T_{thin\ film}$ / ℃ (day 6)	$\Delta T_{thin\text{-}film}$ / ℃
20	20.9	20.8	20.8	20.9	21.0	20.9	0.2
80	76.2	76.4	76.3	76.0	75.9	76.2	0.6
ΔT	55.3	55.6	55.5	55.1	54.9	55.3	0.6

3.9 Chapter summary

In chapter 3, all the experimental procedures used to fabricate, process and characterise the chalcogenide glasses investigated during the work described in this thesis were overviewed. Sections 3.1 and 3.2 listed the chemicals used during this project and the personal codes. The steps for preparing the chalcogenide glasses studied in this thesis were presented in section 3.3, and section 3.4 introduced the technique for preparing chalcogenide glass prisms, whose refractive index will be measured in chapter 4. Section 3.5 describes a hot-pressing technique developed for making chalcogenide glass thin films and bulk samples for ellipsometry measurements. The hot-pressed chalcogenide glass thin films will be characterised in chapters 6 and 7 and the refractive index dispersion data of the ellipsometry samples obtained using spectroscopic ellipsometry will be analysed in chapter 5. Section 3.6 presented the Fourier transform infrared (FTIR) spectroscopy used for bulk glass characterisation, thin film measurements and measuring the emission spectra of external beam sources. The central wavelengths of the beam sources used for the minimum deviation measurements (see chapter 4) were determined. The FTIR thin film measurements and their errors were also presented in this section. The thermal mechanical analysis (TMA) for measuring the viscosity-temperature properties and thermal expansion coefficient (TEC) of chalcogenide glasses were introduced in

section 3.7. These data will be essential for a successful hot pressing and determining the thermo-optic coefficient of a chalcogenide glass, as will be discussed in chapter 7. A new temperature-controlled holder was designed and manufactured, which will be used to heat and cool a chalcogenide glass prism and thin film fot the thermo-optic coefficient measurements in chapter 7. Its thermal performance was shown in section 3.8.

References

[3.1] Dantanarayana, H.G., Abdel-Moneim, N., Tang, Z., Sojka, L., Sujecki, S., Furniss, D., Seddon, A.B., Kubat, I., Bang, O. and Benson, T.M., 2014. Refractive index dispersion of chalcogenide glasses for ultra-high numerical-aperture fiber for mid-infrared supercontinuum generation. *Optical Materials Express*, *4*(7), pp.1444-1455.

[3.2] Fang, Y., Jayasuriya, D., Furniss, D., Tang, Z.Q., Markos, C., Sujecki, S., Seddon, A.B. and Benson, T.M., 2016, July. Characterising refractive index dispersion in chalcogenide glasses. In *Transparent Optical Networks (ICTON), 2016 18th International Conference on* (pp. 1-5). IEEE.

[3.3] Seddon, A.B., Pan, W.J., Furniss, D., Miller, C.A., Rowe, H., Zhang, D., McBrearty, E., Zhang, Y., Loni, A., Sewell, P. and Benson, T.M., 2006. Fine embossing of chalcogenide glasses–a new fabrication route for photonic integrated circuits. *Journal of Non-Crystalline Solids*, *352*(23-25), pp.2515-2520.

[3.4] Abdel-Moneim, N.S., Mellor, C.J., Benson, T.M., Furniss, D. and Seddon, A.B., 2015. Fabrication of stable, low optical loss rib-waveguides via embossing of sputtered chalcogenide glass-film on glass-chip. *Optical and Quantum Electronics*, *47*(2), pp.351-361.

[3.5] Parnell, H., 2018. *Towards a Ge-Sb-Se/S hyperspectral imaging probe for early cancer diagnosis (Do*ctoral dissertation, University of Nottingham).

[3.6] Lamontagne, J., Dumas, P., Mouillet, V. and Kister, J., 2001. Comparison by Fourier transform infrared (FTIR) spectroscopy of different ageing techniques: application to road bitumens. *Fuel*, *80*(4), pp.483-488.

[3.7] Lezal, D., 2003. Chalcogenide glasses-survey and progress. *Journal of Optoelectronics and Advanced Materials*, *5*(1), pp.23-34.

[3.8] Gordon, I.E., Rothman, L.S., Hill, C., Kochanov, R.V., Tan, Y., Bernath, P.F., Birk, M., Boudon, V., Campargue, A., Chance, K.V. and Drouin, B.J., 2017. The HITRAN2016 molecular spectroscopic database. *Journal of Quantitative Spectroscopy and Radiative Transfer*, *203*, pp.3-69.

[3.9] Shiryaev, V.S., Adam, J.L., Zhang, X.H., Boussard-Pl édel, C., Lucas, J. and Churbanov, M.F., 2004. Infrared fibers based on Te–As–Se glass system with low optical losses. *Journal of Non-Crystalline Solids*, *336*(2), pp.113-119.

[3.10] Swanepoel, R., 1985. Determining refractive index and thickness of thin films from wavelength measurements only. *Journal of the Optical Society of America A*, *2*, pp.1339-1343.

[3.11] Swanepoel, R., 1984. Determination of surface roughness and optical constants of inhomogeneous amorphous silicon films. *Journal of Physics E Scientific Instruments*, *17*, pp.896-903.

[3.12] Savage, S.D., Miller, C.A., Furniss, D. and Seddon, A.B., 2008. Extrusion of chalcogenide glass preforms and drawing to multimode optical fibers. *Journal of Non-Crystalline Solids*, *354*(29), pp.3418-3427.

[3.13] Furniss, D. and Seddon, A.B., 2008. Thermal analysis of inorganic compound glasses and glass-ceramics. *Principles and Applications of Thermal Analysis*, pp.410-449.

[3.14] Gent, A.N., 1960. Theory of the parallel plate viscometer. *British Journal of Applied Physics*, *11*, pp.85-87.

[3.15] Morse, P.M., 1929. Diatomic molecules according to the wave mechanics. II. Vibrational levels. *Physical Review*, *34*(1), pp.57-64.

[3.16] Bergman, T.L., Incropera, F.P., DeWitt, D.P. and Lavine, A.S., 2011. *Fundamentals of heat and mass transfer*. John Wiley & Sons.

Chapter 4: Measuring the refractive index of chalcogenide glasses using the minimum deviation method

One goal of this PhD Project is to determine the refractive index of chalcogenide glasses at mid-infrared (MIR) wavelengths using the minimum deviation method. Due to the high accuracy, the results obtained using the minimum deviation method presented in this chapter will be taken as the benchmark values for the techniques developed later.

Section 4.1 presents the basic theory of the minimum deviation method. Section 4.2 then presents the experimental setup and operations of the minimum deviation measurement in our laboratory, and a commercial silica prism will be used to analyse the errors of the minimum deviation measurement using our setup in section 4.3. In section 4.4, the refractive indices of chalcogenide prisms (manufactured as described in section 3.4) at different wavelengths are measured using the minimum deviation method. In section 4.5, measured refractive index data is used to explore various extrapolations to the refractive index of Ge-As-Se-Te glass system. Finally, a summary of this chapter will be made in section 4.6.

4.1 Basic theory of the minimum deviation method.

As a beam enters a transparent material from air with an incident angle [4.1], the beam is deflected, based on the incident angle and the material's refractive index, according to Snell's law. A beam travelling through a prism is deflected twice: once entering, and again when exiting (See Figure 4.1-1(a)). The deviation angle is defined as the sum of these two deflections as shown in Figure 4.1-1(a). It is assumed that the angle of incidence at the output face is less than the critical angle.

When a laser beam travels through a prism with a certain incident angle, the minimum deviation position will be achieved as shown in Figure 4.1-1(b), which makes the sum of the two deflections a minimum. Applying Snell's law, and using geometric optics, an expression for refractive index *n* can be obtained as [4.1]:

$$\mathrm{n} = \frac{\sin[(\alpha+\theta)/2]}{\sin(\alpha/2)} \qquad (4.1)$$

where α is the apex angle of prism, and θ is the minimum deviation angle (see Figure 4.1-1).

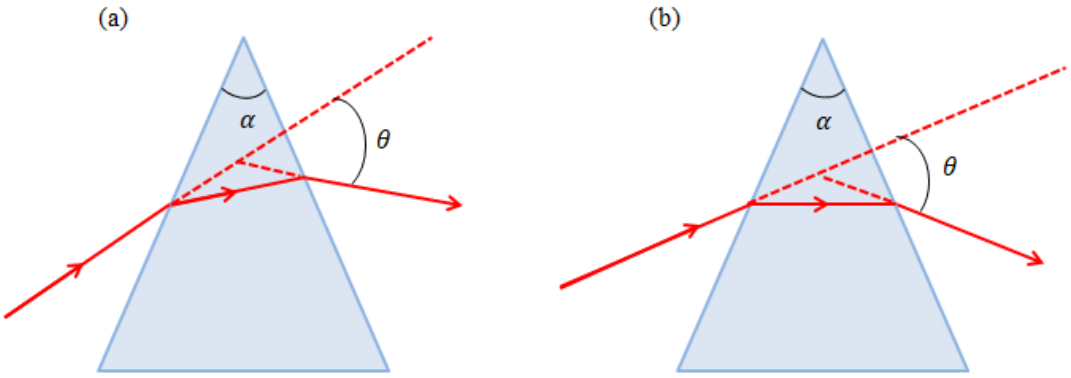


Figure 4.1- 1. Schematic diagram showing (a) the deflections of a beam travelling through a prism with an apex angle of α; (b) the minimum deviation position for a beam incident with a certain angle; the sum of the two deflections is a minimum.

For apex angle α measurement, a laser beam was launched on the surface of the prism. The prism was adjusted to let the incident beam reflect back along its own path (see Figure 4.1-2(a)). The angle of this position was measured as α_1. The prism was rotated to let the other surface reflect the beam back along its own path and this angle was recorded as α_2 (see Figure 4.1-2(b)). The apex angle α can then be calculated using Eq. (4.2) [4.2].

$$\alpha = \alpha_1 - \alpha_2 - 180^\circ \ . \qquad (4.2)$$

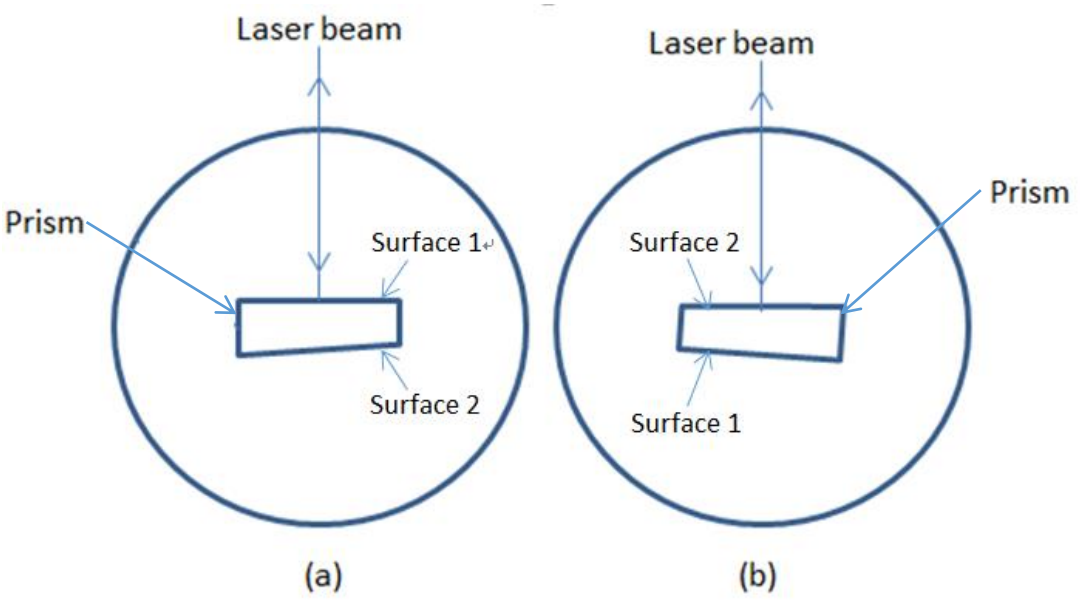


Figure 4.1- 2. Schematic diagram of apex angle measurement: (a) one surface of the prism was adjusted to let the incident beam reflect back along its own path; (b) the prism was rotated to let the other surface reflect the beam back along its own path.

4.2 Experimental setup and operations.

The experimental setup is illustrated in Figure 4.2-1. The major components of the apparatus used for the minimum deviation measurement incorporate a laser source (a 651nm He-Ne class I laser, < 400 µW) fibre coupled with the Agilent fibre coupled diode (1465-1575nm 40mW), other MIR beam sources (3.1 µm interband-cascade laser (ICL) from NRL, SuperK mid-infrared supercontinuum source (1.1-4.2 µm, 450 mW) from NKT Photonics, used in conjunction with a band pass filter (centre wavelength: 3.8 µm; FWHM: 180 nm), or a 6.45 µm optical parametric oscillator (OPO) (Chromacity spark FIR, Chromacity Ltd.)), a 1550 nm fibre collimator (model: F230FC-1550, Thorlabs) used for collimating the 651 nm laser source and the 1465-1575 nm tunable laser (see Figure 4.2-1), a prism table with a prism holder on it (E. R. Watts & Son. Ltd. No. 50336), and a plane mirror (Diameter: 48 mm) mounted on the rotation table 2 as shown in Figure 4.2-1. A screen with an aperture (diameter: ~ 3 mm) is placed in front of the beam source. When using the visible beam source, a sheet of white paper with an aperture (diameter: ~ 3 mm) in its centre was used as the screen (see Figure 4.2-2(a)). When using the invisible beam sources, a liquid crystal film with an aperture (diameter: ~ 3 mm) in its centre was used as the screen (see Figure 4.2-2(b)). The optical components were mounted on an optical

bench (Supplier: Ealing, Size: 178 cm L × 90 cm W × 10 cm H) by screws (size: M6). The plane mirror was connected to the rotation table 2 and the prism was mounted on the rotation table 1, as shown in Figure 4.2-1. The surface of the prism, which is at the rotation centre of the rotation table, is defined as surface 1. The other surface of the prism is called surface 2.

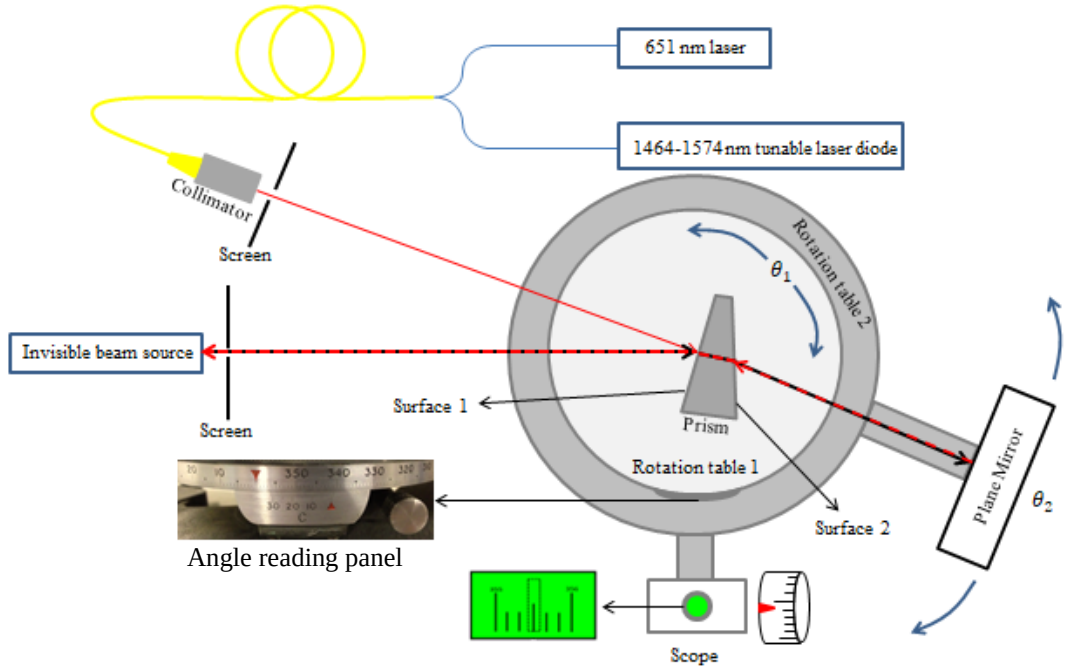
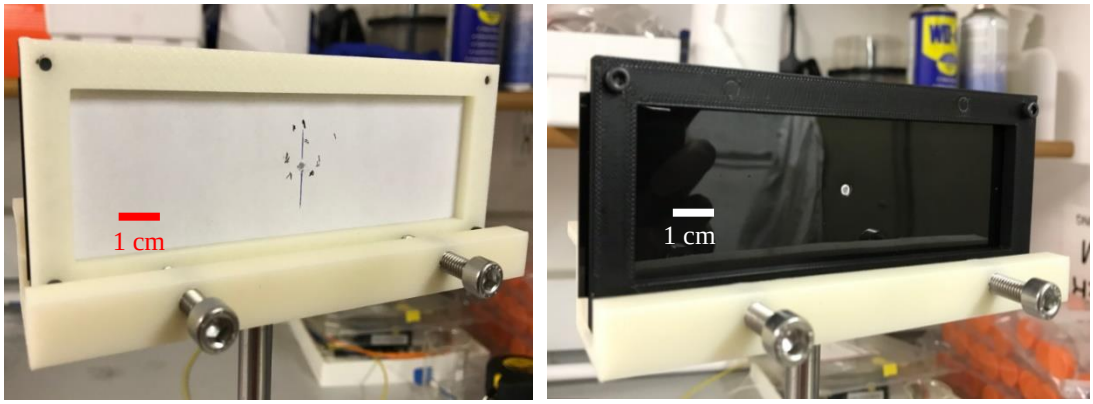


Figure 4.2- 1. Schematic diagram of experimental setup for measuring refractive index using minimum deviation method. The prism was on the rotation table 1 and the mirror was connected to the rotation table 2.



(a) (b)

Figure 4.2- 2. The screens with an aperture (diameter: ~ 3 mm) in the centre used in the minimum deviation measurement for detecting (a) the visible light sources and (b) the invisible light sources.

Before the minimum deviation measurements, all lasers used in the measurements were aligned to be parallel to the optical bench. Then the plane mirror was adjusted

to let the required beam reflect back along its own optical path and the position of the plane mirror was read out from the scope (see Figure 4.2-1) to an accuracy of 5 seconds. This reading was recorded as the zero position reading $\theta_2{}'$, which was used for calculating the minimum deviation angle later.

The prism was placed on the holder and secured using plasticine. Then the rotation table 1 was rotated to find the angles at which each of surface 1 and surface 2 reflected the beam back along its optical own path. These two readings were recorded as α_1 and α_2 respectively. The apex angle can then be calculated from Eq. (4.2).

After that, the rotation table 1 was rotated continuously in the same clockwise direction. The light ray was observed to rotate in the same direction as the prism up to a certain point, at which the light beam would change its direction of travel. This position is the minimum deviation position. The plane mirror was adjusted to reflect the beam along its own optical path and the reading of the rotation table 2 was written down as $\theta_2{}''$.

The minimum deviation angle was calculated as $\theta = |\theta_2{}'' - \theta_2{}'|$. The refractive index was calculated by Eq. (4.1). The results of the measurements will be presented and discussed in the following sub-sections.

4.3 Analysis the errors of the minimum deviation measurements in our laboratory using a commercial LAF 850322 right-angled prism

In order to investigate the accuracy and error of the minimum deviation measurements based on the optical setup in our laboratory, a commercial silica prism (LAF 850322 right-angled prism) was used for some initial measurements. The accuracy and error of the minimum deviation measurements in our laboratory will be illustrated in this section.

4.3.1. The LAF 850322-silica-glass prism

The LAF 850322 glass prism has a right angle and two 45 °angles as shown in Figures 4.3-1 and 4.3-2.

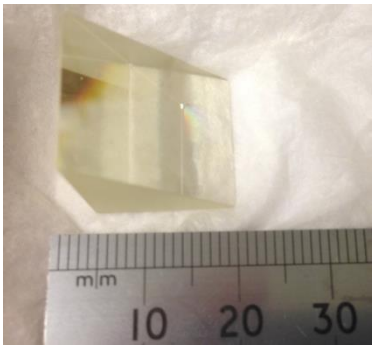


Figure 4.3- 1. Picture of the LAF 850322-silica-glass prism with a right angle.

A schematic diagram of the minimum deviation position of the prism is shown in Figure 4.3-2 with the definitions of surface 1 and surface 2 which were also discussed in section 4.2.

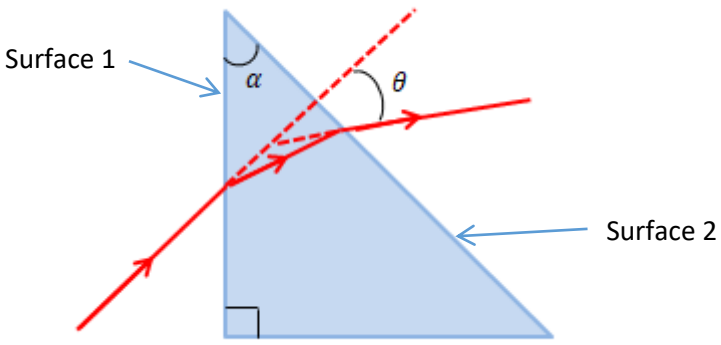


Figure 4.3- 2. Schematic diagram of the minimum deviation position. θ is the deviation angle, α is the top angle of the prism.

According to SCHOTT optical glass data sheets [4.3], the refractive index of the LAF 850322 prism at certain wavelengths and at a temperature of 20 ℃ are as shown in Table 4-1.

Table 4- 1. The refractive index of LAF 850322 glass at certain wavelengths (Temperature: 20 °C). [4.3]

Wavelength (nm)	768.2	706.5	656.3	587.6	546.1	486.1	478.0	435.8	404.7
Refractive index	1.8330	1.8382	1.8426	1.8503	1.8565	1.8689	1.8705	1.8845	1.8981

A Sellmeier dispersion formula to the above data is given in [4.3] as:

$$n^2 - 1 = \frac{2.000\lambda^2}{\lambda^2 - 0.012\mu m^2} + \frac{0.299\lambda^2}{\lambda^2 - 0.054\mu m^2} + \frac{1.807}{\lambda^2 - 156.5\mu m^2} \quad (4.3)$$

where n is the refractive index and λ is the wavelength in units of μm. For this initial measurement, the wavelength of the laser source was 651 nm. Therefore, the refractive index of LAF 850322 at this wavelength and at 20 ℃ was calculated to be 1.8432 according to Eq. (4.3). Note that in the present work, a two-term Sellmeier equation is used to describe the refractive index of a chalcogenide glass rather than a three-term Sellmeier equation like Eq. (4.3). This will be described in detail in section 5.4.

Knowing the refractive index and the nominal apex angle ($\alpha = 45°$) of the LAF 850322 prism, theoretically, the minimum deviation angle can be calculated according to Eq. (4.1), which yields $\theta_t = 44.72°$. A 1 % error in the apex angle ($\alpha_e = 45° \pm 0.45°$) leads to an error of $\pm$ 0.0102 in determining the refractive index of the LAF850322 prism according to Eq. (4.1). A 1% error in the minimum deviation angle ($\theta_e = 44.72° \pm 0.4472°$) results in an error of $\pm$ 0.0072 in determining the refractive index using Eq. (4.1). Thus an estimate of the error introduced by measurements in both the apex angle and the minimum deviation method has been obtained.

4.3.2. The results of the refractive index of LAF 850322 prism

The experiments were undertaken at room temperature (measured at 21.1 ℃ using a mercury thermometer). The definitions of surface 1, surface 2, and zero position are given in section 4.2. The raw data from the minimum deviation measurements is shown in Table 4-2. This was then used to determine the refractive index of the LAF850322 prism as shown in Table 4-3.

The average refractive index obtained using surface 1 as the incident surface (labelled surface 1 in Table 4-3) was 1.8441 with a standard deviation of precision of 0.0002, as shown in Table 4-3. Compared to the refractive index calculated from the Schott data [4.3], which is 1.8432 at the wavelength of 651 nm, the accuracy is ~0.049 %. Using surface 2 as the incidence surface, the average refractive index is

1.8441 with a standard deviation of precision of 0.0002 as shown in Table 4-3. The accuracy to the reference value is ~0.049 %.

Section 4.3.1 described how a 1 % error in apex angle would cause a 0.6 % error in calculating the refractive index, and a 1 % error in minimum deviation angle would lead to a 0.42 % error in refractive index. Table 4-3 shows that the standard deviation of the measured apex angle was 0.0081 while the standard deviations of measured minimum deviation angle were 0.0058 for the surface 1 measurements and 0.0080 for the surface 2 measurements. Therefore, the errors in apex angle measurement would cause more errors than those in minimum deviation angle in calculating the refractive index. For the measurements of the apex angle, the average apex angle is 45°00′37″ (see Table 4-3). The error with respect to the nominal apex angle (45 °) is ~0.019 %.

For the measurement of minimum deviation angle shown in Table 4-3, the standard deviation of the results obtained using the surface 1 is ~1.37 times less than when using the surface 2. It is mainly because in the surface 1 case when finding the minimum deviation position, the screen used to detect the beam deviation by the prism was placed 5 m away from the prism. However, for surface 2, due to the limited space in the lab (the optical setup was placed near a wall), the distance between the screen and the prism was limited to 0.6 m. Increasing the distance between the prism and screen can increase the accuracy of finding the minimum deviation position. In the case of surface 2, a plane mirror can be used to increase the optical path of the deviated beam in order to reduce the error in the future. Furthermore, according to Figure 4.2-1, surface 2 of the prism is not located exactly at the rotation centre of the stage, which might introduce futher errors in determining the minimum deviation position.

Table 4- 2. Minimum deviation measurement results of LAF 850322 right angle prism. (Every time one measurement starts, alignment was done again. Therefore, no means and no standard deviations are evaluated from the data.)

Measurements	zero position	Apex angle measurement		Minimum deviation measurement		Final zero position
		Surface 1	Surface 2	Surface 1	Surface 2	
1	15°43′30″	113°23′	338°23′	330°56′26″	60°30′41″	15°43′16″
2	15°43′30″	113°27′	338°28′	330°56′21″	60°30′48″	15°43′12″
3	15°43′26″	113°52′	338°53′	330°56′33″	60°30′36″	15°43′14″
4	15°43′22″	114°06′	339°07′	330°56′25″	60°30′34″	15°43′34″
5	15°43′18″	114°03′	339°03′	330°56′20″	60°31′21″	15°42′51″
6	15°43′15″	116°23′	341°24′	330°55′30″	60°30′10″	15°43′14″
7	15°43′10″	116°45′	341°45′	330°55′35″	60°30′44″	15°43′19″
8	15°43′34″	115°38′	340°39′	330°56′04″	60°30′54″	15°43′01″
9	15°43′25″	115°37′	340°38′	330°55′49″	60°30′58″	15°43′14″
10	15°43′22″	115°29′	340°30′	330°56′10″	60°30′11″	15°43′15″
11	15°42′46″	115°24′	340°25′	330°56′05″	60°31′14″	15°43′02″
12	15°43′02″	115°46′	340°47′	330°55′30″	60°31′14″	15°43′00″
13	15°43′31″	115°23′	340°23′	330°55′38″	60°30′57″	15°42′53″
14	15°43′32″	115°28′	340°28′	330°55′55″	60°30′37″	15°43′01″
15	15°43′18″	115°33′	340°34′	330°55′45″	60°31′24″	15°43′00″

Table 4- 3. The results of the refractive index, apex angle and minimum deviation angle calculated from Table 4-2.

Measurements	Apex angle	Minimum deviation angle		Refractive index	
		Surface 1	Surface 2	Surface 1	Surface 2
1	45°00′00″	44°47′04″	44°47′11″	1.84428	1.84431
2	45°01′00″	44°47′09″	44°47′18″	1.84392	1.84396
3	45°01′00″	44°46′53″	44°47′10″	1.84385	1.84393
4	45°01′00″	44°46′57″	44°47′12″	1.84387	1.84394
5	45°00′00″	44°46′58″	44°48′03″	1.84425	1.84454
6	45°01′00″	44°47′45″	44°46′55″	1.84409	1.84386
7	45°00′00″	44°47′35″	44°47′34″	1.84442	1.84441
8	45°01′00″	44°47′30″	44°47′20″	1.84402	1.84397
9	45°01′00″	44°47′36″	44°47′33″	1.84405	1.84403
10	45°01′00″	44°47′12″	44°46′49″	1.84394	1.84383
11	45°01′00″	44°46′41″	44°48′28″	1.84380	1.84428
12	45°01′00″	44°47′32″	44°48′12″	1.84403	1.84421
13	45°00′00″	44°47′53″	44°47′26″	1.84450	1.84438
14	45°00′00″	44°47′37″	44°47′05″	1.84443	1.84428
15	45°01′00″	44°47′33″	44°48′06″	1.84403	1.84418
Average	45°00′37″	44°47′20″	44°47′29″	1.84410	1.84414
s.d.	0.00811	0.00583	0.00799	0.00022	0.00022

4.3.3. Errors in the minimum deviation measurement using the LAF 850322 prism

Before measuring the refractive index of chalcogenide glass prisms, it is crucial to know the error that is likely to be introduced in each part of the procedure for the minimum deviation measurement. In this section, the error in each part of this setup will be discussed.

4.3.3.1 Error in determining zero position

To find zero position, the beam was allowed to pass through the window of the prism holder without mounting a prism. The plane mirror was then adjusted to retro-reflect the laser source back along its own path. However, because the 651 nm laser beam was not perfectly collimated, the image of the reflected beam on the screen was larger than the aperture. The figure of the spot caused by the beam after 2.94-metres of travel can be seen in Figure 4.3-3. Hence, some errors were occurred in determining the zero position.

Table 4-4 shows that the error in determining the zero position was less $\pm$ 22", which was mainly attributed to the beam was not being perfectly collimated i.e. the spot caused by the reflected beam would be enlarged which led to the error.

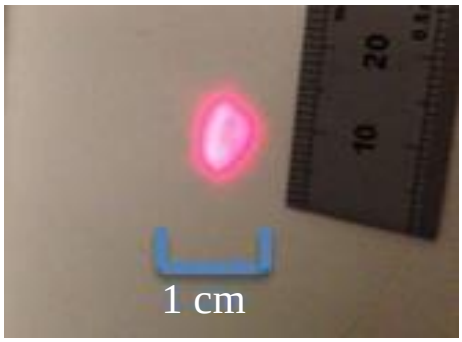


Figure 4.3- 3. The size of spot on the wall which is 2.94 m away from the 651 nm laser source.

To reduce the error in determining the zero position, a well collimated beam and a screen with a smaller aperture will be preferred.

Table 4- 4. Data of finding the zero angle position (moving the mirror).

	1st measurement		2nd measurement		3rd measurement		4th measurement	
	zero position	Final zero position	zero position	Final zero position	zero position	Final zero position	zero position	Final zero position
1	15°43′38″	15°43′06″	15°43′20″	15°43′05″	15°43′48″	15°43′10″	15°43′26″	15°43′48″
2	15°43′32″	15°43′08″	15°43′39″	15°43′10″	15°43′21″	15°43′06″	15°43′05″	15°43′25″
3	15°43′31″	15°43′24″	15°43′27″	15°43′20″	15°43′34″	15°43′16″	15°43′25″	15°43′35″
4	15°43′15″	15°43′35″	15°43′26″	15°43′11″	15°43′16″	15°43′20″	15°43′25″	15°43′33″
5	15°43′34″	15°43′06″	15°43′36″	15°43′16″	15°43′11″	15°43′19″	15°43′30″	15°43′28″
Average	15°43′30″	15°43′16″	15°43′30″	15°43′12″	15°43′26″	15°43′14″	15°43′22″	15°43′34″
s.d.	0.00219	0.00326	0.00193	0.00143	0.00372	0.00149	0.00244	0.00220
error:	±15″	±19″	±10″	±8″	±22″	±8″	±17″	±14″

Zero position: measured before mounting the prism.
Final zero position: measured after dismounting the prism.

4.3.3.2 Error in reading out the minimum deviation position

When the minimum deviation angle position was decided, the plane mirror was used to retro-reflect the beam back along its own path. The angle of mirror was read out from the scope, as shown in Figure 4.2-1. This reading would be used to calculate the minimum deviation angle with the zero position. However, because of the non-perfect quality of beam and the surfaces of the prism, some errors were introduced when judging when the beam perfectly aligned with the aperture on the screen. In order to quantify this error, the measurements were repeated by moving the mirror without changing the minimum deviation position.

Table 4-5 shows the results from repeated measurements. These presented indicate that the error in reading out the minimum deviation position is less than $\pm 41"$, which was mainly due to the quality of the 651 nm laser beam. The imperfect collimation of the beam would enlarge the spot on the screen after travelling 1.96 metres, which would cause errors in reading out the angles. Images of the spots on the screen are shown in Figure 4.3-4:

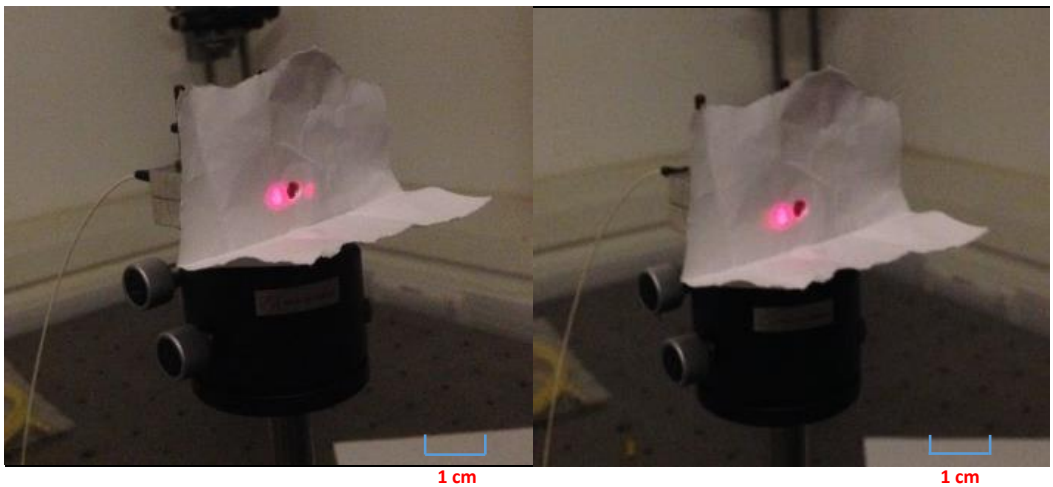


Figure 4.3- 4. The 651 nm wavelength spot caused by the reflected beam when measuring the minimum deviation position (left is when the incident surface is surface 2 and right is surface 1).

The quality of the beam can be improved by changing to a better collimation system and the surface quality of the chalcogenide glass prisms can be improved by careful polishing.

Table 4- 5. Repeated measurements of the minimum deviation position by moving the plane mirror only to estimate the error in reading out the minimum deviation position.

	1st measurement		2nd measurement		3rd measurement		4th measurement	
	Surface 1	Surface 2	Surface 1	Surface 2	Surface 1	Surface 2	Surface 1	Surface 2
1	330°57′14″	60°30′24″	330°56′34″	60°31′00″	330°56′29″	60°31′00″	330°56′30″	60°31′29″
2	330°56′00″	60°30′40″	330°56′08″	60°30′44″	330°56′36″	60°30′33″	330°56′05″	60°30′52″
3	330°56′12″	60°30′29″	330°56′41″	60°30′20″	330°56′55″	60°30′44″	330°55′51″	60°31′43″
4	330°56′29″	60°31′06″	330°56′31″	60°30′06″	330°56′03″	60°30′34″	330°55′42″	60°30′50″
5	330°56′50″	60°30′15″	330°56′21″	60°30′59″	330°56′40″	60°30′37″	330°55′24″	60°31′29″
Mean:	330°56′33″	60°30′35″	330°56′27″	60°30′38″	330°56′33″	60°30′42″	330°55′54″	60°31′17″
s.d.	0.00737	0.00488	0.00319	0.00597	0.00474	0.00277	0.00617	0.00598
Error:	±41″	±31″	±19″	±32″	±30″	±18″	±36″	±27″

4.3.3.3 Error in minimum deviation measurement (re-measurement of the minimum deviation position)

To find the minimum deviation position, the prism was rotated continuously in the same clockwise direction. The light ray was observed to rotate in the same direction as the prism up to a certain point, at which the light beam would change its direction of travel. This is the minimum deviation position. Then the plane mirror was used to retro-reflect the beam back along its own path for reading out the angle. However, the minimum deviation position was judged by eye, which led to some errors. Moreover, this kind of error contained the reading error described in section 4.3.3.2. The measurements for finding the minimum deviation position were repeated by rotating the prism.

Table 4-6 shows the results of the repeated measurements of the minimum deviation position. They indicate that the error is less $\pm 1'46"$ when surface 2 was used as the incident surface. As described in section 4.3.2, when using surface 2 as the incident surface, the distance between the prism and the screen used for detecting the deviated beam was ~ 0.6 m. However, when using surface 1 as the incident surface, the screen used for detecting the deviated beam was placed 5 m away from the prism. The error when using surface 1 is less than $\pm 55"$ as shown in Table 4-6. All of these findings confirm the conclusion in section 4.3.2 that increasing the distance between the prism and screen can reduce the error when finding the minimum deviation position. The error arises mainly from the quality of the beam and judging the minimum deviation position by eye.

The maximum error recorded in Table 4-6 is $\pm 1'46"$ which corresponds to an error of ~0.065 % in the minimum deviation angle. An error of around 0.065 % in the minimum deviation angle will lead to an error of 0.025 % in calculating the refractive index according to Eq. (4.1).

4.3.3.4 Error in reading out the position for apex angle measurements

In the apex angle measurement described in section 4.1, the surfaces 1 and 2 of the prism were adjusted to retro-reflect the beam back along its own path. The angular positions of the surface 1 and surface 2 were read out from the angle reading panel

(see Figure 4.2-1). The readout errors in measuring the positions are shown for five measurements in Table 4-7. The results presented indicate that the error of reading out the positions of the surface 1 and surface 2 is less than $\pm 1.5'$, which is mainly attributed to the non-perfect quality of the 651 nm laser beam.

4.3.3.5 Error in measuring the apex angle

The method of determining the apex angle was described in section 4.1. Table 4-8 shows the results of five measurements which indicate that the error in determining the apex angle is less than 0.11 %. This leads to an error of 0.06 % in calculating the refractive index (see section 4.1) using Eq. (4.1).

Table 4- 6. Repeated measurements of the minimum deviation position by re-rotating the rotation stage to estimate the error in determining the minimum deviation position.

	1st measurement		2nd measurement		3rd measurement		4th measurement	
	Surface 1	Surface 2	Surface 1	Surface 2	Surface 1	Surface 2	Surface 1	Surface 2
1	330°55′53″	60°30′53″	330°56′40″	60°29′45″	330°56′34″	60°31′21″	330°55′54″	60°30′09″
2	330°56′12″	60°31′00″	330°56′21″	60°30′53″	330°56′04″	60°30′15″	330°57′12″	60°30′20″
3	330°55′35″	60°31′05″	330°56′09″	60°29′27″	330°57′20″	60°30′16″	330°56′29″	60°30′22″
4	330°57′17″	60°30′41″	330°56′40″	60°32′34″	330°56′55″	60°31′00″	330°56′10″	60°30′58″
5	330°57′14″	60°29′45″	330°55′56″	60°31′21″	330°55′50″	60°30′07″	330°56′20″	60°31′00″
Average:	330°56′26″	60°30′41″	330°56′21″	60°30′48″	330°56′33″	60°30′36″	330°56′25″	60°30′34″
s.d.:	0.01165	0.00806	0.00480	0.01879	0.00480	0.01879	0.00911	0.00813
Error:	±51″	±56″	±25″	±1′46″	±47″	±45″	±47″	±26″

Table 4- 7. The reading errors in measuring the positions of the surface 1 and surface 2 in apex angle measurements.

	1st measurement		2nd measurement		3rd measurement		4th measurement		5th measurement	
	Surface 1	Surface 2	Surface 1	Surface 2	Surface 1	Surface 2	Surface 1	Surface 2	Surface 1	Surface 2
1	338°23′	113°23′	338°27′	113°26′	338°52′	113°49′	339°07′	114°06′	339°03′	114°04′
2	338°23′	113°23′	338°28′	113°27′	338°51′	113°52′	339°08′	114°07′	339°03′	114°03′
3	338°25′	113°21′	338°28′	113°26′	338°52′	113°51′	339°07′	114°06′	339°03′	114°03′
4	338°23′	113°24′	338°29′	113°27′	338°53′	113°51′	339°09′	114°08′	339°03′	114°03′
5	338°24′	113°22′	338°28′	113°26′	338°53′	113°52′	339°07′	114°06′	339°04′	114°04′
Mean	338°23′36″	113°22′36″	338°28′00″	113°26′24″	338°52′12″	113°51′00″	339°07′36″	114°06′36″	339°03′12″	114°03′24″
s.d.	0.01333	0.01700	0.01054	0.00816	0.01247	0.01826	0.01333	0.01333	0.00667	0.00816
Error	±1′	±1.5′	±1′	±0.5′	±1′	±1.5′	±0.5′	±1′	±0.5′	±0.5′

Table 4- 8. The errors in determining the apex angle of the prism.

	1st measurement	2nd measurement	3rd measurement	4th measurement	5th measurement
1	45°00′	45°01′	45°03′	45°01′	44°59′
2	45°00′	45°01′	44°59′	45°01′	45°00′
3	45°04′	45°02′	45°01′	45°01′	45°00′
4	44°59′	45°02′	45°02′	45°01′	45°00′
5	45°02′	45°02′	45°01′	45°01′	45°00′
Mean:	45°01′	45°01′36″	45°01′	45°01′	44°59′48″
s.d.:	0.02867	0.00653	0.01633	0	0.00133
Error:	±3′	±0.5′	±2′	±0	±0.1′

4.3.4 Section summary

Based on our setup for the minimum deviation method in Figure 4.2-1, the refractive index of the LAF850322 commercial prism at a wavelength of 651 nm was determined to be 1.8441 with a standard deviation of less than 0.0002. The accuracy to the reference value (n = 1.8432 at a wavelength of 651 nm calculated from the Schott data [4.3]) is better than 0.05%. Since surface 2 is not located at the rotation axis of the rotation stage and the distance between the prism and the screen used for detecting the deviated beam was limited, more errors were introduced in determining the refractive index using this surface as the incidence surface.

The average apex angle measured is 45°00′37″ (s.d.= 0.0081). The difference between the measured value and the reference value (45 °) is 0.023%. The maximum error of measuring the apex angle is 0.11% which will lead to an error of 0.06 % in calculating the refractive index.

The error of minimum deviation position measurement is 0.065 % which will cause an error of 0.025% in calculating the refractive index.

In section 4.3.3, each error in the minimum deviation measurement using the current setup in the University of Nottingham was investigated. The error of this measurement can be improved by:

1. Improving the beam quality to be well-colimated;
2. Ensuring good quality of prism surfaces;
3. Using a smaller aperture on the screen;
4. Increasing the optical path of the setup;
5. Manufacturing a prism with a larger apex angle.

4.4 Measuring the refractive indices of chalcogenide glasses using the minimum deviation method

This section describes measurements of the refractive indices of chalcognenide glass prisms (listed in Table 3.4-1) at wavelengths of 651 nm (only for $Ge_{7.5}As_{25.5}S_{67}$ at. %), 1464 nm to 1574 nm, 3100 nm, 3800 nm and 6450 nm. The standard deviation of the measurements will be shown for each prism. These results will be taken as benchmark values in late chapters where new techniques for determining the refractive index of the chalcogenide glasses based on the Swanepoel method [4.5] are developed.

4.4.1 The refractive indices of $Ge_{7.5}As_{25.5}S_{67}$, $As_{40}Se_{60}$, $Ge_{16}As_{24}Se_{15.5}Te_{46}$ at. % and $Ge_{20}Sb_{10}Se_{70}$ at. % at different wavelengths.

Detailed information on the $Ge_{7.5}As_{25.5}S_{67}$ at. % (YRFP001), $As_{40}Se_{60}$ at. % (YRFP004), $Ge_{16}As_{24}Se_{15.5}Te_{44.5}$ at. % (YRFP003) and $Ge_{20}Sb_{10}Se_{70}$ at. % (YRFP005) prisms studied was shown in Table 3.4-2 in section 3.4. The target apex angle of the $As_{40}Se_{60}$ at. % (YRFP004), $Ge_{16}As_{24}Se_{15.5}Te_{46}$ at. % (YRFP003) prisms was 10 º; this was limited by the amount of material available. The target apex angle of the $Ge_{7.5}As_{25.5}S_{67}$ at. % (YRFP002) and $Ge_{20}Sb_{10}Se_{70}$ at. % (YRFP005) was 20 º. The optical setup for measuring the refractive indices of the chalcogenide glass prisms was shown in Figure 4.2-1. The data obtained was fitted with a standard two-term Sellmeier equation of the form [4.4]:

$$n^2(\lambda) = a + \frac{b\lambda^2}{\lambda^2 - a_1^2} + \frac{c\lambda^2}{\lambda^2 - a_2^2} \qquad (4.4)$$

where a, b, c, a_1 and a_2 are all fitting parameters.

For $Ge_{7.5}As_{25.5}S_{67}$ at. % (M122MINSCGDJ), the refractive indices at the wavelengths of 651 nm, 1464 nm to 1574 nm with an interval of 10 nm (since the data points are very close to each other, only a single point at the wavelength of 1504

nm is shown in Figure 4.4-1(a) for clarity), and 3100 nm are shown in Figure 4.4-1(a). The best Sellmeier fit to these data points is also shown in Figure 4.4-1(a) yielding the Sellmeier coefficients presented in Table 4-9. Table 4-9 also presents the values of R^2 (coefficient of determination) to indicate the fitting quality. The closer the R^2 value is to 1, the better the fit is. The measured apex angle and the values of the refractive indices at different wavelengths of $Ge_{7.5}As_{25.5}S_{67}$ at. % and $As_{40}Se_{60}$ at. % are listed, along with the standard deviation, in Table 4-10. Since the beam sources at wavelengths of 3800 nm and 6450 nm were only available late in the PhD period, at which time the respect interests of the group had shifted to Ge-As-Se-Te and Ge-Sb-Se materials, the refractive index of $Ge_{7.5}As_{25.5}S_{67}$ at. % at wavelengths of 3800 nm and 6450 nm were not measured.

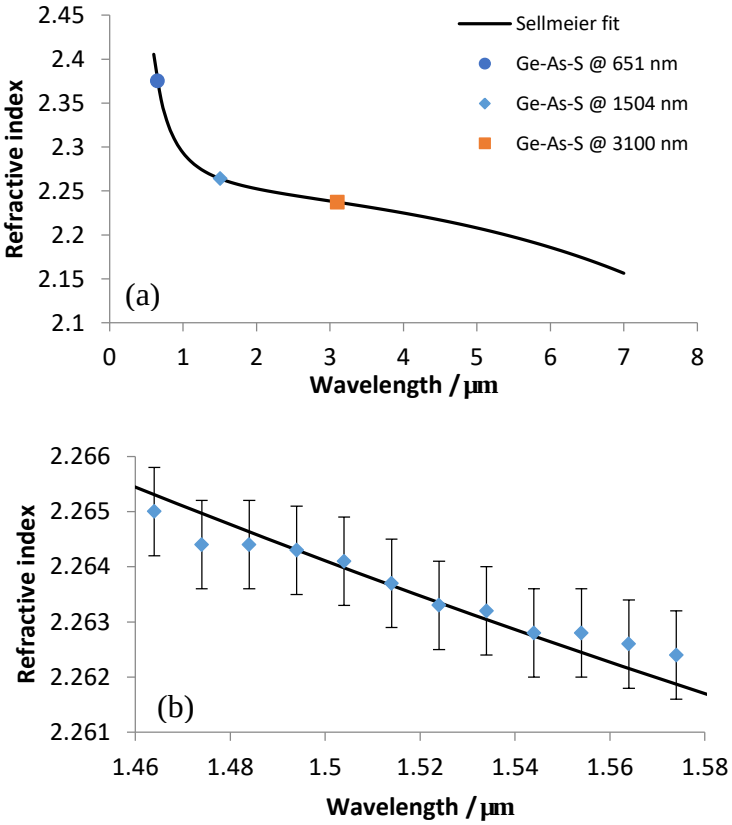


Figure 4.4- 1. (a) The refractive indices of the $Ge_{7.5}As_{25.5}S_{67}$ at. % (M122MINSCGDJ) prism at different wavelengths with the best Sellmeier fit; (b) the refractive indices of the Ge-As-S prism over the wavelengths range from 1.464 μm to 1.574 μm with an interval of 0.01 μm. The measurements were measured at ambient room temperature.

Table 4- 9. The Sellmeier coefficients for the refractive indices of the $Ge_{7.5}As_{25.5}S_{67}$ at. % (M122MINSCGDJ), $As_{40}S_{60}$ at. % (M130MINSCGDJ), $Ge_{16}As_{24}Se_{15.5}Te_{44.5}$ at. % (M140MINSCGDJ) and $Ge_{20}Sb_{10}Se_{70}$ at. % (M135HAP) prisms together with the residual error R^2.

Sellmeier coefficients	a	b	c	a_1	a_2	R^2
Ge-As-S	3.051	2.000	1.585	0.3115	15.52	0.9999
As-Se	4.062	3.726	3.244	0.3979	58.92	0.9999
Ge-As-Se-Te	3.332	6.676	0.9153	0.5022	64.37	0.9998
Ge-Sb-Se	4.831	1.626	2.512	0.4883	53.55	0.9993

Table 4- 10. The measured apex angle and the values of the refractive indices of the $Ge_{7.5}As_{25.5}S_{67}$ at. % (M122MINSCGDJ) and $As_{40}Se_{60}$ at. % (M130MINSCGDJ) prisms with the standard deviations. The measurements were measured at ambient room temperature.

Wavelength /nm	Apex angle (Ge-As-S)	RI (Ge-As-S)	s.d.	Apex angle (As-Se)	RI (As-Se)	s.d.
651	20 °17 ’	2.3754	0.0006	-	-	-
1464	20 °13 ’	2.2650	0.0006	10 °15 ’	2.8430	0.0013
1474	20 °13 ’	2.2644	0.0006	10 °15 ’	2.8420	0.0013
1484	20 °13 ’	2.2644	0.0006	10 °15 ’	2.8415	0.0013
1494	20 °13 ’	2.2643	0.0006	10 °15 ’	2.8406	0.0013
1504	20 °13 ’	2.2641	0.0006	10 °15 ’	2.8404	0.0013
1514	20 °13 ’	2.2637	0.0006	10 °15 ’	2.8395	0.0013
1524	20 °13 ’	2.2633	0.0006	10 °15 ’	2.8391	0.0013
1534	20 °13 ’	2.2632	0.0006	10 °15 ’	2.8380	0.0013
1544	20 °13 ’	2.2628	0.0006	10 °15 ’	2.8371	0.0013
1554	20 °13 ’	2.2628	0.0006	10 °15 ’	2.8370	0.0013
1564	20 °13 ’	2.2626	0.0006	10 °15 ’	2.8364	0.0013
1574	20 °13 ’	2.2624	0.0006	10 °15 ’	2.8358	0.0013
3100	20 °18 ’	2.2373	0.0020	10 °13 ’	2.8006	0.0020
3800	-	-	-	10 °14 ’	2.7952	0.0010
6450	-	-	-	10 °14 ’	2.7863	0.0010

When measuring the refractive index of $Ge_{7.5}As_{25.5}S_{67}$ at. % using the 651 nm He-Ne laser, the refractive index was measured to be 2.3754 with a standard deviation of less than 0.0006 as shown in Figure 4.4-1(a) and Table 4-10. When measuring the refractive indices of this prism using the tunable laser diode, the wavelengths of the laser were selected from 1464 nm to 1574 nm with an interval of

10 nm. The refractive indices of $Ge_{7.5}As_{25.5}S_{67}$ at. % over this narrow wavelength range are shown in Figure 4.4-1(b). The standard deviations were less than 0.0006 as shown in Table 4-10. When using the ICL at a wavelength of 3100 nm for the minimum deviation measurement, the measured refractive index is 2.2373 (see Figure 4.4-1(a)) with a standard deviation of less than 0.0020 as shown in Table 4-10. The larger standard deviation is attributed to the poorer beam quality of the ICL compared to that of the well-collimated fibre coupled tunable laser. Table 4-10 shows that the measured apex angle is very slightly different when using the different lasers, which is attributed to the fact that the incident position on the non-perfectly-flat surface changed after the alignment. The apex angle can be determined as shown in Table 4-10 with an error of $\pm 1'$, which will lead to a $\pm$ 0.0011 error in calculating the refractive index.

$As_{40}Se_{60}$ at. % (M130MINSCGDJ) is not transparent to the 651 nm He-Ne laser. The refractive indices at the wavelengths of 1464 nm to 1574 nm with an interval of 10 nm (since the data points are very close to each other, only a single point at the wavelength of 1504 nm are shown in Figure 4.4-2(a)), 3100 nm, 3800 nm and 6450 nm are shown in Figure 4.4-2(a). The best Sellmeier fit to these data points is shown in Figure 4.4-2(a), yielding the Sellmeier coefficients in Table 4-9. The measured apex angle and the values of the refractive indices at different wavelengths of $As_{40}Se_{60}$ at. %, with their standard deviation, are listed in Table 4-10.

When measuring the refractive indices of this $As_{40}Se_{60}$ at. % prism using the tunable laser diode, the wavelengths of the laser were selected from 1464 nm to 1574 nm with an interval of 10 nm. The refractive indices of $As_{40}Se_{60}$ at. % over this wavelength range are shown in Figure 4.4-2(b). The standard deviations are less than 0.0013 as shown in Table 4-10. When using the ICL (at a wavelength of 3100 nm) for the minimum deviation measurement, the measured refractive index was 2.8006 (see Figure 4.4-1(a)) with a standard deviation of less than 0.0020, as shown in Table

4-10. Compared to the corresponding $Ge_{7.5}As_{25.5}S_{67}$ at. % measurements, these larger standard deviations are attributed to the smaller apex angle, as shown in Table 4-10. In this case, the apex angle can be determined as shown in Table 4-10 with an error of $\pm 1'$, which will lead to an error of less than $\pm$ 0.0030 in calculating the refractive index. When measuring the refractive index of the $As_{40}Se_{60}$ at. % prism using the SuperK supercontinuum source, used in conjunction with a 3.8 μm band pass filter, the refractive index was measured to be 2.7952 with a standard deviation of less than 0.0010 as shown in Figure 4.4-2(b) and Table 4-10. The refractive index at a wavelength of 6.45 μm was measured to be 2.7863 with a standard deviation of less than 0.0010 as shown in Figure 4.4-2(b) and Table 4-10. Since the beams were well collimated for these two latter light sources, the standard deviations of precision are less than those obtained using the ICL (at a wavelength of 3100 nm).

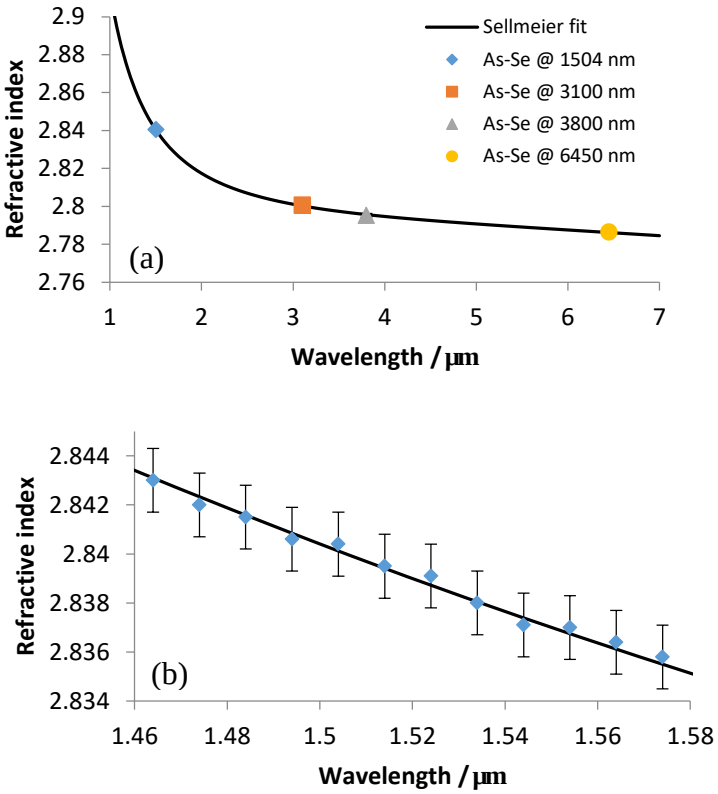


Figure 4.4- 2. (a) The refractive indices of the $As_{40}Se_{60}$ at. % prism (M130MINSCGDJ) at different wavelengths with the best Sellmeier fit; (b) the refractive indices of the $As_{40}Se_{60}$ at. % prism over the wavelength range from 1.464 μm to 1.574 μm with an interval of 0.01 μm. The measurements were measured at ambient room temperature.

The refractive indices of the $Ge_{16}As_{24}Se_{15.5}Te_{44.5}$ at. % (M140MINSCGDJ) and $Ge_{20}Sb_{10}Se_{70}$ at. % (M135HAP) prisms at the wavelengths of 1464 nm to 1574 nm with an interval of 10 nm (since the data points are very close to each other, only a single point at the wavelength of 1504 nm is shown in Figures 4.4-3(a) and 4.4-4(a)), 3100 nm, 3800 nm and 6450 nm are shown in Figures 4.4-3 and 4.4-4. The best Sellmeier fit to these data points is shown in Figures 4.4-3and 4.4-4, yielding the Sellmeier coefficients presented in Table 4-9. The measured apex angle and the values of the refractive indices at different wavelengths of the $Ge_{16}As_{24}Se_{15.5}Te_{44.5}$ at. % and $Ge_{20}Sb_{10}Se_{70}$ at. % prisms, together with the standard deviation of the measurements, are listed in Table 4-11.

For $Ge_{16}As_{24}Se_{15.5}Te_{44.5}$ at. % (M140MINSCGDJ), the refractive indices at the wavelengths from 1464 nm to 1574 nm with an interval of 10 nm are shown in Figure 4.4-3(b) with a standard deviation of precision less than 0.0012 (see Table 4-11). When using the ICL (at a wavelength of 3100 nm), the refractive index was measured to be 3.1920 with a standard deviation of precision less than 0.0023, which was relatively large due to the poor beam quality. Due to the good beam quality of SuperK supercontinuum source with a 3.8 μm band pass filter and the OPO (at a wavelength of 6450 nm), the refractive index of $Ge_{16}As_{24}Se_{15.5}Te_{44.5}$ at. % was determined to be 3.1820 and 3.1682 at these wavelengths, respectively, with a standard deviation less than 0.0010. The apex angle was measured to be $10°16'$ with an error of less than $\pm 1'$. This error will lead to an error of less than ± 0.0038 in determining the refractive index.

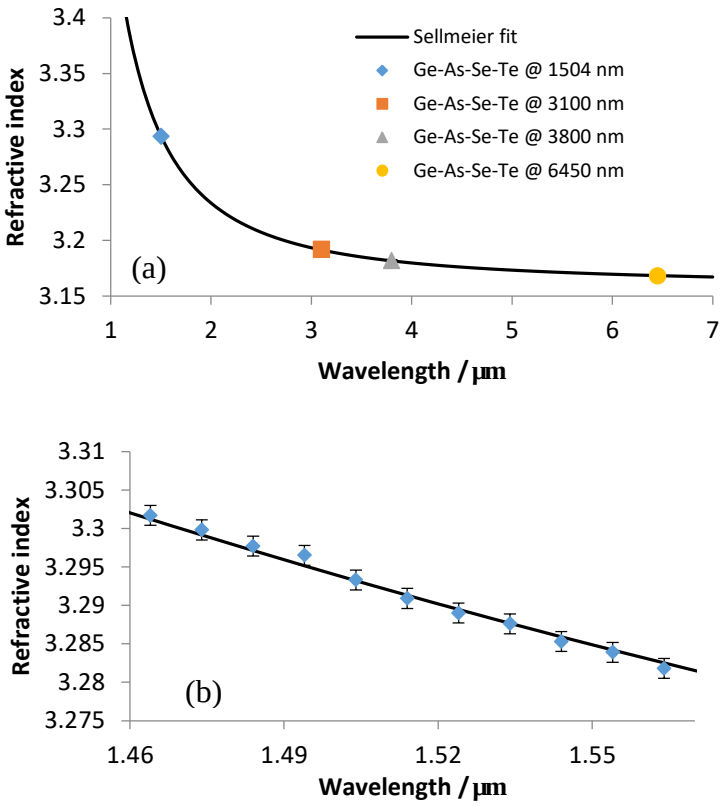


Figure 4.4- 3. (a) The refractive indices of the $Ge_{16}As_{24}Se_{15.5}Te_{44.5}$ at. % (M140MINSCGDJ) prism (YRFP003) at different wavelengths with the best Sellmeier fit; (b) the refractive indices of the $Ge_{16}As_{24}Se_{15.5}Te_{44.5}$ at. % (M140MINSCGDJ) prism over the wavelength range from 1.464 μm to 1.574 μm with an interval of 0.01 μm. The measurements were measured at ambient room temperature.

For $Ge_{20}Sb_{10}Se_{70}$ at. % (M135HAP), the refractive indices at the wavelengths from 1464 nm to 1574 nm with an interval of 10 nm are shown in Figure 4.4-4(b) with a standard deviation of precision less than 0.0004 (see Table 4-11). When using the ICL (at a wavelength of 3100 nm), the refractive index was measured to be 2.5465 with a relatively large standard deviation of precision less than 0.0008, which was attributed to the poor beam quality. Due to the good beam quality of SuperK supercontinuum source with a 3.8 μm band pass filter and the OPO (at a wavelength of 6450 nm), the refractive index of $Ge_{20}Sb_{10}Se_{70}$ at. % was determined to be 2.5447and 2.5354 at these wavelengths, respectively, with a standard deviation less than 0.0006. Due to the larger apex angle ($\sim 20^\circ 05' \pm 1'$) compared to that of the $Ge_{16}As_{24}Se_{15.5}Te_{44.5}$ at. % prism, the standard deviations of the measured refractive

index at different wavelengths were improved, as shown in Table 4-11. In this case, an error of $\pm 1'$ in apex angle will lead to an error in refractive index of less than ± 0.0014. Therefore, in order to reduce the error in the refractive index, a prism with larger apex angle is preferred. This confirms the discussion in section 4.3.

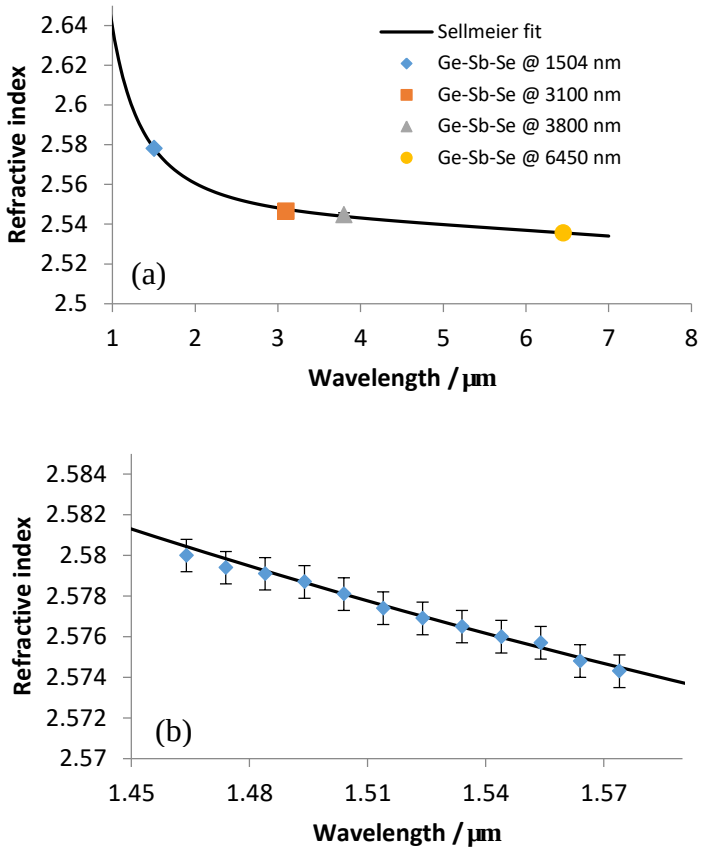


Figure 4.4- 4. (a) The refractive indices of the $Ge_{20}Sb_{10}Se_{70}$ at. % (M135HAP) prism (YRFP005) at different wavelengths with the best Sellmeier fit; (b) the refractive indices of the $Ge_{20}Sb_{10}Se_{70}$ at. % (M135HAP) prism over the wavelength range from 1.464 µm to 1.574 µm with an interval of 0.01 µm. The measurements were measured at ambient room temperature.

Table 4- 11. The measured apex angle and the values of the refractive indices of the $Ge_{16}As_{24}Se_{15.5}Te_{44.5}$ at. % (M140MINSCGDJ) and $Ge_{20}Sb_{10}Se_{70}$ at. % (M135HAP) prisms with the standard deviations. The measurements were measured at ambient room temperature.

Wavelength /nm	Apex angle (Ge-As-Se-Te)	RI (Ge-As-Se-Te)	s.d.	Apex angle (Ge-Sb-Se)	RI (Ge-Sb-Se)	s.d.
1464	10 °16 ’	3.3017	0.0012	20 °05 ’	2.5800	0.0004
1474	10 °16 ’	3.2998	0.0012	20 °05 ’	2.5794	0.0004
1484	10 °16 ’	3.2977	0.0012	20 °05 ’	2.5791	0.0004
1494	10 °16 ’	3.2965	0.0012	20 °05 ’	2.5787	0.0004
1504	10 °16 ’	3.2933	0.0012	20 °05 ’	2.5781	0.0004
1514	10 °16 ’	3.2909	0.0012	20 °05 ’	2.5774	0.0004
1524	10 °16 ’	3.2890	0.0012	20 °05 ’	2.5769	0.0004
1534	10 °16 ’	3.2876	0.0012	20 °05 ’	2.5765	0.0004
1544	10 °16 ’	3.2853	0.0012	20 °05 ’	2.5760	0.0004
1554	10 °16 ’	3.2839	0.0012	20 °05 ’	2.5757	0.0004
1564	10 °16 ’	3.2818	0.0012	20 °05 ’	2.5748	0.0004
1574	10 °16 ’	3.2804	0.0012	20 °05 ’	2.5743	0.0004
3100	10 °16 ’	3.1920	0.0023	20 °06 ’	2.5465	0.0008
3800	10 °16 ’	3.1820	0.0010	20 °05 ’	2.5447	0.0006
6450	10 °16 ’	3.1682	0.0010	20 °05 ’	2.5354	0.0005

4.4.2 The refractive indices of other chalcogenide glasses at wavelengths of 3.1 μm, 3.8 μm and 6.45 μm.

In section 4.4.1, the refractive indices of the $Ge_{7.5}As_{25.5}S_{67}$ at. % (M122MINSCGDJ, YRFP002), $As_{40}Se_{60}$ at. % (M130MINSCGDJ, YRFP004), $Ge_{16}As_{24}Se_{15.5}Te_{46}$ at. % (M140MINSCGDJ, YRFP003) and $Ge_{20}Sb_{10}Se_{70}$ at. % (M135HAP, YRFP005) prisms were measured at some wavelengths in the near-infrared (NIR) and mid-infrared (MIR) regions by the minimum deviation method. A two-term Sellmeier equation was applied to fit the data points over the respective measurement wavelength range. In this Project, the wavelength range of primary interest is the MIR region. Therefore, the refractive indices of some chalcogenide prisms manufactured from glass of additional compositions ($Ge_{14.3}As_{27}Se_{15.5}Te_{43.2}$ at. % (M178DJ, YRFP006), $Ge_{20}As_{20}Se_{14}Te_{46}$ at. % (M112DJ, YRFP007), $Ge_{15}As_{25}Se_{19}Te_{41}$ at. % (M193DJ, YRFP008), distilled $Ge_{16}As_{24}Se_{15.5}Te_{44.5}$ at. %

(M188SCGDJ, YRFP009) and $Ge_{20}Sb_{10}Se_{67}S_3$ at. % (M191HAP, YRFP0010)) were measured at the wavelengths of 3.1 and 6.45 μm using the ICL and the OPO, respectively. Since the SuperK supercontinuum source had to be returned to NKT before these prisms were manufactured, the refractive index at the wavelength of 3.8 μm was not measured.

The measured apex angles and refractive indices of the $Ge_{14.3}As_{27}Se_{15.5}Te_{43.2}$ at. % (M178DJ), $Ge_{20}As_{20}Se_{14}Te_{46}$ at. % (M112DJ), $Ge_{15}As_{25}Se_{19}Te_{41}$ at. % (M193DJ), distilled $Ge_{16}As_{24}Se_{15.5}Te_{44.5}$ at. % (M188SCGDJ) and $Ge_{20}Sb_{10}Se_{67}S_3$ at. % (M191HAP) prisms are shown in Table 4-12. This refractive index data will be taken as benchmark values for the modified Swanepoel method described in chapter 6.

Table 4- 12. The measured apex angle and refractive index of the $Ge_{14.3}As_{27}Se_{15.5}Te_{43.2}$ at. % (M178DJ), $Ge_{20}As_{20}Se_{14}Te_{46}$ at. % (M112DJ), $Ge_{15}As_{25}Se_{19}Te_{41}$ at. % (M193DJ), distilled $Ge_{16}As_{24}Se_{15.5}Te_{44.5}$ at. % (M188SCGDJ) and $Ge_{20}Sb_{10}Se_{67}S_3$ at. % (M191HAP) prisms. The measurements were measured at room temperature (23±0.5 ℃).

Wavelength	3.1 μm	6.45 μm	Wavelength	3.1 μm	6.45 μm
Apex angle ($Ge_{14.3}As_{27}Se_{15.5}Te_{43.2}$)	20 °11 ’	20 °10 ’	Apex angle (distilled $Ge_{16}As_{24}Se_{15.5}Te_{44.5}$)	10 °18 ’	10 °16 ’
Refractive index (s.d.) ($Ge_{14.3}As_{27}Se_{15.5}Te_{43.2}$)	3.2035 (0.0012)	3.1841 (0.0011)	Refractive index (s.d.) (distilled $Ge_{16}As_{24}Se_{15.5}Te_{44.5}$)	3.1853 (0.0016)	3.1637 (0.0014)
Apex angle ($Ge_{20}As_{20}Se_{14}Te_{46}$)	10 °08 ’	10 °09 ’	Apex angle ($Ge_{20}Sb_{10}Se_{67}S_3$)	20 °09’	20 °09’
Refractive index (s.d.) ($Ge_{20}As_{20}Se_{14}Te_{46}$)	3.1662 (0.0020)	3.1432 (0.0010)	Refractive index (s.d.) ($Ge_{20}Sb_{10}Se_{67}S_3$)	2.5322 (0.0007)	2.5223 (0.0006)
Apex angle ($Ge_{15}As_{25}Se_{19}Te_{41}$)	10 °12 ’	10 °12 ’			
Refractive index (s.d.) ($Ge_{15}As_{25}Se_{19}Te_{41}$)	3.1550 (0.0014)	3.1324 (0.0009)			

4.4.3 Repeatability of the minimum deviation measurements using the 3100 nm ICL source

As described in section 4.4.2, the beam quality of the 3100 nm ICL source is relatively poor. As a way to determine the repeatability of the minimum deviation measurements using the 3100 nm ICL source, the $Ge_{16}As_{24}Se_{15.5}Te_{44.5}$ at. % (YRFP003) and $Ge_{20}Sb_{10}Se_{70}$ at. % (YRFP005) prisms were re-measured several times over a four-month time period.

The refractive index of the $Ge_{16}As_{24}Se_{15.5}Te_{44.5}$ at. % prism measured on different days is shown in Figure 4.4-5. The first two data points in Figure 4.4-5 were measured at room temperatures of 24.3 ℃ and 24.8 ℃, respectively. The last four points were measured at room temperatures of 21.8 ℃, 21.2 ℃, 21.3 ℃ and 21.1 ℃, respectively. There is little variance in the measured refractive index from day to day, and all of the measured refractive index values are well within the standard deviation errors of each other. The average refractive index of the $Ge_{16}As_{24}Se_{15.5}Te_{44.5}$ at. % prism across the six independent measurements is 3.1920, and is within an envelope of $\Delta n = 0.0014$, resulting in an error of refractive index within ± 0.0007.

The refractive index of the $Ge_{20}Sb_{10}Se_{70}$ at. % prism measured on different days is shown in Figure 4.4-6. The seven data points in Figure 4.4-6 were measured at room temperatures of 24.0 ℃, 24.8 ℃, 25.1 ℃, 23.3 ℃, 23.5 ℃, 23.8 ℃ and 24.2 ℃, respectively. There is little variance in the measured refractive index from day to day, and most of the measured refractive index values are well within the standard deviation errors of each other. The average refractive index of the $Ge_{20}Sb_{10}Se_{70}$ at. % prism across the seven independent measurements is 2.5462, and is within an envelope of $\Delta n = 0.0022$, resulting in an error of refractive index within ± 0.0011.

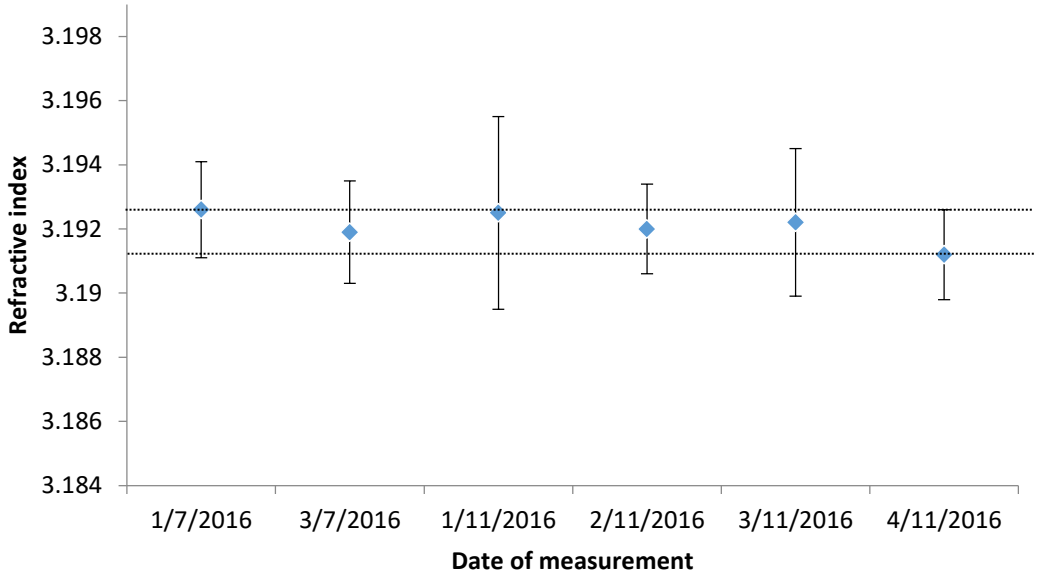


Figure 4.4- 5. The refractive index of the $Ge_{16}As_{24}Se_{15.5}Te_{44.5}$ at. % (M140MINSCGDJ) prism (YRFP003) measured independently at a wavelength of 3.1 µm on the dates indicated.

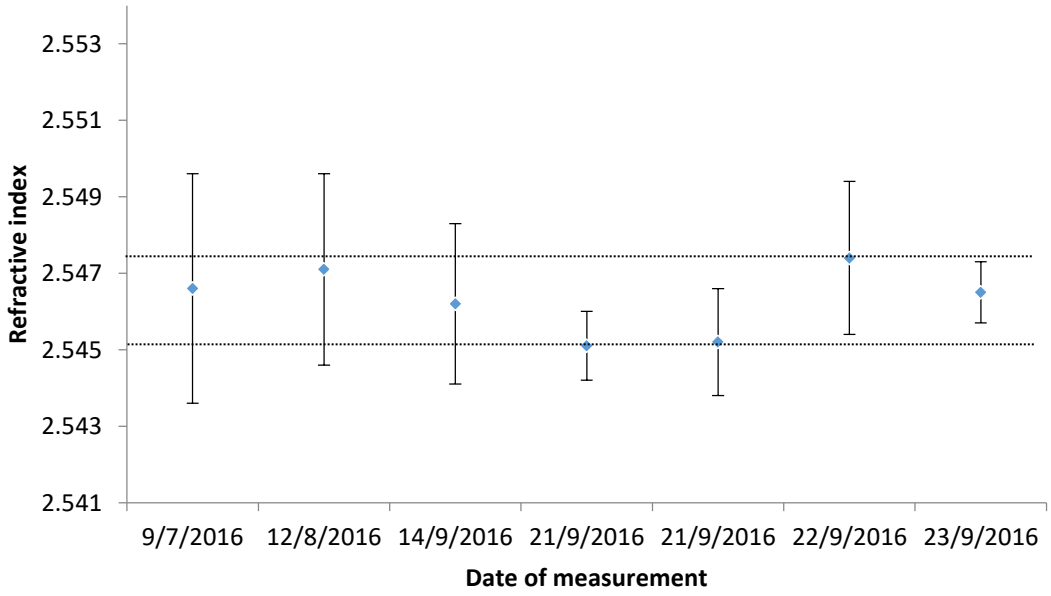


Figure 4.4- 6. The refractive index of the $Ge_{20}Sb_{10}Se_{70}$ at. % (M135HAP) prism measured independently at a wavelength of 3.1 µm on the dates indicated.

4.4.4 Section summary

The refractive indices of the chalcogenide prisms listed in Table 3.4-2 were measured at different wavelengths using the minimum deviation method. When using a 651 nm He-Ne laser source, the refractive index of the $Ge_{7.5}As_{25.5}S_{67}$ at. % (M122MINSCGDJ) prism can be determined with a standard deviation less than 0.0006. The refractive indices of the $Ge_{7.5}As_{25.5}S_{67}$ at. % (M122MINSCGDJ), $As_{40}Se_{60}$ at. % (M130MINSCGDJ), $Ge_{16}As_{24}Se_{15.5}Te_{44.5}$ at. % (M140MINSCGDJ) and $Ge_{20}Sb_{10}Se_{70}$ at. % (M135HAP) prims were measured at the wavelengths from 1474 to 1574 nm with an interval of 10 nm using a tunable laser diode. For the prism with 10 ^{o}target apex angle, the standard deviation of the refractive index data was less than 0.0013. For the prism with 20 ^{o}target apex angle, the standard deviation of the refractive index data was improved from less than 0.0013 to less than 0.0006. For the measurements using a 3100 nm ICL, due to its relatively poor beam quality, the standard deviation of the measured refractive index increased up to 0.0023. The SuperK supercontinuum source used conjunction with a 3.8 μm band pass filter and 6.45 μm OPO were successfully used to provide the refractive index data with a standard deviation of precision of less than 0.0010. The refractive index data were then fitted to a two-term Sellmeier equation over the wavelength measurement range.

The repeatability of the minimum deviation measurements using the ICL was analysed using the $Ge_{16}As_{24}Se_{15.5}Te_{44.5}$ at. % (M140MINSCGDH) and $Ge_{20}Sb_{10}Se_{70}$ at. % (M135HAP) prisms. The average refractive index of the $Ge_{16}As_{24}Se_{15.5}Te_{44.5}$ at. % prism across the six independent measurements was 3.1920 at a wavelength of 3.1 μm with an error of refractive index within ± 0.0007. For the $Ge_{20}Sb_{10}Se_{70}$ at. % prism, the average refractive index across the seven independent measurements was 2.5462 at a wavelength of 3.1 μm with an error in refractive index within ± 0.0011.

4.5 Extrapolating the refractive index data of the $Ge_xAs_{z-x}Se_{100-z-y}Te_y$ at. % glass system

As mentioned in sections 4.4.1 and section 4.4.2, the refractive indices of Ge-As-Se-Te with different glass compositions ($Ge_{16}As_{24}Se_{15.5}Te_{44.5}$ at. % (M140MINSCGDJ), $Ge_{14.3}As_{27}Se_{15.5}Te_{43.2}$ at. % (M178DJ), $Ge_{20}As_{20}Se_{14}Te_{46}$ at. % (M112DJ), $Ge_{15}As_{25}Se_{19}Te_{41}$ at. % (M193D) and distilled $Ge_{16}As_{24}Se_{15.5}Te_{44.5}$ at. % (M188SCGDJ)) were measured using the minimum deviation method. Based on the data obtained, the refractive index of Ge-As-Se-Te with different compositions can be predicted.

To conduct a systematic investigation of the composition dependence of refractive index in the Ge-As-Se-Te glass system, the refractive indices of $Ge_xAs_{z-x}Se_{100-z-y}Te_y$ at. % (x is the atomic % of Ge in Ge-As-Se-Te; y is the atomic % of Te in Ge-As-Se-Te; z is the sum in atomic % of Ge and As) measured using the 3.1 μm ICL source and obtained from QinetiQ are listed in Table 4-13. Based on the different glass composition of $Ge_xAs_{z-x}Se_{100-z-y}Te_y$ at. % presented in Table 4-13, the range of x, y, z in present work can be determined, yielding $10 \leq x \leq 25$, $40 \leq y \leq 50$ and $30 \leq z \leq 40$.

Table 4- 13. The measured refractive index and estimated refractive index of Ge-As-Se-Te with different compositions from our group and QinetiQ data [4.6] with the errors.

	Ge/ at. %	As/ at. %	Se/ at. %	Te/ at. %	Refractive index (Prism or literature)	Estimation	Error
Data from Mid-infrared photonics Group, University of Nottingham	15	25	19	41	3.155 @ 3.1 μm 3.132 @ 6.45 μm	3.155 @ 3.1 μm 3.131 @ 6.45 μm	0% @ 3.1 μm -0.03% @ 6.45 μm
	16	24	15.5	44.5	3.192 @ 3.1 μm 3.168 @ 6.45 μm	3.192 @ 3.1 μm 3.168 @ 6.45 μm	Initial value
	20	20	14	46	3.166 @ 3.1 μm 3.143 @ 6.45 μm	3.166 @ 3.1 μm 3.142 @ 6.45 μm	0% @ 3.1 μm -0.03% @ 6.45 μm
	14.3	27	15.5	43.2	3.204 @ 3.1 μm 3.184 @ 6.45 μm	3.208 @ 3.1 μm 3.184 @ 6.45 μm	0.12% @ 3.1 μm 0% @ 6.45 μm
QinetiQ (2004)	15	25	14	46	3.267 @ 2 μm 3.198 @ 9 μm	3.259 @ 2 μm 3.197 @ 9 μm	-0.24% @ 2 μm -0.03% @ 9 μm
	20	20	14	46	3.2 @ 2 μm 3.138 @ 9 μm	3.2 @ 2 μm 3.138 @ 9 μm	Initial value
	19	11	17	53	3.196 @ 2 μm 3.115 @ 9 μm	3.184 @ 2 μm 3.122 @ 9 μm	-0.38% @ 2 μm 0.22% @ 9 μm
	25	15	14	46	3.140 @ 2 μm 3.078 @ 9 μm	3.142 @ 2 μm 3.080 @ 9 μm	0.06% @ 2 μm 0.06% @ 9 μm

The refractive indices of Ge-As-Se-Te with different compositions synthesised in our group were measured at a wavelength of 3.1 μm. Results are presented in Table 4-13. By analysing the refractive index change with changing the composition of $Ge_{15}As_{25}Se_{19}Te_{41}$ at. % (x=15; y=41; z=40), $Ge_{16}As_{24}Se_{15.5}Te_{44.5}$ at. % (x=16; y=44.5;

z=40) and $Ge_{20}As_{20}Se_{14}Te_{46}$ at. % (x=20; y=46; z=40), a 1 atomic % composition change from Ge to As (x reduced by 1) increased the refractive index by ~0.012 at a wavelength of 3.1 μm. This value is in a good agreement with that analysed from QinetiQ data [4.6], also shown in Table 4-13, which is 0.012. The analysis of the refractive index change with changing compositions of these three glasses yielded that a 1 atomic % composition change from Se to Te (y increased by 1) increased the refractive index by ~0.014 at a wavelength of 3.1 μm; this is also in a good agreement with QinetiQ data (0.013 to 0.020) [4.6] as shown in Table 4-13. According to [4.7], a 1 atomic % composition change from Ge to As in Ge-As-Se-Te glass system increased the refractive index by 0.0126 ± 0.0026. Furthermore, a 1 atomic % composition change from Ge/As to Se/Te (z reduced by 1) increased the refractive index by 0.004. Therefore, when $10 \leq x \leq 25$, $40 \leq y \leq 50$ and $30 \leq z \leq 40$, assuming the refractive index of $Ge_xAs_{z-x}Se_{100-z-y}Te_y$ at. % to be the initial value $n_{initial}$, the refractive index of $Ge_{x'}As_{z'-x'}Se_{100-z'-y'}Te_{y'}$ at. %, $n_{estimate}$, can be predicted by:

$$n_{estimate} = n_{initial} + 0.012(x - x') + 0.014(y' - y) + 0.004(z - z') \qquad (4.4)$$

The predicted refractive index of $Ge_{14.3}As_{27}Se_{15.5}Te_{43.2}$ at. % (x=14.3; y=43.2; z=41.3) using Eq. (4.4) is 3.208 at the wavelength of 3.1 μm as shown in Table 4-13. Compared to the experimental benchmark value from the minimum deviation method (3.204 at the wavelength of 3.1 μm), the error is less than 0.12 %. Assuming the the refractive index of $Ge_{16}As_{24}Se_{15.5}Te_{44.5}$ at. % at a wavelength of 6.45 μm as the initial value, the predicted refractive indices of $Ge_{20}As_{20}Se_{14}Te_{46}$ at. %, $Ge_{20}As_{20}Se_{14}Te_{46}$ at. % and $Ge_{14.3}As_{27}Se_{15.5}Te_{43.2}$ at. % at a wavelength of 6.45 μm were obtained using Eq. (4.4), as shown in Table 4-13. Compared to the results obtained using the minimum deviation method, the errors were less than 0.03%.

In order to further investigate the error of the prediction, the benchmark QinetiQ data [4.6] was used, assuming the refractive index of $Ge_{20}As_{20}Se_{14}Te_{46}$ at. % as the

initial value. At a wavelength of 9 μm, the error from the predicted refractive index using Eq. (4.4) to the measured values is less than 0.22 % as shown in Table 4.13. At the wavelength of 2 μm, the error from the predicted refractive index obtained using Eq. (4.4) to the measured values increased with the atomic % of Te increasing, which is attributed to the red shift of the optical bandgap with increasing the atomic % of Te in the Ge-As-Se-Te glass.

In conclusion, when the composition of $Ge_xAs_{z-x}Se_{100-z-y}Te_y$ at. % is within the range of $10 \leq x \leq 25$, $40 \leq y \leq 50$ and $30 \leq z \leq 40$, the refractive index can be extrapolated from measured data with an error of less than 0.22 %. This extrapolation is very useful for predicting core/cladding composition for the design of step-index fibres.

4.6 Chapter summary

The main focus of this chapter was to measure the refractive index of the chalcogenide glasses using the prism minimum deviation method. The measured results will be taken as the benchmark values in the following chapters. The most important points from chapter 4 are summarised below:

- A setup for the minimum deviation measurement was successfully established up in our laboratory.
- In order to investigate the accuracy and error of the minimum deviation measurements based on the optical setup in our laboratory, a commercial silica prism (LAF 850322 right-angled prism) was used for initial measurements. Based on our setup for the minimum deviation method in Figure 4.2-1, the refractive index of the LAF850322 commercial prism was determined with an accuracy of better than 0.05 % compared to the reference value calculated from the Schott data [4.3]. The standard deviations of the refractive index using the

two surfaces of the prism as the incident surface are less than 0.0002. The errors in each part of the measurement were analysed.

- The refractive index of chalcogenide glass prisms was successfully determined using the minimum deviation method. When using a 651 nm He-Ne laser source, the refractive index of the $Ge_{7.5}As_{25.5}S_{67}$ at. % (M122MINSCGDJ) prism can be determined with a standard deviation less than 0.0006. The refractive indices of the $Ge_{7.5}As_{25.5}S_{67}$ at. % (M122MINSCGDJ), $As_{40}Se_{60}$ at. % (M130MINSCGDJ), $Ge_{16}As_{24}Se_{15.5}Te_{44.5}$ at. % (M140MINSCGDJ) and $Ge_{20}Sb_{10}Se_{70}$ at. % (M135HAP) prims were measured at the wavelengths from 1464 to 1574 nm with an interval of 10 nm using a tunable laser diode. For prisms with a 10 ° target apex angle, the standard deviation of the refractive index data was less than 0.0013. For prisms with a 20 °target apex angle, the standard deviation of the refractive index data was improved from less than 0.0013 to less than 0.0006. For the measurements using the 3.1 μm ICL source, due to the relatively poor beam quality, the standard deviation of the measured refractive index increased up to 0.0023. The SuperK supercontinuum source used with a 3.8 μm band pass filter and a 6.45 μm OPO Chromacity lasers source were successfully used to provide refractive index data, each with a standard deviation of precision less than 0.0010. The refractive index data over the wavelength measurement range were then successfully fitted to a two-term Sellmeier equation.
- The repeatability of the minimum deviation measurements using a 3.1 μm ICL source was analysed using $Ge_{16}As_{24}Se_{15.5}Te_{44.5}$ at. % (M140MINSCGDJ) and $Ge_{20}Sb_{10}Se_{70}$ at. % (M135HAP) prisms. The average refractive index of the $Ge_{16}As_{24}Se_{15.5}Te_{44.5}$ at. % prism across six independent measurements over a four-month time period is 3.1920 at a wavelength of 3.1 μm with an error of refractive index within ± 0.0007. For the $Ge_{20}Sb_{10}Se_{70}$ at. % prism, the average refractive index across seven independent measurements, taken over a period of two months, is 2.5462 at a wavelength of 3.1 μm with an error of refractive index within ± 0.0011.

- After analysing the refractive index change with changing composition of Ge-As-Se-Te ($Ge_{16}As_{24}Se_{15.5}Te_{44.5}$ at. % (M140MINSCGDJ), $Ge_{14.3}As_{27}Se_{15.5}Te_{43.2}$ at. % (M178DJ), $Ge_{20}As_{20}Se_{14}Te_{46}$ at. % (M112DJ) and $Ge_{15}As_{25}Se_{19}Te_{41}$ at. % (M193D)), an interpolation scheme for predicting the refractive index of $Ge_xAs_{z-x}Se_{100-z-y}Te_y$ at. % within the range of $10 \leq x \leq 25$, $40 \leq y \leq 50$ and $30 \leq z \leq 40$ was set up with an error of less than 0.22 %.

References

[4.1] Malitson, L.H., 1965. Interspecimen Comparison of the Refractive Index of Fused Silica. *Journal of the Optical Society of America*, *55*(1205), pp.1917-1983.

[4.2] Fang, Y., Jayasuriya, D., Furniss, D., Tang, Z.Q., Markos, C., Sujecki, S., Seddon, A.B. and Benson, T.M., 2016, July. Characterising refractive index dispersion in chalcogenide glasses. In *Transparent Optical Networks (ICTON), 2016 18th International Conference on* (pp. 1-5). IEEE..

[4.3] Schott, A. G. (2011). Optical glass data sheets. *Germany Google Scholar*.

[4.4] Dantanarayana, H.G., Abdel-Moneim, N., Tang, Z., Sojka, L., Sujecki, S., Furniss, D., Seddon, A.B., Kubat, I., Bang, O. and Benson, T.M., 2014. Refractive index dispersion of chalcogenide glasses for ultra-high numerical-aperture fiber for mid-infrared supercontinuum generation. *Optical Materials Express*, *4*(7), pp.1444-1455.

[4.5] Swanepoel, R., 1985. Determining refractive index and thickness of thin films from wavelength measurements only. *Journal of the Optical Society of America A*, *2*, pp.1339-1343.

[4.6] Tikhomirov, V.K., Furniss, D., Seddon, A.B., Savage, J.A., Mason, P.D., Orchard, D.A. and Lewis, K.L., 2004. Glass formation in the Te-enriched part of the quaternary Ge–As–Se–Te system and its implication for mid-infrared optical fibres. *Infrared Physics & Technology*, *45*(2), pp.115-123.

[4.7] Aio, L.G., Efimov, A.M. and Kokorina, V.F., 1978. Refractive index of chalcogenide glasses over a wide range of compositions. *Journal of Non-Crystalline Solids*, *27*(3), pp.299-307.

Chapter 5: Refractive index models for chalcogenide glasses

The accurate refractive indices of some chalcogenide glasses at the wavelengths of 651 nm, 1464 to 1574 nm, 3100 nm, 3800 nm and 6450 nm were successfully measured by the minimum deviation method in Chapter 4. However, due to the limitation of beam sources, it is not possible to make continuous refractive index dispersion measurements using this technique.

Refractive index dispersion data are crucial for designing chalcogenide glass step-index fibres (SIF) for mid-infrared (MIR) supercontinuum generation (SCG). However, little dispersion data is available at MIR wavelengths for the chalcogenide glasses. In this chapter, the dispersion data of chalcogenide glasses will be presented over the wavelength range from 0.4 μm to 33 μm, covering the visible (VIS: 0.4 to 0.7 μm), the near-infrared (NIR: 0.7 to 3 μm) and some of the mid-infrared (MIR: 3 to 50 μm) spectral regions, by means of spectroscopic ellipsometry. Once the dispersion data have been measured at several wavelengths, a proper refractive index model is required to interpolate the data points and represent the characteristic. Therefore, different complex refractive index models will be introduced and applied to fit the data points. The proper refractive index models, which will be used to improve Swanepoel method in chapter 6, can be verified by yielding the best fitting qualities.

Section 5.1 will introduce complex refractive index and two commonly used refractive index models for the real part of refractive index. In section 5.2, the basic theory of ellipsometry will be introduced and the refractive index dispersion of five different chalcogenide glasses taken from the literature will be presented. Section 5.3 will define the transparent windows for chalcogenide glasses. In section 5.4, different linear refractive index models will be applied to fit the ellipsometry data over the wavelength range from the lower wavelength edge of the transparent

window to 2 μm and within the whole transparent window, and comparisons between them will be made. Section 5.5 will discuss the physical interpretation of the parameters used in a two-term Sellmeier model. In section 5.6, the numerical aperture of a proposed core-cladding fibre design will be presented. In section 5.7, the material dispersion for the chalcogenide glasses introduced in section 5.2 will be calculated and discussed. Finally, a summary of this chapter will be made in section 5.8.

5.1 Refractive index models

5.1.1 Complex refractive index and permittivity

When light passes through a medium, some part of it will usually be attenuated. This can be taken into account by defining a complex refractive index [5.1]:

$$\underline{n} = n + i\kappa \qquad (5.1)$$

where n is the real part of the refractive index which is related to the phase velocity and κ is the imaginary part of the refractive index which is also known as the extinction coefficient.

For most naturally occurring materials, which are non-magnetic at optical frequencies, the relation between the complex relative permittivity $\underline{\varepsilon_r}$, with real and imaginary parts ε_r and $\widetilde{\varepsilon_r}$, and the complex refractive index $\underline{n}$, with real and imaginary parts n and κ, is

$$\underline{\varepsilon_r} = \varepsilon_r + i\widetilde{\varepsilon_r} = \underline{n}^2 = (n + i\kappa)^2. \qquad (5.2)$$

The real and imaginary parts of $\underline{\varepsilon_r}$ can be expressed by:

$$\varepsilon_r = n^2 - \kappa^2 \qquad (5.3)$$

$$\widetilde{\varepsilon_r} = 2n\kappa. \qquad (5.4)$$

The real and imaginary parts of $\underline{n}$ can thus be expressed by:

$$n = \sqrt{\frac{|\underline{\varepsilon_r}| + \varepsilon_r}{2}}, \quad (5.5)$$

$$\kappa = \sqrt{\frac{|\underline{\varepsilon_r}| - \varepsilon_r}{2}} \quad (5.6)$$

where $|\underline{\varepsilon_r}| = \sqrt{{\varepsilon_r}^2 + \widetilde{\varepsilon_r}^2}$ is the complex modulus.

Many dispersive models for refractive index dispersion exist. Some models model only the real part of the refractive index, such as the Cauchy model and Sellmeier model [5.2]. Some models model both the real and imaginary parts of the refractive index, such as the Drude model [5.2] and the Tauc-Lorentz model [5.3]. In the present work, only the real part of refractive index was investigated. Therefore, the Cauchy and Sellmeier models will be further applied to fit the ellipsometry data points (real part of refractive index) in this chapter and to modify the Swanepoel method [5.4] in chapter 6. The Lorentz and Drude model will not be introduced in detail here.

5.1.2 Cauchy model

The Cauchy dispersion model [5.5] is the most simplified and the very first model developed. However, the Cauchy model approximation is only valid away from band gaps, where the imaginary part of refractive index is very small. In other words, the model is valid in the optically transparent regions [5.6]. The Cauchy equation is shown in Eq. (5.7):

$$n^2(\lambda) = A_1 + \frac{A_2}{\lambda^2} + \frac{A_3}{\lambda^4} \quad (5.7)$$

where n is the real part of refractive index, λ is the wavelength and A_1, A_2 and A_3, are fitting parameters.

The model according to the Eq. (5.7), assumes that the band gap, where a resonance in refractive index occurs, is at zero frequency. Hence, the Cauchy model cannot be used if the band gap of the material falls within the wavelength range of interest [5.6].

5.1.3 Sellmeier model

The Sellemier model was firstly derived by Sellmeier in 1871 [5.7], and is one of the most widely used models to describe the refractive index dispersion. Similar to the Cauchy model, the Sellmeier model is valid away from band gaps. However, the Sellmeier model can be applied to model materials with multiple band gaps in the frequency range of interest, which is unlike the Cauchy model [5.6]. The Sellmeier model of the real part of refractive index is given as:

$$n^2(\lambda) = A + \sum_{i=1}^{N_s} \frac{B_i \lambda^2}{\lambda^2 - {C_i}^2} \qquad (5.8)$$

where A, B_i and C_i are experimentally determined Sellmeier coefficients, and N_s is the number of Sellmeier coefficients used. In this work, when N_s = 1, the model in Eq. (5.8) is referred to the one-term Sellmeier model. The two-term Sellmeier model is defined when N_s = 2.

Eq. (5.8) models multiple infinite material resonances at N_s wavelengths for which the relevant term becomes singular when $\lambda = C_i$. For the two-term Sellmeier model, one resonance in the ultraviolet (UV) and another in the infrared (IR) is sufficient for most solid materials for a wide frequency range away from absorption bands [5.6]. This will be further discussed in section 5.4.

5.2 Refractive index dispersion measurements on chalcogenide glasses by means of spectroscopic ellipsometry

Several refractive index models for refractive index dispersion exist. Some of them (the Cauchy model and Sellmeier model [5.2]) can only determine the real part of the refractive index. Some models model both the real and imaginary parts of the refractive index, such as the Drude model [5.2] and the Tauc-Lorentz model [5.3]. In the present work, only the real part of refractive index of chalcogenide glasses was investigated; the Cauchy and Sellmeier models are not only simple in concept but also material dispersion can be obtained from the second derivatives of Eqs. (5.7) and (5.8). Therefore, the Cauchy model and Sellmeier model will be applied and further compared in this chapter.

Bulk chalcogenide glass samples ($Ge_{16}As_{24}Se_{15.5}Te_{44.5}$ at. % (M150MINSCGDJ), $As_{40}Se_{60}$ at. % (M005MINSCGNM), $Ge_{10}As_{23.4}Se_{66.6}$ at. % (M007MINSCGNM), $Ge_{16.5}As_{16}Ga_3Se_{64.5}$ at. % (ZQT007), Pr^{3+} doped $Ge_{16}As_{21}Ga_1Se_{62}$ at. % (M022MINREZQT)), whose preparation procedures are described in section 3.6.2, were sent to J. A. Woollam co. Inc. for spectroscopic-ellipsometry analysis.

The basic theory of spectroscopic ellipsometry was illustrated in section 2.5.3. The chalcogenide sample were analysed by spectroscopic ellipsometry with the incidence angle from 55 ° to 75 ° in 10 ° intervals. The incidence angle was close to the Brewster angle, which allowed most sensitivity to the reflectance differences between s- and p- polarised light as discussed in section 2.5.3. The Woollam VUV VASE rotating analyser ellipsometer was used to measure the refractive index dispersion of the samples from 140 nm to 2500 nm. It was purged with dry nitrogen gas to eliminate the atmospheric absorption of light below 190 nm by oxygen and water vapour. The Woollam IR-VASE rotating analyser was used for the 1.7 μm – 33 μm wavelength-range measurements. The IR-VASE integrates a FTIR

interferometer source, a rotating compensator ellipsometer, wire-grid polarisers and a DTGS detector. The data points obtained from the spectroscopic ellipsometry were fitted by different refractive index models. The proper refractive index model will provide the best fit to the data points, which will be used to determine some optical properties of the chalcogenide glasses (continuous refractive index versus wavelengths, numerical aperture and material dispersion) here and improve the Swanepoel method [5.4] in chapter 6.

Spectroscopic ellipsometry measures the change of polarisation upon reflection and compares it to a model. The thickness and refractive index of a sample can be determined by matching the spectral of the amplitudes Ψ and phase Δ of the oscillations versus wavenumber spectra. The Tauc-Lorentz and Cody-Lorentz models were used to model the absorption spectra of the chalcogenide glass samples. A Sellmeier dispersion function was used to model the real part of permittivity of each glass composition. The extinction coefficients of each glass composition were obtained using the Kramers-Kronig relationships: $\varepsilon_r = n^2 - \kappa^2$ and $\widetilde{\varepsilon_r} = 2n\kappa$. The accuracy of this technique is limited by surface effects [5.8] as a thin contamination layer, oxide layer, or small defects on the surface can all potentially yield different optical constants for the glass.

The refractive indices and extinction coefficients of $Ge_{16}As_{24}Se_{15.5}Te_{44.5}$ (M150MINSCGDJ), $As_{40}Se_{60}$ (M005MINSCGNM), $Ge_{10}As_{23.4}Se_{66.6}$ (M007MINSCGNM), $Ge_{16.5}As_{16}Ga_3Se_{64.5}$ (ZQT007) and Pr^{3+} doped $Ge_{16}As_{21}Ga_1Se_{62}$ (M022MINREZQT) obtained from the Woollam VUV VASE and IR-VASE instruments were shown in Figure 5-1 as solid and dashed lines respectively.

From the inset to Figure 5-1, a steeply rising extinction coefficient with decreasing wavelengths starts from ~ 1445 nm ($Ge_{16}As_{24}Se_{15.5}Te_{44.5}$ at. %), ~ 700 nm ($As_{40}Se_{60}$ at. %), ~ 665 nm ($Ge_{10}As_{23.4}Se_{66.6}$ at. %), ~ 650 nm ($Ge_{16.5}As_{16}Ga_3Se_{64.5}$ at. %) and ~

650 nm (Pr^{3+} doped $Ge_{16}As_{21}Ga_1Se_{62}$ at. %). The extinction coefficients reach maximum values of ~ 1.95 for $Ge_{16}As_{24}Se_{15.5}Te_{44.5}$ at. %, ~ 1.85 for $As_{40}Se_{60}$ at. %, ~ 1.6 for $Ge_{10}As_{23.4}Se_{66.6}$ at. %, ~ 1.5 for $Ge_{16.5}As_{16}Ga_3Se_{64.5}$ at. % and ~ 1.6 for Pr^{3+} doped $Ge_{16}As_{21}Ga_1Se_{62}$ at. %. According to Dantanarayana *et al.* [5.9], the wavelengths at which the extinction coefficients begin to increase are proposed to be associated with their optical band gaps. In [5.10], Zakery and Elliott reported the optical band-gaps as corresponding to wavelengths of 701 nm for the $As_{40}Se_{60}$ at. % and 645 nm for the $Ge_9As_{25}Se_{66}$ at. %, which is in agreement with the onset of rising extinction coefficient with decreasing wavelength of 700 nm for the $As_{40}Se_{60}$ at. % and ~ 665 nm for $Ge_{10}As_{23.4}Se_{66.6}$ at. %. Therefore, the optical band-gaps of $Ge_{16}As_{24}Se_{15.5}Te_{44.5}$ at. %, $Ge_{16.5}As_{16}Ga_3Se_{64.5}$ at. % and Pr^{3+} doped $Ge_{16}As_{21}Ga_1Se_{62}$ at. % can be roughly estimated from the results shown in the inset to Figure 5-1 as ~ 1300 nm (~ 0.954 eV), ~ 650 (~ 1.907 eV) nm and ~ 650 nm (~ 1.907 eV) respectively.

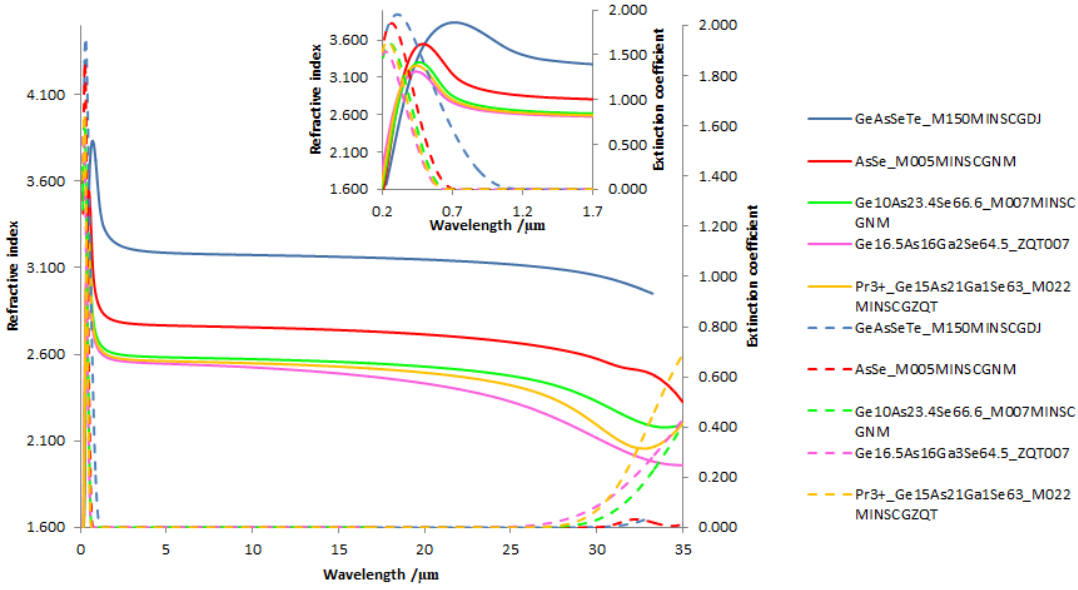


Figure 5- 1. The refractive indices (solid lines) and extinction coefficients (dashed lines) of $Ge_{16}As_{24}Se_{15.5}Te_{44.5}$ at. % (M150MINSCGDJ), $As_{40}Se_{60}$ at. % (M005MINSCGNM), $Ge_{10}As_{23.4}Se_{66.6}$ at. % (M007MINSCGNM), $Ge_{16.5}As_{16}Ga_3Se_{64.5}$ at. % (ZQT007), Pr^{3+} doped $Ge_{16}As_{21}Ga_1Se_{62}$ at. % (M022MINSCGZQT) calculated from ellipsometry measurements. Inset shows detail over the wavelength range from 0.2 µm to 1.7 µm.

5.3 Optically transparent window

For the applications of fibre optics and optical waveguides, the principal interest is generally in real part of refractive index of a chalcogenide glass within its transparent window. Therefore, it is crucial to know the transparent windows for chalcogenide glasses.

Dantanarayana *et al.* defined the transparent window of a chalcogenide glass to be the range of wavelengths over which the extinction coefficient was smaller than 0.0005 [5.9]. Therefore, the transparent windows of $Ge_{16}As_{24}Se_{15.5}Te_{44.5}$ at. % (M140MINSCGDJ), $As_{40}Se_{60}$ at. % (M005MINSCGNM), $Ge_{10}As_{23.4}Se_{66.6}$ at. % (M007MINSCGNM), $Ge_{16.5}As_{16}Ga_3Se_{64.5}$ at. % (ZQT007), Pr^{3+} doped $Ge_{16}As_{21}Ga_1Se_{62}$ at. % (M022MINSCGZQT) can be determined according to the extinction coefficient plots in Figure 5-1. For $Ge_{16}As_{24}Se_{15.5}Te_{44.5}$ at. %, the transparent window is from ~ 1.44 μm to ~ 29.46 μm. For $As_{40}Se_{60}$ at. % and $Ge_{10}As_{23.4}Se_{66.6}$ at. %, the transparent windows are from ~ 0.7 μm to ~ 30 μm. The transparent window for $Ge_{16.5}As_{16}Ga_3Se_{64.5}$ at. % is from ~ 0.65 μm to ~ 23.5 μm and for Pr^{3+} doped $Ge_{16}As_{21}Ga_1Se_{62}$ at. %, it is from ~ 0.65 μm to ~ 26 μm.

5.4 Fits to the ellipsometry data

As discussed in sections 5.1 and 5.2, the Cauchy and Sellmeier models are not only simple in concept but also material dispersion can be obtained from the second derivatives of Eqs. (5.7) and (5.8). Furthermore, the Cauchy and Sellmeier models are valid in the transparent window of a glass. In chapter 6, an appropriate refractive index model for chalcogenide glasses over the wavelength range from the lower wavelength edge of the transparent window to 2 μm and within the whole transparent window will be required to modify the Swanepoel method [5.4]. Therefore, in order to determine the proper refractive index for chalcogenide glasses within these two wavelength ranges, the Cauchy and Sellmeier models, in this

section, will be applied to interpolate the ellipsometry data (real part of the refractive index) over the wavelength range from the lower wavelength edge of the transparent window to 2.5 μm (obtained using the Woollam VUV VASE rotating analyser ellipsometer) and within the whole transparent window (obtained using the Woollam VUV VASE and IR-VASE instruments) by using the Matlab curve fitting tool (cftool in Matlab). A good refractive index model will be verified by yielding a good model fit to the experimental data (R^2 (coefficient of determination) is close to 1; *MSE* (mean of square error) is low).

5.4.1 Fits to the ellipsometry data (real part of the refractive index) over the wavelength range from the lower wavelength edge of the transparent window to 2.5 μm

The models used to fit the refractive index of the chalcogenide glasses within their transparent windows (defined in section 5.3) **over the wavelength range from the lower wavelength edge of the transparent window to 2.5 μm** were the two-term Cauchy, three-term Cauchy, one-term Sellmeier and two-term Sellmeier models.

Since the Cauchy model is a simple polynomial, least square fitting methods can produce stable model parameters. However, for the Sellmeier models, the initial parameters of C_1, $C_2 \ldots$ are required when using a linear least square fitting algorithm to avoid the model becoming unbounded at resonance frequencies [5.9]. Since the Sellmeier model becomes unbounded at resonance frequencies, the C_n parameters must be placed outside of the transparent window. In this wavelength range, the effect of the MIR fundamental vibrational absorption band of chalcogenide glasses is expected to be negligible. Therefore, a one-term Sellmeier fit (C_1 in optical bandgap electronic absorption region) with an additional constant term is expected to be sufficient for describing the refractive index dispersion within this region. According to [5.6], a two-term Sellmeier fit (C_1 in optical bandgap electronic absorption region and C_2 in MIR fundamental vibrational absorption region) with an additional constant term is sufficient to determine the refractive

index of chalcogenide glasses away from the absorption bands. Both the one-term Sellmeier and two-term Sellmeier models with a constant term were used here to fit the experimental data from Woollam.

The model fittings of two-term Cauchy, three-term Cauchy, one-term Sellmeier and two-term Sellmeier obtained for $Ge_{16}As_{24}Se_{15.5}Te_{44.5}$ at. % (M150MINSCGDJ), $As_{40}Se_{60}$ at. % (M005MINSCGNM), $Ge_{10}As_{23.4}Se_{66.6}$ at. % (M007MINSCGNM), $Ge_{16.5}As_{16}Ga_{3}Se_{64.5}$ at. % (ZQT007) and Pr^{3+} doped $Ge_{16}As_{21}Ga_{1}Se_{62}$ at. % (M022MINREZQT) over the wavelength range from the lower wavelength edge of the transparent window to 2.5 μm are plotted along with the refractive index measurements in Figures 5-2(a) and 5-2(b). In Figure 5-2, these four models can fit the refractive index of chalcogenide glasses within the transparent windows but fail to describe the refractive index behaviour near the optical gap at lower wavelengths.

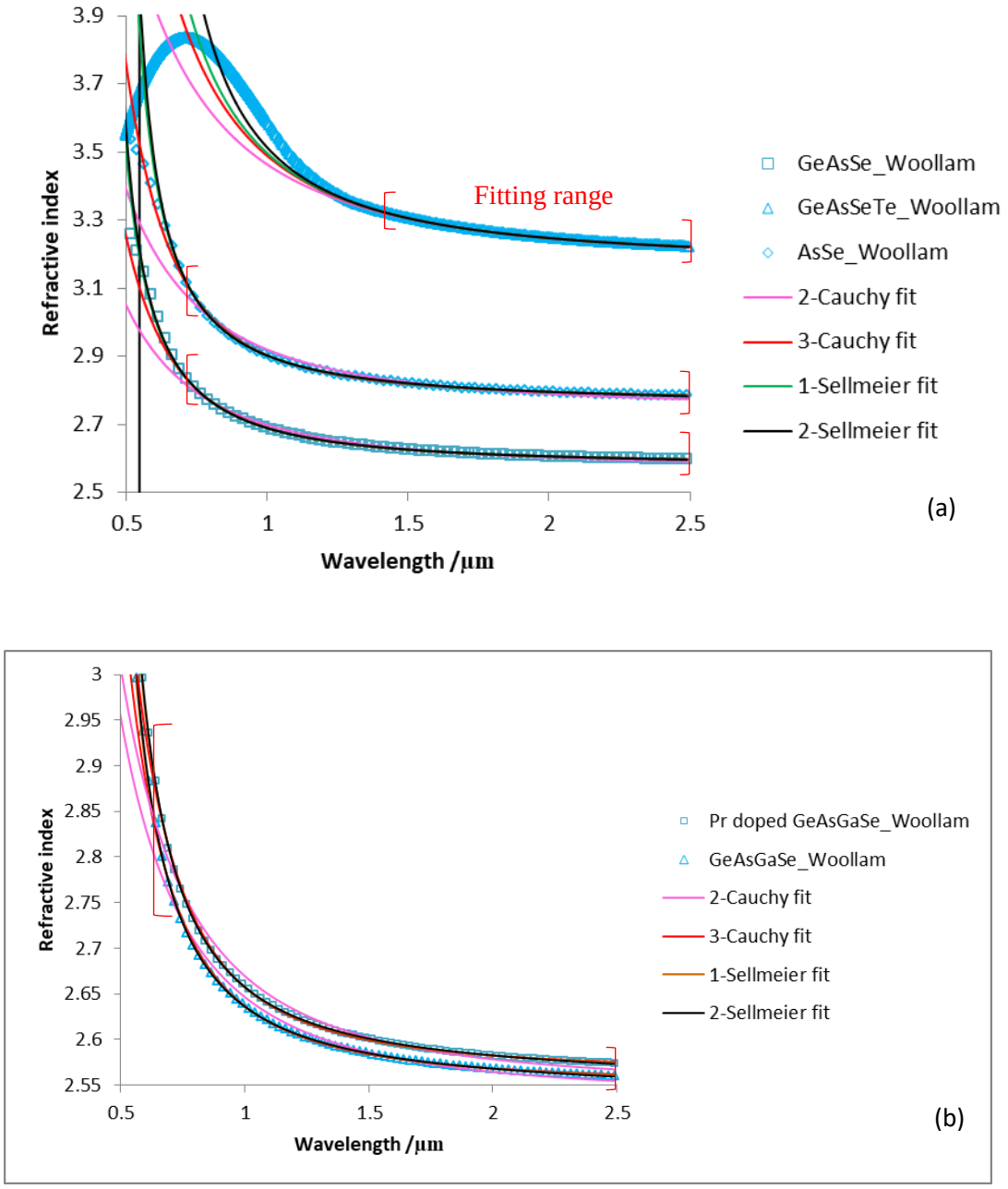


Figure 5- 2. Fitting the refractive index of (a) $Ge_{16}As_{24}Se_{15.5}Te_{44.5}$ at. % (M150MINSCGDJ), $As_{40}Se_{60}$ at. % (M005MINSCGNM), $Ge_{10}As_{23.4}Se_{66.6}$ at. % (M007MINSCGNM); (b) $Ge_{16.5}As_{16}Ga_3Se_{64.5}$ at. % (ZQT007) and Pr^{3+} doped $Ge_{16}As_{21}Ga_1Se_{62}$ at. % (M022MINSCGZQT) glasses with two-term Cauchy (pink), three-term Cauchy (red), one-term Sellmeier (green) and two-term Sellmeier (black) models over the wavelength range from the lower wavelength edge of the transparent window to 2.5 μm. The red brackets indicate the fitting range.

For the Cauchy models, fitting parameters were simply produced by using a least squares fitting method as shown in Table 5-1. The R^2 and *MSE* in Table 5-1 indicate that the three-term Cauchy model can fit the refractive index of the chalcogenide

glasses slightly better than the two-term Cauchy model. For the one-term Sellmeier model, the values of C_1 varies from 0.1 μm to 1.445 μm for the $Ge_{16}As_{24}Se_{15.5}Te_{44.5}$ at. % glass and from 0.1 μm to 0.7 μm for both the $As_{40}Se_{60}$ at. % and $Ge_{10}As_{23.4}Se_{66.6}$ at. % glasses. The fitting qualities of the one-term Sellmeier model were slightly better than those of the three-term Cauchy model as shown in Table 5-1. In order to test whether introducing a second Sellmeier term in the one-term Sellmeier model could achieve a lower fitting error, the two-term Sellmeier model was fitted with the extra term C_2. When C_2 was placed in the MIR fundamental vibrational absorption region, it was given an initial value of 30 μm and was allowed to vary from 30 μm to 100 μm. From Table 5-1, it is found that introducing a second Sellmeier term in the Sellmeier model could not significantly lower the fitting error below that obtained by the one-term Sellmeier model over the wavelength range from the lower wavelength edge of the transparent window to 2.5 μm. From Figure 5-2 and Table 5-1, it is found that the three-term Cauchy, one-term Sellmeier and two-term Sellmeier can provide good fits to the refractive index of the chalcogenide glasses over the wavelength range from the lower wavelength edge of the transparent window to 2.5 μm.

Table 5- 1. The fitting parameters and qualities yielded from the fits to the $Ge_{16}As_{24}Se_{15.5}Te_{44.5}$ at. % (M150MINSCGDJ), $As_{40}Se_{60}$ at. % (M005MINSCGNM), $Ge_{10}As_{23.4}Se_{66.6}$ at. % (M007MINSCGNM), $Ge_{16.5}As_{16}Ga_3Se_{64.5}$ at. % (ZQT007) and Pr^{3+} doped $Ge_{16}As_{21}Ga_1Se_{62}$ at. % (M022MINSCGZQT) glasses with different models over the wavelength range from the lower wavelength edge of the transparent window to 2.5 μm.

	Two-term Cauchy	Three-term Cauchy		One-term Sellmeier	Two-term Sellmeier
Ge-As-Se-Te (1445 nm to 2500 nm)					
A_1	10.06	9.998	A	1.507	5.007
A_2	1.936	1.711	B_1	8.588	5.142
A_3		0.3721	C_1	0.4460	0.7957
			B_2		22.12
			C_2		65.03
Fitting quality					
R^2	0.9997	1		1	1
MSE	1.632×10^{-7}	5.670×10^{-9}		2.034×10^{-9}	6.750×10^{-9}
As-Se (700 nm to 2500 nm)					
A_1	7.535	7.681	A	4.891	5.253
A_2	0.9886	0.4621	B_1	2.765	2.442
A_3		0.2860	C_1	0.4663	0.4807
			B_2		27.42
			C_2		60.51
Fitting quality					
R^2	0.9770	0.9985		0.9997	0.9999
MSE	1.559×10^{-4}	1.015×10^{-5}		1.955×10^{-6}	9.212×10^{-7}
Ge-As-Se (700 nm to 2500 nm)					
A_1	6.606	6.678	A	3.843	4.071
A_2	0.6736	0.4166	B_1	2.825	2.610
A_3		0.1391	C_1	0.4080	0.4177
			B_2		10.66
			C_2		65.34
Fitting quality					
R^2	0.9885	0.9997		0.9999	1
MSE	4.174×10^{-5}	1.210×10^{-6}		1.956×10^{-7}	8.285×10^{-8}

Table 5- 1. The fitting parameters and qualities yielded from the fits to the $Ge_{16}As_{24}Se_{15.5}Te_{44.5}$ at. % (M150MINSCGDJ), $As_{40}Se_{60}$ at. % (M005MINSCGNM), $Ge_{10}As_{23.4}Se_{66.6}$ at. % (M007MINSCGNM), $Ge_{16.5}As_{16}Ga_3Se_{64.5}$ at. % (ZQT007) and Pr^{3+} doped $Ge_{16}As_{21}Ga_1Se_{62}$ at. % (M022MINSCGZQT) glasses with different models over the wavelength range from the lower wavelength edge of the transparent window to 2.5 μm. (continued)

	Two-term Cauchy	Three-term Cauchy		One-term Sellmeier	Two-term Sellmeier
Ge-As-Ga-Se (640 nm to 2500 nm)					
A_1	6.434	6.507	A	4.131	4.456
A_2	0.5693	0.3277	B_1	2.365	2.064
A_3		0.1153	C_1	0.4009	0.4163
			B_2		18.26
			C_2		62.31
Fitting quality					
R^2	0.9842	0.9990		0.9997	0.9999
MSE	5.619×10^{-5}	3.461×10^{-6}		9.773×10^{-7}	4.564×10^{-7}
Pr^{3+} doped Ge-As-Ga-Se (640 nm to 2500 nm)					
A_1	6.488	6.573	A	4.080	4.376
A_2	0.6374	0.3507	B_1	2.480	2.209
A_3		0.1370	C_1	0.4098	0.4228
			B_2		19.5
			C_2		64.62
Fitting quality					
R^2	0.9823	0.9990		0.9997	0.9999
MSE	7.759×10^{-5}	4.560×10^{-6}		1.116×10^{-6}	6.021×10^{-7}

The percentage errors in fitting the refractive index of the $Ge_{16}As_{24}Se_{15.5}Te_{44.5}$ at. % (M150MINSCGDJ) and $As_{40}Se_{60}$ at. % (M005MINSCGNM) glasses over the wavelength range from the lower wavelength edge of the transparent window to 2.5 μm with two-term Cauchy, three-term Cauchy, one-term Sellmeier and two-term Sellmeier models are plotted in Figures 5-3(a) and 5-3(b). The percentage errors in fitting the refractive index of the $Ge_{10}As_{23.4}Se_{66.6}$ at. % (M007MINSCGNM), $Ge_{16.5}As_{16}Ga_3Se_{64.5}$ at. % (ZQT007) and Pr^{3+} doped $Ge_{16}As_{21}Ga_1Se_{62}$ at. % (M022MINREZQT) glasses are similar to those seen for $As_{40}Se_{60}$ at. %, and are shown in Figure B1 in appendix B. The fitting errors of two-term Cauchy model are

within 0.05 % for $Ge_{16}As_{24}Se_{15.5}Te_{44.5}$ at. % and larger than 0.3 % for $As_{40}Se_{60}$ at. %, which is the worst among these four models in the wavelength range from the lower wavelength edge of the transparent window to 2.5 μm, as shown in Figure 5-3. The three-term Cauchy model improved the fitting with the error less than 0.02 % for $Ge_{16}As_{24}Se_{15.5}Te_{44.5}$ at. % and less than 0.1 % for $As_{40}Se_{60}$ at. % in this wavelength range. The Sellmeier models (one-term Sellmeier and two-term Sellmeier models) could achieve lower modelling errors than the Cauchy models with the error less than 0.008 % for $Ge_{16}As_{24}Se_{15.5}Te_{44.5}$ at. % and less than 0.05 % for $As_{40}Se_{60}$ at. % as shown in Figure 5-3.

In summary, the two-term Cauchy model proved to be the worst refractive index model for chalcogenide glasses over the wavelength range from the lower wavelength edge of the transparent window to 2.5 μm when compared to the other models. The three-term Cauchy model significantly improved the fitting performance, which makes it suitable to describe the refractive index dispersion of chalcogenide glasses in this wavelength range. Moreover, the best fits were achieved by the one-term Sellmeier and two-term Sellmeier models, which were also thus considered as suitable refractive index models for chalcogenide glasses over the wavelength range from the lower wavelength edge of the transparent window to 2.5 μm.

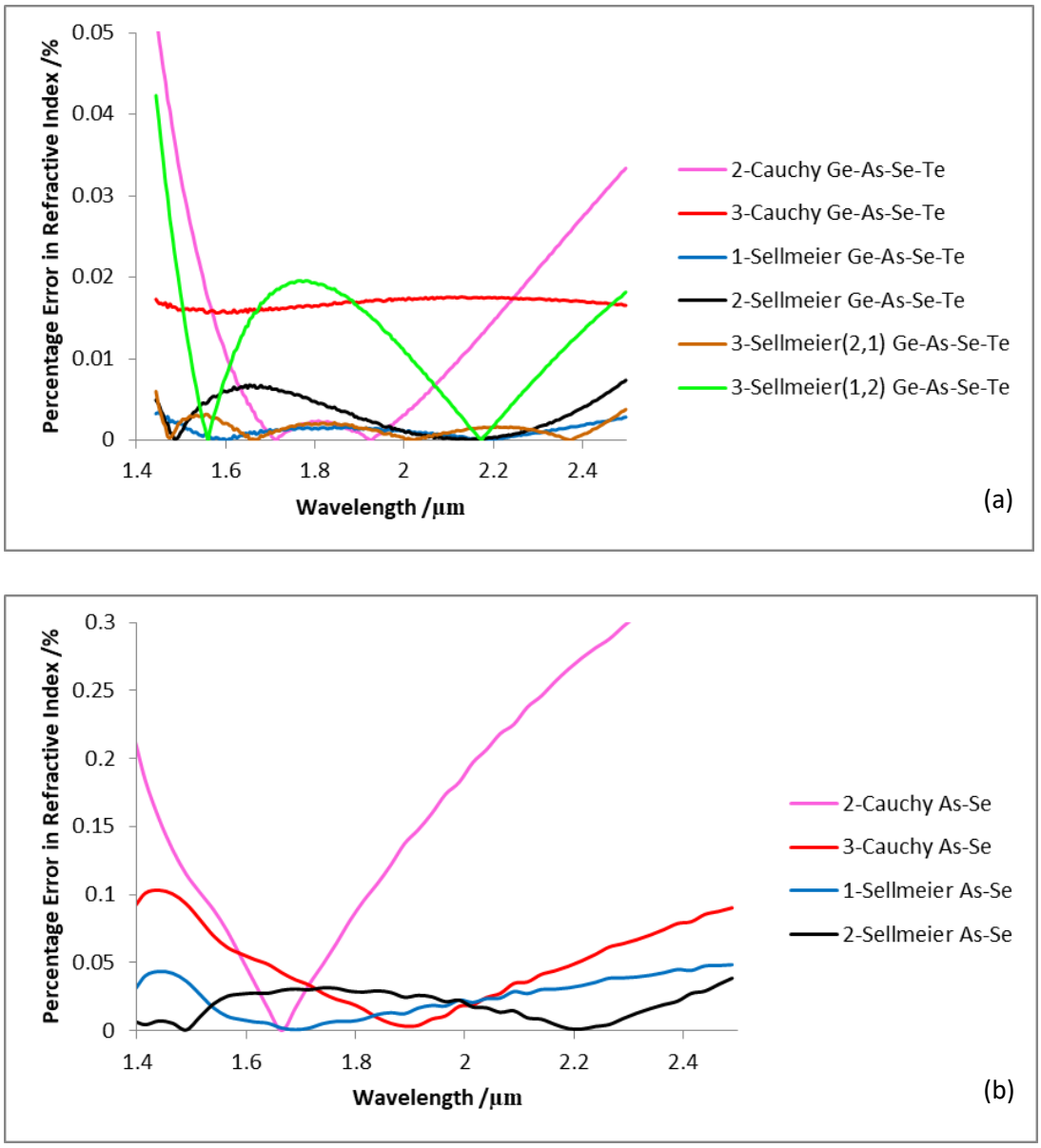


Figure 5- 3. The error in fitting the refractive index of the (a) $Ge_{16}As_{24}Se_{15.5}Te_{44.5}$ at. % (M150MINSCGDJ) and (b) $As_{40}Se_{60}$ at. % (M005MINSCGNM) glasses with two-term Cauchy (pink), three-term Cauchy (red), one-term Sellmeier (blue) and two-term Sellmeier (black) models over the wavelength range from the lower wavelength edge of the transparent window to 2.5 µm.

5.4.2 Fits to the ellipsometry data (real part of the refractive index) over the whole transparent window

In order to find a proper model to describe the refractive index dispersion of chalcogenide glasses ($Ge_{16}As_{24}Se_{15.5}Te_{44.5}$ at. % (M150MINSCGDJ), $As_{40}Se_{60}$ at. % (M005MINSCGNM), $Ge_{10}As_{23.4}Se_{66.6}$ at. % (M007MINSCGNM),

$Ge_{16.5}As_{16}Ga_3Se_{64.5}$ at. % (ZQT007) and Pr^{3+} doped $Ge_{16}As_{21}Ga_1Se_{62}$ at. % (M022MINREZQT)) **over their respective transparent windows**, the two-term Cauchy, three-term Cauchy, one-term Sellmeier, two-term Sellmeier and three-term Sellmeier models were applied to fit the refractive index data of the chalcogenide glasses in their transparent windows (defined in Section 5.3) by using the Matlab curve fitting tool (cftool in Matlab).

Since the Cauchy model is a simple polynomial, least square fitting methods can produce stable model parameters. For the one-term Sellmeier model, the optical gap resonant wavelength C_1 was placed outside of the transparent window to avoid the model becoming unbounded at resonance frequencies. The initial values of C_1 varied from 0.1 μm to the start points of the transparent windows (1.445 μm for $Ge_{16}As_{24}Se_{15.5}Te_{44.5}$ at. %, 0.7 μm for $As_{40}Se_{60}$ at. % and $Ge_{10}As_{23.4}Se_{66.6}$ at. % and 0.64 μm for $Ge_{16.5}As_{16}Ga_3Se_{64.5}$ at. % and Pr^{3+} doped $Ge_{16}As_{21}Ga_1Se_{62}$ at. %). For the two-term Sellmeier model (C_1 in optical bandgap electronic absorption region and C_2 in MIR fundamental vibrational absorption region) with a constant term, due to the discontinuity of the Sellmeier model at C_1 and C_2, these fitting parameters were allowed to vary below the start points of the transparent windows (1.445 μm for $Ge_{16}As_{24}Se_{15.5}Te_{44.5}$ at. %, 0.7 μm for $As_{40}Se_{60}$ at. % and $Ge_{10}As_{23.4}Se_{66.6}$ at. % and 0.64 μm for $Ge_{16.5}As_{16}Ga_3Se_{64.5}$ at. % and Pr^{3+} doped $Ge_{16}As_{21}Ga_1Se_{62}$ at. %) and above the end points of the transparent windows (29.46 μm for $Ge_{16}As_{24}Se_{15.5}Te_{44.5}$ at. %, 30 μm for $As_{40}Se_{60}$ at. % and $Ge_{10}As_{23.4}Se_{66.6}$ at. %, 23.44 μm for $Ge_{16.5}As_{16}Ga_3Se_{64.5}$ at. % and 26 μm for Pr^{3+} doped $Ge_{16}As_{21}Ga_1Se_{62}$ at. %) respectively.

In order to test whether a lower modelling error can be reduced by introducing a third Sellmeier term, the two three-term Sellmeier models were fitted with the extra term: B_3, and C_3, near the optical bandgap electronic absorption (named: three-term Sellmeier (2,1)) and the MIR fundamental vibrational absorption (named: three-term

Sellmeier (1,2)), respectively. When C_3 was placed near the optical bandgap electronic absorption region, the initial value of C_3 varied from 0.1 μm to the start points of the transparent windows (1.445 μm for $Ge_{16}As_{24}Se_{15.5}Te_{44.5}$ at. %, 0.7 μm for $As_{40}Se_{60}$ at. % and $Ge_{10}As_{23.4}Se_{66.6}$ at. % and 0.64 μm for $Ge_{16.5}As_{16}Ga_3Se_{64.5}$ at. % and Pr^{3+} doped $Ge_{16}As_{21}Ga_1Se_{62}$ at. %). When C_3 was placed near the MIR fundamental vibrational absorption region, the initial value of C_3 varied above the end points of the transparent windows (29.46 μm for $Ge_{16}As_{24}Se_{15.5}Te_{44.5}$ at. %, 30 μm for $As_{40}Se_{60}$ at. % and $Ge_{10}As_{23.4}Se_{66.6}$ at. %, 23.44 μm for $Ge_{16.5}As_{16}Ga_3Se_{64.5}$ at. % and 26 μm for Pr^{3+} doped $Ge_{16}As_{21}Ga_1Se_{62}$ at. %).

The fits of the two-term Cauchy, three-term Cauchy, one-term Sellmeier, two-term Sellmeier, three-term Sellmeier (2,1) and three-term Sellmeier (1,2) models to the refractive index data of the $Ge_{16}As_{24}Se_{15.5}Te_{44.5}$ at. % and $As_{40}Se_{60}$ at. % glasses are plotted in Figures 5-4(a) and 5-4(b). The fits to $Ge_{10}As_{23.4}Se_{66.6}$ at. %, $Ge_{16.5}As_{16}Ga_3Se_{64.5}$ at. % and Pr^{3+} doped $Ge_{16}As_{21}Ga_1Se_{62}$ at. % are similar to those for $Ge_{16}As_{24}Se_{15.5}Te_{44.5}$ at. % and $As_{40}Se_{60}$ at. %, and are displayed in Figure B2 in appendix B. The parameters and qualities yielded from the fits are shown in Table 5-2. The percentage errors in fitting the refractive indices of the $Ge_{16}As_{24}Se_{15.5}Te_{44.5}$ at. % and $As_{40}Se_{60}$ at. % glasses over their respective transparent windows with these models are shown in Figures 5-5(a) and 5-5(b) while those for $Ge_{10}As_{23.4}Se_{66.6}$ at. %, $Ge_{16.5}As_{16}Ga_3Se_{64.5}$ at. % and Pr^{3+} doped $Ge_{16}As_{21}Ga_1Se_{62}$ at. % are shown in Figure B3 in appendix B. Figures 5-4 and 5-5 reveal that the two-term Cauchy, three-term Cauchy and one-term Sellmeier models cannot closely describe the refractive index dispersion of $Ge_{16}As_{24}Se_{15.5}Te_{44.5}$ at. % and $As_{40}Se_{60}$ at. % over their transparent windows; the error is larger than 1 % for $Ge_{16}As_{24}Se_{15.5}Te_{44.5}$ at. % and larger than 2 % for $As_{40}Se_{60}$ at. %. These results confirm that the Cauchy model cannot be used if the band gap falls within the range of interest. Because the one-term Sellmeier model only has one resonance term, this model cannot be applied to model materials such as chalcogenide glasses with band gaps influencing the wavelength range of interest.

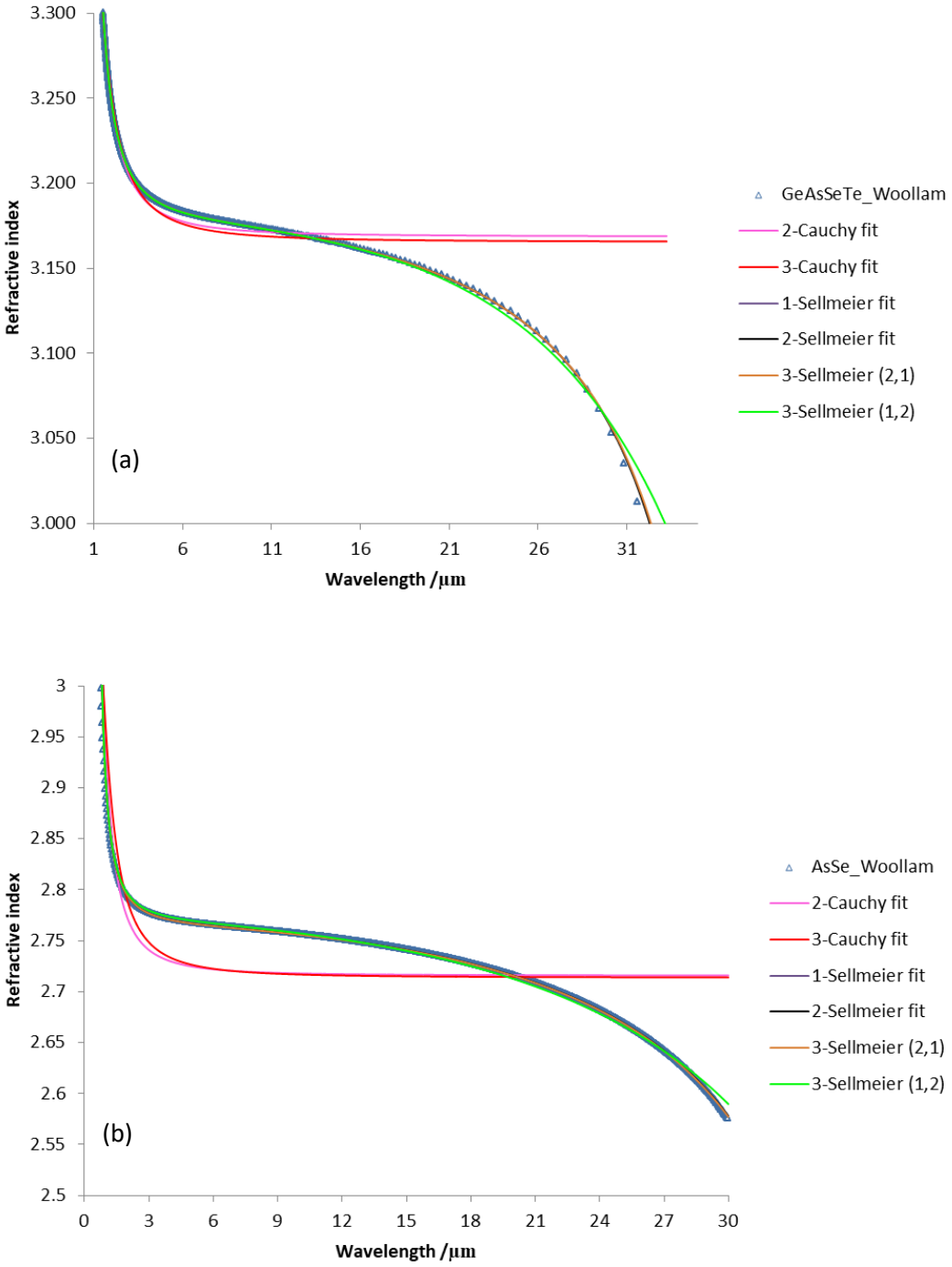


Figure 5- 4. The fits of the two-term Cauchy, three-term Cauchy, one-term Sellmeier, two-term Sellmeier, three-term Sellmeier (2,1) and three-term Sellmeier (1,2) models to the refractive index data of the (a) $Ge_{16}As_{24}Se_{15.5}Te_{44.5}$ at. % (M150MINSCGDJ) and (b) $As_{40}Se_{60}$ at. % (M005MINSCGNM) glasses over their respective transparent window.

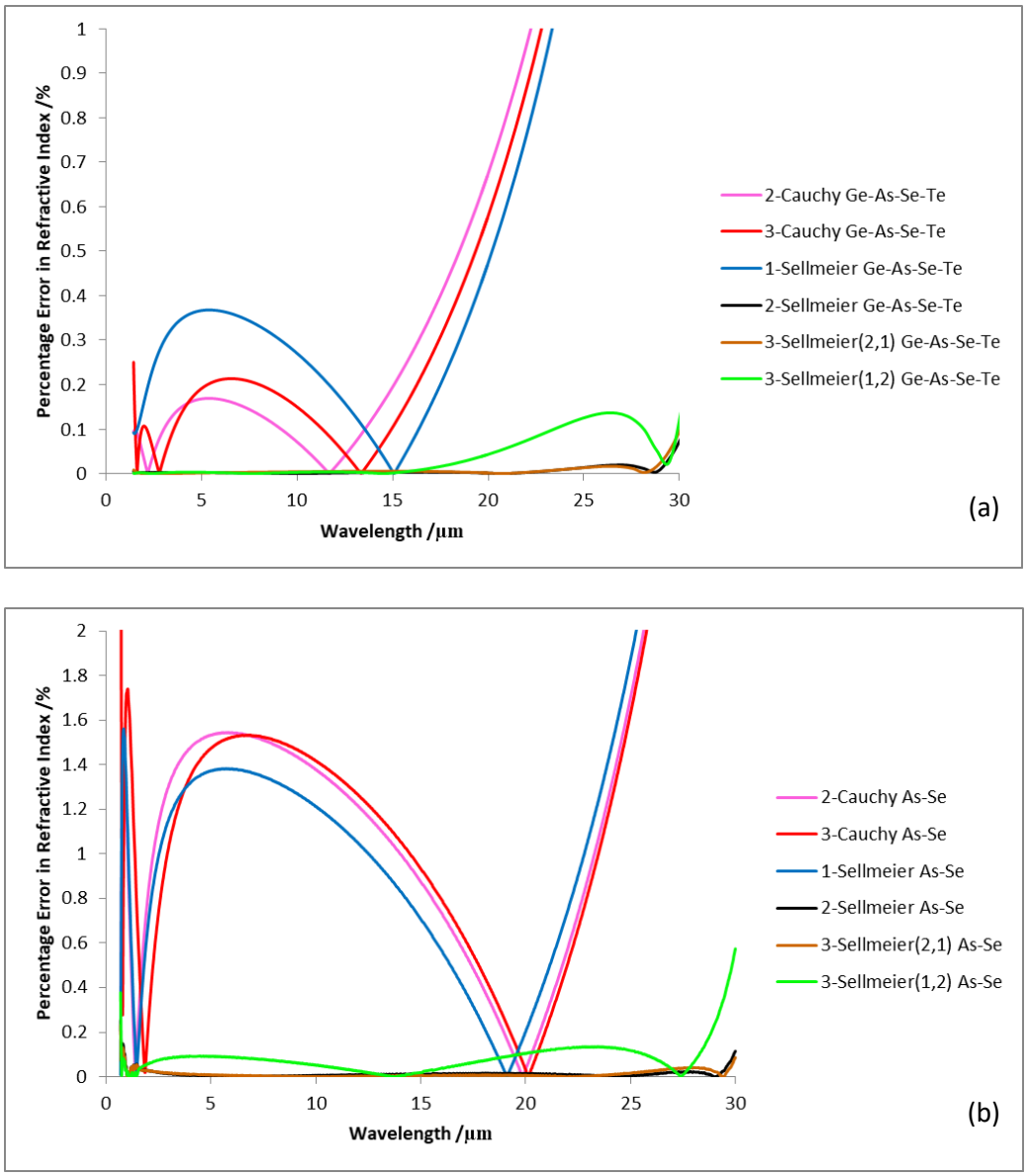


Figure 5- 5. The percentage errors in fitting the refractive index of the (a) $Ge_{16}As_{24}Se_{15.5}Te_{44.5}$ at. % (M150MINSCGDJ) and (b) $As_{40}Se_{60}$ at. % (M005MINSCGNM) glasses over their respective transparent window with the two-term Cauchy, three-term Cauchy, one-term Sellmeier, two-term Sellmeier, three-term Sellmeier (2,1) and three-term Sellmeier (1,2) models.

Unlike the two-term Cauchy, three-term Cauchy and one-term Sellmeier models, the two-term Sellmeier model has one Sellmeier term in the optical bandgap electronic absorption region and one in the MIR fundamental vibrational absorption region. Therefore, it is suitable to describe the refractive index dispersion of chalcogenide glasses over their transparent windows as shown in Figure 5-4. The error plots presented in Figure 5-5 show that for both $Ge_{16}As_{24}Se_{15.5}Te_{44.5}$ at. % and

$As_{40}Se_{60}$ at. %, the two-term Sellmeier model can fit the experimental refractive index data well, with the error less than 0.1 %. From Figure 5-5, it is also found that the fitting errors aren't significantly improved by using the three-term Sellmeier (2,1) model. Moreover, the fitting error of the three-term Sellmeier (1,2) model increased from less than 0.1 % to less than 0.2 % over the wavelegnth range from 1.5 μm to 30 μm for $Ge_{16}As_{24}Se_{15.5}Te_{44.5}$ at. % and $As_{40}Se_{60}$ at. % compared to the two-term Sellmeier model. Therefore, the lowest modelling errors were produced by the two-term Sellmeier and three-term Sellmeier (2,1) models with the error less than 0.1 % over the wavelength range from 1.5 μm to 30 μm. Introducing a third Sellmeier term to the two-term Sellmeier model cannot significantly improve the fitting performance, which is in good agreement with the findings of [5.9].

The parameters and qualities yielded from the fits are shown in Table 5-2. Table 5-2 also show that the Cauchy models (two-term Cauchy and three-term Cauchy models) cannot correctly describe the refractive index dispersion of the chalcogenide glasses within their respective transparent windows with R^2 less than 0.9364 for $Ge_{16}As_{24}Se_{15.5}Te_{44.5}$ at. % and less than 0.4386 for the other four compositions. The higher R^2 for $Ge_{16}As_{24}Se_{15.5}Te_{44.5}$ at. % found is attributed to the fact that more data points were collected at shorter wavelengths. From Figure 5-4(a), it is easily found that the Cauchy models failed to fit the refractive index data especially at the longer wavelengths. As discussed above, the one-term Sellmeier model also failed to closely fit the refractive index data with R^2 less than 0.9317 for $Ge_{16}As_{24}Se_{15.5}Te_{44.5}$ at. % and less than 0.4262 for the other four compositions. However, the two-term Sellmeier model (C_1 inoptical bandgap electronic absorption region and C_2 in MIR fundamental vibrational absorption region) with a constant term provided good fits to the refractive index data with the R^2 better than 0.9999 for all these five chalcogenide glass compositions as shown in Table 5-2. It is found that, compared to the two-term Sellmeier model, the three-term Sellmeier (2,1) model cannot significantly improve the fitting performance. However, compared to the two-term

Sellmeier model and the three-term Sellmeier model (2,1), the three-term Sellmeier (1,2) model made the fitting performance worse although R^2 remains better than 0.9977.

In summary, the two-term Sellmeier model can successfully describe the refractive index dispersion of the chalcogenide glasses over their respective transparent windows with the best fitting quality (R^2 better than 0.9999) and lowest fitting errors (less than 0.1 %). Introducing an extra Sellmeier term does not significantly improve the fitting performance. Therefore, the two-term Sellmeier model was considered to be an effective model for the refractive index dispersion of chalcogenide glasses in the MIR region. The two-term Sellmeier fits to the refractive index data here will be used to calculate the numerical aperture and material dispersion in the following sections. Moreover, in chapter 6, the two-term Sellmeier model will be applied to improve the original Swanepoel method [5.4] in order to extend this method into the MIR region.

Table 5- 2. The fitting parameters and qualities yielded from the fits to the $Ge_{16}As_{24}Se_{15.5}Te_{44.5}$ at. % (M150MINSCGDJ), $As_{40}Se_{60}$ at. % (M005MINSCGNM), $Ge_{10}As_{23.4}Se_{66.6}$ at. % (M007MINSCGNM), $Ge_{16.5}As_{16}Ga_3Se_{64.5}$ at. % (ZQT007) and Pr^{3+} doped $Ge_{16}As_{21}Ga_1Se_{62}$ at. % (M022MINSCGZQT) glasses with different models over their respective transparent windows.

	Two-term Cauchy	Three-term Cauchy		One-term Sellmeier	Two-term Sellmeier	Three-term Sellmeier (2,1)	Three-term Sellmeier (1,2)
Ge-As-Se-Te (1.445 μm to 29.46 μm)							
A_1	10.04	10.02	A	-595	0.813	1.515	0.2898
A_2	2.045	2.472	B_1	605	9.282	8.763	9.804
A_3		-1.132	C_1	-0.05806	0.4304	0.4481	0.4201
			B_2		0.5471	0.5586	389.1
			C_2		39.52	39.74	64.43
			B_3			-0.1817	-392.6
			C_3			0.5239	64.83
Fitting quality							
R^2	0.9316	0.9364		0.9317	1	1	0.9999
MSE	1.037×10^{-4}	9.663×10^{-5}		1.038×10^{-4}	6.157×10^{-9}	1.102×10^{-8}	9.470×10^{-8}
As-Se (0.7 μm to 30 μm)							
A_1	7.375	7.364	A	-114.5	4.635	3.356	4.756
A_2	1.238	1.752	B_1	121.9	3.010	2.369	2.907
A_3		-0.3926	C_1	0.1	0.4551	0.4720	0.4572
			B_2		0.8702	0.8681	1.007
			C_2		41.01	40.96	46.84
			B_3			1.919	0.3702
			C_3			0.2299	46.82
Fitting quality							
R^2	0.4254	0.4386		0.4245	0.9999	0.9999	0.9977
MSE	2.147×10^{-3}	2.095×10^{-3}		2.148×10^{-3}	3.388×10^{-7}	2.908×10^{-7}	8.720×10^{-6}

Table 5-2. The fitting parameters and qualities yielded from the fits to the $Ge_{16}As_{24}Se_{15.5}Te_{44.5}$ at. % (M150MINSCGDJ), $As_{40}Se_{60}$ at. % (M005MINSCGNM), $Ge_{10}As_{23.4}Se_{66.6}$ at. % (M007MINSCGNM), $Ge_{16.5}As_{16}Ga_3Se_{64.5}$ at. % (ZQT007) and Pr^{3+} doped $Ge_{16}As_{21}Ga_1Se_{62}$ at. % (M022MINSCGZQT) glasses with different models over their respective transparent windows. (continued)

	Two-term Cauchy	Three-term Cauchy		One-term Sellmeier	Two-term Sellmeier	Three-term Sellmeier (2,1)	Three-term Sellmeier (1,2)
Ge-As-Se (0.7 μm to 29.76 μm)							
A_1	6.389	6.374	A	-90.73	3.545	3.498	2.651
A_2	0.9874	1.682	B_1	97.12	3.118	2.061	3.998
A_3		-0.5274	C_1	0.1	0.3944	0.4116	0.3607
			B_2		0.6178	0.6183	187.5
			C_2		36.68	36.68	58.46
			B_3			1.104	-193.2
			C_3			0.3486	59.5
Fitting quality							
R^2	0.2709	0.2952		0.2699	0.9999	0.9999	0.9983
MSE	3.147×10^{-3}	3.042×10^{-3}		3.152×10^{-3}	3.805×10^{-7}	3.790×10^{-7}	7.383×10^{-6}
Ge-As-Ga-Se (0.64 μm to 23.44 μm)							
A_1	6.202	6.185	A	-2265	4.010	4.035	3.994
A_2	0.8481	1.440	B_1	2271	2.485	2.034	2.501
A_3		-0.3835	C_1	0.01932	0.3944	0.3988	0.3936
			B_2		2.360	2.437	95.24
			C_2		44.97	45.53	60.93
			B_3			0.4274	-95.69
			C_3			0.3792	62.49
Fitting quality							
R^2	0.3847	0.4183		0.3846	1	0.9999	0.9999
MSE	2.262×10^{-3}	2.139×10^{-3}		2.263×10^{-3}	1.757×10^{-7}	1.876×10^{-7}	2.302×10^{-7}

Table 5-2. The fitting parameters and qualities yielded from the fits to the $Ge_{16}As_{24}Se_{15.5}Te_{44.5}$ at. % (M150MINSCGDJ), $As_{40}Se_{60}$ at. % (M005MINSCGNM), $Ge_{10}As_{23.4}Se_{66.6}$ at. % (M007MINSCGNM), $Ge_{16.5}As_{16}Ga_3Se_{64.5}$ at. % (ZQT007) and Pr^{3+} doped $Ge_{16}As_{21}Ga_1Se_{62}$ at. % (M022MINSCGZQT) glasses with different models over their respective transparent windows. (continued)

	Two-term Cauchy	Three-term Cauchy		One-term Sellmeier	Two-term Sellmeier	Three-term Sellmeier (2,1)	Three-term Sellmeier (1,2)
Pr doped Ge-As-Ga-Se (0.64 μm to 26 μm)							
A_1	6.333	6.323	A	-75.18	3.909	4.186	3.756
A_2	0.831	1.228	B_1	81.51	2.647	3.141	2.795
A_3		-0.2586	C_1	0.1001	0.4016	0.3931	0.3948
			B_2		0.7718	0.774	65.22
			C_2		36.37	36.4	58.12
			B_3			-0.771	-70.09
			C_3			0.2808	61.04
Fitting quality							
R^2	0.4224	0.4449		0.4262	0.9999	0.9999	0.9997
MSE	1.630×10^{-3}	1.580×10^{-3}		1.633×10^{-3}	1.782×10^{-7}	1.893×10^{-7}	9.563×10^{-7}

5.5 Physical interpretation of parameters of the two-term Sellmeier model

As discussed in section 5.4.2, the two-term Sellmeier model (C_1 in optical bandgap electronic absorption region and C_2 in MIR fundamental vibrational absorption region) was considered to be an effective model for the refractive index dispersion of chalcogenide glasses in the MIR region. When using a two-term Sellmeier model to fit the refractive index data, several different sets of Sellmeier coefficients can be obtained depending on the choice of resonant wavelengths C_1 and C_2. According to Dantanarayana *et al.* [5.14], a unique two-term Sellmeier model, with physical interpretations on C_1 and C_2, would be an advantage in giving insight not only into the dispersion characteristic but also into the electronic and vibrational characteristic of the material. The knowledge of the optical bandgaps and the fundamental vibrational absorption bands of the chalcogenide glasses studied in this thesis has been reviewed in sections 2.3.3.1 and 2.3.2, respectively. In this sub-section, the

physical significance of C_1 and C_2 in the two-term Sellmeier model will be discussed.

According to [5.9], C_2 in a two-term Sellmeier model is associated with vibrational band resonance absorption. Therefore, the refractive index dispersion might be predicted from the knowledge of the fundamental resonant absorptions of a chalcogenide glass. For the $As_{40}Se_{60}$ at. % glass, the position of the fundamental vibrational band calculated from its second overtone band occurs at 41.7 μm [5.11]; this band is attributed to stretching of $AsSe_3$ pyramid units in the $As_{40}Se_{60}$ at. % glass structural matrix [5.11]. Figure 5-6 show a plot of absorbances as a function of wavelengths for the $As_{40}Se_{60}$ at. % glass manufactured in our laboratory (Melting code: M179CMDF). The position of the second overtone of the fundamental vibrational absorption band is observed to occur at 20.58 μm. The fundamental vibrational band was thus calculated to occur at 2×20.58 μm = 41.16 μm. From Table 5-2, the C_2 value generated from the best two-term Sellmeier fit is 41.01 μm, which fits well with the calculated fundamental vibrational band occurring at 41.16 μm. This suggested, for the $As_{40}Se_{60}$ at. % glass, the C_2 value from the two-term Sellmeier model is associated with the vibrational band resonance absorption.

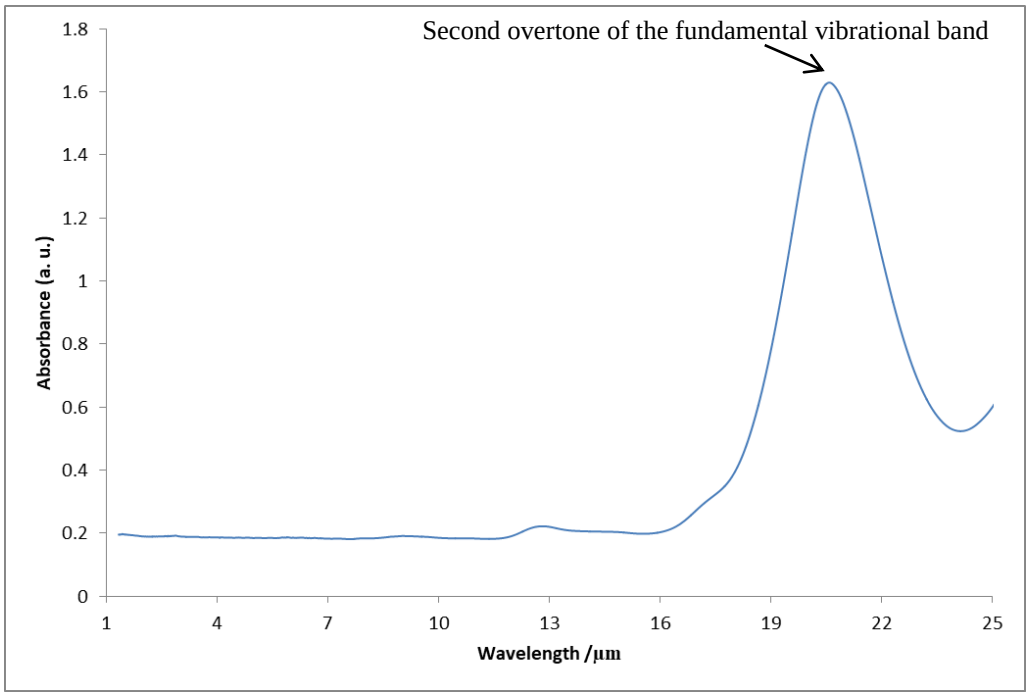


Figure 5- 6. The FTIR transmission spectrum of the $As_{40}Se_{60}$ at. % glass (M179CMDF) at a temperature of 20 ℃, showing the position of the second overtone of the fundamental vibrational absorption band.

C_1 in a two-term Sellmeier model is associated with the optical bandgap absorption. For the $As_{40}Se_{60}$ at. % glass, a less good fit to known resonant absorption is found for the C_1 value from the two-term Sellmeier model than the C_2 value from the two-term Sellmeier model was also found in [5.9]. Zakery and Elliott reported the optical bandgap as corresponding to wavelengths of 701 nm for the $As_{40}Se_{60}$ at. % [5.10], which is different from the C_1 value for the $As_{40}Se_{60}$ at. % glass here of 455 nm. From Figure 5-1, the extinction coefficient of the $As_{40}Se_{60}$ at. % glass obtained from spectroscopic ellipsometry at a wavelength of 701 nm is less than 0.0005, which is low enough to lie within the as-defined transparent window (see section 5.3). Since the two-term Sellmeier fitting requires the resonant wavelength be placed outside the transparent window, it suggests that the two-term Sellmeier model for this chalcogenide glass being wholly predictable from known absorption coefficient.

Since the C_2 value of the $As_{40}Se_{60}$ at. % glass was well associated to the position of the fundamental absorption band, the Sellmeier parameters shown in Table 5-2 for

$As_{40}Se_{60}$ at. % are considered a unique and complete dispersion relationship in the transparent window. The advantages of having a unique set of coefficients is that the dispersion and glass structure or even molecular structure can be correlated from a literature of glass chemical composition/molecular structure and unique two-term Sellmeier coefficients. With refinement, this might enable one to reverse engineer glasses to design a suitable glass composition for a particular application requiring certain dispersion characteristics. For the other compositions investigated in this chapter, since the knowledge of the fundamental vibrational band is currently not available, a unique set of the two-term Sellmeier coefficients cannot be determined.

5.6 Step-index fibre and numerical aperture

Step-index fibre (SIF) based on the $As_{40}Se_{60}$ at. % (M005MINSCGNM) core and $Ge_{10}As_{23.4}Se_{66.6}$ at. % (M007MINSCGNM) cladding glasses has been successfully fabricated for mid-infrared supercontinuum generation [5.12]. This fibre generated a MIR supercontinuum spanning 1.4 μm to 13.3 μm [5.12]. An ultra-high-numerical aperture (NA) SIF fibre based on the $Ge_{16}As_{24}Se_{15.5}Te_{44.5}$ at. % (M150MINSCGDJ) core and $Ge_{10}As_{23.4}Se_{66.6}$ at. % (M007MINSCGNM) cladding has also been fabricated for MIR supercontinuum generation [5.13].

The NA of a SIF composed of a designed glass pair is determined from:

$$\mathrm{NA} = \sqrt{{n_1}^2 - {n_2}^2} \qquad (5.9)$$

where n_1 is the real part of the refractive index for the core glass and n_2 is the real part of the refractive index for the cladding glass. The two-term Sellmeier fits in Table 5-2 were used to calculate the NA of the two core-cladding fibres fabricated. As shown in Figure 5-7, the NA of the $Ge_{16}As_{24}Se_{15.5}Te_{44.5}$ at. % / $Ge_{10}As_{23.4}Se_{66.6}$ at. % glass pair is larger than 1.86 over the wavelength range from 0.5 to 30 μm. For the $As_{40}Se_{60}$ at. % / $Ge_{10}As_{23.4}Se_{66.6}$ at. % glass pair, the SIF has a calculated NA

larger than 0.97 over the wavelength range from 0.5 to 30 μm. The ultra-high NA can strongly guide light (MIR radiation) in the core and allow theoretically a MIR supercontiuum to be unhindered across the wavelength range, which makes the glass pair a good candidate for SIF MIR supercontinuum generation [5.9].

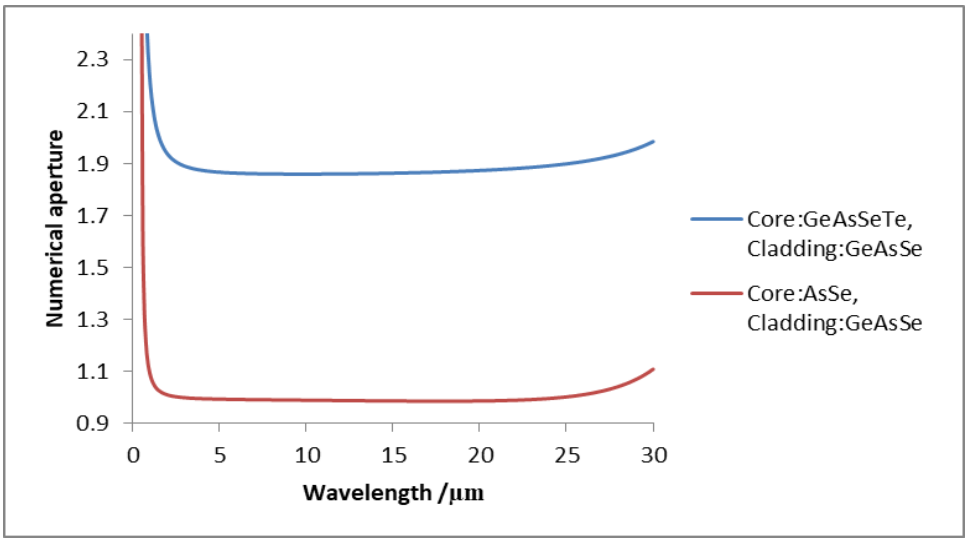


Figure 5- 7. NA variation with wavelength for two high-NA optical fibres of: the $As_{40}Se_{60}$ at. % (M005MINSCGNM) / $Ge_{10}As_{23.4}Se_{66.6}$ at. % (M007MINSCGNM) glass pair (red) and the $Ge_{16}As_{24}Se_{15.5}Te_{44.5}$ at. % (M150MINSCGDJ) / $Ge_{10}As_{23.4}Se_{66.6}$ at. % (M007MINSCGNM) glass pair (blue).

5.7 Material dispersion

Supercontinuum generation (SCG) happens through the interaction of many nonlinear processes to cause extensive spectral broadening, such as self-phase modulation, four-wave mixing and soliton based dynamics [5.14]. Two main regimes for SCG are the soliton fission regime [5.14] and modulation instability regime [5.15, 5.16]. These two regimes have similar physical processes and the pumps are both in the anomalous dispersion regime (where the material dispersion is greater than zero), close to the material zero-dispersion wavelength (ZDW). In the soliton regime, pumping with a high power, femtosecond pulse in the anomalous dispersion regime, close to the material ZDW, allows the solitons to be generated by soliton fission [5.14]. In the modulation instability regime, the solitons will be

generated when the breakup of continuous wave (CW) or quasi-continuous wave fields due to modulation instability [5.15]. It is also possible to create SCG by pumping into the normal dispersion regime [5.12]. When pumping with short pulses in the normal regime, pulse broadening will occurs due to self-phase modulation. When the pulses are not short enough, the pulse broadening will be created by stimulated-Raman scattering. However, as pumping in the normal dispersion regime is less efficient for SCG, the majority of modern sources avoid pumping in the normal dispersion regime [5.17]. Therefore, for achieving MIR SCG based on chalcogenide fibres, it is important to know the material dispersion across the MIR region and the material ZDW for all glasses used.

The two-term Sellmeier fits to the refractive indices of the chalcogenide glasses as shown in Table 5-2 across their transparent window (where κ, defined in section 5.3, is assumed to be zero) allow the calculation of the material dispersion. The material dispersion D was calculated from the standard formula [5.18]:

$$D = -\frac{\lambda}{c}\left(\frac{d^2n}{d\lambda^2}\right) \qquad (5.10)$$

where n is the refractive index at wavelength λ and c is the light velocity in vacuum. The material dispersion obtained from Eq. (5.10), using the second derivative of the refractive index given by the two-term Sellmeier equations with the parameters given in Table 5-2, is shown in Figure 5-8. For the $As_{40}Se_{60}$ at. % (M005MINSCGNM) / $Ge_{10}As_{23.4}Se_{66.6}$ at. % (M007MINSCGNM) glass pair, the ZDW occurs at 7.4 μm and 7.1 μm, respectively, which is in good agreement with [5.9]. For the core material in the $Ge_{16}As_{24}Se_{15.5}Te_{44.5}$ at. % (M150MINSCGDJ) / $Ge_{10}As_{23.4}Se_{66.6}$ at. % (M007MINSCGNM) glass pair, the ZDW of $Ge_{16}As_{24}Se_{15.5}Te_{44.5}$ at. % occurs at 10 μm. As previously stated, the purpose of fabricating the $As_{40}Se_{60}$ at. % / $Ge_{10}As_{23.4}Se_{66.6}$ at. % and $Ge_{16}As_{24}Se_{15.5}Te_{44.5}$ at. % / $Ge_{10}As_{23.4}Se_{66.6}$ at. % SIFs is for SCG. However, most commercially available high-peak-power lasers do not cover the anomalous-dispersion-wavelength ranges of

these two SIFs. Therefore, the SCG can be achieved by either pumping in the normal-dispersion regime or reducing the ZDW by scaling down the fibre core to a few micrometres in diameter. The small-diameter core can be fabricated by either tapering the fibre [5.19] or using microstructured suspended-core structures [5.20]. It is also important to notice that the material dispersion of the $Ge_{16}As_{24}Se_{15.5}Te_{44.5}$ at. % and $As_{40}Se_{60}$ at. % core glasses remains weak out to 20 μm wavelength, as shown in Figure 5-8. For the $Ge_{16.5}As_{16}Ga_3Se_{64.5}$ at. % (ZQT007) glass, Figure 5-8 shows that the ZDW occurs at 5.4 μm. For the Pr^{3+} doped $Ge_{16}As_{21}Ga_1Se_{62}$ at. % (M022MINREZQT) glass, the ZDW locates at 6.5 μm.

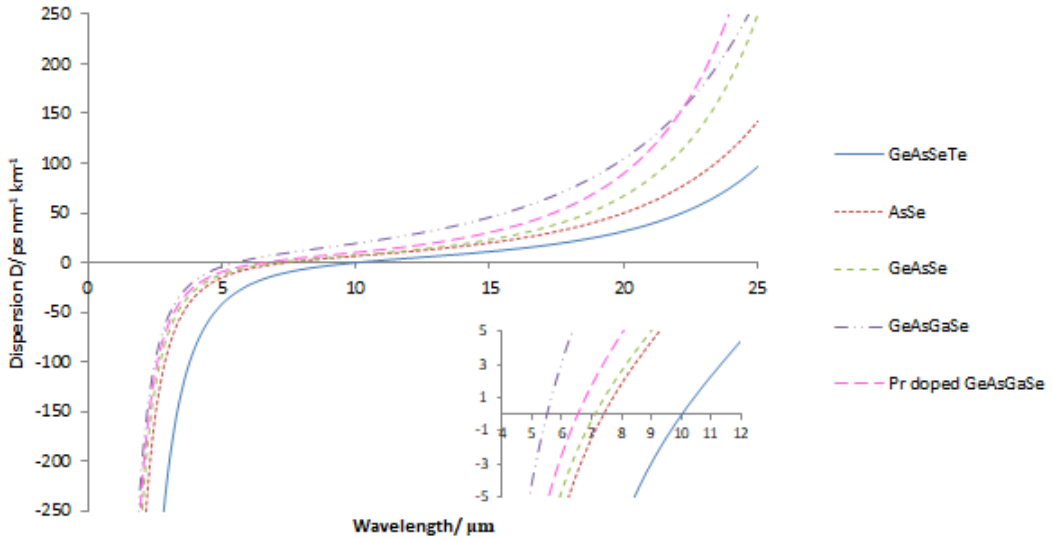


Figure 5- 8. Material dispersion *D* calculated from Eq. (5.10) and the fitted Sellmeier models of the $Ge_{16}As_{24}Se_{15.5}Te_{44.5}$ at. % (M150MINSCGDJ), $As_{40}Se_{60}$ at. % (M005MINSCGNM), $Ge_{10}As_{23.4}Se_{66.6}$ at. % (M007MINSCGNM), $Ge_{16.5}As_{16}Ga_3Se_{64.5}$ at. % (ZQT007) and Pr^{3+} doped $Ge_{16}As_{21}Ga_1Se_{62}$ at. % (M022MINSCGZQT) glasses. Inset: material dispersion close to the material zero dispersion wavelengths.

5.8 Chapter summary

In this chapter, bulk glass samples of $Ge_{16}As_{24}Se_{15.5}Te_{44.5}$ at. % (M150MINSCGDJ), $As_{40}Se_{60}$ at. % (M005MINSCGNM), $Ge_{10}As_{23.4}Se_{66.6}$ at. % (M007MINSCGNM), $Ge_{16.5}As_{16}Ga_3Se_{64.5}$ at. % (ZQT007) and Pr^{3+} doped $Ge_{16}As_{21}Ga_1Se_{62}$ at. % (M022MINREZQT) at. % were analysed for their refractive index and extinction

coefficients by means of spectroscopic ellipsometry over the wavelength range from 0.4 to 33 μm.

From the extinction coefficient data, the wavelengths corresponding to the optical band gaps of $Ge_{16}As_{24}Se_{15.5}Te_{44.5}$ at. %, $As_{40}Se_{60}$ at. %, $Ge_{10}As_{23.4}Se_{66.6}$ at. %, $Ge_{16.5}As_{16}Ga_3Se_{64.5}$ at. % and Pr^{3+} doped $Ge_{16}As_{21}Ga_1Se_{62}$ at. % were estimated to be 700 nm for $As_{40}Se_{60}$ at. %, 665 nm for $Ge_{10}As_{23.4}Se_{66.6}$ at. %, 1300 nm for $Ge_{16}As_{24}Se_{15.5}Te_{44.5}$ at. %, 650 nm for $Ge_{16.5}As_{16}Ga_3Se_{64.5}$ at. % and 650 nm for Pr^{3+} doped $Ge_{16}As_{21}Ga_1Se_{62}$ at. % from the onset of the rising extinction coefficient with decreasing wavelength. According to the definition of the transparent window for a chalcogenide glasses made by Dantanarayana *et al.* [5.14], the transparent windows for $As_{40}Se_{60}$ at. % and $Ge_{10}As_{23.4}Se_{66.6}$ at. % are from ~0.7 to 30 μm, which is in a good agreement with [5.9]. For the $Ge_{16}As_{24}Se_{15.5}Te_{44.5}$ at. %, the transparent window was determined to be from ~ 1.44 μm to ~ 29.46 μm. The transparent window for $Ge_{16.5}As_{16}Ga_3Se_{64.5}$ at. % is from ~ 0.65 μm to ~ 23.5 μm and for Pr^{3+} doped $Ge_{16}As_{21}Ga_1Se_{62}$ at. %, it is from ~ 0.65 μm to ~ 26 μm according to the extinction coefficient data.

To fit the refractive index dispersion data in the wavelength range from the lower wavelength edge of the transparent window to 2.5 μm, two-term Cauchy, three-term Cauchy, one-term Sellmeier and two-term Sellmeier models were applied. Compared to the Cauchy models, the Sellmeier models can provide better fitting performance to the refractive index of chalcogenide glasses within this wavelength range with the error less than 0.008 % for $Ge_{16}As_{24}Se_{15.5}Te_{44.5}$ at. %. For fitting the refractive index of the chalcogenide glasses in their transparent windows, a two-term Sellmeier model, with one resonant optical bandgap electronic absorption and one resonant MIR fundamental vibrational absorption, was determined to be sufficient with good fitting qualities as shown in Table 5-2. However, the Cauchy models and the

one-term Sellmeier model proved to be invalid over the whole transparent window for chalcogenide glasses.

A SIF based on the $As_{40}Se_{60}$ at. % (M005MINSCGNM) core and $Ge_{10}As_{23.4}Se_{66.6}$ at. % (M007MINSCGNM) cladding was successfully fabricated for mid-infrared supercontiuum generation [5.12]. Using the refractive index data presented in this chapter, the numerical aperture of these core-cladding fibres was calculated to be larger than 0.97 over the wavelength range from 0.5 to 30 μm. Another ultra-high-NA SIF based on the $Ge_{16}As_{24}Se_{15.5}Te_{44.5}$ at. % (M150MINSCGDJ) and $Ge_{10}As_{23.4}Se_{66.6}$ at. % (M007MINSCGNM) glass pair was also fabricated for mid-infrared supercontiuum generation [5.13] with the calculated NA in this chapter shown to be larger than 1.86 over the wavelength range from 0.5 to 30 μm.

The two-term Sellmeier fits to the measured refractive index data have also been used to calculate material dispersion characteristics for $Ge_{16}As_{24}Se_{15.5}Te_{44.5}$ at. %, $As_{40}Se_{60}$ at. %, $Ge_{10}As_{23.4}Se_{66.6}$ at. %, $Ge_{16.5}As_{16}Ga_3Se_{64.5}$ at. % and Pr^{3+} doped $Ge_{16}As_{21}Ga_1Se_{62}$ at. %. For $As_{40}Se_{60}$ at. % and $Ge_{10}As_{23.4}Se_{66.6}$ at. %, the ZDW occurs at 7.4 μm and 7.1 μm, respectively, which is in good agreement with [5.14]. For the core material in the $Ge_{16}As_{24}Se_{15.5}Te_{44.5}$ at. % / $Ge_{10}As_{23.4}Se_{66.6}$ at. % glass pair, the ZDW of $Ge_{16}As_{24}Se_{15.5}Te_{44.5}$ at. % occurs at 10 μm. For the $Ge_{16.5}As_{16}Ga_3Se_{64.5}$ at. % glass, the ZDW occurs at 5.4 μm and for the Pr^{3+} doped $Ge_{16}As_{21}Ga_1Se_{62}$ at. % glass, the ZDW locates at 6.5 μm. In the next chapter, a two-term Sellmeier model will be applied to improve the original Swanepoel method [5.4] in order to extend this method into the MIR region.

References

[5.1] Hecht, E., 1998. Optics. *Addison Wesley*, *997*, pp.213-214.

[5.2] Liu, J., 2005. Photonic Devices, *Cambridge University Press*.

[5.3] Jellison Jr, G.E. and Modine, F.A., 1996. Parameterization of the optical functions of amorphous materials in the interband region. *Applied Physics Letters*, *69*(3), pp.371-373.

[5.4] Swanepoel, R., 1985. Determining refractive index and thickness of thin films from wavelength measurements only. *Journal of the Optical Society of America A*, *2*, pp.1339-1343.

[5.5] Jenkins, F.A. and White, H.E., 1937. Fundamentals of optics. *Tata McGraw-Hill Education*.

[5.6] Dantanarayana, H.G., 2012. *Application of TLM for optical microresonators* (Doctoral dissertation, University of Nottingham).

[5.7] Sellmeier, W., 1871. Zur Erkarung der abnormen Farbenfolge im Spectrum einiger. Substanzen. *Annalen der Physik und Chemie*, *219*, pp.272-282.

[5.8] Poelman, D. and Frederic Smet, P., 2003. Methods for the determination of the optical constants of thin films from single transmission measurements: a critical review. *Journal of Physics D Applied Physics*, *36*, pp.1850-1857.

[5.9] Dantanarayana, H.G., Abdel-Moneim, N., Tang, Z., Sojka, L., Sujecki, S., Furniss, D., Seddon, A.B., Kubat, I., Bang, O. and Benson, T.M., 2014. Refractive index dispersion of chalcogenide glasses for ultra-high numerical-aperture fiber for mid-infrared supercontinuum generation. *Optical Materials Express*, *4*(7), pp.1444-1455.

[5.10] Zakery, A. and Elliott, S.R., 2007. *Optical nonlinearities in chalcogenide glasses and their applications* (Vol. 135). Berlin: Springer.

[5.11] Maklad, M.S., Mohr, R.K., Howard, R.E., Macedo, P.B. and Moynihan, C.T., 1974. Multiphonon absorption in As_2S_3-As_2Se_3 glasses. *Solid State Communications*, *15*(5), pp.855-858.

[5.12] Petersen, C.R., Møller, U., Kubat, I., Zhou, B., Dupont, S., Ramsay, J., Benson, T., Sujecki, S., Abdel-Moneim, N., Tang, Z., Furniss, D., Seddon, A.B. and Bang, O., 2014. Mid-infrared supercontinuum covering the 1.4-13.3 mum molecular fingerprint region using ultra-high NA chalcogenide step-index fibre. *Nature Photonics*, *8*, pp.830-834.

[5.13] Jayasuriya, D., 2018. *Towards mid-infrared fibre-optic device and systems for sensing, mapping and imaging* (Doctoral dissertation, University of Nottingham).

[5.14] Dudley, J.M., Genty, G. and Coen, S., 2006. Supercontinuum generation in photonic crystal fiber. *Reviews of Modern Physics*, *78*, pp.1135-1184.

[5.15] Abeeluck, A.K. and Headley, C., 2005. Continuous-wave pumping in the anomalous-and normal-dispersion regimes of nonlinear fibers for supercontinuum generation. *Optics Letters*, *30*(1), pp.61-63.

[5.16] Vanholsbeeck, F., Martin-Lopez, S., Gonz âlez-Herr áez, M. and Coen, S., 2005. The role of pump incoherence in continuous-wave supercontinuum generation. *Optics Express*, *13*(17), pp.6615-6625.

[5.17] Dai, S., Wang, Y., Peng, X., Zhang, P., Wang, X. and Xu, Y., 2018. A review of mid-infrared supercontinuum generation in chalcogenide glass fibers. *Applied Sciences*, *8*(5), p.707.

[5.18] Agrawal, G.P., 2018, March. Nonlinearity of Optical Fibers: A tutorial. In *2018 Optical Fiber Communications Conference and Exposition (OFC)* (pp. 1-3). IEEE.

[5.19] Birks, T.A., Wadsworth, W.J. and Russell, P.S.J., 2000. Supercontinuum generation in tapered fibers. *Optics Letters*, *25*(19), pp.1415-1417.

[5.20] Gao, W., El Amraoui, M., Liao, M., Kawashima, H., Duan, Z., Deng, D., Cheng, T., Suzuki, T., Messaddeq, Y. and Ohishi, Y., 2013. Mid-infrared supercontinuum generation in a suspended-core As_2S_3 chalcogenide microstructured optical fiber. *Optics Express*, *21*(8), pp.9573-9583.

Chapter 6: Swanepoel's method to determine the refractive index of chalcogenide glasses

As discussed in chapter 5, material dispersion data are crucial for designing of chalcogenide glass step-index fibres (SIF) for mid-infrared (MIR) supercontinuum generation (SCG). Spectroscopic ellipsometry, as the most popular technique for measuring refractive index dispersion in the MIR region, has disadvantages of high cost, requiring correct mathematical models and being sensitive to surface defects. Therefore, a new technique was required to obtain the material dispersion data over the transparent windows (defined in section 5.3) of chalcogenide glasses.

A method was presented to determine the refractive index and thickness of a thin film (1 μm, $\alpha - Si:H$ on a glass substrate) in the transparent region by Swanepoel in 1985 [6.1]. This entails obtaining two transmission spectra, one at normal incidence and another at oblique incidence. This method yielded the values of refractive index and thickness to an accuracy of better than 1% in his paper. In 1995, this method was used by Corrales *et al.* to determine the thickness and refractive index of As-Se and Se thin films over the wavelength range from 0.7 to 2 μm to an accuracy of better than 3 % [6.2].

One big goal of this Project is to develop a technique to determine the refractive index dispersion of chalcogenide glasses ($As_{40}Se_{60}$ at. %, $Ge_{20}Sb_{10}Se_{70}$ at. %, $Ge_{16}As_{24}Se_{15.5}Te_{44.5}$ at. % etc.) in the MIR region. The Swanepoel method as an effective technique to measure the refractive index of thin films in the near infrared (NIR) region was considered to be a potential approach for MIR refractive index dispersion determinations.

In section 6.1, the method described in Swanepoel's paper [6.1] was implemented by the author in Matlab; this is referred to the original Swanepoel

method. The original Swanepoel method was then applied to determine the refractive index dispersion of $Ge_{16}As_{24}Se_{15.5}Te_{44.5}$ at. % (M140MINSCGDJ) and $As_{40}Se_{60}$ at. % (M130MINSCGDJ) thin films in the MIR region in section 6.2, where it is shown that the fitting procedures of the Cauchy refractive index model used are poor. In section 6.3, the original Swanepoel method is modified by changing the dispersive model to the three-term Cauchy, one-term Sellmeier and two-term Sellmeier models. The modified Swanepoel methods were applied to determine the refractive index of the $As_{40}Se_{60}$ at. % thin film over the wavelength range from 0.7 to 2 μm using the data in [6.2], and then applied to determine the refractive index dispersion of the $Ge_{16}As_{24}Se_{15.5}Te_{44.5}$ at. % (M140MINSCGDJ) and $As_{40}Se_{60}$ at. % (M130MINSCGDJ) thin films in the MIR region. In this section, the modified Swanepoel method using the two-term Sellmeier model is determined as the best method to determine the refractive index dispersion of chalcogenide glasses ($As_{40}Se_{60}$ at. % and $Ge_{16}As_{24}Se_{15.5}Te_{44.5}$ at. %) in the MIR region; this method is referred to the improved Swanepoel method. In section 6.4, the refractive indices of Ge-As-Se-Te glass system will be presented. In section 6.5, the refractive indices of other chalcogenide glasses will be determined from the improved Swanepoel method. Section 6.6 will investigate the effect of fast quenching on the chalcogenide thin films. In section 6.7, a very small refractive-index contrast in a two-composition thin film will be determined from a simple modification of the improved Swanepoel method. Finally, section 6.8 provides a chapter summary.

6.1 Reproducing the original Swanepoel method

A method was presented to determine the refractive index and thickness of the thin film (1 μm, $\alpha - \mathrm{Si{:}H}$ on a glass substrate) in the transparent region (extinction coefficient $k \approx 0$) by Swanepoel in 1985. [6.1] This entails obtaining two sepctra, one at normal incidence and another at oblique incidence. This method yielded the

values of refractive index and thickness to an accuracy of better than 1% in his paper.

6.1.1 The basic theory of the original Swanepoel method

Most of the material in this sub-section is reproduced from Swanepoel's paper [6.1] for the convenience of the reader.

In the transparent region of the $\alpha - \mathrm{Si{:}\,H}$ thin film (extinction coefficient $k \approx 0$), the expressions for using the envelopes around the maxima and minima of the interference fringes to determine the refractive index are:

$$n^2 = P + (P^2 + s^2)^2 \qquad (6.1)$$

where

$$P = 2s\frac{T_M - T_m}{T_M T_m} + \frac{s^2+1}{2}$$

where s is the substrate refractive index, and T_M and T_m are the maxima and minima of the interference fringes (see Figure 2.5-6 in section 2.5.5). However, this method may cause significant errors in determining the refractive index and thickness of the thin film since the results are very sensitive to the experimental values of T_M and T_m. Therefore, another method was used by Swanepoel to determine the refractive index and thickness [6.1].

It is assumed that a mathematical expression for the dispersion $n(\lambda)$ exists and that n is isotropic. Then $n(\lambda)$ can be represented by three constants x, a and b in the region of $k^2 \ll n^2$ by:

$$n^2 = \frac{a}{\lambda^x} + b \qquad (6.2)$$

where λ is wavelength and *a*, *b* and *x* are fitting coefficients. The dispersive equation in Eq. (6.2) is similar to the Cauchy equation, but in order to have a better fit to the refractive index data, the Cauchy model was altered in [6.1] to have an extra fitting parameter *x* instead of a constant value of wavelength λ.

For normal incidence on a film with the thickness *d* the wavelengths of the transmission extrema are given:

$$2n_0 d = m\lambda_0 \qquad (6.3)$$

where λ_0 is the wavelength at the maxima or minima of the normal incidence transmission spectrum, n_0 is the refractive index of the material at λ_0, and *m* is the order number which has integer values for the maxima and half-integer values for the minima in the case where the thin film has no substrate or the refractive index of thin film is larger than that of the substrate.

Only *m* and the product $n_0 d$ can be determined solely from Eqs. (6.2) and (6.3); thus another experimental equation had to be found to determine the other constants. This was obtained by measuring a second transmission spectrum at an angle of incidence $i > 0$. The equation for the interference extrema then became [6.3]:

$$2n_i d\cos r = m\lambda_i \qquad (6.4)$$

where *r* is the angle of the refraction in the film, λ_i is wavelength at the maxima or minima of the non-normal incidence transmission spectrum, and n_i is the refractive index of the material at λ_i. Eq. (6.4) can be used for a stand-alone thin film or a film on a transparent substrate.

Method A (Determining *n* from the order numbers *m*):

Following [6.1], the order number *m* is now considered not to be a discrete-order number but a continuous mathematical variable. The spectrum for normal incidence

is shifted towards shorter wavelengths by increasing each order number by an amount Δm, where Δm can be different for each m. The shifting in extrema due to oblique incidence, according to Eq. (6.4), can be written in terms of normal incidence as:

$$2n_i d = (m + \Delta m)\lambda_i \qquad (6.5)$$

Following [6.1] it is noted for later discussion that Eqs. (6.4), (6.5), together with Snell's law (Eq. (6.7)), yield:

$$cos\ r = \frac{m}{m+\Delta m}, \qquad (6.6)$$

using:

$$n_i = \frac{sin\ i}{sin\ r}, \qquad (6.7)$$

and that it follows from Eq. (6.3) that two adjacent extrema of the normal-incidence spectrum at wavelengths λ_{01} and λ_{02}, obey

$$m_1 = \frac{n_{01}\lambda_{02}}{2(n_{02}\lambda_{01} - n_{01}\lambda_{02})}.$$

The quantity M now can be determined by the expression:

$$M = \frac{\lambda_{02}}{2(\lambda_{01} - \lambda_{02})} \qquad (6.8)$$

where $M \geq m$. $M = m$ in the non-dispersive case. In the dispersive case, the dispersion of M was described in [6.1] by the approximate form:

$$M = \frac{C_s}{\lambda_0}\left(1 + \frac{D_s}{\lambda_o^y}\right) \qquad (6.9)$$

where C_s, D_s and y are fitting parameters. The value of m at each extremum is now approximately given by

$$m \approx \frac{C_s}{\lambda_0}. \qquad (6.10)$$

Eq. (6.9) can be written in the form of an equation for a straight line:

$$M\lambda_0 = \frac{D}{\lambda_0^y} + C \qquad (6.11)$$

where *D*, *C*, and y are fitting parameters which can then be used to find values of *m* ($\leq M$) where, at each extremum wavelength λ_o, *m* takes an integer value close to transmission maxima and half integer values close to transmission minima.

Substitution of Eq. (6.2) into Eq. (6.3) yields:

$$m^2{\lambda_0}^2 = \frac{A}{{\lambda_0}^x} + B \qquad (6.12)$$

where

$$A = 4ad^2$$

$$B = 4bd^2. \qquad (6.13)$$

Because the order numbers are known, the value of *x* can be obtained by iteration and performing a linear regression of Eq. (6.12); the regression yields the values of *A* and *B*.

Substitution of Eq. (6.2) into (6.5), using Eq. (6.12), and solving forΔm yields

$$\Delta m = [m^2 \frac{\lambda_o^2}{\lambda_i^2} + \frac{A}{\lambda_i^2}(\frac{1}{\lambda_i^x} - \frac{1}{\lambda_0^x})]^{1/2} - m \qquad (6.14)$$

The value of n_i at each value of λ_i can be calculated using Eqs. (6.14), (6.6) and (6.7).

To get the value of thin film thickness, Eq. (6.15) needs to be plotted:

$$\left(\frac{l}{2} + \Delta m\right) = 2d\frac{n_i}{\lambda_i} - m_1, \qquad (6.15)$$

where m_1 is the order number of the first observable extreme, l = 0,1,2,3…. Using $(\frac{l}{2} + \Delta m)$ as ordinate and $\frac{n_i}{\lambda_i}$ as abscissa, a straight line can be plotted. The slope of the line can be used to determine the thickness.

Method B (Determining *n* from the dispersion equation):

The other way to calculate n without knowing m presented in [6.1] will now be considered. From Eqs. (6.3) and (6.4), it follows that

$$n_i \cos r = n_0 \frac{\lambda_i}{\lambda_0}. \qquad (6.16)$$

In the non-dispersive case, Eq. (6.16) can be written as

$$\cos r = n_0 \frac{\lambda_i}{\lambda_0},$$

and n can be calculated from Eq. (6.7).

Substitution of Eq. (6.7) into (6.16) yields

$$n_i^2 - n_0^2 \frac{\lambda_i^2}{\lambda_0^2} = sin^2\, i. \qquad (6.17)$$

Substitution of Eq. (6.2) into (6.17) yields an inhomogeneous equation in a, b, and x. Three such equations can be obtained by considering three different extrema, and a, b, and x can in principle be solved from these equations. To obtain correct values, however, requires that the wavelengths be measured to an accuracy of better than 0.1 nm, which is not obtainable. Method B can, however, be used in the case of thin films where only one or two extrema appear and other methods fail.

From Eq. (6.2), by expanding n_i^2 in a Taylor series around n_0, it follows that

$$n_i^2 = n_0^2 + \frac{ax}{\lambda_0^{x+1}}(\lambda_0 - \lambda_i). \quad (6.18)$$

Substitution of Eq. (6.18) into (6.17) yields

$$n_0^2 = N^2 - \frac{ax}{\lambda_0^{x-1}(\lambda_0+\lambda_i)} \quad (6.19)$$

where

$$N^2 = \frac{\lambda_0^2 sin^2 i}{\lambda_0^2 - \lambda_i^2}. \quad (6.20)$$

Eqs. (6.2) and (6.19) indicate that N^2 can be represented by a function of the form:

$$N^2 = \frac{E}{\lambda^x} + b \quad (6.21)$$

where *E* and *b* are fitting constants. From Eqs. (6.2), (6.21) and (6.19), it follows that

$$\frac{E}{a} = \frac{(1+x)\lambda_0+\lambda_i}{\lambda_0+\lambda_i} \approx 1 + \frac{x}{2} \quad (6.22)$$

x can be determined by finding a good fit to Eq. (6.21). This good fit subsequently yields *E* and *b*. The value of *a* can be determined by Eq. (6.22). Thus the refractive index can be determined.

To determine *m* and *d*, an equation similar to Eq. (6.15) can be written as [6.1]

$$\frac{l}{2} = 2d\frac{n_0}{\lambda_0} - m_1 \quad (6.23)$$

The thickness can be found from the slope of the line and the estimation of first order number m_1 will also be given.

Knowing the extrema of the transmission spectrum, T_M and T_m, Eq. (6.1) can be used to get n_T. Put n_T into Eq. (6.23), the value of d_T and another estimation of m_1 will be given.

Taking the average of three values of thickness and using Eq. (6.3), the refractive index can be calculated. Then a fit of these final values to Eq. (6.1) yields the expression for refractive index against wavelength.

6.1.2 Reproducing the results given in Swanepoel's paper using Matlab.

Matlab codes were written by the author to reproduce the results presented in Swanepoel's paper [6.1]. The wavelengths at the maxima and minima of the normal incident transmission spectrum λ_0 and the wavelengths at the maxima and minima of the transmission spectrum with 30 °incident angle (see Table 6.1-1) were provided by [6.1], and will be used in this section.

6.1.2.1 Determining the order numbers of each extreme.

The values of λ_0 (see Table 6.1-1) were used to determine the quantity *M* according to Eq. (6.8); the values of *M* are shown in Table 6.1-1. The error between the reproduced values and those from Swanepoel's paper is less than 2.5 %.

To obtain the value of *m* at each extreme, a linear regression of Eq. (6.11) was performed by iterating the value of *y* to obtain the best fit as shown in Figure 6.1-1. The value of the coefficient of determination R^2 (the closer the R^2 value is to 1, the better the fit is) [6.4] is 0.9996 with y = 4.1, which is different from the value in the Swanepoel's paper (y = 4.5). In the case of best fitting (y = 4.1), the calculated order numbers at each extreme, m_y from the approximation (6.10), are shown in Table 6.1-1 as well as the values of m_y when y = 4.5. From Table 6.1-1, both sets of results when y = 4.1 and y = 4.5, are sufficient to determine the first order number

(the order number of the first observable extreme of the transmission spectra within the detection range) which is 6.5 in Swanepoel's paper [6.1].

Table 6.1- 1. Comparison between *M* and m_y obtained using Matlab codes developed by the author and those in the Swanepoel paper [6.1].

λ_0 /nm	857.6	802.3	755.4	715.2	680.4	650.3	623.9	600.8
λ_i /nm	844.0	790.1	744.4	705.3	671.6	642.3	616.8	594.3
M (Swanepoel)	7.3	8.1	9.0	10.0	11.0	12.1	13.2	
M (This work)	7.3	8.1	8.9	9.8	10.8	11.8	13.0	
m_y (Swanepoel)	6.7	7.1	7.6	8.0	8.4	8.8	9.2	9.5
m_y (This work, y=4.1)	6.5	6.9	7.3	7.7	8.1	8.5	8.9	9.2
m_y (This work, y=4.5)	6.6	7.1	7.5	7.9	8.3	8.7	9.1	9.4

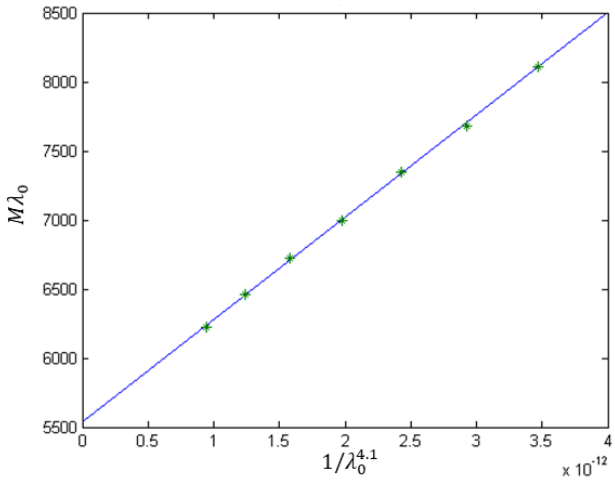


Figure 6.1- 1. The best fit to Eq. (6.11) using the data presented in [6.1] with *y*=4.1. The coefficient of determination R^2 is 0.9996.

6.1.2.2 Determining n from the order numbers m (Method A).

The actual values of *m* are used in Eq. (6.12), iterating *x* in steps of 0.1 from 3.5 to 5.5. The best fit was obtained with *x* = 4.2 yielding

$$m^2{\lambda_0}^2 = \frac{A}{{\lambda_0}^{4.2}} + B$$

$$A = 3.027 \times 10^{18}$$

$$B = 2.962 \times 10^{7}$$

The values of *A*, *B* and *x* obtained are the same as those presented in Swanepoel's paper. Δm was calculated from Eq. (6.14) and n_i was calculated from Eqs. (6.6) and (6.7). The results of Δm and n_i are compared to those found in Swanepoel's paper [6.1] in Table 6.1-2. It is easily found that the values of Δm and n_i are the same as those presented in [6.1].

Table 6.1- 1. The results of calculated Δm and n_i comparing to those in Swanepoel's paper [6.1].

λ_0 /nm	857.6	802.3	755.4	715.2	680.4	650.3	623.9	600.8
λ_i /nm	844.0	790.1	744.4	705.3	671.6	642.3	616.8	594.3
Δm (Swanepoel)	0.1154	0.1224	0.1294	0.1355	0.1391	0.1449	0.1464	0.1516
Δm (This work)	0.1154	0.1224	0.1294	0.1355	0.1391	0.1449	0.1464	0.1516
n_i (Swanepoel)	2.688	2.708	2.726	2.751	2.798	2.820	2.881	2.904
n_i (This work)	2.688	2.708	2.726	2.751	2.798	2.812	2.881	2.904

The plot of Eq. (6.15) with R^2 = 0.9996 is shown in Figure 6.1-2. In Figure 6.1-2, a straight line through – m_1 with the slope of 2078, yields a value for *d* of *d* = 1039 nm, which is the same as the value quoted in [6.1]. Then the constants *a* and *b* can be calculated from Eq. (6.13), yielding the equation for $n(\lambda)$:

$$n^2 = \frac{7.017 \times 10^{11}}{\lambda^{4.4}} + 6.860 \qquad (6.24)$$

In [6.1], $a = 7.016 \times 10^{11}$ and *b* = 6.865.

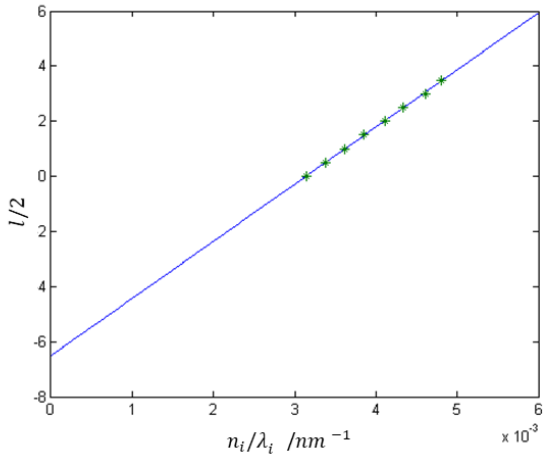


Figure 6.1- 2. Plot of $\frac{l}{2} + \Delta m$ as a function of n_i/λ_i to determine the thickness *d*.

6.1.2.3 Determining n from the dispersion equation (Method B).

Following the method B described in section 6.1.1, the values of *N* can be obtained from Eq. (6.20) using the values of λ_0 and λ_i presented in [6.1] (see Table 6.1-3); the results are shown in Table 6.1-3. The values of *N* in this work are the same as those reported in Swanepoel's paper [6.1]. Then the best fit of Eq. (6.21) yields $E = 7.952 \times 10^{12}$ and b = 6.947 with x = 4.4. All these values are the same as those presented in [6.1].

The calculated values of *E/a* from Eq. (6.22) vary from 3.218 to 3.212. Hence, the average value 3.215 was taken as the value of *E/a*. The equation for $n(\lambda)$ thus is:

$$n^2 = \frac{2.473\times10^{12}}{\lambda^{4.4}} + 6.9473. \qquad (6.25)$$

The values of n_0 were calculated from Eq. (6.25) at each wavelength as shown in Table 6.1-3. The results are the same as those presented in Swanepoel's paper.

Table 6.1- 2. The values of *N* and n_0 obtained in this work comparing to those in Swanepoel's paper [6.1].

λ_0 /nm	857.6	802.3	755.4	715.2	680.4	650.3	623.9	600.8
λ_i /nm	844.0	790.1	744.4	705.3	671.6	642.3	616.8	594.3
N (Swanepoel)	2.819	2.878	2.941	3.016	3.119	3.198	3.324	3.408
N (This work)	2.819	2.878	2.941	3.016	3.119	3.198	3.324	3.408
n_o (Swanepoel)	2.693	2.713	2.736	2.762	2.792	2.826	2.862	2.901
n_o (This work)	2.693	2.713	2.736	2.762	2.792	2.826	2.862	2.901

To determine the first order number and the thickness *d*, a best fit of Eq. (6.23) was plotted, as shown in Figure 6.1-3, yielding the value of the first order number as 6.5 and a slope of 2072, and a value for *d* of:

$$d = 1036 \text{ nm}$$

which is the same as that reported in [6.1].

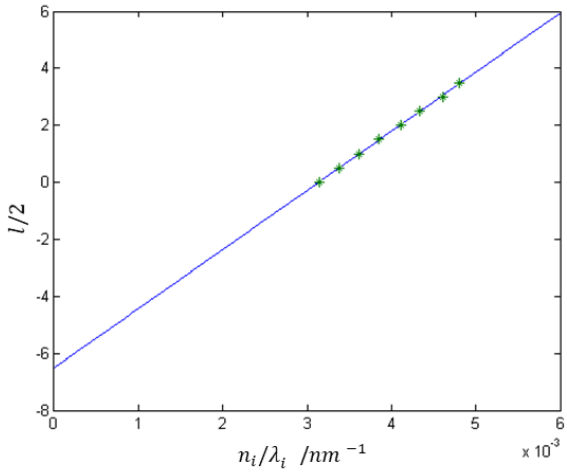


Figure 6.1- 3. Plot of $\frac{l}{2}$ as a function of n_0/λ_0 to determine the thickness *d* from Eq. (6.23).

6.1.2.4 Determining the thickness d_T and refractive index n_T from the transmittance.

The values of transmittance T_M and T_m presented in [6.1] at each extreme are shown in Table 6.1-3. n_T can be determined from Eq. (6.1) as shown in Table 6.1-4. The error with respect to the results in [6.1] is less than 0.04 %.

Table 6.1- 3. The values of n_T obtained from the transmittance T_M and T_m comparing to those in Swanepoel's paper [6.1].

λ_0 /nm	857.6	802.3	755.4	715.2	680.4	650.3	623.9	600.8
λ_i /nm	844.0	790.1	744.4	705.3	671.6	642.3	616.8	594.3
T_M	0.920	0.920	0.915	0.895	0.860	0.805	0.73	0.64
T_m	0.560	0.555	0.545	0.535	0.515	0.485	0.45	0.41
n_T (This work)	2.680	2.699	2.730	2.742	2.773	2.818	2.854	2.881
n_T (Swanepoel)	2.680	2.699	2.731	2.742	2.773	2.818	2.855	2.881

A plot of Eq. (6.23) using the values of n_T yields a value for d_T of

$$d_T = 1040\ nm.$$

The value of d_T obtained in this work is the same as that presented in Swanepoel's paper.

6.1.2.5 Determining the refractive index and thickness by making an agreement between methods A and B.

The values of x in Eq. (6.12) obtained by method A is 4.2 while that in Eq. (6.21) obtained by method B is 4.4. Therefore, x was determined to be 4.3 as an average value.

Taking the average value for the thickness d of 1038 nm, the final values of n can now be determined using Eq. (6.3); these results are shown in Table 6.1-4. From

Table 6.1-4, both results are seen to be the same which means the results presented in [6.1] were well reproduced. This indicates that the Matlab code developed can be applied to determine the refractive index dispersion of chalcogenide thin films.

Table 6.1- 4. The comparison between the final refractive index *n* and that in Swanepoel's paper [6.1].

λ_0 /nm	857.6	802.3	755.4	715.2	680.4	650.3	623.9	600.8
λ_i /nm	844.0	790.1	744.4	705.3	671.6	642.3	616.8	594.3
n (This work)	2.685	2.705	2.729	2.756	2.785	2.819	2.855	2.894
n (Swanepoel)	2.685	2.705	2.729	2.756	2.785	2.819	2.855	2.894

A fit of these final values to Eq. (6.2) yields:

$$n^2 = \frac{1.319 \times 10^{12}}{\lambda^{4.3}} + 6.890$$

where these two fitting parameters are the same as those presented in [6.1].

6.2 Determining the refractive index of $Ge_{16}As_{24}Se_{15.5}Te_{44.5}$ at. % and $As_{40}Se_{60}$ at. % thin films using the original Swanepoel method

The original Swanepoel method was well reproduced in section 6.1. Efforts are made in this section to use this original Swanepoel method to determine the refractive index and thickness of hot-pressed $Ge_{16}As_{24}Se_{15.5}Te_{44.5}$ at. % (melting code: M140MINSCGDJ; hot pressing code: YRFFP007) and $As_{40}Se_{60}$ at. % (melting code: M130MINSCGDJ; hot pressing code: YRFFP003) thin films.

The $Ge_{16}As_{24}Se_{15.5}Te_{44.5}$ (M140MINSCGDJ) at. % and $As_{40}Se_{60}$ at. % (M130MINSCGDJ) thin films were hot-pressed from optical fibres as described in section 3.5.2. The interference transmission spectra of the $Ge_{16}As_{24}Se_{15.5}Te_{44.5}$ at. % and the $As_{40}Se_{60}$ at. % thin films are shown respectively in Figures 6.2-1(a) and

6.2-1(b). The beam source used in the FTIR spectrometer is a Globar^{TM} and the detector used is a DLaTGSD301 which has a usable wavelength range from 2 to 25 μm.

The solid curves in Figure 6.2-1 represent the interference transmission spectrum for normal incidence whereas the dotted spectrum is that for an incidence angle of 30 º. Because the accuracy of the calculation depends on $(\lambda_0 - \lambda_i)$, the angle of non-normal incidence should be large enough to get sufficient displacement but, as described in section 3.6.5, not so large that the lateral spreading of the beam would introduce errors in the case of non-uniform films. No particular significance should be attached to the actual values of transmission of the oblique angle of incidence spectrum (dotted curve, red) because the effects of polarisation can influence its magnitude for large angles of incidence [6.2]. Another method to get sufficient displacement between the normal and angled incidence results is to decrease the thickness of the thin film. As discussed in section 3.5.2, decreasing the thickness of the thin film will result in increasing difficulties in collecting complete samples after the hot-pressing. Thin films having nominal thicknesses of 20 μm and 25 μm provide sufficient displacements between the two sets of fringes and yet were strong enough to be collected and handled.

Since the interference fringes obtained at wavelengths below 2.85 μm are influenced by atmospheric water absorption at wavelengths around 2.7 μm, and the displacements $(\lambda_0 - \lambda_i)$ were relatively small at these measurement wavelengths, which led to errors in determining the thickness of the thin film as well as of the refractive index, the extrema at wavelengths below 2.85 μm were not selected when determining the thickness of the thin film.

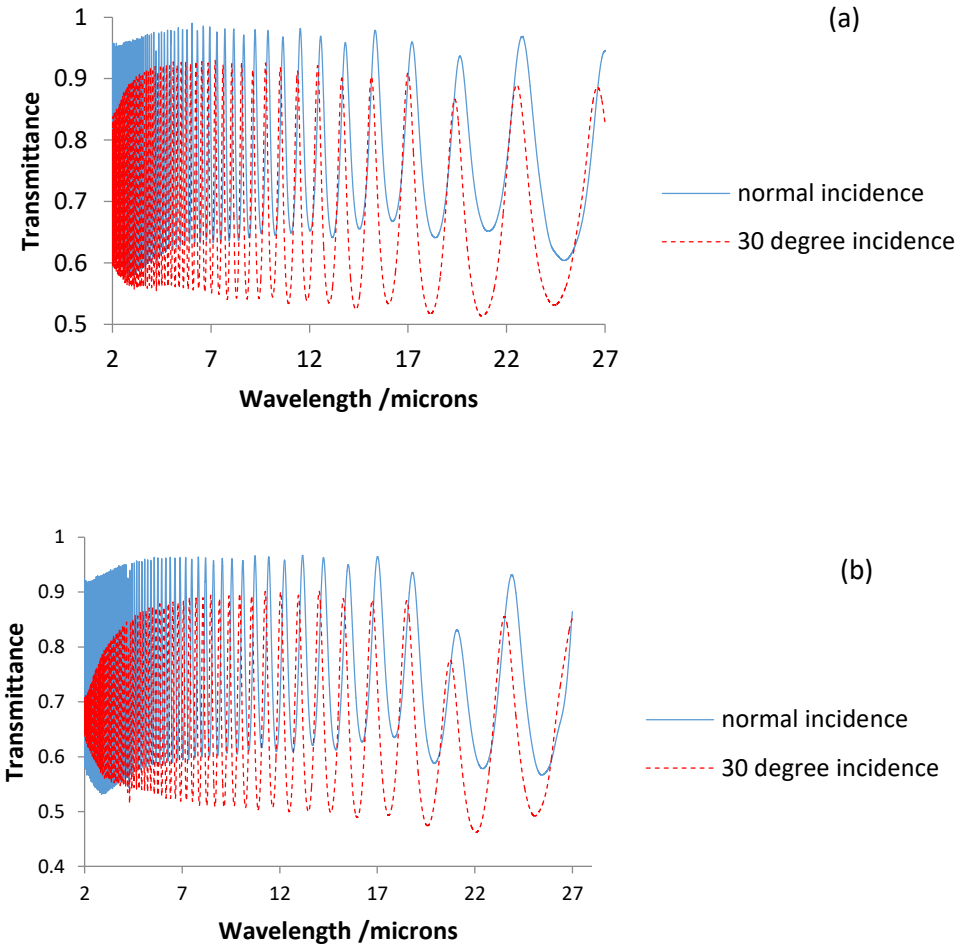


Figure 6.2- 1. Transmission spectra for: (a) a 20 µm target thick pressed $Ge_{16}As_{24}Se_{15.5}Te_{44.5}$ at. % (M140MINSCGDJ) sample at normal incidence (solid curve, blue) and at an incident angle of 30 °(dotted curve, red) and (b) a 25 µm target thick pressed $As_{40}Se_{60}$ at. % (M130MINSCGDJ) sample at normal incidence (solid curve, blue) and at an incident angle of 30 °(dotted curve, red).

From Figure 6.2-1(b), an obvious dip at ~ 21 µm was observed in the transmission spectrum of the $As_{40}Se_{60}$ at. % thin film; this dip was identified by Moynihan' group [6.6] as the second overtone of the fundamental stretching band due to $AsSe_3$ pyramid units in an As_2Se_3 glass structural matrix itself. The details were discussed in section 5.5.

6.2.1 Determining the order numbers at each extreme for the $Ge_{16}As_{24}Se_{15.5}Te_{44.5}$ at. % and $As_{40}Se_{60}$ at. % thin films.

Some wavelengths of the extrema of the $Ge_{16}As_{24}Se_{15.5}Te_{44.5}$ at. % (M140MINSCGDJ) and $As_{40}Se_{60}$ at. % (M130MINSCGDJ) thin films found in Figure 6.2-1 are listed in Table 6.2-1. The quantities M of the $Ge_{16}As_{24}Se_{15.5}Te_{44.5}$ at. % and $As_{40}Se_{60}$ at. % thin films were determined by Eq. (6.8) and are also shown in Table 6.2-1.

To obtain the value of m at each extreme, a linear regression of Eq. (6.11) was done in Matlab with iterating the value of y to perform the best fit as shown in Figure 6.2-2. For $Ge_{16}As_{24}Se_{15.5}Te_{44.5}$ at. %, the value of R^2 is 0.3162 with y = 3.6 as shown in Figure 6.2-2(a). The order number at the wavelength of 22.786 μm can thus be determined to be 6, as shown in Table 6.2-1. For $As_{40}Se_{60}$ at. %, the value of R^2 is 0.0261 with y = 6 as shown in Figure 6.2-2(b). Therefore, the order number at the wavelength of 23.896 μm can be obtained from the approximation (6.10) which is 7.

Since the fitting qualities in Figure 6.2-2 were poor, another method needs to be applied to check whether this method is sufficient to determine the order numbers at each extreme of the transmission plots for the chalcogenide thin films. The data of the $As_{40}Se_{60}$ at. % thin film is used here for an illustration. According to Eq. (6.3), the refractive index at each extreme can be determined by the thickness of the thin film d, the order numbers m and the wavelength λ_0 at each extreme. For most chalcogenide glasses, the refractive index is within the range of 2.0 to 3.3. The thickness of the thin film d is within the range of 25 μm (target thickness) to 35 μm. The first observable extreme of the transmission spectrum in Figure 6.2-1(b) was determined to be at the wavelength of 23.896 μm, which is a maximum extreme. According to Eq. (6.3), the range of the order number at the first observable extreme in Figure 6.1-2(b) is from 4.1 to 9.7. Assuming the thickness d for the thin film is 30

μm, iterating the first order number m in steps of 1 from 1 to 9 (m has integer values for the maxima and half-integer values for the minima of the interference fringes [6.1]), the refractive indices at different order numbers calculated after making the above assumptions are shown in Figure 6.2-3. For the refractive indices calculated, assuming the order numbers at the first extreme of 8 and 9 (red and pink dots in Figure 6.2-3 respectively), the refractive index increases with increasing wavelength which does not agree with the expected refractive index dispersion of chalcogenide glasses [6.5]. For the refractive indices calculated assuming the order numbers at the first extreme of 5 and 6 (light blue and green dots in Figure 6.2-3 respectively), the $dn/d\lambda$ of $As_{40}Se_{60}$ at. % is much larger than that in [6.5]. Therefore, the correct order number at the first extreme of the transmission spectrum in Figure 6.2-1(b) should be 7 which is in agreement with the result determined from the approximation of Eq. (6.10). This method for determining the order number at the first observable extreme also suite for other chalcogenide glasses.

Table 6.2- 1. The values of M, m_y and the actual order numbers m at each first observable extreme obtained for the hot-pressed $Ge_{16}As_{24}Se_{15.5}Te_{44.5}$ at. % (M140MINSCGDJ) and $As_{40}Se_{60}$ at. % (M130MINSCGDJ) thin films.

Ge-As-Se-Te								
λ_0 /μm	22.786	21.052	19.635	18.381	17.203	16.217	15.334	…
M	6.1	6.9	7.3	7.3	8.2	8.7	9.1	…
m_y	6.1	6.6	7.1	7.6	8.1	8.6	9.1	…
m	6	6.5	7	7.5	8	8.5	9	…
As-Se								
λ_0 /μm	23.896	22.411	21.087	19.934	18.803	17.880	17.015	…
M	7.5	8.0	8.6	8.3	9.7	9.8	10.2	…
m_y	7.3	7.8	8.2	8.7	9.3	9.7	10.2	…
m	7	7.5	8	8.5	9	9.5	10	…

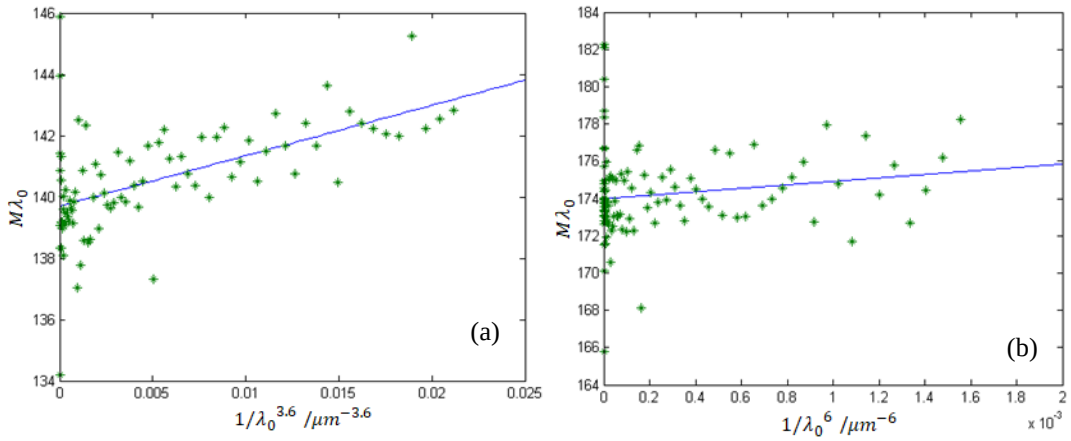


Figure 6.2- 2 . Plot of $M\lambda_0$ as a function of n_0/λ_0 to determine the quantity M for (a) the $Ge_{16}As_{24}Se_{15.5}Te_{44.5}$ at. % (M140MINSCGDJ) and (b) $As_{40}Se_{60}$ at. % (M130MINSCGDJ) thin films.

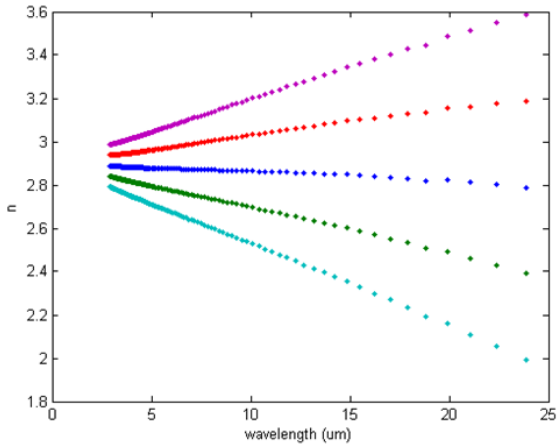


Figure 6.2- 3. Refractive indices of the $As_{40}Se_{60}$ at. % (M130MINSCGDJ) thin film calculated assuming the order numbers at the first observable extreme (at the wavelength of 23.896 μm) of 5 (light blue), 6 (green), 7 (blue), 8 (red), and 9 (pink).

6.2.2 Determining n from the order number m for the $Ge_{16}As_{24}Se_{15.5}Te_{44.5}$ at. % and $As_{40}Se_{60}$ at. % thin films.

The actual values of *m* obtained in section 6.2.1 (see Table 6.2-1) are used in Eq. (6.12), iterating *x* in steps of 0.1 from 1 to 6. The best fits were obtained with $x = 1$ yielding

$$m^2\lambda_0^2 = \frac{2.028\times10^3}{\lambda^1} + 1.893\times10^4 \quad \text{for } Ge_{16}As_{24}Se_{15.5}Te_{44.5} \text{ at. \%}$$

$$m^2\lambda_0^2 = \frac{3.506\times10^3}{\lambda^1} + 2.901\times10^4 \quad \text{for } As_{40}Se_{60} \text{ at. \%}$$

The best fits to Eq. (6.12) for $Ge_{16}As_{24}Se_{15.5}Te_{44.5}$ at. % (M140MINSCGDJ) and $As_{40}Se_{60}$ at. % (M130MINSCGDJ) are shown in Figure 6.2-4. For $Ge_{16}As_{24}Se_{15.5}Te_{44.5}$ at. %, the best fitting from the original Swanepoel method is shown in Figure 6.2-4(a). The quanlity of the fits is quantified via the values of R^2 (coefficient of determination) and *MSE* (mean of square error) [6.3], which were discussed in section 5.4. Note that a good fit to data would give a R^2 approaching 1 and a *MSE* of 0. The value of R^2 is 0.8997 and *MSE* is 3.584×10^3. For $As_{40}Se_{60}$ at. %, the value of R^2 is 0.6702 and *MSE* is 4.686×10^4. The poor fittings shown in Figures 6.2-4(a) and 6.2-4(b) indicate that a dispersion equation based on Eq. (6.2) is not appropriate to describe the refractive index dispersion of chalcogenide thin films in the MIR region.

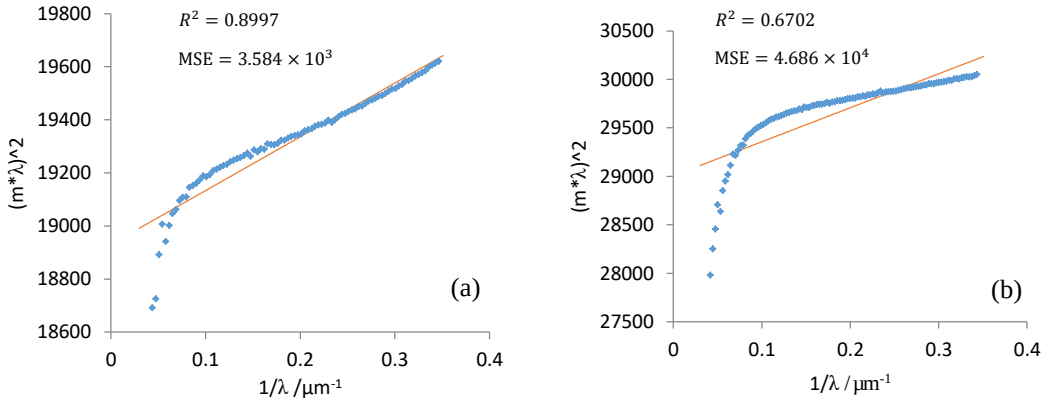


Figure 6.2- 4. Best fits to Eq. (6.12) using the experimental data for (a) the $Ge_{16}As_{24}Se_{15.5}Te_{44.5}$ at. % (M140MINSCGDJ) and (b) $As_{40}Se_{60}$ at. % (M130MINSCGDJ) thin films.

Δm was calculated from Eq. (6.14) and n_i was calculated from Eqs. (6.6) and (6.7). The results of Δm and n_i for $Ge_{16}As_{24}Se_{15.5}Te_{44.5}$ at. % and $As_{40}Se_{60}$ at. % obtained using the original Swanepoel method are shown in Tables 6.2-2 and 6.2-3.

Figure 6.2-5 shows a plot of $\frac{l}{2} + \Delta m$ as a function of n_i/λ_i. Eq. (6.15) shows that the gradient of this straight line plot is 2*d*. For $Ge_{16}As_{24}Se_{15.5}Te_{44.5}$ at. %, the slope of the straight line is 43.68 µm, yielding the value of thickness for the $Ge_{16}As_{24}Se_{15.5}Te_{44.5}$ at. % thin film of 21.84 µm (target thickness: 20 µm). For $As_{40}Se_{60}$ at. %, the slope of the straight line is 61.96 µm, yielding the value of thickness for the $As_{40}Se_{60}$ at. % thin film of 30.98 µm (target thickness: 25 µm). The difference between the calculated thickness and the target thickness can be attributed to the quality of the shims (see section 3.6.5.2), short hot-pressing time or the high glass melt viscosity during the hot pressing.

Table 6.2- 2. Calculation of refractive index of the $Ge_{16}As_{24}Se_{15.5}Te_{44.5}$ at. % (M140MINSCGDJ) thin film from the original Swanepoel method.

λ_0 /µm	λ_i /µm	T_M	T_m	M	m_y	m	Δm	n_i	N	n_0	n_T	n
22.786	22.509	0.899	0.576	6.1	6.1	6	0.0740	3.212	3.216	3.212	1.996	3.158
21.052	20.760	0.904	0.584	7.0	6.6	6.5	0.0916	3.010	3.013	3.008	1.914	3.159
19.635	19.370	0.909	0.591	7.3	7.1	7	0.0963	3.045	3.049	3.044	1.909	3.159
18.381	18.136	0.915	0.597	7.3	7.6	7.5	0.1017	3.067	3.072	3.066	1.938	3.160
17.203	16.996	0.922	0.603	8.2	8.1	8	0.0980	3.224	3.229	3.224	1.916	3.160
16.217	16.013	0.928	0.607	8.7	8.6	8.5	0.1089	3.154	3.159	3.153	1.894	3.161
…												
3.042	3.005	0.935	0.539	46.7	45.9	46	0.5660	3.217	3.244	3.212	2.124	3.206
3.010	2.974	0.934	0.538	48.3	46.4	46.5	0.5673	3.230	3.258	3.225	2.123	3.206
2.979	2.943	0.934	0.538	47.7	46.9	47	0.5853	3.198	3.225	3.192	2.122	3.207
2.948	2.912	0.934	0.538	48.4	47.4	47.5	0.5862	3.212	3.240	3.207	2.124	3.207
2.918	2.883	0.933	0.537	49.0	47.9	48	0.5930	3.210	3.238	3.205	2.123	3.208
2.888	2.853	0.933	0.537		48.4	48.5	0.5993	3.210	3.239	3.205	2.087	3.209

Table 6.2- 3. Calculation of refractive index of the $As_{40}Se_{60}$ at. % (M130MINSCGDJ) thin film from the original Swanepoel method.

λ_0 /µm	λ_i /µm	T_M	T_m	M	m_y	m	Δm	n_i	N	n_0	n_T	n
23.896	23.517	0.899	0.576	7.5	7.3	7	0.1213	2.720	2.819	2.817	2.064	2.703
22.411	22.043	0.904	0.584	8.0	7.8	7.5	0.1333	2.687	2.768	2.766	2.045	2.716
21.087	20.732	0.909	0.591	8.6	8.2	8	0.1440	2.671	2.739	2.737	2.031	2.726
19.934	19.579	0.915	0.597	8.3	8.7	8.5	0.1611	2.604	2.662	2.659	2.020	2.738
18.803	18.513	0.922	0.603	9.7	9.2	9	0.1466	2.804	2.857	2.855	2.012	2.734
17.880	17.584	0.928	0.607	9.8	9.7	9.5	0.1655	2.714	2.760	2.757	2.007	2.745
…	…											
3.040	2.991	0.935	0.539	57.8	57.6	57	0.9311	2.800	2.814	2.799	2.223	2.800
3.014	2.966	0.934	0.538	57.3	58.1	57.5	0.9341	2.808	2.822	2.807	2.224	2.800
2.988	2.941	0.934	0.538	58.4	58.6	58	0.9296	2.826	2.841	2.826	2.225	2.800
2.962	2.916	0.934	0.538	59.5	59.1	58.5	0.9392	2.824	2.839	2.824	2.226	2.800
2.938	2.891	0.933	0.537	60.7	59.6	59	0.9554	2.812	2.827	2.812	2.227	2.800
2.914	2.867	0.933	0.537	-	60.1	59.5	0.9717	2.800	2.816	2.800	2.229	2.801

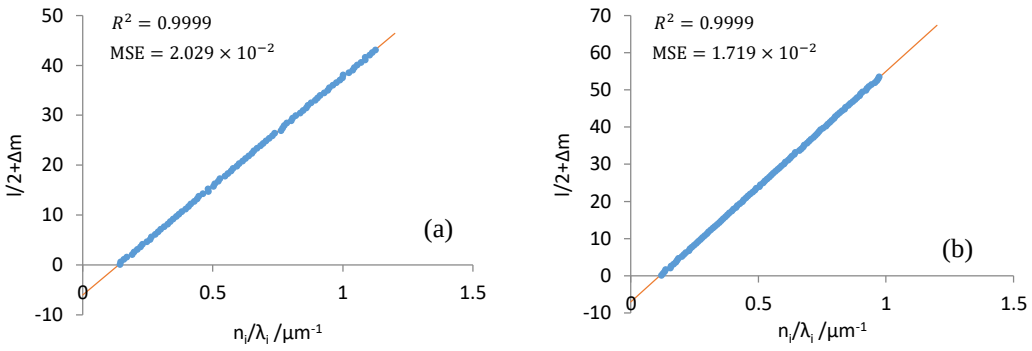


Figure 6.2- 5. . Plot of $\frac{l}{2} + \Delta m$ as a function of n_i/λ_i to determine the thickness d from the original Swanepoel method for (a) the $Ge_{16}As_{24}Se_{15.5}Te_{44.5}$ at. % (M140MINSCGDJ) thin film and (b) the $As_{40}Se_{60}$ at. % (M130MINSCGDJ) thin film.

The constants *a* and *b* were determined from Eq. (6.13), yielding the equation for $n(\lambda)$

$$n^2 = \frac{1.064}{\lambda^1} + 9.926 \quad \text{for } Ge_{16}As_{24}Se_{15.5}Te_{44.5} \text{ at. \%} \qquad (6.26)$$

$$n^2 = \frac{0.7057}{\lambda^1} + 7.591 \quad \text{for } As_{40}Se_{60} \text{ at. \%} \qquad (6.27)$$

6.2.3 Determining *n* from the dispersion equation for the $Ge_{16}As_{24}Se_{15.5}Te_{44.5}$ at. % and $As_{40}Se_{60}$ at. % thin films.

The values of *N* can be determined from Eq. (6.20) as shown in Tables 6.1-2 and 6.1-3. Iterating *x* in steps of 0.1 from 1 to 6 in Eq. (6.21), best fits to Eq. (6.21) in Figure 6.2-6 are obtained for *x* = 1:

$$N^2 = \frac{1.874}{\lambda^1} + 9.854. \quad \text{for } Ge_{16}As_{24}Se_{15.5}Te_{44.5} \text{ at. \%}$$

$$N^2 = \frac{7.7848\times10^{-1}}{\lambda^1} + 7.709. \quad \text{for } As_{40}Se_{60} \text{ at. \%}$$

For $Ge_{16}As_{24}Se_{15.5}Te_{44.5}$ at. %, the best fit in Figure 6.2-6 (a) yields $E = 1.874$ and $b = 9.854$ with $R^2 = 0.4500$ and $MSE = 3.358 \times 10^{-2}$. For $As_{40}Se_{60}$ at. %, the best fit in Figure 6.2-6 (b) yields $E = 7.7848 \times 10^{-1}$ and $b = 7.709$ with $R^2 = 0.2993$ and $MSE = 1.102 \times 10^{-2}$. The data points at longer wavelengths ($\lambda > 15\ \mu m, \frac{1}{\lambda} < 0.067\ \mu m^{-1}$) are scattered which is due to the effects of multi-phonon absorption bands of $Ge_{16}As_{24}Se_{15.5}Te_{44.5}$ at. % and $As_{40}Se_{60}$ at. %.

The values of *a* can be determined from Eq. (6.22) for $Ge_{16}As_{24}Se_{15.5}Te_{44.5}$ at. % and $As_{40}Se_{60}$ at. %. Then the equations for $n(\lambda)$ are:

$$n^2 = \frac{1.249}{\lambda^1} + 9.854. \quad \text{for } Ge_{16}As_{24}Se_{15.5}Te_{44.5} \text{ at. \%} \qquad (6.28)$$

$$n^2 = \frac{0.5190}{\lambda^1} + 7.709. \quad \text{for } As_{40}Se_{60} \text{ at. \%} \qquad (6.29)$$

Figure 6.2-7 show plots of $\frac{l}{2}$ as a function of n_0/λ_0. For $Ge_{16}As_{24}Se_{15.5}Te_{44.5}$ at. %, the slope of the straight line is 43.66 µm, yielding the value of the thin film thickness as 21.83 µm (target thickness: 20 µm). For $As_{40}Se_{60}$ at. %, the slope of the straight line is 61.82 µm, yielding the value of thickness as 30.91 µm (target thickness: 25 µm).

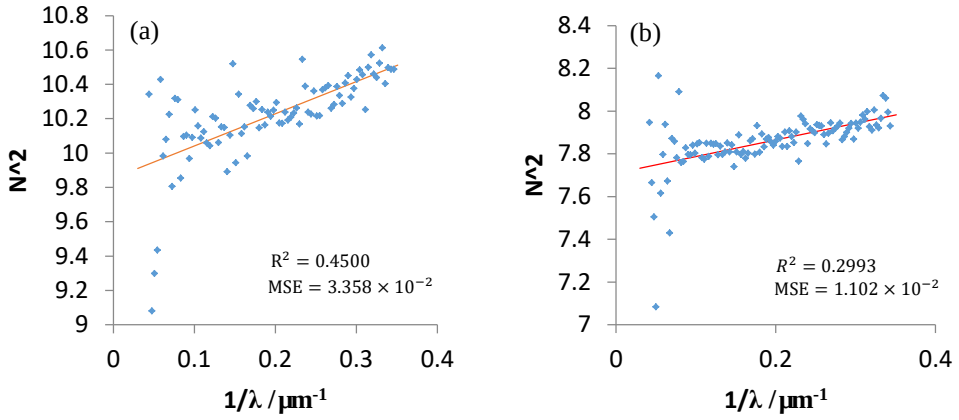


Figure 6.2- 6. Plot of the best fit for Eq. (6.21) to determine the constants *E* and *b* for (a) the $Ge_{16}As_{24}Se_{15.5}Te_{44.5}$ at. % (M140MINSCGDJ) thin film and (b) the $As_{40}Se_{60}$ at. % (M130MINSCGDJ) thin film.

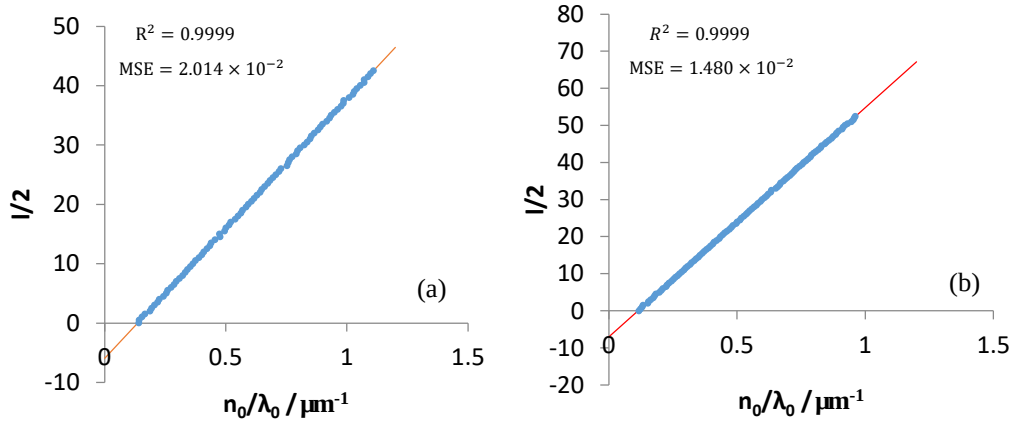


Figure 6.2- 7. Plots of $\frac{l}{2}$ as a function of n_0/λ_0 to determine the thickness *d* for (a) the $Ge_{16}As_{24}Se_{15.5}Te_{44.5}$ at. % (M140MINSCGDJ) thin film and (b) the $As_{40}Se_{60}$ at. % (M130MINSCGDJ) thin film.

6.2.4 Determining *n* from the transmittance of the interference spectrum for the $Ge_{16}As_{24}Se_{15.5}Te_{44.5}$ at. % and $As_{40}Se_{60}$ at. % thin films.

As described in section 6.1, the refractive index of a thin film can be determined using the envelopes around the maxima and minima of the transmission interference fringes according to Eq. (6.1). The values of $n(\lambda)$ determined from sections 6.2.2 and 6.2.3 are now compared with those obtained from the transmission values rather than the wavelengths at which extrema occur. To get the maximum and minimum transmittance values at each extreme, the envelopes of T_M and T_m were constructed to the normal-incidence transmittance spectrum presented in Figure 6.2-1, as shown in Figure 6.2-8. The values of T_M and T_m of $Ge_{16}As_{24}Se_{15.5}Te_{44.5}$ at. % (M140MINSCGDJ) and $As_{40}Se_{60}$ at. % (M130MINSCGDJ) at some wavelengths are shown in Tables 6.2-2 and 6.2-3. The values of n calculated from Eq. (6.1) for the $Ge_{16}As_{24}Se_{15.5}Te_{44.5}$ at. % and $As_{40}Se_{60}$ at. % stand-alone thin films are shown as n_T, using a value for the substrate refractive index of $s = 1$ (i.e. the thin film is in air).

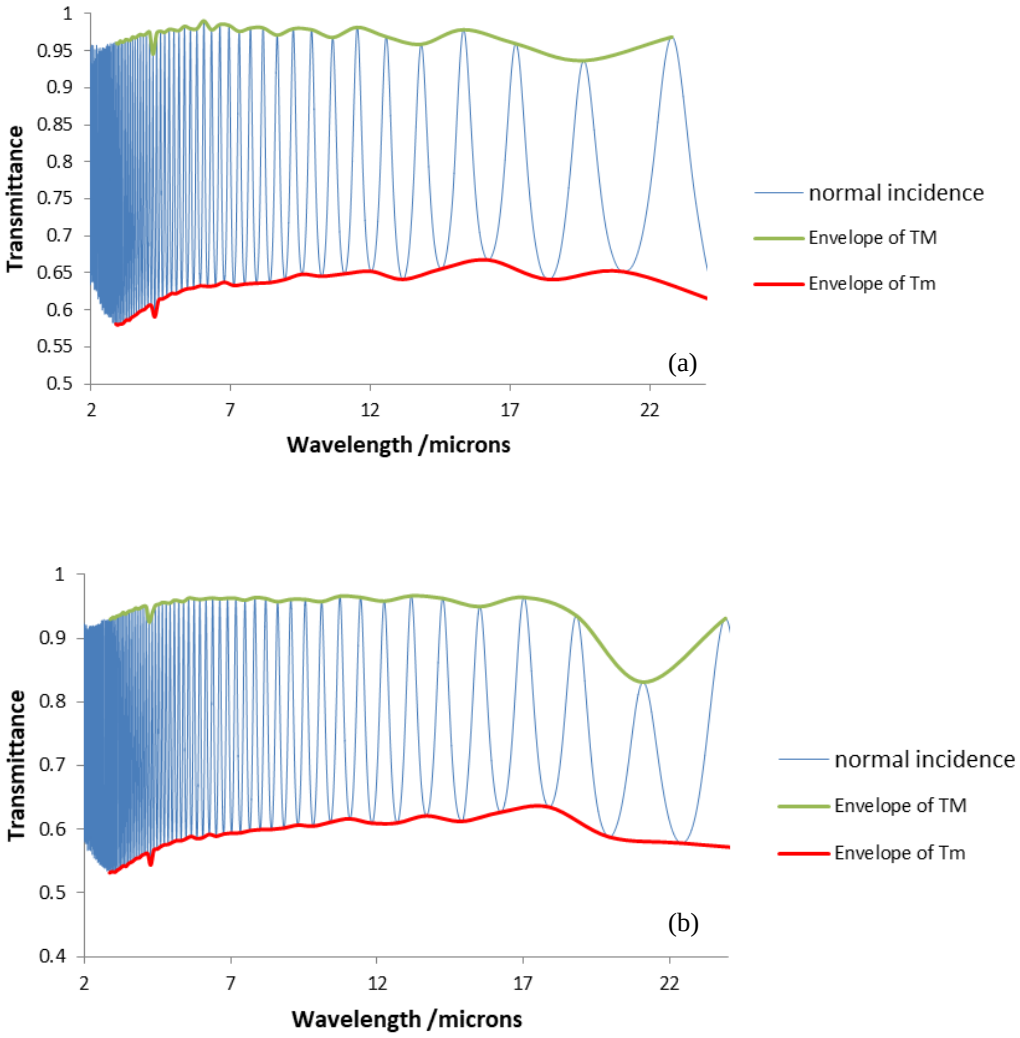


Figure 6.2- 8. The normal-incidence transmittance spectra of (a) the $Ge_{16}As_{24}Se_{15.5}Te_{44.5}$ at. % (M140MINSCGDJ) thin film and (b) the $As_{40}Se_{60}$ at. % (M130MINSCGDJ) thin film with the envelopes of T_M and T_m.

A best fit to Eq. (6.23), shown in Figure 6.2-9(a), yields an estimation to the order number for the first extreme of 4.8 and a slope of 64.74 μm for $Ge_{16}As_{24}Se_{15.5}Te_{44.5}$ at. %, yielding a value for d_T of

$d_T = 32.37\ \mu m.$ for $Ge_{16}As_{24}Se_{15.5}Te_{44.5}$ at. %

with R^2 = 0.9994 and *MSE* = 0.094. For $As_{40}Se_{60}$ at. %, a best fit to Eq. (6.12), shown in Figure 6.2-9(b) yields an estimation to the order number for the first extreme of 5.3 and a slope of 75.24 μm, yielding a value for d_T of

$d_T = 37.62\ \mu m.$ for $As_{40}Se_{60}$ at. %

The value of R^2 is 0.9992 and the mean standard error is 0.1976. Since the correct values of the order number of the first observable extreme have been shown in section 6.2.1 to be 6 for $Ge_{16}As_{24}Se_{15.5}Te_{44.5}$ at. % and 7 for $As_{40}Se_{60}$ at. %, the incorrect values of the order number of the first extreme determined here indicate that the transmittances presented in Figure 6.2-8 are not sufficient to provide accurate results. Both of the thicknesses determined here are higher than those determined in sections 6.2.2 (21. 84 μm for $Ge_{16}As_{24}Se_{15.5}Te_{44.5}$ at. % and 30.98 μm for $As_{40}Se_{60}$ at. %) and 6.2.3 (21. 83 μm for $Ge_{16}As_{24}Se_{15.5}Te_{44.5}$ at. % and 30.91 μm for $As_{40}Se_{60}$ at. %). In the case of a non-uniform hot-pressed thin film, the transmission spectra shrink and then lead to smaller values of T_M and larger values of T_m [6.2]. Eq. (6.1) then yields values of n_T that are too small, as shown in Table 6.2-2, and a value of d_T that is too large. Eq. (6.1) requires that T_M and T_m be measured to an accuracy of better than 0.5 % to yield an accuracy of 1 % in calculating n [6.1]. Moreover, Eq. (6.1) is valid only for homogeneous thin films with uniform thickness [6.7]. Even small inhomogeneities have a large influence on the experimental values of transmittance and can easily results in errors in determining the refractive index of up to 100 %. In this work, the transmission spectra were obtained from a FTIR spectrometer. The measured values of the transmittance are influenced by a careless background collection, material and air absorption bands in MIR region and the non-uniform thickness of the thin film. Due to the unacceptable large errors in n_T and d_T determined directly from the transmittance envelope, d_T cannot be taken into the calculation of the final thickness. However, this method can be used to indicate how nonuniform the thin film is.

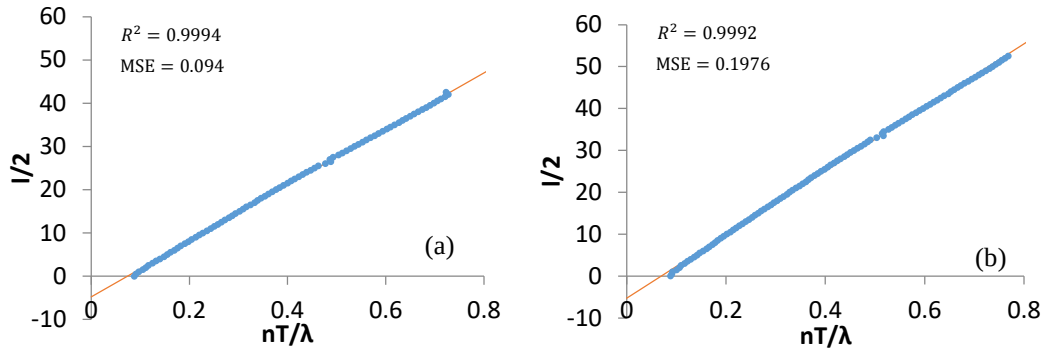


Figure 6.2- 9. Plot of *I/2* as a function of n_T/λ_0 for (a) the $Ge_{16}As_{24}Se_{15.5}Te_{44.5}$ at. % (M140MINSCGDJ) thin film and (b) the $As_{40}Se_{60}$ at. % (M130MINSCGDJ) thin film.

6.2.5 Determining the final thickness and refractive index of the $Ge_{16}As_{24}Se_{15.5}Te_{44.5}$ at. % and $As_{40}Se_{60}$ at. % thin films

The values of *x* for $Ge_{16}As_{24}Se_{15.5}Te_{44.5}$ at. % (M140MINSCGDJ) and $As_{40}Se_{60}$ at. % (M130MINSCGDJ) obtained in sections 6.2.2 and 6.2.3 are both 1. The Swanepoel method is sensitive to the calculated sample thickness, as indicated by Eq. (6.3). A 0.01 µm difference in thickness will lead to a refractive index difference of 0.0015 for the $Ge_{16}As_{24}Se_{15.5}Te_{44.5}$ at. % thin film and 0.0009 for the $As_{40}Se_{60}$ at. % thin film. For $Ge_{16}As_{24}Se_{15.5}Te_{44.5}$ at. %, the difference between the thickness obtained in section 6.2.2 and that obtained in section 6.2.3 is 0.01 µm which, as indicated, leads to a refractive index difference of ~ 0.0015. For $As_{40}Se_{60}$ at. %, the difference between the thickness obtained in section 6.2.2 and that obtained in section 6.2.3 is 0.07 µm which leads to a refractive index difference of ~ 0.006. Taking the average value for the thickness *d* of ~ 21.84 µm for $Ge_{16}As_{24}Se_{15.5}Te_{44.5}$ at. % and 30.95 µm for $As_{40}Se_{60}$ at. %, the final values of *n* can now be determined using Eq. (6.3), which were shown in the last column of Tables 6.2-2 and 6.2-3.

Fits of these final values to Eq. (6.2), as shown in Figures 6.2-10 for $Ge_{16}As_{24}Se_{15.5}Te_{44.5}$ at. % and 6.2-11 for $As_{40}Se_{60}$ at. %, yields

$$n^2 = \frac{0.9212}{\lambda^1} + 7.572 \quad \text{for } Ge_{16}As_{24}Se_{15.5}Te_{44.5} \text{ at. \%} \qquad (6.30\ a)$$

$$n^2 = \frac{0.9212}{\lambda^1} + 7.572. \quad \text{for } As_{40}Se_{60} \text{ at. \%} \qquad (6.30\ b)$$

with $R^2 = 0.8983$ for $Ge_{16}As_{24}Se_{15.5}Te_{44.5}$ at. % and $R^2 = 0.7763$ for $As_{40}Se_{60}$ at. %. For $Ge_{16}As_{24}Se_{15.5}Te_{44.5}$ at. %, the errors of the fit to data points over the wavelength range from 3 to 24 μm are within 0.2 % out to a wavelength of 16 μm, and then increase up to 0.8 % at the wavelength of 24 μm as the blue line shown in Figure 6.2-12. For $As_{40}Se_{60}$ at. %, the errors are within 0.5 % out to a wavelength of 17 μm and then increase up to 2 % at the wavelength of 24 μm as the red line shown in Figure 6.2-12. The poor fits in Figures 6.2-10 and 6.2-11 obtained using the original Swanepoel method indicate that the original dispersive equation in Eq. (6.2) is not appropriate to describe the refractive index dispersion of chalcogenide thin films in the MIR region. Therefore, in order to apply the Swanepoel method to determine the refractive index dispersion of chalcogenide glasses in MIR region, other dispersive equations are required.

The minimum deviation method using the setup in MIR Photonics Group, University of Nottingham, can determine the refractive index of chalcogenide glasses with a standard deviation of precision less than 0.001. As discussed in chapter 4, these results are taken as benchmark value. The refractive indices of the $Ge_{16}As_{24}Se_{15.5}Te_{44.5}$ at. % (M140MINSCGDJ) and $As_{40}Se_{60}$ at. % (M130MINSCGDJ) prisms at wavelengths of 3.1 and 3.8 μm are shown as red filled triangles in Figures 6.2-10 and 6.2-11. The difference in refractive index for $Ge_{16}As_{24}Se_{15.5}Te_{44.5}$ at. % between the results obtained from the minimum deviation measurements and those obtained from the original Swanepoel method is less than 0.0121 (0.38 %). The equivalent difference for $As_{40}Se_{60}$ at. % is less than 0.0017

(0.06%). However, due to the use of the "seemingly inappropriate" dispersive model which causes the poor fits to the experimental data in Figures 6.2-4, 6.2-6 6.2-10 and 6.2-11, the results of refractive index and thickness cannot be trusted.

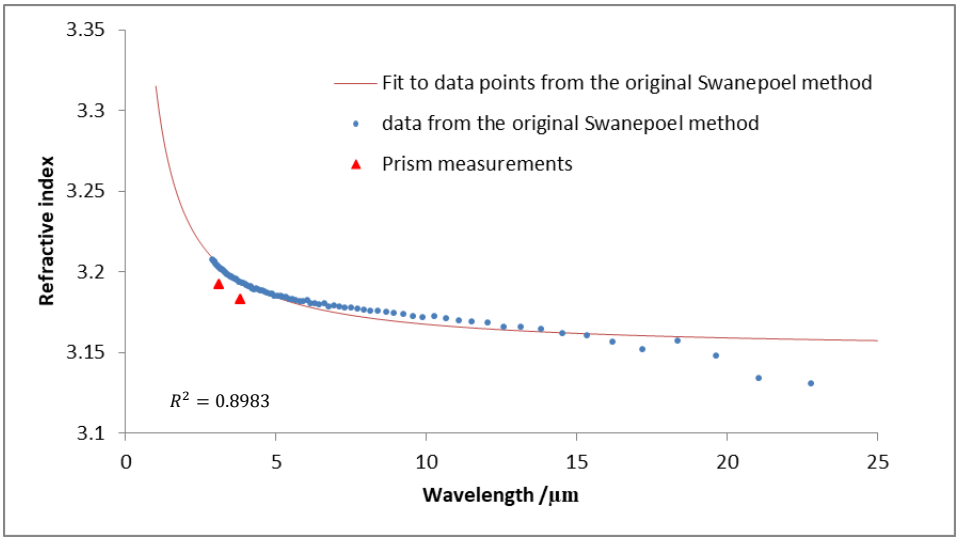


Figure 6.2- 10. The fit to the final refractive index (temperature of the measurements: 23.1 ± 0.5 ℃) of $Ge_{16}As_{24}Se_{15.5}Te_{44.5}$ at. % (M140MINSCGDJ) from the original Swanepoel method compared to the bench mark obtained from the prism measurements at 3.1 and 3.8 μm (see Table 4-11 in section 4.4.1) shown as red filled triangles.

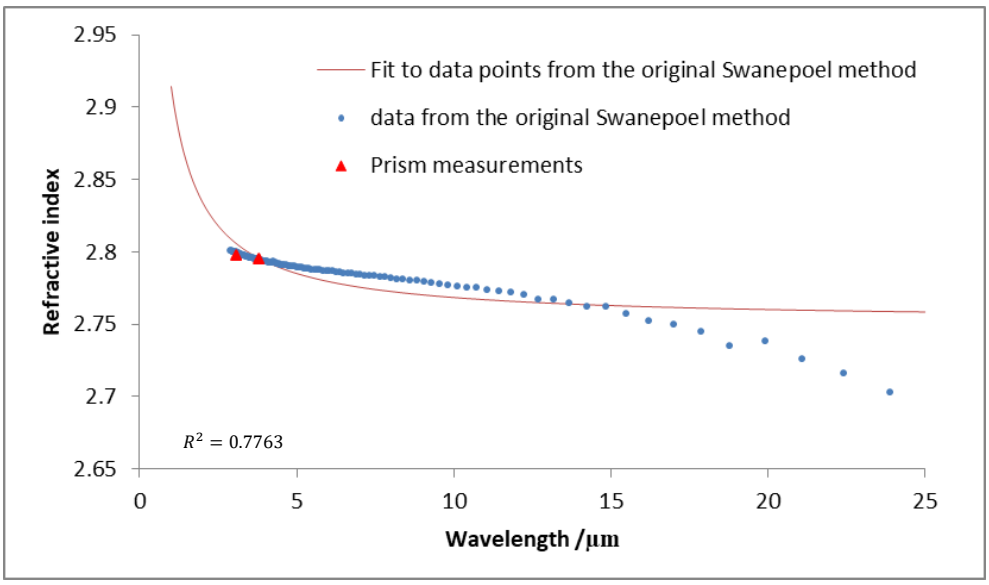


Figure 6.2-11. The fit to the final refractive index (temperature of the measurements: 23.1 ± 0.5 ℃) of $As_{40}Se_{60}$ at. % (M130MINSCGDJ) from the original Swanepoel method compared to the bench mark obtained from the prism measurements at 3.1 and 3.8 μm (see Table 4-10 in section 4.4.1) shown as red filled triangles.

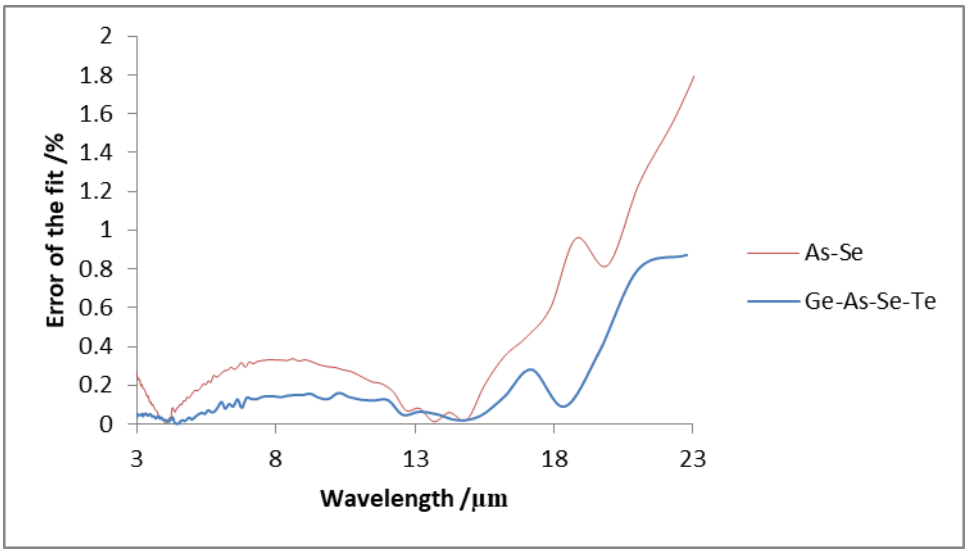


Figure 6.2- 12. Errors of the fits to the final refractive index values for the $Ge_{16}As_{24}Se_{15.5}Te_{44.5}$ at. % (Ge-As-Se-Te) (M140MINSCGDJ) and $As_{40}Se_{60}$ at. % (As-Se) (M130MINSCGDJ) thin films.

6.3 Modifying the Swanepoel method by using three-term Cauchy, one-term Sellmeier and two-term Sellmeier models.

The poor fittings to experimental data illustrated in Figures 6.2-4, 6.2-6 and 6.2-10 in section 6.2 indicate that the Cauchy dispersive equation used in the original Swanepoel method is not appropriate to describe the refractive index dispersion of chalcogenide glasses in the MIR region. Therefore, the values of thickness and refractive index determined from the original Swanepoel method cannot be trusted at MIR wavelengths. In order to extend this method into the MIR region, other dispersive models are required.

Section 5.4.1 confirmed that three-term Cauchy, one-term Sellmeier and two-term Sellmeier models are suitable refractive index models for chalcogenide glasses over the wavelength range from the lower wavelength edge of the transparent window to 2.5 µm compared to the two-term Cauchy model. Therefore, in order to apply the Swanepoel method to determine the refractive index of chalcogenide glasses within

this wavelength range, three-term Cauchy, one-term Sellmeier and two-term Sellmeier models will be used to modify the original Swanepoel method.

Section 5.4.2 confirmed that the two-term Sellmeier model is sufficient to determine the refractive index of chalcogenide glasses over their whole transparent windows (the wavelength range of the thin film measurements (3 – 25 μm) are typically within the transparent windows of chalcogenide glasses, as discussed in section 5.3). Therefore, the original Swanepoel method will be modified by using a two-term Sellmeier model as the dispersive equation. By successfully determining the refractive index of $As_{40}Se_{60}$ at. % (melting code: M130MINSCGDJ; hot pressing code: YRFFP003) and $Ge_{16}As_{24}Se_{15.5}Te_{44.5}$ at. % (melting code: M140MINSCGDJ; hot pressing code: YRFFP007) in the MIR region in this section, this method will be referred to **the improved Swanepoel method**.

6.3.1 The basic theory of the modified Swanepoel method by using the three-term Cauchy, one-term Sellmeier and two-term Sellmeier models

In this sub-section, the three-term Cauchy, one-term Sellmeier and two-term Sellmeier models are used as the dispersive equation instead of Eq. (6.2) in order to modify the original Swanepoel method.

The three-term Cauchy equation used as the dispersion equation was

$$n^2(\lambda) = \frac{a}{\lambda^{2x}} + \frac{b}{\lambda^x} + c \qquad (6.31)$$

where $n(\lambda)$ is the refractive index as a function of wavelength, and a, b and c are coefficients that can be determined for a material by fitting the equation to measured refractive indices at known wavelengths. Following [6.1], the three-term Cauchy model was altered to have an extra fitting parameter x in order to have a better fit.

The one-term Sellmeier equation is:

$$n^2(\lambda) = a + \frac{b\lambda^2}{\lambda^2 - a_1^2}, \qquad (6.32)$$

where a and b are dimensionless fitting coefficients (different from those which appear in Eq. (6.31)) and a_1 indicates the single resonant absorption wavelength assumed in the model.

The two-term Sellmeier Equation is given in Eq. (6.33):

$$n^2(\lambda) = a + \frac{b\lambda^2}{\lambda^2 - a_1^2} + \frac{c\lambda^2}{\lambda^2 - a_2^2}, \qquad (6.33)$$

where a, b and c are dimensionless fitting coefficients. a_1 and a_2 indicate the two resonant absorption wavelengths assumed in the model.

All the steps of the Swanepoel method are similar to those described in section 6.1. Due to the different dispersive models, some expressions of the equations will appear in modified forms as indicated below.

Method A (Determining n from the order numbers m):

Substitutions of Eqs. (6.31), (6.32) and (6.33) into (6.2) yield:

$$Three - term\ Cauchy: \qquad m^2\lambda_0^2 = \frac{A}{\lambda_0^{2x}} + \frac{B}{\lambda_0^x} + C, \qquad (6.34)$$

$$One - term\ Sellmeier: \qquad m^2\lambda_0^2 = A + \frac{B\lambda^2}{\lambda^2 - a_1^2}, \qquad (6.35)$$

$$Two - term\ Sellmeier: \qquad m^2\lambda_0^2 = A + \frac{B\lambda^2}{\lambda^2 - a_1^2} + \frac{C\lambda^2}{\lambda^2 - a_2^2}, \qquad (6.36)$$

where:

$$A = 4ad^2; \quad B = 4bd^2; \; C = 4cd^2. \qquad (6.37)$$

The order numbers *m* at each extreme are required before the fitting coefficients in the dispersive models can be determined. The intermediate quantity *M* is given in Eq. (6.8). In the dispersive case, the dispersions of *M* were represented by the approximation forms [6.1]:

$$Three-term\ Cauchy: \qquad M=\frac{C}{\lambda_0}\left(1+\frac{D_1}{\lambda_0^{y}}+\frac{D_2}{\lambda_0^{2y}}\right) \tag{6.38}$$

$$One-term\ Sellmeier: \qquad M=\frac{E_1}{\lambda_0}\left(1+\frac{F_1}{1-(\frac{b_1}{\lambda_0})^2}\right) \tag{6.39}$$

$$Two-term\ Sellmeier: \qquad M=\frac{E_2}{\lambda_0}\left(1+\frac{F_2}{1-(\frac{b_1}{\lambda_0})^2}+\frac{G_2}{1-(\frac{b_2}{\lambda_0})^2}\right) \tag{6.40}$$

where *C*, D_1 and D_2 are the fitting parameters in Eq. (6.38). For Eqs. (6.39) and (6.40), E_1, F_1, E_2, F_2 and G_2 are the dimensionless coefficients. b_1 and b_2 indicate the absorption wavelengths. For the one-term Sellmeier model, b_1 indicates the optical bandgap electronic absorption wavelength, while, for the two-term Sellmeier model, b_1 and b_2 are associated with optical bandgap electronic absorption and vibrational band resonance absorption, respectively. The first term in Eqs. (6.38), (6.39) and (6.40) reflects the $1/\lambda$ relation between *m* and λ according to Eq. (6.3). In Eq. (6.38) and (6.40), the second and third terms in parentheses approximate the effect of dispersion while, in Eq. (6.39), the second term in parentheses describes the effect of dispersion. Other forms of Eqs. (6.38), (6.39) and (6.40) are used to determine the best fits to experimental data:

$$Three-term\ Cauchy: \qquad M\lambda_0=C+\frac{D_1}{\lambda_0^{y}}+\frac{D_2}{\lambda_0^{2y}} \tag{6.41}$$

$$One-term\ Sellmeier: \qquad M\lambda_0=E_1+\frac{F_1}{1-(\frac{b_1}{\lambda_0})^2} \tag{6.42}$$

$$Two-term\ Sellmeier: \qquad M\lambda_0=E_2+\frac{F_2}{1-(\frac{b_1}{\lambda_0})^2}+\frac{G_2}{1-(\frac{b_2}{\lambda_0})^2}. \tag{6.43}$$

The fitting coefficients determined the best fits of Eqs. (6.41), (6.42) and (6.43) to experimental data. The values of m at each extreme for three-term Cauchy and one-term Sellmeier models are now approximately given by:

$$Three-term\ Cauchy: \qquad m = \frac{C}{\lambda_0} \tag{6.44}$$

$$One-term\ Sellmeier: \qquad m = \frac{E_1+F_1}{\lambda_0} \tag{6.45}$$

For the two-term Sellmeier model, when the measurement spectrum is close to the wavelength of b_1, the main dispersive term is the second term in Eq. (6.43). The value of m at each extreme is approximated by:

$Two-term\ Sellmeier, wavelength\ close\ to\ b_1$:

$$m \cong \left(E_2 + \frac{G_2}{1-\left(\frac{b_2}{\lambda_0}\right)^2}\right)/\lambda_0. \tag{6.46}$$

When the measurement spectrum is close to the wavelength of b_2, the main dispersive term is the third term in Eq. (6.43). The value of m at each extreme is approximated by:

$Two-term\ Sellmeier, wavelength\ close\ to\ b_2$:

$$m \cong \left(E_2 + \frac{F_2}{1-\left(\frac{b_1}{\lambda_0}\right)^2}\right)/\lambda_0 \tag{6.47}$$

Substitution of Eqs. (6.31), (6.32) and (6.33) into Eq. (6.5), using Eqs. (6.34), (6.35) and (6.36) respectively, and solving for Δm yields:

$Three-term\ Cauchy$:

$$\Delta m = [m^2 \frac{\lambda_o^2}{\lambda_i^2} + \frac{A}{\lambda_i^2}(\frac{1}{\lambda_i^{2x}} - \frac{1}{\lambda_0^{2x}}) + \frac{\mathrm{B}}{\lambda_i^2}(\frac{1}{\lambda_i^x} - \frac{1}{\lambda_0^x})]^{1/2} - m, \quad (6.48)$$

$One-term\ Sellmeier$:

$$\Delta m = [m^2 \frac{\lambda_o^2}{\lambda_i^2} + \frac{B}{\lambda_i^2}(\frac{1}{1-(\frac{a_1}{\lambda_i})^2} - \frac{1}{1-(\frac{a_1}{\lambda_0})^2})]^{1/2} - m, \quad (6.49)$$

$Two-term\ Sellmeier$:

$$\Delta m = [m^2 \frac{\lambda_o^2}{\lambda_i^2} + \frac{B}{\lambda_i^2}(\frac{1}{1-(\frac{a_1}{\lambda_i})^2} - \frac{1}{1-(\frac{a_1}{\lambda_0})^2}) + \frac{\mathrm{C}}{\lambda_i^2}(\frac{1}{1-(\frac{a_2}{\lambda_i})^2} - \frac{1}{1-(\frac{a_2}{\lambda_0})^2})]^{1/2} - m. \quad (6.50)$$

The value of n_i at each wavelength for the different dispersive models can be calculated using Eqs. (6.48), (6.49), (6.50), (6.6) and (6.7).

The values of thickness can be determined by the plots of Eq. (6.15).

Method B (Determining n from the dispersion equation):

Expanding n_i^2 in a Taylor series around n_0 in Eqs, (6.31), (6.32) and (6.33) yields:

$Three-term\ Cauchy$:

$$n_i^2 = n_0^2 + \frac{2ax}{\lambda_0^{2x+1}}(\lambda_0 - \lambda_i) + \frac{bx}{\lambda_0^{x+1}}(\lambda_0 - \lambda_i), \quad (6.51)$$

$One-term\ Sellmeier$:

$$n_i^2 = n_0^2 - \frac{2ba_1^2\lambda_i}{({\lambda_i}^2 - a_1^2)^2}(\lambda_0 - \lambda_i), \quad (6.52)$$

$Two-term\ Sellmeier$:

$$n_i^2 = n_0^2 - \frac{2ba_1^2\lambda_i}{({\lambda_i}^2 - a_1^2)^2}(\lambda_0 - \lambda_i) - \frac{2ca_2^2\lambda_i}{({\lambda_i}^2 - a_2^2)^2}(\lambda_0 - \lambda_i). \quad (6.53)$$

Substitutions of Eqs. (6.51), (6.52) and (6.53) into Eq. (6.17) yield:

$Three-term\ Cauchy$:

$$n_0^2 = N^2 - \frac{2ax}{\lambda_0^{2x-1}(\lambda_0+\lambda_i)} - \frac{bx}{\lambda_0^{x-1}(\lambda_0+\lambda_i)}, \quad (6.54)$$

$One-term\ Sellmeier$:

$$n_0^2 = N^2 - \frac{2ba_1^2\lambda_i\lambda_0^2}{\left(\lambda_i{}^2-a_1^2\right)^2(\lambda_0+\lambda_i)}, \quad (6.55)$$

$Two-term\ Sellmeier$:

$$n_0^2 = N^2 - \frac{2ba_1^2\lambda_i\lambda_0^2}{\left(\lambda_i{}^2-a_1^2\right)^2(\lambda_0+\lambda_i)} - \frac{2ca_2^2\lambda_i\lambda_0^2}{\left(\lambda_i{}^2-a_2^2\right)^2(\lambda_0+\lambda_i)}, \quad (6.56)$$

where N was defined in Eq. (6.20). N^2 can be represented by other forms for the different models by combining Eq. (6.31) and Eq. (6.54), Eq. (6.32) and Eq. (6.55), Eq. (6.33) and Eq. (6.56):

$Three-term\ Cauchy$: $$N^2 = \frac{D_1}{\lambda^{2x}} + \frac{D_2}{\lambda^x} + c, \quad (6.57)$$

$One-term\ Sellmeier$: $$N^2 = a + \frac{F_1\lambda^2}{\lambda^2-a_1^2}, \quad (6.58)$$

$Two-term\ Sellmeier$: $$N^2 = a + \frac{F_2\lambda^2}{\lambda^2-a_1^2} + \frac{G_2\lambda^2}{\lambda^2-a_2^2}. \quad (6.59)$$

The best fits of Eqs. (6.57), (6.58) and (6.59) to experimental data yield the fitting coefficients in the equations. For the three-term Cauchy model, from Eqs. (6.31), (6.57) and (6.54), the expressions for *a* and *b* are shown in Eq. (6.60). For the one-term Sellmeier model, the expression for *b* can be determined in Eq. (6.61) using Eqs. (6.32), (6.58) and (6.55). For the two-term Sellmeier model, the equations of *b* and *c* can be obtained from Eq. (6.33), (6.59) and (6.56), as shown in Eq. (6.62).

$Three-term\ Cauchy$:

$$a = \frac{D_1(\lambda_0+\lambda_i)}{(2x+1)\lambda_0+\lambda_i},\ b = \frac{D_2(\lambda_0+\lambda_i)}{(x+1)\lambda_0+\lambda_i}; \tag{6.60}$$

$One-term\ Sellmeier$:

$$b = F_1/[1+\frac{2a_1^2\lambda_i}{({\lambda_i}^2-a_1^2)(\lambda_0+\lambda_i)}]; \tag{6.61}$$

$Two-term\ Sellmeier$:

$$b = F_2/[1+\frac{2a_1^2\lambda_i}{({\lambda_i}^2-a_1^2)(\lambda_0+\lambda_i)}],\quad c = G_2/[1+\frac{2a_2^2\lambda_i}{({\lambda_i}^2-a_2^2)(\lambda_0+\lambda_i)}]. \tag{6.62}$$

The values of n_0 can now be determined from Eqs. (6.54), (6.55) and (6.56). The values of thickness can be determined by the plots of Eq. (6.23).

6.3.2 Determining the refractive index of $As_{40}Se_{60}$ at. % thin film over the wavelength range from 0.7 to 2 μm using the modified Swanepoel methods.

The refractive index and average thickness of a thermally evaporated $As_{40}Se_{60}$ at. % thin film over the wavelength range from 0.7 to 2 μm was determined by Corrales *et al.* [6.2] to an accuracy better than 3 % using the original Swanepoel method [6.1]. In this section, the results of [6.2] are reproduced; the modified Swanepoel methods using three different models outlined in the previous sub-section (three-term Cauchy, one-term Sellmeier and two-term Sellmeier models) are then applied to determine the refractive index and thickness of the $As_{40}Se_{60}$ at. % thin film using the data in [6.2]. The comparisons between these four methods are presented in this section.

6.3.2.1 Determining n from the order number m for $As_{40}Se_{60}$ at. % thin film using the data from Corrales et al. [6.2]

The wavelengths λ_0 at extremes of the normal-incidence spectrum in [6.2] are shown in Table 6.3-1. The values of λ_0 (see Table 6.3-1) were used to determine

the quantity M of the $As_{40}Se_{60}$ at. % thin film in [6.2] according to Eq. (6.8); the values of M are shown in Table 6.3-1.

Best fits of Eq. (6.38), (6.39) and (6.40) to experimental data were plotted to obtain the values of m at each extreme as shown in Figure 6.3-1 yielding:

$$Original\ (two-term\ Cauchy):\ M\lambda_0 = 0.6524 + \frac{4.144}{\lambda_0^3}$$

$$Three-term\ Cauchy:\quad M\lambda_0 = 02568 + \frac{0.4439}{\lambda_0^2} + \frac{4.094}{\lambda_0^4}$$

$$One-term\ Sellmeier:\quad M\lambda_0 = 0.4894 + \frac{3.547}{1-(\frac{0.4225}{\lambda_0})^2}$$

$$Two-term\ Sellmeier:\quad M\lambda_0 = -2.782 + \frac{6.640}{1-\left(\frac{0.3464}{\lambda_0}\right)^2} - \frac{169.5}{1-(\frac{63.87}{\lambda_0})^2}.$$

For the best fit using the original Swanepoel method, as shown in Figure 6.3-1(a), the value of R^2 is 0.9407 and the value of *MSE* is 1.573×10^{-2} with y = 3.0. For the Swanepoel method modified by using three-term Cauchy model, the best fit in Figure 6.3-1(b) yields $R^2 = 0.9399$ and $MSE = 1.573 \times 10^{-2}$. For the Swanepoel method modified by using the one-term Sellmeier model, the best fit in Figure 6.3-1(b) yields $R^2 = 0.9379$ and $MSE = 1.648 \times 10^{-2}$. The best fit obtained from the Swanepoel method modified by using two-term Sellmeier model in Figure 6.3-1(d) yields $R^2 = 0.9390$ and $MSE = 1.618 \times 10^{-2}$.

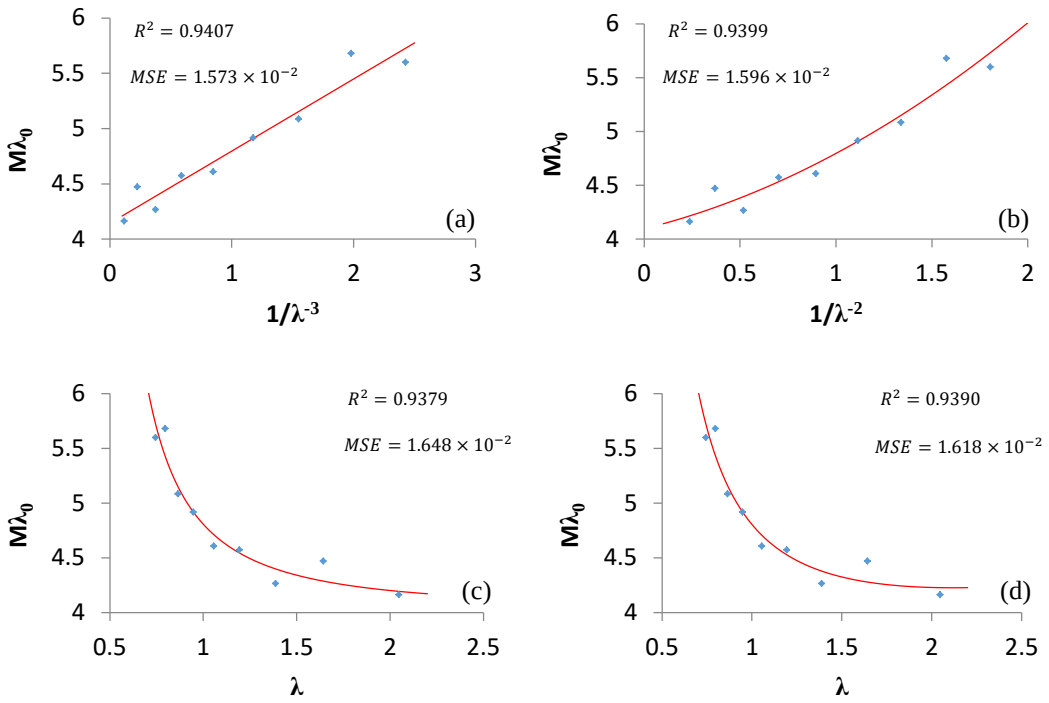


Figure 6.3- 1. Plot of $M\lambda_0$ as a function of n_0/λ_0 using the experimental data of Corrales *et al.* [6.2] to determine the quantity M from the Swanepoel method using (a) the original dispersive model, (b) three-term Cauchy model, (c) one-term Sellmeier model and (d) two-term Sellmeier model.

The values of m can then be determined by Eqs. (6.10), (6.44), (6.45) and (6.46) as shown in Table 6.3-1. From Table 6.3-1, it is found that these four methods can all determine the correct order numbers at each extreme of the $As_{40}Se_{60}$ at. % thin film in the experimental wavelength range considered in [6.2] (over the wavelength range from ~ 0.7 μm to ~ 2 μm).

Table 6.3- 1. The values of *M* and order numbers *m* obtained from the original and modified Swanepoel methods applied to the experimental data of Corrales *et al.* [6.2].

λ_0 /μm	M	m (original)	m (three-term Cauchy)	m (one-term Sellmeier)	m (two-term Sellmeier)	m
2.0478	2.0	2.0	2.0	2.0	2.0	2
1.6435	2.7	2.5	2.5	2.5	2.4	2.5
1.3883	3.1	3.0	3.0	2.9	2.8	3
1.194	3.8	3.5	3.4	3.4	3.3	3.5
1.0561	4.4	3.9	3.9	3.8	3.7	4
0.9475	5.2	4.4	4.3	4.3	4.1	4.5
0.8642	5.9	4.8	4.7	4.7	4.5	5
0.7965	7.1	5.2	5.1	5.1	4.9	5.5
0.7443	7.5	5.6	5.5	5.4	5.2	6
0.6979	-	5.9	5.9	5.8	5.6	6.5

The correct values of *m* are used in Eqs. (6.12), (6.34), (6.35) and (6.36). The best fits are shown in Figure 6.3-2 for the four different dispersive models yielding:

$$Original\ (two-term\ Cauchy):\ \ m^2{\lambda_0}^2 = \frac{1.320}{{\lambda_0}^3} + 16.67 \qquad (6.63)$$

$$Three-term\ Cauchy:\ \ m^2\lambda_0^2 = \frac{0.493}{\lambda_0^4} + \frac{0.945}{\lambda_0^2} + 16.560, \qquad (6.64)$$

$$One-term\ Sellmeier:\ \ m^2\lambda_0^2 = 9.889 + \frac{6.594\lambda^2}{\lambda^2 - 0.4328^2}, \qquad (6.65)$$

$$Two-term\ Sellmeier:\ \ m^2\lambda_0^2 = 11.23 + \frac{5.406\lambda^2}{\lambda^2 - 0.4551^2} + \frac{148\lambda^2}{\lambda^2 - 61.87^2}, \qquad (6.66)$$

The fitting coefficients in Eq. (6.63) are the same as those in [6.2] and the fit is shown in Figure 6.3-2(a) with $R^2 = 0.9957$ and $MSE = 6.440 \times 10^{-3}$. For Eq. (6.64), the fitting quality was slightly improved by changing the dispersive model

from a two-term Cauchy model to a three-term Cauchy model as shown in Figure 6.3-2(b). The fitting quality was further improved by using a one-term Sellmeier model with $R^2 = 0.9968$ and $MSE = 4.788 \times 10^{-3}$ as shown in Figure 6.3-2(c). From Figure 6.3-2, the best fit was provided by the two-term Sellmeier model with $R^2 = 0.9970$ and $MSE = 4.500 \times 10^{-3}$, as shown in Figure 6.3-2(d).

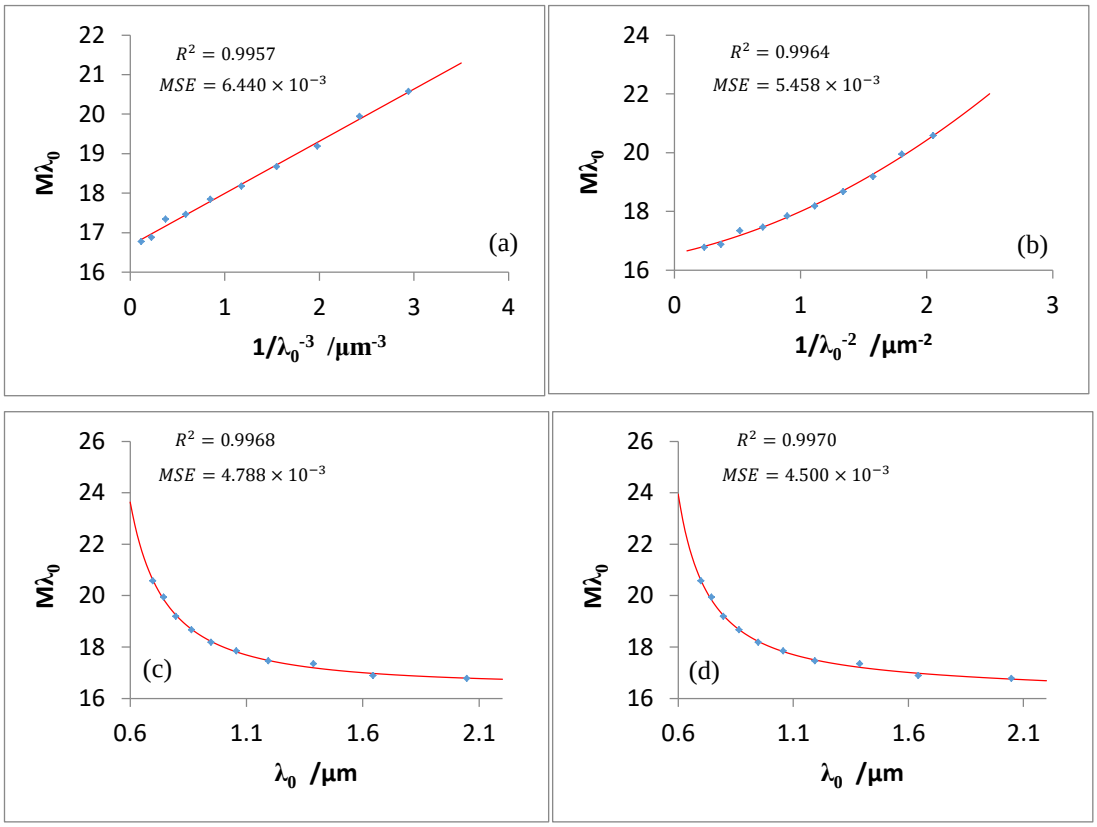


Figure 6.3- 2. Best fits to (a) Eq. (6.12), (b) Eq. (6.34), (c) Eq. (6.35) and (d) Eq. (6.36) using the data from Corrales *et al.* [6.2] for the $As_{40}Se_{60}$ at. % thin film.

The values of Δm were calculated from Eqs. (6.14), (6.48), (6.49) and (6.50) as listed in Table 6.3-2. The Δm reproduced here is the same as that presented in [6.2]. The agreement between these four different dispersive models is better than 5 %.

The values of n_i were then calculated from Eqs. (6.6) and (6.7) with the agreement better than 2.3 %, as shown in Table 6.3-3. From Tables 6.3-2 and 6.3-3, it is found that the difference of Δm and n_i increased as the wavelength decreased, which

indicates that the Sellmeier models are more wavelength sensitive than the Cauchy models when the wavelength is close to the optical bandgap.

Table 6.3- 2. The values of Δm determined from the Swanepoel method with the four different dispersive models using the data from Corrales *et al.* [6.2].

λ_0 /μm	λ_i /μm	m	Δm (original)	Δm (three-term Cauchy)	Δm (one-term Sellmeier)	Δm (two-term Sellmeier)
2.0478	2.0478	2	0.0366	0.0367	0.0368	0.0371
1.6435	1.6435	2.5	0.0455	0.0456	0.0457	0.0459
1.3883	1.3883	3	0.0537	0.0537	0.0538	0.0539
1.1940	1.194	3.5	0.0611	0.0611	0.0611	0.0610
1.0561	1.0561	4	0.0675	0.0674	0.0672	0.0671
0.9475	0.9475	4.5	0.0725	0.0723	0.0720	0.0718
0.8642	0.8642	5	0.0788	0.0787	0.0784	0.0782
0.7965	0.7965	5.5	0.0803	0.0804	0.0803	0.0803
0.7443	0.7443	6	0.0822	0.0827	0.0833	0.0836
0.6979	0.6979	6.5	0.0836	0.0845	0.0866	0.0875

Table 6.3- 3. The values of n_i determined from the Swanepoel method with the four different dispersive models using the data from Corrales *et al.* [6.2].

λ_0 /μm	λ_i /μm	m	n_i (original)	n_i (three-term Cauchy)	n_i (one-term Sellmeier)	n_i (two-term Sellmeier)
2.0478	2.0115	2	2.649	2.645	2.642	2.632
1.6435	1.6149	2.5	2.657	2.654	2.651	2.646
1.3883	1.3649	3	2.678	2.677	2.675	2.674
1.1940	1.1748	3.5	2.710	2.711	2.711	2.713
1.0561	1.0401	4	2.756	2.759	2.762	2.765
0.9475	0.9342	4.5	2.819	2.822	2.828	2.832
0.8642	0.8527	5	2.849	2.851	2.857	2.860
0.7965	0.7870	5.5	2.959	2.957	2.958	2.958
0.7443	0.7362	6	3.051	3.043	3.032	3.026
0.6979	0.6910	6.5	3.147	3.130	3.094	3.077

Plots of $\frac{l}{2} + \Delta m$ as a function of n_i/λ_i are shown in Figure 6.3-3 to determine the thickness of the $As_{40}Se_{60}$ at. % thin film. From Figure 6.3-3(a), the gradient of the plot is 1.493 μm yielding the thickness of the $As_{40}Se_{60}$ at. % thin film as 0.747 μm; this value is given as 0.758 μm in [6.2]. Applying the three-term Cauchy model as the dispersive model, the value of R^2 was improved from 0.9940 to 0.9950 and *MSE* was reduced from 1.259×10^{-2} to 1.060×10^{-2}, as shown in Figure 6.3-3(b). The thickness was determined to be 0.748 μm. For the one- term Sellmeier model, the plot of $\frac{l}{2} + \Delta m$ as a function of n_i/λ_i is shown in Figure 6.3-3(c) yielding the value of thickness as 0.750 μm with $R^2 = 0.9965$ and $MSE = 7.392 \times 10^{-3}$. The fitting quality in Figure 6.3-3(c) is better than those in Figures 6.3-3(a) and 6.3-3(b). For the two-term Sellmeier model, the plot provides the best fit to the data with $R^2 = 0.9965$ and $MSE = 7.392 \times 10^{-3}$, as shown in Figure

6.3-3(d), yielding the thickness as 0.751 μm. The agreement between the values of thickness determined from the Swanepoel method using the four different dispersive models is better than 0.53 % over the wavelength range from ~ 0.7 μm to ~ 2 μm.

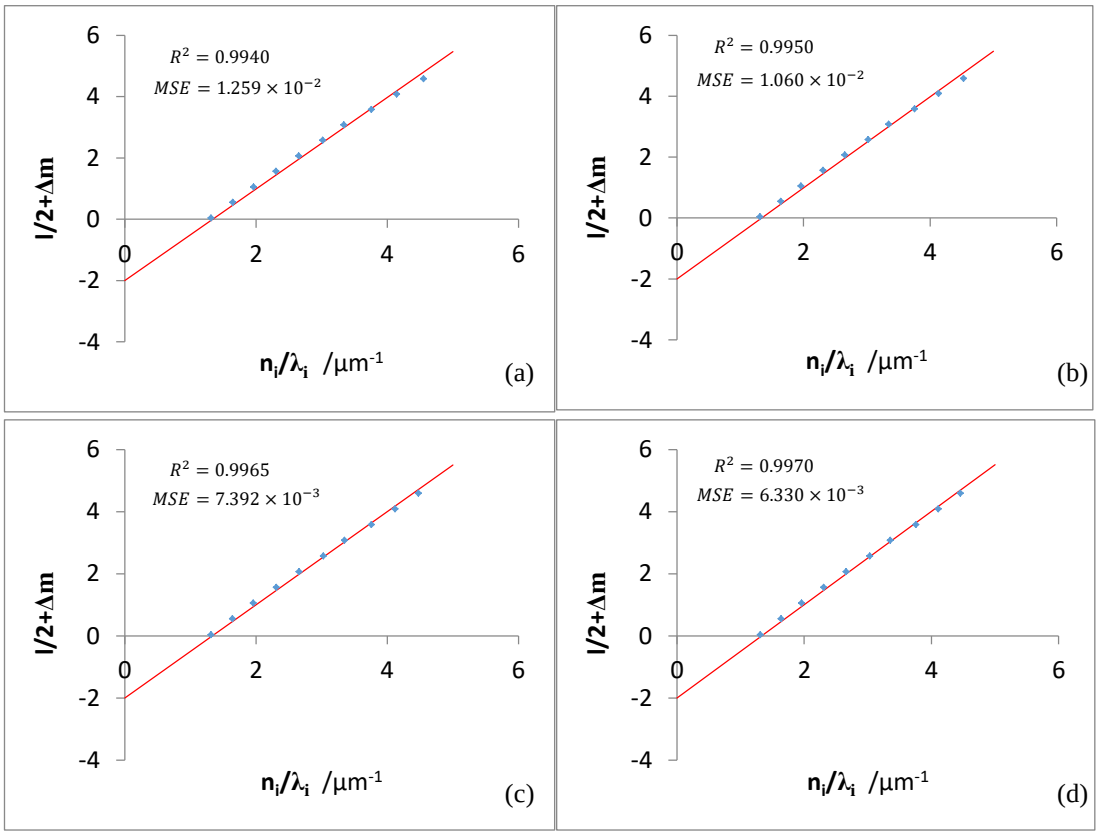


Figure 6.3- 3. Plot of $l/2 + \Delta m$ as a function of n_i/λ_i using the data in [6.2] to determine the thickness d from the Swanepoel method using (a) original dispersive model; (b) three-term Cauchy model; (c) one-term Sellmeier model; (d) two-term Sellmeier model.

The constants in Eqs. (6.2), (6.31), (6.32) and (6.33) can now be all determined yielding:

$$Original\ (two-term\ Cauchy):\quad n^2(\lambda) = \frac{5.922\times10^{-1}}{\lambda^3} + 7.479 \qquad (6.67)$$

$$Three-term\ Cauchy:\quad n^2(\lambda) = \frac{2.204\times10^{-1}}{\lambda^4} + \frac{4.226\times10^{-1}}{\lambda^2} + 7.403 \qquad (6.68)$$

$$One-term\ Sellmeier:\quad n^2(\lambda) = 4.396 + \frac{2.931\lambda^2}{\lambda^2 - 0.4328^2} \qquad (6.69)$$

$$Two-term\ Sellmeier: \quad n^2(\lambda) = 4.978 + \frac{2.396\lambda^2}{\lambda^2 - 0.4551^2} + \frac{6.339\lambda^2}{\lambda^2 - 61.87^2}, \qquad (6.70)$$

6.3.2.2 Determining n from the dispersion equation for the $As_{40}Se_{60}$ at. % thin film using the data from Corrales et al. [6.2]

The values of N can be determined from Eq. (6.20) as shown in Table 6.3-4. The best fits to Eqs. (6.21), (6.57), (6.58) and (6.59), as shown in Figure 6.3-4, yield:

$$Original\ (two-term\ Cauchy): \quad N^2 = \frac{1.502}{\lambda^{3.7}} + 7.036 \qquad (6.71)$$

$$Three-term\ Cauchy: \quad N^2 = \frac{1.136}{\lambda^4} + \frac{0.486}{\lambda^2} + 6.930, \qquad (6.72)$$

$$One-term\ Sellmeier: \quad N^2 = 0.592 + \frac{6.049\lambda^2}{\lambda^2 - 0.4952^2}, \qquad (6.73)$$

$$Two-term\ Sellmeier: \quad N^2 = 0.592 + \frac{6.049\lambda^2}{\lambda^2 - 0.4952^2} + \frac{1.01\times10^{-6}\lambda^2}{\lambda^2 - 100^2}. \qquad (6.74)$$

Eq. (6.71) is the same as that given in Corrales *et al.* [6.2] with $R^2 = 0.9988$ and $MSE = 4.070 \times 10^{-3}$, as shown in Figure 6.3-4(a). Applying the three-term Cauchy model as the dispersive model, the value of R^2 was improved from 0.9988 to 0.9989 and *MSE* was reduced from 4.070×10^{-3} to 3.758×10^{-3}, as shown in Figure 6.3-4(b). When using an one-term Sellmeier model as the dispersive model, the fitting quality is the lowest as shown in Figure 6.3-4(c). From Figure 6.3-4(d), introducing an extra Sellmeier term doesn't improve the fitting quality. However, the value of the fitting parameter c ($c = 1.01 \times 10^{-6}$) in Eq. (6.74) indicates that this term is not required when fitting the refractive index of chalcogenide glasses in the experimental wavelength range considered in [6.2] (over the wavelength range from ~ 0.7 μm to ~ 2 μm).

Table 6.3- 4. The values of N and n_0 determined for the data of Corrales *et al.* [6.2] from the Swanepoel method with the four different dispersive models.

λ_0 /μm	λ_i /μm	N	n_0 (original)	n_0 (three-term Cauchy)	n_0 (one-term Sellmeier)	n_0 (two-term Sellmeier)
2.0478	2.0115	2.667	2.654	2.652	2.331	2.331
1.6435	1.6149	2.692	2.663	2.661	2.346	2.346
1.3883	1.3649	2.735	2.681	2.681	2.380	2.380
1.1940	1.1748	2.799	2.707	2.709	2.434	2.434
1.0561	1.0401	2.883	2.741	2.745	2.507	2.507
0.9475	0.9342	2.995	2.787	2.794	2.607	2.607
0.8642	0.8527	3.075	2.788	2.796	2.666	2.666
0.7965	0.7870	3.247	2.875	2.883	2.824	2.824
0.7443	0.7362	3.398	2.937	2.943	2.954	2.954
0.6979	0.6910	3.565	3.000	3.003	3.089	3.089

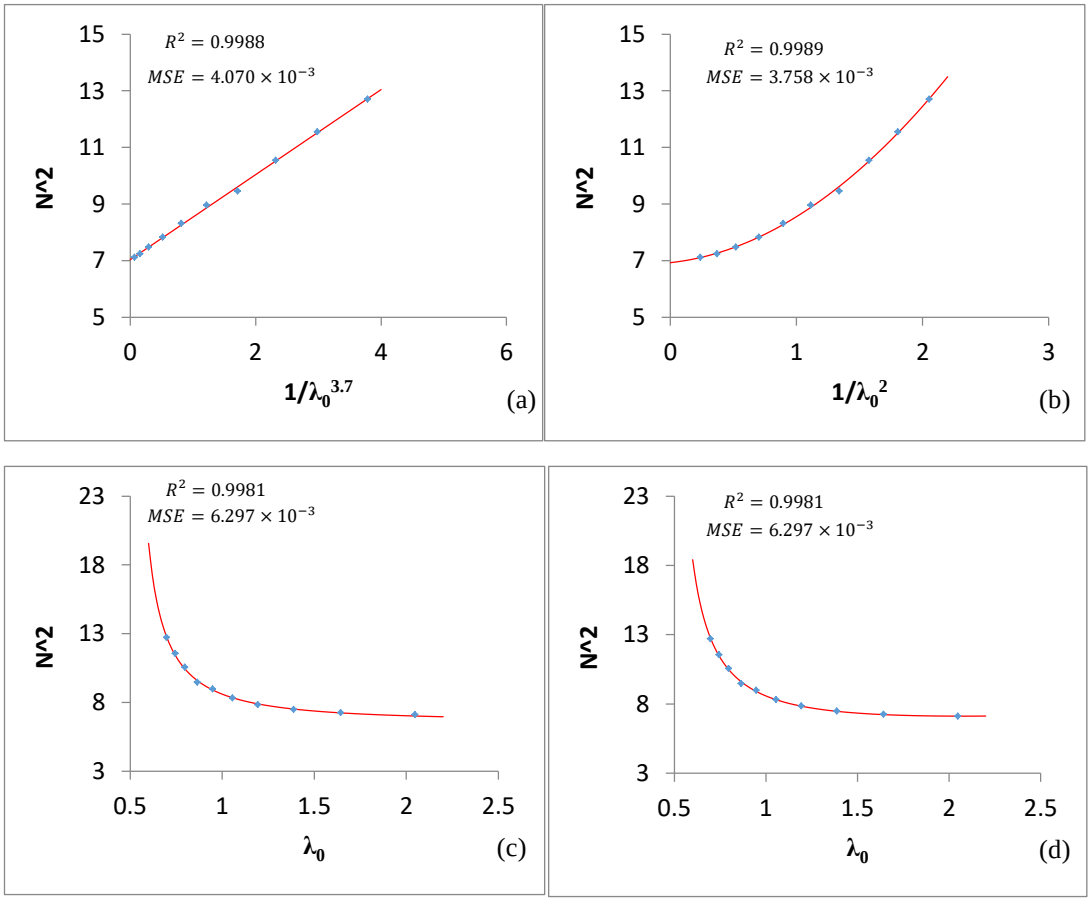


Figure 6.3- 4. Plot of the best fits to determine the fitting coefficients for: (a) Eq. (6.21); (b) Eq. (6.57); (c) Eq. (6.58) and (d) Eq. (6.59) using the data from [6.2].

With the fitting coefficients of Eqs. (6.21), (6.57), (6.58) and (6.59) obtained, the values of E/a in Eq. (6.22), D_1/a and D_2/b in Eq. (6.60), F_1/b in Eq. (6.61), F_1/b and F_2/c in Eq. (6.62) were determined and are listed in Table 6.3-5. The values of E/a at each extreme from the original Swanepoel method is the same as those reported in [6.2]. From the values of D_1/a and D_2/b for the three-term Cauchy model, the average values were taken to be 3.014 and 2.007 respectively. However, for the one-term Sellmeier model, the values of F_1/b vary from 1.064 to 2.051, which caused a large variation in determining the constant b in Eq. (6.32) and therefore n_0. This variation indicates that the present variation of the Swanepoel method using an one-term Sellmeier model is not valid when the measurement wavelengths are close to the resonant wavelength a_1. For the values of F_1/b for the two-term Sellmeier model in Table 6.3-5, because the measurement wavelengths lie close to the optical bandgap of $As_{40}Se_{60}$ at. %, the values of F_1/b show a large variation, from 1.064 to 2.051, which is the same as that observed for the one-term Sellmeier model. Since the measurement wavelengths are far from the MIR vibrational absorption band of $As_{40}Se_{60}$ at. %, the effect of the second Sellmeier term is negligible in the experimental wavelength range considered in [6.2], with the values of F_2/c varying from 0.0049 to 0.0085.

Table 6.3- 5. The values of *E/a* in Eq. (6.22), D_1/a and D_2/b in Eq. (6.60), F_1/b in Eq. (6.61), F_1/b and F_2/c in Eq. (6.62) at each extreme using the data from [6.2].

λ_0 /μm	E/a (original)	D_1/a (three-term Cauchy)	D_2/b (three-term Cauchy)	F_1/b (one-term Sellmeier)	F_1/b (two-term Sellmeier)	F_2/c (two-term Sellmeier)
2.0478	2.867	3.018	2.009	1.064	1.064	0.0085
1.6435	2.866	3.018	2.009	1.103	1.103	0.0085
1.3883	2.866	3.017	2.008	1.150	1.150	0.0083
1.194	2.865	3.016	2.008	1.214	1.214	0.0080
1.0561	2.864	3.015	2.008	1.291	1.291	0.0075
0.9475	2.863	3.014	2.007	1.388	1.388	0.0070
0.8642	2.862	3.013	2.007	1.506	1.506	0.0066
0.7965	2.861	3.012	2.006	1.652	1.652	0.0059
0.7443	2.860	3.011	2.005	1.822	1.822	0.0054
0.6979	2.859	3.010	2.005	2.051	2.051	0.0049

The values of n_0 for the four different dispersive models can be determined from Eqs. (6.19), (6.54), (6.55) and (6.56), as shown in Table 6.3-4. The values of n_0 from the original (single Cauchy term) Swanepoel method are same as those reported in [6.2]. The n_0 determined from the modified Swanepoel method using a three-term Cauchy model is in a good agreement with that determined from the original Swanepoel method with an error of less than 0.3 %. From Table 6.3-4, it is found that both the one-term Sellmeier model and the two-term Sellmeier model cannot correctly determine n_0, which is because the Sellmeier model becomes more sensitive to wavelengths when the measurement wavelengths lie very close to resonant wavelengths; this caused large variations in determining the values of F_1/b (one-term Sellmeier model), F_1/b (two-term Sellmeier model) and F_2/c (two-term

Sellmeier model), as shown in Table 6.3-5, and thus leads to large errors in determining the values of n_0, as shown in Table 6,3-4.

Plots of $\frac{l}{2}$ as a function of n_0/λ_0 are shown in Figure 6.3-5 to determine the thickness of the As-Se thin film. From Figure 6.3-5(a), the gradient of the plot is 1.500 μm yielding the thickness of the As-Se thin film as 0.750 μm, which is the same as the value presented in [6.2]. Applying the three-term Cauchy model as the dispersive model, the value of R^2 was the same as that from the original Swanepoel method but the *MSE* was slightly reduced from 8.682×10^{-4} to 7.563×10^{-4}, as shown in Figure 6.3-5(b). The thickness was determined to be 0.748 μm. The poor fitting qualities in Figures 6.3-5(c) and 6.3-5(d) yielded the thickness of 0.638 μm and the order number of the first extreme as 1.365, which indicates that the Sellmeier models are not valid when the measurement wavelengths are close to optical bandgap. Therefore, in the experimental wavelength range considered in [6.2] (over the wavelength range from ~ 0.7 μm to ~ 2 μm), the thickness and refractive index of the $As_{40}Se_{60}$ at. % thin film cannot be correctly determined by the Swanepoel method when using the one-term and two-term Sellmeier models.

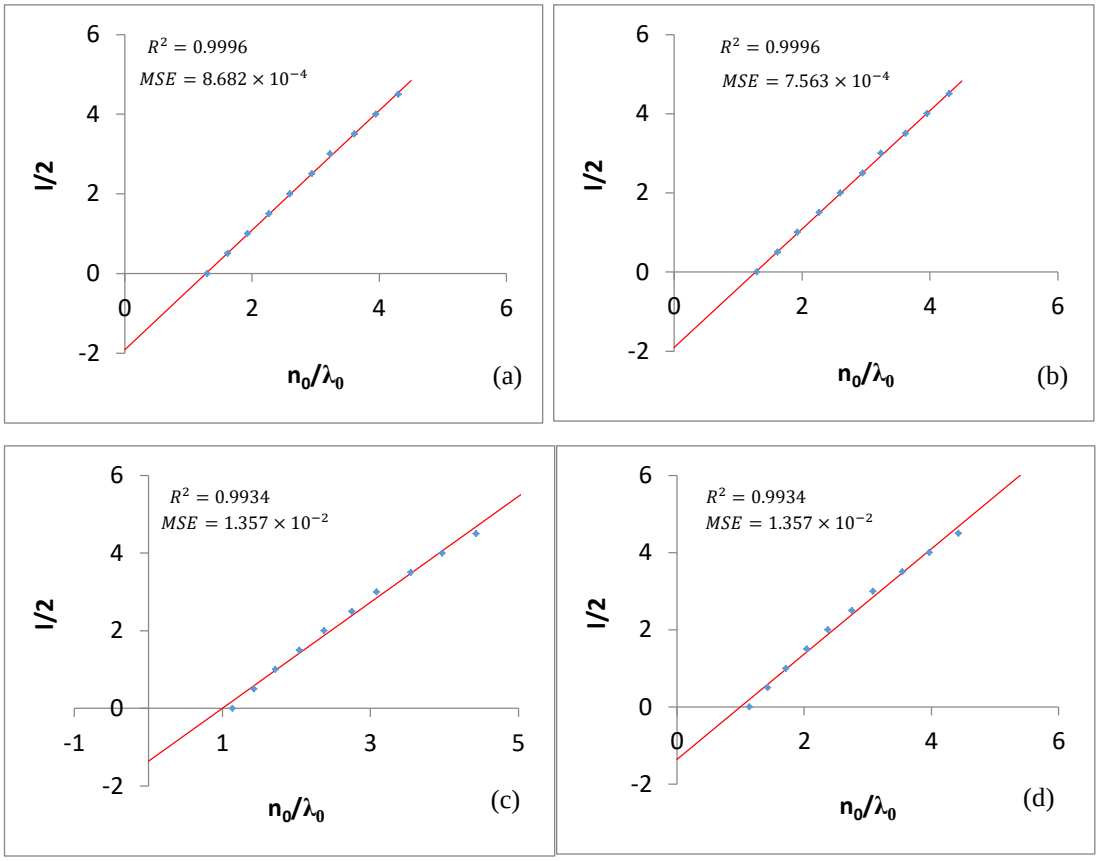


Figure 6.3- 5. Plot of $\frac{I}{2}$ as a function of n_0/λ_0 using the data from [6.2] to determine the thickness *d* for the $As_{40}Se_{60}$ at. % thin film from the Swanepoel method using (a) original dispersive model; (b) three-term Cauchy model; (c) one-term Sellmeier model; (d) two-term Sellmeier model.

6.3.2.3 The final values of thickness and refractive index for $As_{40}Se_{60}$ at. % thin film using the data from Corrales et al. [6.2]

For the original (single Cauchy term) Swanepoel method, the thickness determined from the two procedures above is 747 nm and 750 nm respectively. Taking an average value for *d* of 749 nm, the final values of refractive index can now be determined from *m* and *d* using Eq. (6.3). These values are shown in Table 6.3-6. In [6.2], the final thickness is stated as being 754 nm, which is different from the value obtained here. The final values of refractive index in [6.2] are listed in Table 6.3-6. It is found that a 0.5 % error in thickness can lead to a ~ 0.7 % error in determining the refractive index.

For the Swanepoel method modified by using the three-term Cauchy model, the thicknesses determined by methods A and B are the same i.e 748 nm. Therefore, the final thickness is taken to be 748 nm. The values of refractive index at each wavelength are determined using Eq. (6.3), as shown in Table 6.3-6. The difference between the refractive index values determined by the modified approach using the three-term Cauchy model and those obtained from the original Swanepoel method using the two-term Cauchy model is less than 0.15 %.

For the one-term and two-term Sellmeier models, the large variations in determining *b* in Table 6.3-5 and poor fits to determine *d* in Figures 6.3-5(c) and (d), when using method B to determine the thickness and refractive index for the $As_{40}Se_{60}$ at. % thin film, are attributed to the fact that the Sellmeier model becomes more sensitive to wavelength when the measurement wavelengths lie very close to resonant wavelengths; this caused large variations in determining the values of F_1/b (one-term Sellmeier model), F_1/b (two-term Sellmeier model) and F_2/c (two-term Sellmeier model), as shown in Table 6.3-5, and thus led to large errors in determining the values of n_0, as shown in Table 6.3-4. Therefore, for method B, the thickness and refractive index of the $As_{40}Se_{60}$ at. % thin film cannot be correctly determined in the wavelength range of the present study by the Swanepoel method modified by using the one-term and two-term Sellmeier models. The thickness determined from method A for the one-term Sellmeier model is 750 nm, which is taken as the final value. For the two-term Sellmeier model, the final thickness is 751 nm which is only determined from method A. The final values of refractive index determined from the Swanepoel method using these two models are shown in Table 6.3-6. The difference between the refractive index values determined by the modified approach using the Sellmeier models (the one-term and two-term Sellmeier models) and those obtained from the original Swanepoel method using the two-term Cauchy model is less than 0.26 %.

The refractive indices determined by these four methods over the wavelength range from ~ 0.7 μm to ~ 2 μm are in good agreement. The thickness differences among these four methods are less than 3 nm. The error in refractive index among these four methods is less than 0.4 %. Since the final values of refractive index were calculated from Eq. (6.3), the Swanepoel method in both the original and modified forms is sensitive to the calculated wavelength. A 1 nm difference in thickness can lead to a 0.003 difference in refractive index.

Table 6.3- 6. The final values of refractive index of the $As_{40}Se_{60}$ at. % thin film at each wavelength within the experimental range from 0.6979 μm to 2.0478 μm determined from the original and modified Swanepoel methods using the data from [6.2] compared to the results from [6.2].

λ_0 /μm	λ_i /μm	n (Corrales *et al.* [6.2])	n (original)	n (three-term Cauchy)	n (one-term Sellmeier)	n (two-term Sellmeier)
2.0478	2.0478	2.715	2.734	2.738	2.730	2.727
1.6435	1.6435	2.724	2.743	2.746	2.739	2.736
1.3883	1.3883	2.761	2.780	2.784	2.777	2.773
1.1940	1.1940	2.770	2.790	2.793	2.786	2.782
1.0561	1.0561	2.801	2.820	2.824	2.816	2.813
0.9475	0.9475	2.827	2.846	2.850	2.843	2.839
0.8642	0.8642	2.865	2.885	2.888	2.881	2.877
0.7965	0.7965	2.904	2.924	2.928	2.921	2.917
0.7443	0.7443	2.961	2.981	2.985	2.977	2.973
0.6979	0.6979	3.007	3.028	3.032	3.024	3.020

The final values of refractive index shown in Table 6.3-6 were then fitted by Eqs. (6.2), (6.31), (6.32) and (6.33) yielding

$$Original\ (two-term\ Cauchy): \quad n^2(\lambda) = \frac{5.896\times10^{-1}}{\lambda^{3.0}} + 7.451 \tag{6.75}$$

$$Three-term\ Cauchy: \quad n^2(\lambda) = \frac{2.178\times10^{-1}}{\lambda^4} + \frac{4.278\times10^{-1}}{\lambda^2} + 7.398 \tag{6.76}$$

$$One-term\ Sellmeier: \quad n^2(\lambda) = 4.386 + \frac{2.940\lambda^2}{\lambda^2-0.4324^2} \tag{6.77}$$

$$Two-term\ Sellmeier: \quad n^2(\lambda) = 5.025 + \frac{2.354\lambda^2}{\lambda^2-0.4572^2} + \frac{65.54\lambda^2}{\lambda^2-60.1^2}, \tag{6.78}$$

The fits of Eqs. (6.75), (6.76), (6.77) and (6.78) to the respective final values of refractive index from each model in Table 6.3-6 are shown in Figure 6.3-6. From Figures 6.3-6(a) and 6.3-6(b), it is shown that the three-term Cauchy model provides a better fitting quality than the original dispersive model (two-term Cauchy model). From Figure 6.3-6(c), the fitting quality of the one-term Sellmeier model is better than those from the original dispersive and three-term Cauchy models. The best fit to the final values of refractive index is from the two-term Sellmeier model with $R^2 = 0.9969$ and $MSE = 2.779 \times 10^{-5}$ as shown in Figure 6.3-6(d).

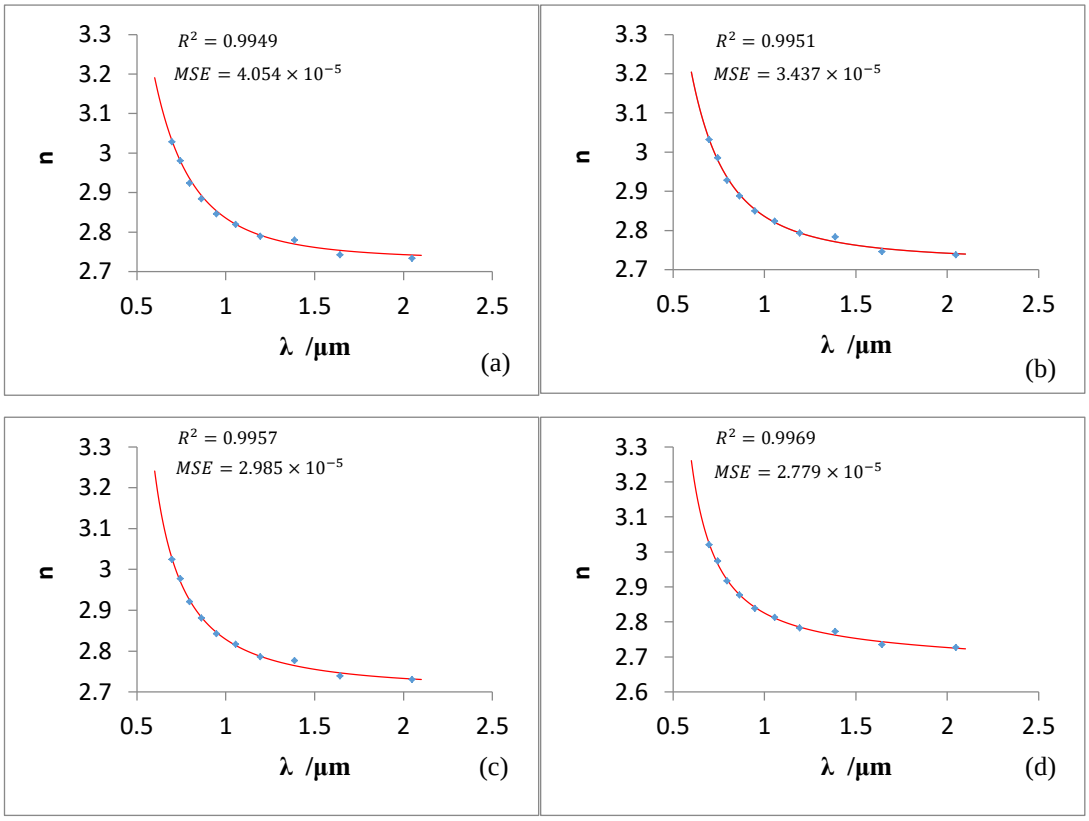


Figure 6.3- 6. The fits to the final values of refractive index for the $As_{40}Se_{60}$ at. % thin film using the data from [6.2] determined from the (a) original Swanepoel method and the improved Swanepoel method using the (b) three-term Cauchy model, (c) one-term Sellmeier model and (d) two-term Sellmeier model.

The errors of the fits to the final refractive index values are shown as a function of wavelength in Figure 6.3-7. It is found that all these four variants of the Swanepeol method provide an error of less than 0.47 %. The best fit was from the two-term Sellmeier model with the error of less than 0.38 % over the wavelength range from 0.7 µm to 2 µm. In the wavelength region close to optical band gap, the Cauchy models provide better fitting performances than the Sellmeier models as shown in Figure 6.3-7, which shows that compared to the Cauchy models, the Sellmeier models are more wavelength sensitive when the measurement region lies very close to the resonant wavelengths.

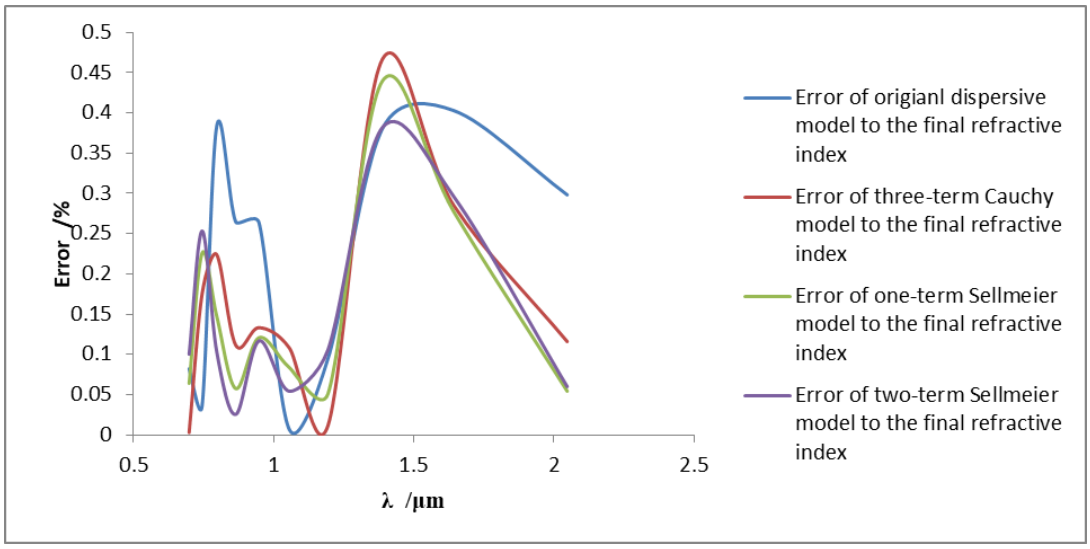


Figure 6.3- 7. The errors of the fits from the original Swanepoel method and the modified Swanepoel method using the three-term Cauchy, one-term Sellmeier and two-term Sellmeier models to the final values of refractive index using the data from [6.2].

6.3.2.4 Section summary

The original Swanepoel method, which used a two-term Cauchy model as the dispersive equation, was modified by changing the dispersive model from the two-term Cauchy model to three-term Cauchy, one-term Sellmeier and two-term Sellmeier models. The modified Swanepoel methods were successfully applied to determine the refractive index of $As_{40}Se_{60}$ at. % over the wavelength range from ~ 0.7 μm to ~ 2 μm using the data in [6.2]. The Swanepoel methods using these four different models can fit their final refractive index data with an error of less than 0.47 %. The lowest errors were achieved by using the two-term Sellmeier model as the dispersive model.

6.3.3 Determining the refractive index of $Ge_{16}As_{24}Se_{15.5}Te_{44.5}$ at. % and $As_{40}Se_{60}$ at. % thin film in mid-infrared (MIR) region using the improved Swanepoel method.

As previously discussed in chapter 5, the Cauchy models and one-term Sellmeier model are valid models for the refractive index dispersions of chalcogenide glasses only in the wavelength range from the lower wavelength edge of the transparent

window to 2.5 μm. Two-term Sellmeier and three-term Sellmeier models are considered to be more suitable refractive index models for chalcogenide glasses and operation at longer wavelengths [6.7]. However, according to section 5.4.2, compared to the two-term Sellmeier model, a three-term Sellmeier model cannot significantly improve the fitting performance. The results in section 6.3.2 also show that the modified Swanepoel method using the two-term Sellmeier model can be effectively applied to determine the refractive index of $As_{40}Se_{60}$ at. % over the wavelength range from ~ 0.7 μm to ~ 2 μm. Therefore, the two-term Sellmeier model is considered to be a very effective refractive index model for chalcogenide glasses across their entire transparent windows.

In this sub-section, the modified Swanepoel method using the two-term Sellmeier model as the dispersive model is applied to determine the refractive index and thickness of hot-pressed $Ge_{16}As_{24}Se_{15.5}Te_{44.5}$ at. % (melting code: M140MINSCGDJ; hot pressing code: YRFFP007) and $As_{40}Se_{60}$ at. % (melting code: M130MINSCGDJ; hot pressing code: YRFFP003) thin films, whose transmission spectra at wavelengths from 1 μm to 27 μm were shown in Figure 6.2-1. The comparison between the results obtained from the modified Swanepoel method using the two-term Sellmeier model and those from the original (two-term Cauchy model) Swanepoel method (see section 6.2) will be discussed in this section to show the improvements gained.

6.3.3.1 Determining n from the order number m for $Ge_{16}As_{24}Se_{15.5}Te_{44.5}$ at. % and $As_{40}Se_{60}$ at. % thin films in MIR region.

The values of *M* that were calculated from Eq. (6.8), using the wavelengths at which adjacent extrema occur at normal incidence, are shown in Tables 6.3-7 and 6.3-8. These values were fitted to Eq. (6.43) iterating b_1 in steps of 0.0001 μm from 0 to 1.5 μm and b_2 in steps of 0.01 μm from 32 μm to 100 μm for $Ge_{16}As_{24}Se_{15.5}Te_{44.5}$ at. %, since the resonance wavelength b_1 and b_2 must be initially placed outside

the transparent window fitting region to avoid the Sellmeier model becoming unbounded [6.5]. For $As_{40}Se_{60}$ at. %, b_1 was varied from 0 to 0.7 μm in steps of 0.0001 μm and b_2 was iterated from 30 μm to 100 μm in steps of 0.01 μm. A good fit was obtained for both $Ge_{16}As_{24}Se_{15.5}Te_{44.5}$ at. % and $As_{40}Se_{60}$ at. % yielding estimates for *m* at each extreme wavelength λ_0, termed m_y following the notation of [6.1], as

$$m_y\lambda_0 = 123.20 + \frac{16.19}{1-(\frac{1.22}{\lambda_0})^2} + \frac{1.04\times10^{-6}}{1-(\frac{100.00}{\lambda_0})^2} \quad \text{for } Ge_{16}As_{24}Se_{15.5}Te_{44.5} \text{ at. \%} \quad (6.79)$$

$$m_y\lambda_0 = 142.60 + \frac{519.80}{1-\left(\frac{0.70}{\lambda_0}\right)^2} + \frac{5.33\times10^{-6}}{1-\left(\frac{100.00}{\lambda_0}\right)^2} \quad \text{for } As_{40}Se_{60} \text{ at. \%} \quad (6.80)$$

where λ_0 is in units of μm. The values of *M* from Eq. (6.8) and m_y from Eqs. (6.79) and (6.80) are shown in Tables 6.3-7 and 6.3-8, together with the actual values of *m* deduced. From Tables 6.2-2, 6.2-3, 6.3-7 and 6.3-8, it can be seen that both the original Swanepoel method and the modified Swanepoel method are able to determine the actual order number *m* of the fringes in Figure 6.2-1.

The actual values of *m* are used in Eq. (6.36), iterating a_1 in steps of 0.0001 μm from 0 to 1.5 μm and a_2 in steps of 0.01 μm from 32 μm to 100 μm for $Ge_{16}As_{24}Se_{15.5}Te_{44.5}$ at. %. For $As_{40}Se_{60}$ at. %, a_1 was iterated from 0 to 0.7 μm in steps of 0.0001 μm and a_2 was iterated from 30 μm to 100 μm in steps of 0.01 μm. The best fit was obtained for $a_1 = 0.4051$ μm and $a_2 = 41.85$ μm in the case of $Ge_{16}As_{24}Se_{15.5}Te_{44.5}$ at. %, which is shown in Figure 6.3-8(a) and $a_1 = 0.6584$ μm and $a_2 = 58.30$ μm in the case of $As_{40}Se_{60}$ at. % as shown in Figure 6.3-8(b) yielding:

$$m^2\lambda_0^2 = 1.118 + \frac{1.924\times10^4\lambda^2}{\lambda^2-0.4051^2} + \frac{1353\lambda^2}{\lambda^2-41.85^2} \quad \text{for } Ge_{16}As_{24}Se_{15.5}Te_{44.5} \text{ at. \%} \quad (6.81)$$

$$m^2\lambda_0^2 = 2.425\times10^4 + \frac{5524\lambda^2}{\lambda^2-0.6584^2} + \frac{8832\lambda^2}{\lambda^2-58.30^2} \text{ for } As_{40}Se_{60} \text{ at. \%} \quad (6.82)$$

Table 6.3- 7. Calculations of refractive index of the $Ge_{16}As_{24}Se_{15.5}Te_{44.5}$ at. % (M140MINSCGDJ) thin film from the modified Swanepoel method using the two-term Sellmeier model.

λ_0	λ_i	M	m_y	m	Δm	n_i	N	n_0	n
				Ge-As-Se-Te					
22.786	22.509	6.1	6.1	6	0.0770	3.150	3.216	-	3.131
21.052	20.760	7.0	6.6	6.5	0.0944	2.967	3.013	-	3.134
19.635	19.370	7.3	7.1	7	0.0985	3.011	3.049	-	3.148
18.381	18.136	7.3	7.6	7.5	0.1036	3.040	3.071	-	3.158
17.203	16.996	8.2	8.1	8	0.0994	3.201	3.229	-	3.152
16.217	16.013	8.7	8.6	8.5	0.1102	3.136	3.159	-	3.157
…	…								
3.042	3.005	46.7	46.8	46	0.5650	3.214	3.244	-	3.205
3.010	2.974	48.3	47.4	46.5	0.5669	3.227	3.258	-	3.205
2.979	2.943	47.7	47.9	47	0.5864	3.195	3.225	-	3.206
2.948	2.912	48.4	48.4	47.5	0.5875	3.209	3.240	-	3.207
2.918	2.883	49.0	49.0	48	0.5944	3.207	3.238	-	3.208
2.888	2.853		49.5	48.5	0.6008	3.206	3.238	-	3.208
d = 21.83 μm. $n_{3.1\,\mu m}$ *from the minimum deviation method* = 3.1920									

Table 6.3- 8. Calculations of refractive index of the $As_{40}Se_{60}$ at. % (M130MINSCGDJ) thin film from the improved Swanepoel method.

λ_0	λ_i	M	m_y	m	Δm	n_i	N	n_0	n
				As-Se					
23.896	23.5169	7.5	7.3	7	0.1213	2.720	2.819	-	2.710
22.411	22.0428	8.0	7.8	7.5	0.1333	2.687	2.768	-	2.723
21.087	20.7323	8.6	8.2	8	0.1440	2.671	2.739	-	2.733
19.934	19.5787	8.3	8.7	8.5	0.1611	2.604	2.661	-	2.745
18.803	18.5132	9.7	9.2	9	0.1466	2.804	2.857	-	2.742
17.880	17.5843	9.8	9.7	9.5	0.1655	2.714	2.760	-	2.752
…	…								
3.040	2.991	57.8	57.6	57	0.9311	2.800	2.814	-	2.807
3.014	2.966	57.3	58.1	57.5	0.9341	2.808	2.822	-	2.807
2.988	2.941	58.4	58.6	58	0.9296	2.826	2.841	-	2.807
2.962	2.916	59.5	59.1	58.5	0.9392	2.824	2.839	-	2.808
2.938	2.891	60.7	59.6	59	0.9554	2.812	2.827	-	2.808
2.914	2.867	-	60.1	59.5	0.9717	2.800	2.816	-	2.808
d = 30.88 μm. $n_{3.1\,\mu m}$ *from the minimum deviation method* = 2.7972.									

For $Ge_{16}As_{24}Se_{15.5}Te_{44.5}$ at. %, the best fitting from the original Swanepoel method was shown in Figure 6.2-4(a). The value of R^2 (correlation coefficient) is 0.8997 and *MSE* (mean squares error) is 3.584×10^3. After the modification of the method using the two-term Sellmeier model of refractive index, the fitting is shown in Figure 6.3-8(a) with R^2 = 0.9954 and *MSE* = 1.621×10^2. Applying the original Swanepoel method to $As_{40}Se_{60}$ at. %, R^2 of the best fit is 0.6702 and the *MSE* is 4.686×10^4, as shown in Figure 6.2-4(b). From Figure 6.3-8(b), the best fit from the modified Swanepoel method yields R^2 = 0.9980 and *MSE* = 2.858×10^2. The poor fits from the original Swanepoel method indicate that the original dispersive model is not appropriate to describe the refractive index dispersion of chalcogenide thin films in the mid-infrared region. In contrast, a good quality fitting to the $m\lambda_0$ data, as in Eq. (6.36), was obtained by using a two-term Sellmeier model as the dispersive equation.

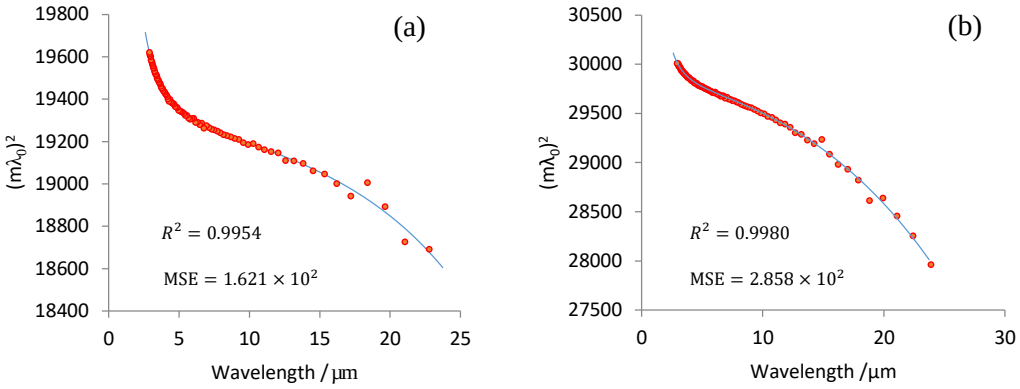


Figure 6.3- 8. (a), (b) are the best fit to Eq. (6.36) in the modified Swanepoel method using the two-term Sellmeier model, Eq. (6.81), for (a) $Ge_{16}As_{24}Se_{15.5}Te_{44.5}$ at. % (M140MINSCGDJ), and Eq. (6.82), for (b) $As_{40}Se_{60}$ at. % (M130MINSCGDJ).

Δm was calculated from Eq. (6.50) and n_i was calculated from Eqs. (6.6) and (6.7). The results of Δm and n_i for $Ge_{16}As_{24}Se_{15.5}Te_{44.5}$ at. % and $As_{40}Se_{60}$ at. % from the modified method (two-term Sellmeier model) are shown in Tables 6.3-7 and 6.3-8. Plots of $l/2+\Delta m$ as a function of n_i/λ_i are shown in Figure 6.3-9; Eq. (6.15) shows that the gradient of this straight line plot is 2*d*. The slope of the straight line is 43.66 µm for $Ge_{16}As_{24}Se_{15.5}Te_{44.5}$ at. % and 61.76 µm for $As_{40}Se_{60}$ at. %,

yielding values for d of $d = 21.83 \pm 0.02$ µm (target thickness: 20 µm) and $d = 30.88 \pm 0.02$ µm (target thickness: 25 µm), respectively. The difference between the calculated thickness and the target thickness can be attributed to the quality of the shims, short hot-pressing time or the high glass-melt viscosity during the hot pressing as discussed in section 6.2.2.

From Figure 6.3-9(a) and Figure 6.2-5(a), the *MSE* from the modified (two-term Sellmeier model) method for the $Ge_{16}As_{24}Se_{15.5}Te_{44.5}$ at. % measurement was 4.302×10^{-4} lower than that from the original (two-term Cauchy model) Swanepoel method. The *MSE* from the modified method for $As_{40}Se_{60}$ at. % was 2.425×10^{-3} lower than that from the original method, as shown in Figure 6.3-9(b) and Figure 6.2-5(b). Although the quality of the line fitting was similar, the values of Δm from the original method were obtained from the poor fitting in Figure 6.2-4, which would have led to an error in determining the film thickness *d*. In the case of $Ge_{16}As_{24}Se_{15.5}Te_{44.5}$ at. %, the thickness determination was better by 0.01 µm in the modified method, which would have led to a ~ 0.001 difference in refractive index. In the case of $As_{40}Se_{60}$ at. %, the observed difference of thickness was 0.1 µm which would have led to a refractive index difference of ~ 0.009.

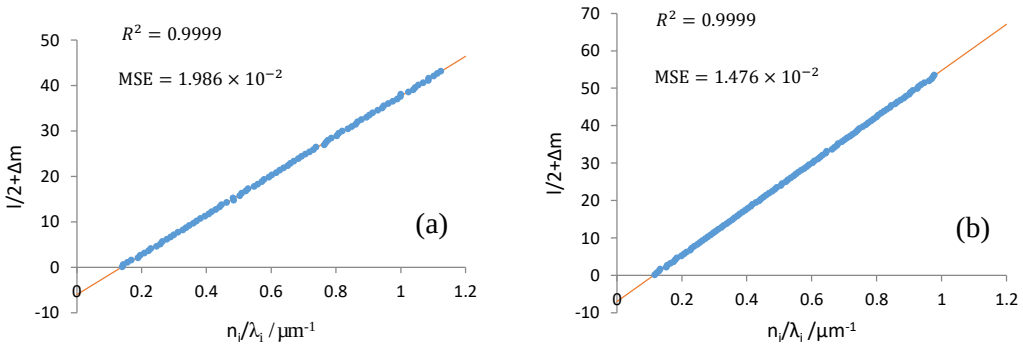


Figure 6.3- 9. Plot of $1/2+\Delta m$ as a function of n_i/λ_i for: (a) $Ge_{16}As_{24}Se_{15.5}Te_{44.5}$ at. % (M140MINSCGDJ) thin film from modified (two-term Sellmeier model) Swanepoel method; (b) $As_{40}Se_{60}$ at. % (M130MINSCGDJ) thin film from modified (two-term Sellmeier model) Swanepoel method.

6.3.3.2 Determining n from the dispersion equation for $Ge_{16}As_{24}Se_{15.5}Te_{44.5}$ at. % and $As_{40}Se_{60}$ at. % thin films in MIR region

As previously discussed in section 6.3.2, for method B, the modified Swanepoel method using the two-term Sellmeier model cannot correctly determine the thickness and refractive index of chalcogenide glasses when the measurement wavelengths are close to the resonant wavelengths. Here, the wavelength range of the measurements is from 3 to 25 μm for $Ge_{16}As_{24}Se_{15.5}Te_{44.5}$ at. % (M140MINSCGDJ) and $As_{40}Se_{60}$ at. % (M130MINSCGDJ). As mentioned in section 5.2, the estimated location of the optical band-gap for $Ge_{16}As_{24}Se_{15.5}Te_{44.5}$ at. % (M150MINSCGDJ) is at 1.3 μm. The MIR vibrational absorption band was indicated by the best Sellmeier fit to the ellipsometry data, which locates at 39.52 μm. For $As_{40}Se_{60}$ at. %, the optical band-gap was reported to be at 0.7 μm [6.8], which is in a good agreement with the estimation found in section 5.2. The MIR vibrational absorption band was calculated to be at 41.7 μm [6.6], which is also in good agreement with the location estimated by the best two-term Sellmeier fits to the ellipsometry data in section 5.5 and [6.5]. Therefore, in this case, the wavelength range of the measurements is not too close to the optical band-gaps and the MIR vibrational absorption bands of $Ge_{16}As_{24}Se_{15.5}Te_{44.5}$ at. % and $As_{40}Se_{60}$ at. %. Method B will be applied to determine the refractive indices and thicknesses of $Ge_{16}As_{24}Se_{15.5}Te_{44.5}$ at. % (melting code: M140MINSCGDJ; hot pressing code: YRFFP007) and $As_{40}Se_{60}$ at. % (melting code: M130MINSCGDJ; hot pressing code: YRFFP003) thin films.

The values of N can be calculated from Eq. (6.20) as shown in Tables 6.3-7 and 6.3-8. The values of N are used in Eq. (6.59), iterating a_1 in steps of 0.0001 μm from 0 to 1.5 μm and a_2 in steps of 0.01 μm from 32 μm to 100 μm for $Ge_{16}As_{24}Se_{15.5}Te_{44.5}$ at. %. For $As_{40}Se_{60}$ at. %, a_1 was iterated from 0 to 0.7 μm in steps of 0.0001 μm and a_2 was iterated from 30 μm to 100 μm in steps of 0.01 μm. The best fit was obtained for $a_1 = 1.500$ μm and $a_2 = 100.0$ μm in the case of

$Ge_{16}As_{24}Se_{15.5}Te_{44.5}$ at. %, which is shown in Figure 6.3-10(a) and $a_1 = 0.6319$ μm and $a_2 = 99.99$ μm in the case of $As_{40}Se_{60}$ at. % as shown in Figure 6.3-10(b) yielding:

$$N^2 = 9.169 + \frac{0.9907\lambda^2}{\lambda^2 - 1.500^2} + \frac{8.984\lambda^2}{\lambda^2 - 100.0^2} \quad \text{for } Ge_{16}As_{24}Se_{15.5}Te_{44.5} \text{ at. \%} \quad (6.83)$$

$$N^2 = 4.435 + \frac{3.382\lambda^2}{\lambda^2 - 0.6319^2} + \frac{2.637\lambda^2}{\lambda^2 - 99.99^2} \quad \text{for } As_{40}Se_{60} \text{ at. \%} \quad (6.84)$$

with R^2 = 0.4984 for $Ge_{16}As_{24}Se_{15.5}Te_{44.5}$ at. % and R^2 = 0.3166 for $As_{40}Se_{60}$ at. %, and where λ is assumed to be in units of μm. In method B, a high accuracy of the values of wavelengths is required [6.1]. As previously discussed in section 3.6.5.2, air absorption bands (CO_2, H_2O), and impurities absorption bands (Se-H, Ge-O, Si-O and As-O) and multi-phonon absorption bands of chalcogenide glasses exist in the MIR region, which can change the observed wavelengths of the extremes. Therefore, the scattered data points visible in Figure 6.3-10 are attributed to the effects of the absorption bands within the wavelengths of measurements, which caused difficulty in the fitting. Due to the poor fitting in Figure 6.3-10, the Sellmeier fits with physical meaning cannot be obtained as shown in Eqs. (6.83) and (6.84); the resonant wavelengths a_1 and a_2 for $Ge_{16}As_{24}Se_{15.5}Te_{44.5}$ at. % in Eq. (6.83) and the vibrational absorption resonant wavelength a_2 for $As_{40}Se_{60}$ at. % in Eq. (6.84) were fitted at 100 μm (the maximum of the search range of 30 to 100 μm specified in the algorithm).

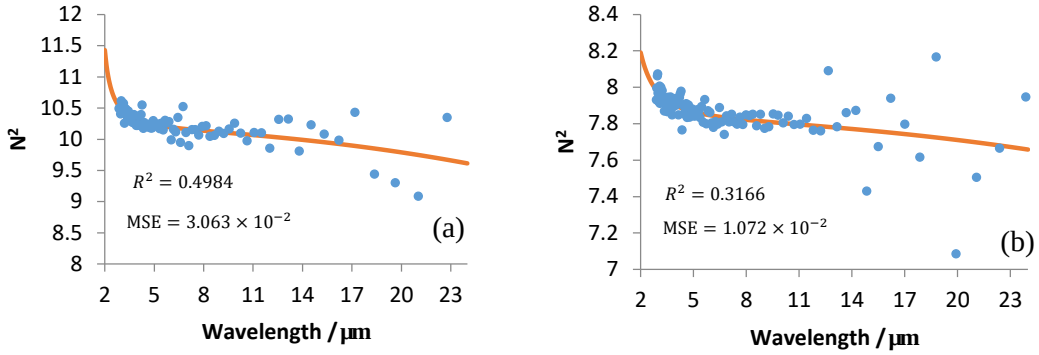


Figure 6.3- 10. Plots of the best fits to determine the fitting coefficients of Eq. (6.59) for (a) $Ge_{16}As_{24}Se_{15.5}Te_{44.5}$ at. % (M140MINSCGDJ) and (b) $As_{40}Se_{60}$ at. % (M130MINSCGDJ).

After obtaining the fitting coefficients in Eqs. (6.83) and (6.84) for $Ge_{16}As_{24}Se_{15.5}Te_{44.5}$ at. % and $As_{40}Se_{60}$ at. %, respectively, Eq. (6.62) can then be used to determine the values of F_1/b and F_2/c for $Ge_{16}As_{24}Se_{15.5}Te_{44.5}$ at. % and $As_{40}Se_{60}$ at. %; the results are shown in Table 6.3-9. For $Ge_{16}As_{24}Se_{15.5}Te_{44.5}$ at. %, the values of F_1/b vary from 1.004 to 1.051, which causes the values of b to vary from 0.986 to 0.718. For the value of F_2/c, the variation is from -0.0469 to 0.0052 as shown in Table 6.3-9, which causes the values of c to vary from -191.45 to 1720.61. For $As_{40}Se_{60}$ at. %, the values of F_1/b vary from 1.001 to 1.380, which causes the values of b vary from 3.380 to 3.216. For the value of F_2/c, the variation is from -0.0501 to 0.0072 as shown in Table 6.3-9, which causes the values of c to vary from -52.64 to 366.65. With the values of c increasing as the wavelength decreased, the values of n_0^2 in Eq. (6.56) will become negative, which make it impossible to obtain correct values for n_0. The large variation in determining the value of c may be attributed to the effects of the absorption bands within the wavelength range of measurements (mainly multi-phonon absorptions).

When using method B to determine the refractive index and thickness of the chalcogenide thin films, a high accuracy of the values of wavelengths is required [6.1]. However, air absorption bands (CO_2, H_2O), and impurities absorption bands (Se-H, Ge-O, Si-O and As-O) and multi-phonon absorption bands of chalcogenide

glasses within the MIR region changed the apparent positions of the extremes, which caused the data points in Figure 6.3-10 to be scattered. Due to the variations in determining the constants b and c, the correct values of n_0 cannot be determined. Therefore, method B is not suitable to determine the refractive index and thickness of chalcogenide glasses in the MIR region.

Table 6.3- 9. The values of F_1/b and F_2/c in Eq. (6.62) for $Ge_{16}As_{24}Se_{15.5}Te_{44.5}$ at. % (M140MINSCGDJ) and $As_{40}Se_{60}$ at. % (M130MINSCGDJ) at each extreme of their respective transmission spectrum.

λ_0 /μm	F_1/b (Ge-As-Se-Te)	F_2/c (Ge-As-Se-Te)	F_1/b (As-Se)	F_2/c (As-Se)
22.786	1.004	-0.0469	1.001	-0.0501
21.052	1.005	-0.0377	1.001	-0.0424
19.635	1.006	-0.0319	1.001	-0.0361
18.381	1.007	-0.0271	1.001	-0.0305
17.203	1.008	-0.0235	1.001	-0.0274
16.217	1.009	-0.0198	1.001	-0.0233
…				
3.042	1.330	0.0051	1.046	0.0071
3.010	1.339	0.0051	1.047	0.0071
2.979	1.349	0.0052	1.048	0.0070
2.948	1.359	0.0052	1.049	0.0070
2.918	1.369	0.0052	1.050	0.0071
2.888	1.380	0.0052	1.051	0.0072

6.3.3.3 The final values of thickness and refractive index for $Ge_{16}As_{24}Se_{15.5}Te_{44.5}$ at. %and $As_{40}Se_{60}$ at. % thin films in the MIR region.

Section 6.3.3.2 shows that method B of the modified Swanepoel method using the two-term Sellmeier model cannot correctly determine the refractive index and thickness of chalcogenide glasses. The thicknesses of the $Ge_{16}As_{24}Se_{15.5}Te_{44.5}$ at. % (melting code: M140MINSCGDJ; hot pressing code: YRFFP007) and $As_{40}Se_{60}$ at. % (melting code: M130MINSCGDJ; hot pressing code: YRFFP003) thin films can however be determined from method A to be 21.83 ± 0.02 μm and 30.88 ± 0.02 μm respectively, as presented in section 6.3.3.1.

With *d* and *m* known, the final values of refractive index at the wavelength of extremes, which are shown in Tables 6.3-7 and 6.3-8, may be determined from Eq. (6.3). The fits of these final values to Eq. (6.3) from the modified Swanepoel method using the two-term Sellmeier model are shown in Figures 6.3-11(a) and 6.3-11(b), which yield:

$$n^2 = 5.259 + \frac{4.837\lambda^2}{\lambda^2 - 0.5771^2} + \frac{0.7964\lambda^2}{\lambda^2 - 43.72^2} \quad \text{for } Ge_{16}As_{24}Se_{15.5}Te_{44.5} \text{ at. \%} \qquad (6.85)$$

$$n^2 = 3.463 + \frac{4.341\lambda^2}{\lambda^2 - 0.3920^2} + \frac{2.124\lambda^2}{\lambda^2 - 56.31^2} \quad \text{for } As_{40}Se_{60} \text{ at. \%} \qquad (6.86)$$

In our previous study of a Sellmeier refractive index model fit to $As_{40}Se_{60}$ at. % ellipsometry data [6.5], several different sets of Sellmeier coefficients could be obtained depending on the choice of $\boldsymbol{a_n}$ parameters in the Sellmeier fit. It is important that the two-term Sellmeier model lends itself to a physical interpretation as this could open the way to the model being a predictive tool. According to [6.5], for the two-term Sellmeier model, the $\boldsymbol{a_1}$ coefficient was proposed to be linked to the optical band gap and $\boldsymbol{a_2}$ was proposed to be associated with vibrational band resonant fundamental absorption. The value of $\boldsymbol{a_2}$ in [6.5] was 41.395 μm which fitted well with the position of the fundamental As-Se stretching band calculated to

occur at 41.7 μm [6.6]. Performing a fit to the present experimental data for the refractive index of $As_{40}Se_{60}$ at. %, but now fixing the value of $\boldsymbol{a_2}$ to that which was used in [6.1], yields:

$$n^2 = 4.196 + \frac{3.602\lambda^2}{\lambda^2 - 0.43834^2} + \frac{0.975\lambda^2}{\lambda^2 - 41.395^2} \qquad \text{for } As_{40}Se_{60} \text{ at. \%}$$

with R^2 = 0.9975. The plot is visually indistinguishable from the plot of Figure 6.3-11(b). Compared to the best fit in Figure 6.3-11(b), the R^2 decreases from 0.9987 to 0.9975. The difference between the two fits may be attributed to the limited experimental wavelength region (2 μm to 25 μm) and to the effect of the material absorption (at 20.8 μm - which is the first overtone of the As-Se fundamental stretching vibrational absorption at 41.7 μm [6.6]). For the $Ge_{16}As_{24}Se_{15.5}Te_{44.5}$ at. % glass no bandgap information is available, and no obvious material absorption was noticed in the transmission spectrum and thus only a best Sellmeier fit to the experimental data is presented.

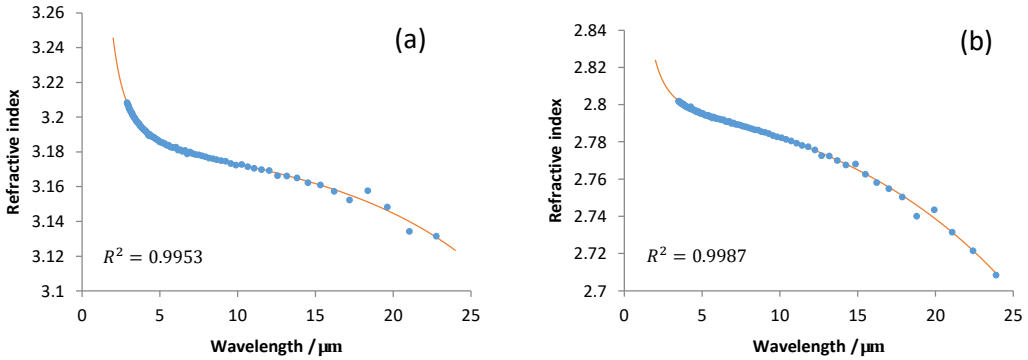


Figure 6.3- 11. The fits to the final refractive index values (temperature of the measurements: 23.1±0.5 ℃) of: (a) $Ge_{16}As_{24}Se_{15.5}Te_{44.5}$ at. % (M140MINSCGDJ) from the improved Swanepoel method; (b) $As_{40}Se_{60}$ at. % (M130MINSCGDJ) from the improved Swanepoel method.

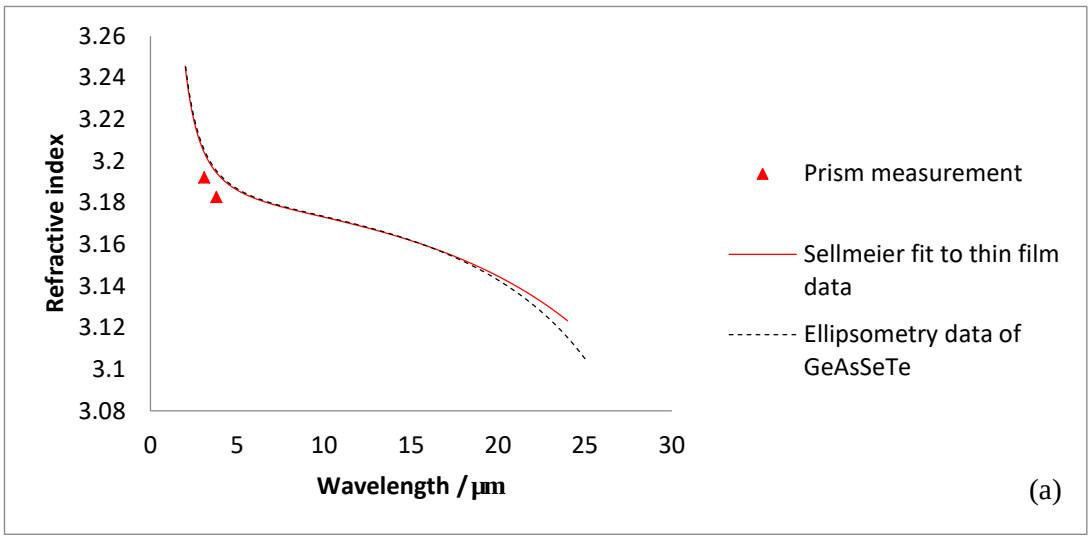
Compared to the results produced by the original (two-term Cauchy model) Swanepoel method as shown in Figures 6.2-10 for $Ge_{16}As_{24}Se_{15.5}Te_{44.5}$ at. %, the two-term Sellmeier dispersive equation introduced in the Swanepoel method provided a better fit to the refractive index data than the original dispersive equation,

with R^2 improved from 0.8983 to 0.9953 as shown in Figures 6.2-10 and 6.3-11(a). For the $As_{40}Se_{60}$ at. % thin film, the fit from the modified (two-term Sellmeier model) Swanepoel method is far better than that from the original method, as shown in Figures 6.2-11 and 6.3-11(b). From Figures 6.2-11, it is obvious that the original two-term Cauchy dispersive equation could not encompass the entire transparent window of chalcogenide glasses whereas Figure 6.3-11(b) shows the two-term Sellmeier model can. The results confirm the findings of [6.5] that a two-term Sellmeier model, with one resonant absorption in the glass optical bandgap region and one resonant absorption in the fundamental vibrational absorption spectral region in the mid-infrared, is sufficient for fitting the refractive index dispersion across the transparent window of each glass. Therefore, the modified Swanepoel method using the two-term Sellmeier model is hitherto referred to as **the improved Swanepoel method**.

The refractive indices of $Ge_{16}As_{24}Se_{15.5}Te_{44.5}$ at. % and $As_{40}Se_{60}$ at. % from the present thin film measurements, a prism minimum deviation measurement [6.9] and ellipsometry are compared in Figure 6.3-12. The prism and thin film measurements for $Ge_{16}As_{24}Se_{15.5}Te_{44.5}$ at. % were also made on glass from the same glass-melt-batch (M140MINSCGDJ) but the ellipsometry measurements were made on $Ge_{16}As_{24}Se_{15.5}Te_{44.5}$ at. % glass from a different glass-melt-batch (M150MINSCGDJ). The prism and thin film measurements for $As_{40}Se_{60}$ at. % were also made on glass from the same glass-melt-batch (M130MINSCGDJ) but the ellipsometry measurements are those reported in [6.5] and were made on $As_{40}Se_{60}$ at. % glass from a different glass-melt-batch (M005MINSCGNM). As discussed in section 4.4, the minimum deviation method in our laboratory is able to determine the refractive index of chalcogenide prisms with a standard deviation of less than 0.001; these results were taken as benchmark value. From Figure 6.3-12(a), the differences in refractive index for the $Ge_{16}As_{24}Se_{15.5}Te_{44.5}$ at. % from the thin film measurements and from the minimum deviation measurements are 0.0119 (0.37 %) at a wavelength

of 3.1 μm and 0.0128 (0.4 %) at a wavelength of 3.8 μm which might be attributed to their different thermal history (that is, the difference in quenching and annealing of the bulk glass to make the prism and after hot-pressing to make the thin film). In contrast, since the thin film and ellipsometry samples of Ge-As-Se-Te were both hot-pressed in a similar manner, which provided a similar thermal history, this provides understanding of why the error in refractive index between them is less than 0.17% from 2 to 25 μm. For $As_{40}Se_{60}$ at. %, the difference in refractive index between the thin film measurements and ellipsometry is greater than that for the $Ge_{16}As_{24}Se_{15.5}Te_{44.5}$ at. %, but is still less than 1.05 % from 2 to 25 μm, and is subject to unintentional compositional differences between the different glass batches which were prepared and then melted independently of one another. From Figure 6.3-12(b), the differences in refractive index between the thin film measurements and the prism minimum deviation measurements are 0.0079 (0.28 %) at a wavelength of 3.1 μm and 0.0051 (0.18 %) at a wavelength of 3.8 μm. Moreover, the difference in the refractive index from the improved Swanepoel method and that given for As_2Se_3 in the commercial Schott glass IRG26 form [6.10] is less than 0.0043.

The Swanepoel method in both the original and modified forms is sensitive to the calculated sample thickness, as indicated by Eq (6.3). The surfaces of the thin films of $Ge_{16}As_{24}Se_{15.5}Te_{44.5}$ at. % and $As_{40}Se_{60}$ at. % produced were both not perfect. However, according to [6.1], these kinds of glass surface undulation and glass surface defects (so long as they are limited in size relative to the wavelength of the light) do not affect the wavelength values of the extrema and hence the method used still yields correct and accurate values for refractive index and thickness.



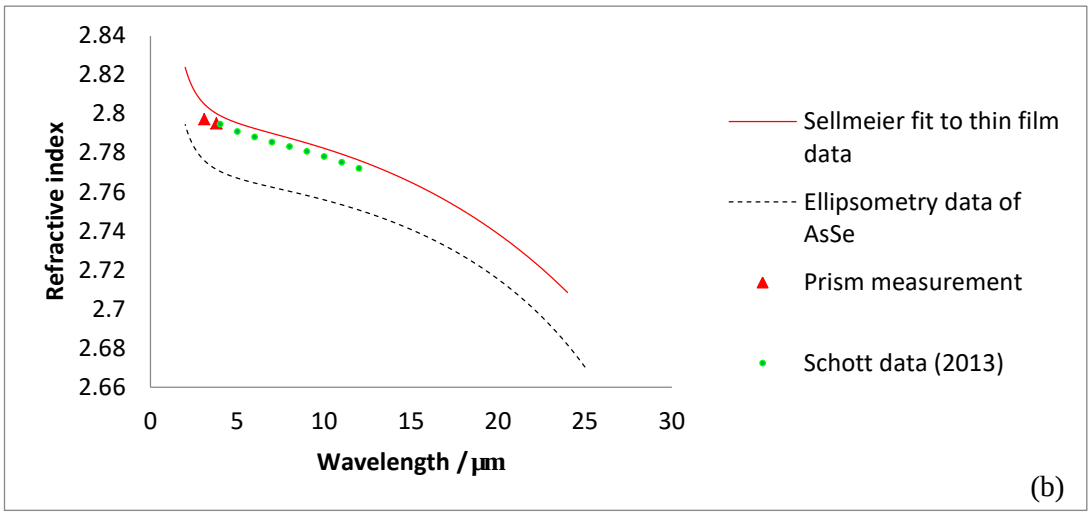


Figure 6.3- 12. Sellmeier fit to the final refractive index values of (a) $Ge_{16}As_{24}Se_{15.5}Te_{44.5}$ at. % (M140mINSCGDJ) and (b) $As_{40}Se_{60}$ at. % (M130MINSCGDJ) from FTIR thin film measurements compared to the data from minimum deviation measurement (see Tables 4-10 and 4-11 in section 4.4.1), ellipsometry (see Figure 5-1 in section 5.2) and Schott [6.10].

6.3.3.4 Reproducibility of the improved Swanepoel method using the two-term Sellmeier model

Section 6.3.3.3 shows that the modified Swanepoel method using a two-term Sellmeier model (improved Swanepoel method) as the dispersive model can successfully determine the refactive index of chalcogenide glasses ($Ge_{16}As_{24}Se_{15.5}Te_{44.5}$ at. % (melting code: M140MINSCGDJ; hot pressing code: YRFFP007) and $As_{40}Se_{60}$ at. % (melting code: M130MINSCGDJ; hot pressing code: YRFFP003)) over the wavelength range from 2 µm to 25 µm to an accuracy of better than 0.4 %. In order to further investigate the reproducibility of this technique, the refractive indices of five $As_{40}Se_{60}$ at. % thin films (two $As_{40}Se_{60}$ at. % thin films from YRFFP002 and three $As_{40}Se_{60}$ at. % thin films from YRFFP003) and seven $Ge_{16}As_{24}Se_{15.5}Te_{44.5}$ at. % thin films (four $Ge_{16}As_{24}Se_{15.5}Te_{44.5}$ at. % thin films from YRFFP007 and three $Ge_{16}As_{24}Se_{15.5}Te_{44.5}$ at. % thin films from YRFFP012) were determined. The best Sellmeier fits of the $As_{40}Se_{60}$ at. % and $Ge_{16}As_{24}Se_{15.5}Te_{44.5}$ at. % thin films are shown in Figure 6.3-13. For $As_{40}Se_{60}$ at. %, the Sellmeier coefficientts of the fits in Figure 6.3-13(a) are shown in Table 6.3-10. For $Ge_{16}As_{24}Se_{15.5}Te_{44.5}$ at. %, the Sellmeier coefficients of the fits in Figure 6.3-13(b) are shown in Table 6.3-11.

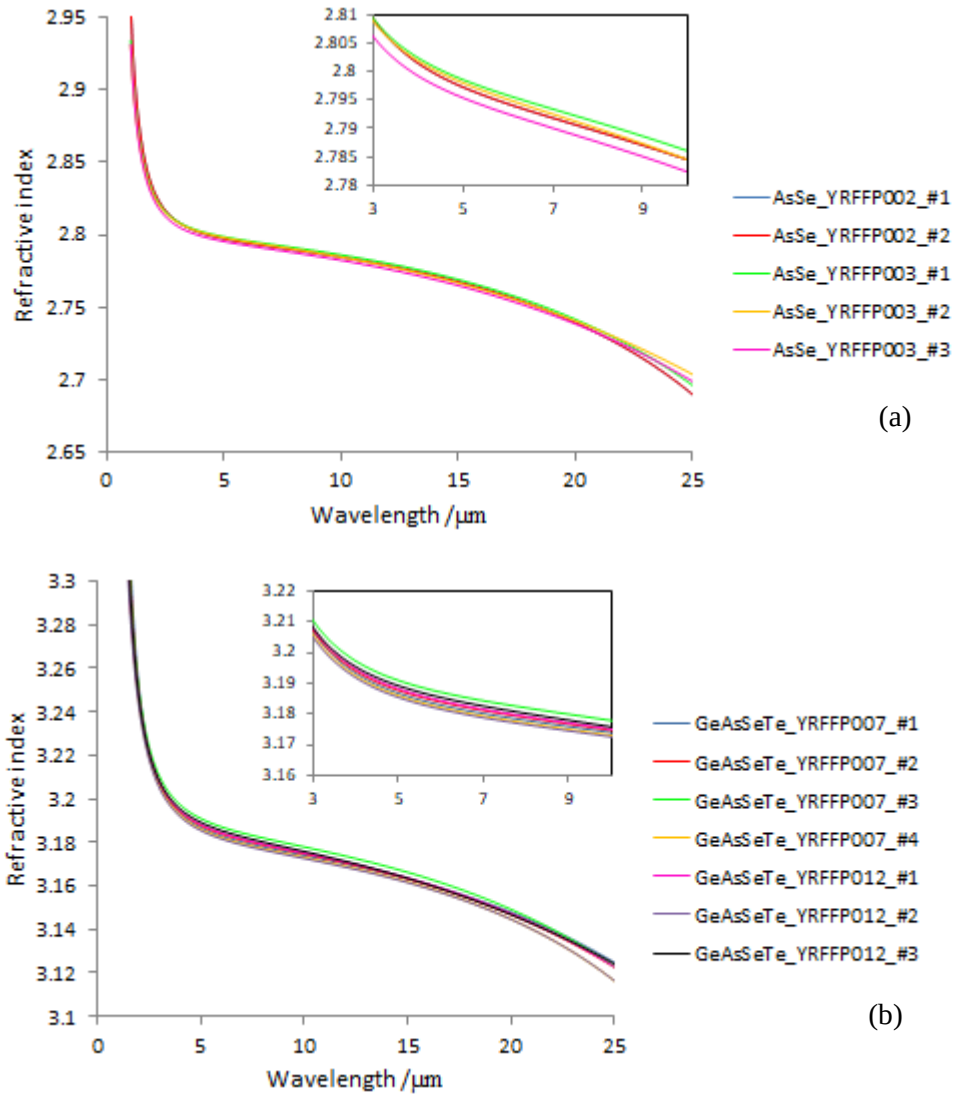


Figure 6.3- 13. The refractive indices from 2 to 25 μm wavelength obtained using the improved Swanepoel method for: (a) the five $As_{40}Se_{60}$ at. % (M130MINSCGDJ) thin films and (b) seven $Ge_{16}As_{24}Se_{15.5}Te_{44.5}$ at. % (M140MINSCGDJ) thin films. Inset: refractive indices from 3 μm to 10 μm.

Table 6.3- 10. The Sellmeier coefficients for five $As_{40}Se_{60}$ at. % (M130MINSCGDJ) thin films (two from YRFFP002 and three from YRFFP003).

Sellmeier coefficients	a	b	c	a_1 (VIS)	a_2 (MIR)	R^2
YRFFP002_#1	3.191	4.617	1.023	0.4108	41.69	0.9894
YRFFP002_#2	4.181	3.640	1.358	0.4301	46.02	0.9971
YRFFP003_#1	2.749	5.071	1.268	0.3668	45.39	0.9972
YRFFP003_#2	3.105	4.715	3.554	0.3746	70.47	0.9987
YRFFP003_#3	3.463	4.341	2.124	0.3920	56.31	0.9987

Table 6.3- 11. The Sellmeier coefficients for seven $Ge_{16}As_{24}Se_{15.5}Te_{44.5}$ at. % (M140MINSCGDJ) thin films (four from YRFFP007 and three from YRFFP012).

Sellmeier coefficients	a	b	c	a_1 $(VIS\ or\ NIR)$ /μm	a_2 (MIR) /μm	R^2
YRFFP007_#1	8.026	2.076	1.153	0.8647	52.34	0.9802
YRFFP007_#2	7.899	2.213	1.471	0.8216	56.15	0.9777
YRFFP007_#3	7.086	3.045	1.134	0.7093	49.83	0.9975
YRFFP007_#4	5.477	4.619	0.8011	0.5885	43.79	0.9986
YRFFP012_#1	5.389	4.723	1.285	0.5797	53.26	0.9995
YRFFP012_#2	3.863	6.229	0.7634	0.5085	43.25	0.9977
YRFFP012_#3	7.670	2.455	3.477	0.7685	80.88	0.9965

Figure 6.3-14 shows the standard deviations of precision for the refractive indices presented in Figure 6.3-13 as the blue line for $As_{40}Se_{60}$ at. % and the red line for $Ge_{16}As_{24}Se_{15.5}Te_{44.5}$ at. %. Figure 6.3-14 shows that the standard deviations of precision for refractive index of $As_{40}Se_{60}$ at. % and $Ge_{16}As_{24}Se_{15.5}Te_{44.5}$ at. % thin films are less 0.002 over the wavelength range from 3 to 23 μm. However, due to the different fitting values of the Sellmeier optical bandgap resonant wavelength a_1, as shown in Tables 6.3-10 and 6.3-11, the standard deviations of precisions in Figure 6.3-14 increase with decreasing wavelengths below 3 μm. Since the optical bandgap of $Ge_{16}As_{24}Se_{15.5}Te_{44.5}$ at. % locates at a longer wavelength than that of $As_{40}Se_{60}$ at. %, as discussed in section 5.2, the standard deviation of precision in determining refractive index for $Ge_{16}As_{24}Se_{15.5}Te_{44.5}$ at. % will be larger than that of $As_{40}Se_{60}$ at. % at shorter wavelengths in the measurement range, as shown in Figure 6.3-14. Figure 6.3-14 also shows that the standard deviations of precision in determining refractive index for $As_{40}Se_{60}$ at. % and $Ge_{16}As_{24}Se_{15.5}Te_{44.5}$ at. % will increase with increasing wavelength at longer wavelengths. These increases are attributed to the different values of the Sellmeier MIR vibrational absorption resonant wavelength a_2 as shown in Table 6.3-11. Since the MIR vibrational absorption of $Ge_{16}As_{24}Se_{15.5}Te_{44.5}$ at. % locates at a longer wavelength than that of $As_{40}Se_{60}$ at. %, the standard deviation of precision for $Ge_{16}As_{24}Se_{15.5}Te_{44.5}$ at. % is expected to be smaller than that of $As_{40}Se_{60}$ at. % at these longer wavelengths as indicated in Figure 6.3-14.

Repeated measurements showed that the refractive index dispersion is determined by the improved method with a standard deviation of precision in determining refractive index of less than 0.002 for the $As_{40}Se_{60}$ at. % thin films and $Ge_{16}As_{24}Se_{15.5}Te_{44.5}$ at. % thin films over the wavelength range from 3 to 23 µm. However, the standard deviation of precision for refractive index will increase out of this wavelength range due to the different values of the Sellmeier resonant wavelengths suggested by the best Sellmeier fits.

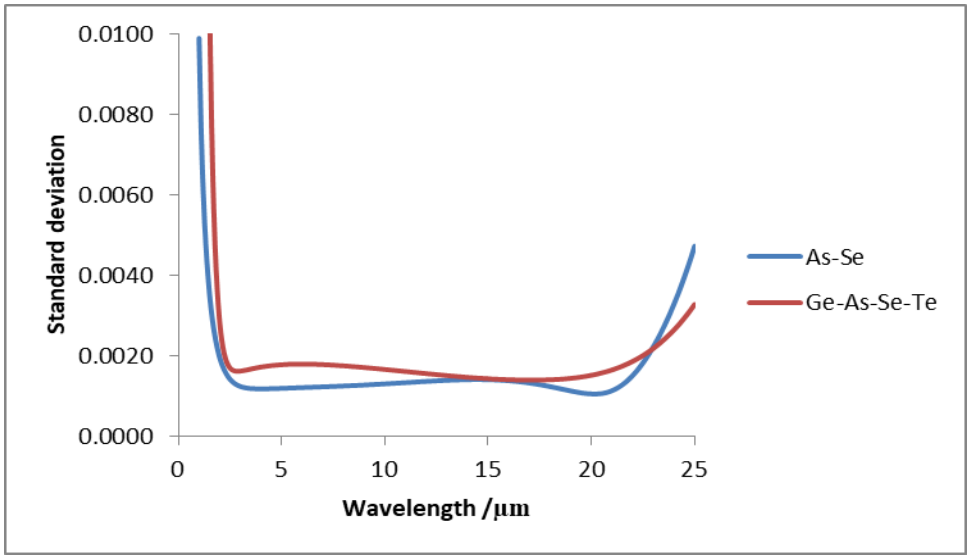


Figure 6.3- 14. The standard deviations of precision for the refractive indices of: (a) $As_{40}Se_{60}$ at. % (M130MINSCGDJ) in Figure 6.3-13 (a) and (b) $Ge_{16}As_{24}Se_{15.5}Te_{44.5}$ at. % (M140MINSCGDJ) in Figure 6.3-13 (b).

6.3.3.5 Section summary

A hot-pressing technique was used to fabricate chalcogenide glass thin films of 20 µm and 25 µm target thickness from fibres. The characteristic interference fringes in the spectral transmission of these thin films were obtained over the wavelength range from 2 to 25 µm by FTIR spectroscopy. The Swanepoel method [6.1] was modified to include a two-term Sellmeier model as the dispersive equation and was successfully applied to determine the refractive index of $Ge_{16}As_{24}Se_{15.5}Te_{44.5}$ at. % (melting code: M140MINSCGDJ; hot pressing code: YRFFP007) and $As_{40}Se_{60}$ at. %

(melting code: M130MINSCGDJ; hot pressing code: YRFFP003) thin films over the wavelength range from 2 μm to 25 μm to an accuracy of better than 0.4 %. It was shown that the original Swanepoel method [6.1] failed to correctly determine the refractive index dispersion of the chalcogenide glasses studied in the MIR spectral region because it uses an inappropriate Cauchy-like dispersive equation. Therefore, the modified Swanepoel method using the two-term Sellmeier model was referred to as **the improved Swanepoel method**. The average thicknesses of the non-uniform thin films were also determined by the improved Swanepoel method presented. Repeated measurements showed that the refractive index dispersion is determined by the improved method with a standard deviation of precision less than 0.002 for the $As_{40}Se_{60}$ at. % (M130MINSCGDJ) thin films and $Ge_{16}As_{24}Se_{15.5}Te_{44.5}$ at. % (M140MINSCGDJ) thin films over the wavelength range from 3 to 23 μm.

6.4 Refractive indices and material dispersions of Ge-As-Se-Te glasses.

Compared to other chalcogenide glasses, Ge-As-Se-Te glasses have the properties of higher refractive index, lower phonon energy and transparency out to longer wavelengths [6.11]. In order to achieve good interface quality of a core-cladding optical fibre formed from these glasses, thermal matching, e.g. of glass transition temperature and viscosity/temperature behaviour of the core and cladding materials, is considered to be a key factor [6.12]. The wide range of composition in Ge-As-Se-Te glass system provides a possibility of good thermal matching. Ge-As-Se-Te glasses with different compositions ($Ge_{16}As_{24}Se_{15.5}Te_{44.5}$ at. % (melting code: M140MINSCGDJ), $Ge_{14.3}As_{27}Se_{15.5}Te_{43.2}$ at. % (M178DJ), $Ge_{20}As_{20}Se_{14}Te_{46}$ at. % (M112DJ), distilled $Ge_{16}As_{24}Se_{15.5}Te_{44.5}$ at. % (M188SCGDJ) and $Ge_{16}As_{24}Se_{19}Te_{41}$ at. % (M193DJ)) were successfully manufactured by Dr. Dinuka Jayasuriya at the time the work was undertaken a PhD candidate in the MIR Photonics Group, University of Nottingham, UK, with matched thermal properties [6.12] for fabricating step-index fibres (SIFs). It is crucial to know the refractive

index changes with changing the compositions in the Ge-As-Se-Te glass system in order to evaluate the optical confinement of these core-cladding fibres.

In the next section, the refractive indices of different Ge-As-Se-Te thin films are reported by the improved Swanepoel method. The numerical aperture of the ultra-high NA SIF for supercontiuum generation (SCG) and low NA SIF formed from Ge-As-Se-Te glasses of different compositions will be calculated. Moreover, the material dispersion of Ge-As-Se-Te glasses will be obtained according to Eq. (5.10) in section 5.7.

6.4.1 Refractive indices of the Ge-As-Se-Te thin films

The thin films of $Ge_{16}As_{24}Se_{15.5}Te_{44.5}$ at. % (M140MINSCGDJ), $Ge_{14.3}As_{27}Se_{15.5}Te_{43.2}$ at. % (M178DJ), $Ge_{20}As_{20}Se_{14}Te_{46}$ at. % (M112DJ), distilled $Ge_{16}As_{24}Se_{15.5}Te_{44.5}$ at. % (M188SCGDJ) and $Ge_{16}As_{24}Se_{19}Te_{41}$ at. % (M193DJ) were successfully hot-pressed separately following the schedule in section 3.5.2. The maximum temperature used during the hot pressing of each glass was 215 ℃ due to the matched viscosities. The thin films were then annealed at their own onset-T_g for 1 hour and allowed to cool down naturally.

The refractive indices of $Ge_{16}As_{24}Se_{15.5}Te_{44.5}$ at. % (M140MINSCGDJ), $Ge_{14.3}As_{27}Se_{15.5}Te_{43.2}$ at. % (M178DJ), $Ge_{20}As_{20}Se_{14}Te_{46}$ at. % (M112DJ), distilled $Ge_{16}As_{24}Se_{15.5}Te_{44.5}$ at. % (M188SCGDJ) and $Ge_{16}As_{24}Se_{19}Te_{41}$ at. % (M193DJ) obtained using the improved Swanepoel method are shown in Figure 6.4-1. The results from the minimum deviation method (discussed in section 4.4) are shown in Figure 6.4-1 for comparison purpose and were taken as benchmark values.

From Figure 6.4-1, $Ge_{14.3}As_{27}Se_{15.5}Te_{43.2}$ at. % exhibits the highest refractive index over the wavelength range from 2 to 25 μm. The differences in the refractive index for the $Ge_{14.3}As_{27}Se_{15.5}Te_{43.2}$ at. % from the thin film measurement and from the minimum deviation method are 0.013 (0.40 %) at a wavelength of 3.1 μm and ~

0.009 (0.27 %) at a wavelength of 6.45 μm. The discussions for the refractive index of $Ge_{16}As_{24}Se_{15.5}Te_{44.5}$ at. % (M140MINSCGDJ) were mentioned in section 6.3.3. This nominal composition was selected to be the core material for both the high-NA SIF fibre for SCG and the low-NA SIF fibre for sensing as mentioned in section 5.6. In order to reduce the optical loss and remove impurity absorption bands, the nominal composition of $Ge_{16}As_{24}Se_{15.5}Te_{44.5}$ at. % was distilled (M188SCGDJ) [6.10]. The refractive index of the distilled $Ge_{16}As_{24}Se_{15.5}Te_{44.5}$ at. % is lower than that without distillation as shown in Figure 6.4-1. The difference is less than 0.009 over the wavelength from 2 to 25 μm. This is attributed to the small composition difference caused by the distillation. The differences in refractive index for the distilled $Ge_{16}As_{24}Se_{15.5}Te_{44.5}$ at. % from the thin film measurement and from the minimum deviation method are 0.103 (0.32 %) at the wavelength of 3.1 μm and ~ 0.008 (0.26 %) at the wavelength of 6.45 μm. $Ge_{20}As_{20}Se_{14}Te_{46}$ has a lower refractive index than the distilled $Ge_{16}As_{24}Se_{15.5}Te_{44.5}$ at. % from both thin film measurements and prism measurements. The difference in refractive index for the $Ge_{20}As_{20}Se_{14}Te_{46}$ at. % to the benchmark value is 0.015 (0.47 %) at the wavelength of 3.1 μm. From Figure 6.4-1, $Ge_{16}As_{24}Se_{19}Te_{41}$ at. % exhibits the lowest refractive index amongst these five compositions over the wavelength from 2 to 25 μm. The differences in refractive index for the $Ge_{16}As_{24}Se_{19}Te_{41}$ at. % from the thin film measurement and from the minimum deviation method are 0.015 (0.47 %) at the wavelength of 3.1 μm. This composition was selected to be the cladding material for the low-NA SIF fibre targeting sensing applications.

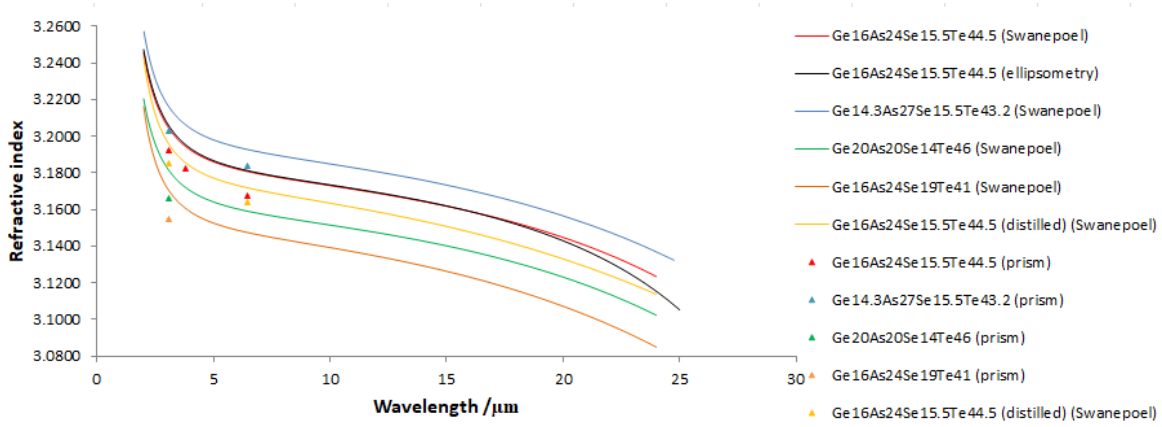


Figure 6.4- 1. The refractive indices of $Ge_{16}As_{24}Se_{15.5}Te_{44.5}$ at. % (M140MINSCGDJ), $Ge_{14.3}As_{27}Se_{15.5}Te_{43.2}$ at. % (M178DJ), $Ge_{20}As_{20}Se_{14}Te_{46}$ at. % (M112DJ), distilled $Ge_{16}As_{24}Se_{15.5}Te_{44.5}$ at. % (M188SCGDJ) and $Ge_{16}As_{24}Se_{19}Te_{41}$ at. % (M193DJ) measured using the improved Swanepoel method. The results from the minimum deviation method (discussed in section 4.4) shown were taken as benchmark values here.

6.4.2 The numerical apertures of the ultra-high NA and low-NA fibres.

An ultra-high-numerical aperture (NA) SIF fibre based on the distilled $Ge_{16}As_{24}Se_{15.5}Te_{44.5}$ at. % (M188SCGDJ) core and $Ge_{10}As_{23.4}Se_{66.6}$ at. % (M007MINSCGNM) cladding has been fabricated for MIR supercontinuum generation [6.10]. A SC spectrum over the wavelength range from 2 to 14 μm was successfully obtained based on this fibre. The refractive index of the distilled $Ge_{16}As_{24}Se_{15.5}Te_{44.5}$ at. % was obtained from the improved Swanepoel method as mentioned in section 6.4.1 and the refractive index of the $Ge_{10}As_{23.4}Se_{66.6}$ at. % was obtained from spectroscopic ellipsometry as shown in section 5.4.2. The NA of this SIF was calculated using Eq. (5.9) and is shown as a function of wavelength in Figure 6.4-2(a). As shown in Figure 6.4-2(a), the NA of the distilled $Ge_{16}As_{24}Se_{15.5}Te_{44.5}$/ $Ge_{10}As_{23.4}Se_{66.6}$ at. % glass pair is larger than 1.82 over the wavelength range from 2 to 25 μm.

A low-NA SIF fibre based on the distilled $Ge_{16}As_{24}Se_{15.5}Te_{44.5}$ at. % core and $Ge_{16}As_{24}Se_{19}Te_{41}$ at. % cladding was designed for chemical sensing [6.12]. The NA of this SIF was calculated by Eq. (5.10) using the results in section 6.4.1 and is

shown as a function of wavelength in Figure 6.4-2(b). As shown in Figure 6.4-2(b), the NA is less than 0.40 over the wavelength range from 3 to 18 μm.

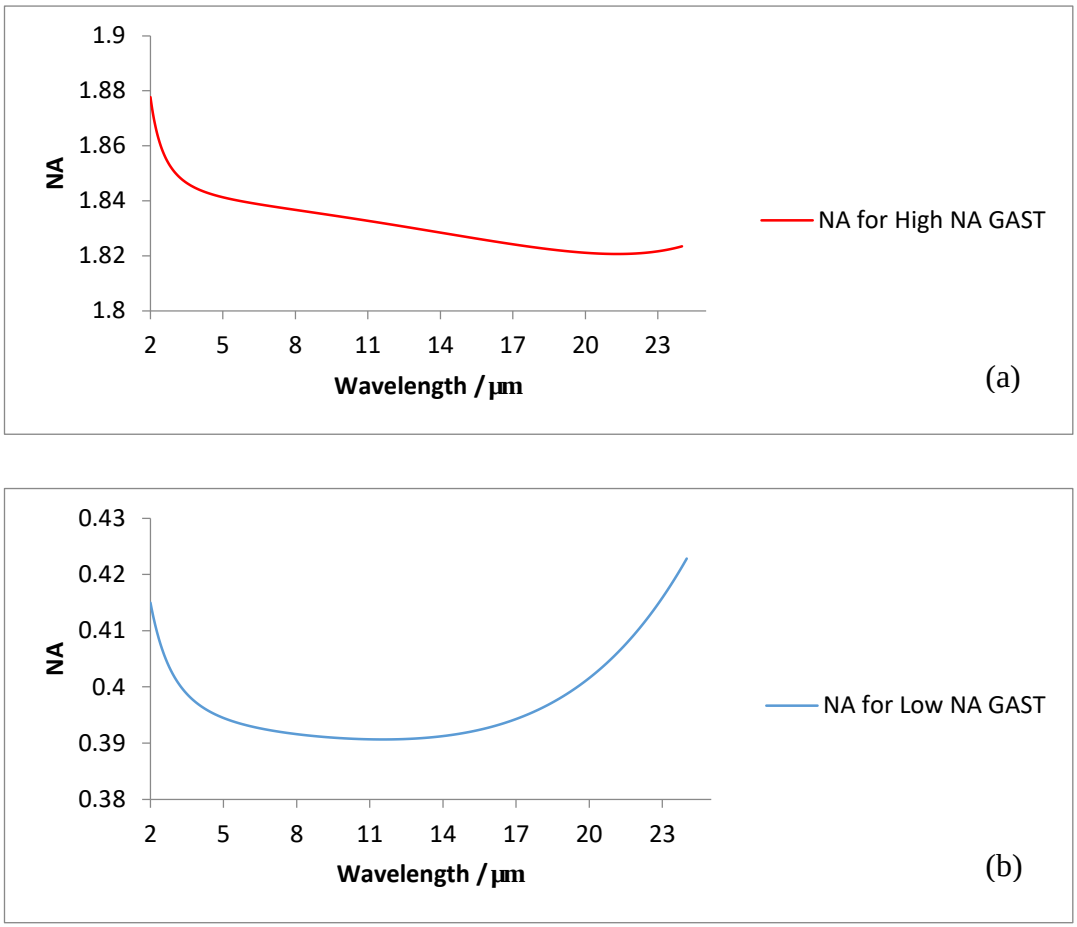


Figure 6.4- 2. The numerical aperture of (a) the Ultra-high-numerical aperture (NA) SIF fibre based on the distilled $Ge_{16}As_{24}Se_{15.5}Te_{44.5}$ at. % (M188SCGDJ) core and $Ge_{10}As_{23.4}Se_{66.6}$ at. % (M007MINSCGNM) cladding and (b) the low-NA SIF fibre based on the distilled $Ge_{16}As_{24}Se_{15.5}Te_{44.5}$ at. % (M188SCGDJ) core and $Ge_{16}As_{24}Se_{19}Te_{41}$ at. % (M193DJ) cladding.

6.4.3 Material dispersions of Ge-As-Se-Te glasses

With the continuous refractive index of the $Ge_{16}As_{24}Se_{15.5}Te_{44.5}$ at. % (M140MINSCGDJ), $Ge_{14.3}As_{27}Se_{15.5}Te_{43.2}$ at. % (M178DJ), $Ge_{20}As_{20}Se_{14}Te_{46}$ at. % (M112DJ), distilled $Ge_{16}As_{24}Se_{15.5}Te_{44.5}$ at. % (M188SCGDJ) and $Ge_{15}As_{25}Se_{19}Te_{41}$ at. % (M193DJ) over the wavelength range from 2 to 25 μm obtained in section 6.4.1, the material dispersions of different compositions (see Figure 6.4-3) can be calculated according to Eq. (5.10). As shown in Figure 6.4-3, the material

dispersions for all these five compositions remain weak out to 25 μm wavelength. The zero dispersion wavelengths of the $Ge_{16}As_{24}Se_{15.5}Te_{44.5}$ at. %, $Ge_{14.3}As_{27}Se_{15.5}Te_{43.2}$ at. %, $Ge_{20}As_{20}Se_{14}Te_{46}$ at. %, distilled $Ge_{16}As_{24}Se_{15.5}Te_{44.5}$ at. % and $Ge_{16}As_{24}Se_{19}Te_{41}$ at. % can be determined from the inset to Figure 6.4-3. Figure 6.4-3 shows that the zero dispersion wavelength of $Ge_{16}As_{24}Se_{15.5}Te_{44.5}$ at. % occurs at ~ 9.67 μm, which is lower than measured using ellipsometry (~ 10.00 μm) presented in section 5.7. This difference might be attributed to the different thermal history, the small composition difference and the less realistic Sellmeier fit based on data from the limited wavelength range (2 to 25 μm). After the distillation, the zero dispersion wavelength occurs at ~ 9.30 μm, which is due to the different composition between the $Ge_{16}As_{24}Se_{15.5}Te_{44.5}$ at. % and the distilled $Ge_{16}As_{24}Se_{15.5}Te_{44.5}$ at. %. For $Ge_{14.3}As_{27}Se_{15.5}Te_{43.2}$ at. %, the zero dispersion wavelength occurs at ~ 9.58 μm as shown in the inset to Figure 6.4-3. For $Ge_{20}As_{20}Se_{14}Te_{46}$, the zero dispersion wavelength occurs at ~ 9.50 μm. From the inset to Figure 6.4-3, the $Ge_{16}As_{24}Se_{19}Te_{41}$ at. % exhibits the lowest zero dispersion wavelength which is ~ 9.10 μm. This indicates that the zero dispersion wavelength will shift to shorter wavelength with less atomic % of Te in Ge-As-Se-Te. However, as no information on the position of the fundamental vibrational absorption bands of Ge-As-Se-Te was available, the Sellmeier fit to the refractive index of Ge-As-Se-Te is based on numerical fits to the data only, but this causes an error of less than ± 0.20 μm in determining the zero dispersion wavelength.

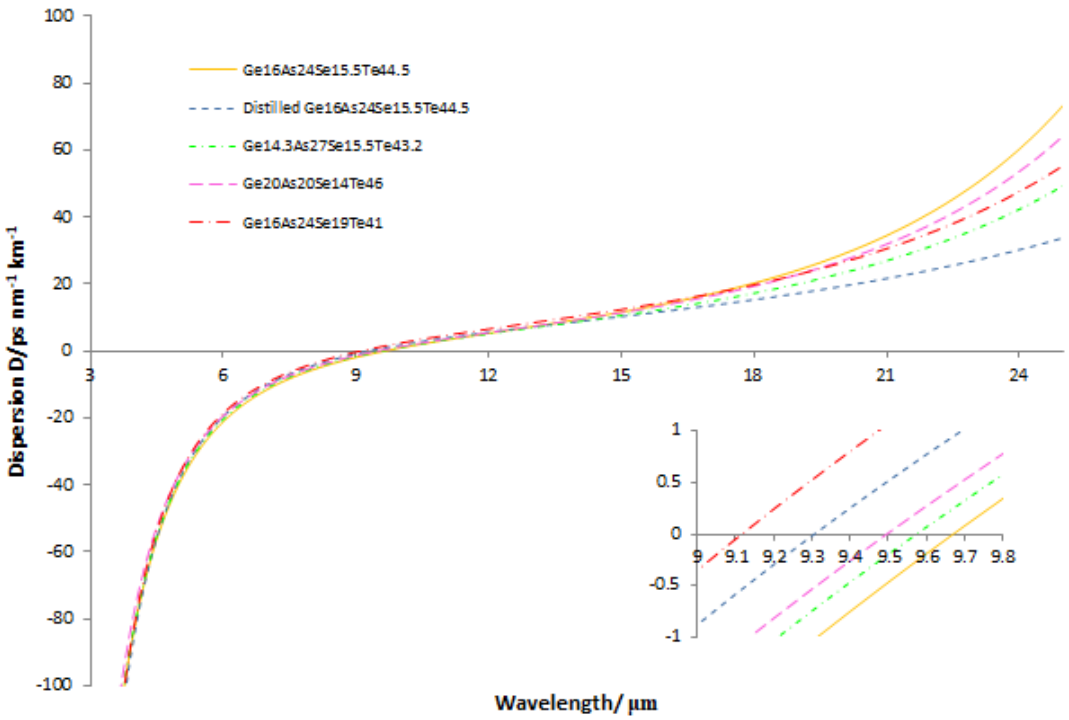


Figure 6.4- 3. Material dispersion *D* calculated from Eq. (5.10) and the fitted Sellmeier models of $Ge_{16}As_{24}Se_{15.5}Te_{44.5}$ at. % (M140MINSCGDJ), $Ge_{14.3}As_{27}Se_{15.5}Te_{43.2}$ at. % (M178DJ), $Ge_{20}As_{20}Se_{14}Te_{46}$ at. % (M112DJ), distilled $Ge_{16}As_{24}Se_{15.5}Te_{44.5}$ at. % (M188SCGDJ) and $Ge_{16}As_{24}Se_{19}Te_{41}$ at. % (M193DJ). Inset: material dispersion close to the material zero dispersion wavelength

6.5 The refractive index of other chalcogenide glasses.

The refractive indices of other chalcogenide thin films ($Ge_{20}Sb_{10}Se_{70}$ at. % (M135HAP), $Ge_{20}Sb_{10}Se_{67}S_3$ at. % (M157HAP), Tb^{3+} doped Ge-As-Ga-Se (ZQT081), Ce^{3+} doped Ge-As-In-Se (M125MINREHS), CeI_3 doped Ge-As-Ga-Se-I (M168MINREDFZQT)) were determined by the improved Swanepoel method, as reported in this section. The manufacturing procedure followed the description in section 3.5.2.

$Ge_{20}Sb_{10}Se_{70}$ at. % (M135HAP) / $Ge_{20}Sb_{10}Se_{67}S_3$ at. % (M157HAP) core / cladding glasses were selected to make low numerical aperture step-index fibres (SIF) for bio- and chemical-sensing [6.13]. In order to make sure the proper confinement of the SIF, the refractive index data for the core and cladding glasses becomes

crucial. The refractive indices of $Ge_{20}Sb_{10}Se_{70}$ at. % and $Ge_{20}Sb_{10}Se_{67}S_3$ at. % obtained using the improved Swanepoel method are shown in Figure 6.5-1 compared with the results obtained by the author from the minimum deviation measurements (see section 4.4). Figure 6.5-1 shows that the refractive index of $Ge_{20}Sb_{10}Se_{70}$ at. % from thin film measurement is higher than that of the cladding $Ge_{20}Sb_{10}Se_{67}S_3$ at. %, which indicates a proper confinement from the cladding glass. From Figure 6.5-1, the differences in refractive index for the $Ge_{20}Sb_{10}Se_{70}$ at. % from the thin film measurement and from the minimum deviation method are 0.0059 (0.23 %) at the wavelength of 3.1 µm, 0.0045 (0.18 %) at the wavelength of 3.8 µm and 0.0050 (0.20 %) at the wavelength of 6.45 µm. For $Ge_{20}Sb_{10}Se_{67}S_3$ at. %, the differences in refractive index from the thin film measurement and from the minimum deviation method are 0.0083 (0.33 %) at the wavelength of 3.1 µm and 0.0065 (0.26 %) at the wavelength of 6.45 µm as shown in Figure 6.5-1. Further discussions about these two compositions will be provided in section 6.7.

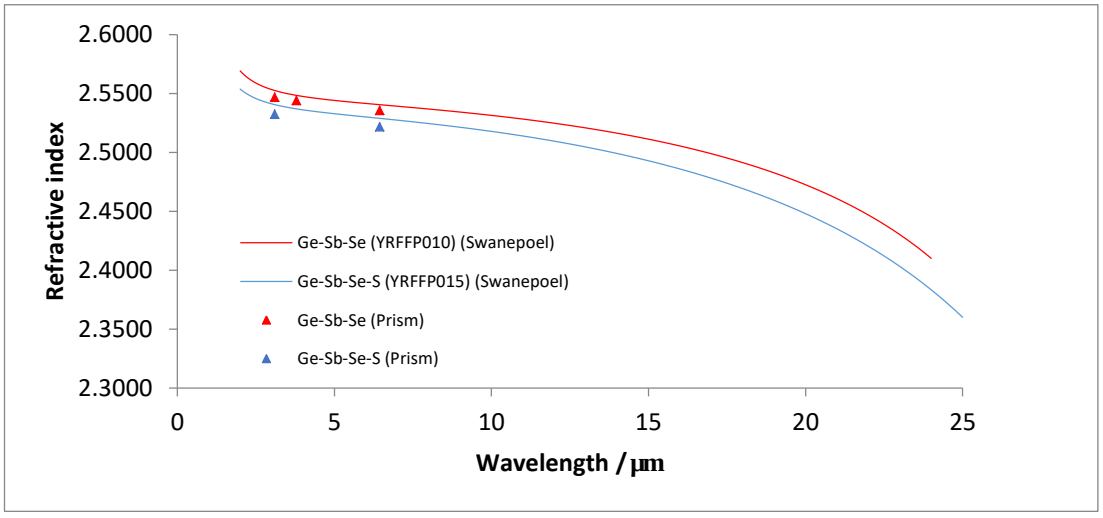


Figure 6.5- 1. The refractive indices of the $Ge_{20}Sb_{10}Se_{70}$ at. % (Ge-Sb-Se) (M135HAP) and $Ge_{20}Sb_{10}Se_{67}S_3$ at. % (Ge-Sb-Se-S) (M157HAP)) thin films obtained using an improved Swanepoel method compared with the results from the minimum deviation measurements.

In order to offer photoluminescence (PL) emission or a bright narrow MIR source in the MIR region from 3 to 10 µm wavelength, rare-earth ions are added into

chalcogenide host glasses in our laboratory and form trivalent ions during glass melting. The refractive indices of Tb^{3+} doped Ge-As-Ga-Se (ZQT081), Ce^{3+} doped Ge-As-In-Se (M125MINREHS) and CeI_3 doped Ge-As-Ga-Se-I (M168MINREDFZQT) are shown in Figure 6.5-2. This refractive index data was useful to PL emission studies [6.14] and fibre lasing modelling work undertaken within the Mid-infrared Photonics Group and George Green Institute for Electromagnetic Research at University of Nottingham.

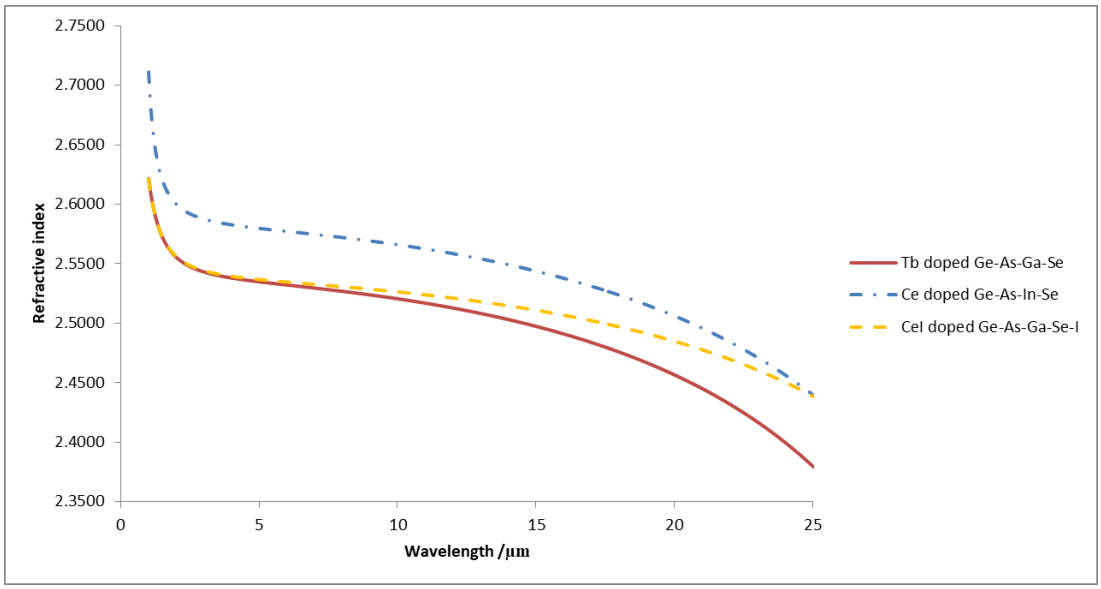


Figure 6.5- 2. The refractive index of the Tb^{3+} doped Ge-As-Ga-Se (ZQT081), Ce^{3+} doped Ge-As-In-Se (M125MINREHS) and CeI_3 doped Ge-As-Ga-Se-I (M168MINREDFZQT) thin films obtained from the improved Swanepoel method.

6.6 Effect of fast quenching.

One big goal in this Project is to determine the refractive index of chalcogenide glass fibres. The main difference between the hot-pressed thin film presented here and the optical fibre is the different quenching condition. A hot-pressed thin film was annealed at the glass on-set T_g for 1 hour as mentioned in section 3.5. For a chalcogenide fibre, it was drawn at the temperature ~ 100 ℃ above T_g (where the viscosity is $10^{4.5} pa \cdot s$) and then cooled down to room temperature within 1 second. According to [6.8] and the literature reviewed in section 2.3.3.4, the optical

properties of evaporated chalcogenide thin films are affected by different heat-treatment procedures. The evaporated chalcogenide films without annealing exhibit a lower refractive index than those with annealing. Moreover, annealing at different T_g and for different annealing durations also results in different optical properties of evaporated chalcogenide films [6.8]. In order to investigate the effects of fast quenching on the refractive index of hot-pressed thin films, the hot-pressed thin film was cooled down without annealing at T_g. Nitrogen was filled into the hot-pressing chamber to increase the cooling rate to ~ 75 ℃/h, which is the fastest that could be achieved based on our setup (see section 3.5). The refractive indices of the well-annealed distilled $Ge_{16}As_{24}Se_{15.5}Te_{44.5}$ at. % (YRFFP019) and $Ge_{14.3}As_{27}Se_{15.5}Te_{43.2}$ at. % (YRFFP016) thin films and the fast-quench distilled $Ge_{16}As_{24}Se_{15.5}Te_{44.5}$ at. % (YRFFP023) and $Ge_{14.3}As_{27}Se_{15.5}Te_{43.2}$ at. % (YRFFP025) thin films are shown in Figure 6.6-1. Figure 6.6-1 shows that the refractive index of the fast-quenched chalcogenide thin film is similar to that of the well-annealed thin film. But no firm conclusion can be drawn about the refractive index of a quenched fibre since the thin-film quenching rate is less than that of a fibre to be.

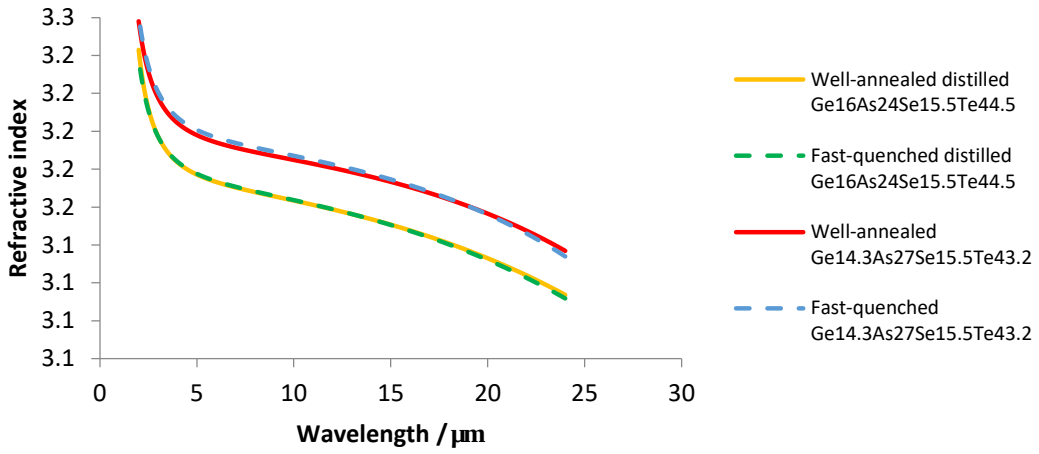


Figure 6.6- 1. The refractive indices of the well-annealed distilled $Ge_{16}As_{24}Se_{15.5}Te_{44.5}$ at. % (YRFFP019, M188SCGDJ) and $Ge_{14.3}As_{27}Se_{15.5}Te_{43.2}$ at. % (YRFFP016, M178DJ) thin films and the fast-quench distilled $Ge_{16}As_{24}Se_{15.5}Te_{44.5}$ at. % (YRFFP023, M188SCGDJ) and $Ge_{14.3}As_{27}Se_{15.5}Te_{43.2}$ at. % (YRFFP025, M178SCG) thin films.

6.7 Determining small refractive index contrast in chalcogenide glass pairs at mid-infrared wavelengths.

$Ge_{20}Sb_{10}Se_{70}$ (i.e Ge-Sb-Se) / $Ge_{20}Sb_{10}Se_{67}S_3$ (i.e Ge-Sb-Se-S) at. % core / cladding glasses were selected to make low numerical aperture step-index fibres (SIF) for bio- and chemical-sensing as previously discussed in section 6.5. In this section, a new technique is presented to determine the small refractive contrast of such a low numerical aperture (NA) glass pair at mid-infrared wavelengths. An unstructured fibre of the core composition ($Ge_{20}Sb_{10}Se_{70}$ at. % (M135HAP)) was hot-pressed together with an unstructured fibre of the cladding composition ($Ge_{20}Sb_{10}Se_{67}S_3$ at. % (M157HAP)) to form a two-composition thin film, with the advantages of the two glasses having the same thermal history and post-fibre processing. The details of the sample preparation were introduced in section 3.5.2. The transmission spectra of the Ge-Sb-Se and Ge-Sb-Se-S from the two-composition thin film were obtained using FTIR spectroscopy as described in section 3.6.5.

6.7.1 Ge-Sb-Se/S glasses: molecular structure

(The following is taken directly from the submitted version of reference: Determining small refractive index contrast in chalcogenide-glass pairs at mid-infrared wavelengths. Y.Fang *et al. Manuscript accepted by Opt.Mat. Exp.)*

"The $Ge_{20}Sb_{10}Se_{70}$ at. % core glass is a non-stoichiometric composition which has excess selenium and is equivalent to: $20GeSe_2$-$5Sb_2Se_3$-15Se. This composition has an average coordination number of 2.5 rather than the value of 2.6 found for the stoichiometric composition: $20GeSe_2$-$5Sb_2Se_3$.

Sati *et al.* [6.15] found that for glasses in the series: $Ge_{40-x}Sb_xSe_{60}$ (x=8, 12, 15, 18 and 20) with average coordination number < 2.67 (posited as a secondary topological

threshold) the structure consists of deformed tetrahedra and pyramids, in which at least one Se atom is substituted by Ge or Sb atoms.

According to Boolchand *et al.* [6.16], the larger bond strength of ≡(Ge-S)- and =(Sb-S)-, as compared to ≡(Ge-Se)- and =(Sb-Se)-, should result in formation of the former in preference to the latter during glass-melting and quenching.

S is smaller than Se and forms stronger bonds and hence the vibrational frequency, ν, of ≡[Ge-S], =[Sb-S] atomic bonds is expected to be higher than that of ≡[Ge-Se]- and =[Sb-Se]- chemical bonds according to the Szigetti equation [6.17]:

$$\nu \propto (f / m)^{1/2} \tag{6.87}$$

where: m is the reduced mass of the two vibrating atoms forming the bond and f is the bond force constant related to chemical bond strength. Therefore, vibrational absorption bands of the S-containing cladding glass are expected at higher frequency compared to the Se-only-containing core glass. Moreover, S is less heavy and less polarisable than Se, so the refractive index of the S-containing cladding glass is expected to be lower than that of the Se-only-containing core glass.

6.7.2 Analysis of observed MIR vibrational absorption bands

The normal-incidence transmission spectra, spanning the wavelength region: 15 to 27 μm obtained at different spatial regions of the Ge-Sb-Se / Ge-Sb-Se-S two-composition thin film are shown in Figure 6.7-1. As the incoming beam shifted from the Ge-Sb-Se part to the Ge-Sb-Se-S part of the thin film, that is from points 1 to 6 in Figure 6.7-1, the extrema of each transmission spectrum shifted gradually to shorter wavelength. Since the thickness variation across the thin film was less than 0.01 μm, the shift of the extrema indicated that the Ge-Sb-Se thin film had a higher refractive index than the Ge-Sb-Se-S thin film, as predicted from glass structural considerations (see section 6.7.1).

In Figure 6.7-1(a), points 2 and 5 are anticipated to correspond most closely to the Ge-Sb-Se and Ge-Sb-Se-S core and cladding glass compositions because these points are sited in the middle of the corresponding pressed fibre region and are neither near the fibre-edges nor near the interface between the two pressed fibres. The interference transmission spectrum collected at point 5 of the Ge-Sb-Se-S cladding glass shows some obvious absorption dips above 25 μm, at: 25.5 μm (small shoulder) and 26.1 μm (strong) (both highlighted in inset on Figure 6.7-1(a)). In contrast, the interference transmission spectrum collected at point 2 of the Ge-Sb-Se core glass exhibits smooth interference fringes only, with no obvious absorption. To understand these spectral changes in the MIR region, the fundamental, overtone and combination vibrational modes of the constituent chemical bonds which may be responsible are considered.

Petit *et al.* [6.18], in studying the two glass series: $(1-x)GeS_2–xSb_2S_3$ (with increasing x) and $Ge_{0.23}Sb_yS_{0.77-y}$ (with increasing y), reported stretching vibrational absorption at 26.3 μm of $[GeS_4]$ tetrahedra. Thus, it is proposed that the strong vibrational absorption found at 26.1 μm in the interference transmission spectrum collected at point 5 in the inset to Figure 6.7-1(a) for the Ge-Sb-Se-S cladding glass is due to ≡[Ge-S]- within tetrahedral $[GeSSe_3]$ units in the cladding glass structure. El-Sayed [6.19] has reported the experimental and theoretical MIR vibrational absorption bands of the glass series: $Ge_{28-x}Sb_xSe_{72}$ at. % with increasing x. The calculated wavelength of a band attributed to fundamental =[Sb-Se]- was 49.8 μm. The small shoulder at 25.5 μm observed here in the interference transmission spectrum of the cladding glass therefore may be assigned as the second overtone of fundamental =[Sb-Se]- vibrational absorption at 49.8 μm in pyramidal units of $[SbSe_3]$ or $[SbSSe_2]$. However, the analogous second overtone of =[Sb-Se]- vibrational absorption in pyramidal $[SbSe_3]$ or $[SbSSe_2]$ units, expected at ~ 20 μm (i.e. at approximately half the wavelength of the fundamental band at 40.49 μm observed for the glass series $Ge_{28-x}Sb_xSe_{72}$ at. % by El-Sayed [6.19]) was not

observed either in the interference transmission spectra of the cladding or the core glasses."

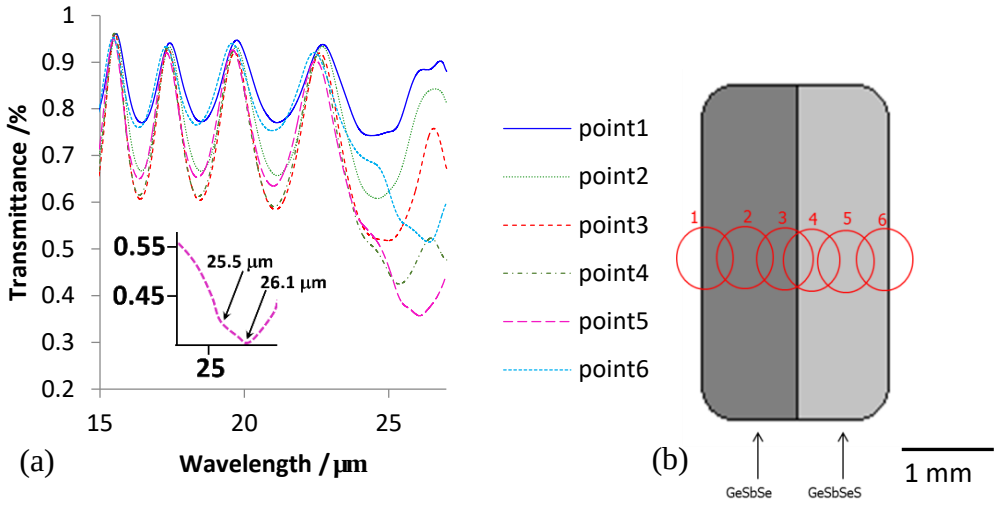


Figure 6.7- 1. (a) The transmission spectra at different locations (shown schematically in (b)) of a two-composition ($Ge_{20}Sb_{10}Se_{70}$ at. % (M135HAP) / $Ge_{20}Sb_{10}Se_{67}S_3$ at. % (M157HAP)) = (core / cladding glasses) thin film. Points 2 and 5 were most representative of the core glass and cladding glass, respectively, without edge or interfacial effects. There are no vibrational absorption bands evident for the spectrum taken at point 2 for the core glass. Yet, in the spectrum taken at point 5 for the cladding glass, two vibrational absorption bands are evident at 25.5 μm (small shoulder) and 26.1 μm (strong band), (as indicated in inset on (a)); the chemical bond vibrations responsible are identified in the text.

6.7.3 Simple approach for determining which material has the larger refractive index in the two-composition (Ge-Sb-Se and Ge-Sb-Se-S) thin film

To design and successfully fabricate small NA, step-index optical fibres, it is crucial that the core and cladding glasses are batched and melted accurately to retain a higher refractive index of the core relative to the cladding glass. Glass-distillation purification procedures can inadvertently adversely affect the NA of a fabricated chalcogenide glass SIF, particularly if the NA is small – Experience within the Mid-infrared Photonics Group and George Green Institute for Electromagnetic Research at University of Nottingham suggest particular difficulties in achieving fibre-NA ≤ 0.2. A simple method was developed here to compare the refractive

indices of two different glasses in the two-composition thin film by using the normal-incidence transmission spectra only.

The transmittance spectra of Ge-Sb-Se and Ge-Sb-Se-S at normal incidence collected from the two-structural thin film are shown in Figure 6.7-2. The data in Figure 6.7-2 are measured separately from those shown in Figure 6.7-1, but in regions close to locations 2 and 5. For normal incidence on a thin film with thickness *d*, the wavelengths of the transmittance extrema are given by Eq. (6.3).

The refractive index contrast of an optical fibre is given by [6.20]:

$$\Delta = \frac{(n_{core}^2 - n_{clad}^2)}{2n_{core}^2} = \frac{1}{2}\left[1 - \left(\frac{n_{clad}}{n_{core}}\right)^2\right] \tag{6.88}$$

where n_{core} is the refractive index in the core and n_{clad} is the refractive index in the cladding. When $n_{clad} > n_{core}$, the refractive index contrast Δ is negative. When $n_{clad} < n_{core}$, Δ is positive. Assuming that the two materials in the two-composition thin film have the same thickness, the refractive index ratio at each extreme for these two materials can be determined by:

$$\frac{n_1(\lambda_{1m})}{n_2(\lambda_{2m})} = \frac{\lambda_{1m}}{\lambda_{2m}} \tag{6.89}$$

where *m* is the order number at each extreme, λ_{1m} is the wavelength at the maxima or minima of the normal incidence transmittance spectrum of the Ge-Sb-Se part of the two-composition thin film, and λ_{2m} is that of Ge-Sb-Se-S. n_1 is the refractive index of Ge-Sb-Se at the wavelength of λ_{1m} and n_2 is the refractive index of Ge-Sb-Se-S at λ_{2m}. Since these two materials have a very small refractive index difference, the difference in wavelength at each extreme is small, as shown in Figure 6.7-2. In the transparency region of interest for most chalcogenide glasses, since the difference between λ_{1m} and λ_{2m} is very small, the difference between $n_1(\lambda_{1m})$ and $n_1(\lambda_{2m})$ is less than 0.0001. Therefore, $n_1(\lambda_{1m})$ and $n_2(\lambda_{2m})$ can be

considered to be evaluated at approximately the same wavelength. Substituting Equation (6.90) into (6.89) the yields:

$$\Delta = \frac{1}{2}\left[1 - \left(\frac{\lambda_{2m}}{\lambda_{1m}}\right)^2\right]. \qquad (6.90)$$

The refractive index contrast Δ determined by the single measurement at normal-incidence is shown as a function of wavelength in Figure 6.7-3. Comparing the two refractive index contrast results obtained at 3.1 and 6.45 μm wavelength, respectively, with that calculated from refractive index measurements for each composition using the minimum deviation method on bulk glass prisms [6.9], Δ obtained from the normal-incidence only measurement is around 0.0025 lower. This difference is mainly attributed to a thickness difference which must have existed across the two-composition thin film. In this case, the thickness variation was 0.04 μm which led to a 0.004 change in refractive index. The thickness variation was typically < 0.05 μm, leading to an error of less than ±0.0020 in determining Δ. This also means that this simple method can only correctly determine which glass has larger refractive index in a two-composition thin film when the refractive index difference between the two glasses (n_{core} - n_{clad}) is > 0.005.

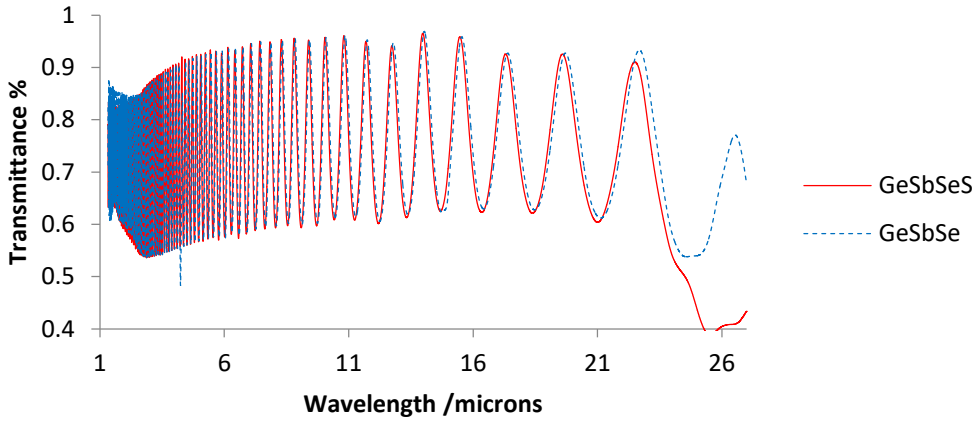


Figure 6.7- 2. The transmittance spectra of $Ge_{20}Sb_{10}Se_{70}$ at. % (M135HAP) (dash curve) and $Ge_{20}Sb_{10}Se_{67}S_3$ at. % (M157HAP) (solid curve) regions of the two-structural thin film at normal incidence.

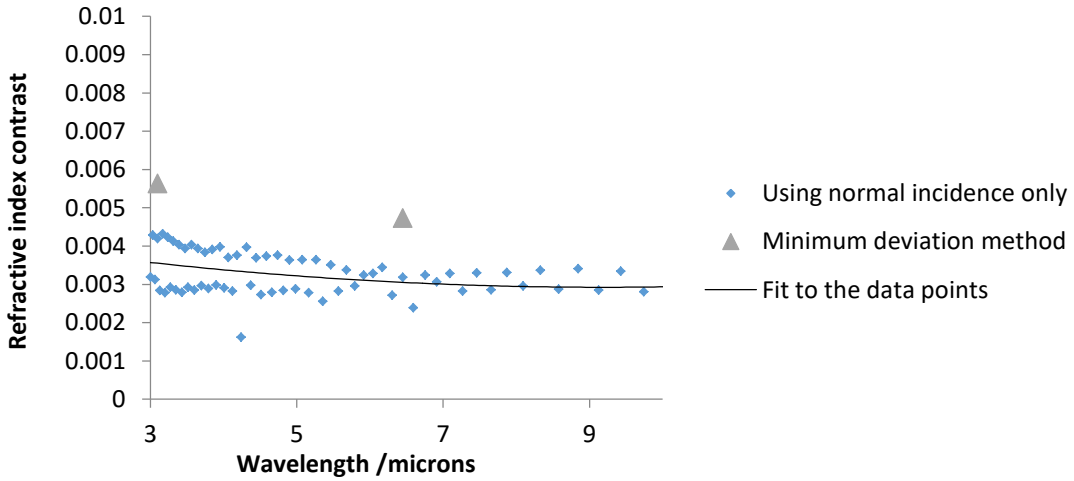


Figure 6.7- 3. The refractive index contrasts of the two-composition thin film: $Ge_{20}Sb_{10}Se_{70}$ at. % (M135HAP) and $Ge_{20}Sb_{10}Se_{67}S_3$ at. % (M157HAP), determined by a single measurement at normal incidence and the minimum deviation method at ambient temperature.

6.7.4 Determining the refractive indices of Ge-Sb-Se and Ge-Sb-Se-S glasses in the two-composition thin film.

In most cases, a very small thickness difference (less than 0.05 μm) existed across the composite, two-composition sample; as noted in section 6.7.2 this would have caused some error in determining the refractive index contrast. In order to determine the thickness of each part of the two-structural thin film, and to get the actual value of the refractive index contrast between the Ge-Sb-Se and Ge-Sb-Se-S thin films (measured in regions close to locations 2 and 5 in the schematic of Figure 6.7-1(b)), the improved Swanepoel method described in section 6.3 and [6.21] was applied.

The Sellmeier equations of Ge-Sb-Se and Ge-Sb-Se-S for the two-composition thin film from the improved Swanepoel method were obtained as:

$$n^2 = 5.469 + \frac{1.006\lambda^2}{\lambda^2 - 0.6472^2} + \frac{1.189\lambda^2}{\lambda^2 - 40.82^2} \qquad \text{for } Ge_{20}Sb_{10}Se_{70} \text{ at. \%} \qquad (6.91)$$

$$n^2 = 4.956 + \frac{1.458\lambda^2}{\lambda^2 - 0.5022^2} + \frac{0.8864\lambda^2}{\lambda^2 - 35.97^2} \qquad \text{for } Ge_{20}Sb_{10}Se_{67}S_3 \text{ at. \%} \qquad (6.92)$$

with $R^2 = 0.9976$ for Ge-Sb-Se and $R^2 = 0.9991$ for Ge-Sb-Se-S. This data can be compared to those obtained for the single glass thin films as discussed in section 6.5.

As previously discussed in section 5.5, the a_1 coefficient in the two-term Sellmeier equation was proposed to be linked to the optical bandgap and a_2 was proposed to be associated with vibrational band resonant fundamental absorption band due to chemical bond vibration of the glass matrix. From Eqs. (6.91) and (6.92), the a_1 coefficient of $Ge_{20}Sb_{10}Se_{67}S_3$ (0.5022 μm) is at a shorter wavelength than that of $Ge_{20}Sb_{10}Se_{70}$ (0.64720 μm), which is in agreement with the hypothesis that introducing S into the Ge-Sb-Se glass system will shift the optical bandgap to shorter wavelength.

(The following is taken directly from the submitted version of reference: Determining small refractive index contrast in chalcogenide-glass pairs at mid-infrared wavelengths. Y.Fang *et al. Manuscript accepted by Opt.Mat. Exp.)*

"The a_2 coefficient of the $Ge_{20}Sb_{10}Se_{70}$ at. % core glass, which is 40.82 μm in Eq. (6.91), is in good agreement with a literature value of 40.49 μm for MIR vibrational absorption attributed to =[Sb-Se]- in [$SbSe_3$] pyramids in a $Ge_{20}Sb_8Se_{72}$ at. % glass, observed by El-Sayed [6.15] when studying the glass series $Ge_{28-x}Sb_xSe_{72}$ at. %, with increasing x. For the $Ge_{20}Sb_{10}Se_{70}$ at. % core glass here, the a_2 coefficient of the $Ge_{20}Sb_{10}Se_{70}$ at. % core glass of 40.82 μm is therefore also assigned to vibrational absorption due to =[Sb-Se]- in [$SbSe_3$] pyramids.

The a_2 coefficient of the $Ge_{20}Sb_{10}Se_{67}S_3$ at. % cladding glass, which is 35.97 μm in Eq. (6.92), appears to be reasonably matched in wavelength to vibrational absorption at 34.5 μm observed by Petit *et al.* [6.18] in MIR spectra of the two glass series: $(1-x)GeS_2–xSb_2S_3$ and $Ge_{0.23}Sb_yS_{0.77-y}$; they found that this absorption band tended to broaden and intensify to cover the range 27.8 to 38.5 μm as Sb and/or

Sb_2Se_3 was increased. Petit *et al.* [6.18] attributed this band to vibrational absorption of [SbS_3] pyramidal units. The a_2 coefficient (35.97 μm) of the Sellmeier model for the $Ge_{20}Sb_{10}Se_{67}S_3$ at. % cladding glass is therefore assigned as =[Sb-S]- vibrational absorption absorption within [SbSSe] pyramidal units in the $Ge_{20}Sb_{10}Se_{67}S_3$ at. % cladding glass.

It is interesting to note that the fundamental vibrational absorption of antimony chalcogenide (=[Sb-Se] and =[Sb-S]-) chemical bonding controls the value of the a_2 coefficient in the Sellmeier modelling rather than the vibrational absorption of the Ge bonding analogues. The phonon energy of the Sb bonding is at lower energy due to the heavier relative atomic mass of Sb (121.76) compared to Ge (72.64), and weaker chemical bonding of Sb. Note, that the a_2 coefficient of the Ge-Sb-Se-S cladding glass is at shorter wavelength than a_2 of the Ge-Sb-Se core glass, which is in agreement with the observation that introducing S into the Ge-Sb-Se glass system will form tetrahedral [$Ge(S)_x(Se)_{4-x}$] and pyramidal [$Sb(S)_y(Se)_{3-y}$] structural units (see section 6.7.1), tending to blue-shift associated vibrational absorption bands towards shorter wavelength." Of course, accurate positions of the MIR fundamental vibrational absorption bands due to the chalcogenide-glass matrix chemical bonds beyond 25 μm can be determined experimentally by using a MIR detector with a wider wavelength range, which was not available to the author at the time measurements were made.

The refractive indices of Ge-Sb-Se and Ge-Sb-Se-S obtained for the two-composition thin film from the improved Swanepoel method are shown in Figure 6.7-4. For comparison purposes, single material $Ge_{20}Sb_{10}Se_{70}$ at. % (melting code: M135HAP; hot pressing code: YRFFP010) and $Ge_{20}Sb_{10}Se_{67}S_3$ at. % (melting code: M157HAP; hot pressing code: YRFFP015) thin films were prepared by means of the hot-pressing technique and each thin film underwent a tailored annealing dwell at its onset-T_g (as measured by differential scanning calorimetry, for method

see: [6.22]) for 1 h while cooling. In Figure 6.7-4, it is found that the error between the results from the two-composition thin film and those from the well-annealed single thin films (presented in section 6.5) is less than 0.12 % over the wavelength range from 3 to 25 μm.

The refractive indices of the Ge-Sb-Se core glass and Ge-Sb-Se-S cladding glass from the two-composition thin film and single glass thin films of each composition obtained from the two-term Sellmeier fitting equations at wavelengths of: 3.1, 5, 6.45, 10 and 15 μm, are shown in Table 6.7-1, as well as the results from minimum deviation measurements on polished prisms at wavelengths of 3.1 and 6.45 μm (see section 4.4). As discussed in section 4.4, the minimum deviation prism method in our laboratory can determine the refractive indices of bulk chalcogenide-glasses with a standard deviation of precision of < 0.001. If the prism minimum deviation values are arbitrary taken as benchmark value, then a 0.2 % error between the thin film measurements and prism measurements was observed. This difference might be attributable to the different thermal history (fictive temperature) of the thin film and prisms; a glass melt has been quenched and annealed prior to grinding and polishing a prism at room temperature, whereas a thin film's most recent thermal history (which will have eradicated any prior history due to fibre drawing etc.) was the hot-pressing thermal schedule which concluded with an annealing step. It is important to note that neither of these thermal histories reflects the thermal history of a chalcogenide glass SIF or unstructured fibre, taken directly from the draw tower, unless the drawn fibre is subsequently annealed.

The refractive index difference (n_{core} - n_{clad}) of Ge-Sb-Se and Ge-Sb-Se-S prisms was 0.0144 at the wavelength of 3.1 μm, and 0.0131 at 6.45 μm. These values are close to those determined from two-structural thin film using the improved Swanepoel method, which were 0.013 at the wavelength of 3.1 μm and 0.012 at 6.45 μm, respectively. With the refractive index of Ge-Sb-Se and Ge-Sb-Se-S in the

two-composition thin film determined, the refractive index contrast can be calculated from Eq. (6.88), which is shown in Figure 6.7-5.

The thickness of each of the Ge-Sb-Se and Ge-Sb-Se-S pressed films in the two-composition thin sample at the locations near point 2 and 5 in Figure 6.7-1, calculated from the improved Swanepoel method, are 27.92 ± 0.02 μm and 27.96 ± 0.02 μm, respectively. This observed thickness variation of 0.04 μm leads to a 0.004 change in the refractive index difference. Thus, applying the simple technique of using the transmission spectra at normal-incidence, the refractive contrast can be determined when the refractive index difference between two glasses is > 0.005.

To establish the absolute values and thicknesses of each glass, repeated measurements were made on the two-structural thin film using the improved Swanepoel method. Repeated measurements showed that the refractive indices of chalcogenide-glasses were determined by the improved Swanepoel method with a standard deviation of precision less than 0.002 (see section 6.3.3.4). The refractive index contrast was determined with an error of less than ± 0.0005 comparing well with that determined by means of the prism minimum deviation method (assumed bench mark) as shown in Figure 6.7-5. Comparing the results shown in Figures 6.7-3 and 6.7-5, it is seen that applying the improved Swanepoel method gives refractive index contrast results in much closer agreement to those obtained from the refractive indices measured separately for each material using the prism minimum deviation method than the simple single normal-incidence measurement approach introduced in section 6.7.3.

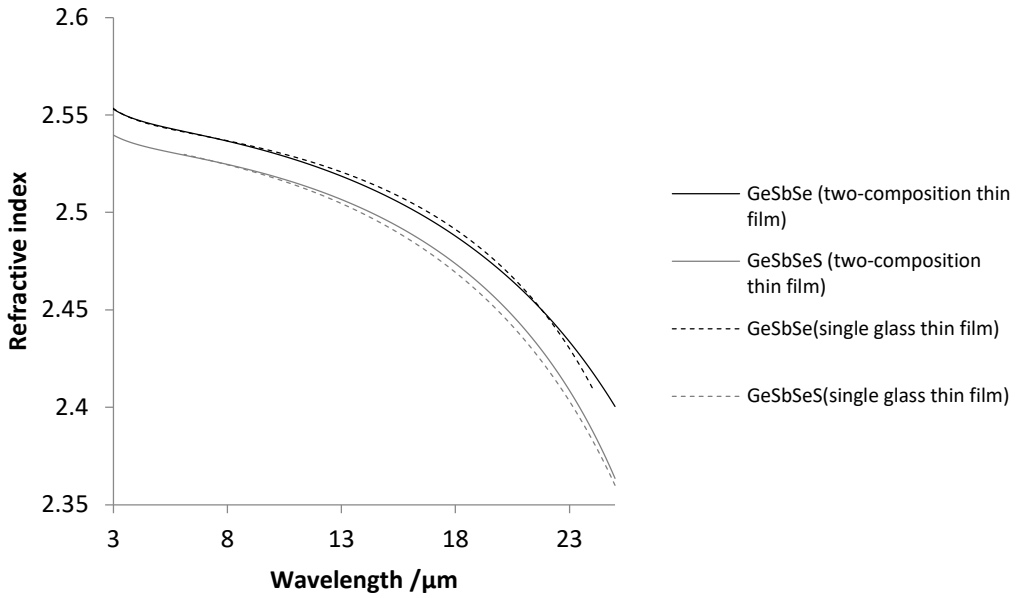


Figure 6.7- 4. The refractive indices of $Ge_{20}Sb_{10}Se_{70}$ at. % (M135HAP) and $Ge_{20}Sb_{10}Se_{67}S_3$ at. % (M157HAP) from two-composition hot-pressed thin film (YRFFP027) compared with those measured for single glass thin films (same batch). All measurements were made using the improved Swanepoel method.

Table 6.7- 1. The refractive indices of $Ge_{20}Sb_{10}Se_{70}$ at. % (M135HAP) and $Ge_{20}Sb_{10}Se_{67}S_3$ at. % (M157HAP) from two-composition hot-pressed thin film (YRFFP027), the individual glass thin films (same batch) and minimum deivation measurements on prisms (same batch) at the wavelengths of 3.1, 5, 6.45, 10 and 15µm. Measurements were made at ambient temperature.

Sample measured	3.1 µm	5 µm	6.45 µm	10 µm	15 µm
Ge-Sb-Se (Two-composition hot-pressed thin film)	2.552	2.544	2.541	2.530	2.508
Ge-Sb-Se (Single material hot-pressed thin film)	2.553	2.544	2.542	2.531	2.511
Ge-Sb-Se-S ((Two-composition hot-pressed thin film)	2.539	2.532	2.529	2.519	2.496
Ge-Sb-Se-S (Single material hot-pressed thin film)	2.540	2.533	2.530	2.518	2.493
Ge-Sb-Se (Prism)	2.5466	-	2.5354	-	-
Ge-Sb-Se-S (Prism)	2.5322	-	2.5223	-	-

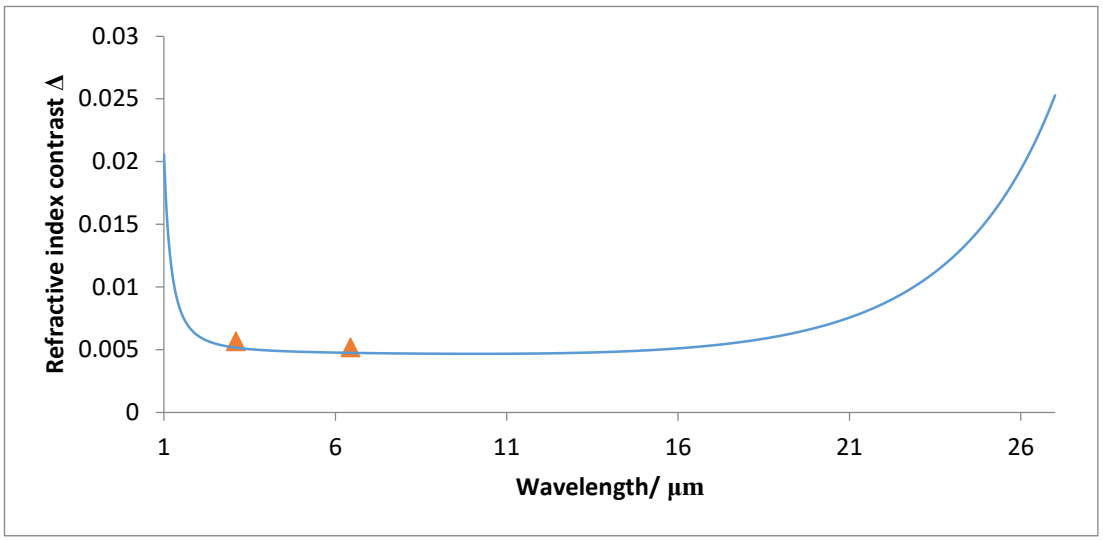


Figure 6.7- 5. The refractive index contrast of the two-composition hot-pressed thin film ($Ge_{20}Sb_{10}Se_{70}$ at. % (M135HAP) core glass; $Ge_{20}Sb_{10}Se_{67}S_3$ at. % (M157HAP) cladding glass) determined by the improved Swanepoel method (solid curve) and minimum deviation method (triangles).

6.7.5 Numerical aperture and dispersion.

Step-index fibre (SIF) based on the Ge-Sb-Se core and Ge-Sb-Se-S cladding glasses has been successfully fabricated [6.13,6.23]. The numerical aperture (NA) of the SIF composed of the designed glass pair is defined in section 5.6 as $NA = \sqrt{n_1^2 - n_2^2}$. Here, n_1 and n_2 are the refractive indices of the core Ge-Sb-Se glass, and the cladding Ge-Sb-Se-S glass respectively. As shown in Figure 6.7-6, the NA, calculated using the refractive index data from the two-composition thin film (Eqs. (6.91) and (6.92)), is around 0.26 over the wavelength range from 3 to 15 µm. The numerical aperture difference between the thin film measurements and prism measurements is less than 0.011, as also presented in Figure 6.7-6. Taking the results from prism measurements as benchmark value, the error in the NA from the thin film measurements was less than 4 %. Since the optical bandgap of the Ge-Sb-Se glass is located at a longer wavelength than that of the Ge-Sb-Se-S glass, the NA was observed to decrease with increasing wavelength at shorter wavelengths in the presented range. Due to the far-infrared fundamental vibrational absorption band of

the Ge-Sb-Se-S locating at shorter wavelength compared to that of the Ge-Sb-Se glass, the NA was found to increase gradually in the longer wavelength region (15 to 26 μm) measured.

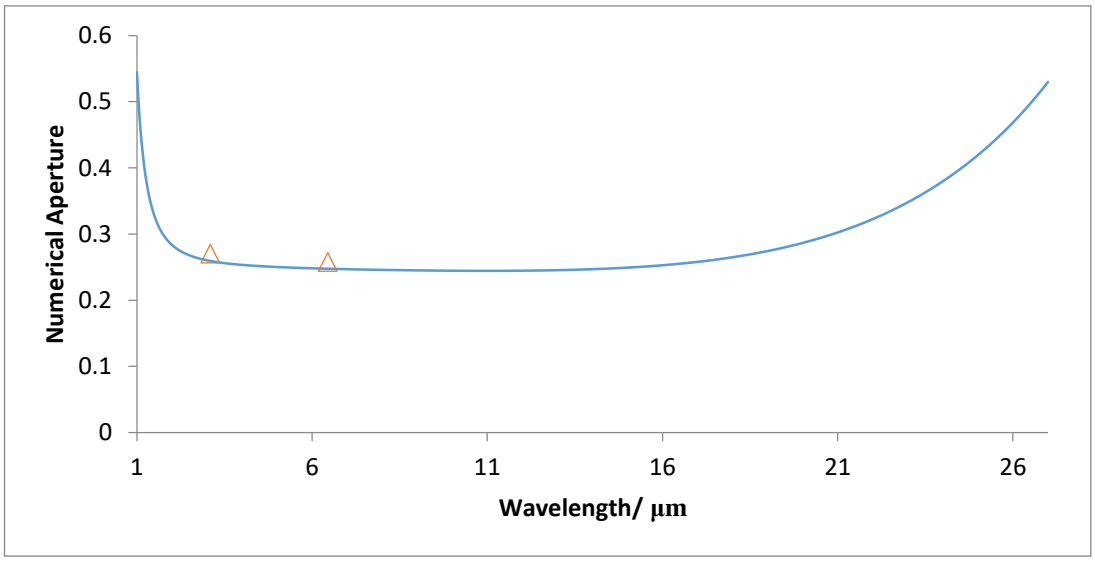


Figure 6.7- 6. The NA of step-index fibres based on the $Ge_{20}Sb_{10}Se_{70}$ at. % (M135HAP) core glass and $Ge_{20}Sb_{10}Se_{67}S_3$ at. % (M157HAP) cladding glass. (The blue solid curve is from thin film measurements; the red triangles are from prism measurements.)

The material dispersion *D*, is important data for the design of supercontinuum generation and low dispersion systems; it was calculated here from Eq. (5.10) (see section 5.7). The material dispersions of Ge-Sb-Se and Ge-Sb-Se-S obtained from Eq. (5.10), using the second derivative of the refractive index data from the two-composition thin film given by Eqs. (6.91) and (6.92) respectively, are shown in Figure 6.7-7. From Figure 6.7-7, the material zero dispersion wavelengths for Ge-Sb-Se and Ge-Sb-Se-S are seen to be at 6.3 and 6.1 μm respectively. This indicates that 3 atomic % S, added into the Ge-Sb-Se glass system in place of Se, causes the zero dispersion wavelength to shift to a shorter wavelength, by 0.2 μm. This trend is in good agreement with results obtained replacing Se with S in the $As_{40}Se_{60}$ at. % glass system where the zero dispersion wavelength was shifted from 7.2 μm for $As_{40}Se_{60}$ at. % [6.24] to 4.81 μm for $As_{40}S_{60}$ at. % [6.25]. Note that the

material dispersion of both Ge-Sb-Se and Ge-Sb-Se-S remains only weakly dependent on wavelength out to 16 µm wavelength.

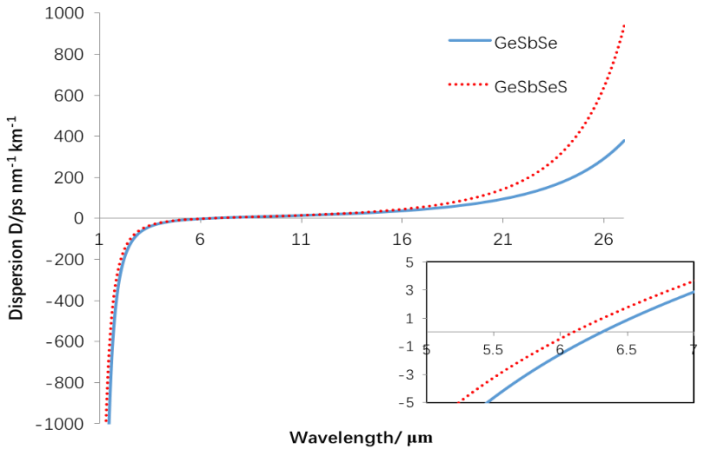


Figure 6.7- 7. Material dispersion *D* calculated from Eq. (5.10) and the fitted Sellmeier models of $Ge_{20}Sb_{10}Se_{70}$ at. % (M135HAP) and $Ge_{20}Sb_{10}Se_{67}S_3$ at. % (M157HAP). Inset: material dispersion close to the material zero dispersion wavelength.

6.7.6 Section summary

A new technique has been developed to determine the small refractive index contrast of two glasses with the same thermal history. The two-composition thin glass film was prepared by a hot-pressing technique. The characteristic interference fringes in the spectral transmission of the two different glasses in the thin film were obtained over the wavelength range from 2 to 27 µm by FTIR spectroscopy; the longer wavelength cut-off was limited by the detector available. Only using the transmission spectra at normal-incidence, the refractive contrast can be determined over the wavelength range from 2 to 25 µm with an error of less than 0.0020 due to a typically thickness variation of < 0.05 µm of the two-composition thin film. To determine the absolute values of the refractive index and thicknesses of each glass in the two-composition thin film, the improved Swanepoel method was applied. Over the wavelength range 3 to 25 µm, the refractive index can be determined with a standard deviation of precision < 0.002 and the refractive index contrast can be

determined with an error of ± 0.0005. The SIF NA was determined from this technique with an error of ± 0.011, compared to the value of SIF NA from the prism minimum deviation method, on samples made from the same glass melts. 3 at. % S replacing Se pro rata in the Ge-Sb-Se glass system (to formulate the cladding glass composition relative to the core glass composition) was shown to blue-shift the VIS optical bandgap and MIR fundamental vibrational absorption bands, lower the refractive index by 0.013 at a wavelength of 3.1 μm and by 0.012 at a wavelength of 6.45 μm, and move the zero dispersion wavelength to shorter wavelength: shifted from 6.3 to 6.1 μm.

6.7 Chapter summary.

The main focus of this chapter was to improve the Swanepoel method to determine the refractive index of chalcogenide glasses in the MIR region. The most important points from chapter 5 are summarised below:

- The original Swanepoel method [6.1] was well reproduced using Matlab codes developed by the author. The results obtained from the present work using the data in [6.1] were the same as those presented in [6.1]. When applied to determine the refractive index of hot-pressed $As_{40}Se_{60}$ at. % (YRFFP003, M130MINSCGDJ) and $Ge_{16}As_{24}Se_{15.5}Te_{44.5}$ at. % (YRFFP007, M140MINSCGDJ) thin films, the original Swanepoel method became invalid due to the dispersive equation (two-term Cauchy model) used in [6.1] being inappropriate for these chalcogenide glasses at MIR wavelengths. Therefore, in order to extend this method into the MIR region, other dispersive models are required.
- The original Swanepoel method was modified by changing the dispersive model from a two-term Cauchy model to three-term Cauchy, one-term Sellmeier and two-term Sellmeier models. The difference between the refractive index values determined by the two Cauchy models in the

Swanepoel method is less than 0.15 %. The difference between the refractive index values determined by the modified approach using the Sellmeier models (the one-term and two-term Sellmeier models) and those obtained from the original Swanepoel method using the two-term Cauchy model is less than 0.26 %. The Swanepoel methods using these four different models were able to fit their refractive index data with an error less than 0.47 %. The lowest errors were achieved by using the two-term Sellmeier model as the dispersive model.

- For MIR refractive index measurements, the Swanepoel method [6.1] was modified to include a two-term Sellmeier model as the dispersive equation (defined as the improved Swanepoel method in this thesis) and was successfully applied to determine the refractive index of $Ge_{16}As_{24}Se_{15.5}Te_{44.5}$ at. % and $As_{40}Se_{60}$ at. % thin films over the wavelength range from 2 μm to 25 μm to an accuracy of better than 0.4 %. It was shown that the original Swanepoel method [6.1] failed to correctly determine the refractive index dispersion of the chalcogenide glasses studied in the MIR spectral region because it uses a Cauchy-like dispersive equation which was shown to be inappropriate. The average thicknesses of the non-uniform thin films were also determined by the improved Swanepoel method presented. Repeated measurements showed that the refractive index dispersion is determined by the improved method with a standard deviation of precision less than 0.002 for $As_{40}Se_{60}$ at. % thin films and $Ge_{16}As_{24}Se_{15.5}Te_{44.5}$ at. % thin films over the wavelength range from 3 to 23 μm.
- The improved Swanepoel method was successfully applied to determine the refractive index of Ge-As-Se-Te glasses with different compositions ($Ge_{16}As_{24}Se_{15.5}Te_{44.5}$ (M140MINSCGDJ), $Ge_{14.3}As_{27}Se_{15.5}Te_{43.2}$ (M178DJ), $Ge_{20}As_{20}Se_{14}Te_{46}$ (M112DJ), distilled $Ge_{16}As_{24}Se_{15.5}Te_{44.5}$ (M188SCGDJ) and $Ge_{16}As_{24}Se_{19}Te_{41}$ (M193DJ) in the MIR region with an accuracy of less than 0.47 % compared to benchmark values obtained using the minimum

deviation method. The NA of a "high-NA" SIF fibre based on the distilled $Ge_{16}As_{24}Se_{15.5}Te_{44.5}$ at. % core and the $Ge_{10}As_{23.4}Se_{66.6}$ at. % (M007MINSCGNM) cladding was calculated to be larger than 1.82 over the wavelength range from 2 to 25 μm. The NA of a "low-NA" SIF fibre based on the distilled $Ge_{16}As_{24}Se_{15.5}Te_{44.5}$ at. % core and $Ge_{16}As_{24}Se_{19}Te_{41}$ at. % cladding was calculated to be less than 0.40 over the wavelength range from 3 to 18 μm. The material disperions of these five compositions were also successfully obtained, which showed that the zero dispersion wavelength might shift to shorter wavelength with less atomic % of Te in Ge-As-Se-Te. Refractive index data for other chalcogenide glasses was also successfully determined by the improved Swanepoel method, which was very useful to the design of SIF fibres for sensing, PL emission and fibre lasing.

- A new technique has been developed to determine the small refractive index contrast of two glasses with the same thermal history and post-fibre processing by fabricating a two-composition thin film. Only using the transmittance spectra at normal incidence, the refractive contrast can be determined when the refractive index difference between the two glasses is larger than 0.005. The improved Swanepoel method was then applied to determine the actual values of the refractive index in the two-composition thin film with a standard deviation of precision less than 0.002. The refractive index contrast can be determined with an error of ±0.0005. Compared to the value of the numerical aperture obtained by means of the minimum deviation method, the numerical aperture was determined from this technique with an error of less than 0.011. 3 atomic % S replacing Se in the Ge-Sb-Se glass system was shown to blue-shift the near-infrared optical bandgap and far-infrared fundamental vibrational absorption bands, lower the refractive index by 0.013 at a wavelength of 3.1 μm and by 0.012 at a wavelength of 6.45 μm, and make the zero dispersion wavelength locate at a shorter wavelength (shifted from 6.3 to 6.1 μm).

References

[6.1] Swanepoel, R., 1985. Determining refractive index and thickness of thin films from wavelength measurements only. *Journal of the Optical Society of America A*, *2*, pp.1339-1343.

[6.2] Corrales, C., Ramírez-Malo, J.B., Fernández-Peña, J., Villares, P., Swanepoel, R. and Márquez, E., 1995. Determining the refractive index and average thickness of AsSe semiconducting glass films from wavelength measurements only. *Applied Optics*, *34*(34), pp.7907-7913.

[6.3] Crawford, F.S., 1968. *Waves* (Vol. 3). Tata McGraw-Hill Education.

[6.4] Nagelkerke, N.J., 1991. A note on a general definition of the coefficient of determination. *Biometrika*, *78*(3), pp.691-692.

[6.5] Dantanarayana, H.G., Abdel-Moneim, N., Tang, Z., Sojka, L., Sujecki, S., Furniss, D., Seddon, A.B., Kubat, I., Bang, O. and Benson, T.M., 2014. Refractive index dispersion of chalcogenide glasses for ultra-high numerical-aperture fiber for mid-infrared supercontinuum generation. *Optical Materials Express*, *4*(7), pp.1444-1455.

[6.6] Maklad, M.S., Mohr, R.K., Howard, R.E., Macedo, P.B. and Moynihan, C.T., 1974. Multiphonon absorption in As_2S_3-As_2Se_3 glasses. *Solid State Communications*, *15*(5), pp.855-858.

[6.7] Swanepoel, R., 1984. Determination of surface roughness and optical constants of inhomogeneous amorphous silicon films. *Journal of Physics E Scientific Instruments*, *17*, pp.896-903.

[6.8] Zakery, A. and Elliott, S.R., 2007. *Optical nonlinearities in chalcogenide glasses and their applications* (Vol. 135). Berlin: Springer.

[6.9] Fang, Y., Jayasuriya, D., Furniss, D., Tang, Z.Q., Markos, C., Sujecki, S., Seddon, A.B. and Benson, T.M., 2016. Characterising refractive index dispersion in chalcogenide glasses. In *Transparent Optical Networks (ICTON), 2016 18th International Conference on* (pp. 1-5). IEEE.

[6.10] Schott Glass Inc., 2013. Schott Infrared Chalcogenide Glass-IRG26.

[6.11] Agrawal, G.P., 2000. Nonlinear fiber optics. In *Nonlinear Science at the Dawn of the 21st Century* (pp. 195-211). Springer, Berlin, Heidelberg.

[6.12] Jayasuriya, D., 2018. *Towards mid-infrared fibre-optic device and systems for sensing, mapping and imaging* (Doctoral dissertation, University of Nottingham).

[6.13] Parnell, H., 2018. *Towards a Ge-Sb-Se/S hyperspectral imaging probe for early cancer diagnosis (D*octoral dissertation, University of Nottingham).

[6.14] Sojka, L., Tang, Z., Furniss, D., Sakr, H., Fang, Y., Beres-Pawlik, E., Benson, T.M., Seddon, A.B. and Sujecki, S., 2017. Mid-infrared emission in Tb^{3+}-doped selenide glass fiber. *Journal of the Optical Society of America B Optical Physics*, *34*(27), pp.A70-A79.

[6.15] Sati, D.C., Kovalskiy, A., Golovchak, R. and Jain, H., 2012. Structure of $Sb_xGe_{40-x}Se_{60}$ glasses around 2.67 average coordination number. *Journal of Non-Crystalline Solids*, *358*(2), pp.163-167.

[6.16] Boolchand, P., Chen, P. and Vempati, U., 2009. Intermediate Phases, structural variance and network demixing in chalcogenides: The unusual case of group V sulfides. *Journal of Non-Crystalline Solids*, *355*(37-42), pp.1773-1785.

[6.17] France, P.W., Drexhage, M.G., Parker, J.M., Moore, M.W., Carter, S.F. and Wright, J.V., 1991. Fluoride Glass Optical Fibers (Blackie, London, 1990).

[6.18] Petit, L., Carlie, N., Adamietz, F., Couzi, M., Rodriguez, V. and Richardson, K.C., 2006. Correlation between physical, optical and structural properties of sulfide glasses in the system Ge–Sb–S. *Materials Chemistry and Physics*, *97*(1), pp.64-70.

[6.19] El-Sayed, S.M., 2003. Far-infrared studies of the amorphous $Sb_xGe_{28-x}Se_{72}$ glassy semiconductor. *Semiconductor Science Technology*, *18*, pp.337-341.

[6.20] Senior, J. M., & Jamro, M. Y., 2009. *Optical fiber communications: principles and practice*. Pearson Education.

[6.21] Fang, Y., Jayasuriya, D., Furniss, D., Tang, Z.Q., Markos, C., Sujecki, S., Seddon, A.B. and Benson, T.M., 2017. Determining the refractive index dispersion and thickness of hot-pressed chalcogenide thin films from an improved Swanepoel method. *Optical and Quantum Electronics*, *49*(7), p.237.

[6.22] Furniss, D. and Seddon, A.B., 2008. Thermal analysis of inorganic compound glasses and glass-ceramics. *Principles and Applications of Thermal Analysis*, pp.411-442.

[6.23] Parnell, H., Furniss, D., Tang, Z., Neate, N.C., Benson, T.M. and Seddon, A.B., 2018. Compositional dependence of crystallization in Ge–Sb–Se glasses relevant to optical fiber making. *Journal of the American Ceramic Society*, *101*(1), pp.208-219.

[6.24] Amorphous material Inc., 2013. AMTIR-2 Information.

[6.25] Dudley, J. M., & Taylor, J. R. (Eds.), 2010. *Supercontinuum generation in optical fibers*. Cambridge University Press.

Chapter 7: The effect of temperature on the optical properties of chalcogenide glasses

In chapter 6, an improved Swanepoel method was successfully developed to determine the refractive index dispersion of chalcogenide glasses in the MIR region. The main focus in this chapter is to investigate the effect of temperature on the optical properties (transparent window, refractive index, numerical aperture, material dispersion and so on) of chalcogenide glasses.

A temperature-controlled holder for bulk-glass FTIR samples and thin films within the FTIR spectrometer (Bruker IFS 66 v/s), and also for prisms was designed and manufactured as introduced in section 3.8. This enables investigation of the effect of temperature on the optical properties of chalcogenide glasses in this chapter.

The thermo-optic coefficient of a material, a very important aspect of infrared optical design, is the change in refractive index with temperature (dn/dT). Although many studies have focused on the physical and optical characteristic of chalcogenide glasses, little dn/dT data is available for chalcogenide glasses in the MIR region [7.1,7.2]. In this chapter, the dn/dT of chalcogenide-glass prisms (the preparation procedure was described in section 3.4) will be measured using the minimum deviation method. In order to obtain the continuous dn/dT data in the MIR region, a novel technique is developed based on the improved Swanepoel method introduced in chapter 6.

Section 7.1 will analyse the FTIR spectra for a selection of chalcogenide glasses ($As_{40}Se_{60}$ at. % (M179CMDF), $Ge_{16}As_{24}Se_{15.5}Te_{44.5}$ at. % (M140MINSCGDJ), $Ge_{20}Sb_{10}Se_{70}$ at. % (M223ZQTDM) and $Ge_{20}Sb_{10}Se_{67}S_3$ at. % (M191HAP)) at different temperatures. Section 7.2 will present the thermo-optic coefficients of these

four chalcogenide glasses measured at certain wavelengths using the minimum deviation prism method. To obtain the thermo-optic coefficients of chalcogenide glasses at MIR wavelengths, a FTIR continuous dn/dT method is developed as described in section 7.3. The material dispersion and numerical aperture (NA) as a function of temperature will also be presented in this section. Finally, a summary of the results and methods presented in this chapter will be made in section 7.4.

7.1 Thermal-FTIR analysis for chalcogenide glasses

The FTIR spectra of chalcogenide glasses ($As_{40}Se_{60}$ at. % (M179CMDF), $Ge_{16}As_{24}Se_{15.5}Te_{44.5}$ at. % (M140MINSCGDJ), $Ge_{20}Sb_{10}Se_{70}$ at. % (M223ZQTDM) and $Ge_{20}Sb_{10}Se_{67}S_3$ at. % (M191HAP)) at set temperatures (water bath temperature) of 20, 40 60 and 80 ℃ are studied here. When the water bath was heated or cooled to a set temperature, the sample would be left for 20 mins to obtained a stable temperature. The actual sample temperature at each set temperature measured using a self-adhesive thermocouple (K-type) was 21.8±0.2 ℃, 37.8±0.2 ℃, 55.9±0.3 ℃ and 74.0±0.3 ℃, respectively. The FTIR samples were prepared following the procedure in section 3.6.2. The optical setup was discussed in section 3.6.3. The thermal performance of the thermal holder was shown in section 3.8. Before measurements, the temperature of sample holder was set to be 20 ℃, and the FTIR spectrometer was purged with dry air (Parker Filtration, FTIR purge gas generator, 75-52-12VDC) for 15 mins to minimise the effect of air absorptions. Then a background spectrum was recorded using the chosen aperture size of 12 mm. After the background spectrum was recorded, the sample was mounted on the thermally controlled holder. The FTIR spectrum of the sample at certain temperatures was collected after a 15-minute dry-air purging.

7.1.1 Thermal-FTIR analysis for $Ge_{16}As_{24}Se_{15.5}Te_{44.5}$ at. % bulk glass

The absorbance spectra of $Ge_{16}As_{24}Se_{15.5}Te_{44.5}$ at. % at temperatures of 21.8±0.2 ℃, 37.8±0.2 ℃, 55.9±0.3 ℃ and 74.0±0.3 ℃ are shown in Figure 7.1-1. The major absorption band located within the transparent window is at ~ 13 μm, which might be a combination band due to the stretching vibration of oxide impurities (Ge-O, Te-O) [7.3,7.4] and the multiphonon absorption band.

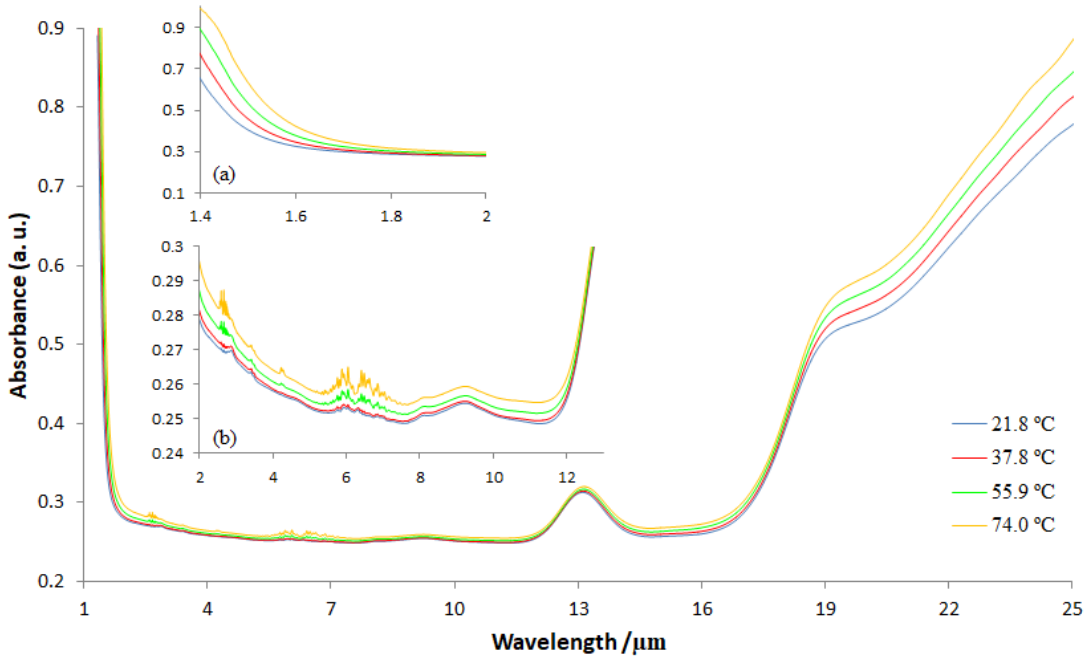


Figure 7.1- 1. The FTIR absorbance spectra of $Ge_{16}As_{24}Se_{15.5}Te_{44.5}$ at. % (M140MINSCGDJ) at temperatures of 21.8±0.2 ℃ (blue), 37.8±0.2 ℃ (red), 55.9±0.3 ℃ (green) and 74.0±0.3 ℃ (purple) over the wavelength from 1 to 25 μm. Inset: The FTIR absorbance spectra of Ge-As-Se-Te at the temperature of 21.8 ℃ (blue), 37.8 ℃ (red), 55.9 ℃ (green) and 74.0 ℃ (purple) (a) in the NIR region and (b) over the wavelength from 2 to 13 μm.

Inset (a) to Figure 7.1-1 appears to show the optical band gap of $Ge_{16}As_{24}Se_{15.5}Te_{44.5}$ at. % shifts to longer wavelengths with increasing the temperatures. From inset (b) to Figure 7.1-1, it is revealed that several absorption bands were present across the wavelength range from 2 to 13 μm. The thermally-dependent absorption bands from the measured atmosphere were observed at ~ 2.9 μm, 4.2 μm and 6.2 μm, which can be associated with O-H band absorption

[7.4,7.5], CO_2 absorption [7.5] and molecular H_2O bending absorption [7.5,7.6], respectively. These impurity absorptions are likely to be an artefact from the measured atmosphere [7.5,7.7-7.10] but may also have a contribution from these species being dissolved in the glass itself. Se-H exhibits an absorption band at 3.42 μm and 4.52 μm [7.4], which appears to be not thermally sensitive as shown in inset (b) to Figure 7.1-1. Two other thermally-independent absorption bands were found to be the glass Ge-O band at ~ 8 μm [7.11,7.12] and the glass Si-O band at ~ 9 μm [7.4]. Inset (b) to Figure 7.1-1 reveals that the impurity bands in the glass are not sensitive to temperature in the range from 21.8 ℃ to 74.0 ℃. However, the absorption bands from the measured atmosphere were observed to be temperature-dependent.

In the short wavelength cutoff region ($\lambda \leq 4.1$ μm) (see inset (b) to Figure 7.1-1), the absorption curve follows the standard Urbach edge [7.13] behaviour which, as discussed in section 2.3.3.1, occurs when free electrons in the mobility edge absorb sufficient photon energy and jump across the optical gap into the conduction band. The absorption ($\Delta\alpha_{el}$) increases with higher temperature in accordance with the following empirical relationship [7.14]:

$$\Delta\alpha_{el} = C(T)\exp\left(\frac{d(T)}{\lambda}\right) - C\exp(d/\lambda) \qquad (7.1)$$

where $C(T)\exp\left(\frac{d(T)}{\lambda}\right)$ is the electronic absorption at temperature T and $C\exp(d/\lambda)$ is the electronic absorption at room temperature; $C(T)$ and $d(T)$ are temperature-dependent constants.

In the Ge-As-Se-Te glass system, since tellurium exhibits a semi-metallic character, the free-electron concentration increases with temperature due to the smaller optical band gap (0.90 - 0.98 eV) [7.14]. This free-electron concentration would contribute to the absorbance spectrum as free-carrier absorption depending on the temperature. The free-carrier absorption, an indirect process involving both a

photon and phonon, occurs when electrons in the lower conduction band absorb radiation and are excited to a higher conduction band (intraband absorption) or states in different bands (interband absorption). With temperatures increasing, these electrons are scattered inelastically by lattice vibrations, transferring energy to the lattice of the material. The free-carrier absorption (α_{fc}) is reported to follow the empirical relationship [7.15,7.16]:

$$\alpha_{fc} = \mathrm{G}\lambda^{m} + G_0 \exp(-E_0/k_B T) \qquad (7.2)$$

where the first term in Eq. (7.2) represents the intraband absorption which is temperature-independent and the second term in Eq. (7.2) represents the interband absorption which is temperature-dependent. G is the constant for optical phonon scattering, m lies between 1.5 and 3.5, G_0 is a material constant and T is the temperature. Following Eq. (7.2), the free-carrier absorption is increased by increasing the temperature.

The absorbance in the electronic edge region ($\lambda \leq 4.1\ \mu m$) is attributed to both electronic and free-carrier absorption [7.14] as shown in inset (b) to Figure 7.1-1. At lower temperatures ($\mathrm{T} \leq 30℃$), the absorption is predominantly due to electronic absorption. With temperature increasing, free-carrier absorption would start to contribute to the absorption.

Between the electronic and multiphonon edge ($5\ \mu m \leq \lambda \leq 11\ \mu m$), the loss is due to free-carrier absorption, wavelength-dependent scattering and Rayleigh scattering [7.14]. However, the change in Rayleigh scattering loss with temperature in the Ge-As-Se-Te glass system was found to be negligible and wavelength-independent scattering is not expected to change noticeably with temperature [7.17]. Therefore, free-carrier absorption may be dominant in this region at high temperature, as shown in inset (b) to Figure 7.1-1.

Beyond 11 μm, for these tellurium-containing glasses, the absorbance is perhaps mainly attributed to free-carrier absorption (as also suggested by Nguyen, Sanghera *et al.* [7.17]) and multiphonon absorption as shown in Figure 7.1-1. The multiphonon absorption is directly due to nonlinearities in the electric dipole moment according to [7.18], and indirectly from anharmonic interaction between IR-active phonons and photons according to [7.19]. The multiphonon absorption increases with temperature and follows the relationship according to [7.14]:

$$\Delta\alpha_{mp} = A(T)\exp(b(T)\lambda) - C\exp(b\lambda) \qquad (7.3)$$

where the first term in Eq. (7.3) represents the multiphonon absorption at temperature T and the second term is the multiphonon absorption at room temperature. $A(T)$ and $b(T)$ are temperature-dependent constants and λ is the wavelength. In the 11-12 μm regions, the change in the multiphonon absorption does not appear to increase as significantly as the free-carrier absorption [7.14]. However, with wavelength increasing, the multiphonon absorption starts to dominate, as shown in Figure 7.1-1.

As a result of the red-shifting optical band gap and increased absorbance due to free-carrier absorption and multiphonon absorption at higher temperature, the transparent window of Ge-As-Se-Te becomes narrower and less transparent as shown in Figure 7.1-1.

7.1.2 Thermal-FTIR analysis for $Ge_{20}Sb_{10}Se_{70}$ at. % and $Ge_{20}Sb_{10}Se_{67}S_3$ at. % bulk glasses

The FTIR transmission spectra of bulk $Ge_{20}Sb_{10}Se_{70}$ at. % (M223ZQTDM) and $Ge_{20}Sb_{10}Se_{67}S_3$ at. % (M191HAP) glasses at room temperature (~23.1 ℃) are shown in Figure 7.1-2. Unlike $Ge_{16}As_{24}Se_{15.5}Te_{44.5}$ at. %, the absorbance of $Ge_{20}Sb_{10}Se_{70}$ at. % and $Ge_{20}Sb_{10}Se_{67}S_3$ at. % remains low in the NIR region ($\lambda \leq 2\ \mu m$) as shown in Figure 7.1-2, which indicates that the optical bandgaps for these two compositions are located at shorter wavelengths than those for $Ge_{16}As_{24}Se_{15.5}Te_{44.5}$ at. %.

Inset (a) to Figure 7.1-2 reveals that several absorption bands were present across the 2-10 μm wavelength region. For $Ge_{20}Sb_{10}Se_{70}$ at. %, Se-H exhibits two of its fundamental vibrational absorptions at 4.52 μm and 3.42 μm [7.4]. With introducing 3 atomic % S into $Ge_{20}Sb_{10}Se_{70}$ at. %, H is gathered by S which exhibits a strong absorption at 4.03 μm. Therefore, the Se-H absorption band at 4.52 μm and 3.42 μm becomes weaker as shown in inset (a) in Figure 7.1-2. A Ge-O absorption band at ~ 8 μm [7.11,7.12] and a Si-O absorption band at ~ 9 μm [7.4] are also observed in inset (a) to Figure 7.1-2 for both $Ge_{20}Sb_{10}Se_{70}$ at. % and $Ge_{20}Sb_{10}Se_{67}S_3$ at. %.

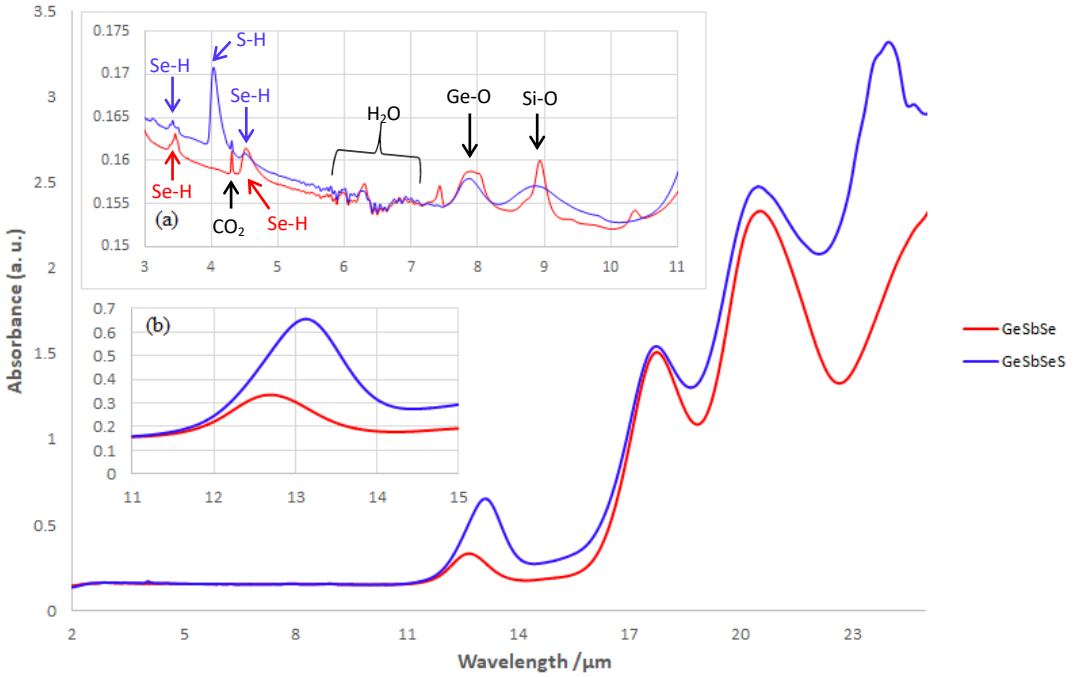


Figure 7.1- 2. FTIR absorbance spectra for $Ge_{20}Sb_{10}Se_{70}$ at. % (M223ZQTDM) and $Ge_{20}Sb_{10}Se_{67}S_3$ at. % (M191HAP) at room temperature over the wavelength from 2 to 25 μm. Inset: (a) FTIR absorbance spectra for $Ge_{20}Sb_{10}Se_{70}$ at. % and $Ge_{20}Sb_{10}Se_{67}S_3$ at. % from 3 to 11 μm; (b) absorption bands locate at ~ 13 μm for $Ge_{20}Sb_{10}Se_{70}$ at. % and $Ge_{20}Sb_{10}Se_{67}S_3$ at. %.

For $Ge_{20}Sb_{10}Se_{70}$ at. %, an obvious absorption band was observed at 12.69 μm, which might be attributed to Ge-O impurity [7.20]. However, with introducing 3 atomic % S into Ge-Sb-Se, the peak of the band shifted to 13.13 μm (see inset (b) to Figure 7.1-2), which might be a combination band due to the Ge-O band and the multiphonon absorption band. Interestingly, an absorption band at ~ 26 μm was

found in the interference transmission spectrum of $Ge_{20}Sb_{10}Se_{67}S_3$ at. % (see Figure 6.7-1). Therefore, the absorption band at 13.13 μm might be attributed to the Ge-O band and the second overture of the multiphonon absorption band at ~ 26 μm (more evidence for this assertion will be shown later). Figure 7.1-2 shows that two obvious multiphonon absorption bands locate at ~ 17.8 μm (17.75 μm for $Ge_{20}Sb_{10}Se_{70}$ at. % and 17.73 μm for $Ge_{20}Sb_{10}Se_{67}S_3$ at. %) and ~ 20.5 μm (20.54 μm for $Ge_{20}Sb_{10}Se_{70}$ at. % and 20.49 μm for $Ge_{20}Sb_{10}Se_{67}S_3$ at. %) for both compositions. The band at ~ 20.5 μm is the second overtone of the fundamental vibrational absorption band due to a $GeSe_4$ tetrahedral unit [7.21].

The FTIR absorbance spectra of $Ge_{20}Sb_{10}Se_{70}$ at. % and $Ge_{20}Sb_{10}Se_{67}S_3$ at. % at temperatures of 21.8±0.2 ℃, 37.8±0.2 ℃, 55.9±0.3 ℃ and 74.0±0.3 ℃ are shown in Figure 7.1-3. Insets (i) to Figures 7.1-3(a) and 7.1-3(b) reveal that the impurities absorption bands (Se-H, S-H, Ge-O and Si-O bands) are not sensitive to temperature within this temperature range. Temperature-dependent absorption bands associated with the atmosphere were also observed at ~ 2.9 μm, 4.2 μm and 6.2 μm, which were associated with the O-H band absorption, CO_2 absorption and molecular H_2O bending absorption, respectively [7.5]. Unlike tellurium-based glass, which possesses a semi-metallic character, free-carrier absorption is not so likely to occur in $Ge_{20}Sb_{10}Se_{70}$ at. % and $Ge_{20}Sb_{10}Se_{67}S_3$ at. %. Therefore, the absorption would not be expected to significantly increase with increasing temperatures between the electronic and multiphonon edges, as confirmed by the absorbance data shown in insets (i) to Figures 7.1-3(a) and 7.1-3(b). Therefore, it is concluded that the presence of tellurium in chalcogenide glasses, especially at high levels, is likely to be detrimental in field applications of these glasses.

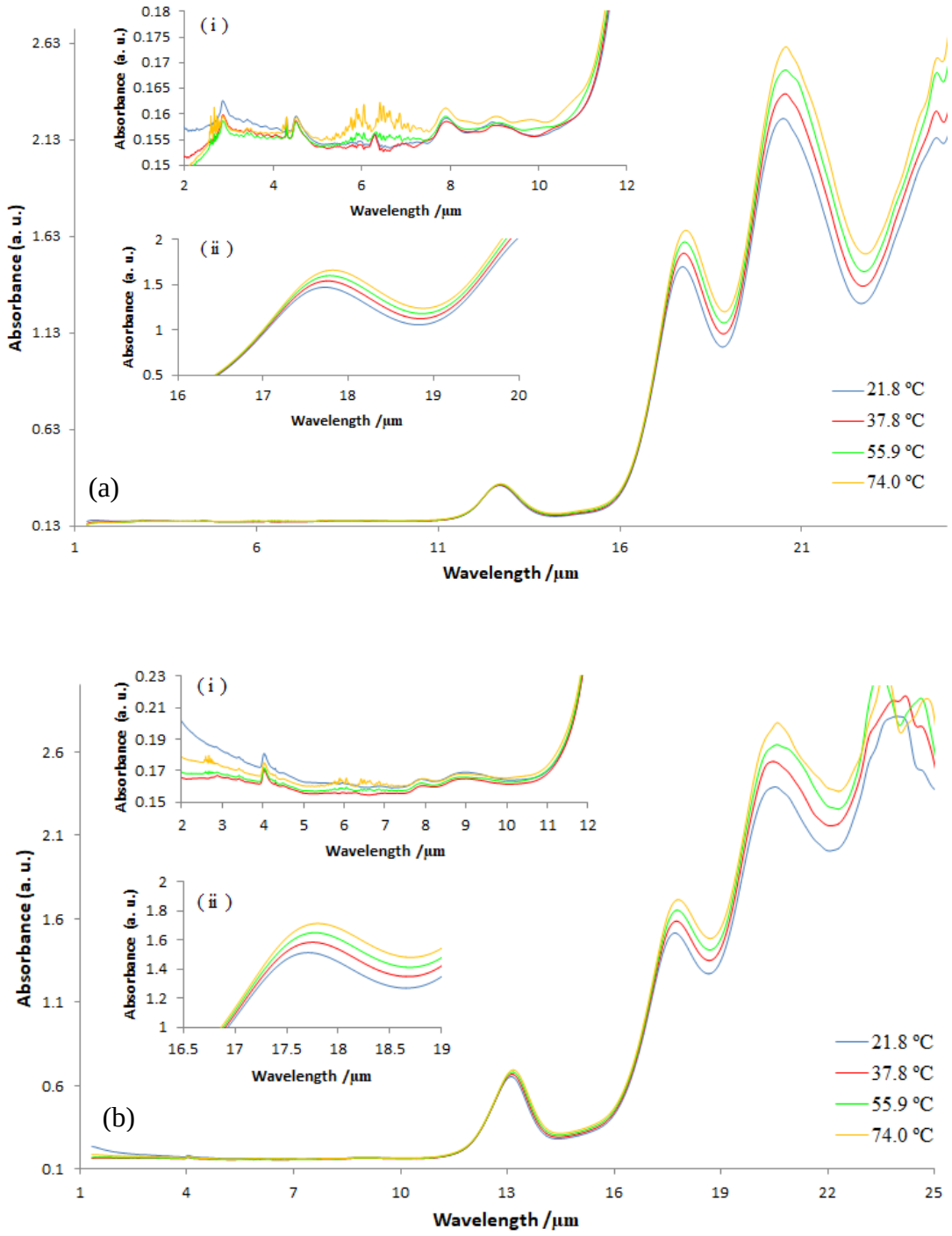


Figure 7.1- 3. The FTIR absorbance spectra of (a) $Ge_{20}Sb_{10}Se_{70}$ at. % (M223ZQTDM) (inset: (i) the absorbance spectra of $Ge_{20}Sb_{10}Se_{70}$ at. % from 2 to 12 µm at temperatures of 21.8±0.2 ℃, 37.8±0.2 ℃, 55.9±0.3 ℃ and 74.0±0.3 ℃; (ii) the multiphonon absorption band at ~ 17.8 µm;) and (b) $Ge_{20}Sb_{10}Se_{67}S_3$ at. % (M191HAP) (inset: (i) the absorbance spectra of $Ge_{20}Sb_{10}Se_{67}S_3$ at. % from 2 to 12 µm at different temperatures; (ii) the multiphonon absorption band at ~ 17.8 µm; at temperatures of 21.8±0.2 ℃, 37.8±0.2 ℃, 55.9±0.3 ℃ and 74.0±0.3 ℃).

The absorption band at 12.69 μm for $Ge_{20}Sb_{10}Se_{70}$ at. % is not sensitive to increasing temperature as shown in Figure 7.1-3(a). According to Eq. (7.3), multiphonon absorption will increase with temperature. Therefore, it is inferred that this absorption band is mainly attributable to the impurity absorption (Ge-O [7.20]). Due to the small composition difference between $Ge_{20}Sb_{10}Se_{70}$ at. % and $Ge_{20}Sb_{10}Se_{67}S_3$ at. %, the Ge-O absorption band at 12.69 μm was expected to exist. With introducing 3 atomic % S into $Ge_{20}Sb_{10}Se_{70}$ at. %, the peak of the absorption band at 12.69 μm was shifted to 13.13 μm. Moreover, this band in $Ge_{20}Sb_{10}Se_{67}S_3$ at. % becomes more sensitive to temperature as shown in Figure 7.1-3(b). Therefore, the absorption band at 13.13 μm for $Ge_{20}Sb_{10}Se_{67}S_3$ at. % is proposed to be a combination band due to the Ge-O band and S-related-multiphonon absorption.

Insets (ii) to Figures 7.1-3(a) and 7.1-3(b) reveal that the peak of multiphonon absorption band at ~ 17.8 μm slightly shifts to longer wavelengths with increasing temperature (peak position: 17.73, 17.76, 17.78, 17.82 μm at temperatures of 21.8 ℃, 37.8 ℃, 55.9 ℃ and 74.0 ℃, respectively, for $Ge_{20}Sb_{10}Se_{70}$ at. %; 17.71, 17.75, 17.77, 17.80 μm at temperatures of 21.8 ℃, 37.8 ℃, 55.9 ℃ and 74.0 ℃, respectively, for $Ge_{20}Sb_{10}Se_{67}S_3$ at. %). The same effects were also observed at the multiphonon absorption bands at ~20.5 μm for $Ge_{20}Sb_{10}Se_{70}$ at. % and $Ge_{20}Sb_{10}Se_{67}S_3$ at. %, as shown in Figure 7.1-3. The red shifts indicate the fundamental vibrational absorption bands shift to longer wavelengths with increasing temperature.

7.1.3 Analysis of multiphonon combination bands in $As_{40}S_{60}$ at. %

Lucovsky and Martin [7.22] have suggested that in As_2Y_3 (Y=S or Se) glass the AsY_3 pyramidal group is only weakly coupled vibrationally by the As-Y-As group and that the infrared and Raman spectra correspond to those for an AsY_3 molecule superimposed on the As-Y-As spectrum. Their model was supported by the infrared spectra studies of $As_{40}S_{60}$ at. % and $As_{40}Se_{60}$ at. % glasses from Moynihan's group

[7.23]. In [7.23], the combination bands of $As_{40}Se_{60}$ at. % were analysed using an $AsSe_3$ stretch frequency $v_A' = 240\ cm^{-1}$ (41.7 μm) and an As-Se-As stretch frequency $v_B' = 340\ cm^{-1}$ (29.4 μm).

As previously discussed in section 7.1.1, the multiphonon absorption exhibits a temperature-dependence following the relationship in Eq. (7.3). Therefore, as temperature increasing, the location of the overtone bands for the fundamental multiphonon absorptions can be indicated by an absorbance that increases with temperature.

The FTIR absorbance spectra of $As_{40}Se_{60}$ at. % (M179CMDF) at temperatures of 21.8±0.2 ℃, 37.8±0.2 ℃, 55.9±0.3 ℃ and 74.0±0.3 ℃ are displayed in Figure 7.1-4. The positions of possible combination bands according to [7.23] are shown in the inset to Figure 7.1-4. A huge temperature-dependent absorption band was found at ~ 20.6 μm (see Figure 7.1-4), which is very close to the second overtone of fundamental vibrational band due to the $AsSe_3$ unit at 20.85 μm. Moreover, this band slightly shifted to longer wavelengths with increasing temperature. An obvious increase of absorbance with temperature was found in the wavelength range from 17 to 18 μm (see inset in Figure 7.1-4) which is in a good agreement with the suggestion that a combination band at ~17.2 μm ($v_A' + v_B'$) is located within this region [7.23]. Between 13.5 μm and 16 μm, the absorbance exhibits a temperature-dependence which is attributed to the third overtone ($3\,v_A'$) of fundamental vibrational band due to the $AsSe_3$ unit, which is at 13.89 μm, and the second overtone ($2v_B'$) of the vibrational absorption band due to the As-Se-As stretch unit, which is at ~14.7 μm. The obvious absorption band at ~12.8 μm is not sensitive to temperature, and might be attributed to impurity absorption (possibly As-O [7.3, 7.24]). The inset to Figure 7.1-4 also reveals that the rest of combination bands don't cause a significant temperature-dependent increase in the absorption. Furthermore, the first several combinations correspond clearly to the prominent

features in the absorbance spectra (maximum at 20.6 μm, shoulder at 17.2 μm and maximum at 14.7 μm at the temperature of 20 ℃).

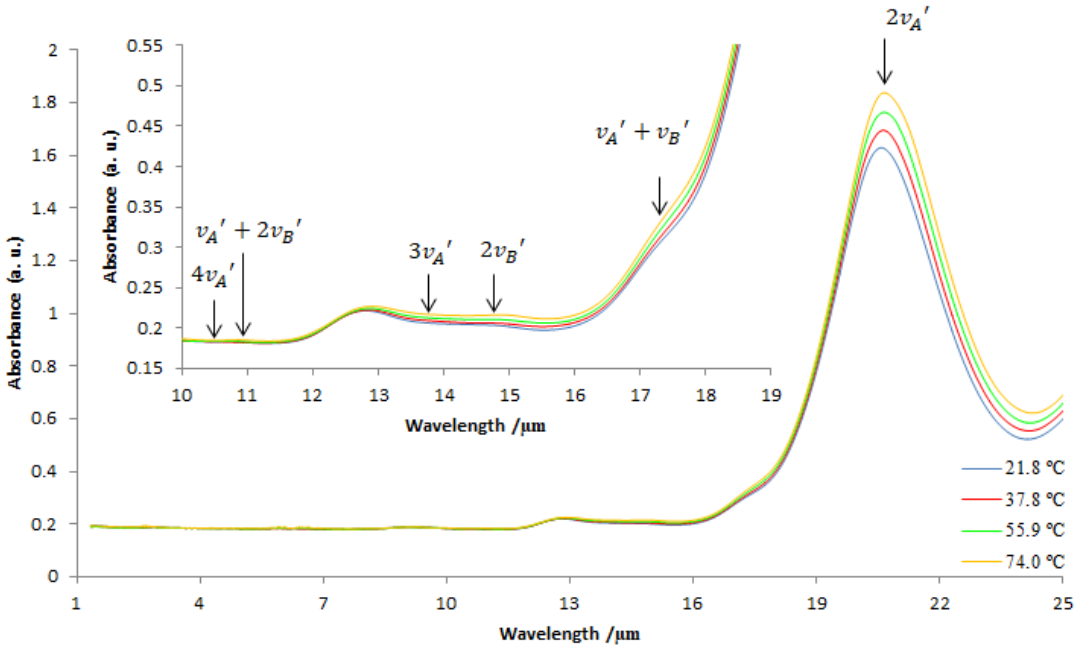


Figure 7.1- 4. The FTIR absorbance spectra of $As_{40}Se_{60}$ at. % (M179CMDF) at temperatures of 21.8±0.2 ℃, 37.8±0.2 ℃, 55.9±0.3 ℃ and 74.0±0.3 ℃ over the wavelength range from 1 to 25 μm. Inset: The FTIR absorbance spectra of $As_{40}Se_{60}$ at. % (M179CMDF) at temperatures of 21.8±0.2 ℃, 37.8±0.2 ℃, 55.9±0.3 ℃ and 74.0±0.3 ℃ with the position of possible combination bands from Moynihan's group [7.23] indicated.

7.2 Thermo-optic coefficients of chalcogenide glasses using the minimum deviation method.

As described in section 2.5.1, the minimum deviation method was considered as the most accurate method to determine the refractive index of prisms at certain wavelengths. The optical setup for the minimum deviation method in our laboratory can determine the refractive index of chalcogenide prisms to four decimal places, as discussed in section 4.4.

A thermally-controlled holder was designed for heating or cooling a chalcogenide glass prism as described in section 3.8; this enabled the investigation of thermo-optic coefficients (dn/dT) for chalcogenide glass prisms.

In this section, the thermo-optic coefficients and thermal polarisability coefficients of the chalcogenide glasses will be determined using the minimum deviation method. The error of using this method to determine the dn/dT of chalcogenide glasses will also be analysed.

7.2.1 Thermo-optic coefficient (dn/dT) and thermal polarisability coefficient of a chalcogenide glass

The variation in the refractive index of a chalcogenide glass with a change in temperature is described as thermo-optic behaviour, and is an extremely important, and often overlooked, aspect of infrared optical design [7.25]. The refractive index change with temperature is attributed to the thermal excitation of phonons (and electrons in some cases), and can be either positive or negative in sign depending on the composition of the glass. A positive refractive index change in response to an applied thermal load is responsible for phenomena such as thermal lensing, self-focusing and laser damage (at high intensities), and spectral instabilities in laser resonators [7.26]. Furthermore, for supercontiuum generation (SCG), this refractive index change with temperature is likely to change the confinement of a step-index fibre (SIF) and material dispersion. Despite its importance, little dn/dT data is available for chalcogenide glasses in the MIR region [7.1,7.2,7.27], possibly because it often only begins to impact device design when high-precision optics are necessary [7.28] but this is now becoming a near-term probality especially with the lenses now being developed for night-sights.

The thermo-optic coefficient (dn/dT) can be measured with the minimum deviation setup (described in section 4.2) used in conjunction with the

thermally-controlled prism holder (described in section 3.8). The expression of dn/dT follows:

$$\frac{\mathrm{dn}}{\mathrm{dT}} = \frac{n_h - n_l}{T_h - T_l} \qquad (7.4)$$

where n_h is the refractive index at a higher temperature T_h and n_l is the refractive index at a lower temperature T_l. Schematic diagrams of using the minimum deivation method to measure the refractive index of the chalcogenide glass with a positive or negative dn/dT are shown in Figure 7.2-1.

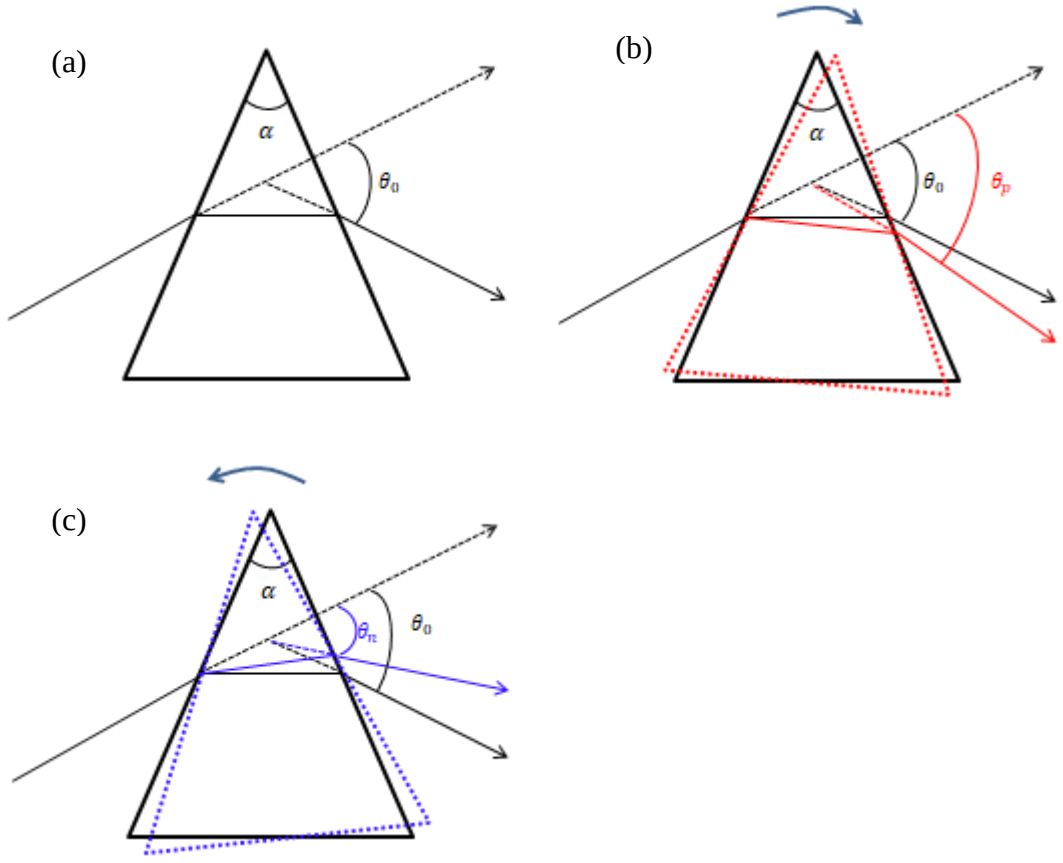


Figure 7.2- 1. Schematic diagrams showing (a) the minimum deviation deflections of a beam travelling through a chalcogenide prism with an apex angle of α; (b) the minimum deviation deflections of a beam travelling through the chalcogenide prism with a positive thermo-optic coefficient; (c) the minimum deviation deflections of a beam travelling through the chalcogenide prism with a negative thermo-optic coefficient.

At lower temperature T_l, the minimum deviation position of the chalcogenide glasses (defined in section 4.1) is shown in Figure 7.2-1(a) with the minimum deviation deflections of θ_0 and apex angle of α. Therefore, the refractive index n_l at the temperature of T_l can be calculated from Eq. (4.1). With temperature increasing to a higher temperature T_h, the minimum deviation position of the chalcogenide prism with a positive dn/dT is shown in Figure 7.2-1(b). Due to the positive dn/dT, the minimum deviation defection will increase from θ_0 to θ_p. Therefore, the refractive index n_h at the temperature of T_h will be higher than n_l according to Eq. (4.1). For a chalcogenide prism formed from negative dn/dT material, the minimum deviation deflection θ_n at higher temperature T_h will become smaller compared to that at lower temperature as shown in Figure 7.2-1(c). This leads to a smaller n_h compared to n_l according to Eq. (4.1).

The thermal Lorentz-Lorenz model, which models the change in refractive index with temperature, was first presented by [7.29] and is:

$$\frac{dn}{dT} = \frac{(n^2-1)(n^2+2)}{6n}(\varphi - \beta) \qquad (7.5)$$

where φ is related to the thermal polarisation coefficient and β is related to the thermal expansion coefficient. From Eq. (7.5), the thermo-optic coefficient is affected by volumetric expansion with temperature and the electronic polarisation of the atoms with temperature, which will result in positive ($\varphi > \beta$) or negative ($\varphi < \beta$) dn/dT as reported in [7.1,7.2]. The relation was simplified by Hilton [7.30]:

$$\frac{1}{n^3}\frac{dn}{dT} = \frac{1}{6}\frac{1}{R_m}\frac{dR_m}{dT} - 3TEC \qquad (7.6)$$

where TEC is thermal expansion coefficient and $\frac{1}{R_m}\frac{dR_m}{dT}$ is the thermal polarisability coefficient (TPC). Using this Hilton approximation with the measured *n*, dn/dT and TEC, the thermal polarisability coefficient can be determined.

Results for the measured thermo-optic coefficients and calculated thermal polarisability of chalcogenide glasses will be presented in sub-section 7.2.4.

7.2.2 Thermo-optic and thermal polarizability coefficients of $As_{40}Se_{60}$ at. % and $Ge_{16}As_{24}Se_{15.5}Te_{44.5}$ at. % obtained from prism measurements.

7.2.2.1 Thermo-optic coefficient of $As_{40}Se_{60}$ at. % and $Ge_{16}As_{24}Se_{15.5}Te_{44.5}$ at. % obtained from prism measurements

The experimental setup for measuring the refractive index of $As_{40}Se_{60}$ at. % (prism code: YRFP004; melting code: M130MINSCGDJ) and $Ge_{16}As_{24}Se_{15.5}Te_{44.5}$ at. % (prism code: YRFP003; melting code: M140MINSCGDJ) prisms as a function of temperature was shown in Figure 4.2-1 (section 4.2). The refractive indices of $As_{40}Se_{60}$ at. % and $Ge_{16}As_{24}Se_{15.5}Te_{44.5}$ at. % at wavelengths of 1494 nm, 1524 nm, 1554 nm and 3100 nm are shown in Tables 7-1 and 7-2, respectively, as a function of temperature (T_{prism}). Each data point in Tables 7-1 and 7-2 is taken as the average of 10 measurements; the standard deviation of precision on refractive index at the wavelengths of 1494 nm, 1524 nm and 1554 nm is less than 0.0006 and the standard deviation of precision on refractive index at 3100 nm is less than 0.001. The error in measuring the prism temperature is less than 0.2 ℃ (see section 3.8.1.3).

Table 7- 1. The refractive index (*n*) at different prism temperatures T_{prism}, the apex angle and thermal expansion coefficient (TEC) of the $As_{40}Se_{60}$ at. % (M130MINSCGDJ) prism (YRFP004). The error of the measured prism temperature was less than ±0.2 ℃. The measured thermo-optic coefficients of $As_{40}Se_{60}$ at. % were positive at wavelengths of 1494, 1524, 1554 and 3100 nm. The standard deviation of precision on refractive index at the wavelengths of 1494 nm, 1524 nm and 1554 nm is less than 0.0004 and the standard deviation of precision on refractive index at 3100 nm is less than 0.001.

	T_{prism} / ℃	*n* at 1494 nm	*n* at 1524 nm	*n* at 1554 nm	*n* at 3100 nm
As-Se					
	16.0	2.8519	2.8496	2.8472	2.7970
	19.9	2.8521	2.8497	2.8474	-
	28.8	2.8523	2.8498	2.8476	2.7973
	37.1	2.8526	2.8500	2.8478	-
	41.2	-	-	-	2.7975
	45.2	2.8527	2.8502	2.8479	-
	53.7	2.8528	2.8505	2.848	2.7978
	62.1	2.853	2.8508	2.8483	-
	70.4	2.8532	2.851	2.8484	2.7981
Apex angle: 10 °13 ′		TEC=22.4±0.5 ppm/ ℃			

Table 7- 2. The refractive index (*n*) at different prism temperatures T_{prism}, the apex angle and thermal expansion coefficient (TEC) of the $Ge_{16}As_{24}Se_{15.5}Te_{44.5}$ at. % (M140MINSCGDJ) prism (YRFP003). The error of the measured prism temperature was less than ±0.2 ℃. The measured thermo-optic coefficients of $Ge_{16}As_{24}Se_{15.5}Te_{44.5}$ at. % were positive at wavelengths of 1494, 1524, 1554 and 3100 nm. The standard deviation of precision for refractive index at the wavelengths of 1494 nm, 1524 nm and 1554 nm is less than 0.0006 and the standard deviation of precision for refractive index at 3100 nm is less than 0.001.

	T_{prism} / ℃	*n* at 1494 nm	*n* at 1524 nm	*n* at 1554 nm	*n* at 3100 nm
Ge-As-Se-Te					
	15.7	3.2935	3.2869	3.2814	3.1917
	20	3.2944	3.2881	3.2827	-
	24.1	3.2953	3.2889	3.2832	-
	28.3	3.2962	3.2897	3.2841	3.1946
	32.6	3.2972	3.2905	3.285	-
	36.9	3.2983	3.2916	3.2861	-
	41.2	3.2993	3.2927	3.2870	3.1970
	45.5	3.3004	3.2938	3.2882	-
	49.7	3.302	3.2953	3.2897	-
	53.9	3.3033	3.2969	3.2912	3.1994
	58.3	3.3045	3.298	3.2923	-
	62.5	3.3057	3.2994	3.2933	-
	66.7	3.3073	3.3008	3.2946	-
	71.1	3.3089	3.3022	3.2959	3.2035
Apex angle: 10 °16′ TEC=16.6±0.5 ppm/ ℃					

The refractive index of the $As_{40}Se_{60}$ at. % prism measured at wavelengths of 1494, 1524 and 1554 nm at different temperatures is presented in Figure 7.2-2(a). It is found that the refractive index decreases with increasing wavelength at each temperature, which is in agreement with the published behaviour of the refractive index dispersion of the chalcogenide glass [7.35]. The error bar shown for each refractive index data point at different prism temperatures indicates the standard deviation error in determining the refractive index, which is ± 0.0004 at wavelengths of 1494, 1524 and 1554 nm and ±0.0010 at a wavelength of 3100nm.

The temperature variation at each measurement temeperature is less than ± 0.2 ℃, which is too small to show in Figure 7.2-2. Due to the small Δn over the temperature of 16.0 to 70.4 ℃, a linear fit applied to the data provides a R^2 (coefficient of determination, R^2 approching 1 means a good fit) of better than 0.9770. The thermo-optic coefficient (dn/dT) can be directly obtained as the slope of the linear fits, which are shown in Figure 7.2-2. The error of the measured dn/dT at these wavelengths is within $\pm 15.6\ \mathrm{ppm/℃}$ (as will be further illustrated in the following sub-section). The literature value provided in [7.31] (30.7 ppm/℃) is in the error range of the measured thermo-optic coefficients presented in Figure 7.2-2. The refractive index of the $As_{40}Se_{60}$ at. % prism measured at a wavelength of 3100 nm at different temperatures is shown in Figure 7.2-2(b). The error bar shown for each data point indicates the standard deviation error in determining the refractive index, which is 0.001. A linear fit to the data points in Figure 7.2-2(b) yielded the value of dn/dT as 20.2 ppm/℃ with a R^2 of 0.9969. The error of the measured dn/dT at this wavelength is within $\pm 26.0\ \mathrm{ppm/℃}$. As discussed in section 4.4, the error in determining the refractive index of the chalcogenide glasses at a wavelength of 3100 nm is larger than that at wavelengths around 1500 nm due to the poorer beam quality of the ICL source used. Despite the large error bar, Figure 7.2-2 suggests that $As_{40}Se_{60}$ at. % exhibits a linear change in refractive index with temperature (dn/dT = 22.4, 26.1, 20.9 and 20.2 ppm/ ℃ at wavelengths of 1494, 1524, 1554, 3100 nm, respectively) over the measurement range at the wavelengths of 1494, 1524, 1554 nm and 3100 nm.

The refractive index of the $Ge_{16}As_{24}Se_{15.5}Te_{44.5}$ at. % prism measured at 1494, 1524 and 1554 nm at different temperatures is presented in Figure 7.2-3(a). The error bar shown for each data point indicates the standard deviation error in determining the refractive index, which is 0.0006. Linear fits were used to fit the data points with a R^2 of better than 0.9905. However, when a quadratic fit ($y = ax^2 + bx + c$, where a, b and c are fitting parameters) was applied to fit the data points, the refractive

index variation with temperature was suggested to be nonlinear with the R^2 improved from 0.9905 to 0.9979 as shown in Figure 7.2-3(a). For $Ge_{16}As_{24}Se_{15.5}Te_{44.5}$ at. %, the optical bandgap occurs at longer wavelengths compared to that of $As_{40}Se_{60}$ at. %. The measurement region here (1494nm to 1554 nm) locates at the standard Urbach edge in the short wavelength cutoff region (defined in section 7.1.1) as shown in the inset (a) to Figure 7.1-1. From the inset (a) to Figure 7.1-1, the optical bandgap of $Ge_{16}As_{24}Se_{15.5}Te_{44.5}$ at. % will shift to longer wavelengths with increasing temperature. Therefore, the suggested nonlinear behaviour of dn/dT of $Ge_{16}As_{24}Se_{15.5}Te_{44.5}$ at. % in this wavelength (1494 nm to 1554 nm) and temperature (15.7 ℃ to 71.1 ℃) measurement range is not only attributed to the thermal excitation of phonons, but also to the red-shift optical bandgap with temperature. A quadratic fit is confirmed to provide an effective fit to the refractive index of $Ge_{16}As_{24}Se_{15.5}Te_{44.5}$ at. % with temperature in this region, as shown in Figure 7.2-3(a). The dn/dTs of $Ge_{16}As_{24}Se_{15.5}Te_{44.5}$ at. % at different measurement temperatures (15.7, 20.0, 24.1, 28.3, 32.6, 36.9, 41.2, 45.5, 49.7, 53.9, 58.3, 62.5, 66.7 and 71.1 ℃) at wavelengths of 1494, 1524 and 1554 nm with an error of $\pm 15.4\ \mathrm{ppm/℃}$, is shown in Figure 7.2-4. The refractive index of the $Ge_{16}As_{24}Se_{15.5}Te_{44.5}$ at. % prism measured at a wavelength of 3100 nm at different temperatures is shown in Figure 7.2-3(b) with a standard deviation error of 0.001. Since this measurement wavelength locates out of the standard Urbach edge, a linear fit was sufficient enough to fit the data points with a R^2 of 0.9976 yielding the dn/dT at a wavelength of 3100 nm to be 213.0 ppm/℃ with an error of $\pm 25.6\ \mathrm{ppm/℃}$ as shown in Figure 7.2-3(b).

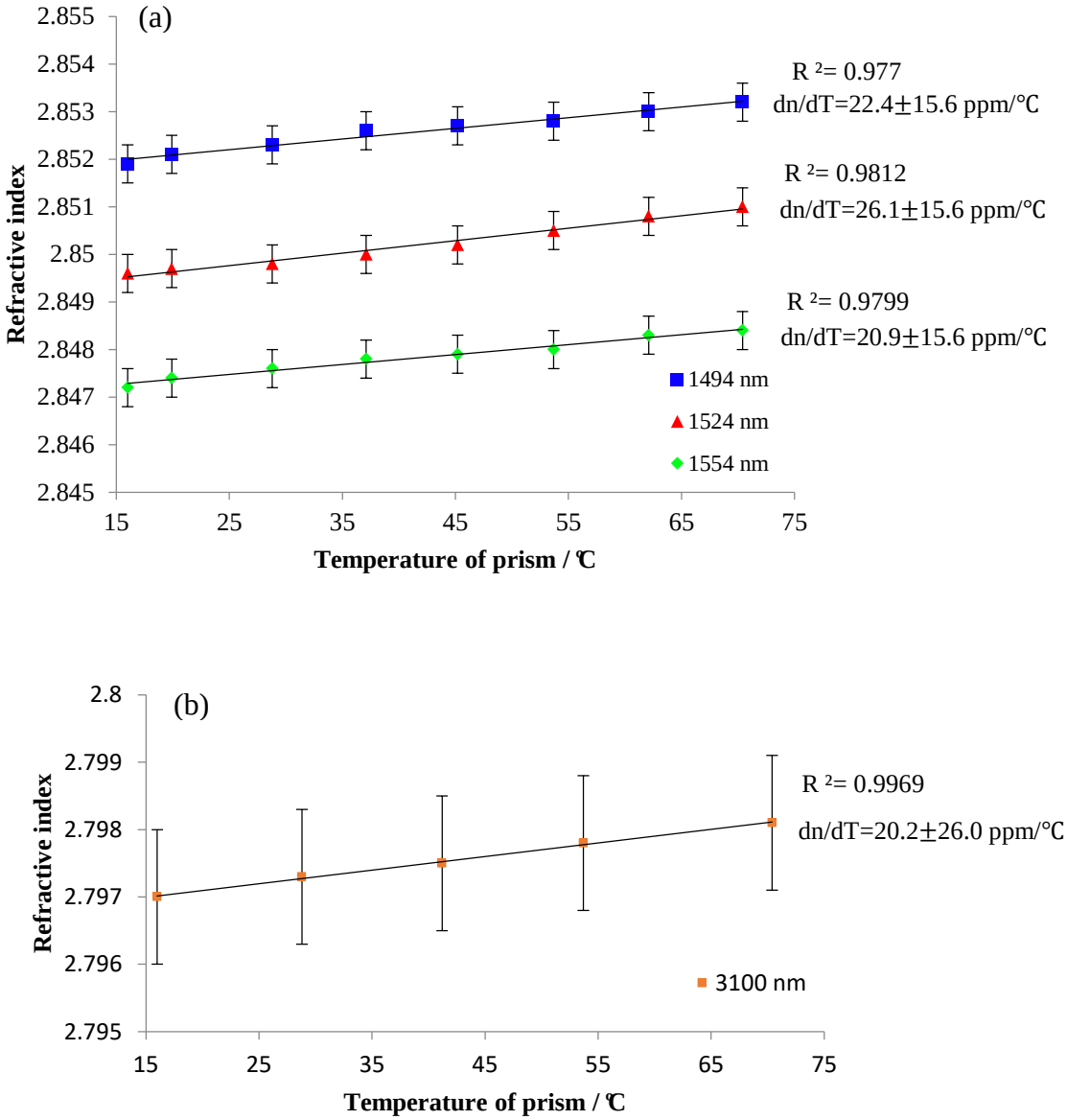


Figure 7.2- 2. The refractive index of the $As_{40}Se_{60}$ at. % (M130MINSCGDJ) prism (YRFP004) varies with temperature at the wavelength of: (a) 1494 nm, 1524 nm, 1554 nm and (b) 3100 nm. The thermo-optic coefficients (dn/dT) are obtained from the linear fits and the R^2 (coefficient of determination) of the fits are given. The temperature variation at each measurement point was less than ±0.2 ℃, which is too small to show in the figure.

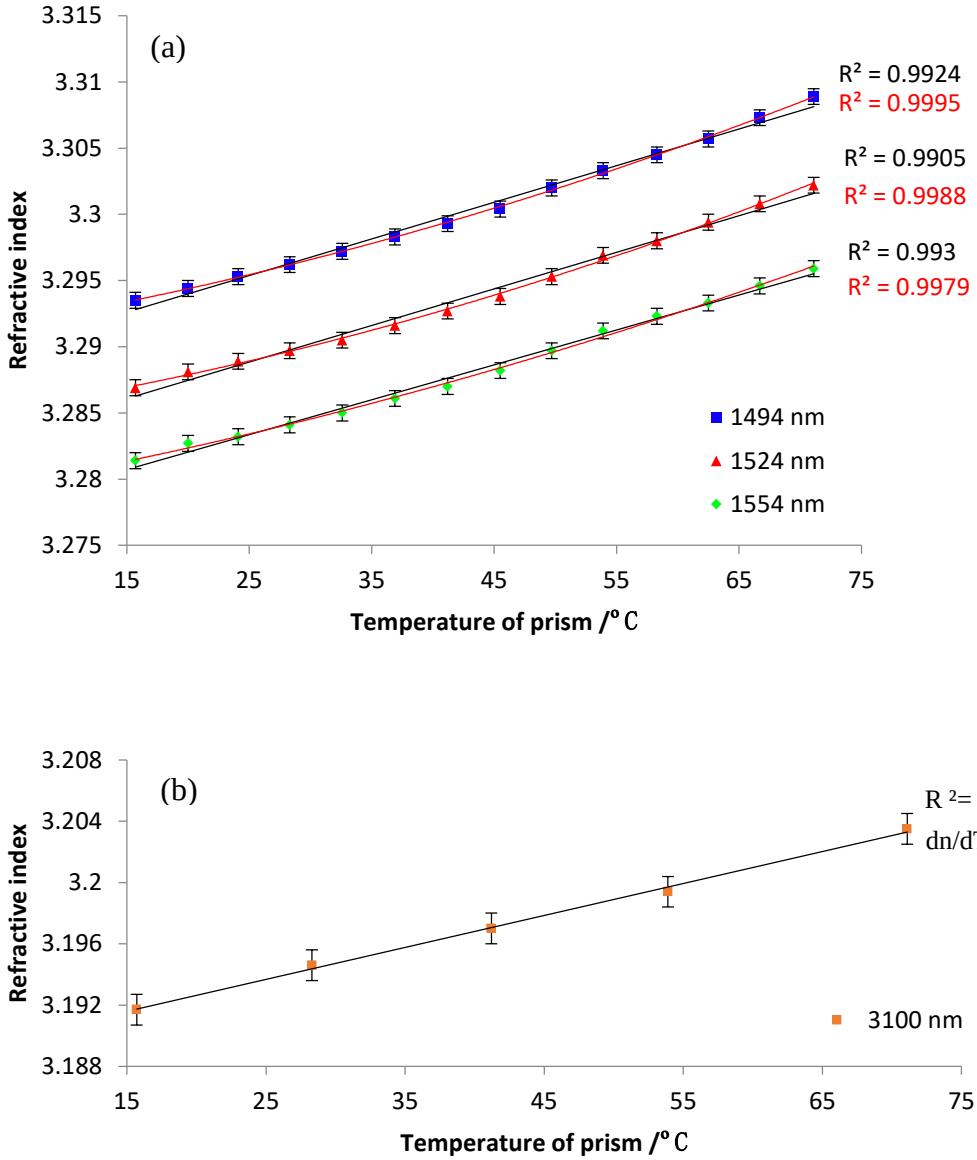


Figure 7.2- 3. The refractive index of the $Ge_{16}As_{24}Se_{15.5}Te_{44.5}$ at. % (M140MINSCGDJ) prism (YRFP003) with temperature at the wavelengths of (a) 1494, 1524, 1554 nm with linear (black) and quadratic (red) fits applied to the data points, and (b) 3100 nm with a linear fit applied to the data points the R^2 (coefficient of determination) of the fits are given. The thermo-optic coefficient (dn/dT) in Figure 7.2-3(b) was obtained from the linear fit. The temperature variation at each measurement point was less than ±0.2 ℃, which is too small to show in the figure.

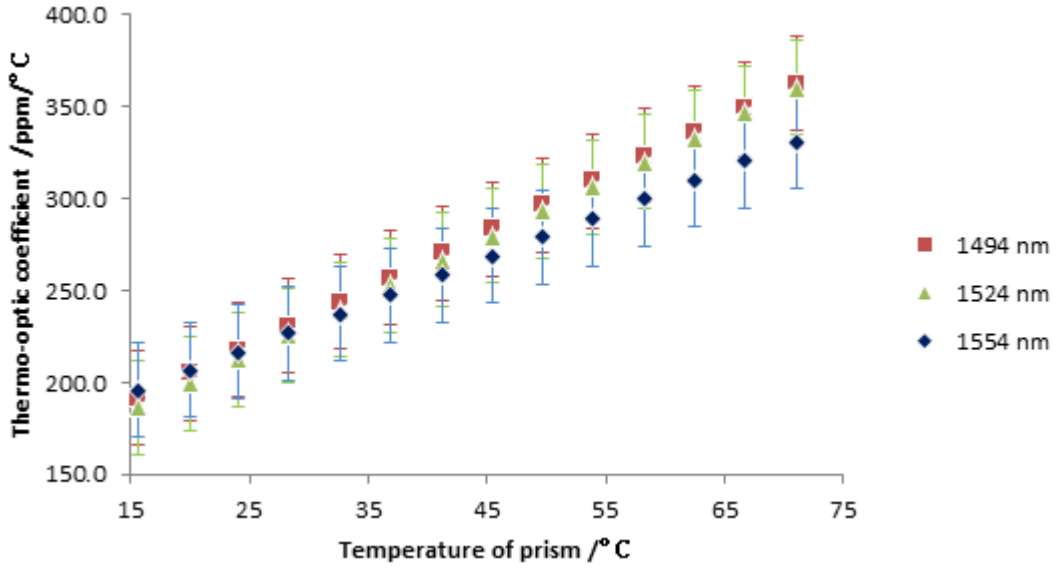


Figure 7.2- 4. Thermo-optic coefficients of the $Ge_{16}As_{24}Se_{15.5}Te_{44.5}$ at. % (M140MINSCGDJ) prism (YRFP003) as a function of temperature at the wavelengths of 1494, 1524 and 1554 nm. The magnitude of the error bar at each data point is 15.4 ppm/ ℃. The temperature variation at each measurement point was less than ±0.2 ℃, which is too small to show in the figure.

7.2.2.2 Error analysis

The absolute error for the dn/dT measurements was calculated using an equation that was firstly presented by Zhou *et al.* [7.32]:

$$\Delta\frac{dn}{dT} = \pm\sqrt{\left[\frac{2}{(T_2-T_1)^2}\Delta n^2 + \frac{2(n_2-n_1)^2}{(T_2-T_1)^4}\Delta T^2\right]} \qquad (7.7)$$

where Δn is the error associated with the refractive index measurements, ΔT is the error associated with measuring the temperature, T_1 and T_2 are the lowest measured temperature and the highest measured temperature respectively, and n_1 and n_2 are the refractive index at the temperatures of T_1 and T_2, respectively. In the present experimental setup, the maximum temperature variation ΔT was less than 0.3 ℃, as previously stated in section 3.8.1.

For measuring the dn/dT of the $As_{40}Se_{60}$ at. % (M130MINSCGDJ) prism using the tunable laser diode at the wavelengths of 1494, 1524 and 1554 nm, the refractive index at the lowest temperature ($T_1 = 16.0$ ℃) and the highest temperature

($T_1 = 71.4$ ℃) is shown in Table 7-1 with a standard error of 0.0006. Therefore, the error of dn/dT can be determined by substituting these values into Eq. (7.7), which yields ± 15.6 ppm/℃. For measuring the dn/dT of the $As_{40}Se_{60}$ at. % prism using the ICL at a wavelength of 3100 nm, the refractive indices at the lowest temperature ($T_1 = 16.0$ ℃) and the highest temperature ($T_1 = 71.4$ ℃) are shown in Table 7-1 with a standard error of 0.001. The error in dn/dT was determined to be ± 26.0 ppm/℃. Following the same procedure the errors of measuring the dn/dT for the $Ge_{16}As_{24}Se_{15.5}Te_{44.5}$ at. % (M140MINSCGDJ) prism using the tunable laser diode and ICL are ± 15.4 ppm/℃ and ± 25.6 ppm/℃, respectively.

From Eq. (7.7), the error in the dn/dT measurements can in principle be effectively reduced by broadening the measurement temperature window and reducing the error in determining refractive index. The error in refractive index measurement could be reduced by using a prism with a larger apex angle, improving the beam quality of the laser source and increasing the optical path between the optical components. The temperature window could in principle be broadened by heating the sample holder by another liquid such as oil which has a higher boiling point than water.

7.2.2.3 Thermal polarisability coefficient of $As_{40}Se_{60}$ at. %and $Ge_{16}As_{24}Se_{15.5}Te_{44.5}$ at. %

Eq. (7.6) shows that the thermal polarisability coefficient (TPC) of a glass can be determined once the refractive index, thermal expansion coefficient (TEC) and thermo-optic coefficient of the glass are known. The TECs of the As-Se and Ge-As-Se-Te glasses were provided by Dr. Dinuka Jayasuriya at the time the work was undertaken a PhD candidate in the Mid-infrared Photonics Group, University of Nottingham UK.

For $As_{40}Se_{60}$ at. % (M130MINSCGDJ), the linear TEC from 30 to 100 ℃ was determined to be 22.4 ppm/℃. The thermal polarisability coefficients at the wavelengths of 1494, 1524 and 1554 nm were calculated from Eq. (7.6) and are

shown in Table 7-3. The thermal polarisability coefficient calculated at the wavelength of 3100 nm is shown in Table 7-4. Since the TEC exhibits linearity within this temperature range, the behaviour of the thermal polarisability coefficient is similar to that of dn/dT, which decreases with increasing wavelength. The TPC result presented for $As_{40}Se_{60}$ at. % is in good agreement with [7.1], which is quoted 406.5 ppm/℃ at a wavelength of 4515 nm.

Table 7- 3. Measured thermo-optic coefficients, refractive indices, thermal expansion coefficients (TEC) and calculated thermal polarisability coefficients (TPCs) of $As_{40}Se_{60}$ at. % (M130MINSCGDJ) at the wavelengths of 1494, 1524 and 1554 nm.

Wavelength / (nm)	dn/dT / (ppm/℃) ± 15.6	n at 19.9 ℃ ±0.0006	TEC / (ppm/℃) ± 0.5	TPC / (ppm/℃)
1494	22.4	2.8521	22.4	409.0
1524	26.1	2.8497	22.4	410.0
1554	20.9	2.8474	22.4	408.6

Table 7- 4. Measured thermo-optic coefficients, refractive indices, thermal expansion coefficients (TEC) and calculated thermal polarisability coefficients (TPCs) of $As_{40}Se_{60}$ at. % (M130MINSCGDJ) and $Ge_{16}As_{24}Se_{15.5}Te_{44.5}$ at. % (M140MINSCGDJ) at the wavelength of 3100 nm.

Composition	dn/dT / (ppm/℃) ± 25.5	n at ~ 28.5 ℃ ±0.0010	TEC / (ppm/℃) ± 0.5	TPC / (ppm/℃)
As-Se	20.2	2.7973	22.4	403.5
Ge-As-Se-Te	213.0	3.1946	16.6	338.0

For $Ge_{16}As_{24}Se_{15.5}Te_{44.5}$ at. % (M140MINSCGDJ), the linear TEC from 30 to 100 ℃ was determined to be 16.6 ppm/℃. The thermo-optic coefficient of $Ge_{16}As_{24}Se_{15.5}Te_{44.5}$ at. % is ~ 10 times higher than that of $As_{40}Se_{60}$ at. %. Eq. (7.6) indicates that a high refractive index, high thermal polarisability coefficient or low thermal expansion coefficient would lead to a high thermo-optic coefficient. Compared to $As_{40}Se_{60}$ at. %, $Ge_{16}As_{24}Se_{15.5}Te_{44.5}$ at. % has a higher refractive index and lower thermal expansion coefficient as shown in Table 7.4. Since the dn/dT varied with temperature, as discussed in section 7.2.2.1, the calculated thermal polarisability was different at different temperatures as shown in Figure 7.2-5. The

thermal polarisability coefficient at the wavelength of 3100 nm is shown in Table 7-4. It is also found that the thermal polarisability coefficient decreases with increasing wavelength. Compared to $As_{40}Se_{60}$ at. %, $Ge_{16}As_{24}Se_{15.5}Te_{44.5}$ at. % has a lower thermal polarisability coefficient.

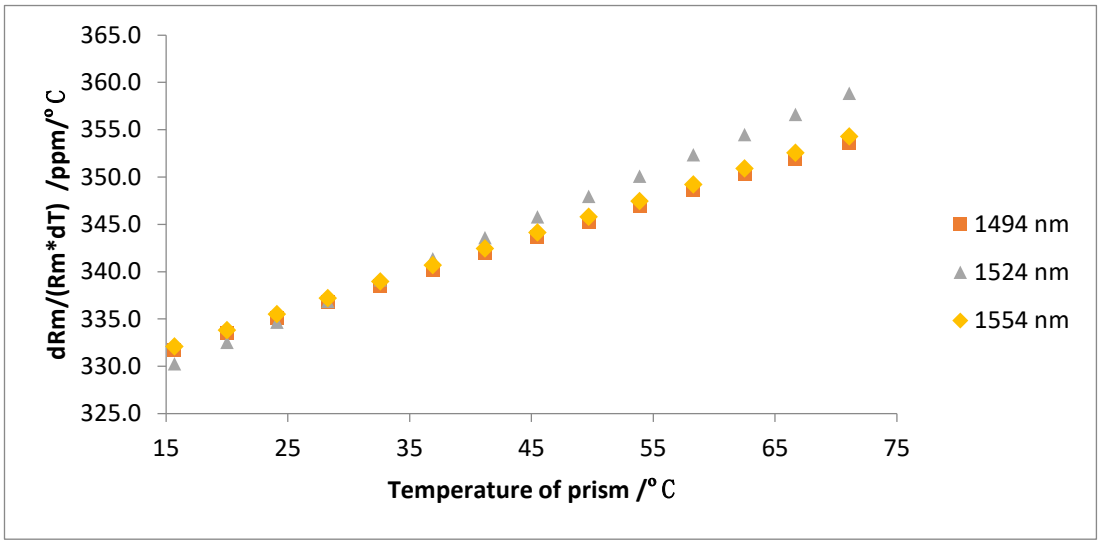


Figure 7.2- 5. The thermal polarisability coefficient of $Ge_{16}As_{24}Se_{15.5}Te_{44.5}$ at. % (M140MINSCGDJ) as a function of temperature at the wavelengths of 1494, 1524 and 1554 nm. The temperature variation at each measurement point was less than ±0.2 ℃, which is too small to show in the figure.

7.2.3 Thermo-optic and thermal polarisability coefficients obtained from the $Ge_{20}Sb_{10}Se_{70}$ at. % and $Ge_{20}Sb_{10}Se_{67}S_3$ at. % prism measurements.

$Ge_{20}Sb_{10}Se_{70}$ / $Ge_{20}Sb_{10}Se_{67}S_3$ (atomic %) core / cladding step-index fibres (SIF) have been successfully fabricated for bio- and chemical-sensing [7.33]. The numerical aperture of this SIF was designed to be ~ 0.27 at the wavelength of 3100 nm at the room temperature. The numerical aperture was obtained from both the minimum deviation method and the improved Swanepoel method (see section 6.7). Since the refractive indices of most chalcogenide glasses are temperature-dependent [7.1,7.2], the numerical aperture is likely to vary with temperature. Therefore, it is crucial to know the thermo-optic coefficients of the core and cladding material, and

hence the variation of the numerical aperture with temperature in order to understand the guiding properties of the SIF, such as the number of modes it supports.

7.2.3.1 Thermo-optic coefficient of $Ge_{20}Sb_{10}Se_{70}$ at. % and $Ge_{20}Sb_{10}Se_{67}S_3$ at. % determined from prism measurements

The refractive index of $Ge_{20}Sb_{10}Se_{70}$ at. % (prism code: YRFP005; melting code: M135HAP) and $Ge_{20}Sb_{10}Se_{67}S_3$ at. % (prism code: YRFP010; melting code: M191HAP) at wavelengths of 1494 nm, 1524 nm, 1554 nm and 3100 nm are shown in Table 7-5 as a function of temperature (T_{prism}). Each refractive index data point in Table 7-5 is taken as the average of 10 measurements; the standard deviation of precision at the wavelengths of 1494 nm, 1524 nm and 1554 nm is less than 0.0004 and the standard deviation of precision at 3100 nm is less than 0.0008. The lower standard deviation error presented here (in comparison to the results for $As_{40}Se_{60}$ at. % and $Ge_{16}As_{24}Se_{15.5}Te_{44.5}$ at. % presented in sub-section 7.2.2) is attributed to a larger prism apex angle used (target apex angle: 20 °) compared to those of the $As_{40}Se_{60}$ at. % and $Ge_{16}As_{24}Se_{15.5}Te_{44.5}$ at. % prisms (target apex angle: 10 °).

The refractive index variations with temperature of $Ge_{20}Sb_{10}Se_{70}$ at. % at wavelengths of 1494, 1524 and 1554 nm are shown in Figure 7.2-6(a). As shown in Figure 7.2-6(a), the refractive index decreased with increasing wavelengths. The error bar shown for each refractive index data point at different prism temperatures indicates the standard deviation error in determining the refractive index, which is ±0.0004 at wavelengths of 1494, 1524 and 1554 nm and ±0.0008 at a wavelength of 3100nm. The temperature variation at each measurement temeperature is less than 0.2 ℃, which is too small to show in Figure 7.2-6. Since this wavelength range is not within the standard Urbach edge in the short wavelength cutoff region of $Ge_{20}Sb_{10}Se_{70}$ at. %, as shown in Figure 7.1-2 in section 7.1.2, a linear fit is sufficient to fit the data points yielding a R^2 of better than 0.9418 as shown in Figure 7.2-6(a). The dn/dT at wavelengths of 1494, 1524 and 1554 nm can be obtained by the slope

of the linear fit with an error of ± 10.7 ppm/℃ (calculated from Eq. (7.7)) as shown in Figure 7.2-6(a).

Table 7- 5. The refractive index (n) at different prism temperatures T_{prism} of the $Ge_{20}Sb_{10}Se_{70}$ at. % (M135HAP) and $Ge_{20}Sb_{10}Se_{67}S_3$ at. % (M191HAP) prisms, and the thermal expansion coefficient (TEC) of the $Ge_{20}Sb_{10}Se_{70}$ at. % glass (M135HAP). The temperature variation at each measurement point was less than ±0.2 ℃. The measured thermo-optic coefficients of $Ge_{20}Sb_{10}Se_{70}$ at. % (M135HAP) and $Ge_{20}Sb_{10}Se_{67}S_3$ at. % (M191HAP) were positive at wavelengths of 1494, 1524, 1554 and 3100 nm. The standard deviation of precision on refractive index at the wavelengths of 1494 nm, 1524 nm and 1554 nm is less than 0.0004 and the standard deviation of precision on refractive index at 3100 nm is less than 0.0008.

	T_{prism} / ℃	n at 1494 nm	n at 1524 nm	n at 1554 nm	n at 3100 nm
GeSbSe					
	16.2	2.5789	2.5770	2.5756	2.5458
	36.5	2.5794	2.5776	2.5762	2.5466
	52.7	2.5801	2.5782	2.5765	2.5475
	68.9	2.5809	2.5792	2.5775	2.5485
Apex angle: 20 °06′	TEC =19.5±0.5 ppm/ ℃				
GeSbSeS					
	15.6	2.5630	2.5622	2.5609	2.5320
	37.9	2.5638	2.5627	2.5618	2.5327
	55.8	2.5652	2.5641	2.5627	2.5332
	73	2.5658	2.5647	2.5633	2.5339
Apex angle: 20 °11′	TEC was not measured.				

The refractive index variations of $Ge_{20}Sb_{10}Se_{67}S_3$ at. % with temperature at the wavelengths of 1494, 1524 and 1554 nm are shown in Figure 7.2-6(b). According to section 6.7, introducing 3 atomic % S into $Ge_{20}Sb_{10}Se_{70}$ at. % shifted the optical bandgap towards shorter wavelengths. Morevoer, Figure 7.1-2 in section 7.1.2 showed that this wavelength region (1494 nm to 1554 nm) is out of the standard Urbach edge in the short wavelength cutoff region of $Ge_{20}Sb_{10}Se_{67}S_3$ at. %. Therefore, a linear fit was applied to the data points in Figure 7.2-6(b) yielding a R^2 of better than 0.9504. The thermo-optic coefficients at wavelengths of 1494, 1524

and 1554 nm obtained from the linear fits are shown in Figure 7.2-6(b) with an error of ± 9.9 ppm/℃. The lower error in determining the dn/dT here (in comparison to the error in determining the dn/dT of $Ge_{20}Sb_{10}Se_{70}$ at. %) is mainly attributed to the larger measurement temperature window as described in section 3.8.1.

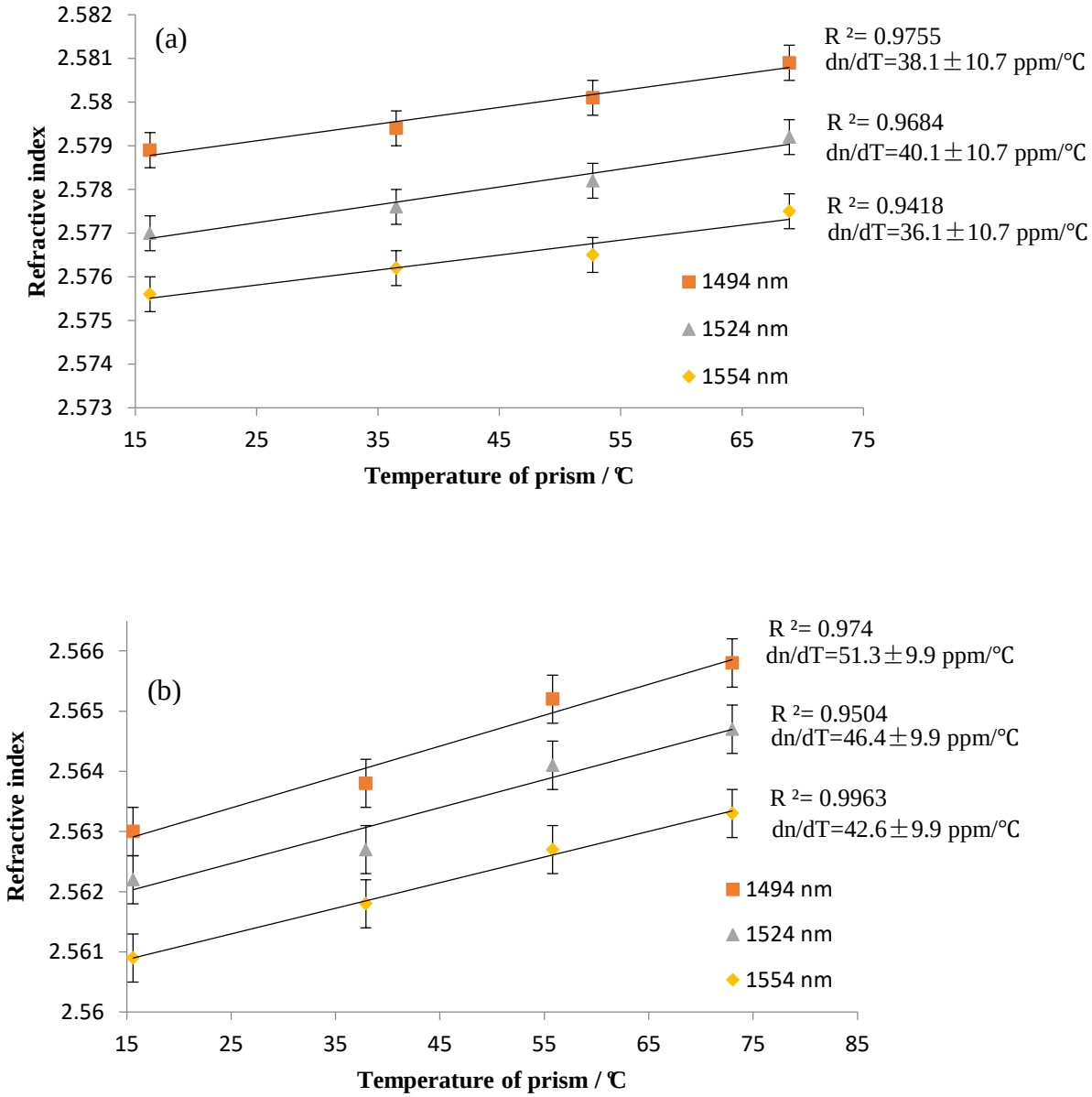


Figure 7.2- 6. The refractive index variations with temperature at wavelengths of 1494, 1524 and 1554 nm for (a) $Ge_{20}Sb_{10}Se_{70}$ at. % (M135HAP) and (b) $Ge_{20}Sb_{10}Se_{67}S_3$ at. % (M191HAP). The thermo-optic coefficients (dn/dT) are obtained from the linear fits the R^2 (coefficient of determination) of the fits are given. The temperature variation at each measurement point was less than ±0.2 ℃, which is too small to show in the figure.

The refractive indices of the $Ge_{20}Sb_{10}Se_{70}$ at. % and $Ge_{20}Sb_{10}Se_{67}S_3$ at. % prisms measured at a wavelength of 3100 nm at different temperatures are shown in Figure 7.2-7. The error bar shown for each data point indicates the standard deviation error, which is 0.0008. For $Ge_{20}Sb_{10}Se_{70}$ at. %, a linear fit to the data points in Figure 7.2-7(a) yielded a value of dn/dT of 49.7 ppm/℃ with a R^2 of 0.9927. The error of the measured dn/dT is within $\pm$ 21.5 ppm/℃. For $Ge_{20}Sb_{10}Se_{67}S_3$ at. %, a linear fit to the data points in Figure 7.2-7(b) yielded a value of dn/dT of 32.5 ppm/℃ with an R^2 of 0.9969. The error of the measured dn/dT is within $\pm$ 19.7 ppm/℃. According to Figure 7.2-7, $Ge_{20}Sb_{10}Se_{67}S_3$ at. % has a lower dn/dT than $Ge_{20}Sb_{10}Se_{70}$ at. % at the wavelength of 3100 nm. However, this difference is within the measurement error.

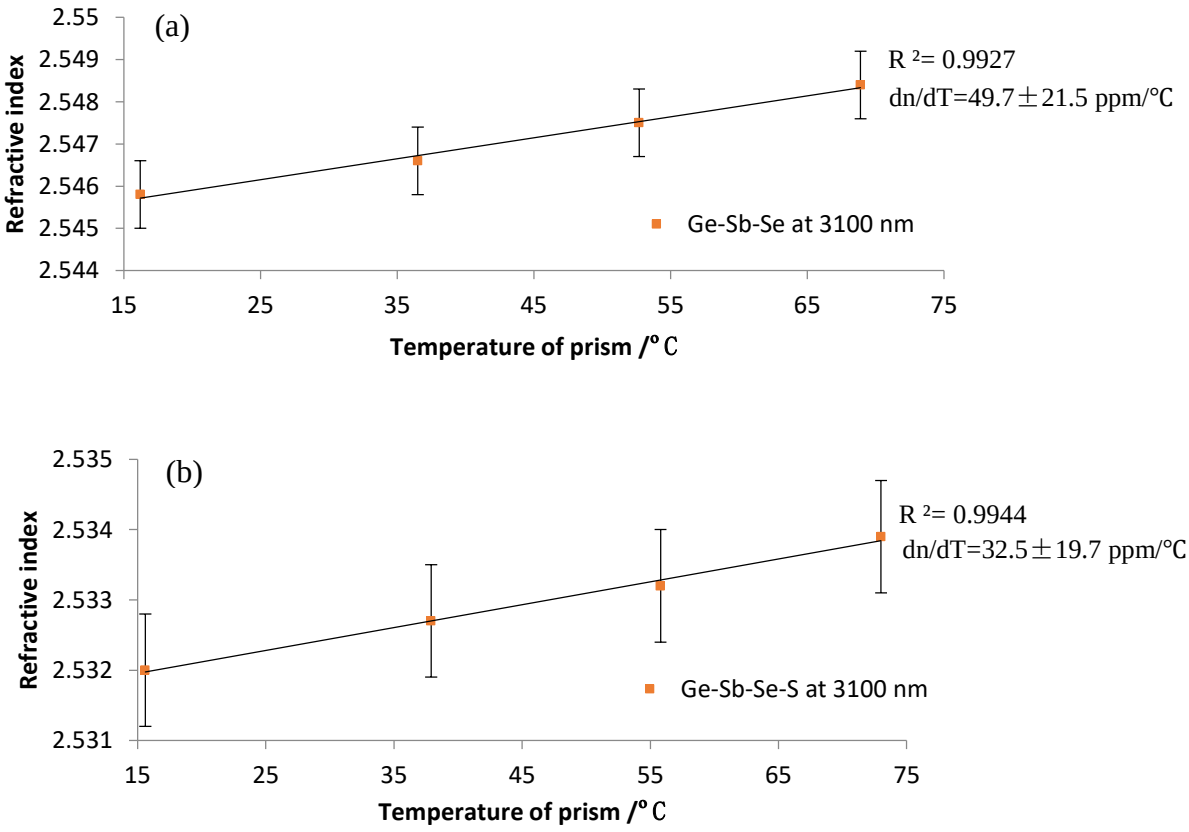


Figure 7.2- 7. The refractive index variations with temperature at the wavelength of 3100 nm for (a) $Ge_{20}Sb_{10}Se_{70}$ at. % (M135HAP) and (b) $Ge_{20}Sb_{10}Se_{67}S_3$ at. % (M191HAP). The thermo-optic coefficients (dn/dT) are obtained from the linear fits the R^2 (coefficient of determination) of the fits are given.

With the refractive index variations with temperature known at different wavelengths for $Ge_{20}Sb_{10}Se_{70}$ at. % and $Ge_{20}Sb_{10}Se_{67}S_3$ at. %, the numerical aperture variation with temperature at different wavelengths can be determined with an error of ± 0.0080. Since the difference between the thermo-optic coefficients of $Ge_{20}Sb_{10}Se_{70}$ at. % and $Ge_{20}Sb_{10}Se_{67}S_3$ at. % is within the measurement error, it is difficult to tell which material has a higher dn/dT. However, due to the small dn/dT differences, the NA changes by less than 0.0256 from 15 to 72 ℃.

7.2.3.2 Thermal polarisability coefficient of $Ge_{20}Sb_{10}Se_{70}$ at. %

Similar to the discussion in section 7.2.2.3, the thermal polarisability coefficient (TPC) of the $Ge_{20}Sb_{10}Se_{70}$ at. % glass can be obtained once the refractive index, thermal expansion coefficient (TEC) and thermo-optic coefficient of the glass are known according to Eq. (7.6). The TEC of the $Ge_{20}Sb_{10}Se_{70}$ at. % glass was kindly measured by Dr. Harriet Parnell at the time the work was undertaken a PhD candidate in the MIR Photonics Group, University of Nottingham UK. However, the TEC of the $Ge_{20}Sb_{10}Se_{67}S_3$ at. % is still missing (see Table 7-5).

The linear TEC of $Ge_{20}Sb_{10}Se_{70}$ at. % from 30 to 100 ℃ was determined to be 19.5 ppm/℃. The TPC at the wavelengths of 1494 nm, 1524 nm, 1554 nm and 3100 nm were calculated from Eq. (7.6) and are shown in Table 7-6.

Table 7- 6. Measured thermo-optic coefficients, refractive indices, thermal expansion coefficients (TEC) and calculated thermal polarizability coefficients (TPCs) of $Ge_{20}Sb_{10}Se_{70}$ at. % (M135HAP) at the wavelengths of 1494 nm, 1524 nm, 1554 nm and 3100 nm.

Wavelength / (nm)	dn/dT / (ppm/℃) ± 10.7	*n* at 16.2 ℃ ±0.0004	TEC / (ppm/℃) ± 0.5	TPC / (ppm/℃)
1494	38.1	2.5789	19.5	364.3
1524	40.1	2.5770	19.5	365.1
1554	36.1	2.5756	19.5	363.7
Wavelength / (nm)	dn/dT / (ppm/℃) ± 21.5	*n* at 16.2 ℃ ±0.0008	TEC / (ppm/℃) ± 0.5	TPC / (ppm/℃)
3100	49.7	2.5458	19.5	369.1

7.3 A FTIR continuous dn/dT method to determine the thermo-optic coefficient of chalcogenide glasses.

In section 7.2, the thermo-optic coefficients of the chalcogenide glasses ($As_{40}Se_{60}$ at. % (M130MINSCGDJ), $Ge_{16}As_{24}Se_{15.5}Te_{44.5}$ at. % (M140MINSCGDJ), $Ge_{20}Sb_{10}Se_{70}$ at. % (M135HAP) and $Ge_{20}Sb_{10}Se_{67}S_3$ at. % (M191HAP)) were determined using the minimum deviation method with an error of less than ± 15.6 ppm/℃ when using the 1464 – 1574 nm tunable laser diode (see section 4.2) and with an error of less than ± 25.6 ppm/℃ when using the 3.1 μm ICL (see section 4.2). Due to the limitation in available beam sources, the dn/dT data at many interesting wavelengths in the MIR region could not be obtained.

In chapter 6, the improved Swanepoel was successfully developed, which can determined the refractive index of chalcogenide glasses across the MIR region with the standard deviation of precision less than 0.002. Unlike the minimum deviation method, this technique can obtain a continuous refractive index curve over the wavelength range from 2 to 25 μm. However, with a measurement range of temperature from 20 ℃ to 80 ℃, a ± 0.002 difference in refractive index can lead to an error in dn/dT of ± 67 ppm/℃ in the worst case. Therefore, a more accurate method is required to determine the continuous thermo-optic coefficient of chalcogenide glasses across the MIR region.

In this sub-section, a method, based on Fourier transform infrared (FTIR) transmission spectra measured at different temperatures, is developed to obtain the continuous thermo-optic coefficients of chalcogenide glasses in the MIR region.

7.3.1 Basic theory

For normal incidence on an optical thin film with thickness of *d*, the wavelengths of the transmission extrema can be expressed by:

$$2nd = m\lambda \qquad (7.8)$$

where λ is the wavelength at the maxima or minima of the normal incidence transmission spectrum, n is the refractive index at the wavelength of λ and m is the order number of the extrema, which has integer values for the maxima and half-integer values for the minima. When the thin film is cooled down to a lower temperature T_l, Eq. (7.8) becomes:

$$n_l = \frac{m\lambda_l}{2d_l} \qquad (7.9)$$

where λ_l is the wavelength at the maxima or minima of the same order m in the normal incidence transmission spectrum at the temperature T_l, d_l is the thickness of the thin film at the temperature of T_l and n_l is the refractive index of the thin film at the wavelength of λ_l. As discussed in section 6.3.3, the values of d_l can be determined to a standard deviation of precision of less than 0.02 μm by changing the dispersive model of refractive index from a Cauchy-like model to a two-term Sellmeier model.

When the thin film is heated up to a higher temperature T_h, the thickness d_h of the thin film at the temperature T_h will be calculated by:

$$d_h = d_l(1 + \mathrm{TEC} * (T_h - T_l)) \qquad (7.10)$$

where TEC is defined as the thermal expansion coefficient, which was determined by thermal mechanical analysis (TMA), as described in section 3.7. With d_h known and the normal incidence of transmission spectrum for the thin film at the temperature of T_h obtained, the refractive index for the thin film at T_h is given as:

$$n_h = \frac{m\lambda_h}{2d_h} \qquad (7.11)$$

where λ_h is the wavelength at the maxima or minima of the same order m in the normal incidence transmission spectrum at the temperature of T_h and n_h is the refractive index at the wavelength of λ_h. The wavelengths λ_l and λ_h, which appear in Eq. (7.9) and (7.11), are not the same, so a dispersive model is introduced.

As discussed in sections 5.4.2 and 6.3.3, a two-term Sellmeier model (see Eq. (5.8 in section 5.1.3)), a two-term Sellmeier model was effective to describe the refractive index dispersion of a chalcogenide glass in the mid-infrared region; this was also confirmed by us in [7.35].

Two-term Sellmeier fits are then applied to the refractive index data obtained from Eqs. (7.9) and (7.11). The thermo-optic coefficient (dn/dT) of the thin film from 20 ℃ to 80 ℃ can now be determined as:

$$\frac{\mathrm{dn}}{\mathrm{dT}} = \frac{\text{Sellmeier fit } (\mathrm{n}_h) - \text{Sellmeier fit } (\mathrm{n}_l)}{T_h - T_l}. \qquad (7.12)$$

A linear variation of dn/dT has been assumed, as used by [7.1,7.2] in the temperature range from 20 ℃ to 100 ℃ and in the transparent region away from the absorption tail. The error of this method will be analysed in the following sections.

7.3.2 Determining thermo-optic coefficients of chalcogenide glasses ($As_{40}Se_{60}$ at. % and $Ge_{16}As_{24}Se_{15.5}Te_{44.5}$ at. %) using the FTIR continuous dn/dT method.

In order to determine the error and accuracy of the technique proposed in section 7.3.1, a chalcogenide thin film with a low thermo-optic coefficient ($As_{40}Se_{60}$ at. % (melting code: M130MINSCGDJ, thin film code: YRFFP003)) and a chalcogenide thin film with a high thermo-optic coefficient ($Ge_{16}As_{24}Se_{15.5}Te_{44.5}$ at. % (melting code: M188SCGDJ, thin film code: YRFFP019)) were used for the measurements in this section. The manufacturing procedures of these thin films were described in section 3.5.2. The thermal performance of the thermal holder was described in section 3.8.2.

7.3.2.1 *Thermo-optic coefficients of $As_{40}Se_{60}$ at. % and $Ge_{16}As_{24}Se_{15.5}Te_{44.5}$ at. % using the FTIR continuous dn/dT method*

The transmission spectra of the $As_{40}Se_{60}$ at. % (M130MINSCGDJ) and $Ge_{16}As_{24}Se_{15.5}Te_{44.5}$ at. % (M188SCGDJ) thin films at normal incidence at measured temperatures of 21.6 ℃ and 74.6 ℃ are shown in Figures 7.3-1(a) and 7.3-1(b).

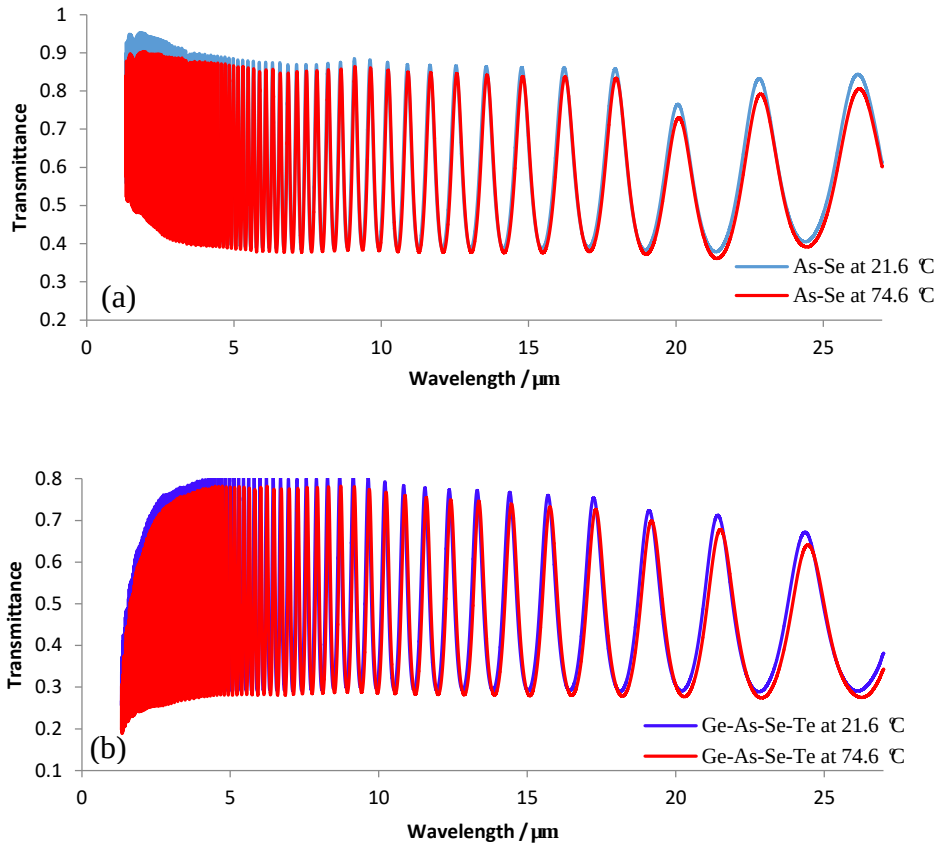


Figure 7.3- 1. The normal transmittance spectra from 15 to 25 μm for (a) $As_{40}Se_{60}$ at. % (As-Se) (M130MINSCGDJ) at the temperature of 21.6 ℃ (blue line) and 74.6 ℃ (red line) and for (b) $Ge_{16}As_{24}Se_{15.5}Te_{44.5}$ at. % (Ge-As-Se-Te) (M188SCGDJ) at the temperature of 21.6 ℃ (blue line) and 74.6 ℃ (red line).

The small, but consistently observed, variation in the magnitude of transmittance extrema with temperature observed in Figures 7.3-1(a) and 7.3-1(b) indicates that the $As_{40}Se_{60}$ at. % and $Ge_{16}As_{24}Se_{15.5}Te_{44.5}$ at. % thin films became less transparent over the wavelength range from 2 to 25 μm with increasing the temperature from 21.6 ℃

to 74.0 ℃; for the case of tellurium-containing chalcogenide glasses then this has been attributed in the past to thermally induced increases of the free-carrier absorption and multi-phonon absorption [7.14]. The obvious dip at ~ 20.5 μm in Figure 7.3-1(a) is attributed to the second overtone of the fundamental vibrational band due to the $AsSe_3$ unit [7.23]. For $Ge_{16}As_{24}Se_{15.5}Te_{44.5}$ at. %, no obvious corresponding dips are observed in Figure 7.3-1(b).

In order to obtain thin film thickness at a temperature of 21.6 ℃, the improved Swanepoel method (defined in section 6.3) was applied to determine the thickness of the $As_{40}Se_{60}$ at. % thin film and of the $Ge_{16}As_{24}Se_{15.5}Te_{44.5}$ at. % thin film at a temperature of 21.6 ℃ yielding $d_l = 29.30 \pm 0.02$ μm and $d_l = 27.40 \pm 0.02$ μm, respectively. The thickness can be determined to a standard deviation of precision of better than 0.02 μm, as discussed in section 6.3.3.4. To obtain the thickness at the higher temperature, the FTIR continuous dn/dT method and the improved Swanepoel method can be applied. For FTIR continuous dn/dT method, the TEC of $As_{40}Se_{60}$ at. % and $Ge_{16}As_{24}Se_{15.5}Te_{44.5}$ at. % were determined by TMA to be 22.4 ppm / ℃ and 16.6 ppm / ℃ over the temperature range from 30 to 100 ℃ (TECs of $As_{40}Se_{60}$ at. % and $Ge_{16}As_{24}Se_{15.5}Te_{44.5}$ at. % were assumed to be linear over the temperature range from 30 to 100 ℃), respectively, with an error of $\pm$ 0.5 ppm / ℃. The thickness of the $As_{40}Se_{60}$ at. % and $Ge_{16}As_{24}Se_{15.5}Te_{44.5}$ at. % thin films at the temperature of 74.6 ℃ can be determined using Eq. (7.10), yielding $d_h = 29.335$ μm and $d_h = 27.426$ μm, respectively. For comparison, the improved Swanepoel method was applied to obtain the thickness of the $As_{40}Se_{60}$ at. % and $Ge_{16}As_{24}Se_{15.5}Te_{44.5}$ at. % thin films at a temperature of 74.6 ℃ directly, yielding $d = 29.33 \pm 0.02$ μm and $d = 27.43 \pm 0.02$ μm, respectively, in good agreement. The calculated TECs from the improved Swanepoel method were 19.3 ppm / ℃ for $As_{40}Se_{60}$ at. % and 20.7 ppm / ℃ for $Ge_{16}As_{24}Se_{15.5}Te_{44.5}$ at. %. The errors in comparison to the results obtained from TMA are 7.6 % and 24.7 %. Since the improved Swanepoel can only

determine the thickness with a standard deviation of precision of less than 0.02, it is not possible to determine the TEC to a high accuracy using this approach.

The order numbers of each extreme in Figures 7.3-1(a) and 7.3-1(b) were determined as described in section 6.3.3. With m, d_l and d_h of the $As_{40}Se_{60}$ at. % and $Ge_{16}As_{24}Se_{15.5}Te_{44.5}$ at. % thin films obtained, the refractive index data points of $As_{40}Se_{60}$ at. % and $Ge_{16}As_{24}Se_{15.5}Te_{44.5}$ at. % at temperatures of 21.6 ℃ and 74.6 ℃ were determined according to Eq. (7.8), as shown in Figures 7.3-2(a) and 7.3-2(b). The respective two-term Sellmeier fits applied to the data points are shown in Figure 7.3-2, and the Sellmeier coefficients for the best fits are shown in Table 7.7. The R^2 coefficient of determination in Table 1 is a statistical measure of how well the refractive index model fit the data points. An R^2 of 1 indicates that the refractive index model perfectly fits the data, and here ranges from 0.9990 to 0.9999.

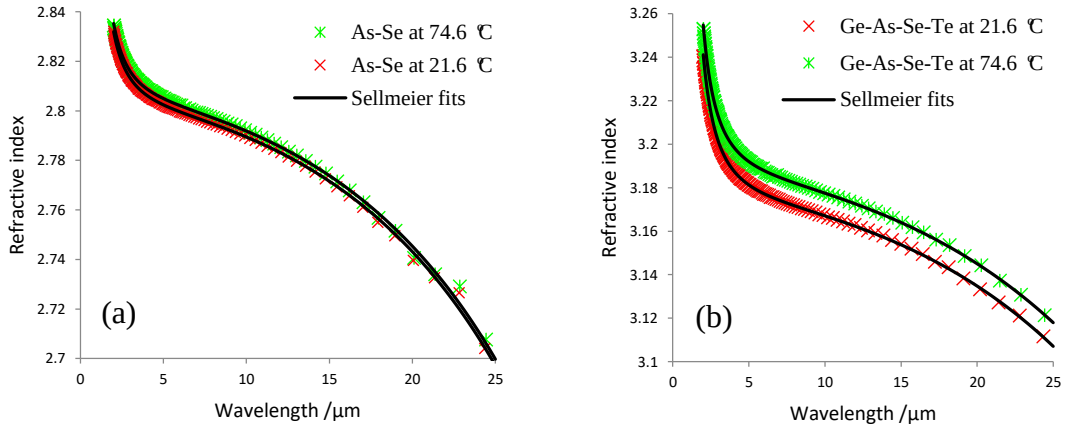


Figure 7.3- 2. The refractive indices at different temperatures obtained using the FTIR continous FTIR method for (a) $As_{40}Se_{60}$ at. % (As-Se) (M130MINSCGDJ) and (b) $Ge_{16}As_{24}Se_{15.5}Te_{44.5}$ at. % (Ge-As-Se-Te) (M188SCGDJ), together with the best Sellmeier fits whose coefficients are shown in Table 1.

The refractive index dispersion of the $As_{40}Se_{60}$ at. % and $Ge_{16}As_{24}Se_{15.5}Te_{44.5}$ at. % thin films at a temperature of 74.6 ℃ was also obtained directly from the improved Swanepoel method. For comparison purposes, the Sellmeier coefficients so obtained are shown in Table 7.7. However, these results are not presented in Figure 7.3-2 as they are indistinguishable from the refractive index results obtained using the FTIR

continuous dn/dT method with differences in refractive index of only 0.0004 for $As_{40}Se_{60}$ at. % and 0.0015 for $Ge_{16}As_{24}Se_{15.5}Te_{44.5}$ at. % over the wavelength range from 2 to 25 μm.

Table 7- 7. Sellmeier coefficients for $As_{40}Se_{60}$ at. % (As-Se) (M130MINSCGDJ) and $Ge_{16}As_{24}Se_{15.5}Te_{44.5}$ at. % (Ge-As-Se-Te) (M188SCGDJ) thin films from the FTIR continuous dn/dT method described in this section, and the improved Swanepoel method (defined in section 6.3).

Sellmeier coefficients	A	B_1	B_2	C_1 (VIS)	C_2 $(MIR\ or\ FIR)$	R^2
As-Se @ 21.6 ℃	5.212	2.631	1.474	0.5056	47.36	0.9990
As-Se @ 74.6 ℃	5.589	2.268	1.545	0.5484	56.06	0.9990
As-Se @ 74.6 ℃ (Swanepoel)	5.743	2.116	1.505	0.5728	47.74	0.9990
Ge-As-Se-Te @ 21.6 ℃	6.603	3.468	1.830	0.6684	57.89	0.9999
Ge-As-Se-Te @ 74.6 ℃	7.159	2.979	2.174	0.7299	62.20	0.9999
Ge-As-Se-Te @ 74.6 ℃ (Swanepoel)	6.959	3.169	1.964	0.7106	59.59	0.9999

As discussed in section 5.5, the resonant wavelength C_1 in the visible (VIS) region of the two-term Sellmeier model is that wavelength which corresponds to the position of optical band gap of a material and the other resonant wavelength C_2 in the MIR region corresponds to the location of the fundamental vibrational absorption band. It is important to lend the two-term Sellmeier model to a physical interpretation as this could open the way to the model being a predictive tool. The second overtone of the fundamental vibrational absorption bands of $As_{40}Se_{60}$ at. % (M179CMDF) for a longer optical path-length bulk sample at temperatures of 21.8 ℃ and 74.0 ℃ measured using FTIR spectroscopy were shown in Figure 7.1-4 in section 7.1.3.

From Figure 7.1-4 in section 7.1.3, the second overtone of the fundamental vibrational absorption band of $As_{40}Se_{60}$ at. % (M179CMDF) is located at ~ 20.58 μm

at a temperature of 21.8 ℃. Therefore, the fundamental vibrational absorption band of $As_{40}Se_{60}$ at. % in the MIR region is at the wavelength of ~ 41.16 μm wavelength (2×20.58 μm). As the sample temperature was increased to 74.0 ℃, the second overtone band of $As_{40}Se_{60}$ at. % red shifted to a wavelength of ~ 20.64 μm as shown in Figure 7.1-4; this suggests that the fundamental vibrational absorption band at this temperature locates at ~ 41.28 μm. Performing a fit to the present experimental data for the refractive index of $As_{40}Se_{60}$ at. % at different temperatures, but now fixing the value of C_2 to be 41.16 μm at the lower temperature (21.8 ℃) and to be 41.28 μm at higher temperature (74.0 ℃), yields Sellmeier coefficients as follows:

$$n^2 = 2.831 + \frac{5.006\lambda^2}{\lambda^2 - 0.3788^2} + \frac{0.9845\lambda^2}{\lambda^2 - 41.16^2} \qquad \text{at lower temperature}$$

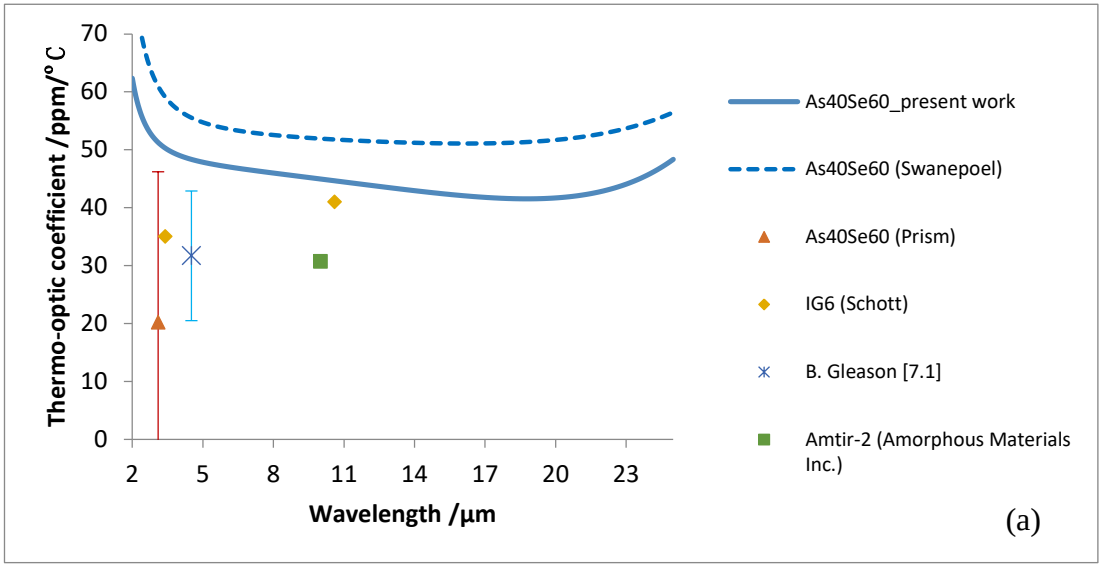
$$n^2 = 4.429 + \frac{2.865\lambda^2}{\lambda^2 - 0.4605^2} + \frac{0.9865\lambda^2}{\lambda^2 - 41.28^2} \qquad \text{at higher temperature}$$

Compared to the best Sellmeier fits to the refractive index experimental data as shown in Table 7-7, the value of R^2 decreased from 0.9992 to 0.9984 for $As_{40}Se_{60}$ at. % at the lower temperature and the value of R^2 decreased from 0.9989 to 0.9980 at the higher temperature. The difference to the best fit may be attributed to the limited experimental wavelength region (2 to 25 μm) and the effects of material absorption.

For $Ge_{16}As_{24}Se_{15.5}Te_{44.5}$ at. %, no band gap information was available; thus only a best fit to the experimental data is presented. From Table 7-7, it is found that with the temperature increasing, the VIS resonant wavelength C_1 obtained from the best two-term Sellmeier fit to the refractive index data of $As_{40}Se_{60}$ at. % and $Ge_{16}As_{24}Se_{15.5}Te_{44.5}$ at. % shifted towards longer wavelengths. These indicate a red shift of the optical bandgap with temperature for $As_{40}Se_{60}$ at. % and $Ge_{16}As_{24}Se_{15.5}Te_{44.5}$ at. %, which is in good agreement with Figure 7.1-1 in section 7.1.1. Table 7-7 also shows that the MIR resonant wavelength C_2 of $As_{40}Se_{60}$ at. % and $Ge_{16}As_{24}Se_{15.5}Te_{44.5}$ at. % shifted towards longer wavelengths, which indicates the fundamental multiphonon absorption band shifts to longer wavelengths with

increasing temperature. These confirm the FTIR absorption spectra observations in Figures 7.1-1 and 7.1-4 for $Ge_{16}As_{24}Se_{15.5}Te_{44.5}$ at. % and $As_{40}Se_{60}$ at. % in section 7.1. The best Sellmeier fits were then used to determine the thermo-optic coefficents according to Eq. (7.12).

The thermo-optic coefficients of the $As_{40}Se_{60}$ at. % (M130MINSCGDJ) and $Ge_{16}As_{24}Se_{15.5}Te_{44.5}$ at. % (M188SCGDJ) thin films over the wavelength range from 2 to 25 μm are shown in Figure 7.3-3. Figure 7.3-3 shows that the dn/dT of $As_{40}Se_{60}$ at. % and $Ge_{16}As_{24}Se_{15.5}Te_{44.5}$ at. % decreases with increasing wavelength in the shorter wavelength region, which is due to the red shift of the optical band gap with temperature. The dn/dT behaviour from 2 to 12 μm is in good agreement with the pubulished dn/dT behaviour of Ge-As-Se glasses [7.2]. At wavelengths > 20 μm, the dn/dT (assumed to be linear over the temperature range from 21.6 ℃ to 74.6 ℃) starts to increase with wavelength as shown in Figure 7.3-3. This is attributed to the red shift of the fundamental multiphonon absorption band with temperature as discussed in section 7.1. The error of this technique in determining the thermo-optic coefficient is less than ±7.0 ppm/℃ for $As_{40}Se_{60}$ at. % and less than ±7.5 ppm/℃ for $Ge_{16}As_{24}Se_{15.5}Te_{44.5}$ at. %, which will be further discussed in the following section. For comparison purposes, the thermo-optic coefficients of an $As_{40}Se_{60}$ at % prism (M130MINSCJDJ) and a $Ge_{16}As_{24}Se_{15.5}Te_{44.5}$ at. % prism (M140MINSCGDJ) at the wavelength of 3.1 μm (3.1 μm Interband cascade laser from NRL) are given in Figures 7.3-3(a) and 7.3-3(b), with an error of less than ±26.0 ppm/℃. Some commercial [7.29,7.34] and published data [7.1] for the thermo-optic coefficient of $As_{40}Se_{60}$ are also shown in Figure 7.3-3(a).



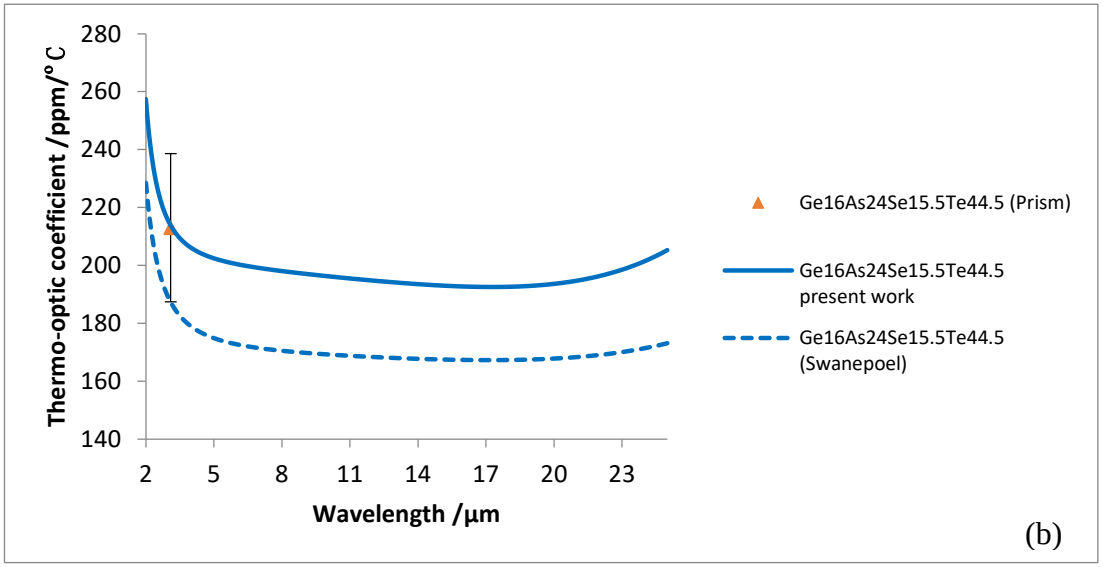


Figure 7.3- 3. The thermo-optic coefficient of: (a) $As_{40}Se_{60}$ at % (M130MINSCGDJ), compared with the result of the $As_{40}Se_{60}$ at % (M130MINSCGDJ) prism obtained using the minimum deviation method, the commercial data [7.31,7.34] and published data [7.1], and (b) $Ge_{16}As_{24}Se_{15.5}Te_{44.5}$ at. % (M188SCGDJ) compared with the result of the $Ge_{16}As_{24}Se_{15.5}Te_{44.5}$ at. % (M140MINSCGDJ) prism obtained using the minimum deviation method. The thermo-optic coefficients of $As_{40}Se_{60}$ at % (M130MINSCGDJ) and $Ge_{16}As_{24}Se_{15.5}Te_{44.5}$ at. % (M188SCGDJ) from the improved Swanepoel method are displayed to compare them with the results obtained from the FTIR continuous dn/dT method.

From Figure 7.3-3(a), it is found that the dn/dT of the $As_{40}Se_{60}$ at % (M130MINSCGDJ) thin film obtained from the FTIR continuous dn/dT method is higher than those obtained using the prism measurement, the commercial data

[7.31,7.34] and the published data [7.1]. As discussed in section 3.5.2, the thin film used here was hot-pressed from an optical fibre, which caused a small composition difference and a different thermal history between the thin film and the preform. To investigate how the composition difference in $As_{40}Se_{60}$ at % affects the thermo-optic coefficient, the dn/dT data of $As_{40}Se_{60}$ at. %, $As_{35}Se_{65}$ at. % and $As_{30}Se_{70}$ at. % in [7.1] is shown in Table 7-8. It inferred from the data presented that replacing 1 atomic % As to Se decreases the thermo-optic coefficient by ~ 7.6 ppm/℃. The thermo-optic coefficient obtained from the improved Swanepoel method is also shown as a function of wavelength in Figure 7.3-3(a). The difference between these results and those obtained from the FTIR continuous dn/dT method is less than 7.6 ppm/℃ from 2 to 25 μm, which is caused by a refractive index difference of merely 0.0004 at the higher temperature between the present method and the improved Swanepoel method.

From Figure 7.3-3(b), the difference between the dn/dT of $Ge_{16}As_{24}Se_{15.5}Te_{44.5}$ at. % (M188SCGDJ) obtained from the FTIR continuous dn/dT method and the benchmark at 3.1μm is less than 0.7 ppm/℃. The thermo-optic coefficient for $Ge_{16}As_{24}Se_{15.5}Te_{44.5}$ at. % (M188SCGDJ) obtained from the improved Swanepoel method is 25.8 ppm/℃ lower than the bench mark as shown in Figure 7.3-3(b). In this case, the refractive index difference at the temperature of 74.6 ℃ between the improved Swanepoel method and the FTIR continuous dn/dT method is less than 0.0015 at the wavelength of 3.1 μm, which lead to a ~28.3 ppm/℃ difference in value of the thermo-optic coefficient.

As previously discussed in chapter 6, the standard deviation of precision in determining the refractive index from the improved Swanepoel method is less than 0.002, which will lead to a ±66.7 ppm/℃ error in determining the thermo-optic coefficient in the worst case. Therefore, the improved Swanepoel method cannot accurately determine the thermo-optic coefficient of chalcogenide glasses. Unlike the

improved Swanepoel method, the FTIR continuous dn/dT method is not sensitive to average thickness and TEC (see the more detailed discussion in the following sub-section). Unlike the minimum deviaiton method, this technique can obtain continuous thermo-optic coefficients of chalcogenide glasses over the wavelength range from 2 to 20 μm with a smaller error of less than ±7.5 ppm/℃ (see section 7.3.2.2).

Table 7- 8. The thermo-optic coefficients of $As_{40}Se_{60}$, $As_{35}Se_{65}$ and $As_{30}Se_{70}$ at. % in [7.1]

As (at %)	Se (at %)	Ref.	Tg	dn/dT (4.515 μm)
40	60	[7.1]	193 ℃	31.7 ppm/℃
35	65	[7.1]	156 ℃	-6.3 ppm/℃
30	70	[7.1]	137 ℃	-43.8 ppm/℃

7.3.2.2 Error and reproducibility of the FTIR continuous dn/dT method

The possible sources of errors on the dn/dT measurements using the FTIR continuous dn/dT method are from Δd (error in determining the average thickness at lower temperature d_l), ΔT (thermal stability), ΔTEC (error of the measured thermal expansion coefficient by TMA) and error in the Sellmeier fit to refractive index dispersion.

As discussed in section 6.3.3, the improved Swanepoel method can determine the average thickness with a standard deviation of precision of less than 0.02 μm. For the $As_{40}Se_{60}$ at. % (melting code: M130MINSCGDJ; hot-pressing code: YRFFP003) and $Ge_{16}As_{24}Se_{15.5}Te_{44.5}$ at. % (melting code: M188SCGDJ; hot-pressing code: YRFFP019) thin films used in the previous section, this standard deviation error will lead to an error of less than ±0.02 ppm/℃ in calculating the dn/dT. Therefore, the FTIR continuous dn/dT method is not sensitive to the average thickness d_l.

As discussed in section 3.8.2, the error in measuring the temperature range ($\Delta T = T_h - T_l$) was < 0.5 ℃. A 0.5 ℃ error in ΔT will lead to an error of ± 1.5 ppm/℃ in determining the dn/dT for the $As_{40}Se_{60}$ at. % glass and an error of ± 2.6 ppm/℃ in determining the dn/dT for the $Ge_{16}As_{24}Se_{15.5}Te_{44.5}$ at. % glass, as shown in Table 7-9. Section 3.7 presented that the thermal expansion can be measured by means of TMA to an error of ± 0.5 ℃. This error in ΔTEC will result in error of ± 2.0 ppm/℃ in determining the dn/dT for $As_{40}Se_{60}$ at. % and an error of ± 1.4 ppm/℃ in determining the dn/dT for $Ge_{16}As_{24}Se_{15.5}Te_{44.5}$ at. %, as shown in Table 7-9.

Table 7- 9. Different sources of errors and the total errors in determining the dn/dT of $As_{40}Se_{60}$ at. % (As-Se) (melting code: M130MINSCGDJ; hot-pressing code: YRFFP003) and $Ge_{16}As_{24}Se_{15.5}Te_{44.5}$ at. % (Ge-As-Se-Te) (melting code: M188SCGDJ; hot-pressing code: YRFFP019) over the wavelength from 2 to 20 μm.

	ΔT (±0.5℃)	ΔTEC (±0.5℃)	Sellmeier fit	Total error
Error (As-Se) / ppm / ℃	±1.5	±2.0	±3.5	±7.0
Error (Ge-As-Se-Te) / ppm / ℃	±2.6	±1.4	±3.5	±7.5

For the two-term Sellmeier fitting, depending on the choice of the resonant wavelengths C_n, several different sets of Sellmeier coefficients can be obtained [7.35]. Different fits to the same refractive index data points may yield different sets of Sellmeier coefficients with the same R^2. To investigate the error on the dn/dT caused by the different Sellmeier fits, the refractive index at the lower temperature n_l and the refractive index at the higher temperature n_h of $As_{40}Se_{60}$ at. % and $Ge_{16}As_{24}Se_{15.5}Te_{44.5}$ at. % were each fitted in five different ways to the two-term Sellmeier model, as shown in Figure 7.3-4. The Sellmeier fitting coefficients and the fitting quality R^2 are shown in Table 7-10. From Figure 7.3-4, it is found that the error from different Sellmeier fits is less than ± 3.5 ppm/℃ for both $As_{40}Se_{60}$ at. % and $Ge_{16}As_{24}Se_{15.5}Te_{44.5}$ at. % over the wavelength from 2 to 20 μm. Since few data points located in the wavelength range from 20 to 25 μm (3 data points for $As_{40}Se_{60}$ at. % and $Ge_{16}As_{24}Se_{15.5}Te_{44.5}$ at. %), and they were affected by the strong

multiphonon absorptions, the error from the fit to the data points was increased in this longer wavelength range, as shown in Figure 7.3-2. This leads to a significant error (up to ±12.5 ppm/℃ at a wavelength of 25 μm for $Ge_{16}As_{24}Se_{15.5}Te_{44.5}$ at. %) in determining the dn/dT within this wavelength region as shown in Figure 7.3-4(b).

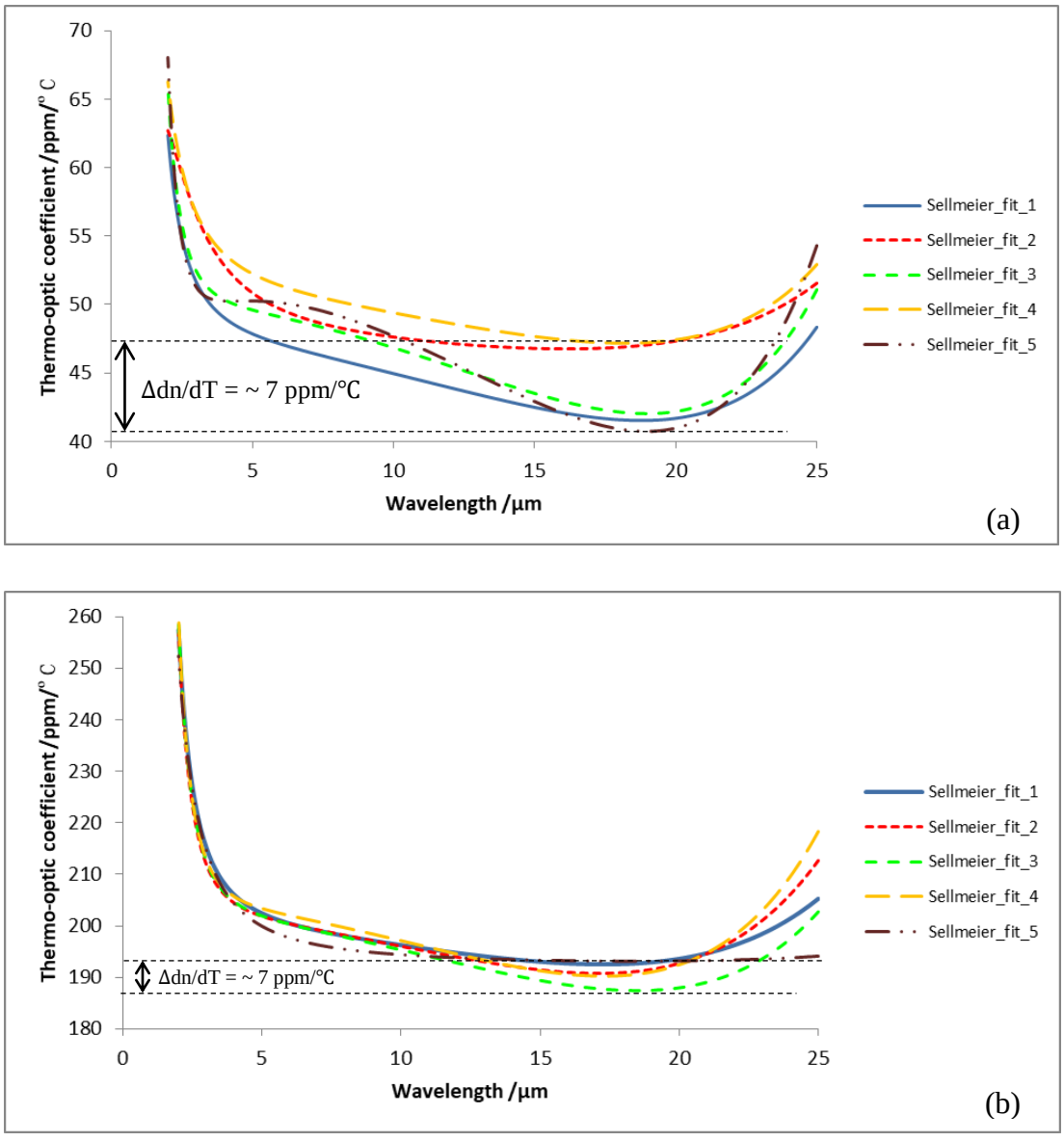


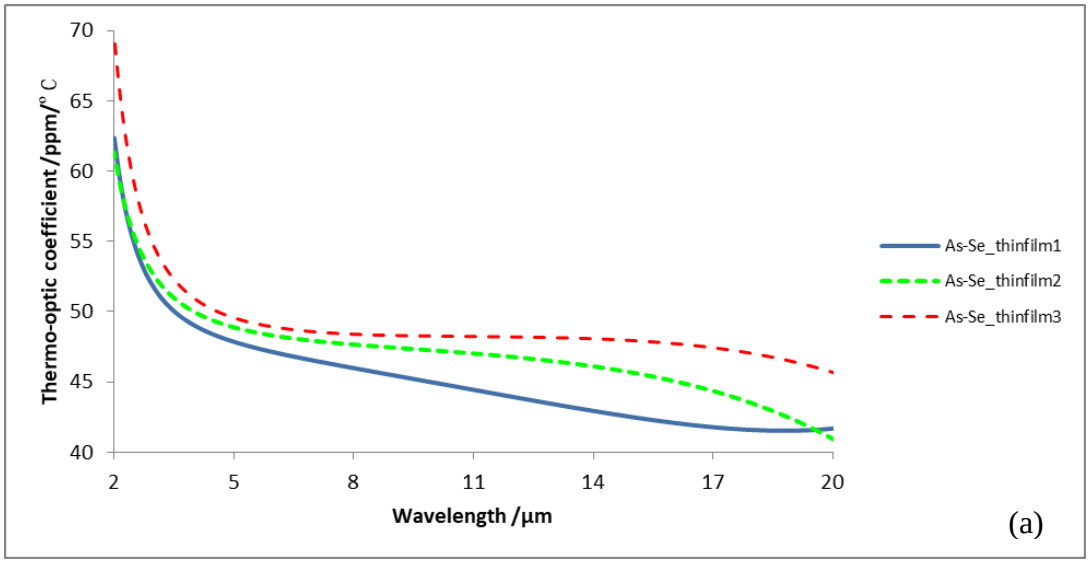
Figure 7.3- 4. The thermo-optic coefficient of: (a) $As_{40}Se_{60}$ at. % (As-Se) (melting code: M130MINSCGDJ; hot-pressing code: YRFFP003) and (b) $Ge_{16}As_{24}Se_{15.5}Te_{44.5}$ at. % (Ge-As-Se-Te) (melting code: M188SCGDJ; hot-pressing code: YRFFP019) obtained using five different Sellmeier fits (see Table 7-10) to the refractive index data points.

To sum up, the error on the dn/dT measurements using the novel method is mainly attributed to ΔT (thermal stability), ΔTEC (error of the measured thermal expansion coefficient by TMA) and error of the Sellmeier fit. When determining the thermo-optic coefficient of a low-dn/dT chalcogenide glass, the error of this technique is less than ±7.0 ppm/℃, as shown in Table 7-9. From Table 7-9, when determining the thermo-optic coefficient of a high-dn/dT chalcogenide glass, the error of this technique is less than ±7.5 ppm/℃. At wavelengths > 20 μm, the error will be dominated by the error in the Sellmeier fits.

Table 7- 10. The different sets of Sellmeier coefficients to the refractive index data points of $As_{40}Se_{60}$ at. % (As-Se) (melting code: M130MINSCGDJ; hot-pressing code: YRFFP003) and $Ge_{16}As_{24}Se_{15.5}Te_{44.5}$ at. % (Ge-As-Se-Te) (melting code: M188SCGDJ; hot-pressing code: YRFFP019).

Sellmeier coefficients	A	B_1	B_2	C_1 (VIS)	C_2 $(MIR\ or\ FIR)$	R^2
As-Se						
Sellmeier 1 @ 21.6 ℃	5.212	2.631	1.474	0.5056	47.36	0.9992
Sellmeier 1 @ 74.6 ℃	5.589	2.268	1.545	0.5484	48.17	0.9989
Sellmeier 2 @ 21.6 ℃	5.236	2.606	1.474	0.5079	47.36	0.9992
Sellmeier 2 @ 74.6 ℃	5.971	1.887	1.556	0.5971	48.29	0.9989
Sellmeier 3 @ 21.6 ℃	2.700	5.141	1.437	0.3674	46.95	0.9992
Sellmeier 3 @ 74.6 ℃	5.062	2.794	1.534	0.4976	48.06	0.9989
Sellmeier 4 @ 21.6 ℃	5.304	2.538	1.480	0.5141	47.43	0.9992
Sellmeier 4 @ 74.6 ℃	5.361	2.496	1.531	0.5247	48.02	0.9989
Sellmeier 5 @ 21.6 ℃	2.700	5.142	1.440	0.3674	46.98	0.9992
Sellmeier 5 @ 74.6 ℃	5.897	1.961	1.591	0.5859	48.70	0.9988
Ge-As-Se-Te						
Sellmeier 1 @ 21.6 ℃	6.603	3.468	1.830	0.6684	57.89	0.9999
Sellmeier 1 @ 74.6 ℃	7.159	2.979	2.174	0.7299	62.20	0.9999
Sellmeier 2 @ 21.6 ℃	6.974	3.099	2.041	0.5514	51.53	0.9999
Sellmeier 2 @ 74.6 ℃	5.221	4.912	1.448	0.5845	52.72	0.9999
Sellmeier 3 @ 21.6 ℃	4.755	5.313	1.372	0.5514	51.53	0.9999
Sellmeier 3 @ 74.6 ℃	6.703	3.434	1.865	0.6859	58.35	0.9999
Sellmeier 4 @ 21.6 ℃	6.202	3.869	1.737	0.6368	56.73	0.9999
Sellmeier 4 @ 74.6 ℃	6.457	3.679	1.762	0.6657	57.0	0.9999
Sellmeier 5 @ 21.6 ℃	5.867	4.203	1.644	0.6143	55.56	0.9999
Sellmeier 5 @ 74.6 ℃	7.054	3.084	2.138	0.7189	61.79	0.9999

As a way to determine the reproducibility of the method proposed here, three $As_{40}Se_{60}$ at. % (M130MINSCGDJ) thin films (thin films 1 and 2 from YRFFP003; thin film 3 from YRFFP002) and three $Ge_{16}As_{24}Se_{15.5}Te_{44.5}$ at. % (M188SCGDJ) thin films from YRFFP019 were used. The manufacturing process for the thin films was as described in section 3.5.2. The thermo-optic coefficients of these three $As_{40}Se_{60}$ at. % thin films are shown in Figure 7.3-5(a). Figure 7.3-5(a) shows that the maximum difference occurs at the wavelength of ~ 17 μm, which is less than 6 ppm/℃. The difference decreases with decreasing wavelength, and is less than 3 ppm/℃ at wavelengths below 10 μm. However, the difference between the thermo-optic coefficients measured for these three thin films is still within the error of this technique (less than ± 7.0 ppm/℃). It is also worth noting that the different thin films might have a very small composition difference, which may also result in a difference in dn/dT. The thermo-optic coefficients of the three $Ge_{16}As_{24}Se_{15.5}Te_{44.5}$ at. % thin films are shown in Figure 7.3-5(b). The difference between them is less than 5 ppm/℃ over the wavelength from 2 to 20 μm, which is again within the error of this technique (less than ± 7.5 ppm/℃).



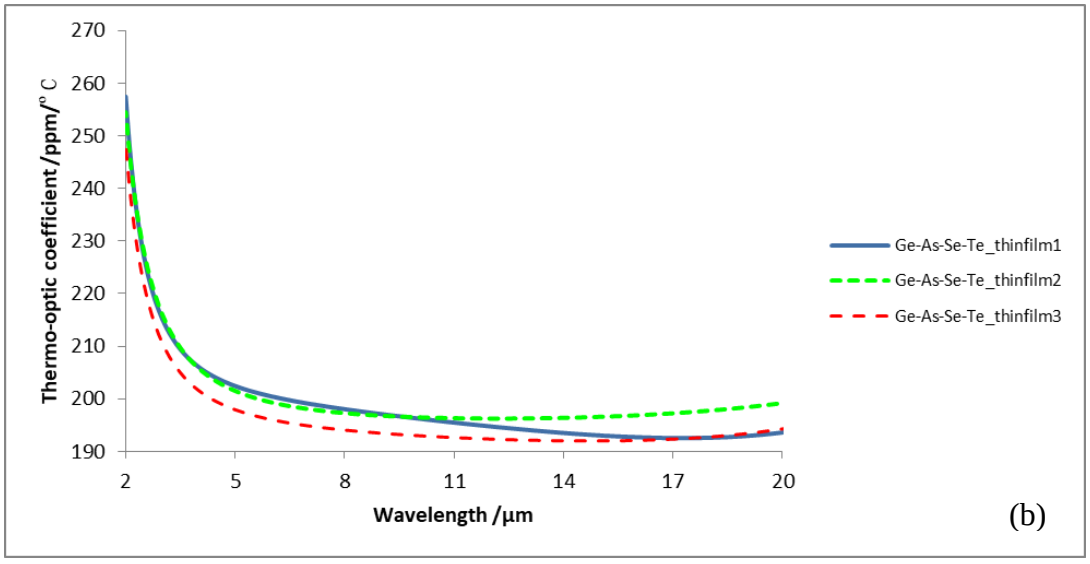


Figure 7.3- 5. The thermo-optic coefficients of three $As_{40}Se_{60}$ at. % (M130MINSCGDJ) thin films (thin films 1 and 2 from YRFFP003; thin film 3 from YRFFP002) and three $Ge_{16}As_{24}Se_{15.5}Te_{44.5}$ at. % (M188SCGDJ) thin films from YRFFP019 obtained using the FTIR continuous dn/dT method.

7.3.2.3 Thermal polarizabilities of $As_{40}Se_{60}$ at. %and $Ge_{16}As_{24}Se_{15.5}Te_{44.5}$ at. %

With the refractive index, TEC and dn/dT of $As_{40}Se_{60}$ at. % and $Ge_{16}As_{24}Se_{15.5}Te_{44.5}$ at. % known, the thermal polarizability coefficients of $As_{40}Se_{60}$ at. % and $Ge_{16}As_{24}Se_{15.5}Te_{44.5}$ at. % over the wavelength from 2 to 25 µm can be obtained according to Eq. (7.6), as shown in Figure 7.3-6. The results calculated from the

prism measurements in section 7.2.4.3 are displayed in Figure 7.3-6 for comparison purpose. Since the TECs of $As_{40}Se_{60}$ at. % and $Ge_{16}As_{24}Se_{15.5}Te_{44.5}$ at. % vary linearly with temperature within this temperature range, the behaviours of the thermal polarizability coefficients are similar to those of dn/dT, which decreases with increasing wavelength at the shorter wavelengths. These observations are in good agreement with the conclusion made in section 7.2.4.3; at wavelenths above 20 μm, the thermal polarizability coefficients of $As_{40}Se_{60}$ at. % and $Ge_{16}As_{24}Se_{15.5}Te_{44.5}$ at. % increase with increasing wavelength because of the red shifts of their fundamental vibrational absorption bands. Figure 7.3-6 shows that the difference in thermal polarisability coefficients obtained using the present method and those obtained using the minimum deivation method is less than 14 ppm/℃ at the wavelength of 3.1 μm. This is attributed to the dn/dT difference mentioned in section 7.3.2.2. For $Ge_{16}As_{24}Se_{15.5}Te_{44.5}$ at. %, due to the similar dn/dT determined using these two methods, the difference of the thermal polarizability coefficients at the wavelength of 3.1 μm is less than 0.04 ppm/℃. $Ge_{16}As_{24}Se_{15.5}Te_{44.5}$ at. % exhibits a lower thermal polarizability coefficient than $As_{40}Se_{60}$ at. % over the wavelength from 2 to 25 μm.

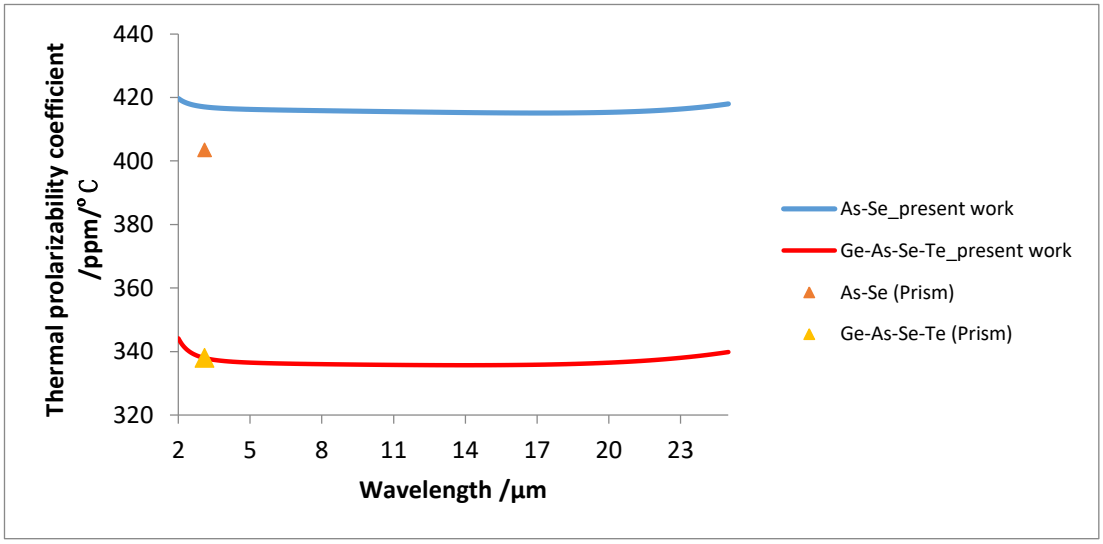


Figure 7.3- 6. Thermal polarizability coefficients of $As_{40}Se_{60}$ at. % (As-Se) (melting code: M130MINSCGDJ; hot-pressing code: YRFFP003) and $Ge_{16}As_{24}Se_{15.5}Te_{44.5}$ at. % (Ge-As-Se-Te) (melting code: M188SCGDJ; hot-pressing code: YRFFP019) compared to the results of the $As_{40}Se_{60}$ at. % (M130MINSCGDJ) and $Ge_{16}As_{24}Se_{15.5}Te_{44.5}$ at. % (M140MINSCGDJ) obtained using the minimum deviation method.

7.3.2.4 Section summary

A FTIR continuous dn/dT method was successfully developed to determine the thermo-optic coefficients of the chalcogenide glasses ($As_{40}Se_{60}$ at. % (melting code: M130MINSCGDJ; hot-pressing code: YRFFP003) and $Ge_{16}As_{24}Se_{15.5}Te_{44.5}$ at. % (melting code: M188SCGDJ; hot-pressing code: YRFFP019)) over the wavelength range from 2 to 20 µm. The error is less than ± 7.0 ppm/°C when applied to a low dn/dT glass ($As_{40}Se_{60}$ at. %) and less than ± 7.5 ppm/°C when applied to a high dn/dT glass ($Ge_{16}As_{24}Se_{15.5}Te_{44.5}$ at. %). Unlike the improved Swanepoel method, the novel method is not so sensitive to the average thickness of the thin film. The error of this technique is mainly attributed to ΔT (thermal stability), ΔTEC (error of the measured thermal expansion coefficient by TMA) and the error of the Sellmeier fitting. The thermal polarizability coefficients of $As_{40}Se_{60}$ at. % and $Ge_{16}As_{24}Se_{15.5}Te_{44.5}$ at. % over the wavelength range from 2 to 20 µm were then determined from the present method.

7.3.3 Assessing the thermal properties of Ge-As-Se-Te thin films with different compositions using the novel method

In this sub-section, the FTIR continuous dn/dT method developed will be applied to determine the thermo-optic coefficients of the distilled $Ge_{16}As_{24}Se_{15.5}Te_{44.5}$ at. % (melting code: M188SCGDJ; hot-pressing code: YRFFP019), $Ge_{14.3}As_{27}Se_{15.5}Te_{43.2}$ at. % (melting code: M178DJ; hot-pressing code: YRFFP025), $Ge_{20}As_{20}Se_{14}Te_{46}$ at. % (melting code: M112DJ; hot-pressing code: YRFFP017) and $Ge_{16}As_{24}Se_{19}Te_{41}$ at. % (melting code: M193DJ; hot-pressing code: YRFFP018) thin films. The manufacturing procedures of these thin films were described in section 3.5.2. The different compositions in Ge-As-Se-Te were developed by Dr. Dinuka Jayasuriya at the time the work was undertaken a PhD candidate in the MIR Photonics Group, University of Nottingham UK, for fabricating the low-NA (numerical aperture) step-index fibres for chemical sensing.

With the refractive index, TEC and dn/dT determined, the thermal polarisability coefficients of Ge-As-Se-Te with different compositions will be calculated using Eq. (7.6). Moreover, determination of the effect of temperature on the material dispersion of Ge-As-Se-Te will be reported in this sub-section.

7.3.3.1 Thermo-optic coefficients of Ge-As-Se-Te thin films

The average thicknesses of the $Ge_{16}As_{24}Se_{15.5}Te_{44.5}$ at. % (M188SCGDJ), $Ge_{14.3}As_{27}Se_{15.5}Te_{43.2}$ at. % (M178DJ), $Ge_{20}As_{20}Se_{14}Te_{46}$ at. % (M112DJ) and $Ge_{16}As_{24}Se_{19}Te_{41}$ at. % (M193DJ) thin films at a temperature of 21.6 ℃ (±0.2 ℃) were determined by the improved Swanepoel method. For $Ge_{16}As_{24}Se_{15.5}Te_{44.5}$ at. %, the average thickness was determined to be 27.40 ± 0.02 µm. For $Ge_{14.3}As_{27}Se_{15.5}Te_{43.2}$ at. %, the average thickness was determined to be 29.35 ± 0.02 µm. For $Ge_{20}As_{20}Se_{14}Te_{46}$ at. %, the thickness at the temperature of 21.6 ℃ is 41.86 ± 0.02 µm and for $Ge_{16}As_{24}Se_{19}Te_{41}$ at. %, the thickness is 36.40 ± 0.02 µm. The

thickness can be determined to a standard deviation of precision of less than 0.02 μm.

The TEC of $Ge_{16}As_{24}Se_{15.5}Te_{44.5}$ (M188SCGDJ) was measured by Dr. Dinuka Jayasuriya at the time the work was undertaken a PhD candidate in the MIR Photonics Group, University of Nottingham UK. The thermal expansion with temperature was found to be linear from 30 ℃ to 100 ℃ with a slope of 16.6 ppm/℃ using TMA (see section 3.7). In present work, the TEC was only measured for one composition by Dr. Jayasuriya. Due to the very small composition difference amongst these four compositions, the TECs of these four compositions were assumed to be 16.6 ppm/℃ with an error of ± 1.0 ppm/℃ in present work.

With TEC and d_l known, d_h at the temperature of 74.6 ℃ (± 0.3 ℃) can be determined from Eq. (7.10) yielding 29.378 μm, 27.426 μm, 41.898 μm and 36.433 μm for the $Ge_{14.3}As_{27}Se_{15.5}Te_{43.2}$ at. % (M178DJ), $Ge_{16}As_{24}Se_{15.5}Te_{44.5}$ at. % (M188SCGDJ), $Ge_{20}As_{20}Se_{14}Te_{46}$ at. % (M112DJ) and $Ge_{16}As_{24}Se_{19}Te_{41}$ at. % (M193DJ) thin films, respectively. The refractive indices at different temperatures for $Ge_{14.3}As_{27}Se_{15.5}Te_{43.2}$ at. %, $Ge_{16}As_{24}Se_{15.5}Te_{44.5}$ at. %, $Ge_{20}As_{20}Se_{14}Te_{46}$ at. % and $Ge_{16}As_{24}Se_{19}Te_{41}$ at. % are shown in Figure 7.3-7 along with the best Sellmeier fits. The Sellmeier coefficients for the best fits are shown in Table 7-11.

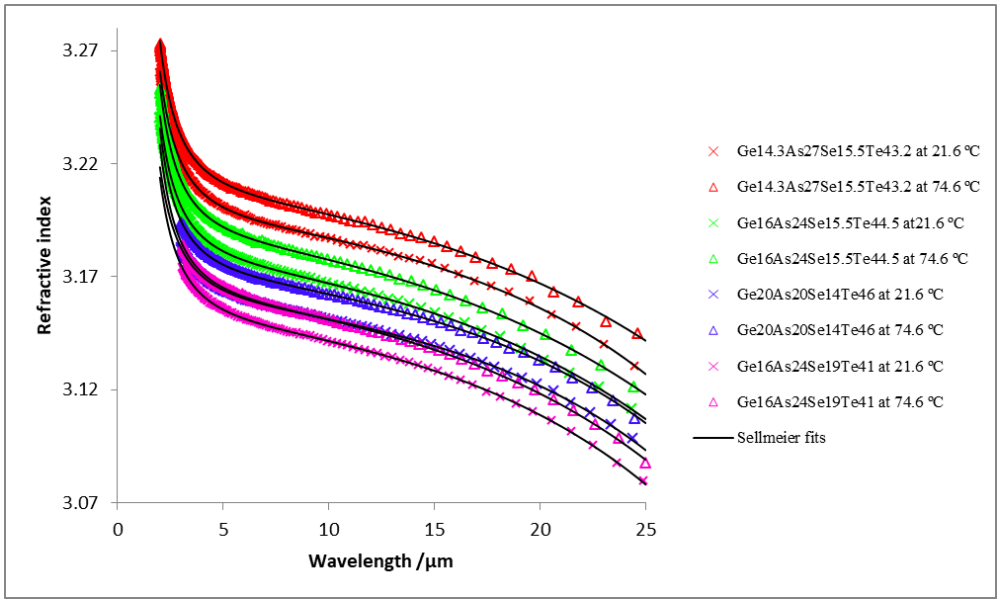


Figure 7.3- 7. The variation of refractive index with wavelength temperatures for $Ge_{14.3}As_{27}Se_{15.5}Te_{43.2}$ at. % (M178DJ), $Ge_{16}As_{24}Se_{15.5}Te_{44.5}$ at. % (M188SCGDJ), $Ge_{20}As_{20}Se_{14}Te_{46}$ at. % (M112DJ) and $Ge_{16}As_{24}Se_{19}Te_{41}$ at. % (M193DJ) along with the best Sellmeier fits to the data points. The Sellmeier coefficients can be found in Table 7-11.

Table 7- 11. The Sellmeier coefficients to the refractive index of $Ge_{14.3}As_{27}Se_{15.5}Te_{43.2}$ at. % (M178DJ), $Ge_{16}As_{24}Se_{15.5}Te_{44.5}$ at. % (M188SCGDJ), $Ge_{20}As_{20}Se_{14}Te_{46}$ at. % (M112DJ) and $Ge_{16}As_{24}Se_{19}Te_{41}$ at. % (M193DJ) at temperatures of 21.6 and 74.6 ℃.

Sellmeier coefficients	A	B_1	B_2	C_1 (VIS)	C_2 (FIR)	R^2
$Ge_{14.3}As_{27}Se_{15.5}Te_{43.2}$ @ 21.6 ℃	5.200	4.991	1.001	0.5707	46.08	0.9998
$Ge_{14.3}As_{27}Se_{15.5}Te_{43.2}$ @ 74.6 ℃	5.958	4.300	1.589	0.6225	56.06	0.9998
$Ge_{16}As_{24}Se_{15.5}Te_{45.5}$ @ 21.6 ℃	3.496	6.572	1.432	0.4992	52.58	0.9999
$Ge_{16}As_{24}Se_{15.5}Te_{45.5}$ @ 74.6 ℃	6.717	3.419	1.805	0.6877	57.53	0.9999
$Ge_{20}As_{20}Se_{14}Te_{46}$ @ 21.6 ℃	8.096	1.869	1.082	0.8669	48.25	0.9997
$Ge_{20}As_{20}Se_{14}Te_{46}$@ 74.6 ℃	8.481	1.554	1.222	0.9550	50.6	0.9997
$Ge_{16}As_{24}Se_{19}Te_{41}$ @ 21.6 ℃	3.934	5.972	1.166	0.5119	47.98	0.9997
$Ge_{16}As_{24}Se_{19}Te_{41}$ @ 74.6 ℃	4.331	5.635	1.393	0.5326	51.57	0.9997

The thermo-optic coefficients of the $Ge_{14.3}As_{27}Se_{15.5}Te_{43.2}$ at. % (M178DJ), $Ge_{16}As_{24}Se_{15.5}Te_{44.5}$ at. % (M188SCGDJ), $Ge_{20}As_{20}Se_{14}Te_{46}$ at. % (M112DJ) and $Ge_{16}As_{24}Se_{19}Te_{41}$ at. % (M193DJ) thin films over the wavelength from 2 to 20 μm were determined according to Eq. (7.12) with an error of less than $\pm$ 9.0 ppm/℃, as shown in Figure 7.3-8. From Figure 7.3-8, $Ge_{20}As_{20}Se_{14}Te_{46}$ at. % has the largest dn/dT amongst these four compositions and it also has the highest Te content. The dn/dTs of $Ge_{14.3}As_{27}Se_{15.5}Te_{43.2}$ at. % and $Ge_{16}As_{24}Se_{15.5}Te_{44.5}$ at. % are very close to each other over the wavelength range from 2 to 17 μm. The difference in dn/dT between these two compositions is seen to apparently increase with increasing wavelengths at wavelengths above 17 μm, which is attributed to the error in the Sellmeier fit. In other words, the data is only thought to be reliable for wavelengths between 3 to 17 μm. Figure 7.3-8 also shows that $Ge_{16}As_{24}Se_{19}Te_{41}$ at. % exhibits the lowest dn/dT and it also has the lowest Te content.

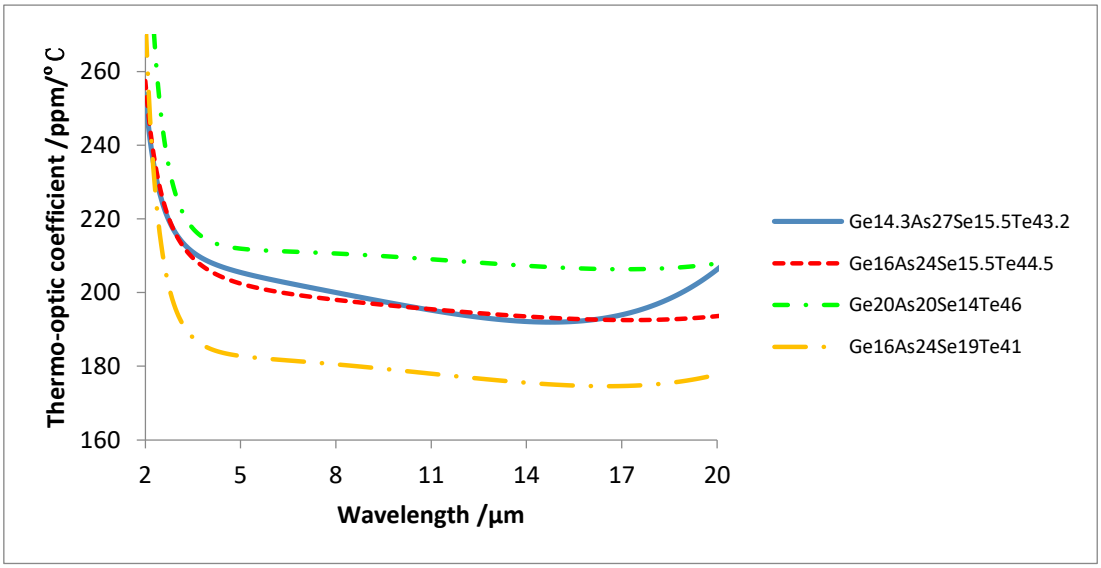


Figure 7.3- 8. The thermo-optic coefficients of the $Ge_{14.3}As_{27}Se_{15.5}Te_{43.2}$ at. % (M178DJ), $Ge_{16}As_{24}Se_{15.5}Te_{44.5}$ at. % (M188SCGDJ), $Ge_{20}As_{20}Se_{14}Te_{46}$ at. % (M112DJ) and $Ge_{16}As_{24}Se_{19}Te_{41}$ at. % (M193DJ) thin films over the wavelength from 2 to 20 μm.

In both [7.1] and [7.2], it was reported that in many cases, the thermo-optic coefficients of Ge-As-Se glasses increased upon decreasing the concentration of Se in the glass system. In order to investigate the relationship between the atomic % of

Se in the Ge-As-Se-Te glass system and the dn/dT, the thermo-optic coefficients of the $Ge_{14.3}As_{27}Se_{15.5}Te_{43.2}$ at. % (M178DJ), $Ge_{16}As_{24}Se_{15.5}Te_{44.5}$ at. % (M188SCGDJ), $Ge_{20}As_{20}Se_{14}Te_{46}$ at. % (M112DJ) and $Ge_{16}As_{24}Se_{19}Te_{41}$ at. % (M193DJ) thin films at wavelengths of 3, 5, 7 and 10 μm are shown in Figure 7.3-9 as a function of the atomic % Se in the Ge-As-Se-Te glass. Figure 7.3-9 shows that the dn/dT does indeed decrease as the atomic percentage of Se decreases in Ge-As-Se-Te; this is in good agreement with [7.1] and [7.2].

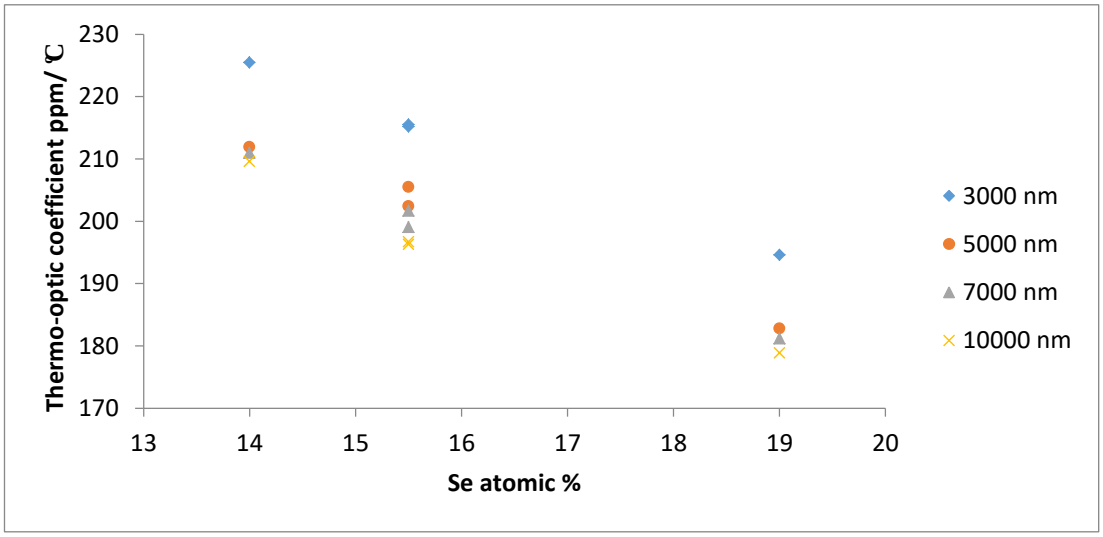


Figure 7.3- 9. The thermo-optic coefficients of the $Ge_{14.3}As_{27}Se_{15.5}Te_{43.2}$ at. % (M178DJ), $Ge_{16}As_{24}Se_{15.5}Te_{44.5}$ at. % (M188SCGDJ), $Ge_{20}As_{20}Se_{14}Te_{46}$ at. % (M112DJ) and $Ge_{16}As_{24}Se_{19}Te_{41}$ at. % (M193DJ) thin films at wavelengths of 3, 5, 7 and 10 μm against the atomic % Se in the Ge-As-Se-Te glass.

7.3.3.2 Thermal polarisability coefficients of Ge-As-Se-Te thin films

With the refractive index, TEC and dn/dT of $Ge_{14.3}As_{27}Se_{15.5}Te_{43.2}$ at. % (M178DJ), $Ge_{16}As_{24}Se_{15.5}Te_{44.5}$ at. % (M188SCGDJ), $Ge_{20}As_{20}Se_{14}Te_{46}$ at. % (M112DJ) and $Ge_{16}As_{24}Se_{19}Te_{41}$ at. % (M193DJ) obtained, the thermal polarisability coefficients of these four different compositions over the wavelength from 2 to 20 μm can be obtained according to Eq. (7.6). Results are shown in Figure 7.3-10. According to Eq. (7.6), the thermal expansion coefficients were assumed to be the same, at 16.6 ppm/℃, with an error of ± 1.0 ppm/℃. The behaviour of the thermal polarisability

coefficients for these four compositions is similar to their dn/dT curves (Figure 7.3-8), as shown in Figure 7.3-10. From Figure 7.3-10, the thermal polarisability coefficients of $Ge_{14.3}As_{27}Se_{15.5}Te_{43.2}$ at. %, $Ge_{16}As_{24}Se_{15.5}Te_{44.5}$ at. % are similar due to their similar compositions. $Ge_{20}As_{20}Se_{14}Te_{46}$ at. % exhibits the highest thermal polarizability coefficient and $Ge_{16}As_{24}Se_{19}Te_{41}$ at. % shows a lower thermal polarizability coefficient over the wavelength range from 3 to 20 μm.

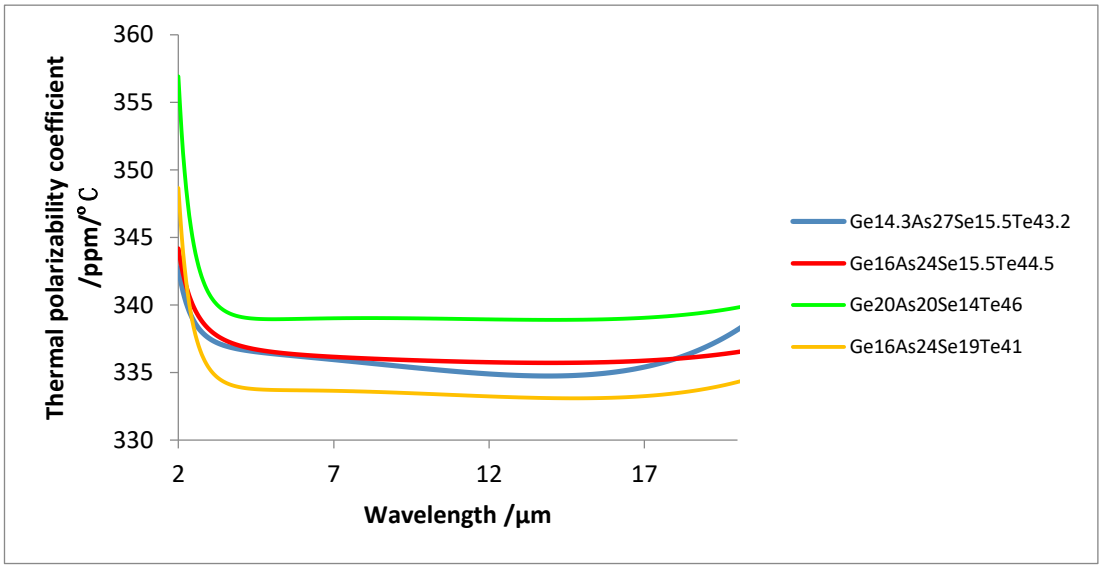


Figure 7.3- 10. The thermal polarisability coefficients of the $Ge_{14.3}As_{27}Se_{15.5}Te_{43.2}$ at. % (M178DJ), $Ge_{16}As_{24}Se_{15.5}Te_{44.5}$ at. % (M188SCGDJ), $Ge_{20}As_{20}Se_{14}Te_{46}$ at. % (M112DJ) and $Ge_{16}As_{24}Se_{19}Te_{41}$ at. % (M193DJ) thin films over the wavelength range from 2 to 20 μm.

7.3.3.3 Variation of the material dispersions of various Ge-As-Se-Te compositions with temperature

An ultra-high-numerical aperture (NA) SIF fibre based on a $Ge_{16}As_{24}Se_{15.5}Te_{44.5}$ at. % (M188SCGDJ) core and $Ge_{10}As_{23.4}Se_{66.6}$ at. % (M007MINSCGNM) cladding has been successfully fabricated and subsequently used for MIR supercontinuum generation (SCG) [7.36]. A SC spectrum covering wavelengths from 2 to 14 μm was successfully obtained based on this fibre. While pumping the fibre for SCG, the temperature of the fibre would inevitably increase due to the high power pump.

Therefore, it is important to know the effect of temperature on the material dispersion of the core glass.

The material dispersions of $Ge_{14.3}As_{27}Se_{15.5}Te_{43.2}$ at. % (M178DJ), $Ge_{16}As_{24}Se_{15.5}Te_{44.5}$ at. % (M188SCGDJ), $Ge_{20}As_{20}Se_{14}Te_{46}$ at. % (M112DJ) and $Ge_{16}As_{24}Se_{19}Te_{41}$ at. % (M193DJ) (see Figure 7.3-11) were calculated using Eq. (5.10) and the best Sellmeier fits. Results are presented in Figure 7.3-11. The inset to Figure 7.3-11 shows details of the zero dispersion wavelengths of $Ge_{14.3}As_{27}Se_{15.5}Te_{43.2}$ at. %, $Ge_{16}As_{24}Se_{15.5}Te_{44.5}$ at. %, $Ge_{20}As_{20}Se_{14}Te_{46}$ at. % and $Ge_{16}As_{24}Se_{19}Te_{41}$ at. % at temperatures of 21.6 ℃ and 74.6 ℃. At lower temperature, the zero dispersion wavelengths of $Ge_{14.3}As_{27}Se_{15.5}Te_{43.2}$ at. %, $Ge_{16}As_{24}Se_{15.5}Te_{44.5}$ at. %, $Ge_{20}As_{20}Se_{14}Te_{46}$ at. % and $Ge_{16}As_{24}Se_{19}Te_{41}$ at. % occur at wavelengths of ~ 9.50 μm, 9.35 μm, 9.33 μm and 9.28 μm, respectively. With the temperature increased to 74.6 ℃, the zero dispersion wavelengths of $Ge_{14.3}As_{27}Se_{15.5}Te_{43.2}$ at. %, $Ge_{16}As_{24}Se_{15.5}Te_{44.5}$ at. %, $Ge_{20}As_{20}Se_{14}Te_{46}$ at. % and $Ge_{16}As_{24}Se_{19}Te_{41}$ at. % shifted towards longer wavelengths and now occur at wavelengths of ~ 9.57 μm, 9.41 μm, 9.38 μm and 9.32 μm, respectively. However, the change in the zero dispersion wavelength is less than 0.1 μm for these four compositions within this temperature range. Figure 7.3-11 also shows that the material dispersion of all four compositions studied remains weak out to 25 μm wavelength. Moreover, all the material dispersions become lower at longer wavelengths as the temperature increases.

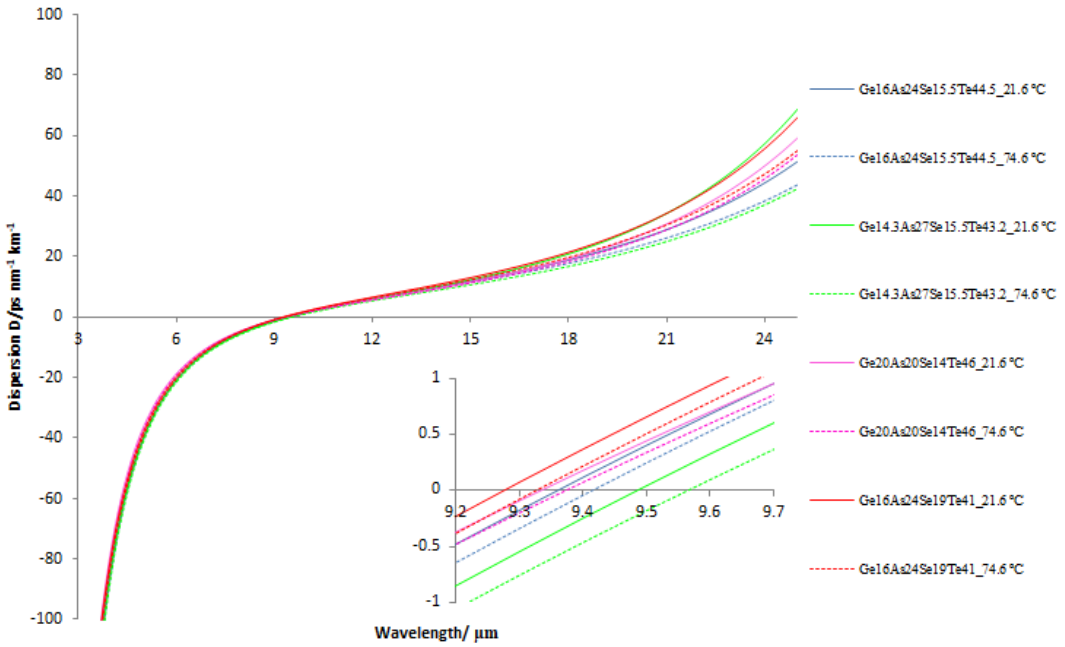


Figure 7.3- 11. Material dispersion *D* calculated from Eq. (5.10) and the fitted Sellmeier models of $Ge_{14.3}As_{27}Se_{15.5}Te_{43.2}$ at. % (M178DJ), $Ge_{16}As_{24}Se_{15.5}Te_{44.5}$ at. % (M188SCGDJ), $Ge_{20}As_{20}Se_{14}Te_{46}$ at. % (M112DJ) and $Ge_{16}As_{24}Se_{19}Te_{41}$ at. % (M193DJ). Inset: material dispersion close to the material zero dispersion wavelengths.

7.4 Chapter summary

The overall aim of this chapter was to determine the effects on the optical properties, including the transparent window, refractive index, numerical aperture, material dispersion, of the chalcogenide glasses investigated in this work. The most important points from chapter 7 are summarised below:

- The FTIR absorbance spectra of the chalcogenide glasses ($As_{40}Se_{60}$ at. % (M179CMDF), $Ge_{16}As_{24}Se_{15.5}Te_{44.5}$ at. % (M140MINSCGDJ), $Ge_{20}Sb_{10}Se_{70}$ at. % (M223ZQTDM) and $Ge_{20}Sb_{10}Se_{67}S_3$ at. % (M191HAP) at temperatures of 21.8 ±0.2 ℃, 37.8±0.2 ℃, 55.9±0.3 ℃ and 74.0±0.3 ℃ were studied here. The transparent windows for these four compositions were determined, and the impurity, atmosphere and multiphonon absorption bands were identified. As temperature increased, the impurity absorption bands were not so sensitive to the increasing temperature while the multiphonon absorption bands exhibited a

temperature-dependent behaviour. For $Ge_{16}As_{24}Se_{15.5}Te_{44.5}$ at. %, the red-shifting optical band gap and increased absorbance due to free-carrier absorption and multiphonon absorption at higher temperature were observed; this resulted in a narrower and less transparent window. By analyzing the FTIR absorbance spetra of $As_{40}Se_{60}$ at. % at temperatures of 21.8 ℃, 37.8 ℃, 55.9 ℃ and 74.0 ℃, it is found that the location of the overtone bands for the fundamental multiphonon absorptions can be estimated by an absorbance that increases with temperature.

- The thermo-optic coefficients (dn/dT) and thermal polarisability coefficients (TPC) of chalcogenide glasses ($As_{40}Se_{60}$ at. % (prism code: YRFP004; melting code: M130MINSCGDJ), $Ge_{16}As_{24}Se_{15.5}Te_{44.5}$ at. % (prism code: YRFP003; melting code: M140MINSCGDJ), $Ge_{20}Sb_{10}Se_{70}$ at. % (prism code: YRFP005; melting code: M135HAP) and $Ge_{20}Sb_{10}Se_{67}S_3$ at. % (prism code: YRFP010; melting code: M191HAP)) were determined using the minimum deviation method in section 7.2. For $As_{40}Se_{60}$ at. %, $Ge_{20}Sb_{10}Se_{70}$ at. % and $Ge_{20}Sb_{10}Se_{67}S_3$ at. %, refractive indices at different temperatures were measured at wavelengths of 1494, 1524, 1554 and 3100 nm. A linear fit was successfully applied to fit the data points, and the dn/dT at each wavelength was obtained from the slope of the linear fit. For $Ge_{16}As_{24}Se_{15.5}Te_{44.5}$ at. %, since the measurement range from 1494 nm to 1554 nm located at the standard Urbach edge in the short wavelength cutoff region and the optical bandgap of $Ge_{16}As_{24}Se_{15.5}Te_{44.5}$ at. % will shift to longer wavelengths with increasing temperature. A quadratic fit was proved to be effective to fit the data points compared to a linear fit. When measuring dn/dT of $Ge_{16}As_{24}Se_{15.5}Te_{44.5}$ at. % using the 3.1 μm ICL, a linear fit was suitable to fit the data points since the wavelength was out of the standard Urbach edge. The error of determining the dn/dT of these four prisms was analysed, and the thermal polarisability coefficients of $As_{40}Se_{60}$ at. %, $Ge_{16}As_{24}Se_{15.5}Te_{44.5}$ at. % and $Ge_{20}Sb_{10}Se_{70}$ at. %

were also calculated with their dn/dT and thermal expansion coefficients obtained.

- The FTIR continuous dn/dT method was developed by the author to obtain the continuous dn/dT of the chalcogenide thin over the wavelength range from 2 to 20 μm. This technique requires the thickness of the thin film at a lower temperature, the thermal expansion coefficient, and the interference transmission spectra of the thin film at normal incidence at a lower temperature and a higher temperature. When considering a chalcogenide glass with a lower dn/dT (~ 40 ppm/℃), this method can determine the dn/dT over the wavelength range from 2 to 20 μm with an error of less than ±7.0 ppm/℃. When assessing a chalcogenide glass with a higher dn/dT (~ 200 ppm/℃), this method can determine the dn/dT over the wavelength range from 2 to 20 μm with an error of less than ±7.5 ppm/℃. The errors in this method was mainly attributed to ΔT (thermal stability), ΔTEC (error of the measured thermal expansion coefficient by TMA) and error of the Sellmeier fit.
- The FTIR continuous dn/dT method developed was then applied to determine the thermo-optic coefficients of the $Ge_{16}As_{24}Se_{15.5}Te_{44.5}$ at. % (M188SCGDJ), $Ge_{14.3}As_{27}Se_{15.5}Te_{43.2}$ at. % (M178DJ), $Ge_{20}As_{20}Se_{14}Te_{46}$ at. % (M112DJ) and $Ge_{16}As_{24}Se_{19}Te_{41}$ at. % (M193DJ) thin films. The results showed that the dn/dT decreased as the atomic percentage of Se decreases in Ge-As-Se-Te; this was in good agreement with [7.1] and [7.2]. Furthermore, the material dispersions of $Ge_{14.3}As_{27}Se_{15.5}Te_{43.2}$ at. %, $Ge_{16}As_{24}Se_{15.5}Te_{44.5}$ at. %, $Ge_{20}As_{20}Se_{14}Te_{46}$ at. % and $Ge_{16}As_{24}Se_{19}Te_{41}$ at. % were also investigated. At a temperature of 21.6 ℃, the zero dispersion wavelengths of $Ge_{14.3}As_{27}Se_{15.5}Te_{43.2}$ at. %, $Ge_{16}As_{24}Se_{15.5}Te_{44.5}$ at. %, $Ge_{20}As_{20}Se_{14}Te_{46}$ at. % and $Ge_{16}As_{24}Se_{19}Te_{41}$ at. % occurred at wavelengths of ~ 9.50 μm, 9.35 μm, 9.33 μm and 9.28 μm, respectively. With the temperature increased to 74.6 ℃, the zero dispersion wavelengths of $Ge_{14.3}As_{27}Se_{15.5}Te_{43.2}$, $Ge_{16}As_{24}Se_{15.5}Te_{44.5}$, $Ge_{20}As_{20}Se_{14}Te_{46}$ and $Ge_{16}As_{24}Se_{19}Te_{41}$ shifted towards longer wavelengths and occurred at

wavelengths of ~ 9.57 μm, 9.41 μm, 9.38 μm and 9.32 μm, respectively. However, the change in the zero dispersion wavelengths is less than 0.1 μm for these four compositions within this temperature range.

References

[7.1] Gleason, B., Richardson, K., Sisken, L. and Smith, C., 2016. Refractive index and thermo-optic coefficients of Ge-As-Se chalcogenide glasses. *International Journal of Applied Glass Science*, *7*(3), pp.374-383.

[7.2] Wang, Y., Qi, S., Yang, Z., Wang, R., Yang, A. and Lucas, P., 2017. Composition dependences of refractive index and thermo-optic coefficient in Ge-As-Se chalcogenide glasses. *Journal of Non-Crystalline Solids*, *459*, pp.88-93.

[7.3] Savage, J.A., Webber, P.J. and Pitt, A.M., 1980. The potential of Ge-As-Se-Te glasses as 3–5 μm and 8–12 μm infrared optical materials. *Infrared Physics*, *20*(5), pp.313-320.

[7.4] Lezal, D., 2003. Chalcogenide glasses-survey and progress. *Journal of Optoelectronics and Advanced Materials*, *5*(1), pp.23-34.

[7.5] Gordon, I.E., Rothman, L.S., Hill, C., Kochanov, R.V., Tan, Y., Bernath, P.F., Birk, M., Boudon, V., Campargue, A., Chance, K.V. and Drouin, B.J., 2017. The HITRAN2016 molecular spectroscopic database. *Journal of Quantitative Spectroscopy and Radiative Transfer*, *203*, pp.3-69.

[7.6] Shiryaev, V.S., Adam, J.L., Zhang, X.H., Boussard-Plédel, C., Lucas, J. and Churbanov, M.F., 2004. Infrared fibers based on Te–As–Se glass system with low optical losses. *Journal of Non-Crystalline Solids*, *336*(2), pp.113-119.

[7.7] Borisevich, V.G., Voitsekhovsky, V.V. and Scripachev, I.V., 1991. Investigation of the influence of extrinsic hydrogen on the optical properties of chalcogenide glasses in the system As-Se. *Vysokochist Vesch*, *1*, p.65.

[7.8] Snopatin, G.E., Churbanov, M.F., Pushkin, A.A., Gerasimenko, V.V., Dianov, E.M. and Plotnichenko, V.G., 2009. High purity arsenic-sulfide glasses and fibers with minimum attenuation of 12 dB/km. *Optoelectronics and Advanced Materials-Rapid Communications*, *3*(7), pp.669-671.

[7.9] Shiryaev, V.S., Adam, J.L., Zhang, X.H., Boussard-Plédel, C., Lucas, J. and Churbanov, M.F., 2004. Infrared fibers based on Te–As–Se glass system with low optical losses. *Journal of Non-Crystalline Solids*, *336*(2), pp.113-119.

[7.10] Churbanov, M.F., Snopatin, G.E., Shiryaev, V.S., Plotnichenko, V.G. and Dianov, E.M., 2011. Recent advances in preparation of high-purity glasses based on arsenic chalcogenides for fiber optics. *Journal of Non-Crystalline Solids*, *357*(11-13), pp.2352-2357.

[7.11] Sanghera, J.S. and Aggarwal, I.D., 1997. Development of chalcogenide glass fiber optics at NRL. *Journal of Non-Crystalline Solids*, *213*, pp.63-67.

[7.12] Sanghera, J. and Aggarwal, I.D., 1998. *Infrared fiber optics*. CRC Press.

[7.13] Urbach, F., 1953. The Long-Wavelength Edge of Photographic Sensitivity and of the Electronic Absorption of Solids. *Physical Review*, *92*, pp.1324-1324.

[7.14] Nguyen, V.Q., Sanghera, J.S., Kung, F.H., Pureza, P.C. and Aggarwal, I.D., 2000. Very large temperature-induced absorptive loss in high Te-containing chalcogenide fibers. *Journal of Lightwave Technology*, *18*(10), pp.1395-1401.

[7.15] Pankove, J.I., 1975. *Optical processes in semiconductors*. Courier Corporation.

[7.16] Bube, R.H., 1992. *Electrons in solids: an introductory survey*. Academic press.

[7.17] Nguyen, V.Q., Sanghera, J.S., Kung, F.H., Aggarwal, I.D. and Lloyd, I.K., 1999. Effect of temperature on the absorption loss of chalcogenide glass fibers. *Applied Optics*, *38*(15), pp.3206-3213.

[7.18] Lax, M. and Burstein, E., 1955. Infrared Lattice Absorption in Ionic and Homopolar Crystals. *Physical Review*, *97*, pp.39-52.

[7.19] Born, M. and Huang, K., 1954. *Dynamical theory of crystal lattices*. Clarendon press.

[7.20] Jiang, C., Wang, X., Zhu, Q., Nie, Q., Zhu, M., Zhang, P., Dai, S., Shen, X., Xu, T., Cheng, C. and Liao, F., 2015. Improvements on the optical properties of Ge–Sb–Se chalcogenide glasses with iodine incorporation. *Infrared Physics & Technology*, *73*, pp.54-61.

[7.21] El-Sayed, S.M., 2003. Far-infrared studies of the amorphous $Sb_xGe_{28-x}Se_{72}$ glassy semiconductor. *Semiconductor Science and Technology*, *18*(4), pp.337-341.

[7.22] Lucovsky, G., 1972. Optic Modes in Amorphous As_2S_3 and As_2Se_3. *Physical Review B*, *6*, pp.1480-1489.

[7.23] Maklad, M.S., Mohr, R.K., Howard, R.E., Macedo, P.B. and Moynihan, C.T., 1974. Multiphonon absorption in As_2S_3-As_2Se_3 glasses. *Solid State Communications*, *15*(5), pp.855-858.

[7.24] Inagawa, I., Iizuka, R., Yamagishi, T. and Yokota, R., 1987. Optical and thermal properties of chalcogenide Ge-As-Se-Te glasses for IR fibers. *Journal of Non-Crystalline Solids*, *95*, pp.801-808.

[7.25] Musgraves, J.D., Danto, S. and Richardson, K., 2014. Thermal properties of chalcogenide glasses. In *Chalcogenide Glasses* (pp. 82-112).

[7.26] Nishii, J., Morimoto, S., Inagawa, I., Iizuka, R., Yamashita, T. and Yamagishi, T., 1992. Recent advances and trends in chalcogenide glass fiber technology: a review. *Journal of Non-Crystalline Solids*, *140*, pp.199-208.

[7.27] Gleason, B., 2015. *Designing optical properties in infrared glass*. *(D*octoral dissertation, Clemson University).

[7.28] Mangin, J., Mennerat, G. and Villeval, P., 2011. Thermal expansion, normalized thermo-optic coefficients, and condition for second harmonic generation of a Nd: YAG laser with wide temperature bandwidth in $RbTiOPO_4$. *Journal of the Optical Society of America. B, Optical physics*, *28*(4), pp.873-881.

[7.29] Prod'homme, L., 1960. A new approach to the thermal change in the refractive index of glasses. *Phys. Chem. Glasses*, *1*(4), pp.119-122.

[7.30] Hilton, A.R. and Jones, C.E., 1967. The thermal change in the nondispersive infrared refractive index of optical materials. *Applied Optics*, *6*(9), pp.1513-1517.

[7.31] Amorphous material Inc., 2013. AMTIR-2 Information.

[7.32] Zhou, T., Zhang, J.F., Hu, B.Q. and Yang, H.G., 1994. Measurements of the thermo-optic coefficient of a barium fluoride single crystal. *Applied Optics*, *33*(13), pp.2620-2623.

[7.33] Parnell, H., 2018. *Towards a Ge-Sb-Se/S hyperspectral imaging probe for early cancer diagnosis (D*octoral dissertation, University of Nottingham).

[7.34] Schott Glass Inc., 2013. Schott Infrared Chalcogenide Glasses-IRG 6.

[7.35] Dantanarayana, H.G., Abdel-Moneim, N., Tang, Z., Sojka, L., Sujecki, S., Furniss, D., Seddon, A.B., Kubat, I., Bang, O. and Benson, T.M., 2014. Refractive index dispersion of chalcogenide glasses for ultra-high numerical-aperture fiber for mid-infrared supercontinuum generation. *Optical Materials Express*, *4*(7), pp.1444-1455.

[7.36] Jayasuriya, D., 2018. *Towards mid-infrared fibre-optic device and systems for sensing, mapping and imaging* (Doctoral dissertation, University of Nottingham).

Chapter 8: Conclusions and suggestions for future work

This Thesis has reported on work carried out to assess the optical properties of chalcogenide glasses relevant to the development of MIR light sources and fibre-sensing. The main focus of this Project was to develop a technique based on the Swanepoel method [8.1] to determine the refractive index dispersion of a hot-pressed chalcogenide thin film in the MIR region. The main conclusions drawn from the work undertaken in this work are presented in section 8.1. In section 8.2, some future work for the further development of the underlying research themes are suggested by the Author.

8.1 Conclusions

8.1.1 Measuring the refractive index of chalcogenide glasses using the minimum deviation method (chapter 4)

- The minimum deviation method has been proven in the past to be suitable for measuring the refractive index of the chalcogenide glasses up to four decimal places [8.2]. This technique exhibits a high accuracy and the results obtained using this technique are not sensitive to the thin oxide layer on the surface of a chalcogenide prism. However, the sample preparation is time-consuming.
- The experimental setup of measuring refractive index using the minimum deviation method was successfully established in our laboratory (see Figure 4.2-1 in section 4.2). This setup allows the measurement of the refractive index of a prism at multiple wavelengths from the visible, via the near-infrared, to the mid-infrared region. All minimum deviation experiments reported in Chapter 4 were conducted nominally at room temperature but not strictly isothermally. In practice that meant the measurements were conducted between 20 to 25 ℃. From the later results of conducting refractive index measurements at controlled

and isothermed temperatures up to about 75 ℃ (see chapter 7) then it is possible to say that the variation of refractive index due to temperature fluctuation alone at nominally room temperature would have been less than ±0.0003 for $As_{40}Se_{60}$ at. % (M130MINSCGDJ), $Ge_{20}Sb_{10}Se_{70}$ (M135HAP) and $Ge_{20}Sb_{10}Se_{67}S_3$ at. % (M191HAP), and less than ±0.0011 for $Ge_{16}As_{24}Se_{15.5}Te_{44.5}$ at. % (M140MINSCGDJ), $Ge_{14.3}As_{27}Se_{15.5}Te_{43.2}$ at. % (M178SDJ), $Ge_{20}As_{20}Se_{14}Te_{46}$ at. % (M112DJ), distilled $Ge_{16}As_{24}Se_{15.5}Te_{44.5}$ at. % (M188SCGDJ) and $Ge_{15}As_{25}Se_{19}Te_{41}$ at. % (M193DJ).

- In order to investigate the error and accuracy of the minimum deviation measurements using the current setup, a commercial silica prism (LAF850322 right-angled prism) was used. Using the present experimental setup, the refractive index of the LAF850322 right-angled prism was determined to be 1.8441 at a wavelength of 651 nm with a standard deviation of ~0.0002. The error to the reference value (1.8432 at a wavelength of 651 nm) is ~ 0.049%. The measured apex was 45°00′37″ with an error of ~0.019% compared to the nominal apex angle (45°). When measuring the refractive index of the LAF850322 right-angled prism, a 1% error in apex angle would lead to a 0.6% error in calculating the refractive index, and a 1% error in the minimum deviation angle would lead to a 0.42 % error in determining the refractive index.
- The chalcogenide glass prisms investigated in this project ($Ge_{7.5}As_{25.5}S_{67}$ at. % (M122MINSCGDJ), $As_{40}Se_{60}$ at. % (M130MINSCGDJ), $Ge_{16}As_{24}Se_{15.5}Te_{44.5}$ at. % (M140MINSCGDJ), $Ge_{14.3}As_{27}Se_{15.5}Te_{43.2}$ at. % (M178DJ), $Ge_{20}As_{20}Se_{14}Te_{46}$ at. % (M122DJ), $Ge_{15}As_{25}Se_{19}Te_{41}$ at. % (M193DJ), $Ge_{20}Sb_{10}Se_{70}$ at. % (M135HAP) and $Ge_{20}Sb_{10}Se_{67}S_3$ at. % (M191HAP)) were prepared using the traditional glass-melting and annealing, then grinding and polishing techniques, as described in section 3.4. To ensure good quality of prism surfaces, epoxy resin was used to hold the glass around to ensure the flatness and each surface of the prism was ground and polished to a 1 μm finish. Considering that a larger apex angle can significantly reduce the standard

deviation of the resulting refractive index and that the beam may not be able to pass through the prism if the apex angle is too large, a 20 °prism apex angle is a good choice for all chalcogenide glasses of refractive index from 2.2 to 3.5. This latter conclusion is a significant step forward for the MIR Photonics Group as in the past it had been assumed that for refractive indices of ~2.2 to 2.7 then a 10 ° apex angle was optimal. In this Project, the $Ge_{7.5}As_{25.5}S_{67}$ at. %, $As_{40}Se_{60}$ at. %, $Ge_{16}As_{24}Se_{15.5}Te_{44.5}$ at. %, $Ge_{20}As_{20}Se_{14}Te_{46}$ at. % and $Ge_{15}As_{25}Se_{19}Te_{41}$ at. % prisms were manufactured to have a nominal apex angle of 10 ° due to non-availability of sufficient material to use a larger apex angle. The $Ge_{7.5}As_{25.5}S_{67}$ at. %, $Ge_{14.3}As_{27}Se_{15.5}Te_{43.2}$ at. %, $Ge_{20}Sb_{10}Se_{70}$ at. % and $Ge_{20}Sb_{10}Se_{67}S_3$ at. % prisms were manufactured to have a nominal apex angle of 20 °.

- Using the minimum deviation method, the refractive index of the $Ge_{7.5}As_{25.5}S_{67}$ at. % prism (YRFP001) was measured at wavelengths of 651 nm, 1464 nm to 1574 nm with an interval of 10 nm, and at 3100 nm. The refractive indices of the $As_{40}Se_{60}$ at. % (YRFP004), $Ge_{16}As_{24}Se_{15.5}Te_{44.5}$ at. % (YRFP004) and $Ge_{20}Sb_{10}Se_{70}$ at. % (YRFP005) prisms were successfully measured at wavelengths of 1464 nm to 1574 nm with an interval of 10 nm and 3100 nm, 3800 nm and 6450 nm, using the light sources of Agilent fibre coupled diode (1464 nm-1575 nm, 40 mW), interband-cascade laser (ICL) (centre wavelength: 3.1 μm, NRL), SuperK continuum MIR source (1.1-4.2 μm, 450 mW, NKT photonics) used in conjunction with a 3.8 μm bandpass filter, and 6.45 μm optical parametric oscillator (OPO) (Chromacity spark FIR, Chromacity Ltd.), respectively. The refractive index data were then successfully fitted to a two-term Sellmeier model over the wavelength measurement range, with a R^2 of better than 0.9993; this indicates that the two-term Sellmeier model is a suitable refractive index model for fitting the refractive index of a chalcogenide glass in the MIR region.

- When using **the 651 nm He-Ne laser** to measure the refractive index of the 20 º apex angle $Ge_{7.5}As_{25.5}S_{67}$ at. % prism, the standard deviation was less than 0.0006. When using **the Agilent fibre coupled diode (tunable wavelength range from 1464 nm to 1574 nm)**, the refractive indices of the 10 ºapex angle prisms ($As_{40}Se_{60}$ at. % and $Ge_{16}As_{24}Se_{15.5}Te_{44.5}$ at. %) can be determined with a standard deviation of less than 0.0013. For the prisms with 20 ºtarget apex angle ($Ge_{7.5}As_{25.5}S_{67}$ at. % and $Ge_{20}Sb_{10}Se_{70}$ at. %), the standard deviation on precision of the refractive index data improved from 0.0013 to 0.0006. This confirms the fact that a larger apex angle can significantly reduce the error in determining refractive index using the minimum deviation method. When using the **ICL** for the minimum deviation measurements at 3100 nm, the standard deviation of the measured refractive index increased up to 0.0020 for the 20 ºtarget apex angle prisms, and up to 0.0023 for the 10 ºtarget apex angle prisms. This confirms that a good beam quality can reduce the error in the minimum deviation measurements. Since the **SuperK continuum mid-infrared source**, used in conjunction with a 3.8 μm bandpass filter, and **6.45 μm OPO** each provided a well-collimated beam, the refractive index at these two wavelengths was determined with a standard deviation of less than 0.0010.
- The refractive indices of some chalcogenide prisms ($Ge_{14.3}As_{27}Se_{15.5}Te_{43.2}$ at. % (YRFP006), $Ge_{20}As_{20}Se_{14}Te_{46}$ at. % (YRFP007), $Ge_{15}As_{25}Se_{19}Te_{41}$ at. % (YRFP008), distilled $Ge_{16}As_{24}Se_{15.5}Te_{44.5}$ at. % (YRFP009) and $Ge_{20}Sb_{10}Se_{67}S_3$ at. % (YRFP0010)) were measured at the wavelengths of 3.1 and 6.45 μm using the ICL and the OPO, respectively. These refractive index data were taken as benchmark values for the modified Swanepoel method, as described in Chapter 6.
- The repeatability of the minimum deviation measurements using the 3100 nm ICL source was investigated using the $Ge_{16}As_{24}Se_{15.5}Te_{44.5}$ and $Ge_{20}Sb_{10}Se_{70}$ prisms. The average refractive index of the $Ge_{16}As_{24}Se_{15.5}Te_{44.5}$ prism across six independent measurements over a four-month time period is 3.1920 with an

error of refractive index within ± 0.0007. For the $Ge_{20}Sb_{10}Se_{70}$ prism, the average refractive index across seven independent measurements, taken over a period of two months, is 2.5462 with an error of refractive index within ± 0.0011.

- After analysing the refractive index change with changing composition of Ge-As-Se-Te, an interpolation scheme for estimating the refractive index of $Ge_xAs_{z-x}Se_{100-z-y}Te_y$ within the range of $10 \leq x \leq 25$, $40 \leq y \leq 50$ and $30 \leq z \leq 40$ was set up with an error of less than 0.22 % (typically ± 0.007 on a refractive index of 3.4) compared to QinetiQ data [8.3]. This estimation is very useful for designing core/cladding composition for step-index fibres.

8.1.2 Refractive index models for chalcogenide glasses in near-infrared (NIR) and mid-infrared (MIR) regions (chapter 5)

- This chapter focused on analysing the refractive index and extinction coefficient of bulk glass samples of $Ge_{16}As_{24}Se_{15.5}Te_{44.5}$ at. % (M150MINSCGDJ), $As_{40}Se_{60}$ at. % (M005MINSCGNM), $Ge_{10}As_{23.4}Se_{66.6}$ at. % (M007MINSCGNM), $Ge_{16.5}As_{16}Ga_3Se_{64.5}$ at. % (ZQT007), Pr^{3+} doped $Ge_{16}As_{21}Ga_1Se_{62}$ at. % (M022MINREZQT) by means of spectroscopic ellipsometry over the wavelength range from 0.4 to 33 μm.
- Based on the extinction coefficient data obtained from spectroscopic ellipsometry, the wavelengths at which the extinction coefficients begin to increase in shorter wavelengths for the $As_{40}Se_{60}$ at. % (700 nm) and $Ge_{10}As_{23.4}Se_{66.6}$ at. % (665 nm), glasses were found to be associated with their published optical bandgap (701 nm for $As_{40}Se_{60}$ at. % and 645 nm for $Ge_9As_{25}Se_{66}$ at. %). Therefore, the optical band gaps of $Ge_{16}As_{24}Se_{15.5}Te_{44.5}$ at. %, $As_{40}Se_{60}$ at. %, $Ge_{10}As_{23.4}Se_{66.6}$ at. %, $Ge_{16.5}As_{16}Ga_3Se_{64.5}$ at. % and Pr^{3+} doped $Ge_{16}As_{21}Ga_1Se_{62}$ at. % could be predicted to be 700 nm for $As_{40}Se_{60}$ at. %, 665 nm for $Ge_{10}As_{23.4}Se_{66.6}$ at. %, 1300 nm for $Ge_{16}As_{24}Se_{15.5}Te_{44.5}$ at. %, 650

nm for $Ge_{16.5}As_{16}Ga_3Se_{64.5}$ at. % and 650 nm for Pr^{3+} doped $Ge_{16}As_{21}Ga_1Se_{62}$ at. %, respectively, from the onset of the rising extinction coefficient with decreasing wavelength.

- According to [8.4], the transparent window of a chalcogenide glass can be defined as the range of wavelengths over which the extinction coefficient is smaller than 0.0005. Based on this definition, the transparent windows of the chalcogenide glasses investigated in this chapter were determined using their extinction coefficient data obtained from spectroscopic ellipsometry. The transparent windows for $As_{40}Se_{60}$ at. % and $Ge_{10}As_{23.4}Se_{66.6}$ at. % are from ~0.7 to 30 μm, which is in a good agreement with [8.4]. For the $Ge_{16}As_{24}Se_{15.5}Te_{44.5}$ at. %, the transparent window was determined to be from ~ 1.44 μm to ~ 29.46 μm. The transparent window for $Ge_{16.5}As_{16}Ga_3Se_{64.5}$ at. % is from ~ 0.65 μm to ~ 23.5 μm and for Pr^{3+} doped $Ge_{16}As_{21}Ga_1Se_{62}$, it is from ~ 0.65 μm to ~ 26 μm according to the extinction coefficient data.
- Two commonly used refractive index models (the Cauchy model and the Sellmeier model) for real part of refractive index within the glass transparent region were introduced. The Cauchy and Sellmeier models were then applied to interpolate the ellipsometry data (real part of the refractive index) over the wavelength range from the lower wavelength edge of the transparent window to 2.5 μm (obtained using the Woollam VUV VASE rotating analyser ellipsometer) and within the whole transparent window (obtained using the Woollam VUV VASE and IR-VASE instruments) by using the Matlab curve fitting tool (cftool in Matlab) since they are valid in the transparent window of a glass and material dispersion can be obtained from the second derivatives of these two models.
- When applying the two-term Cauchy, three-term Cauchy, one-term Sellmeier and two-term Sellmeier models to fit the refractive index data of the $Ge_{16}As_{24}Se_{15.5}Te_{44.5}$ at. %, $As_{40}Se_{60}$ at. %, $Ge_{10}As_{23.4}Se_{66.6}$ at. %, $Ge_{16.5}As_{16}Ga_3Se_{64.5}$ at. % and Pr^{3+} doped $Ge_{16}As_{21}Ga_1Se_{62}$ at. % glasses **over the wavelength range from the lower wavelength edge of the transparent**

window to 2.5 μm, the two-term Cauchy model proved to be the worst of these refractive index model. Introducing a third Cauchy term was found to significantly improve the fitting performance, which makes the three-term Cauchy model suitable to describe the refractive index dispersion of chalcogenide glasses in this wavelength region. Furthermore, the best fits were provided by the one-term Sellmeier and two-term Sellmeier models, which were also thus considered as suitable refractive index models.

- When applying the two-term Cauchy, three-term Cauchy, one-term Sellmeier, two-term Sellmeier and three-term Sellmeier models to fit the refractive index data of the $Ge_{16}As_{24}Se_{15.5}Te_{44.5}$ at. %, $As_{40}Se_{60}$ at. %, $Ge_{10}As_{23.4}Se_{66.6}$ at. %, $Ge_{16.5}As_{16}Ga_3Se_{64.5}$ at. % and Pr^{3+} doped $Ge_{16}As_{21}Ga_1Se_{62}$ at. % glasses **within their entire transparent windows**, the Cauchy models and the one-term Sellmeier model failed to describe the refractive index dispersion since they cannot be applied to model materials with multiple band gaps in the frequency range of interest. The two-term Sellmeier model (C_1 in optical bandgap electronic absorption band spectral region and C_2 in MIR fundamental vibrational absorption band region) successfully described the refractive index dispersion of the chalcogenide glasses in this wavelength region with the best fitting quality (R^2 better than 0.9999) and lowest fitting errors (less than 0.1 %). Moreover, introducing an extra Sellmeier term beyond two terms did not significantly improve the fitting performance. Therefore, the two-term Sellmeier model was concluded to be a suitable refractive index dispersion model of chalcogenide glasses over the glass transparent window, and were therefore applied to improve the original Swanepoel method [8.1] in order to extend this method into the MIR region, as discussed in chapter 6.
- According to [8.4], C_1 in a two-term Sellmeier model is associated with the optical bandgap absorption and C_2 in a two-term Sellmeier model is associated with vibrational band resonance absorption. For $As_{40}Se_{60}$ at. %, a unique set of Sellmeier coefficients, with the C_2 associated well with the position of the

calculated (from its second overtone band in the FTIR transmission spectrum) fundamental vibrational absorption band, was presented. It is suggested that, with the short and long wavelength resonant, intrinsic absorption of the chalcogenide glass composition known, the refractive index dispersion might be predictable. For the other compositions ($Ge_{16}As_{24}Se_{15.5}Te_{44.5}$ at. %, $Ge_{10}As_{23.4}Se_{66.6}$ at. %, $Ge_{16.5}As_{16}Ga_3Se_{64.5}$ at. % and Pr^{3+} doped $Ge_{16}As_{21}Ga_1Se_{62}$ at. %) investigated in this chapter, since knowledge of the fundamental vibrational bands is not available – simply requiring further data collection - a unique set of the two-term Sellmeier coefficients cannot be determined.

- Previously, a SIF based on the $As_{40}Se_{60}$ at. % core and $Ge_{10}As_{23.4}Se_{66.6}$ at. % cladding was successfully fabricated for a record MIR fibre supercontiuum generation [8.5]. Using the refractive index data presented in this chapter, the numerical aperture of these core-cladding fibre was calculated to be larger than 0.97 over the wavelength range from 0.5 to 30 μm, agreeing with published work. Another ultra-high-NA SIF based on the $Ge_{16}As_{24}Se_{15.5}Te_{44.5}$ at. % and $Ge_{10}As_{23.4}Se_{66.6}$ at. % glass pair was also fabricated for MIR supercontiuum generation [8.6] with the newly calculated NA in this chapter shown to be larger than 1.86 over the wavelength range from 0.5 to 30 μm.
- The two-term Sellmeier fits to the measured refractive index data have also been used to calculate material dispersion characteristics for $Ge_{16}As_{24}Se_{15.5}Te_{44.5}$ at. % (M150MINSCGDJ), $As_{40}Se_{60}$ at. % (M005MINSCGNM), $Ge_{10}As_{23.4}Se_{66.6}$ at. % (M007MINSCGNM), $Ge_{16.5}As_{16}Ga_3Se_{64.5}$ at. % (ZQT007), Pr^{3+} doped $Ge_{16}As_{21}Ga_1Se_{62}$ at. % (M022MINREZQT). For $As_{40}Se_{60}$ at. % and $Ge_{10}As_{23.4}Se_{66.6}$ at. %, the calculated ZDW occurred at 7.4 μm and 7.1 μm, respectively, which is in good agreement with [8.4]. For the core material in the $Ge_{16}As_{24}Se_{15.5}Te_{44.5}$ at. % / $Ge_{10}As_{23.4}Se_{66.6}$ at. % glass pair, the ZDW of $Ge_{16}As_{24}Se_{15.5}Te_{44.5}$ at. % occurs at 10 μm. For the $Ge_{16.5}As_{16}Ga_3Se_{64.5}$ at. % glass, the ZDW occurs at 5.4 μm and for the Pr^{3+} doped $Ge_{16}As_{21}Ga_1Se_{62}$ at. % glass, the ZDW locates at 6.5 μm.

8.1.3 Swanepoel's method to determine the refractive index of chalcogenide glasses (chapter 6)

- To reiterate, the main goal in this Project was to modify the method described in Swanepoel's paper [8.1] (referred to the original Swanepoel method) to provide useful refractive index and material dispersion data for the chalcogenide glass compositions designed for MIR light source development and fibre-sensing.
- The basic theory of the original Swanepoel method was introduced, and this method was successfully reproduced using the MATLAB codes written by the author. The results obtained matched those presented by Swanepoel in [8.1].
- For characterising the refractive index of a chalcogenide thin film over the wavelength range from 2 to 25 μm, a hot-pressing technique was developed to fabricate stand-alone chalcogenide glass thin films with the choice of thickness of 20 μm, 25 μm and 30 μm.
- The interference transmission spectra of the hot-pressed thin films ($Ge_{16}As_{24}Se_{15.5}Te_{44.5}$ at. % (M140MINSCGDJ) and $As_{40}Se_{60}$ at. % (M130MINSCGDJ)) over the wavelength range from 1 to 27 μm were successfully obtained using FTIR spectrometry. In the interference transmission spectra, it was possible in some cases to observe the multiphonon absorption bands of the glass overlying the fringes. Since the method described in Swanepoel's paper [8.1] used the extrema of the interference transmission spectra (one at normal incidence and one at oblique incidence) to determine the refractive index of a thin film, the measurement wavelength range was based on the distinguishable extrema obtained. The wavelength range of the distinguishable extrema for the hot-pressed thin film can be optimised by:
    1. Reducing the thickness variation on the wedge-shaped hot-pressed thin film, by using a suitable hot-pressing temperature, increasing the hot-pressing duration or increasing the hot-pressing pressure. The wedge shape was an inescapable error due to the fabrication techinique.

2. Decreasing the beam size by selecting a smaller aperture. Therefore, in the FTIR thin film measurements, a 1 mm aperture was selected.
3. A careful purge using dry air (at least 15 mins) to prevent the interference fringes being distorted by water and CO_2 absorptions.

- The original Swanepoel method to determine the refractive index of the hot-pressed chalcogenide glass thin films ($Ge_{16}As_{24}Se_{15.5}Te_{44.5}$ at. % (M140MINSCGDJ) and $As_{40}Se_{60}$ at. % (M130MINSCGDJ)) became invalid at longer wavelengths due to the inappropriate dispersive equation used by Swanepoel (two-term Cauchy model). For $Ge_{16}As_{24}Se_{15.5}Te_{44.5}$ at. %, the errors of the fit to data points over the wavelength range from 3 to 24 μm were within 0.2 % out to 16 μm, and then increase, with a value of 0.8 % at a wavelength of 24 μm. For $As_{40}Se_{60}$ at. %, the errors are within 0.5 % out to 17 μm and then increase up to 2 % at a wavelength of 24 μm. In order to extend this method into the MIR region, other dispersive models were required.
- The original Swanepoel method of [8.1] was modified by changing the dispersive model from a two-term Cauchy model to three-term Cauchy, one-term Sellmeier and two-term Sellmeier models. The modified Swanepoel methods and the original Swanepoel method were then applied to determine the refractive index of the $As_{40}Se_{60}$ at. % thin film using the data in [8.7]. The difference between the refractive index values determined by the two Cauchy models in the Swanepoel method was less than 0.15 %. The difference between the refractive index values determined by the modified approach using the Sellmeier models (the one-term and two-term Sellmeier models) and those obtained from the original Swanepoel method using the two-term Cauchy model was found to be less than 0.26 %. The Swanepoel methods using these four different models were able to fit their refractive index data with the error less than 0.47 %. The lowest errors were achieved by using the two-term Sellmeier model as the dispersive model.

- Since the two-term Sellemeir model was considered as a suitable refractive index model for chalcogenide glasses in the MIR region according to [8.4] and as described in chapter 5, the modified Swanepoel method using a two-term Sellmeier model was applied to determine the refractive index of the $Ge_{16}As_{24}Se_{15.5}Te_{44.5}$ at. % (M140MINSCGDJ) and $As_{40}Se_{60}$ at. % (M130MINSCGDJ) thin films; the results were compared to those obtained using the original Swanepoel method. By using a suitable refractive index model, refractive indices of the $Ge_{16}As_{24}Se_{15.5}Te_{44.5}$ at. % and $As_{40}Se_{60}$ at. % thin films were successfully determined over the wavelength range from 2 μm to 25 μm with an error of less than 0.4 % (< ± 0.013 on refractive index at a wavelength of 3.1 μm) compared to the results obtained using the minimum deviation method. This difference might be attributed to their different thermal history. The average thicknesses of the non-uniform thin films were also determined by this method. Moreover, compared to the original Swanepoel method, the method using a two-term Sellmeier model significantly reduced the fitting error to the refractive index data points. Therefore, the modified Swanepoel method using a two-term Sellmeier model was christened as **the improved Swanepoel method** in this thesis. Repeated measurements showed that the refractive index dispersion was determined by the improved method with a standard deviation of precision less than ± 0.002 on refractive index for the $As_{40}Se_{60}$ at. % (M130MINSCGDJ) thin films and $Ge_{16}As_{24}Se_{15.5}Te_{44.5}$ at. % (M140MINSCGDJ) thin films over the wavelength range from 3 to 23 μm.
- The improved Swanepoel method was successfully applied to determine the refractive index of Ge-As-Se-Te glasses with different compositions ($Ge_{16}As_{24}Se_{15.5}Te_{44.5}$ at. % (M140MINSCGDJ), $Ge_{14.3}As_{27}Se_{15.5}Te_{43.2}$ at. % (M178DJ), $Ge_{20}As_{20}Se_{14}Te_{46}$ at. % (M112DJ), distilled $Ge_{16}As_{24}Se_{15.5}Te_{44.5}$ at. % (M188SCGDJ) and $Ge_{16}As_{24}Se_{19}Te_{41}$ at. % (M193DJ)) in the MIR region with an accuracy of less than 0.47 % (< ± 0.015 on refractive index at a wavelength of 3.1 μm) compared to the results obtained using the minimum deviation

method. The NA of the high-NA SIF fibre based on the distilled $Ge_{16}As_{24}Se_{15.5}Te_{44.5}$ (M188SCGDJ) core and the $Ge_{10}As_{23.4}Se_{66.6}$ (M007MINSCGNM) cladding was calculated to be larger than 1.82 over the wavelength range from 2 to 25 μm. The NA of the low-NA SIF fibre based on a distilled $Ge_{16}As_{24}Se_{15.5}Te_{44.5}$ (M188SCGDJ) core and a $Ge_{16}As_{24}Se_{19}Te_{41}$ (M193DJ) cladding was calculated to be less than 0.40 over the wavelength range from 3 to 18 μm. The material disperions of the five compositions ($Ge_{16}As_{24}Se_{15.5}Te_{44.5}$ at. % (M140MINSCGDJ), $Ge_{14.3}As_{27}Se_{15.5}Te_{43.2}$ at. % (M178DJ), $Ge_{20}As_{20}Se_{14}Te_{46}$ at. % (M112DJ), distilled $Ge_{16}As_{24}Se_{15.5}Te_{44.5}$ at. % (M188SCGDJ) and $Ge_{16}As_{24}Se_{19}Te_{41}$ at. % (M193DJ)) were also successfully obtained, which showed that the zero dispersion wavelength might shift to shorter wavelength with lower atomic % of Te in Ge-As-Se-Te. The refractive index data for other chalcogenide glasses was also successfully determined by the improved Swanepoel method.

- The investigation on the effects of fast quenching on the refractive index of hot-pressed thin films was also discussed. The results obtained using the improved Swanepoel method showed that the refractive index of the fast-quenched chalcogenide thin film was similar to that of the well-annealed thin film. However, the fast-quenching achieved here in the hot press was nowhere near as fast a quench as is done when drawing optical fibre on a draw tower. Therefore it is surmised that the refractive index dispersion of as-drawn fibre will differ from annealed bulk glass of the same composition but that this has not been possible to investigate during this Project.
- A new technique has been developed to determine the small refractive index contrast of two glasses with the same thermal history. The two-composition thin glass film (core: $Ge_{20}Sb_{10}Se_{70}$ at. % (M135HAP); cladding: $Ge_{20}Sb_{10}Se_{67}S_3$ at. % (M157HAP)) was prepared by a hot-pressing technique. Only using the transmission spectra at normal-incidence, the refractive contrast can be determined over the wavelength range from 2 to 25 μm with an error of less than

± 0.0020 due to a typically thickness variation of < 0.05 μm of the two-composition thin film. To determine the absolute values of the refractive index and thicknesses of each glass in the two-composition thin film, the improved Swanepoel method was applied. Over the wavelength range 3 to 25 μm, the refractive index was determined with a standard deviation of precision < 0.002 and the refractive index contrast was determined with an error of ±0.0005. The SIF NA was determined from this technique with an error of ± 0.011, compared to the value of SIF NA from the prism minimum deviation method, on samples made from the same glass melts. 3 at. % S replacing Se pro rata in the Ge-Sb-Se glass system (to formulate the cladding glass composition relative to the core glass composition) was shown to blue-shift the VIS optical bandgap and MIR fundamental vibrational absorption bands, lower the refractive index by 0.013 at a wavelength of 3.1 μm and by 0.012 at a wavelength of 6.45 μm, and move the zero dispersion wavelength to shorter wavelength: shifted from 6.3 to 6.1 μm.

8.1.4 The effects of temperature on the optical properties of chalcogenide glasses (chapter 7)

This chapter mainly discussed the temperature effects on the optical properties of the chalcogenide glasses ($As_{40}Se_{60}$ at. % (M179CMDF), $Ge_{16}As_{24}Se_{15.5}Te_{44.5}$ at. % (M140MINSCGDJ), $Ge_{20}Sb_{10}Se_{70}$ at. % (M223ZQTDM) and $Ge_{20}Sb_{10}Se_{67}S_3$ at. % (M157HAP)) investigated in this work.

- A temperature-controlled holder was designed and manufactured to heat or cool the temperature of the bulk chalcogenide glasses and chalcogenide glass thin films. The lowest nominal temperature was set to be 15 ℃ to avoid condensation on the sample. The highest nominal temperature was set to be 80 ℃; this was limited by the liquid (water) used in the water bath. The temperature variation between the set temperature and the temperature of the sample can be reduced by using a nylon chamber to reduce the air flow. The actual sample

temperature achieved were 21.8±0.2 ℃, 37.8±0.2 ℃, 55.9±0.3 ℃ and 74.0± 0.3 ℃.

- The FTIR absorbance spectra of chalcogenide glasses ($As_{40}Se_{60}$ at. % (M179CMDF), $Ge_{16}As_{24}Se_{15.5}Te_{44.5}$ at. % (M140MINSCGDJ), $Ge_{20}Sb_{10}Se_{70}$ at. % (M223ZQTDM) and $Ge_{20}Sb_{10}Se_{67}S_3$ at. % (M191HAP)) at temperatures of 21.8 ℃, 37.8 ℃, 55.9 ℃ and 74.0 ℃ were studied and are reported in section 7.1.
- For $Ge_{16}As_{24}Se_{15.5}Te_{44.5}$ at. % (M140MINSCGDJ), the impurity, atmosphere and multiphonon absorption bands were identified from the FTIR spectrum. In the Ge-As-Se-Te glass system, since tellurium exhibits a semi-metallic character, free carrier absorption dominates the absorbance absorption from 5 μm to 12 μm with increasing temperature. As wavelength increased, the multiphonon absorption started to dominate. As a result of the red-shifting optical band gap and increased absorbance due to free-carrier absorption and multiphonon absorption at higher temperature, the transparent window of Ge-As-Se-Te becomes narrower and less transparent. From the absorbance spectra of Ge-As-Se-Te at different temperatures, it was observed that the impurity absorption bands (Se-H bands at 3.42 μm and 4.52 μm, Ge-O band at ~ 8 μm and Si-O band at ~ 8 μm) were not sensitive to temperature within this temperature range while multiphonon absorption band exhibited an obvious temperature-dependent behaviour.
- For both $Ge_{20}Sb_{10}Se_{70}$ at. % (M223ZQTDM) and $Ge_{20}Sb_{10}Se_{67}S_3$ at. % (M191HAP), the impurity, atmosphere and multiphonon absorption bands for each composition were identified. It is found that, with introducing 3 atomic % S into Ge-Sb-Se, H is gathered by S which exhibits a strong absorption at 4.03 μm, which in turn weaken the Se-H absorption band at 4.52 μm and 3.42 μm. With introducing 3 atomic % S into Ge-Sb-Se, the peak of the absorption band at 12.69 μm was shifted to 13.13 μm. By analysing the absorbance spectra of $Ge_{20}Sb_{10}Se_{70}$ at. % and $Ge_{20}Sb_{10}Se_{67}S_3$ at. % at different temperatures, the band at 13.13 μm for $Ge_{20}Sb_{10}Se_{67}S_3$ at. % is a combination band thought due to the

Ge-O band and S related-multiphonon absorption. Moreover, the peaks of multiphonon absorption bands were observed to slightly red-shift to longer wavelength; this indicates the fundamental vibrational absorption band shift to longer wavelengths with increasing temperature.

- The investigation on the multiphonon absorption bands for $As_{40}Se_{60}$ at. % (M179CMDF) was discussed in section 7.1.3. From the FTIR absorbance spectra of $As_{40}Se_{60}$ at. % at temperatures of 21.8 ℃, 37.8 ℃, 55.9 ℃ and 74.0 ℃, an obvious increase of absorbance with temperature was observed at the wavelengths where the multiphonon absorption bands were suggested to occur [8.8]. This indicates that the location of the overtone bands for the fundamental multiphonon absorptions can be estimated by an absorbance that increases with temperature. The obvious multiphonon absorption bands found in the spectra were also identified.
- The thermo-optic coefficients (dn/dT) and thermal polarisability coefficients (TPC) of chalcogenide glasses ($Ge_{16}As_{24}Se_{15.5}Te_{44.5}$ at. % (M140MINSCGDJ), $As_{40}Se_{60}$ at. % (M130MINSCGDJ), $Ge_{20}Sb_{10}Se_{70}$ at. % (M223ZQTDM) and $Ge_{20}Sb_{10}Se_{67}S_3$ at. % (M191HAP)) were determined using the minimum deviation method in section 7.2. The most important observations are:
    1. The refractive indices of the $As_{40}Se_{60}$ at. % (M130MINSCGDJ) and $Ge_{16}As_{24}Se_{15.5}Te_{44.5}$ at. % (M140MINSCGDJ) prisms were measured at wavelengths of 1494, 1524, 1554 and 3100 nm at different temperatures between 15 ℃ and 72 ℃; the standard deviation on refractive index measured at wavelengths of 1494, 1524 and 1554 nm was less than 0.0006 and the standard deviation on refractive index measured at a wavelength of 3100 nm was less than 0.0010.
    2. For $As_{40}Se_{60}$ at. % (M130MINSCGDJ), a linear fit of refractive index versus temperature was found suitable to fit the data points at each wavelength. The dn/dTs of $As_{40}Se_{60}$ at. % at wavelengths of 1494, 1524, 1554 and 3100 nm were determined from the slope of the linear fit, yielding

the dn/dT of 22.4 ppm/℃, 26.1 ppm/℃, 20.9 ppm/℃ and 20.2 ppm/℃ at the wavelengths of 1494, 1524, 1554 and 3100 nm, respectively. The absolute errors on dn/dT were analysed to be ±15.6 ppm/℃ when using the tunable laser diode at wavelengths of 1494, 1524 and 1554 nm, and ± 26.0 ppm/℃ when using the 3.1 μm ICL. With dn/dT and thermal expansion coefficient known, the TPCs of As-Se at wavelengths of 1494, 1524, 1554 and 3100 nm were also determined, which were 409.0 ppm/℃, 410.0 ppm/℃, 408.6 ppm/℃ and 403.5 ppm/℃, respectively.

3. For $Ge_{16}As_{24}Se_{15.5}Te_{44.5}$ at. % (M140MINSCGDJ), the measurement range from 1494 nm to 1554 nm located at the standard Urbach edge in the short wavelength cutoff region and the optical bandgap of $Ge_{16}As_{24}Se_{15.5}Te_{44.5}$ at. % will shift to longer wavelengths with increasing temperature. Therefore, the suggested nonlinear behaviour of dn/dT of Ge-As-Se-Te in this temperature measurement range is not only attributed to the thermal excitation of phonons, but also to the red-shift of the optical bandgap with temperature. To fit the refractive index of Ge-As-Se-Te with temperature in this region, a quadratic fit was confirmed to be effective. Therefore, the dn/dTs at the wavelengths of 1494, 1524 and 1554 nm were different at different temperatures within this temperature range, with an error of ±15.4 ppm/℃. When measuring dn/dT of Ge-As-Se-Te using the 3.1μm ICL, a linear fit was suitable to fit the data points, yielding the dn/dT of 213 ppm/℃ with an error of ±25.6 ppm/℃. Moreover, the thermal polarisability coefficients (TPCs) of Ge-As-Se-Te at the measurement wavelengths were also calculated.
4. Since the $Ge_{20}Sb_{10}Se_{70}$ at. % (M135HAP) and $Ge_{20}Sb_{10}Se_{67}S_3$ at. % (M191HAP) prisms had a larger nominal apex angle (20 °) compared to the $As_{40}Se_{60}$ at. % (M130MINSCGDJ) and $Ge_{16}As_{24}Se_{15.5}Te_{44.5}$ at. % (M140MINSCGDJ) prisms (10 °), the standard deviation of precision of the measured refractive index at different temperatures at wavelengths of 1494,

1524 and 1554 nm was less than 0.0004 and the standard deviation of precision at a wavelength of 3100 nm was less than 0.0008. Since the measurement range was out of the standard Urbach edge in the short wavelength cutoff region for these two compositions, a linear fit of refractive index versus temperature was applied to fit the data points. The dn/dTs at wavelengths of 1494, 1524 and 1554 nm for $Ge_{20}Sb_{10}Se_{70}$ at. % and $Ge_{20}Sb_{10}Se_{67}S_3$ at. % were determined from the slope of the linear fit with an error of less than ±10.7 ppm/℃. When using the ICL, the error of determining the dn/dT increased to less than ±21.5 ppm/℃ due to the poor beam quality as discussed in section 4.4.

- The continuous thermo-optic coefficients (d*n*/d*T*) of the $As_{40}Se_{60}$ at. % (melting code: M130MINSCGDJ; hot-pressing code: YRFFP003) and $Ge_{16}As_{24}Se_{15.5}Te_{44.5}$ at. % (melting code: M188SCGDJ; hot-pressing code: YRFFP019) glass thin films were successfully determined with an error of less than ±7.5 ppm/℃ over the wavelength range from 2 μm to 20 μm using the FTIR continuous *dn/dT* method presented in section 7.3. This technique requires the thickness of the thin film at a lower temperature, the thermal expansion coefficient, and the interference transmission spectra of the thin film at normal incidence at a lower temperature and a higher temperature. A two-term Sellmeier model, with one resonant visible absorption and one resonant far-infrared absorption, was applied to describe the refractive index dispersion of the $Ge_{16}As_{24}Se_{15.5}Te_{44.5}$ at. % and $s_{40}Se_{60}$ at. % glass thin films over the wavelength range from 2 μm to 25 μm. The red shifts of the optical bandgap and the fundamental vibrational absorption band were indicated by the values of the resonant wavelengths C_1 and C_2. Compared to the improved Swanepoel method (defined in section 6.3), the present method was not sensitive to the average thickness of the thin film and thus the error in determining the thermo-optic coefficient is much smaller. Compared to the prism minimum deviation method (see section 4.4), the proposed method provides a much lower error and the

d*n*/d*T* can be easily obtained at arbitrary wavelengths over the wavelength range from 2 μm to 20 μm.

- The method presented in section 7.3 was then applied to determine the thermo-optic coefficients of the $Ge_{16}As_{24}Se_{15.5}Te_{44.5}$ at. % (M188SCGDJ), $Ge_{14.3}As_{27}Se_{15.5}Te_{43.2}$ at. % (M178DJ), $Ge_{20}As_{20}Se_{14}Te_{46}$ at. % (M112DJ) and $Ge_{16}As_{24}Se_{19}Te_{41}$ at. % (M193DJ) thin films. The results showed that the dn/dT decreased as the atomic percentage of Se decreases in Ge-As-Se-Te; this was in good agreement with [8.9] and [8.10]. Furthermore, the material dispersions of $Ge_{14.3}As_{27}Se_{15.5}Te_{43.2}$ at. %, $Ge_{16}As_{24}Se_{15.5}Te_{44.5}$ at. %, $Ge_{20}As_{20}Se_{14}Te_{46}$ at. % and $Ge_{16}As_{24}Se_{19}Te_{41}$ at. % were also investigated. At lower temperature, the zero dispersion wavelengths of $Ge_{14.3}As_{27}Se_{15.5}Te_{43.2}$ at. %, $Ge_{16}As_{24}Se_{15.5}Te_{44.5}$ at. %, $Ge_{20}As_{20}Se_{14}Te_{46}$ at. % and $Ge_{16}As_{24}Se_{19}Te_{41}$ at. % occurred at wavelengths of ~ 9.50 μm, 9.35 μm, 9.33 μm and 9.28 μm, respectively. With the temperature increased to 74.6 ℃, the zero dispersion wavelengths of $Ge_{14.3}As_{27}Se_{15.5}Te_{43.2}$ at. %, $Ge_{16}As_{24}Se_{15.5}Te_{44.5}$ at. %, $Ge_{20}As_{20}Se_{14}Te_{46}$ at. % and $Ge_{16}As_{24}Se_{19}Te_{41}$ at. % shifted towards longer wavelengths and occurred at wavelengths of ~ 9.57 μm, 9.41 μm, 9.38 μm and 9.32 μm, respectively. However, the change in the zero dispersion wavelength was shown to be less than 0.1 μm for these four compositions within this temperature range.

8.2 Future work

In this Project, significant progress has been made in assessing the optical properties, especially refractive index, of chalcogenide glasses fabricated for developing MIR fibre-based light source. The conclusions drawn in section 8.1 have shown that the minimum deviation method, spectroscopic ellipsometry and the improved Swanepoel method were successfully applied to determine the optical properties of the chalcogenide glasses. However, several actions still need to be taken in the future.

8.2.1 Prism minimum deviation measurements

Several actions are suggested to further improve the accuracy of the minimum deviation measurements using the current setup.

1. A good beam quality can significantly reduce the error of the measurements. Section 4.4, has shown that a supercontinuum beam source used conjunction with a band pass filter provided a well-collimated source with a sufficient power for refractive index determination. A broad SCG (a MIR supercontiuum spanning 1.4 μm to 13.3 μm) based on chalcogenide fibres was demonstrated by Petersen *et al.* [8.5] and Thorlabs [8.11] provides IR band pass filters from 1.75 to 9.5 μm. Using this SCG beam source with different IR band pass filters provided by Thorlabs, the refractive index of a chalcogenide glass prism at different specific wavelengths could be obtained.
2. A screen with a smaller aperture can reduce the error in determining the apex angle, which will in turn reduce the error in determining the refractive index. The size of the aperture used was 3 mm in diameter and an aperture with 1 mm diameter will be preferred in future work. Note that a beam source with a higher output power will be required when using the screen with a smaller aperture. A liquid crystal film was used to detect invisible beam sources when using the minimum deviation method in this project. Due to the lack of room-temperature controll in our laboratory, the liquid crystal film sometimes did not operate at the desired temperature, which was likely to have caused some errors in determining the minimum deviation position. Therefore, a room-temperature-controlled system in the laboratory would reduce the error of the minimum deviation measurements.
3. By using several plane mirrors to extend the optical path of the current setup, the error can be further reduced.
4. In this Project, some prisms were manufactured with a nominal apex angle of 10 ^{o}since, in the past, it had been assumed that for refractive indices of ~2.2 to 2.7

then a 10 °apex angle was optimal in the MIR Photonics Group. As discussed in chapter 4, a prism with a larger apex angle can provide a more consistent and accurate result. Therefore, it is suggested that the consistent use of chalcogenide glass prisms with an apex angle of 20 °will be ideal for the minimum deviation measurements.

8.2.2 Spectroscopic ellipsometry

According to Dantanarayana *et al.* [8.4], a unique two-term Sellmeier model, with physical interpretations on C_1 and C_2, would be an advantage in giving insight not only into the dispersion characteristic but also into the electronic and vibrational characteristic of the material. In the present work, a unique set of Sellmeier coefficients was only obtained for the $As_{40}Se_{60}$ at. % glass (M005MINSCGNM) as this was the only material studied for which the information on the fundamental vibrational absorption band was available. For other compositions, the information of the MIR fundamental absorption band can be obtained using a Bruker Vertex 70 spectrometer [8.12]. Using the standard MIR globar, T240/3 ultra-wide range beam splitter and D201/BD wide range DlaTGS detector, the measurement range of the Bruker Vertex 70 spectrometer can easily cover the wavelength range from 1 to ~ 100 μm. In order to see clear features of the chalcogenide glasses in the far-infrared region, and prevent the interference fringes ocurring, the test sample would need to be ground and polished to a thickness in the range from 300 μm to 800 μm. The information of the MIR and FIR fundamental absorption band of the other chalcogenide glasses investigated in this project can thus be obtained.

8.2.3 Improved Swanepoel method

In this Project, the improved Swanepoel method was firstly developed by the author to determine the refractive index of chalcogenide hot-pressed thin films in the MIR region. Since the chalcogenide thin film was hot-pressed from a chalcogenide fibre, the main difference between the hot-pressed thin film and the fibre is an thermal

history. This difference can be eliminated by either ultra-fast-quenching the hot-pressed thin film or annealing the chalcogenide fibres. Therefore, it is worth investigating the fast quenching of the hot-pressed thin film and the optical properties of annealed chalcogenide fibres in future work.

Limited to the current experimental setup, the measurement range of the FTIR thin film measurement can only cover the wavelength range from 1 to 27 μm. Therefore, it is difficult to obtain a unique set of Sellmeier coefficients with a physical interpretation. As mentioned above, using the Bruker Vertex 70 spectrometer, the measurement range can be extended up to 100 μm. Therefore, the extremes near the fundamental absorption band can be obtained, which will allow a unique set of Sellmeier coefficients with a physical interpretation to be obtained for all the chalcogenide glass compositions studied in the present work, and any new compositions synthesized in the future.

Since the beam used in the thin film measurements was not well-collimated, using the supercontinuum generation source may lead to a better accuracy.

Until now, it is still challenging to directly obtain the refractive index of chalcogenide fibres. The final goal in this project is to directly determine the refractive index of chalcogenide fibres. The author believe that, by grinding and polishing a chalcogenide fibre with a larger diameter (≥300 μm) to obtain a sufficient flat surface area [8.13], it is possible in future work to determine the refractive index of a chalcogenide glass fibre using Digital Refractometry [8.14].

References

[8.1] Swanepoel, R., 1985. Determining refractive index and thickness of thin films from wavelength measurements only. *Journal of the Optical Society of America A*, *2*, pp.1339-1343.

[8.2] Zhang, X.H., Guimond, Y. and Bellec, Y., 2003. Production of complex chalcogenide glass optics by molding for thermal imaging. *Journal of Non-Crystalline Solids*, *326*, pp.519-523.

[8.3] Tikhomirov, V.K., Furniss, D., Seddon, A.B., Savage, J.A., Mason, P.D., Orchard, D.A. and Lewis, K.L., 2004. Glass formation in the Te-enriched part of the quaternary Ge–As–Se–Te system and its implication for mid-infrared optical fibres. *Infrared Physics & Technology*, *45*(2), pp.115-123.

[8.4] Dantanarayana, H.G., Abdel-Moneim, N., Tang, Z., Sojka, L., Sujecki, S., Furniss, D., Seddon, A.B., Kubat, I., Bang, O. and Benson, T.M., 2014. Refractive index dispersion of chalcogenide glasses for ultra-high numerical-aperture fiber for mid-infrared supercontinuum generation. *Optical Materials Express*, *4*(7), pp.1444-1455.

[8.5] Petersen, C.R., Møller, U., Kubat, I., Zhou, B., Dupont, S., Ramsay, J., Benson, T., Sujecki, S., Abdel-Moneim, N., Tang, Z., Furniss, D., Seddon, A.B. and Bang, O., 2014. Mid-infrared supercontinuum covering the 1.4-13.3 mum molecular fingerprint region using ultra-high NA chalcogenide step-index fibre. *Nature Photonics*, *8*, pp.830-834.

[8.6] Jayasuriya, D., 2018. *Towards mid-infrared fibre-optic device and systems for sensing, mapping and imaging* (Doctoral dissertation, University of Nottingham).

[8.7] Corrales, C., Ramírez-Malo, J.B., Fernández-Peña, J., Villares, P., Swanepoel, R. and Márquez, E., 1995. Determining the refractive index and average thickness of AsSe semiconducting glass films from wavelength measurements only. *Applied Optics*, *34*(34), pp.7907-7913.

[8.8] Maklad, M.S., Mohr, R.K., Howard, R.E., Macedo, P.B. and Moynihan, C.T., 1974. Multiphonon absorption in As_2S_3-As_2Se_3 glasses. *Solid State Communications*, *15*(5), pp.855-858.

[8.9] Gleason, B., Richardson, K., Sisken, L. and Smith, C., 2016. Refractive index and thermo-optic coefficients of Ge-As-Se Chalcogenide Glasses. *International Journal of Applied Glass Science*, *7*(3), pp.374-383.

[8.10] Wang, Y., Qi, S., Yang, Z., Wang, R., Yang, A. and Lucas, P., 2017. Composition dependences of refractive index and thermo-optic coefficient in Ge-As-Se chalcogenide glasses. *Journal of Non-Crystalline Solids*, *459*, pp.88-93.

[8.11] Thorlabs IR bandpass filter. https://www.thorlabs.com/newgrouppage9.cfm?objectgroup_id=5871, Date of access: 14/02/2019.

[8.12] Bruker Vertex 70v FTIR spectrometer. https://www.bruker.com/products/infrared-near-infrared-and-raman-spectroscopy/ft-ir-research-spectrometers/vertex-series/vertex-70v/overview.html, Date of access: 14/02/2019.

[8.13] Athanasiou, G.S., 2013. *The fabrication of chalcogenide glass fibre photonic components* (Doctoral dissertation, University of Nottingham).

[8.14] Collet, E., 1987. Digital refractometry. *Optics Communications*, *63*(4), pp.217-224.

Appendix A

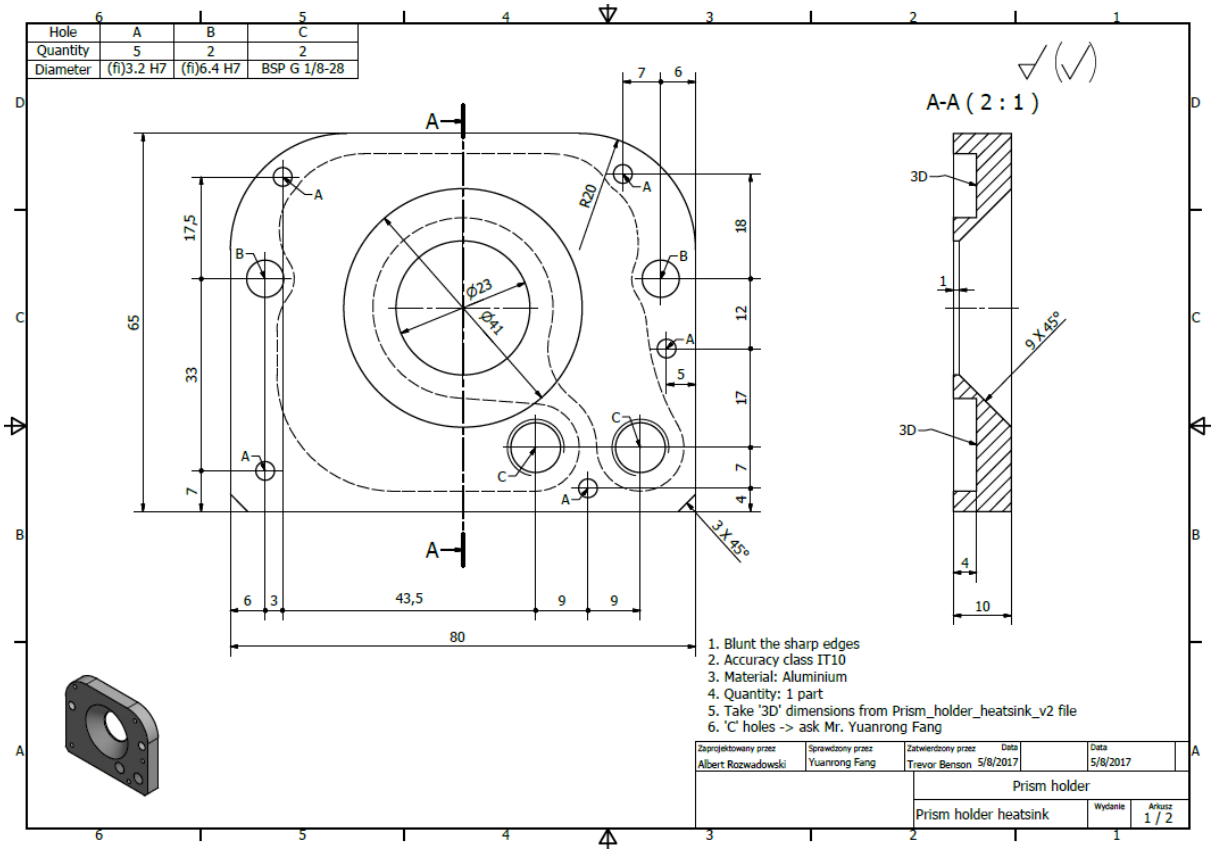


Figure A 1. The front part of the temperature-controlled holder.

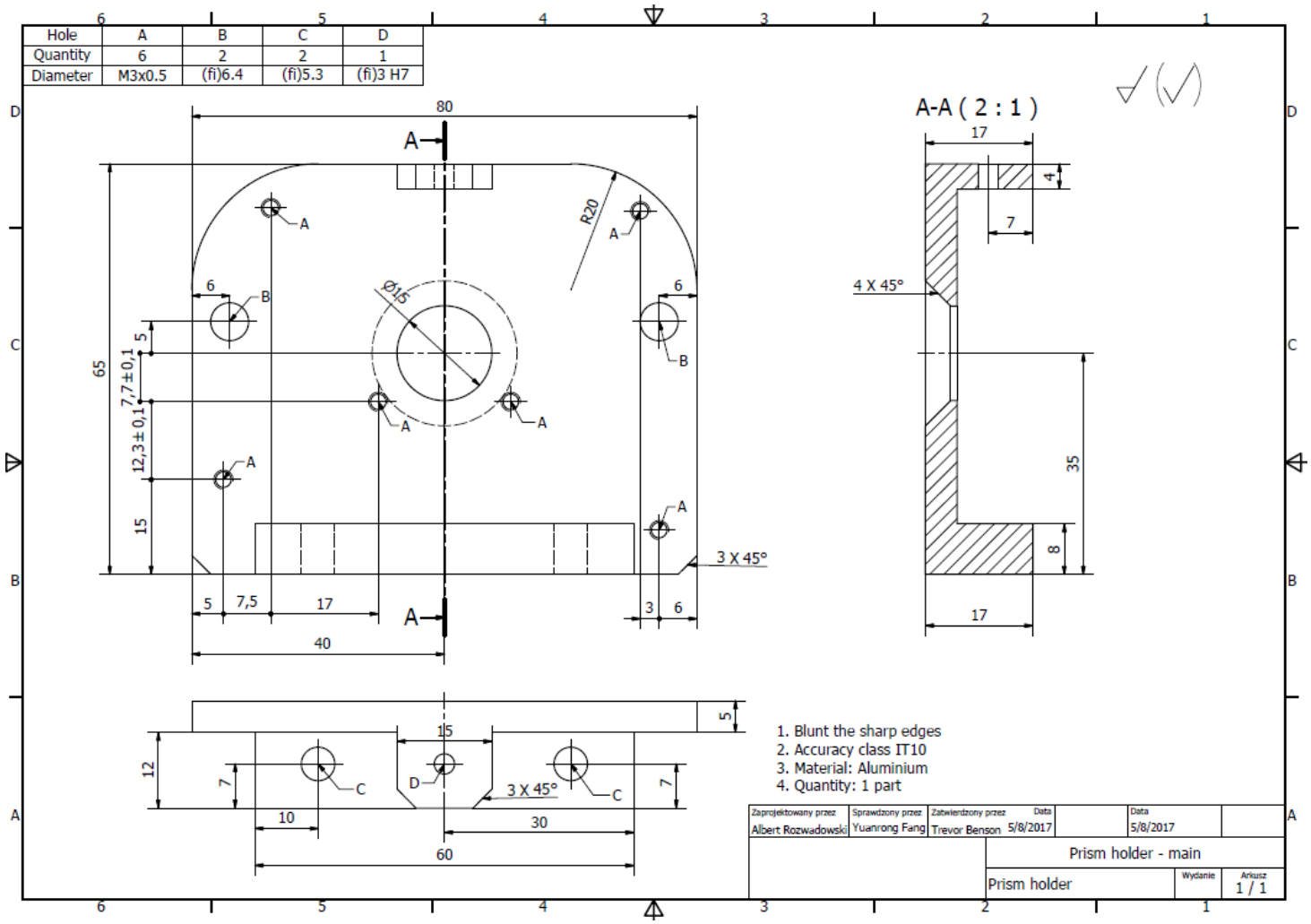


Figure A 2. The rear part of the temperature-controller holder.

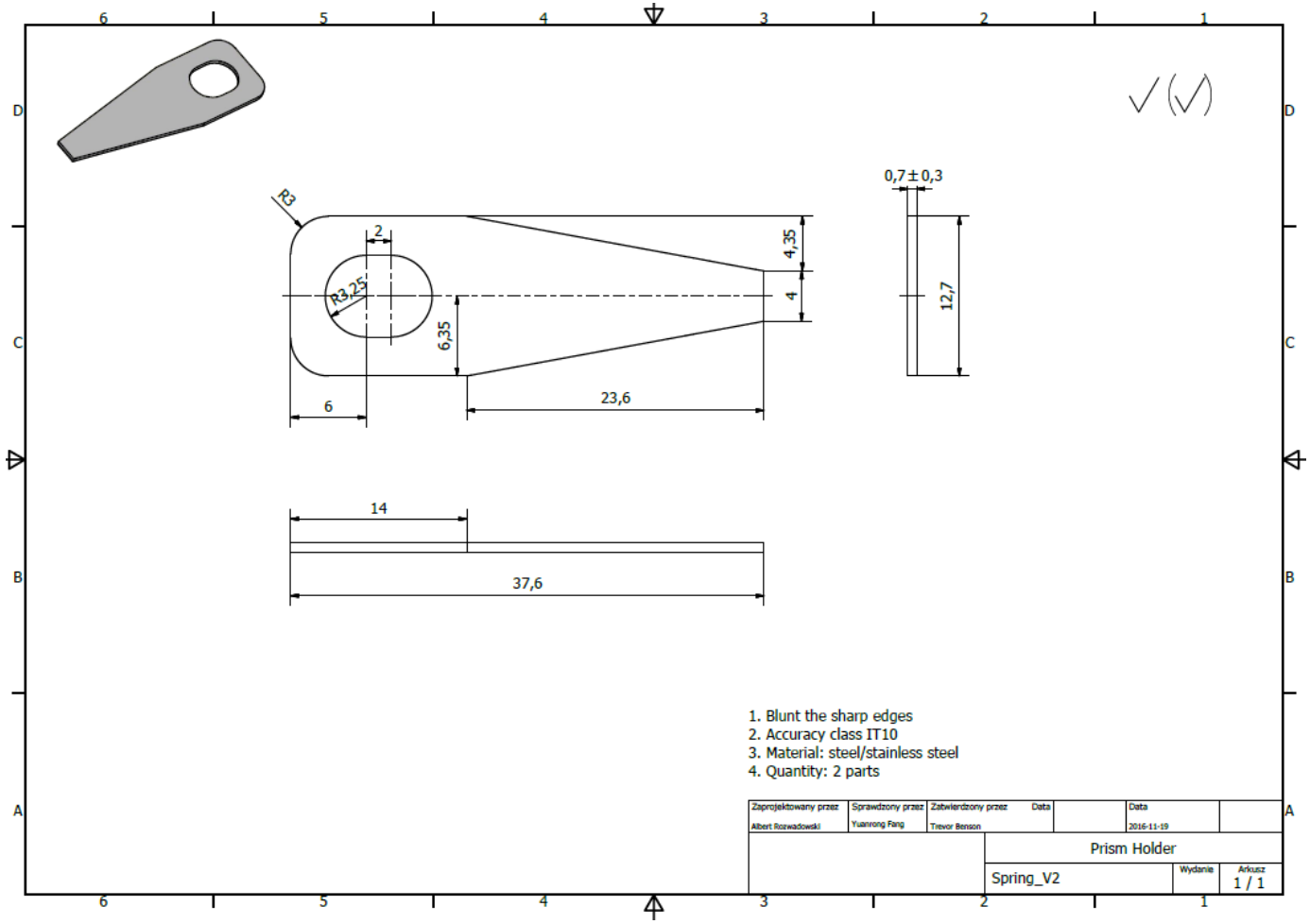
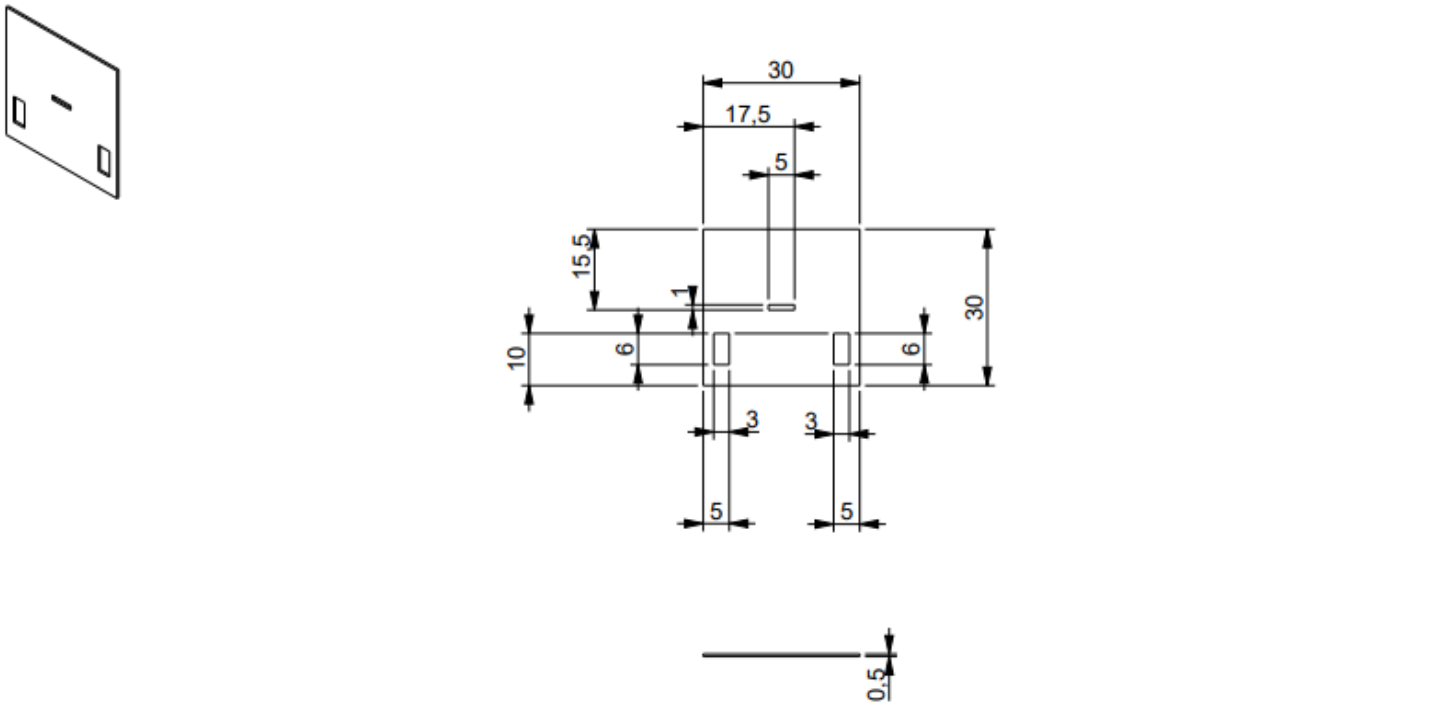


Figure A 3. The components for mounting the sample on the temperature-controller holder.



		DRN: 19-Feb-18		
LINEAR: ±0,1 ANGULAR: ±0,5		REV:		
		ISS. DATE:		
		mid-IR photonics	SIZE A4	DWG NO.
			SCALE 1:1	SHEET 1 of 1

Figure A 4. The detail drawing of a thin film holder designed for the thermo-optic coefficient measurements.

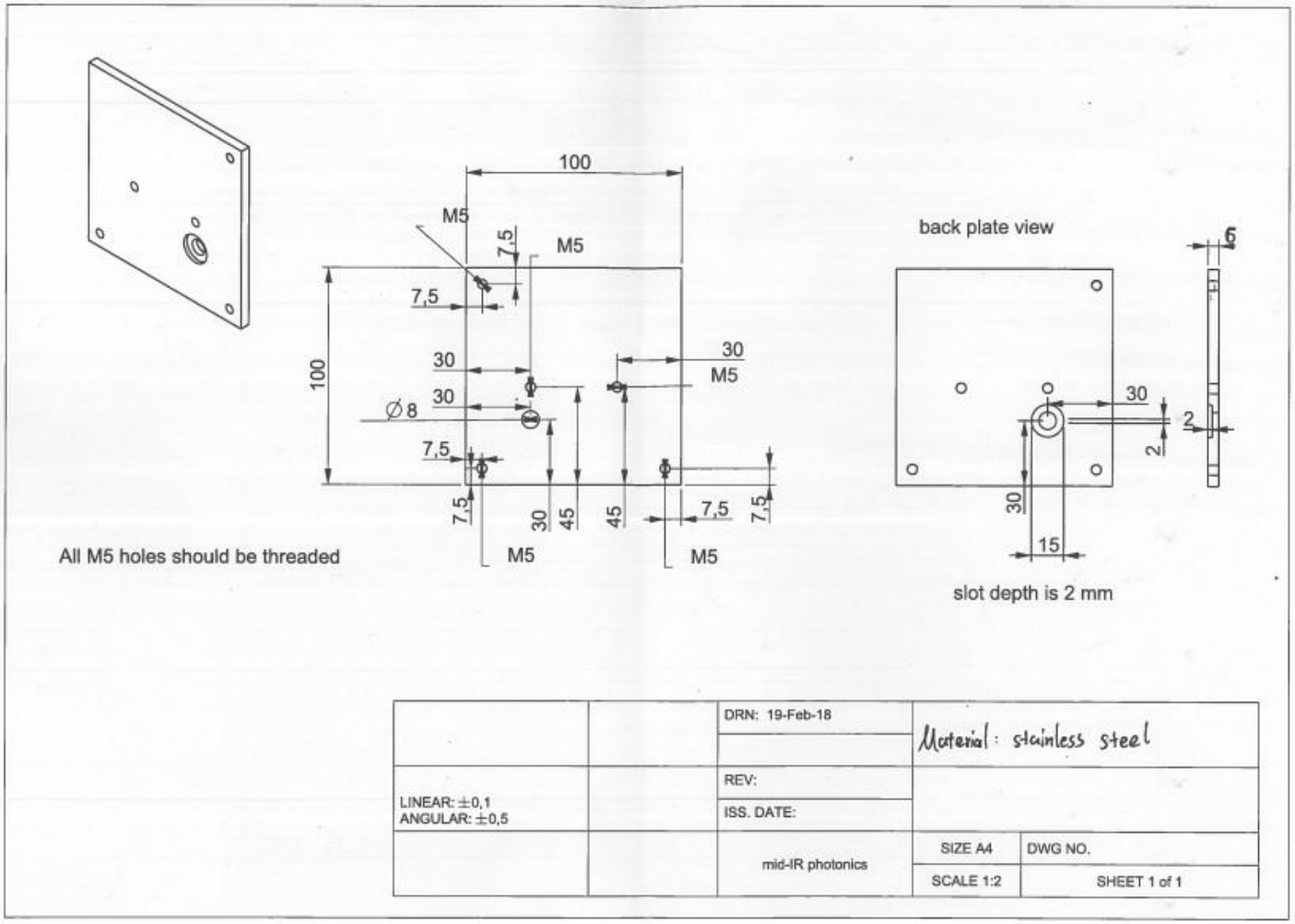


Figure A 5. The top plate of a 3-axis stage

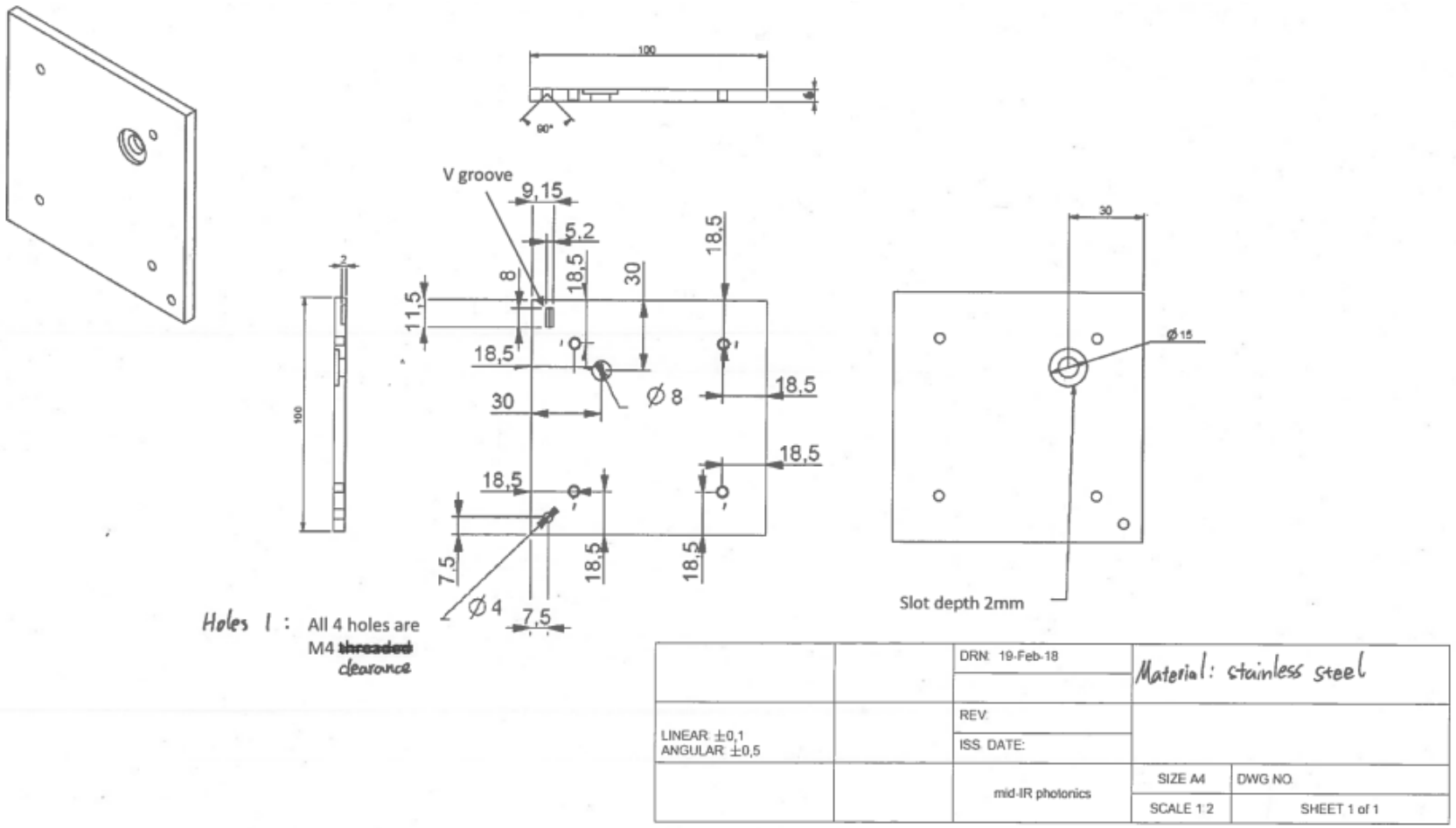


Figure A 6. The bottom plate of a 3-axis stage.

.

Appendix B

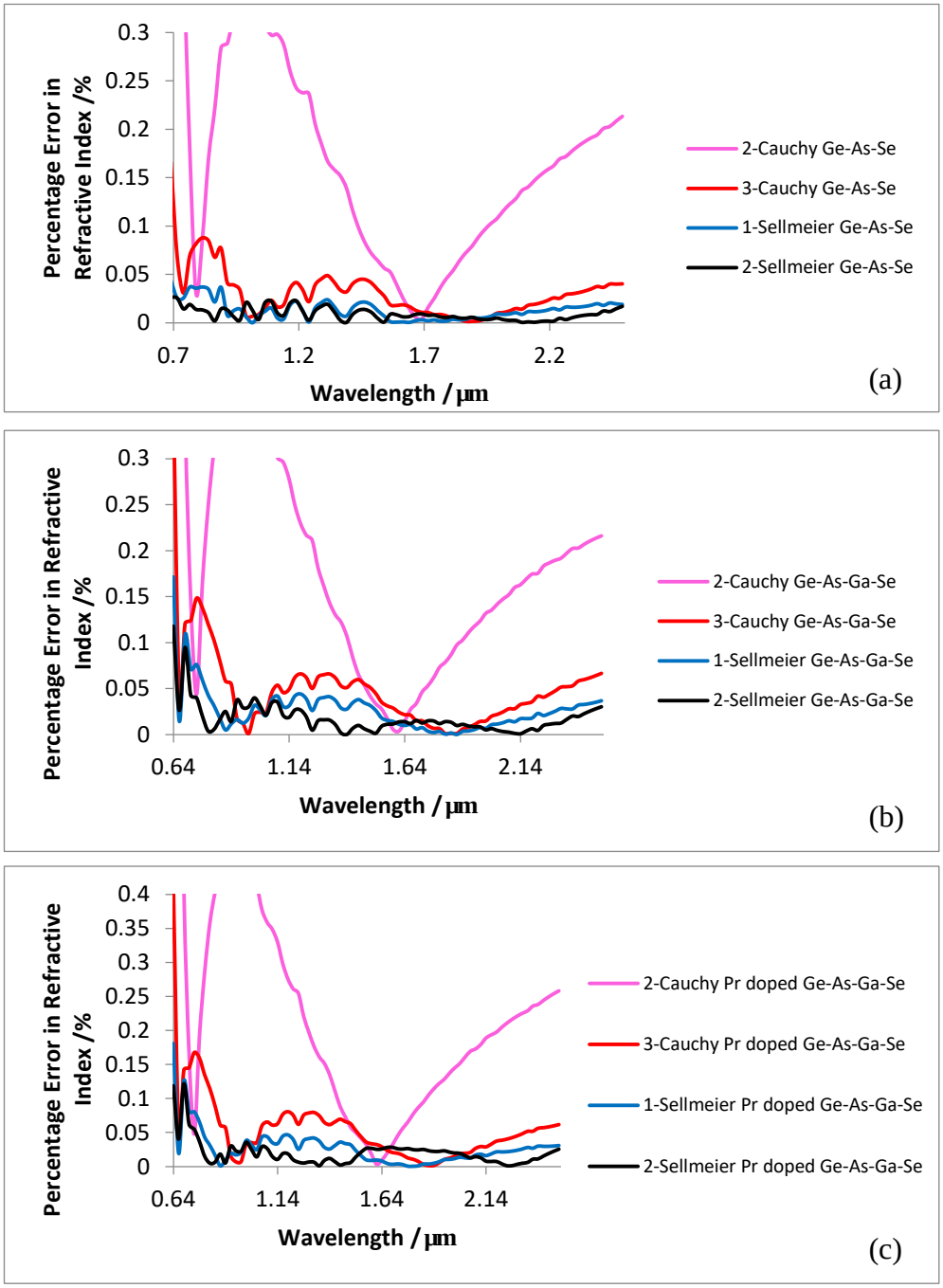


Figure B 1. The error in fitting the refractive index of the (a) $Ge_{10}As_{23.4}Se_{66.6}$ at. % (M007MINSCGNM), (b) $Ge_{16.5}As_{16}Ga_3Se_{64.5}$ at. % (ZQT007) and (c) Pr^{3+} doped $Ge_{16}As_{21}Ga_1Se_{62}$ at. % (M022MINREZQT) glasses with two-term Cauchy (pink), three-term Cauchy (red), one-term Sellmeier (blue) and two-term Sellmeier (black) models.

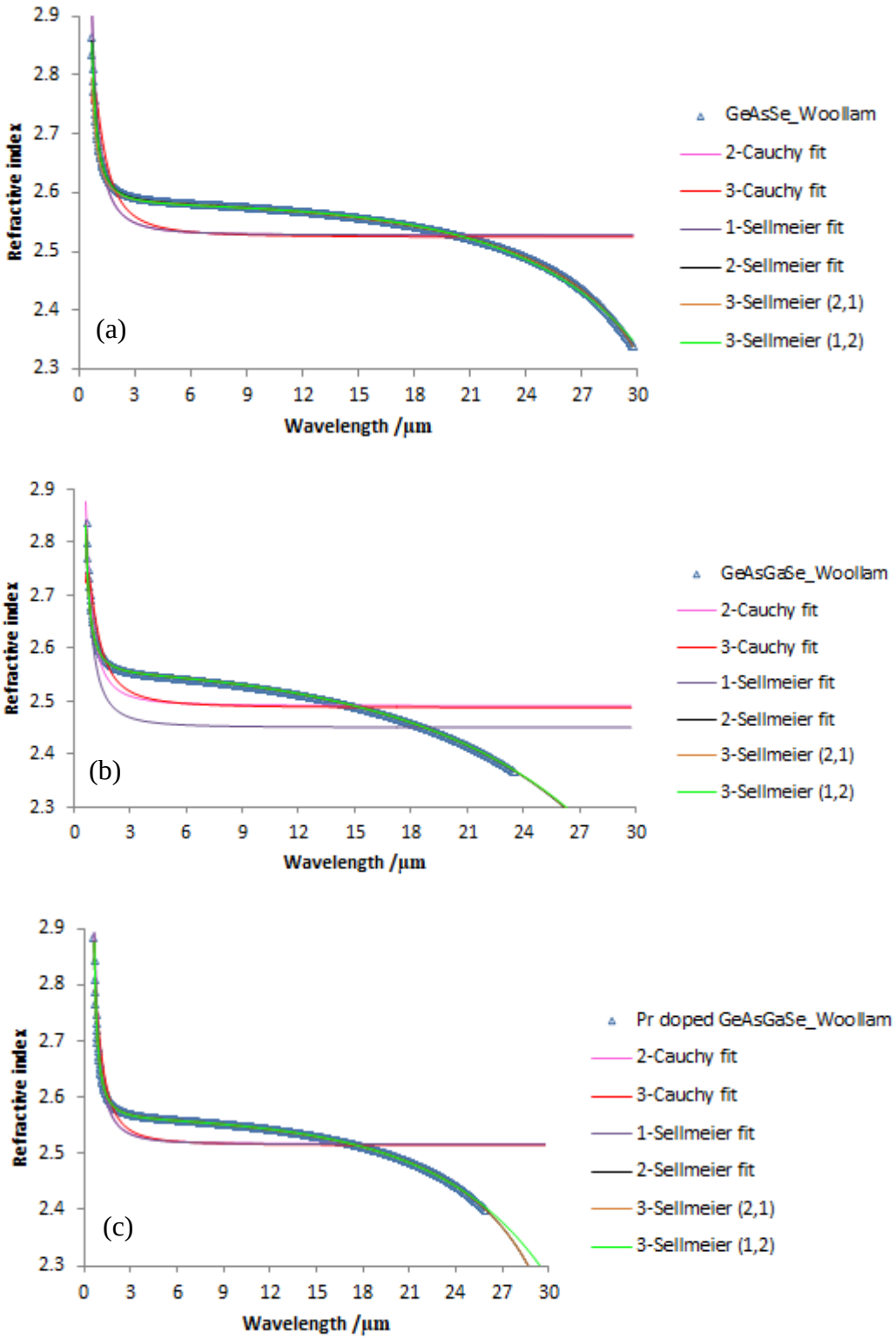


Figure B 2. The fits of the two-term Cauchy, three-term Cauchy, one-term Sellmeier, two-term Sellmeier, three-term Sellmeier (2,1) and three-term Sellmeier (1,2) models to the refractive index data of the (a) $Ge_{10}As_{23.4}Se_{66.6}$ at. % (M007MINSCGNM), (b) $Ge_{16.5}As_{16}Ga_3Se_{64.5}$ at. % (ZQT007) and (c) Pr^{3+} doped $Ge_{16}As_{21}Ga_1Se_{62}$ at. % (M022MINREZQT) glasses over their whole transparent windows.

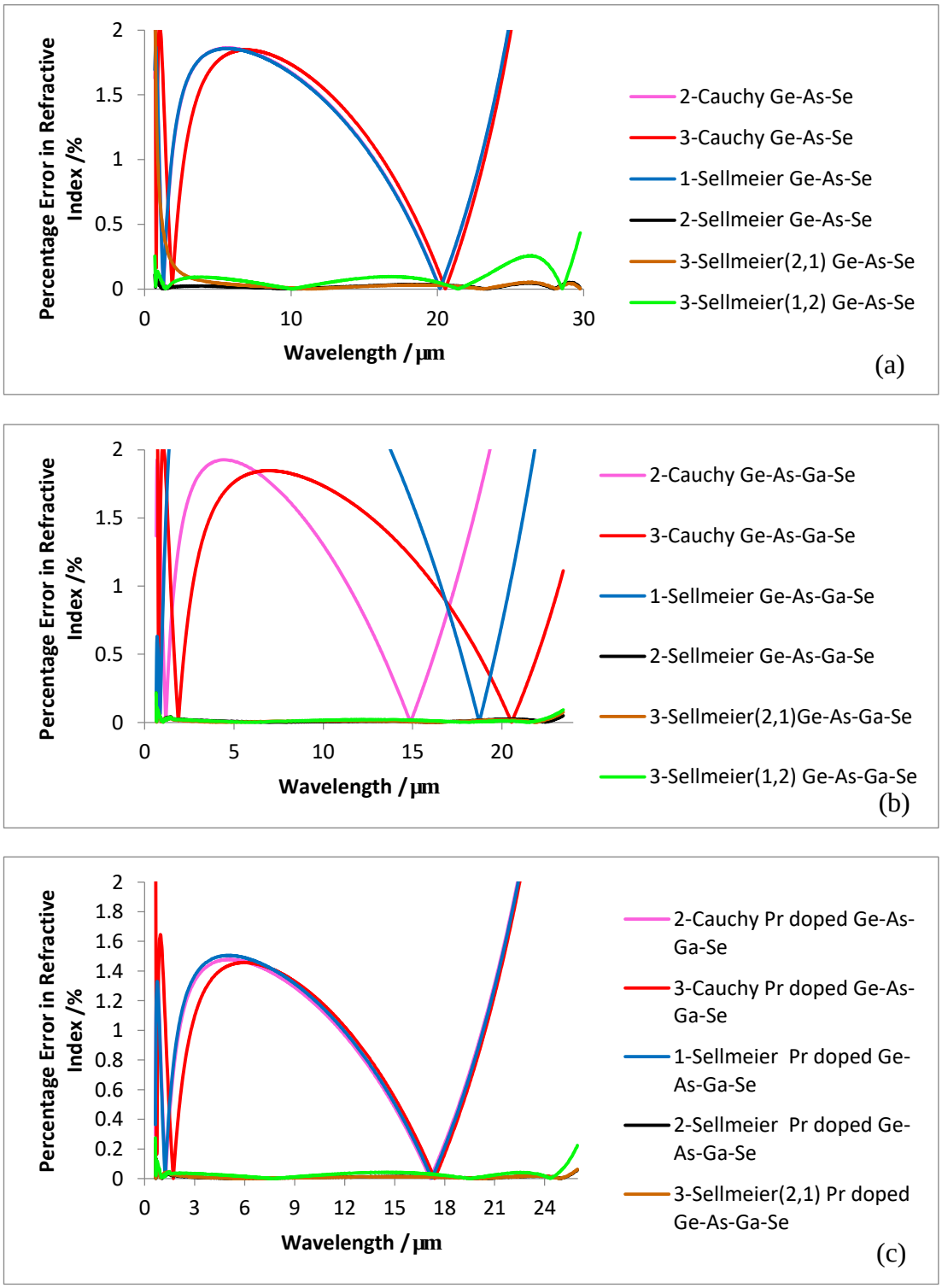


Figure B 3. The percentage errors in fitting the refractive index of the (a) $Ge_{10}As_{23.4}Se_{66.6}$ at. % (M007MINSCGNM), (b) $Ge_{16.5}As_{16}Ga_3Se_{64.5}$ at. % (ZQT007) and Pr^{3+} doped $Ge_{16}As_{21}Ga_1Se_{62}$ at. % (M022MINREZQT) glasses over their whole transparent windows with the two-term Cauchy, three-term Cauchy, one-term Sellmeier, two-term Sellmeier, three-term Sellmeier (2,1) and three-term Sellmeier (1,2) model.